Exploring the interstellar contents of a TeVatron : molecules, dust and star formation in the evolved supernova remnant IC443

Pierre Dell'Ova

PSL UNIVERSITÉ PARIS

THÈSE DE DOCTORAT
DE L'UNIVERSITÉ PSL

Préparée à l'École Normale Supérieure de Paris

Exploring the interstellar contents of a TeVatron: molecules, dust and star formation in the evolved supernova remnant IC443

Soutenue par

Pierre Dell'Ova

Le 9 Décembre 2021

École doctorale n°127

EDAAIF

Spécialité

Astrophysique

Composition du jury :

Hélène Sol	Observatoire de Paris	*Présidente*
Marianne Lemoine-Goumard	Centre d'Études Nucléaires, Bordeaux	*Rapportrice*
Arnaud Belloche	Max-Planck Institute for Radio Astronomy	*Rapporteur*
Isabelle Grenier	Commissariat à l'énergie atomique, Saclay	*Examinatrice*
Javier Goicoechea	Instituto de Física Fundamental, Madrid	*Examinateur*
Franck Le Petit	Observatoire de Paris	*Examinateur*
Marco Padovani	Istituto Nazionale di Astrofisica, Arcetri	*Examinateur*
Maryvonne Gerin	Observatoire de Paris	*Directrice de thèse*
Antoine Gusdorf	École Normale Supérieure	*Directeur de thèse*

ENS | PSL

Résumé

Les supernovae ont un impact majeur sur l'évolution du milieu interstellaire des galaxies. Ces explosions stellaires injectent 10^{51} erg dans leur voisinage direct, soit l'équivalent de l'énergie émise par le Soleil durant toute son existence. Ces événements réguliers à l'échelle d'une galaxie (environ deux par siècles dans la Voie Lactée) produisent une onde de choc rapide (jusqu'à 10^4 km s^{-1}) qui interagit avec le milieu ambiant durant plusieurs centaines de millier d'années. En plus d'être temporairement le siège de l'accélération de rayons cosmiques de haute énergie (TeV−PeV), les restes de supernovae déposent de l'énergie cinétique sur plusieurs dizaines de parsecs avant de se dissiper entièrement sous forme de rayonnement et de turbulence. Cette injection d'énergie et de rayons cosmiques participe à la régulation de la turbulence, à l'enrichissement chimique et à la structuration des multiples phases du milieu interstellaire. De plus, après refroidissement des régions denses comprimées par les chocs plus lents (10^1 km s^{-1}) qui se propagent tardivement, la formation de nouvelles étoiles peut être déclenchée. Situé à 1.8 kpc et âgé d'environ 25,000 ans, le reste de supernova IC443 offre la possibilité d'étudier ces mécanismes de rétroaction avec précision. L'étude des rayons cosmiques est poursuivie à travers le produit de leur interaction avec le milieu interstellaire, source de photons de haute énergie (rayons X/γ) émis *via* quatre mécanismes : décomposition de pions neutres, Bremsstrahlung, effet Compton inverse et rayonnement synchrotron. L'interprétation des observations de rayons γ requiert une connaissance fine des caractéristiques physiques et chimiques de l'environnement, tel que la masse totale du gaz, l'intensité et la distribution en énergie du champ de rayonnement, et la présence de sources d'injection de nouveaux rayons cosmiques. En direction du pic d'intensité des rayons γ, nous avons réalisé de nouvelles observations du reste de supernova IC443 avec le télescope de 30m de l'IRAM ainsi que le télescope APEX. Dans un champ $10' \times 10'$, nos observations spectrales de ^{12}CO, ^{13}CO, C^{18}O et nos observations continuum avec la caméra NIKA2 révèlent le contenu interstellaire de la région avec une résolution angulaire de $10'' - 20''$. À l'aide de modèles de transfert de rayonnement, nous avons d'abord produit des cartes de la masse totale de gaz dans la région à partir de l'émission de ^{12}CO et ^{13}CO. Nous avons ensuite utilisé des modèles d'émission de poussière pour étudier le continuum entre 3.4 μm et 2.0 mm (WISE, Spitzer, LABOCA, NIKA2). L'utilisation des algorithmes Bayésiens PPMAP et HerBIE permet de déterminer la densité de colonne et la température des poussières, ainsi que plusieurs paramètres supplémentaires avec HerBIE. Nos mesures de masses *via* l'émission des poussières et *via* la molécule ^{12}CO sont indépendantes et en accord. Ces mesures indiquent l'existence de deux candidats pour l'interaction du milieu dense avec les rayons cosmiques à l'origine de la production de rayons γ: un amas de gaz choqué de masse $\sim$ 250 M$_\odot$, et un amas de gaz froid et non perturbé de masse $\sim$ 400 M$_\odot$. D'une part, ces cartes de masse posent des contraintes précises sur l'émission de rayons γ *via* la décomposition de pions neutres et le Bremsstrahlung dans la région étudiée. D'autre part, notre carte du champ de rayonnement déterminée *via* HerBIE nous permet aussi de poser une contrainte sur l'effet Compton inverse. Enfin, à l'aide de catalogues de sources ponctuelles nous avons déterminé l'existence de potentielles protoétoiles dans la région. Ces dernières peuvent également participer à l'injection de rayons cosmiques de moyennes énergies (MeV−GeV). Ces résultats pourront être ré-investis en tant que paramètres d'entrée dans un modèle d'émission de rayons γ afin de déterminer la composition (hadronique ou leptonique) et les mécanismes principaux d'interaction des rayons cosmiques avec le milieu interstellaire dans IC443.

Mots clés: *Milieu interstellaire*, *Restes de supernova*, *Cinématique et dynamique*, *Chocs*, *Formation des étoiles*, *Rayons cosmiques*.

Abstract

Supernovae have a major impact on the evolution of the interstellar medium of galaxies. These stellar explosions inject 10^{51} erg into their neighborhood, which is equivalent to the energy emitted by the Sun during its entire existence. These regular events at the scale of a galaxy (about two per century in the Milky Way) produce a fast shock wave (up to 10^4 km s^{-1}) that interacts with the surrounding medium for several hundred thousand years. In addition to being temporary sites of acceleration of high-energy cosmic rays (TeV−PeV), supernova remnants deposit kinetic energy over several tens of parsecs before they entirely decay into radiation and turbulence. This injection of energy and cosmic rays participates in the regulation of the turbulence, the chemical enrichment and the structuring of the multiple phases of the interstellar medium. Moreover, when dense regions are compressed by the slower shocks (10^1 km s^{-1}) that propagate lately, the cold and dense medium that is left after a characteristic cooling time constitutes a potential site for the formation of new stars. Located at 1.8 kpc and about 25,000 years old, the supernova remnant IC443 offers the possibility to study these feedback mechanisms with accuracy. In this kind of objects, the study of cosmic rays is pursued through the product of their interaction with the interstellar medium, which is a source of high energy photons (X-ray/γ-ray) emitted *via* four mechanisms: decay of neutral pions, Bremsstrahlung, inverse Compton scattering and synchrotron radiation. The interpretation of γ-ray observations requires a detailed knowledge of the physical and chemical characteristics of the environment, such as the total mass of the gas, the intensity and energy distribution of the radiation field, and the existence of new cosmic-ray injection sources. In the direction of the γ-ray intensity peak, we have made new observations of the supernova remnant IC443 with the IRAM 30m telescope and the APEX telescope. In a $10' \times 10'$ field of observations, our spectral observations of ^{12}CO, ^{13}CO, C^{18}O pure rotational lines and our continuum observations with the NIKA2 camera reveal the interstellar content of the region with an angular resolution of $10'' - 20''$. Using radiative transfer models, we first produced maps of the total molecular gas mass in the region from the emission of ^{12}CO and ^{13}CO lines. We then used dust emission models to study the continuum between 3.4 µm and 2.0 mm (WISE, Spitzer, LABOCA, NIKA2). The use of the Bayesian algorithms PPMAP and HerBIE allows us to determine the column density and temperature of the dust, as well as several additional parameters with HerBIE. Our mass measurements *via* dust emission and *via* the ^{12}CO molecule are independent and in agreement. These measurements indicate the existence of two candidates for the interaction of the dense medium with cosmic rays at the origin of the γ-ray production: a shocked molecular clump of ~ 250 M$_\odot$, and a cold, quiescent molecular cloudlet of ~ 400 M$_\odot$. On the one hand, these mass maps put precise constraints on the γ-ray emission *via* neutral pion decay and Bremsstrahlung in the studied region. On the other hand, our radiation field map determined *via* HerBIE also allows us to constrain the inverse Compton scattering. Finally, with the help of point-source catalogs we have determined the existence of potential protostars in the region. These protostars can also participate in the injection of medium energy cosmic rays (MeV−GeV). These results can be re-invested as input parameters in a γ-ray emission model in order to determine the composition (hadronic or leptonic) and the main mechanisms of interaction of cosmic rays with the interstellar medium in IC443.

Keywords: *Interstellar medium*, *Supernova remnants*, *Kinematics and Dynamics*, *Shocks*, *Star formation*, *Cosmic rays*.

Remerciements

J'adresse mes remerciements à mon superviseur, Antoine Gusdorf, pour son enthousiasme et sa capacité à transmettre ses connaissances avec rigueur et clarté. Si j'ai appris beaucoup de choses pendant ces trois années, c'est en grande partie grâce à ses enseignements, son intransigeance scientifique et son regard expert sur notre discipline. Je le remercie également pour sa générosité et l'aide qu'il m'a offert à de multiples occasions, chaque fois qu'une difficulté scientifique, logistique ou même personnelle se présentait.

Mes remerciements vont également à ma directrice de thèse, Maryvonne Gerin, pour sa bienveillance et ses encouragements. Pendant ces trois années, chaque rencontre avec Maryvonne était l'occasion de bénéficier d'une expérience et d'une vision scientifique remarquables, sous la forme de suggestions toujours fructueuses.

Je tiens aussi à remercier mes rapporteurs, Arnaud Belloche et Marianne Lemoine-Goumard, qui m'ont fait l'honneur de lire ce long manuscrit et d'assister à ma soutenance de thèse. Leur rigueur et leur application, combinées avec la relecture très assidue de Marco Padovani, ont participé à soigner et parfaire ce document. C'est avec plaisir que je remercie tous les autres membres de mon jury de thèse: Hélène Sol, Isabelle Grenier, Javier Goicoechea et Franck Le Petit.

Je remercie vivement les personnels administratifs de l'École Normale Supérieure qui m'ont porté assistance pendant mon séjour. En particulier, Céline Paris pour l'efficacité et la prévenance dont elle a fait preuve chaque fois que je devais me déplacer en mission; mais aussi Delphine Rolland, dont l'aide a été précieuse pour l'organisation du pot de thèse.

Au même titre, je remercie les personnels de l'Institut de Radioastronomie Millimétrique pour leur hospitalité et leur diligence. Mes nuits blanches à l'observatoire du Pico Veleta resteront des souvenirs impérissables.

Je souhaite également exprimer ma gratitude et mon amitié envers tous nos collaborateurs scientifiques. Ils sont nombreux à m'avoir soutenu dans mon labeur, à avoir partagé leur expertise, participé à mes recherches: Rolf Güsten, Denise Riquelme, Alberto Noriega Crespo, David Neufeld, Martin Houde, Frédéric Galliano, Pierre Cristofari, Andrew Lehmann, Alexandre Marcowith, Marco Padovani, Gabriela Castelletti, Axel Weiss, Bilal Ladjelate, Frédérique Motte, Anaëlle Maury, Pierre Guillard, Nathalie Ysard, Anthony Jones.

Je suis également reconnaissant envers les membres de mon comité de suivi: Franck Le Petit, Catherine Boisson et François Boulanger. Leur sympathie, leurs encouragements et leurs conseils avisés ont participé à renouveler ma motivation et à me donner l'énergie nécessaire pour parvenir au bout du travail qui m'incombait. Guillaume Pineau des Forêts, Pierre Lesaffre, Pierre Cristofari, Alessia Ritacco, Erwan Allys, Benjamin Godard, François Lévrier et Michel Perault sont également remerciés chaleureusement pour leur soutien, notamment pendant les dernières semaines de ma thèse, pendant lesquelles beaucoup d'entre eux ont été volontaires pour m'aider à préparer ma soutenance.

Enfin, je remercie tous mes camarades du département de physique pour leur amitié et leur soutien. Mélanie, le rayon de soleil de notre laboratoire, pour sa joie et sa bonne humeur indestructibles. Thibaud, mon compagnon de pinseria, pour nos dialogues incessants et stimulants. Bruno, le seigneur de la rue Mouffetard, pour sa patience et sa persévérance lorsqu'il s'agissait

de m'arracher de ma zone de confort. Nicolas, l'esthète tourmenté, pour son ouverture d'esprit et son humour insolite. Pablo et Constant, mes nouveaux camarades fraîchement arrivés, pour leurs encouragements lors de la préparation de ma soutenance.

Bien sûr, ces remerciements ne peuvent s'achever sans une pensée pour ma famille et mes amis. Mes parents, pour leur soutien inaltérable et les moments de repos indispensables que furent mes vacances hivernales chez eux. Florian, Romain, Clément et Gaby, mes fidèles compagnons, pour leur fraternité. Mention spéciale pour Quentin, mon acolyte indispensable dont l'humanité m'inspire et suscite mon admiration. Enfin, et surtout, une pensée pour Sarah, mon amie la plus essentielle et ma camarade, ainsi que notre petite complice, Aki.

Un manuscrit de thèse est l'aboutissement de huit années d'apprentissage ininterrompu. Pour terminer, il m'importe donc de signaler ma reconnaissance et mon profond respect envers les maîtres les plus passionnants que j'ai rencontré au cours de mes études, ainsi que ceux qui m'ont inspiré par leur rigueur et leur compétence. Notamment mes professeurs de CPGE Sandrine Fay et Alexandre Boisseau, pour leur virtuosité, mais également Jean-Marcel Rax et Jérôme Perez pour leurs cours captivants, et leur amour de la physique contagieux.

Je dédie ce manuscrit à la mémoire des professeurs de mathématique et de physique-chimie du Lycée Européen de Villers-Cotterêts, mes amis Patrice Cauvin et Michel Montangerand. Parmi la multitude de rencontres et d'événements contingents ayant abouti à la réalisation de cette thèse, ils occupent une place privilégiée.

Note to the reader

This manuscript is organized in four parts that follow a linear progression from the introduction of the scientific context to the presentation of the results obtained during the thesis. Nonetheless, most chapters can be read independently from each other. Reading Chapters 1−2 (part I) entirely is not required, but it is recommended. Chapter 1 contains an expanded introduction to all aspects related to evolved supernova remnants. Readers who are familiar with the subject can jump to section 1.5, in which we state our scientific goals. Chapter 2 provides the interested reader with a comprehensive review of the supernova remnant IC443. Chapters 3−5 (part II) include a brief description of the tools and methods used in this thesis (*e.g.* observation procedures, data reduction tools, radiative transfer analysis, dust emission models); and Chapters 6−7 (part III) contain the description of our new observations of IC443. The complete description of the analysis and new results obtained during the thesis starts in Chapter 6 and ends in Chapter 10 (part IV). Readers who are primarily interested in the results are invited to jump to this part of the manuscript.

Contents

List of terms and abbreviations

2MASS Two-Micron All-Sky Survey . . . 83, 107
ACIS Advanced CCD Imaging Spectrometer . . . 72
AGILE Astro-Rivelatore Gamma a Immagini Leggero . . . 89
ALMA Atacama large millimeter/submillimeter array . . . 46
ANRAO Australian National Radio Astronomy Observatory . . . 90
APEX Atacama Pathfinder EXperiment . . . 40
ASCA Advanced Satellite for Cosmology and Astrophysics . . . 72
BIMA Berkeley Illinois Maryland Array . . . 82
CCSNe Core-collapse supernovae . . . 5
CFHT Canada-France-Hawaii Telescope . . . 34, 85
CGRO Compton Gamma Ray Observatory . . . 88
CIE Collisional ionization equilibrium . . . 11
CMF Core mass function . . . 48
CNM Cold neutral medium . . . 17
CR Cosmic ray . . . 6, 55
CSM Circumstellar medium . . . 6
CSO Caltech Submillimeter Observatory . . . 82
CTA Cherenkov Telescope Array . . . 65
CTTS Classical T Tauri star . . . 316
CUBISM Cube Builder for IRS Spectral Mapping . . . 106
DARTS Data ARchive and Transmission System . . . 266
DN Digital Number . . . 268
DRAO Dominion Radio Astrophysical Observatory . . . 79
DSA Diffusive shock acceleration . . . 21, 56
EGRET Energetic Gamma Ray Experiment Telescope . . . 57, 88
FCRAO Five College Radio Astronomy Observatory . . . 78
FIR Far infrared . . . 7
FUV Far ultraviolet . . . 20
GBT Green Bank Telescope . . . 93
GMC Giant molecular cloud . . . 19
HAeBe Herbig Ae/Be . . . 316
HerBIE HiERarchical Bayesian Inference for dust Emission . . . 142
HIM Hot ionized medium . . . 17
IMF Initial mass function . . . 46
IR Infrared . . . 7
IRS Infrared Spectrograph (*Spitzer*-IRS) . . . 80, 105
IRSA Infrared Science Archive . . . 265
IRSF Infrared Survey Facility . . . 80
ISM Interstellar medium . . . 5
ISO Infrared Space Observatory . . . 80
ISRF Interstellar radiation field . . . 40, 154
KAO Kuiper Airborne Observatory . . . 84
KID Kinetic Inductance Detector . . . 121, 189
KOSMA Kölner Observatorium for Submillimeter Astronomy . . . 92

WR Wolf Rayet 7
WSRT Westerbork Synthesis Radio Telescope 76
XMM-Newton X-ray Multi-Mirror Mission - Newton 72
YSO Young stellar object 44, 313

Part I : Introduction

Chapter 1 | General introduction

Contents

1.1 | Supernova remnants

From the perspective of a distant observer, the brief and dramatic increase in luminosity observed during the early stages of a supernova (SN) explosion is a fascinating sight. Nonetheless, these bright and ephemeral episodes expose a tiny fraction of the chain of events that unfold after the death of a star. For instance, while SN 1987A was visible to the naked eye for approximately 310 days (*e.g.* Fransson *et al.* 2007), the massive amount of kinetic energy released by the explosion will continue to disperse into the interstellar medium for the next few hundred thousand years. Supernovae are among the astronomical phenomena that have been observed since the earliest times, but their currently accepted astrophysical description is recent.

As a matter of fact, it is only in the last century that the dynamical processes following the very last stages of stellar evolution were understood and finally related to these well-known transient observations. In the 1930s, the astronomers Walter Baade and Fritz Zwicky introduced the word supernova[1] and advanced the view that these outbursts could correspond to the collapse of ordinary stars into neutron stars, based on the measurements of the total energy released by these events (Osterbrock, 2001).

However, even before the observations of these *"new stars"*[2] (or *"guest stars"*) gained their current physical interpretation, they were of great importance to ancient astronomers, for they challenged the long-established Aristotelian presumption that change could only occur in the sub-lunar region, the rest of the universe being assumed as static and eternal (Clark and Stephenson, 1982). As we will see, supernova outbursts do represent a strong case against this belief, considering their fundamental role in the dynamic evolution of the turbulent, unstable and ever changing interstellar medium (section 1.1.3).

Once the astrophysical source of these transitory events was identified, an additional decade was necessary to firmly establish the existence of supernova remnants, the final state of these stellar explosions. Walter Baade and Rudolph Minkowski proposed that the optical spectroscopic observations of the Crab Nebula (Minkowski, 1942) and Nova Ophiuchi 1604 (Baade, 1943) could support the assumption that these objects were the dynamical products of supernovae interacting with their environment. These findings were followed by the identification of several supernova remnants with discrete, non thermal radio sources and the discoveries of many other remnants (Baade and Minkowski 1954, Hanbury Brown and Hazard 1952, Harris 1962), paving the way to numerous studies of these objects.

In many respects, the studies of SNe and their remnants brought results of considerable relevance in the recent development of astrophysics and cosmology. In particular, Type Ia SNe play a central role in present day cosmology since their brightness allows them to be detected at high red-shifts (up to $z \sim 1.7$, Riess *et al.* 2007). Most importantly, their use as *standard candles* to measure distances (Branch and Tammann 1992, Riess *et al.* 1998) has led to the discovery that the expansion of the universe is accelerating (Garnavich *et al.* 1998, Perlmutter *et al.* 1998). SNe are also a key agent of the stellar nucleosynthesis of heavier elements (Woosley *et al.*, 1973) and dust synthesis (Todini and Ferrara 2001, Micelotta *et al.* 2018b, Sarangi *et al.* 2018). Supernova remnants (which should be distinguished from "supernovae", see section 1.1.1.3) still represent to this day a paramount class of objects tied with a wide range of open astrophysical questions, essentially interstellar shocks (section 1.2), cosmic star formation history (section 1.3) and cosmic-ray acceleration (section 1.4). In particular, evolved supernova remnants constitute a key ingredient of the life cycle of the interstellar matter, for they participate in the energy injection mechanisms, the dynamical and chemical evolution of the different phases of the interstellar medium (section 1.1.3) and the regulation of star formation. In the next section, we shall begin with a brief description of the stellar physical processes leading to supernovae explosions.

[1] *"the phenomenon of a super-nova represents the transition of an ordinary star into a body of considerably smaller mass"*, Baade and Zwicky (1934).

[2] In Latin, *nova* means "new". This term was coined by Tycho Brahe in his observations record of SN 1572 *De nova et nullius aevi memorio prius visa stella* (Concerning the new and previously unseen stars).

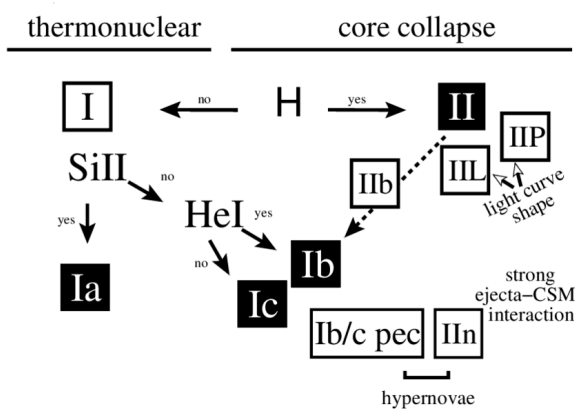

Figure 1.1 The adopted classification scheme of supernovae. Type Ia SNe are associated with the thermonuclear explosion of accreting white dwarfs. Other SN types originate from the core collapse of massive stars. CCSNe with explosion energies $E > 10^{52}$ erg are called hypernovae. Figure from Turatto (2003).

1.1.1 Formation and evolution of a supernova remnant

Supernovae explosions occur when a stellar system reaches the end of its last evolutionary stage and irreversibly breaks out of equilibrium. This section does not aim to describe in details the mechanisms by which these explosions are triggered, but it is necessary to give an insight on the different possible origins of supernova remnants since their long term properties will partially derive from the nature of their progenitor (see Vink 2012 for a detailed review of these explosion mechanisms). Indeed, there are two types of progenitors, arriving at their explosive end with different paths and physical processes (reflected by their distinct lightcurves). Two broad categories are used to describe SNe: core-collapse supernovae and thermonuclear supernovae. In the first case, the explosion energy originates from the gravitational energy released during the collapse of a stellar core, while in the second case it is caused by the explosive-runaway nuclear burning of stellar material. Additionally, an observational classification is used based on the detection of hydrogen absorption lines (Type I and Type II SNe, Minkowski 1941), but we will show in the following sections that these two classification schemes are not consistent with each other, since Type II SNe are systematically core-collapse SNe, but Type I SNe can be either thermonuclear or core-collapse SNe (see Fig. 1.1, Vink 2012).

1.1.1.1 Massive stars

Massive stars ($M > 8M_{\odot}$) end with a violent explosion when the effective pressure support generated by the fusion of nuclear fuel drops below a critical level (Bethe 1990, see Burrows and Vartanyan 2021, Woosley *et al.* 2002 for recent reviews). Most of the gravitational energy released by the collapse is in the form of neutrinos ($\sim 10^{53}$ erg, Vink 2012 and references therein). The explosion mechanism is not well known, but it is thought to be caused by the formation of a proto-neutron star at the core of the progenitor. As the iron core of the progenitor undergoes gravitational collapse in less than a second, the density increases until it reaches that of an atomic nucleus and finally opposes further compression. The core then rebounds and generates a shock wave through the infalling outer layers of the star. This shock-heated gas then expands outward at a velocity of a few thousand kilometers per second, interacting with the circumstellar medium. Observationally, these supernovae have been classified as Type II, Types Ib and Type Ic supernovae based on the atomic lines detected in their spectra, although they result from the same explosion mechanism. Types Ib and Ic are now understood to be explosions of massive stars that have lost their hydrogen-rich (Type Ib) and helium-rich (Type Ic) envelopes as a result of

stellar wind mass loss (*e.g.* Heger *et al.* 2003). This class of supernovae explosions are labeled **core-collapse supernova** (CCSNe).

1.1.1.2 Binary systems

Lower mass stars ($M < 8M_{\odot}$) in binary systems are adequate candidates for a second type of SN explosions (Whelan and Iben, 1973). The majority of these main sequence stars terminate their thermonuclear lives after they eject their outer hydrogen envelopes, leaving behind a compact C/O white dwarf (Salpeter, 1955). In close binary systems, assuming that a companion giant star transfers stellar material to the white dwarf, the mass builds up and eventually reaches the Chandrasekhar limit ($M \simeq 1.38$ M$_{\odot}$, Chandrasekhar 1931). The exact trigger mechanism is not well understood, but once the core density has reached this critical level, the nuclear fusion of carbon and oxygen into iron is set in motion and a runaway thermonuclear reaction occurs. The white dwarf is entirely destroyed by the explosion and the remnants of stellar material are transported by the resulting shock wave (see section 1.1.3). Thermonuclear SNe are associated with spectroscopic class Type Ia (Elias *et al.*, 1985), which have Si absorption lines in their spectra. Hereafter, these supernovae explosions will be designated as **SNIa**.

1.1.1.3 On the distinction between the SN explosion and its remnant

Depending on the mass of the progenitor, CCSNe leave behind either a compact neutron star or a black hole, but in the case of SNIa the white dwarf is completely shattered. In both cases, the so-called supernova remnant (SNR) encompasses the circumstellar leftovers of the SN explosions and their dynamical products. By definition, the term 'supernova remnant' refers to the expanding shock wave propagating through the neighboring interstellar medium (ISM) and the transitory structure resulting from this interaction (hence, a mixture of the ejected stellar material together with the interstellar material swept, heated and ionized by the shock).

Now that the definition of supernova remnants and their relation to SN explosions have been precisely settled, we will provide a more detailed description of the different stages of SNR formation and evolution.

1.1.1.4 Supernova remnants evolution

Upon the SN explosion, the stellar material is expelled at a velocity of a few thousand kilometers per second (*i.e.* up to a fraction of light speed). The total kinetic energy released varies from $E_0 = 10^{51}$ erg for Type Ia SNe[3] and up to $E_0 = 10^{52}$ erg for super-luminous CCSNe (Nicholl *et al.*, 2020). This sudden release of energy drives a blast wave through the ambient ISM that is bound to gradually decelerate as it interacts with the interstellar matter. As a matter of fact, following Woltjer (1972) we can describe three different stages in the expansion of the SNR[4]: *i.)* the **free-expansion phase**, *ii.)* **Sedov-Taylor phase** and *iii.)* **snowplow phase**. However, it should be noted that this evolutionary classification scheme is an oversimplification. These

[3] $E_0 = 10^{51}$ erg corresponds approximately to the energy emitted by the Sun during its entire existence (assuming that it converts 10% of its mass from hydrogen to helium in nuclear fusion: $E_{\odot} = 0.1 \times M_{\odot}c^2 \simeq 1.8 \times 10^{51}$ erg, where $M_{\odot}$ is the mass of the Sun, and c is the light speed).

[4] The description of the different phases of SNR evolution given in this section relies significantly on the chapter thirty-nine of Draine (2011): *Effects of Supernovae on the ISM*.

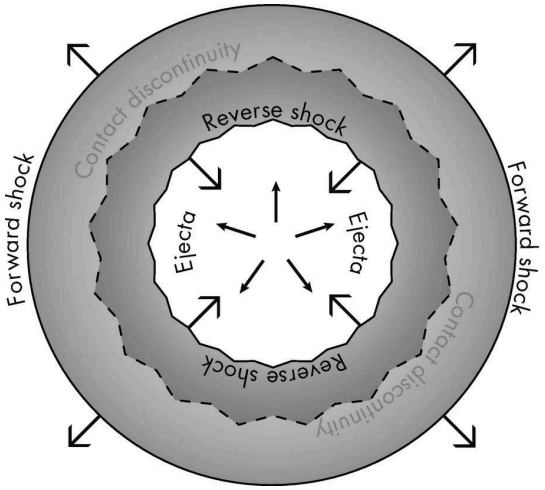

Figure 1.2 Schematic representation of the morphology of the supernova remnant during the free-expansion phase (figure from Vink 2020). In the inner region the ejecta is expanding ballistically. A contact discontinuity separates the forward shock (light gray region) from the reverse shock (dark gray region) that propagates towards the center of the SNR. The forward shock expands and interacts with the ISM, while the reverse shock reheats the interior of the remnant.

different phases allow to study theoretical SNRs using an efficient framework, but the observations show that individual SNRs do not necessarily fit in well defined evolutionary phases. Additionally, different parts of the same SNR might be in different stages depending on the circumstellar density structure corresponding to the initial conditions in which the SN outburst occurred. These initial conditions are shaped by many parameters that can be difficult to determine, such as the nature of the progenitor, the structure of the primordial molecular cloud in which it was born, the impact of stellar winds, *etc.* (*e.g.* Rosado *et al.* 1994, Vink *et al.* 1997).

Free-Expansion phase, or ejecta-driven phase If we neglect relativistic effects and magnetic fields, the modeling of a SNe can be approached using simple assumptions. Let a mass of ejecta $M_{\rm ej}$ with velocity $v_{\rm ej}$ and total energy E_0 be injected into a medium of density n_0 at a time $t = 0$. During the first days after the explosion, the ejecta expands essentially unimpeded, *i.e.* it travels ballistically at nearly constant velocity through the circumstellar medium (CSM):

$$\langle v_{\rm ej}^2 \rangle^{1/2} = \left(\frac{2E_0}{M_{\rm ej}} \right)^{1/2} \tag{1.1}$$

Assuming that $E_0 = 10^{51}$ erg and $M_{\rm ej} = 1.4\ M_\odot$ (SNIa), an estimate of the velocity of the ejecta during the free-expansion phase is ~8450 km s^{-1}, or ~3160 km s^{-1} considering a higher mass CCSNe (10 $M_\odot$). The sound speed in ionized hydrogen is $c_s = \sqrt{\gamma k_{\rm B} T / m_{\rm H}}$ (where $k_{\rm B}$ is the Boltzmann constant, $m_{\rm H}$ is the mass of an hydrogen atom, γ is the adiabatic index and T is the temperature of the gas) thus even within hot circumstellar material ($T = 10^4$ K) the sound speed $c_s \sim 13$ km s^{-1} is far lower than the velocity of the ejecta. Hence the expanding blast drives a fast shock that locally accelerates, heats, compresses and ionizes the gas, providing all the conditions for the production of cosmic rays (CRs) by diffusive shock acceleration (see section 1.4).

During the rapid propagation of the outward shock front, the density of the expanding ejecta and its thermal pressure $p_{\rm ej} \propto \rho_{\rm ej}$ decrease steadily, *i.e.* the ejecta is cooled by adiabatic expansion. A reverse shock is driven into the ejecta when its internal pressure drops below the thermal pressure of the shocked circumstellar medium ($p_{\rm ej} < p_{\rm csm}$). The reverse shock ($v_{\rm rs} \sim 10^3$ km s^{-1}, *e.g.* Leahy and Williams 2017) propagates inward and reheats the ejecta while the main blastwave continues to expand (see Fig. 1.2). During this period of time the shock-heated plasma ($k_{\rm B} T \sim 1$ keV) within the interior of the SNR constitutes a strong source of ultraviolet (UV) radiation and

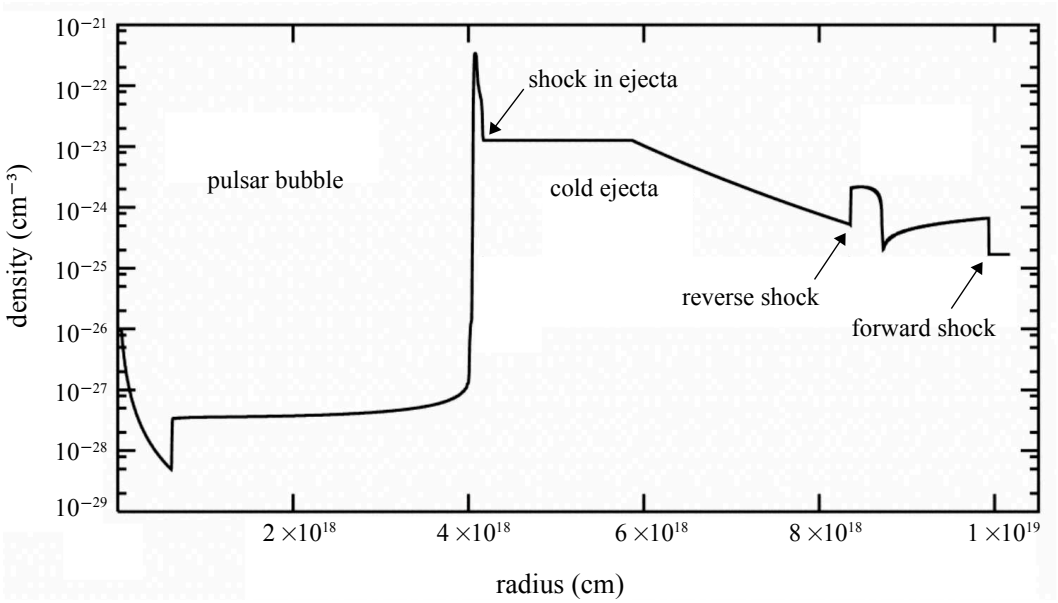

Figure 1.3 Model of the density profile in a supernova remnant as a function of radius (Blondin *et al.*, 2001). The forward and reverse shocks are indicated by the arrows. This model includes a pulsar wind nebula in the cavity, responsible for the formation of an additional shock in the ejecta.

thermal X-rays (McKee, 1974). The X-ray spectrum of the heated ejecta is essentially dominated by bremsstrahlung continuum and K – α lines (O, Ne, Mg, Si, S, Ar and Ca). The ionized gas in the region between the reverse shock and the blastwave also emits near and mid-infrared (IR) fine-structure lines (Fe, Ne, Ar, *e.g.* Isensee *et al.* 2010) but the amount of radiated energy remains negligible with respect to the total kinetic energy released by the explosion. Additionally, the dust formed within the ejecta (Nozawa *et al.* 2011, Bianchi and Schneider 2007, see section 1.1.3.2) can be heated by the aforementioned UV radiation field and collisionaly heated by the reverse shock (Dwek and Arendt, 1992), producing far infrared (FIR) thermal emission (*e.g.* SN1987A, Matsuura *et al.* 2011). However, for a shock velocity $v_s > 100$ km s^{-1}, up to 70% of dust grains can be destroyed by the reverse shock (see section 1.1.3.2, Jones *et al.* 1994, De Looze *et al.* 2017).

The free-expansion phase ends when the initial momentum driven by the blast has met a commensurate resistance opposed by the circumstellar medium. This stage is reached when the expanding ejecta has collided with a mass of material equal to the ejecta mass, hence the radius of the SNR at this moment is given by:

$$r_{\rm SNR} = \left(\frac{3M_{\rm ej}}{4\pi\mu m_{\rm H}}\right)^{1/3} n_0^{-1/3} \tag{1.2}$$

Where $m_{\rm H}$ is the mass of the hydrogen atom, and μ the mean molecular weight. Assuming a progenitor mass $M_{\rm ej} = 1.4\ M_\odot$ (SNIa) and a uniform CSM density $n_0 = 0.1$ cm^{-3} (*e.g.* Leahy 2017) yields the estimate $r_{\rm SNR} \simeq 5$ pc. Using the ejecta velocity previously estimated, this stage is reached at $t = r_{\rm SNR}/\langle v_{\rm ej}^2\rangle^{1/2}$, *i.e.* around 600 years for a typical SNR resulting from a SNIa. These estimates are in fair agreement with observations of young SNRs such as Kepler and Tycho (see Tab.1.1), but there might be discrepancies for non-spherical SNRs and/or SNRs expanding in environments characterized by non-uniform density profiles. In particular, CCSNe are often preceded by a Wolf-Rayet (WR) phase in which the progenitor produces powerful stellar winds

SNR	t_{SNR} (years)	r_{SNR} (pc)	v_{ej} (km s^{-1})	n_0 (cm^{-3})
Cas A	358	2.6	1000 - 1500	1.5
Kepler	410	2.5 - 3.8	1550 - 2000	0.1
Tycho	442	3.7	1500 - 2800	0.2
Crab	958	3.4	1400 - 1500	0.5
SN 1006	1000	7.1 - 7.5	2900 ± 100	0.1
Cygnus Loop	17 000	21.5 - 27	200 - 300	0.1 - 0.2
IC443	30 000	9.6 - 15	65 - 100	10 - 20

Table 1.1 Physical parameters for a sample of SNRs. The parameters t_{SNR}, r_{SNR}, v_{ej} and n_0 are respectively the age and radius of the SNR, ejecta velocities and local ISM densities. These parameters are taken from Chiad *et al.* (2015) (table 1) and references therein. For the most evolved SNRs ($t_{SNR} \gg 1000$ years), the age estimate is very uncertain.

that generate a $\sim r^{-2}$ density profile (van Veelen *et al.*, 2009). In some cases, the CSM into which the blastwave expands may be highly structured due to the impact of the wind phases. For example, a massive O type star will blow a fast wind ($1550 - 3000$ km s^{-1}, *e.g.* Mokiem *et al.* 2007) carving a low-density cavity or "*bubble*" enclosed by a fragmented, shock-heated dense shell made of swept-up ambient material (Castor *et al.* 1975, Weaver *et al.* 1977). Chevalier and Liang (1989) proposed a model to describe the interaction between a massive star SNe and a circumstellar shell. The SNR RCW 86 is a known case of a Type Ia SNe in a wind-blown bubble (Williams *et al.*, 2011).

Sedov-Taylor quasi-adiabatic expansion phase Once the free-expansion phase is over, the reverse shock ($v_{rs} \sim 10^3$ km s^{-1}) has traveled to the center of the SNR and reheated the entire cavity (Draine, 2011). The remnant is now dominated by the swept-up matter and the radiative losses can still be ignored to describe its dynamical evolution ("radiative losses" refer to the energy removal by photons escaping from the SNR). As a matter of fact, during this period of time the SNR radiates primarily through nonthermal emission mechanisms that do not produce energy losses commensurate to the total kinetic energy released by the outburst (see also Fig. 1.11). Most prominently, a radio synchrotron emission halo is produced by the interaction between the accelerated electrons and the local magnetic field. Additionally, γ-rays up to TeV energies are emitted as the result of the interaction of cosmic rays with the ISM (*via* inverse Compton scattering and pion decay, see section 1.4 for a full description of these nonthermal mechanisms).

Since radiative losses are negligible, we consider that the total energy is conserved and the dynamical evolution of the SNR is treated as an adiabatic phase. Hence, the ideal model used to describe the later evolution of the SNR is based on the assumption that the explosion energy E_0 is instantaneously injected into a uniform medium with density ρ_0, with no energy losses. During this phase, the blast wave enters a "*point explosion*" regime that can be described by self-similar solutions of three hydrodynamical variables (density ρ, velocity u, pressure P). These hydrodynamical variables are controlled by the equation of mass conservation,

$$\frac{\partial \rho}{\partial t} + \frac{1}{r^2}\frac{\partial}{\partial r}(r\rho u) = 0 \tag{1.3}$$

the equation of momentum conservation,

$$\frac{\partial u}{\partial t} + u\frac{\partial u}{\partial r} = -\frac{\partial P}{\partial r} \tag{1.4}$$

and the equation of energy conservation,

$$\frac{\partial}{\partial t}(\rho\epsilon + \frac{1}{2}\rho u^2) + \frac{1}{r^2}\frac{\partial}{\partial r}[r^2\rho u(\epsilon + P/\rho + \frac{1}{2}u^2)] = 0 \tag{1.5}$$

Where $\epsilon = P/[(\gamma - 1)\rho]$. This set of equations is consistent with the assumption that we are considering an ideal problem in which radiative losses, finite mass of the ejecta and the pressure of the ambient medium are neglected. The Rankine-Hugoniot jump conditions are derived from the conservation equations of the number of particles (Eq. 1.3), energy (Eq. 1.5) and momentum (Eq. 1.4) on both sides of the SNR shock front. Introducing the dimensionless variables α, v, p, we find that for $0 < r < r_s$ (where r_s is the radius of the blast), self-similar solutions must take the form:

$$\rho(r,t) = \left[\frac{\gamma+1}{\gamma-1}\right]\rho_0\alpha(\xi) \tag{1.6}$$

$$u(r,t) = \left[\frac{4}{5(\gamma+1)}\right]\frac{r}{t}v(\xi) \tag{1.7}$$

$$P(r,t) = \left[\frac{8}{25(\gamma+1)}\right]\rho_0\frac{r^2}{t^2}p(\xi) \tag{1.8}$$

Where $\xi = r(\frac{\rho_0}{E_0 t^2})^{1/5}$ is a dimensionless variable built using dimensional analysis, ρ_0 is the pre-shock density, γ the adiabatic index and $\alpha(\xi)$, $v(\xi)$, $p(\xi)$ are dimensionless functions of $\rho(r,t)$, $u(r,t)$, $P(r,t)$, respectively. The relation $\xi(r,t)$ can be inverted to determine the radius of the spherical blast evolving in the homogeneous and stationary ISM according to the expansion law (Sedov, 1977):

$$r_s = \xi_0\left(\frac{E_0}{\rho_0}\right)^{1/5} t^{2/5} \tag{1.9}$$

Where ξ_0 is a numerical constant of order unity. Hence the rate of expansion of the shock with respect to its radius is given by the derivative dr_s/dt:

$$v_s = \frac{2}{5}\xi_0^{5/2}\left(\frac{E_0}{\rho_0}\right)^{1/2} r_s^{-3/2} \tag{1.10}$$

And finally the temperature within the postshock can be determined using the Rankine-Hugoniot jump conditions:

$$T_s = \frac{2(\gamma-1)}{(\gamma+1)^2}\frac{M_0}{k_B}v_s^2 \tag{1.11}$$

Where v_s is the shock velocity, k_B the Boltzmann constant and M_0 the total mass within the radius of the blast. These relations allow to estimate the physical parameters at $r = r_s$, but we need to solve equations 1.6, 1.7 and 1.8 to determine the profiles of the density, velocity and pressure across the blastwave. The analytical solutions of the dimensionless functions $\alpha(\xi)$, $v(\xi)$ and $p(\xi)$ can be determined by injecting the dimensionless expression of ρ, u and P in Eq. 1.3, Eq. 1.4 and 1.5. After some re-organization, the equation of mass conservation becomes:

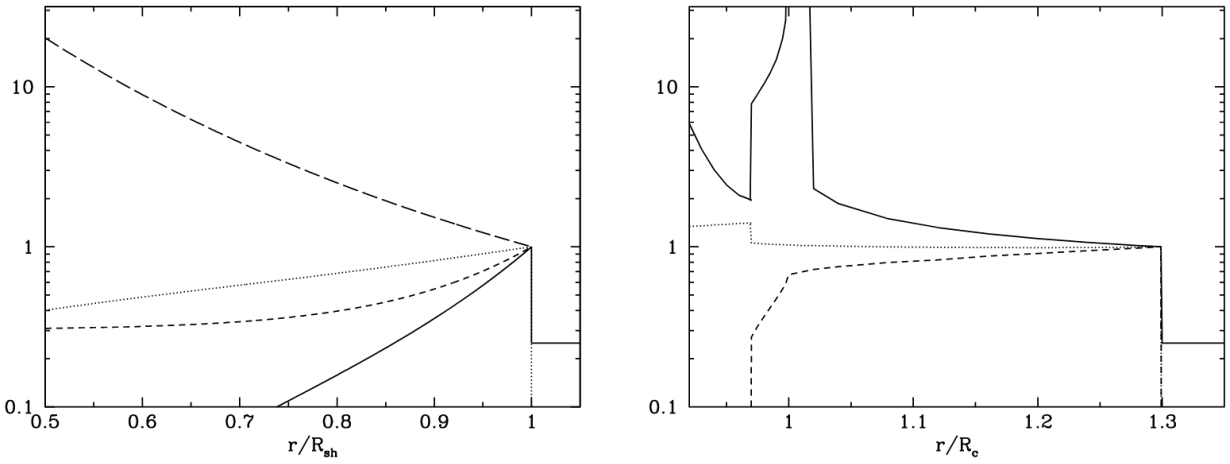

Figure 1.4 The structure of a SNR as given by the self-similar models of Sedov (1959) (left) and Chevalier (1982a). The values for the parameters have been normalized to the values immediately behind the forward shock. For the Sedov model the radius is expressed in units of the shock radius, for the Chevalier model in units of the contact discontinuity R_c, the border between swept-up and ejecta material. The solid lines show the density, the dotted lines the velocity, and the short-dashed lines the pressure profiles. For the Sedov model the temperature is indicated (long-dashed line). For this model the temperature goes to infinity toward the center. For the Chevalier model the density goes to infinity for $r = R_c$. Note that in the observer frame the velocity drops at the reverse shock. Figure reproduced from Vink (2012).

$$-\xi\frac{d\alpha}{d\xi}+\frac{2}{\gamma+1}\left[2\alpha v+\xi\frac{d}{d\xi}(\alpha\xi)\right]=0 \tag{1.12}$$

the equation of momentum conservation becomes

$$-v-\frac{2}{5}\xi\frac{dv}{d\xi}+\frac{4}{5(\gamma+1)}\left[v^2+v\xi\frac{dv}{d\xi}\right]+\frac{2(\gamma-1)}{5(\gamma+1)\alpha}\left[2p+\xi\frac{dp}{d\xi}\right]=0 \tag{1.13}$$

and the equation of energy conservation becomes

$$-2(p+\alpha v^2)-\frac{2}{5}\xi(p+\alpha v^2)+\frac{4}{5(\gamma+1)}\left[5v(\gamma p+\alpha v^2)+\xi\frac{d}{d\xi}(v[\gamma p+\alpha v^2])\right]=0 \tag{1.14}$$

An analytical solution to this system of equations was found by Sedov (1959) and Taylor (1950), known as the Sedov-Taylor self-similar spherical shock solution, but other self-similar solutions have been proposed to model the early evolution of the blastwave (*e.g.* Chevalier 1982a, Truelove and McKee 1999). The self-similar solutions of Sedov (1959) and Chevalier (1982a) are both shown in Fig.1.4 for pressure, velocity, density and temperature. It follows from all these models that the sudden liberation of a large energy E_0 in a small volume (the *point explosion* model of a SN) results in a blastwave that smoothly and asymptotically transitions from the free-expansion phase to the self-similar Sedov-Taylor solution (Cioffi *et al.*, 1988).

As the expanding blast slows down, the temperature decreases and the main coolants (*e.g.* H_2) reform in the postshock gas: the radiative losses become important, thus the SNR leaves the Sedov-Taylor adiabatic phase. The time at which this happens can be estimated based on the cooling time of the gas interior to the shock front. The energy variations caused by radiative losses inside the SNR can be written as:

$$\Delta E(t) = -\int_0^t \int_0^{r_s} \Lambda(T) 4\pi r^2 dr dt \tag{1.15}$$

Where Λ is the thermal energy removal rate, which determines the amount of energy transported by escaping photons per unit time and volume. Λ is related to the excitation conditions and density of the shocked gas: within the hot postshock gas ($T > 10^4$ K), the gas is assumed to be in collisional ionization equilibrium (thereafter CIE, *i.e.* the ionization of hydrogen provides enough free electrons to collisionaly excite atoms and ions and reach a steady state). These collisions are followed by the spontaneous emission of deexcitation photons that carry away the thermal energy of the gas. Hence the rate of energy removal by radiative losses can be written as:

$$\Lambda(T) = n_e n_H f(T) \tag{1.16}$$

Where n_e and n_H are respectively the electron and hydrogen densities, and $f(T)$ is the radiative cooling function that depends on the exact elemental abundances and modeling of atomic physics.

For $10^5 < T < 10^{7.3}$ K and assuming solar abundances, the radiative cooling function can be adopted following the CHIANTI atomic database (Dere *et al.*, 2009):

$$\Lambda(T)/n_e n_H = \Lambda_0 \, T^{-0.7}, \; \Lambda_0 \sim 1.7 \times 10^{-18} \text{ erg cm}^3 \text{ s}^{-1} \tag{1.17}$$

Hence we have:

$$\Delta E(t) = -\Lambda_0 n_0^2 \frac{4\pi}{3} \Gamma r_s^3 T_s^{-0.7} \int_0^t dt \tag{1.18}$$

Where n_0 is the local density, r_s, v_s and T_s are respectively the shock radius, velocity and temperature, and the constant $\Gamma = \langle (\rho/\rho_0)^2 (T_s/T)^{0.7} \rangle$ is a volume-weighted average over the blastwave that can be determined from the temperature and density profiles derived from the Sedov-Taylor solution. If we inject the Sedov expansion law (Eq.1.9) and the equation of the temperature (Eq.1.11) in this equation, we obtain:

$$\Delta E(t)/E_0 \simeq -1.8 \times 10^{-15} \left(\frac{n_0}{\text{cm}^{-2}}\right)^{1.68} \left(\frac{t}{\text{s}}\right)^{3.04} \tag{1.19}$$

Thus, if we consider that the radiative phase has begun once the energy of the blast has been halved by radiative losses ($\Delta E(t)/E_0 = -1/2$) and assuming that $n_0 = 10$ cm^{-3} (SNe in a dense environment, *e.g.* IC443, Chevalier 1999, Lee *et al.* 2012), this corresponds to a cooling time and duration of the Sedov-Taylor phase of $\sim$ 16 000 years. At this stage, the SNR has a radius $\sim$ 9 pc (Eq.1.9) and the shock has a velocity $\sim$ 220 km s^{-1} (Eq.1.10).

Radiative, pressure-driven snowplow phase Towards the end of the Sedov-Taylor phase, the radiative cooling causes the temperature to drop within the shock front, while the shock-heated gas in the interior of the SNR remains hot. Once the temperature has declined ($T \ll 10^5$ K, Draine 2011), the expanding blastwave is not sustained anymore by the thermal pressure of the shock and the propagation stalls. The cooled postshock gas collapses and forms a thin, dense shell where dynamical instabilities are generated on the basis of preshock density perturbations (Blondin *et al.*, 1998). At this stage, the SNR enters the snowplow phase, during which the blast sweeps the ambient material and builds an increasingly massive radiative (isothermal) shell of

SNR phase	Δt (years)	$r_{\rm SNR}$ (pc)	$v_{\rm ej}$ (km s^{-1})	conserved quantity
Free-expansion	100 - 500	1 - 5	$\sim 10^3$	blastwave velocity
Sedov-Taylor	10 000 - 20 000	5 - 10	$\sim 10^2$	total energy E_0
Snowplow	0.5 - 1 Myr	20 - 50	$10 - 10^2$	radial momentum

Table 1.2 Physical parameters corresponding to each phase of supernova remnant evolution. The parameters Δt, $r_{\rm SNR}$ and $v_{\rm ej}$ are respectively the duration of the phase, radius of the SNR (at the end of the phase) and ejecta velocities.

cool gas around a low-density, high-pressure and hot central cavity. The localized condensations of the sheet-like cold shell (compressed up to a factor 100, $n \sim 10^3$ cm^{-3}) and areas of interaction with interstellar clouds produce filamentary structures where the shock is isothermal and radiates photons, effectively cooling the remnant (Hester, 1987). The majority of the energy is radiated in a thin cooling layer characterized by bright emission of optical lines (primarily Hα, [O II], [O III], [S II], [N II], McKee and Cowie 1975, Fesen *et al.* 1985) and IR lines (primarily H_2 rotational transitions, as well as [Fe II], [C II] and [O I] lines, Oliva *et al.* 1989).

Since the energy of photons emitted by excited gas decreases with the velocity of the SNR shocks, over time the prominent wavelength $\lambda = hc/k_{\rm B}T$ (where h is the Planck constant) in which a SNR is bright gradually shifts from the UV/optical domain to the infrared/millimeter range. Additionally, the synchrotron radiation in the thin shell is enhanced by the compression of the magnetic field (van der Laan 1962a, van der Laan 1962b). For an electron of energy $E_{\rm GeV}$ ($E_{\rm GeV} = 1$ corresponds to an energy $E = 1$ GeV), the peak synchrotron frequency is given by:

$$\nu_{\rm GHz} = 4.6 \times 10^{-3} E_{\rm GeV} B_{\mu\rm G} \tag{1.20}$$

Where $B_{\mu\rm G} = 1$ corresponds to a magnetic field $B = 1$ μG, and $\nu_{\rm GHz} = 1$ corresponds to a frequency $\nu = 1$ GHz. Considering a typical preshock magnetic field $B \sim 10$ μG (Crutcher 1999, Heiles and Crutcher 2005), a compression factor ~ 100 and assuming that electrons are sufficiently accelerated to have an energy of order GeV (see section 1.4), this mechanism can account for the bright, nonthermal radio shells observed in evolved SNRs. The radio spectra of most SNRs can be described by a power law $S_\nu \propto \nu^{-\alpha}$ with $\alpha = 0.4 - 0.7$ (Green, 2014).

On its own, the expanding spherical shell decelerates continuously because of the conservation of radial momentum, but it is still driven by the internal pressure of the hot cavity forces that exerts centrifugal force onto it (Cox, 1972a). Hence the momentum-conserving snowplow solution (Oort, 1951) has to be corrected for the contribution of the hot cavity pressure. Since the radiative losses are negligible in the interior of the shell, the gas inside the cavity cools by adiabatic expansion (pV^γ remains constant). Hence, assuming that $\gamma = 5/3$ the pressure p within the interior of the SNR is given by:

$$p = p_0 \left(\frac{r_0}{r_{\rm s}} \right)^5 \tag{1.21}$$

Where p_0 and r_0 are respectively the pressure and radius of the SNR at the beginning of the snowplow phase. The momentum of the spherical shell increases under the effect of the thermal

pressure inside the remnant where the hot gas pushes outward, thus we have:

$$\frac{d}{dt}(M_s v_s) \simeq 4\pi p_0 \left(\frac{r_0^5}{r_s^3}\right) \tag{1.22}$$

where M_s is the mass of the shell. Assuming that the time evolution of the radius is given by a power law of t, dimensional analysis yields:

$$r_s = r_0 (t/t_0)^{2/7} \tag{1.23}$$

$$v_s = \frac{2}{7}\frac{r_0}{t_0}(t/t_0)^{-5/7} \tag{1.24}$$

Where t_0 is the time at which the snowplow phase starts. Using this last expression of the velocity, we can estimate the duration of the blastwave propagation before it finally fades away. Indeed, once the velocity of the expansion has slowed down to the average velocity dispersion in the ISM ($c_s \sim 5-10$ km s^{-1} if we include turbulent motions, *e.g.* Mast and Goldstein 1970), the SNR blast has practically dissipated and merged into the ISM. Using Eq.1.24 this fade away time amounts to ~ 0.8 Myr, and a final radius ~ 30 pc (Eq.1.23) for a SNe evolving in a dense environment ($n_0 = 10$ cm^{-3}). Thus, the last phase of SNR evolution is the most likely to be observed since it lasts longer than the previous stages.

1.1.2 Types of supernova remnants

One would naturally assume that the classification of supernova remnants could be derived from the classification scheme of SN explosions. However, most of the time it is difficult to determine the origin (CCSNe or SNIa) of an individual object, especially for old SNRs ($t_{SNR} \sim 10^4$ years). As a matter of fact, it is reasonable to make the hypothesis that a SNR originates from a CCSNe if it is found to be located in an OB association in which its progenitor might have formed (Westerlund 1969a, Westerlund 1969b), or if a pulsar is found in the vicinity (*e.g.* Kaspi *et al.* 1998). Still, unless precise and clear distance measurements are available, this kind of evidence is weak since it is entirely possible that these spatial correlations are accidental. Likewise, SNRs located high above the Galactic plane are likely to originate from SNIa, since this population of stars is on average older (Vink, 2012). At any rate, it is challenging to determine if a remnant evolved either from a CCSNe or SNIa, thus SNRs have their own classification based on their morphology. There used to be three long-established morphological classes of SNRs: *i.)* shell-type, *ii.)* plerionic and *iii.)* composite (see definitions below). Since the 1980s, a broader classification has developed on the basis of a large amount of new X-rays observations of older SNRs, which showed that the X-ray and radio morphologies are not always correlated. This has led to the introduction of a new class: mixed-morphology SNRs. Hence, nowadays there are four conventional classes of supernova remnants (see Fig.1.5).

***i.* Shell-type supernova remnants** A shell morphology is naturally expected in SNRs, as the blastwave sweeps material through the CSM and builds a dense shell of shock-heated plasma (bright in X-rays and radio wavelengths). Cas A (Reed *et al.*, 1995) and Kepler (van den Bergh and Kamper, 1977) are typical examples of shell-type SNRs.

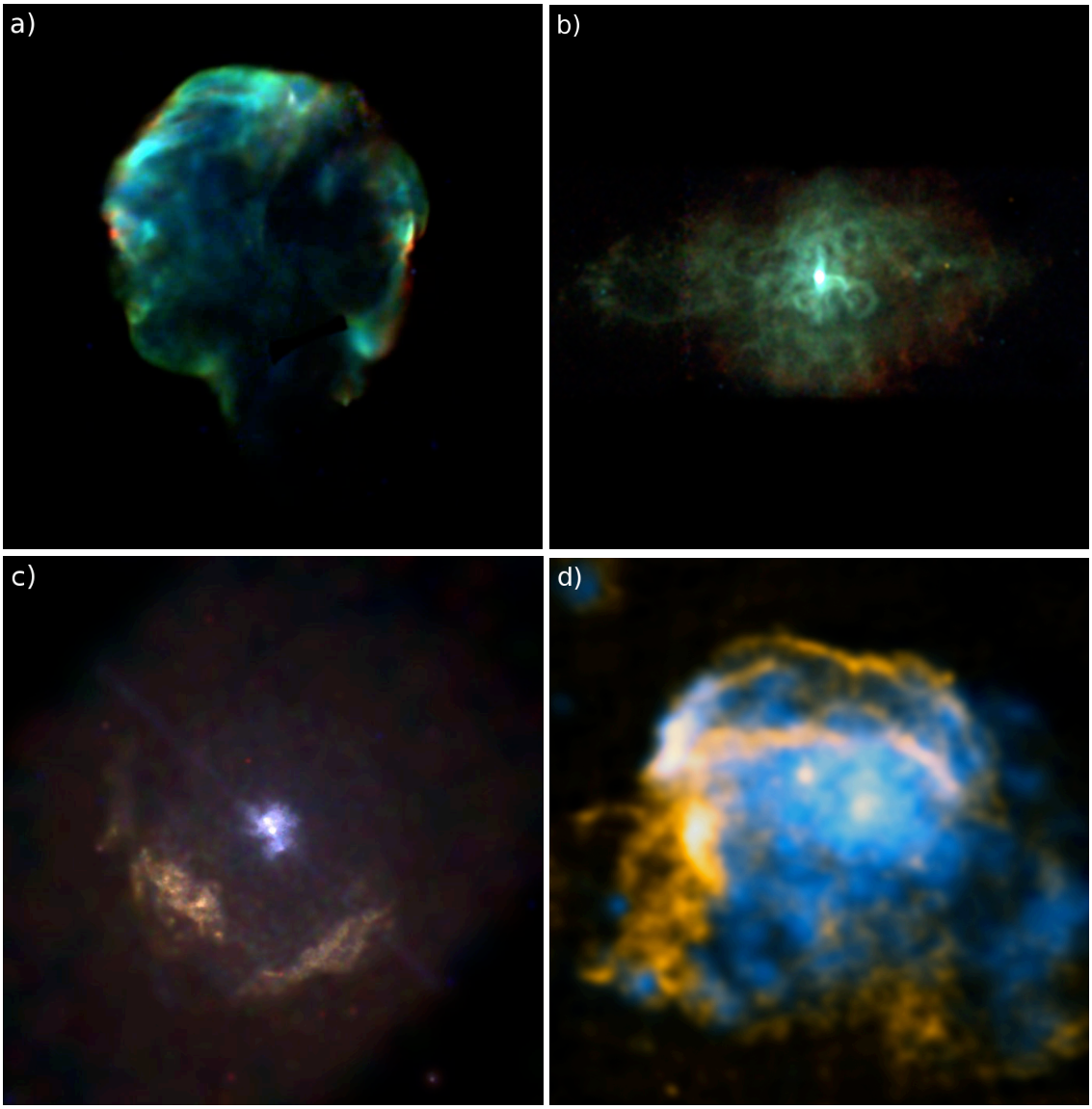

Figure 1.5 The SNR morphological classification illustrated with examples (figure reproduced from Vink 2012). From top left to bottom right: **a)** The Cygnus Loop, a shell-type SNR with a diameter of 3° (∼ 40 pc), as observed by the *ROSAT* PSPC instrument (Levenson *et al.*, 1998), red is very soft emission from ∼0.1-0.4 keV, green ∼0.5-1.2 keV, and blue ∼1.2-2.2 keV. **b)** 3C58, a plerion/pulsar wind nebula, as observed by *Chandra* (Slane *et al.*, 2004). The long axis of this object is ∼7′ (∼ 6 pc). **c)** The composite SNR Kes75 as observed by *Chandra* (Helfand *et al.*, 2003) with the inner pulsar wind nebula, which has a hard X-ray spectrum, powered by the pulsar J1846-0258. The partial shell has a radius of ∼1.4′ (∼ 3 pc). The colors indicate 1-1.7 keV (red, Ne and Mg emission), 1.7-2.5 keV (green, Si/S), and 2.5-5 keV (blue, mostly continuum emission from the pulsar wind nebula). **d)** The "thermal-composite" SNR W28 as observed in X-rays by the *ROSAT* PSPC (blue) and in radio by the VLA (yellow, Dubner *et al.* 2000). In this remnant, the morphology in radio is distinct from the X-ray emission (in contrast to the SNRs shown in the 'a', 'b' and 'c' panels, in which the morphology is reproduced across X-ray and radio wavelengths). The diameter of the shell is 1.5° (∼ 60 pc). (Image credit: Chandra press office, http://chandra.harvard.edu/photo/2008/w28/more.html)

***ii.* Plerionic supernova remnants** CCSNe are expected to produce rapidly rotating neutron stars following the collapse of the progenitor. As their rotation speed decrease, these pulsar continuously lose energy with a rate:

$$\frac{\mathrm{d}E}{\mathrm{d}t} = 4\pi \frac{I}{P^3} \frac{\mathrm{d}P}{\mathrm{d}t} \tag{1.25}$$

Where P is the rotation period and $I \sim 10^{45}$ g cm^2 the moment of inertia (Vink, 2012). This energy loss produces a wind of relativistic electrons and positrons. Within the termination shock, these particles are accelerated and emit synchrotron radiation from radio to soft γ-rays, as well as inverse Compton emission from soft γ-rays to TeV energies (Gaensler and Slane, 2006). As a result, contrary to shell-type SNRs these remnants appear as centrally-filled, with the brightness increasing towards the center (bright in X-rays and radio wavelengths). These objects are known as **pulsar wind nebulae** (PWNe), or plerions[5]. The most striking example of plerion is the Crab nebula (Hester, 2008). In some plerions, the pulsar motion inside the SNR causes the wind bubble to move within the interior and can form a bow-shock nebula, like in the 11 kyr old SNR Vela (Helfand *et al.* 2001, Aharonian *et al.* 2006). One puzzling question about plerions is the absence of a shell. Simulations of the X-ray emission in SNRs evolving in a low-density medium can reproduce the centrally-filled morphology for up to $\sim 10^7$ years, well into the radiative phase (Shelton, 1999).

***iii.* Composite supernova remnants** Composite SNRs are evolved pulsar wind nebulae surrounded by a shell (bright in X-rays and radio wavelengths). A striking example is given by the SNR Kes75 (Su *et al.*, 2009). Shull *et al.* (1989) proposed that the accidental interaction between high-velocity pulsars and old SNR shells can produce these objects (like in CTB 80 or G5.4-1.2, Frail and Kulkarni 1991). However, using Monte Carlo simulations Gaensler and Johnston (1995) computed the probability to observe these associations and concluded that some of the claims of PWNe-SNR associations are merely geometric projections. Hydrodynamical simulations of the interaction between PWNe and shells were proposed to reproduce the morphology of these objects, showing the role of Rayleigh-Taylor instabilities and asymmetries in the surrounding interstellar medium (Blondin *et al.* 2001, van der Swaluw *et al.* 2003).

***iv.* Mixed-morphology supernova remnants** Mixed-morphology SNRs are shell-like in radio, and centrally-filled in X-rays. These objects represent a distinct physical class (Rho and Petre, 1998). In these relatively old SNRs, the X-ray emission is not powered by a pulsar but by thermal emission from the hot plasma within the cavity. Moreover, their emission comes mainly from swept-up material, not from the ejecta. As it is hinted by the presence of OH masers, most of these remnants are interacting with H I and/or molecular clouds (Frail *et al.*, 1996). The enhanced X-ray emission in the interior cavity could be caused by evaporated gas from the clouds these SNRs are interacting with. Thus, the existence of MCs in the vicinity is crucial for the formation of this class of SNR, and it is likely that they have massive progenitors. Well known mixed-morphology SNRs are W28, W44, 3C391 and IC443.

Others Additional classes of SNRs have been found throughout the years, based on morphological *and* non-morphological criteria. For example, the distinct class of oxygen-rich SNRs are

[5] In greek, *pleres* means full (Weiler and Panagia, 1978).

likely to originate from the most massive stars (*e.g.* Cas A, van den Bergh 1988). Likewise, Gaensler (1998) isolated a subset of 17 Galactic SNRs that present a bilateral or "barrel" morphology aligned with the Galactic plane. He proposed that this class of remnants might indicate the extrinsic role played by the Galactic magnetic field in shaping the SNRs, either as a result of magnetic compression or preprocessing of the ISM along the plane.

Evolved supernova remnants In the literature, SNRs are often designated either as "young", "mature" or "old". These labels are not very precisely defined and might change from one author to the other. A general guideline is that the age of young SNRs is less than ~1000 years (corresponding to the ejecta-driven phase), while mature SNRs correspond approximately to the Sedov-Taylor phase and old SNRs are in the radiative snowplow phase (Vink, 2012). Hereafter, we will overlook the early stages of SNR evolution described in section 1.1.1 and focus on the impact of *evolved* SNRs (*i.e.* old SNRs, aged $\geq$ 10 000 yr). The essential object studied in this thesis, the supernova remnant IC443 (see Chapter 2) is in the radiative snowplow phase. The next sections will be centered on a review of the characteristics of evolved (old) SNRs and the critical role played by these objects in the ISM. However, in order to provide the required background and context, we will also systematically introduce the impact of young supernova remnants as briefly as possible (*e.g.* we will describe the mechanisms of dust synthesis in the first decades after the explosion before examining dust properties in the older phases of SNR evolution).

1.1.3 Evolved supernova remnants and their impacts on the interstellar medium

The ubiquity of supernova remnants Supernova remnants are a key parameter of the ISM dynamical and chemical evolution. The Galactic SN explosion rate is estimated around one event per $\tau_{\rm SNR} = 40 \pm 10$ years (Tammann *et al.*, 1994). Assuming that: *i.* the blast wave of a SN sweeps a spherical space of radius $r_{\rm SNR}$ ~15 pc (see section 1.1.1); *ii.* the SNR progenitors are homogeneously distributed in the Galaxy; *iii.* the star populated region of the Milky Way can be modeled by a disk volume of radius $R_{\rm MW} = 20$ kpc and height $H_{\rm MW} = 0.6$ kpc (Rix and Bovy, 2013), *iv.* the age of the Milky Way is $t_{\rm MW}$ ~11.2 Gyr (*e.g.* Krauss and Chaboyer 2003, Bond *et al.* 2013); we can estimate the average number of times an arbitrary region of the Galaxy has been swept by a SNR shock:

$$\frac{4}{3}\frac{t_{\rm MW}}{\tau_{\rm SNR}}\frac{R_{\rm SNR}^3}{R_{\rm MW}^2}\frac{1}{H_{\rm MW}} \sim 5 \tag{1.26}$$

Hence, during its life each cubic centimeter of our Galaxy has been reprocessed several times by the shockwave associated with a SNR. For this reason, supernova remnants are a key ingredient regarding the dynamical evolution of the ISM, the chemistry of the gas and dust phases, and the energy injection at intragalactic scale. SNRs regulate the global energy, pressure and mass balance of the ISM and they provide a mechanism to account for its multiphase structure (see McKee 1990 and Ferrière 2001 for reviews on our current view regarding the characteristics of the multiphase ISM and the role of SNRs in its shaping).

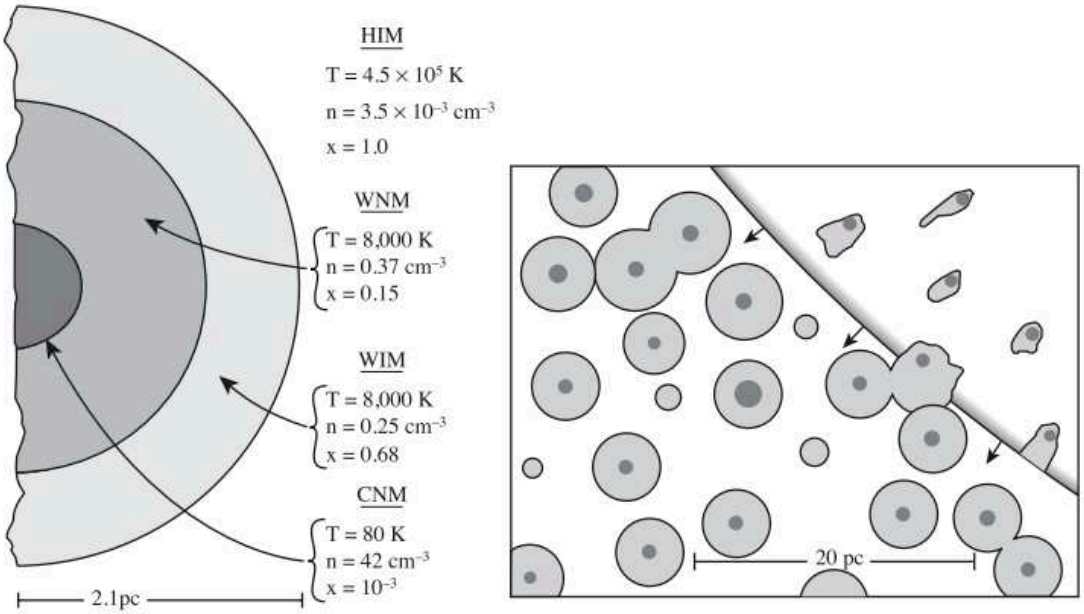

Figure 1.6 *Left*: Three phase model of the ISM by McKee and Ostriker (1977). This figure represents the cross section of a characteristic small cloud. The dark gray region shows the cold core (cold neutral medium, CNM), *i.e.* the interior of the cloud where molecules are shielded from UV radiation (Sternberg *et al.*, 2014). Next is the warm neutral medium (WNM) where thermal instability occurs (Field, 1965). The outer layer, or intercloud region, is gas largely ionized by stellar UV background: the warm ionized medium (WIM). To the exterior of the small cloud is the hot ionized medium (HIM). Typical values of hydrogen density n, temperature T, and ionization fraction $x = n_e/n$ are shown for each component. *Right*: Small-scale structure of the interstellar medium. A cross section of a representative region 30 pc × 40 pc in extent is shown. A supernova blast wave is expanding into the region from the upper right. The radius of the neutral cold cores of the clouds (represented in dark gray) ranges from about 0.4 to 1 pc in this small region; all the clouds with cores have warm envelopes (light gray) of radius ∼ 2.1 pc. A few clouds are too small to have cores. The envelopes of clouds inside the SNR are compressed and distorted by the expanding blast.

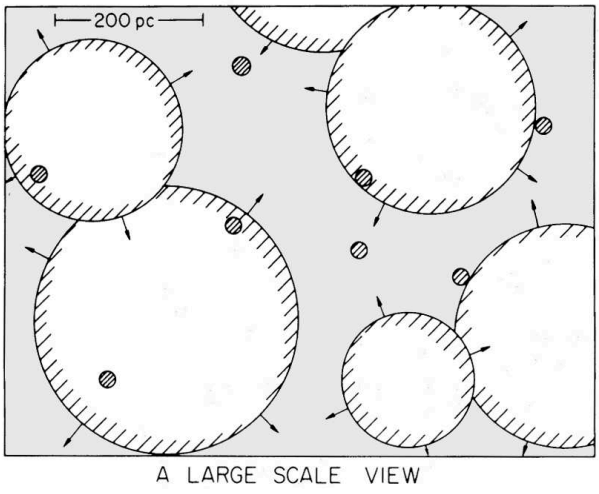

Figure 1.7 Large-scale structure of the interstellar medium (McKee and Ostriker, 1977). The scale here is 20 times greater than in Fig. 1.6: the region is 600 pc × 800 pc. Only clouds with a radius greater than 7 pc are shown (hatched circles). Evolved SNRs of size greater than 180 pc are represented by large expanding circles. Altogether about 9000 clouds, most with a radius ∼ 2.1 pc, would occur in a region this size.

Structuring and regulating the multiphase ISM The morphology of the ISM is shaped by the impact of evolved supernova remnants on their environment. McKee and Ostriker (1977) proposed that SN explosions in an initially cloudy interstellar medium can produce and regulate the evolution of the three-component medium observed in the ISM (see Fig. 1.6 and 1.7) and account for the large amount of low-density, hot gas observed in the Galactic disk (Shapiro and Field 1976, Spitzer 1990, Hollenbach and Tielens 1999).

In this picture, the shocks associated with the expanding blast of SNRs produce large volumes of hot ionized medium and strongly interact with neutral clouds encountered in the vicinity. Very small clouds are rapidly evaporated, and larger clouds have their outer envelope twisted and/or swept up by the blastwave, providing the warm photo-ionized phase of the ISM. The remaining dense, neutral cores of large clouds are exposed and accelerated by the collision with the shell of the SNR, but they survive the passage of the blast. The high-density phase of the ISM is replenished during the snowplow phase as the expanding dense shell collects interstellar material. Hence the mass balance is regulated by the competition between the evaporation of clouds and the compression of swept-up matter; and the energy balance is regulated by the competition between kinetic energy injection and radiation of the coronal gas. Simulations of SN explosions reproduce the multiphase structure of the ISM for a various range of initial conditions (*e.g.* gas densities $10^{-5} - 10^{2}$ cm^{-3}, temperature $10 - 10^{8}$ K, Mach number up to 25 and SN rates $1 - 720$ Myr^{-1}, Gent *et al.* 2013, Gatto *et al.* 2015).

Superbubbles If several massive stars have formed in a cluster of OB associations (Elmegreen and Lada 1977, Lada 1987), they are likely to enter their supernova phase before they have a chance to drift apart. Thus, in a short period of time the combined action of the stellar winds and repeated SN outbursts will excavate a large cavity of coronal gas (low-density, ionized, hot material) surrounded by a large, thin shell of cold gas. In a short time (of order $\sim$ 1 Myr), the remnants of the neighboring SNe will merge and form a single superbubble, which may be hundreds of parsecs across (Mac Low and McCray 1988, *e.g.* Oey 1996 for a study of SNR driven superbubbles in the Magellanic cloud). These superbubbles are a primary source of the hot ionized component of the ISM, believed to fill a fraction $\leq 30\%$ of the Milky Way disk's volume (*e.g.* Ferrière 1998, Könyves *et al.* 2007). Simulations of superbubble evolution in the multiphase ISM have been made based on the assumptions of the clustering of SN activity (*e.g.* Korpi *et al.* 1999). These simulations show that the lifetime of these structures is shorter than 10^{7} yr, during which they expand into irregular, hot cavities of size $\sim$ 200 pc.

1.1.3.1 Energy injection

Supernova remnants are very special astrophysical objects, for they provide the unique opportunity to witness every single mode of large-scale (up to $\sim$ 100 pc) energy injection and energy transport in the interstellar medium, in real time, over up to $\sim 10^{5}$ years. Indeed, the prodigious energy and momentum injected in the environment at the time of the explosion drives large shockwaves that cascade to lower scales, decay into turbulence, heat and ionize the ambient gas, accelerate cosmic rays, amplify the local magnetic field, *etc*. In this section we will briefly present these different mechanisms of energy injection, how they regulate the energy partition of the ISM and how they are met in SNRs.

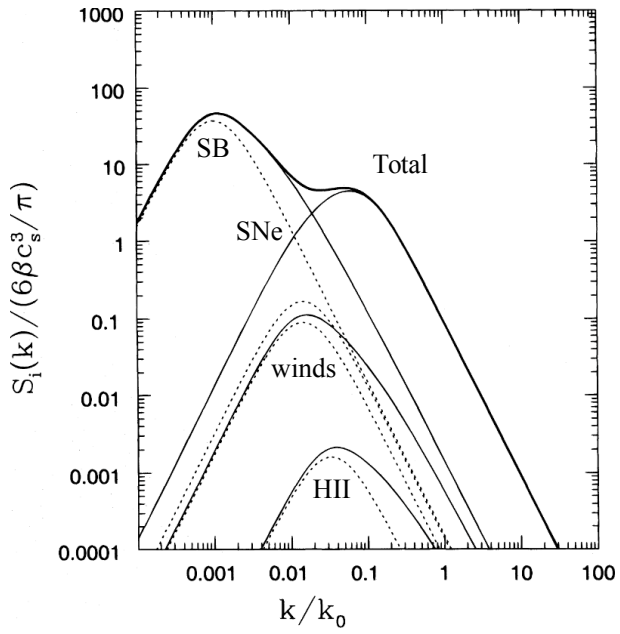

Figure 1.8 Normalized turbulent source functions $S_i(k)$ (where k is the wavenumber of an eddy) for individual supernovae, superbubbles (labelled 'SB'), winds, and H II regions (Spitzer 1982, Ikeuchi and Spitzer 1984, Bykov and Toptygin 1987). Solid lines show the sum of primary and secondary shock contributions for each source; dashed lines show secondary shocks only. The thick line represents the total source function. SNe dominate over most of the spectral range, although superbubbles can dominate on large scales ($k/k_0 < 0.01$). Figure from Norman and Ferrara (1996).

Energetic impact of SNRs: *i.* Kinetic energy injection, shocks and turbulent decay The ISM is globally observed to be turbulent: the electron density spectrum in the WIM has a Kolmogorov-like spectrum over at least 6 orders of magnitudes (Armstrong *et al.*, 1995); CO observations towards giant molecular clouds (GMC) are characterized by suprathermal emission lines (Zuckerman and Evans, 1974). The ISM in the Galactic disk is turbulent (Larson 1981, Scalo 1987, Rosen and Bregman 1995), as well as in most spiral galaxies where the H I velocity dispersion varies between 4 km s^{-1} and 15 km s^{-1} (*e.g.* Dickey *et al.* 1990). Supernova remnant feedback, driven by the expanding blastwave that heats and stirs the ISM over large volumes and periods of time of order $\sim$ 1 Myr, are the dominant contributor to the injection of kinetic energy in the ISM.

SNe and SNRs inject kinetic energy into the turbulent spectrum at large scales, then the energy cascades into small scale turbulent motions (Norman and Ferrara 1996, see Fig. 1.8). In the early phases of the SNR evolution, the kinetic energy is held by fast shocks that will gradually decay into turbulent motions and transport the energy to lower scales where it is dissipated. It has been argued that stellar feedback contributes to turbulence injection (*via* H II regions expansion, radiation pressure, jets from young stellar objects, stellar winds) but the input of SNRs is far greater in magnitude than the aforementioned mechanisms that take effect in the earlier phases of stellar evolution (Mac Low and Klessen, 2004). The major part of the SN kinetic energy will ultimately be converted into interstellar turbulence and radiative losses, but it also marginally accelerates interstellar clouds. Chevalier (1974) obtained an efficiency between 4% and 8% for the kinetic energy transmitted to the cloud motions, the rest being dissipated during cloud collisions.

In the past years, simulations of SN outbursts in stratified and non homogeneous environments have been made to study the injection of momentum over the lifetime of a SNR (*e.g.* Kim and Ostriker 2015, Martizzi *et al.* 2015, Joung and Mac Low 2006) and the relation between the SN rate and the velocity dispersion in the ISM (Dib *et al.*, 2006). These simulations show that SNe driving can account for the typical velocity dispersions measured in diffuse gas ($\sigma \sim 6$ km s^{-1} in Dib *et al.* 2006 simulations). In addition, numerical magnetohydrodynamic simulations show that kinetic energy injection by SNe contribute to regulate the star formation rate in molecular clouds (Hennebelle and Iffrig 2014, Iffrig and Hennebelle 2015, Geen *et al.* 2016).

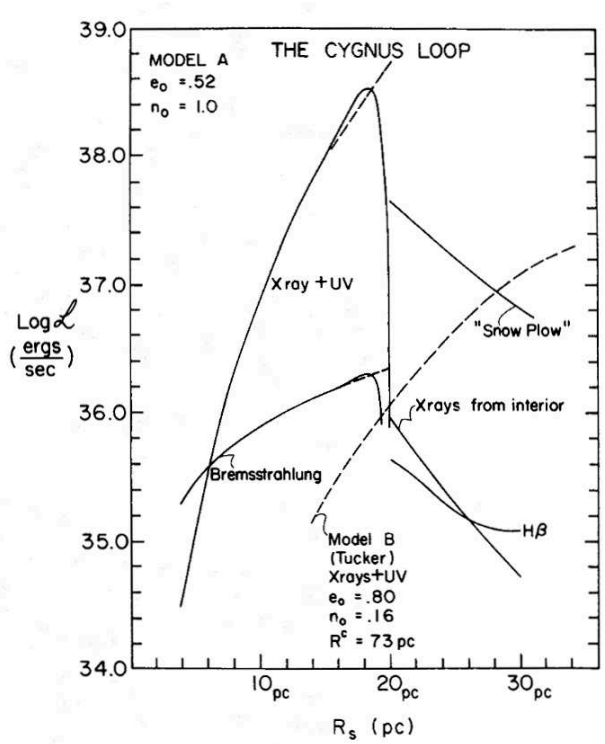

Figure 1.9 Evolution of the total luminosity (shell + cavity) with respect to the shell radius R_s, for a possible model of the Cygnus Loop SNR (Cox 1972a, Cox 1972b). The total energy radiated is 0.52 E_0, where E_0 is the energy released by the SN explosion, and the CSM density is $n_0 = 1$ cm^{-3}. The model from Tucker (1971) is also shown by a dashed curve. For $R_s > 20$ pc, the "snowplow" luminosity curve represents the total luminosity of the filaments, based on a model of a plane shock wave (Cox 1972b). The "snowplow" luminosity of the shock-heated gas is dominated by Lyman, Balmer and forbidden lines (primarily hydrogen and oxygen lines).

Energetic impact of SNRs: *ii.* Thermal energy injection, ionization and radiative transport
Around forty years ago, the first *Copernicus* observations of highly ionized species (*e.g.* O VI lines) and of the diffuse X-ray background around 0.25 keV challenged the previous view according to which the ISM could be described by cold ($T \sim 100$ K) gas clouds embedded in a substrate of warm ($T \sim 10^4$ K) ionized intercloud medium (McCray and Snow, 1979). The observation of this diffuse X-ray background requires the existence of a hot ($T \sim 10^5$ K) coronal phase of the ISM. SNRs heating mechanisms can account for the thermal energy injection required to maintain this hot, ionized phase and reproduce both the far UV (FUV) luminosity and soft X-ray background (Williamson *et al.* 1974, Jenkins and Meloy 1974, Cox and Smith 1974, Shapiro and Field 1976).

Upon the explosion of a SN, the ionizing radiation emitted can have a fairly direct effect, but it represents only an energy of about 10^{44} erg of hard X-rays radiation emitted at the time of the shock breakout (Colgate, 1974), hence a tiny fraction of the total energy ($E_0 \sim 10^{51}$ erg). The optically radiated energy released upon the explosion is $\sim 10^{49}$ erg, a negligible fraction as well, but it grows during the SNR lifespan and represents a significant component of the total energy during the snowplow phase (see Fig. 1.11). As a matter of fact, *over its entire lifetime* about 30% of the SNR energy is emitted as ionizing radiation (Chevalier 1974, Mansfield and Salpeter 1974). This amount of ionizing radiation remains lower than the total ionizing luminosity that is produced by a hot star during its lifetime, but it is deposited over a larger volume, and it extends to X-rays (Chevalier, 1977).

The total energy radiated (both ionizing *and* non-ionizing photons) by the post-shock gas at the end of the shell formation is important. Cox (1972a) calculated that at this stage $\sim$ 52% of the initial blast energy ($E_0 \sim 10^{51}$ erg) is lost via radiative losses, mostly *via* the emission of FUV and X-rays photons (see Fig. 1.9). The subsequent photo-ionization of the cooler portions of the shell forms H II regions which, in turn, will radiate energetic photons, producing photo-dissociation regions in their environment (or "photon-dominated regions", hereafter PDRs, see Hollenbach

and Tielens 1999 for a review). Shock models can also contribute to characterize the injection of thermal energy and consecutive radiative cooling mechanisms (Cox 1972b, Chevalier *et al.* 1980, see section 1.2). Optical spectrophotometric observations of forbidden line ratios ([O I], [S II], Hα) allow to discriminate SNRs from H II regions, and to trace high temperature ($\sim 10^4$ K) and electron densities ($n_e \sim 10^2 - 10^3$ cm^{-3}) in the shocked filamentary structures (*e.g.* Miller 1974, Fesen *et al.* 1985).

Energetic impact of SNRs: *iii.* Magnetic field amplification and CR acceleration The energetic input of SNRs also has an impact on the magnetic field and CR energy densities of the ISM. Blandford and Eichler (1987) proposed that CRs can be accelerated in SNRs shocks *via* the diffusive shock acceleration mechanism (DSA, see section 1.4), but a strongly turbulent and intense local magnetic field ($\geq$ 100 μG) is required to drive this mechanism. Collisionless interstellar shocks should be able to dissipate the kinetic energy injected by SNRs into thermal, magnetic and CR energy (Hoyle and Ireland 1960, Axford *et al.* 1977), but the sum of the equipartition magnetic field and relativistic electron energy densities are likely to be less than or about 1% of the thermal energy density in SNRs (Chevalier, 1982a). Local amplification of the pre-existing magnetic field is required to account for the acceleration of high-energy (TeV) CRs. The scenario of magnetic field amplification is supported by observations in the objects where hard X-ray measurements are available (Völk *et al.*, 2005). In Cas A for instance, X-ray observations with arcsecond spatial resolution show the synchrotron emission located on the filamentary structures where the SNR shocks are propagating (Bamba *et al.* 2003, Vink and Laming 2003). In some extreme regions, these synchrotron losses require magnetic field amplitudes up to 500 μG.

At first the amplification mechanism of the magnetic field was understood based on the adiabatic compression of the gas in the SNR shell: because the magnetic flux is *frozen* into the gas, when the gas density increases, so does the magnetic field amplitude (Heiles and Crutcher, 2005). But in fact this mechanism is not sufficient to produce the observed magnetic fields, and studies of plasma instability theory are required to fully account for the amplification (Voelk *et al.*, 1984). The turbulent motions caused by the Rayleigh-Taylor instability at the contact discontinuity between the shell and the preshock medium can participate in the magnetic field amplification (Jun and Norman, 1996). In fact, both the postshock *and* preshock magnetic fields have to be amplified to drive DSA. The turbulent dynamo fed by the cascade of the SNR kinetic energy injection is likely to dominate the downstream amplification of the magnetic field (Xu and Lazarian 2016, Xu and Lazarian 2017); while the upstream amplification can be modeled by the action of the CR pressure gradient on the ISM (Drury and Downes, 2012). The combination of these processes can account for the enhanced magnetic field and subsequent acceleration of relativistic particles. In section 1.4, we will review the observational evidence for CR acceleration in SNRs, and the impact of CRs on the ISM.

Energy partition of an evolved SNR The time evolution of the energy partition of an SNR is shown in Fig. 1.11 (obtained with a spherically symmetric hydrodynamic model, Chevalier 1974). This figure shows that once the Sedov-Taylor adiabatic phase ends, the kinetic energy gradually decreases and the internal energy is quickly converted into ionizing, non-ionizing and infrared radiation. As an illustrative example, we roughly estimated the energy partition in the evolved SNR IC443 and compared our findings with reference figures (Draine, 2011). The results are

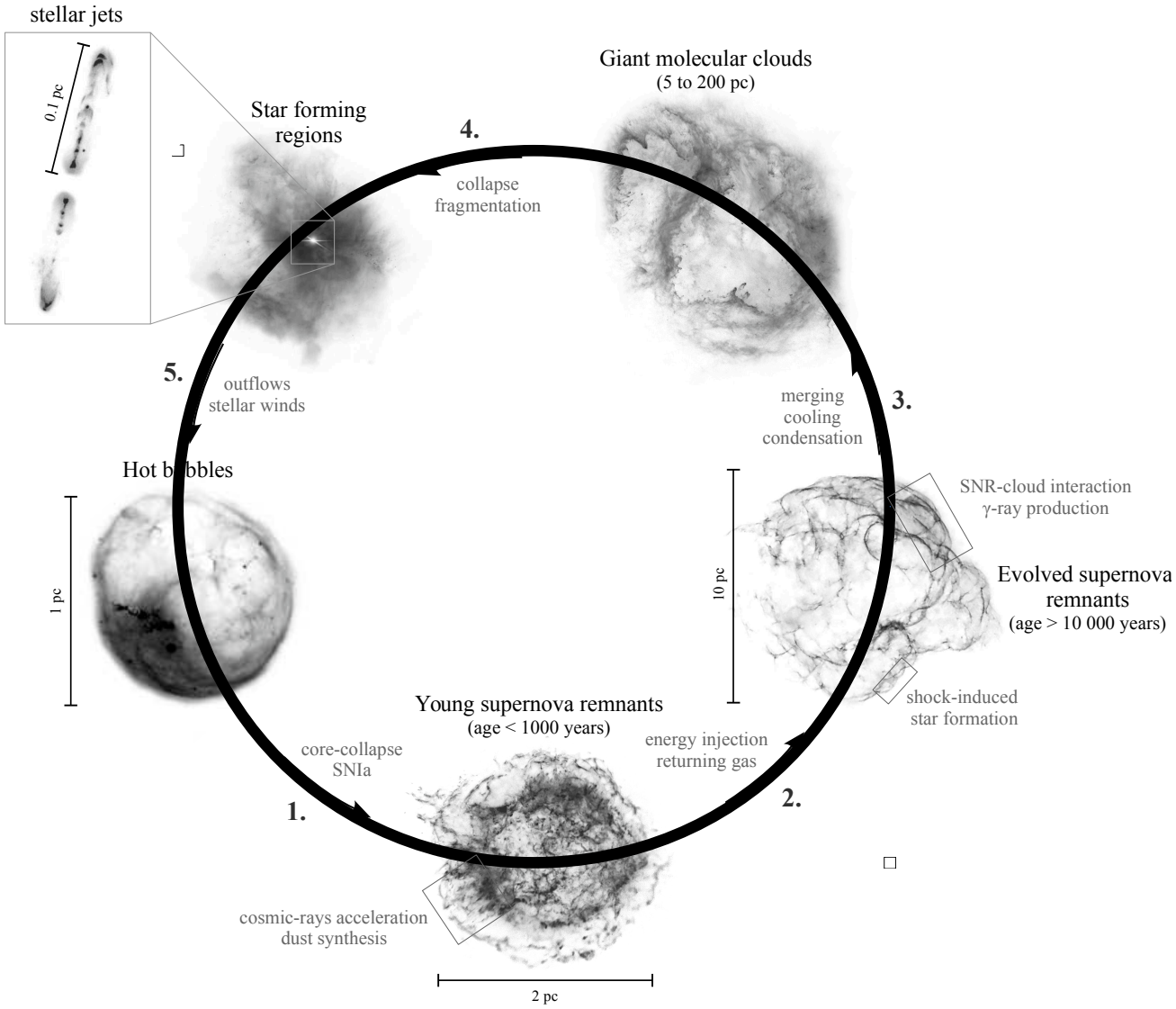

Figure 1.10 Schematic view of the cycle of the interstellar medium, focusing on the role of SNRs. The main feedback, energy injection, material exchange and re-processing mechanisms are indicated in gray for each corresponding stage. For the sake of illustration, grayscale images are extracted from observations of Cas A (young supernova remnant), Simeis 147 (evolved supernova remnant), Westerhout 3-5 (giant molecular clouds), M42 (star forming region) and NGC 7635 (hot bubble). *1.)* Massive stars and accreting white dwarfs explode into SNe, releasing $\sim 10^{51}$ erg into their environment, accelerating CRs and producing dust. *2.)* evolved SNRs stir, heat and ionize the medium, producing the multiphase ISM. Re-processed gas returns to the environment in the form of swept-up material. *3.)* Old SNRs gradually merge with the ISM as they cool and dissipate turbulent energy. New H I and molecular clouds are formed from the dense, quiescent and cold regions of the shell residues. *4.)* Molecular clouds eventually fragment and collapse into star forming regions. *5.)* Protostars inject feedback energy through stellar jets, outflows and winds, producing hot bubbles (H II regions). The most massive stars are the progenitors of the next generation of CCSNe.

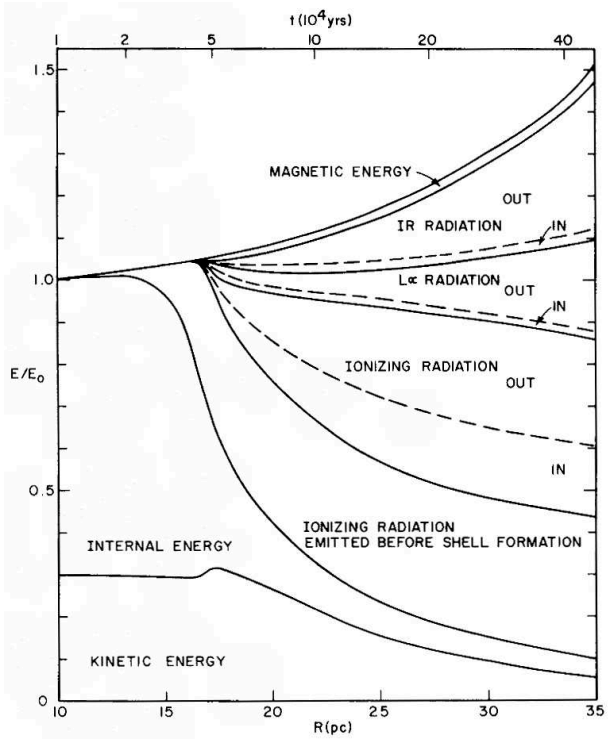

Figure 1.11 Energetics of a spherically symmetric hydrodynamic SNR model (initial energy $E_0 = 3 \times 10^{50}$ erg, local density $n_0 = 1$ cm^{-3}, local magnetic field $B_0 = 3 \times 10^{-6}$ G) as a function of remnant radius under the assumption that the remnant is optically thin at all wavelengths (Chevalier, 1974). Before $R = 10$ pc, the Sedov-Taylor adiabatic solution holds. "In" applies to radiation emitted inside the dense shell, while "Out" applies to that emitted between the shock front and the dense shell. The ratio of internal energy to initial energy E/E_0 increases due to internal energy added by surrounding gas, assumed to be ionized and at $T = 10^4$ K. Figure reproduced from Chevalier (1974).

shown in Table 1.3. Our estimates are based on the measurement obtained in Chapters 9 (analysis of dust thermal emission) and 8 (analysis of ^{12}CO, ^{13}CO and C^{18}O rotational lines). Our estimate of the thermal energy only accounts for the molecular phase, hence we are likely missing the bulk of the thermal energy held by the hot, ionized phase in the cavity of the SNR. In addition, our estimate of the "FIR" energy is restricted to dust emission. Including the contribution by ionic and atomic lines would likely increase this component by a factor $1,25 - 2,5$ (see section 9.1.4). We find that in the IC443 SNR, $E_{\rm kin} \gg E_{\rm CR} \simeq E_{\rm mag} \simeq E_{\rm thermal} \gg E_{\rm FIR}$, where $E_{\rm kin}$ is the turbulent kinetic energy, $E_{\rm CR}$ is the cosmic rays energy, $E_{\rm mag}$ is the magnetic energy, $E_{\rm thermal}$ is the thermal energy and $E_{\rm FIR}$ is the energy held by far-infrared photons. According to Fig. 1.11, this energy partition is approximately consistent with an age $0.5 - 1 \times 10^5$ yr (however, the local density in the molecular cloud that is interacting with the IC443 SNR is higher than the input used in this model: $n = 10 - 20$ cm^{-3}, *e.g.* Akabane 1966).

1.1.3.2 Chemistry

Not only are the SNRs a major source of energy injection, they also contribute to regulate the cycle of the interstellar matter. SNe are a prime source of cosmic dust, a paramount ingredient of the ISM that represents 1%-2% of the mass of the universe (excluding dark matter) and up to 50% of the radiation of some galaxies. Dust is a key agent that regulates the physical and chemical processes responsible for star formation and galaxy evolution, as well as the thermal balance of the ISM. Dust serves as a catalyst for chemical reactions, such as the formation of H_2 molecules on the surface of dust grains. In evolved SNRs, the intertwined chemistry of the gas and dust phases is shaped by the specific conditions corresponding to the propagation of shocks (heating, ionization, compression, destruction, *etc.*). In this section we will give a description of these mechanisms.

Component	$u_{\rm ISM}$(eV cm^{-3})	$u_{\rm SNR}$(eV cm^{-3})	Note
Cosmic microwave background ($T_{\rm CMB}$ = 2.725 K)	0.265	0.265	*a*
Starlight ($h\nu$ < 13.6 eV)	0.54	-	*a*
Far-infrared radiation from dust	0.31	0.39-1.68	*b*
Thermal energy $(3/2)nk_{\rm B}T$ (SNR: molecular phase)	0.49	0.13-390	*c*
Turbulent kinetic energy $(1/2)\rho v^2$ (SNR: molecular phase)	0.22	$26 - 9.3 \times 10^4$	*d*
Magnetic energy $B^2/8\pi$	0.89	559	*e*
Cosmic rays	1.39	400	*f*

a Naturally, the CMB contribution is the same as in the local ISM (Draine, 2011). We cannot accurately estimate the starlight component, although it is likely to be similar as the Draine (2011) figure.
b Inferred from the area under the spectral energy distribution of dust thermal emission, multiplied by $4\pi/c$ to convert from luminosity to energy density (Chapter 9, see Fig. 9.13). The lower boundary represents the average across our $16' \times 16'$ field of observations, and the higher boundary represents the maximum (towards the shocked clump 'G').
c Lower boundary: assuming $T_{\rm kin}$ = 10 K and a local density $n_{\rm H_2} = 10^2$ cm^{-3} for the cold ambient gas (from our analysis of ^{12}CO lines, see Tab. 8.8, Chapter 8). Higher boundary: assuming $T_{\rm kin}$ = 300 K and a local density $n_{\rm H_2} = 10^4$ cm^{-3} for the warm shocked gas (from our analysis of H_2 lines, see Tab. 8.3, Chapter 8).
d Lower boundary: assuming a local density $n_{\rm H_2} = 10^2$ cm^{-3} for the quiescent ambient gas (from our analysis of ^{12}CO lines, see Tab. 8.8, Chapter 8) and velocity dispersion Δv = 5 km s^{-1} (Fig. 6.16). Higher boundary: assuming a local density $n_{\rm H_2} = 10^4$ cm^{-3} for the turbulent shocked gas (from our analysis of H_2 lines, see Tab. 8.3, Chapter 8) and a velocity dispersion Δv = 30 km s^{-1} (Fig. 6.16).
e For an upper limit B = 150 μG, assuming identity with the measurements in clumps B, C and E (Koo *et al.*, 2010).
f Ackermann *et al.* (2013) ("To explain the gamma-ray luminosity, the CR energy density in the clouds should be ~ 400 eV cm^{-3}").

Table 1.3 Comparison of the energy densities in the local ISM and in a typical evolved SNR. The values $u_{\rm ISM}$ (second column) are reproduced from Draine (2011). The values $u_{\rm SNR}$ (third column) are estimated from measurements in the supernova remnant region IC443G (see notes below the table).

Chemical impact of SNRs: *i.* dust formation Stellar winds are strong candidates for the synthesis of cosmic dust, but they cannot fit the short timescales needed to explain the infrared observations in high redshift galaxies (Dunne *et al.*, 2003). Synthesis of dust requires chemical processes that take place at temperature $T \sim 1000 - 2000$ K and high gas densities, thus corresponding to the conditions met in evolved stellar outflows or winds and ejecta of novae and supernovae (Kozasa *et al.*, 2009). It is believed that CCSNe are a prime and most efficient source of dust (Wooden *et al.*, 1993), as the observations support the existence of dust in the ejecta of young SNRs, where the dust can be detected through IR excess (Danziger *et al.*, 1989), intensity decline of the optical curve (Whitelock *et al.*, 1989) and blue-shift displacement of emission lines (Lucy *et al.*, 1989).

Confusion between the pre-existing swept-up ISM dust and the newly formed dust is an issue that can be partially solved by targeting very young SNRs. Observations of very young SNRs confirmed that SNe are dust factories. In SN1987A for example, the time evolution of dust thermal emission has been recorded and the presence of dust in the ejecta was confirmed by high-resolution ALMA observations (Indebetouw *et al.* 2014, Matsuura *et al.* 2015). Dust formation was also observed in the Crab nebula towards the dense filaments where the dust is heated by synchrotron radiation (Gomez *et al.*, 2012). A current issue with the observational studies of dust synthesis is the measurement of dust masses, that differ by two orders of magnitude between IR and sub-millimeter observations.

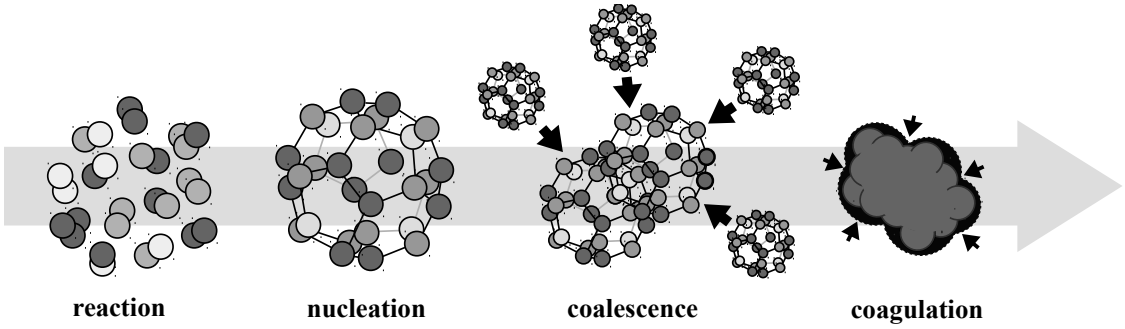

Figure 1.12 Schematic representation of the nucleation (reaction, nucleation) and condensation (coalescence, coagulation) chemical phases leading to the synthesis of molecules, precursor clusters and dust grains in the ejecta of young SNRs. For the sake of simplicity, only C_{28} clusters are represented, but many other clusters participate in the synthesis (Sarangi *et al.*, 2018).

Dust formation is a complex interplay between several physical and chemical mechanisms. The formation of dust grains starts within a year after the SN explosion, and continues for a few years. Theory predicts that a mass 0.02 $M_\odot$ to 0.2 $M_\odot$ is produced (Sarangi *et al.*, 2018), but observations range from 10^{-6} $M_\odot$ to 1 $M_\odot$ (Todini and Ferrara 2001, Nozawa *et al.* 2003). Chemical kinetic models (Cherchneff and Lilly, 2008) are built on the assumption that the processes of dust formation are occurring out of thermodynamic equilibrium. Chemical networks, *i.e.* large sets of chemical reactions coupled to each other have been used to model the formation of dust (*e.g.* Cherchneff and Dwek 2010). The post-explosion abundances are given by nucleosynthesis studies and simulations of the ejecta (Woosley and Weaver 1995, Thielemann *et al.* 1996). The formation process can be described by two phases:

- *Nucleation phase.* The nucleation phase starts within a year from the explosion (hence, during the free expansion phase), and then goes on for a couple of years in the He-rich core of the ejecta. The nucleation process is modeled by a network of reactions in the gas phase. During this stage, clusters of molecules such as $(SiO)_5$, $(MgSiO_3)_2$, C_{28} and Mg_4 start to build up in combination with regular molecules such as CO, SiO, SO, O_2, CS (Sarangi *et al.* 2018 and references therein).

- *Condensation phase.* Following nucleation, the next step is condensation, during which dust precursors in the ejecta grow by coalescence and coagulation of the aforementioned clusters (see Fig. 1.12). This stage is controlled by physical processes such as Brownian diffusion, convective Brownian motion enhancement, gravitational collection, turbulent inertial motion and Van der Waals interactions.

These models predict dust grains made mainly of silicates, amorphous carbon, alumina, silicon, iron and magnesium, but the respective abundances of C-rich and O-rich dust grains depends on the mass of the progenitor.

Chemical impact of SNRs: *ii.* dust destruction and survival Re-processing by the reverse shocks might cause erosion or destruction of the dust grains formed in the cavity of the SNR. Indeed, dust grain destruction is expected in fast shocks (velocity higher than 100 km s^{-1}, Jones

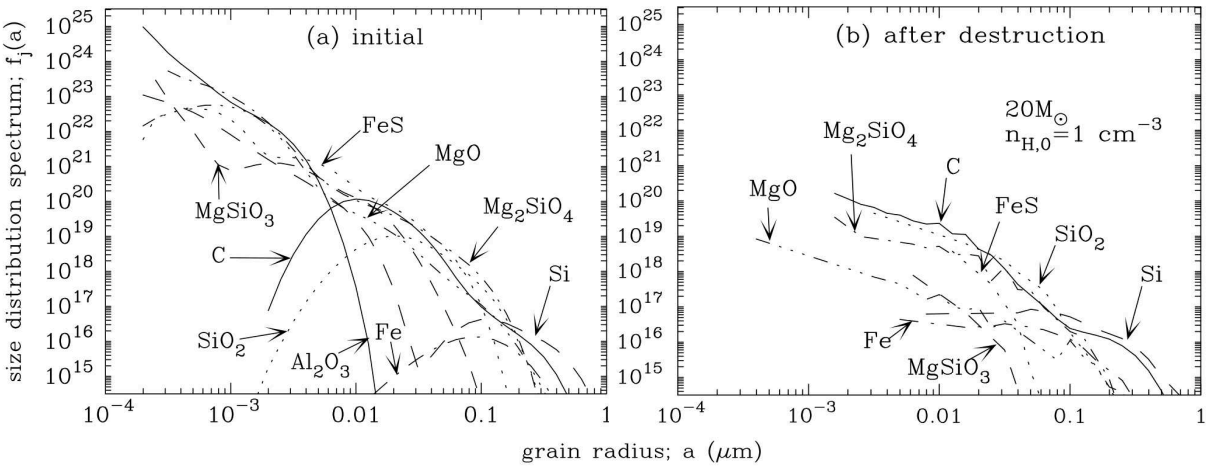

Figure 1.13 Size distributions of the synthesized dust before and after re-processing by the reverse shocks in SNRs. Figure reproduced from Nozawa *et al.* (2007).

et al. 1994), and the destruction rate increases with shock velocity. In the meantime, the forward shock processes and destroys the pre-existing CSM dust. Therefore, shock models are required to determine the role of SNRs both as dust source and sink. In particular, determining the destruction rate of dust by reverse shocks is crucial to know how SNRs effectively integrate new dust in the ISM. In Cas A, De Looze *et al.* (2017) found that the reverse shock destroyed up to 70% of the freshly formed dust, but this fraction varies between 10% and 50% for other SNRs (Micelotta *et al.* 2018b and references therein). Several processes participate in dust erosion and destruction through collisions. Grain-grain collisions can enable fragmentation (shattering) or complete vaporisation of dust grains. Collisions between gas-phase particles and dust grains will lead to either *i.*) ejection of atoms from the grain surface (mantle sputtering, Cowie 1978, Barlow 1978, Tielens *et al.* 1994), *ii.)* dust grain shattering (core sputtering, or *erosion*, Field *et al.* 1997, Flower and Pineau des Forets 1995, Flower *et al.* 1996, May *et al.* 2000) or *iii.*) solid to gas phase transitions caused by heating of the grain (*i.e.* sublimation).

Attempts at modeling the survival rate of dust into the radiative phase of evolved SNRs show that the total destruction rate spans 20% to 100% depending on the initial blast energy E_0 and density of the ambient ISM (Nozawa *et al.* 2007, see Fig. 1.13). Smaller dust grains (radius $a < 0.05$ µm) might be completely destroyed in the reverse-postshock region, but the 0.05 – 0.2 µm dust grains could be trapped in the dense shell while large grains (radius $a > 0.2$ µm) are ejected in the ISM. Thus, it is likely that the survival of dust synthesized in the first stages of SNR evolution can partially account for the FIR emission mechanisms observed in the shells of old, evolved SNRs. Thereupon, Pinheiro Gonçalves *et al.* (2011) presented a total of 39 detections at 24 µm and 70 µm in SNRs using *Spitzer*-MIPS, and Reach *et al.* (2006) found 18 detections with IRAC at 3.6, 4.5, 5.8 and 8 µm. Andersen *et al.* (2011) presented *Spitzer*-MIPS and IRS observations of 14 SNRs and proposed that dust shattering can account for the overabundance (by a factor 2-3) of small grains. Tappe *et al.* (2006) reported the detection of polycyclic aromatic hydrocarbons (PAH) in the SNR N123D (age ~2500 years) and found that large PAHs are more likely to survive shocks (Rho *et al.*, 2011).

Chemical impact of SNRs: *iii.* molecule synthesis and re-processing by shocks SNRs also have a great impact on gas-phase synthesis and chemistry. From the first seconds of a SN event during which the explosion releases synthesized elements heavier than iron through rapid neutron capture (r-process, Wagoner *et al.* 1967) to the specific shock chemistry occurring in evolved SNRs, the ISM is enriched by the formation of new elements and molecules. The first molecules detected in a young SN ejecta (as early as 100 days post-explosion) were the key diatomic species CO and SiO (in SN1987A, Cherchneff and Sarangi 2011; in the Type II SNe SN1995ad, Spyromilio and Leibundgut 1996, SN1998s, Gerardy *et al.* 2000).

It should be noted that there are mainly two types of molecular species formed in young SNe: those involved in the formation processes of dust, and those only depleting gas-phase elements (*e.g.* CO, H_2, O_2). For example, in the early phase of the SNR ($\sim 10^2$ days past explosion), the gas-phase abundance of SiO quickly declines as it depletes into dust (Kotak *et al.*, 2009). Observations strongly support that SNe are a prime source of molecules, like in SN1987A where the formation of CO was detected 112-136 days after the explosion, as well as SiO, CO^+, CS, H_3^+ and H_2; or in the Cas A SNR where CO was also detected (Rho *et al.*, 2009).

Recent efforts were made to improve the modelization of chemical formation and include the synthesis of several additional molecules in SN ejecta (see Petuchowski *et al.* 1989, Lepp *et al.* 1990 for previous models). Cherchneff and Lilly (2008) proposed an approach based on chemical kinetics, with a large network of reactions determining the formation of CO and SiO mainly, but also O_2, CO_2, SiS, SO, H_2. They showed that molecules form very efficiently in the ejecta of massive SNe, accounting for 10% to 40% of the total progenitor mass. The exact abundances of the different formed species depends on the mixing in the ejecta. In particular, mixing of the He core with the hydrogen envelope favors molecular formation. Similarly to dust, the question of the survival of molecules after the re-processing by the reverse shock is fundamental to determine if SNe do enrich their environment with new molecular material. Biscaro and Cherchneff (2014) found that the molecules formed in the first stage are destroyed by reverse shocks, and then reform in the postshock regions. In evolved supernova remnants, the gas-phase chemistry is ruled by the propagation of slow shocks ($v < 100$ km s^{-1}, see section 1.2 for a complete description of shock chemistry in evolved SNRs).

1.1.3.3 Interaction of SNRs with molecular clouds

Evolution of massive stars CCSN progenitors are massive stars (≥ 8 $M_\odot$) that surge through the stellar evolutionary sequence within short timescales (as short as a few million years for the most massive stars, Woosley *et al.* 2002). As a consequence, massive stars might reach the end of their life while they are still embedded in the molecular cloud in which they formed. From an observational perspective, McKee and Cowie (1975) studied SN-cloud interaction in SNRs where the blastwave is driven into interstellar clouds (see Fig. 1.15). Their model can explain the observed characteristics of quasi-stationary floculi in the young SNR Cas A (Reed *et al.*, 1995), as well as optical filaments in old SNRs such as the Cygnus Loop. These bright filaments are viewed as shocked interstellar clouds in which a *secondary shock* is driven with a far lower velocity than the blast expanding in the intercloud medium (*main shock*). Using the notations defined in Fig. 1.15, the velocity of the secondary shock is $v_c \sim v_b(\rho_0/\rho_c)^{1/2}$ (with $\rho_0 \ll \rho_c$, *e.g.* $\rho_0/\rho_c \sim 10^{-2}$).

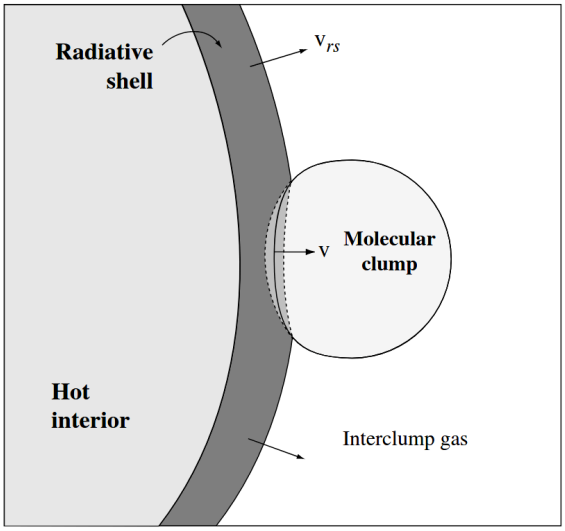

Figure 1.14 Schematic figure representing the interaction of the expanding radiative shell of an evolved SNR, moving at a velocity v_{rs}, with a molecular clump. The interaction generates a dense slab bounded by shock waves (dashed lines) and moving at a velocity v. This figure is extracted from Chevalier (1999) and corresponds to the model used by the authors to study the interaction of a SNR with a clumpy molecular cloud.

Figure 1.15 Schematic representation of the shockwaves that occur when a blast wave produced by a supernova overtakes a cloud of density ρ_c. The gas in region 1 is the hot gas behind the blastwave, region 2 is just behind the bow shock, point 3 is the stagnation point at the surface of the cloud, and region 4 contains the gas which has passed through the cloud shock. The cloud shock moves at velocity v_c; the blastwave shock moves at velocity v_b into the ambient medium of density ρ_0. Figure reproduced from McKee and Cowie (1975).

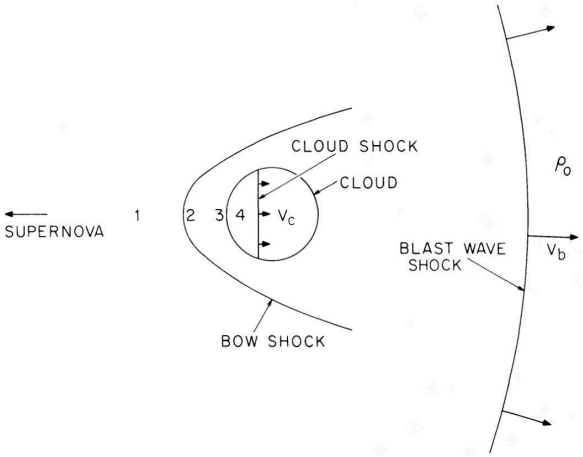

Chevalier (1999) studied the interaction of SNRs with molecular clouds from a theoretical point of view (see Fig. 1.14). Firstly, this kind of interaction is much more likely for the lower end of massive progenitors (early B1-B3 stars, $M \leq 12$ M$_\odot$) because the stellar winds of higher mass stars can clear large regions (> 20 pc) of molecular material, preventing any interaction with the SNR in the "early" phase of the expansion (*i.e.* in the first 10-20 kyr, see Tab. 1.2). Thus, a fraction of Type II SNRs with radius ~ 10 pc are able to interact with molecular clouds. Molecular clouds (MC) are clumpy, they can be described by a collection of dense clumps in a lower density interclump medium with a filling factor ~ 0.1 (Blitz 1993, Williams *et al.* 1995). Hence the shell of evolved SNRs entering the radiative phase ($r \sim 5$ pc) will interact with these dense clumps.

There are several conspicuous candidates for SNR-MC interaction. Frail *et al.* (1996) presented a total of 8 SNRs that show strong OH maser emission, but the most detailed observations are available for W44, W28, W51C and IC443 (Wootten 1981, Koo and Moon 1997a). Shock-excited masers are "signposts" of SNR-MC interaction, since their emission originates from post-shock molecular gas heated by the passage of the SNR through dense molecular gas (Claussen *et al.* 1997a, Koralesky *et al.* 1998, Frail and Mitchell 1998). Therefore, they also allow to localize candidate sites of cosmic-ray acceleration (see section 1.4). From the observations of W44 and IC443, Seta *et al.* (1998) showed that an enhanced ^{12}CO J=2–1/J=1–0 ratio is also a marker of SNR-MC interaction.

SNR feedback on molecular clouds: shocks and particle acceleration Targeted studies of SNRs interacting with molecular clouds show that the mechanical feedback has a substantial impact on the evolution of molecular clouds. Hewitt *et al.* (2009b) reported *Spitzer*-IRS observations of 6 SNRs interacting with MCs. In these SNRs, evidence of shocked molecular gas is given by the presence of the bright pure rotational lines of H_2 S(0) to S(7). Near-IR and millimeter observations in W28 and W44 reveal the extensive presence of shocked H_2 and CO in regions where the blastwave interacts with MCs (Reach *et al.*, 2005). *Spitzer*/IRS observations of the SNRs W44, W28, IC443, 3C391 led to the detection of fine-structure atomic and ionic transitions that originate from slow, nondissociative shocks driven by the remnants (Neufeld *et al.* 2007, Yuan and Neufeld 2011).

In the SNRs W28 and 3C391, *Herschel*/PACS detected H_2O, CO, OH molecular lines and additional fine-structure transitions with fluxes in agreement with models of nondissociative shocks (Neufeld *et al.*, 2014). In the upcoming section 1.2, we will describe into much more details the shock propagation and feedback in SNRs. The particular class of SNRs interacting with MCs also constitute efficient CR accelerators. Models of nonthermal particle injection, acceleration and propagation both in the interclump medium and where the radiative shell interacts with dense clumps show that these regions are sources of hard X-rays and γ-rays (Bykov *et al.* 2000, Torres *et al.* 2003, see section 1.4). Finally, studies of the mechanical feedback of SNRs based on hydrodynamical simulations show that the momentum delivered to dense gas varies by a factor 10 depending on the location of the progenitor with respect to the primordial MC in which it is born, and that a significant fraction of the cloud mass is removed by the explosion (*e.g.* Hennebelle and Iffrig 2014, Iffrig and Hennebelle 2015, Geen *et al.* 2016). We will discuss the impact of SNRs on star formation in section 1.3.

1.2 | Shocks in supernova remnants

1.2.1 Interstellar shocks

Definition A shock is an irreversible[6], pressure-driven fluid dynamical disturbance propagating at a supersonic speed ($v_s > c_s$, where v_s is the disturbance velocity and c_s the sound or signal speed). Supersonic motions require strong pressure gradients generated by the localized injection of large amounts of kinetic energy. At a critical pressure level, a shock front will develop at the leading edge of the disturbance. This is caused by the fact that the shock velocity does not allow the preshock medium ahead of the shockwave to dynamically respond before the shock strikes. In this region where a discontinuity of hydrodynamical variables occurs, the flow is referred to as a shock.

Shocks are ubiquitous in the ISM, since *i.)* the sound speed is small in low-density and low-temperature environments, and *ii.)* the ISM is intermittently disturbed by energetic events releasing kinetic energy that cascades to high-velocity motions of the gas. Hence, supersonic motions are a common phenomenon in our universe, and they represent an important component of the energy budget. There are many sources of shocks (stellar winds, outflows, expanding H II regions,

[6]Shocks are irreversible because entropy is generated when kinetic energy is dissipated into heat (which is then converted into radiation *via* the excitation of chemical species). We describe the mechanisms of energy dissipation in the next paragraphs.

Galactic arms, cloud-cloud collisions, *etc*) but we focus here on the impact of evolved SNRs. We can define the shock strength based on the Mach number $\mathcal{M} = v_s/c_s$, where c_s is the sound speed ahead of the shock. The Mach number can be up to 10^3 in the ISM, which is far larger than what can be obtained in laboratory experiments. In fact, young SNRs provide the strongest shocks, since the velocity of the blastwave is $\sim 10^4$ km s^{-1} during the free-expansion phase. In evolved supernova remnants, the velocity of shocks is $\sim 10 - 10^2$ km s^{-1}, corresponding to a Mach number ~ 10.

There is an abundant literature on hydrodynamical, magneto-hydrodynamical shockwaves (Landau and Lifshitz 1959, Zeldovich and Raizer 1966) and interstellar shocks (McKee and Hollenbach 1980, Hollenbach and McKee 1989, Draine and McKee 1993, Draine 2011, Tielens 2005). In the following sections, we will only provide a description of the essential knowledge required to understand the characteristics of interstellar shocks observed in SNRs.

1.2.1.1 The Rankine-Hugoniot jump relations

Jump conditions In an hydrodynamical shock discontinuity, the density, pressure and velocity variables jump from the preshock to the postshock states of the fluid. These jump conditions can be derived from the fluid equations. The fluid equations are based on the conservation of mass, momentum, energy and magnetic flux (Draine and McKee, 1993):

$$\frac{\partial \rho}{\partial t} + \frac{\partial}{\partial x_k}(\rho v_k) = 0 \tag{1.27}$$

$$\frac{\partial}{\partial t}(\rho v_j) + \frac{\partial}{\partial x_k}\left(\rho v_j v_k + P\delta_{jk} - \sigma_{jk} + \frac{B^2}{8\pi}\delta_{jk} - \frac{1}{4\pi}B_j B_k\right) = 0 \tag{1.28}$$

$$\frac{\partial}{\partial t}u + \frac{\partial}{\partial x_k}(uv_k + q_k) + (P\delta_{jk} - \sigma_{jk})\frac{\partial v_j}{\partial x_k} + \frac{\partial F_k}{\partial x_k} = 0 \tag{1.29}$$

$$\frac{\partial}{\partial t}B_j + \frac{\partial}{\partial x_k}(v_k B_j - v_j B_k) = 0 \tag{1.30}$$

where ρ, v, and P are the density, velocity and pressure; B is the magnetic field, u is the fluid energy density ($u = (3/2)P + u_{\rm int}$, where $u_{\rm int}$ is the internal energy density), q is the heat flux due to thermal conduction, F is the radiative flux, and σ_{jk} is the viscous stress tensor.

The Rankine-Hugoniot equations can be derived in a purely hydrodynamical shock (in which the magnetic field is zero). Under these conditions, we have:

$$\frac{\partial \rho}{\partial t} + \frac{\partial}{\partial x_k}(\rho v_k) = 0 \tag{1.31}$$

$$\frac{\partial}{\partial t}(\rho v_j) + \frac{\partial}{\partial x_k}\left(\rho v_j v_k + P\delta_{jk} - \sigma_{jk}\right) = 0 \tag{1.32}$$

$$\frac{\partial}{\partial t}u + \frac{\partial}{\partial x_k}(uv_k + q_k) + (P\delta_{jk} - \sigma_{jk})\frac{\partial v_j}{\partial x_k} + \frac{\partial F_k}{\partial x_k} = 0 \tag{1.33}$$

In a strong ($\mathcal{M} \gg 1$) purely transverse, plane-parallel steady hydrodynamical shock, the jump conditions describing the transition from the preshock to the postshock variables (ρ_2, v_2, T_2) are:

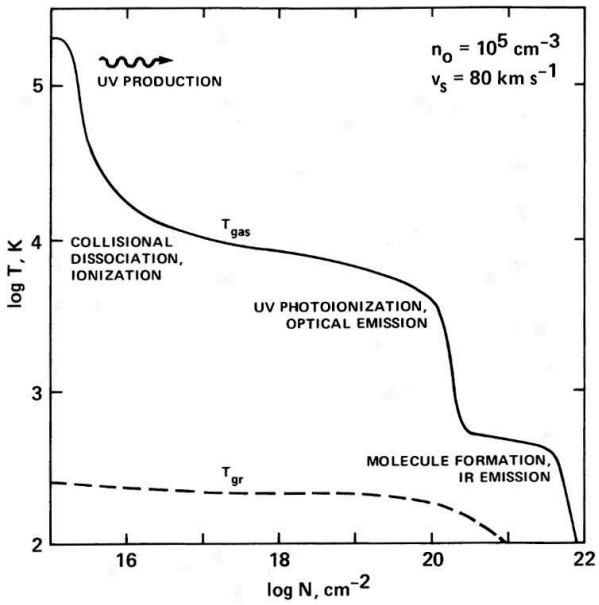

Figure 1.16 The postshock temperature structure of a fast molecular shock (v_s = 80 km s^{-1}). Three regions are delineated: *i.)* the hot, $T \sim 10^5$ K, immediate postshock region, where gas is collisionally dissociated and ionized and UV photons are produced which affect both the preshock and postshock gas *ii.)* the recombination plateau, where the Lyman continuum photons are absorbed, maintaining $T \sim 10^4$ K; and *iii.)* the recombining and molecule forming gas downstream, where chemical energy of H_2 formation can maintain a lower temperature plateau. Note that the grains are weakly coupled to the gas, so that $T_{\rm grain} \ll T_{\rm gas}$. Figure from Hollenbach and McKee (1989).

$$\frac{\rho_2}{\rho_1} = \frac{\gamma+1}{\gamma-1} \tag{1.34}$$

$$v_2 = \frac{\gamma-1}{\gamma+1} v_s \tag{1.35}$$

$$T_2 = \frac{2(\gamma-1)}{(\gamma+1)^2} \frac{\mu v_s^2}{k_B} \tag{1.36}$$

Where v_s is the shock velocity ($v_s \equiv v_1$), γ is the adiabatic index, k_B is the Boltzmann constant, ρ_1 is the preshock density and μ the molecular weight. Thus, for $\gamma = 5/3$, there is a factor 4 between the upstream and downstream densities and velocities.

1.2.1.2 Structure of an interstellar shock

Shocks heat, compress, accelerate, and possibly dissociate and ionize the gas (for a shock velocity $v_s \geq 30$ km s^{-1}). Their exact structure depends on the preshock density, ionization fraction, magnetic field and the shock velocity. Before we describe in details the respective properties of the different types of shocks (fast, slow, radiative, externally irradiated, two-fluids C-type and J-type shocks, *etc.*) we will give a general description of the structure of a shock based on the model of Hollenbach and McKee (1989), corresponding to fast ($v_s = 30 - 150$ km s^{-1}), steady interstellar shocks in molecular gas at densities $n_0 = 10^3 - 10^6$ cm^{-3}. In fact, the most simple shock structures are those found in slow molecular shocks ($v_s \leq 30$ km s^{-1}), but we aim to give a preliminary description that is as broad as possible. Following McKee and Hollenbach (1980) we can describe the structure of a shock by three distinct regions:

***i.)* Radiative precursor** Radiative precursors are radiation fields generated by the downstream shocked gas which can heat, dissociate and ionize the upstream gas. Under these conditions, the shock is described as '*self-irradiated*'. The existence and strength of the radiative precursor depends on the velocity of the shock and local density: self-irradiated shocks are expected if v_s is

large ($v_s \gg 25$ km s^{-1}). In these fast shocks, the ionizing radiation generated by the cooling gas produces a strong radiation field of UV to soft X-ray photons. The photo-ionization front driven in the preshock gas forms a precursor ahead of the fluid shockwave, called the *radiative precursor*. In self-irradiated shocks, molecules and atoms in the upstream gas are ionized and dissociated by the precursor before the hydrodynamical shock strikes.

***ii.)* Shock front** The shock front is a thin region with increased density and temperature (following the Rankine-Hugoniot jump conditions). In a region of thickness smaller than one mean free path[7], the hydrodynamical variables jump from their preshock to postshock values. In this region, the shock heats, accelerates and compresses the gas. The heating is applied to the gas through the dissipation of the kinetic energy. The dissipation is regulated by three different classes of mechanisms depending on the nature of the shock: *i.)* molecular viscosity in high-density, low-velocity molecular shocks; *ii.)* collective motions of charged particles in collisionless, low-density plasma shocks; *iii.)* neutral-ion friction in partially ionized gases. Above a critical shock velocity, molecular species can be collisionaly dissociated in the shock front, possibly increasing the cooling time in the postshock gas (the dominant molecular coolant H_2 can be dissociated if $v > 25$ km s^{-1}, Kwan *et al.* (1977), although O I and C II can also be efficient coolers in dense media).

***iii.)* Relaxation layer** the postshock region or relaxation layer is the area where the gas cools and chemical reactions occur. Figure 1.16 shows the temperature structure of the relaxation layer in a fast shock (Hollenbach and McKee, 1989). In the atomic gas at very high temperature (10^4 K $< T < 5 \times 10^5$ K), the dominant excitation processes that regulate the cooling are the inelastic electronic collisions, but neutral fine structure lines of protons and recombination lines of ionized He, C, N and O contribute as well. At $T < 5 \times 10^3$ K, fine structure transitions of C II, Si II and O I dominate the infrared emission. As the postshock gas cools down, the formation of molecules through high temperature chemical reactions ($T > 1000$ K) produces high abundances of certain molecular species (H_2, OH, CO, H_2O, CH^+, OCS, SO, H_2, SiO). In molecular relaxation layers, H_2, CO, OH, NH_2, CH_3OH and H_2O dominate the cooling *via* the emission of rotational and vibrational infrared lines (Neufeld and Kaufman, 1993). H_2 is the dominant coolant, because it is the most abundant molecule in the ISM. In addition it is an homonuclear molecule, hence it has a negligible line opacity (Le Bourlot *et al.*, 1999).

1.2.1.3 Magnetic precursors

Effect of the magnetic field on magneto-hydrodynamical (MHD) shocks Until now we did not describe the effect of the magnetic field on the dynamics of interstellar shockwaves. If we consider a partially ionized fluid of density ρ_0 in a local magnetic field B_0, the magnetosonic speed is defined by:

$$v_{ms} = \frac{B_0}{\sqrt{4\pi\rho_0}} \tag{1.37}$$

Hence if $v_{ms} > v_s$ for a large enough B_0, then magnetosonic waves (*i.e.* MHD compressive waves) might propagate in the upstream ionized fluid, ahead of the hydrodynamical shock. If the ionization fraction x is different from zero, and not large enough for neutrals and charged particles to

[7] This is true only for J-type shocks, see the next sections.

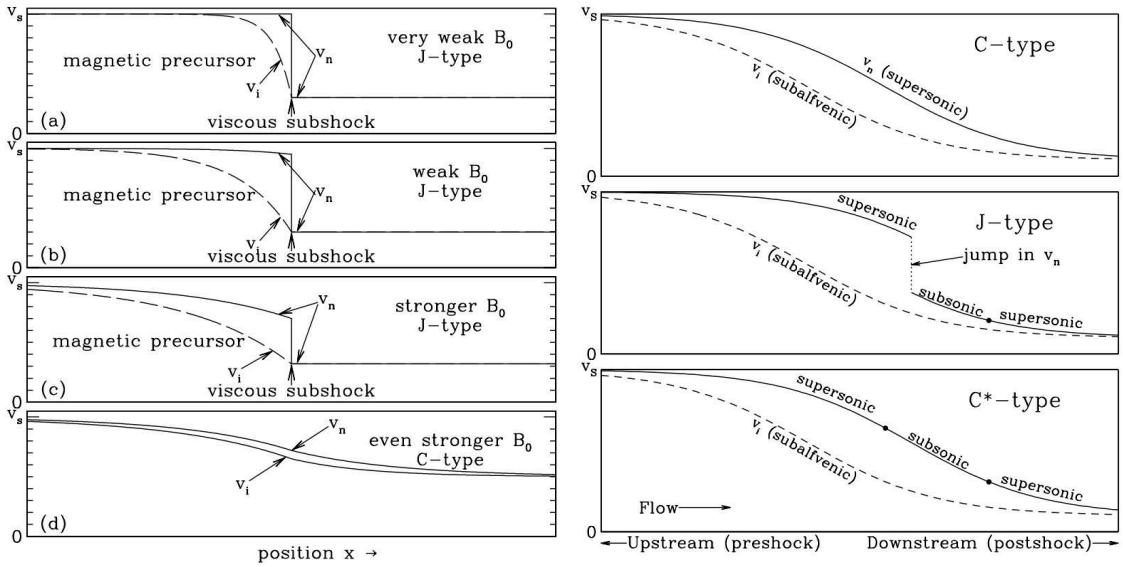

Figure 1.17 *Left panel:* Sequence of two-fluid shocks, with different values of preshock magnetic field strength B_0. As the magnetic field strength B_0 is increased, the magnetic precursor extends further ahead of the viscous subshock (the discontinuity in the neutral velocity), and produces more deceleration of the neutrals. For large enough B_0, the neutrals are decelerated entirely by the magnetic precursor, and the shock becomes C-type. Figure reproduced from Draine (2011). *Right panel:* schematic structures of two-fluid shock waves showing velocities of the neutral and ionized fluids relative to the shock front. Three types of solutions are possible: C-type, J-type, and C* type. Velocities are relative to the shock front. Figure reproduced from Draine and McKee (1993).

be collisionally coupled ($x \ll 10^{-3}$, Mullan 1971) then ions, driven by the magnetic field, stream through the neutrals with a fraction of the shock speed, heating and compressing the upstream gas. This is referred to as a magnetic precursor (Draine, 1980).

J-type and C-type shocks If the magnetic field is large enough, the impact of the magnetic precursor can entirely remove the discontinuity in hydrodynamical variables (see Figure 1.17). This characteristic of two-fluid MHD shocks allows us to introduce two physically distinct classes of shocks: J-type shocks (jump) and C-type (continuous) shocks. In C-type shocks, the variables transition smoothly from preshock to postshock values as a result of the action of the magnetic precursor on the ionized fluid ahead of the shock. The transition from J-type to C-type shocks depends both on the amplitude of the magnetic field and ionization fraction of the gas. In fact, if the ionization fraction is large enough ($x \gg 10^{-3}$), then ionic and neutral species are coupled by friction, and both fluids dynamically react to the perturbation as a whole (*i.e.* the flow can be described by a single fluid). Under these conditions, a J-type shock will occur regardless of the existence of a magnetic precursor. Additionally, C* type shocks are a distinct class of C-type shocks in which a transition to a subsonic flow occurs continuously at a sonic point (in the reference frame of the shockwave, see Figure 1.17, Chernoff 1987, Roberge and Draine 1990, Godard *et al.* 2019).

Shock models in supernova remnants Supernova remnants represent a unique opportunity to test shock models. The injection of 10^{51} erg of kinetic energy into the environment produces fast

shocks that gradually decelerate to lower velocities and interact with interstellar clouds, covering a wide range of shock types and conditions. There cannot be a single model used to study shocks in SNRs, since a large range of velocities ($1 - 10^4$ km s^{-1}), preshock densities ($10^{-2} - 10^7$ cm^{-3}), magnetic fields (1 μG – 5 mG) and ionization fractions ($10^{-8} - 10^{-1}$) can be found in these objects. Several models of steady plane-parallel shocks have been proposed over the past decades (*e.g.* Cox 1972a, Dopita *et al.* 1977, Raymond 1979, Hollenbach and McKee 1979, Hollenbach and McKee 1989).

In the next sections we give a chronological description of the shock models best-suited to each stage of SNR evolution, going from fast shocks (in the early phase of the SNR) to slow molecular shocks (in evolved supernova remnants). In our following description of various shock models, we will ignore collisionless shocks (in which the energy is dissipated *via* wave-particle interaction instead of particle-particle collisions). Most importantly, collisionless shocks accelerate cosmic rays efficiently *via* first order Fermi acceleration (Blandford and Eichler 1987, Jones and Ellison 1991, Malkov and Drury 2001, see section 1.4).

1.2.2 Fast shocks ($10^2 < v < 10^3$ km s^{-1})

Fast shocks ($10^2 < v < 10^3$ km s^{-1}) propagate in young supernova remnants (during the free-expansion phase and early Sedov-Taylor phase, *i.e.* during the first few thousands of years of SNR evolution, see section 1.1.1).

MAPPINGS: fast shocks ($v \gg 10^2$ km s^{-1}) The MAPPINGSIII shock model allows to study interstellar shocks with velocities $v_s = 100 - 1000$ km s^{-1}, magnetic fields $B_0 = 10^{-4} - 10$ μG and preshock densities $n_0 \sim 1$ cm^{-3} (Allen *et al.* 2008, see Sutherland *et al.* 1993 for a description of the previous version: MAPPINGSII). Young SNRs are characterized by fast shocks ($v_s \sim 10^2 - 10^3$ km s^{-1}) during the first thousand years of the blastwave propagation. These high-velocity radiative shocks generate strong local UV photon fields. If the shock is fast enough ($v_s > 170$ km s^{-1}) the ionizing radiation of the hot gas produces a radiative precursor in the upstream gas. The optical emission within the shock front and precursor region is dominated by the photoionized gas, rather than the cooling layers (Dopita and Sutherland, 1996). The computational steps of MAPPINGSIII for the modeling of fast shocks with radiative precursors are the following: *i.)* first an initial shock model is computed; *ii.)* then the photoionized precursor is modeled based on the radiation field returned by the initial shock model; *iii.)* this scheme is repeated, updating the ionization state at each step.

The MAPPINGS shock model is mostly used to study stellar shocks in star-forming galaxies (*e.g.* Ho *et al.* 2014, Rich *et al.* 2010), but it can also be applied to fast radiative shocks found in SNRs interacting with interstellar clouds, in particular towards high-velocity optical filaments (Sutherland *et al.* 1993, *e.g.* Kim *et al.* 2014 in the Cygnus Loop). Most recently, Alarie and Drissen (2019) analyzed the optical emission lines of fast shocks in the IC443 SNR using MAPPINGS. In the northeastern shell of the remnant mapped with the imaging Fourier transform spectrometer SITELLE (CFHT), the shock velocities determined by the model are between 20 and 150 km s^{-1}.

Earlier models and observations of moderately fast shocks in SNRs ($v_s \sim 10^2$ km s^{-1}) As the SN blast wave propagates in the ISM for several thousand years, the velocity of shocks decreases.

The first interstellar shock models developed around the 70s were appropriate for SNRs in the Sedov-Taylor phase and beyond ($v_s \sim 10^2$ km s^{-1}).

Cox (1972a) described the flow structure and luminosity of a plane shockwave, providing the first framework to study interstellar shocks in relatively evolved SNRs (past the free-expansion phase). Based on the observations of the Cygnus Loop SNR filaments and the assumption that these structures are planar sheets of shocked material seen edge-on (Poveda 1965, Parker 1967, Hester 1987), he found that the cooling of the shock heated gas can account for the observed luminosity in O I and Hα for $n_0 = 6$ cm^{-3} and $v_s \sim 100$ km s^{-1}. Dopita *et al.* (1977) analyzed the optical emission from shockwaves in several Galactic and Magellanic clouds SNRs (including Vela X, Puppis A, RCW 89, W 28) and derived elemental abundances based on the line intensities predicted by moderately fast shock models. Raymond (1979) proposed a calculation of the optical and UV emission line intensities in plane-parallel, steady state shocks and compared the results with observations in the Cygnus Loop and Vela SNRs (Raymond *et al.*, 1981).

Among other issues, these early studies explored the possibility to distinguish H II regions from SNRs based on the comparison of observations with line intensities predicted by shock models. Hollenbach and McKee (1979) introduced a shock model for $v_s > 25$ km s^{-1} (updated by Hollenbach and McKee 1989 for 25 kms^{-1} $< v_s <$ 150 km s^{-1}). At 25 km s^{-1}, the velocity of the shock is sufficient to dissociate any preexisting molecule in the gas, and yet molecules are still observed in high-velocity shocks (*e.g.* Shull *et al.* 1977, Kwan and Scoville 1976), including fast SNR shocks (*e.g.* in the W51C SNR interacting with a molecular cloud, Koo and Moon 1997b). Based on chemical networks, shock models like the one introduced by Hollenbach and McKee (1979) can account for the re-formation of H_2 on dust grains in the postshock gas, as well as the formation of several other molecular species (CO, OH, H_2O, *etc.*, see following developments). Refractory grains (graphite, silicate) are expected to survive if $v_s < 300$ km s^{-1} (Draine and Salpeter 1977, Jones *et al.* 1994), hence the postshock gas can be molecular under a wide variety of conditions in fast shocks.

1.2.3 Molecular shocks in evolved supernova remnants ($v < 60$ km s^{-1})

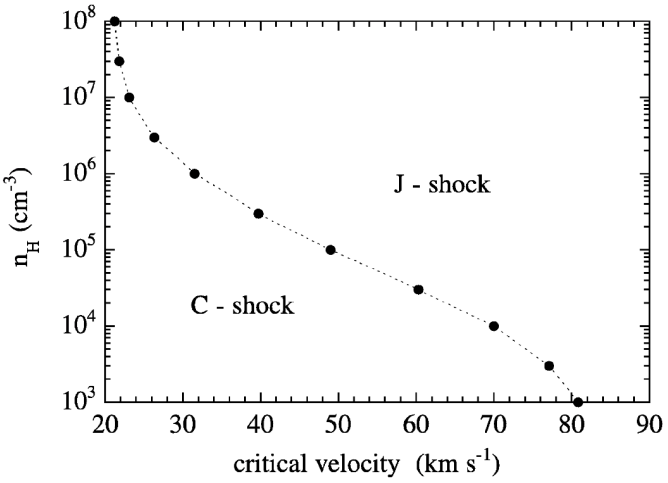

Figure 1.18 Maximum shock velocity, v_{crit}, consistent with the existence of a C-type shockwave, as a function of the preshock gas density, $n = n(H) + 2n(H_2)$. The initial amplitude of the magnetic field is given by $B(\mu G) = [n_H(cm^{-3})]^{1/2}$, and the initial ortho:para H_2 ratio is 3.0. If the shock velocity is higher than v_{crit}, the flow transitions into a J-type shock. Figure reproduced from Le Bourlot *et al.* (2002). See also Fig. 1.21 for an updated description.

Slow molecular shocks ($v_s < 60$ km s^{-1}) propagate in old, evolved supernova remnants , typically in molecular shells interacting with the denser circumstellar environment (during the late Sedov-Taylor phase and Snowplow phase, *i.e.* in SNRs characterized by $t_{SNR} \gg 1$ kyr).

The Paris-Durham molecular shock code The Paris-Durham shock model provides the steady state solution of the plane-parallel MHD equations coupled with cooling functions and a chemical network appropriate to the molecular phase of the ISM (first described in Flower *et al.* 1985, see also Flower *et al.* 2003 and Flower and Pineau des Forêts 2015, with major updates in Lesaffre *et al.* 2013, Godard *et al.* 2019 and Lehmann *et al.* 2020, see the following paragraphs). Non-stationary solutions were described by Lesaffre *et al.* (2004a), Lesaffre *et al.* (2004b) (and references therein), and pseudo-multidimensional solutions were developed by Kristensen *et al.* (2008) (pseudo-2D), Gustafsson *et al.* (2010) (pseudo-3D) and Tram *et al.* (2018).

The code solves a set of coupled, first-order, ordinary differential equations (Flower, 2010) using the DVODE forward integration algorithm (Hindmarsh, 1983). The initial conditions are given by solving the chemical and thermal equations in an uniform slab for 10^7 years, so that the shock propagates in a medium at thermal and chemical equilibrium. Lesaffre *et al.* (2013) refined the model by including a treatment of photo-reactions assuming a moderate irradiation ($G_0 = 1$)[8] in magnetized shocks with densities $n_{\rm H} = 10^2 - 10^4$ cm^{-3} and low to moderate velocities (from 3 to 40 km s^{-1}).

Godard *et al.* (2019) updated the shock model in order to take into account a stronger external radiation field (up to $G_0 \sim 10^4$). Only the version by Lehmann *et al.* (2020) can reproduce self-irradiated shocks with velocities $v_{\rm s} \geq 60$ km s^{-1}. The Paris-Durham shock code was developed with low-mass star formation in sight, in order to provide a tool for the interpretation of IR and sub-millimeter spectroscopic data (Flower and Pineau des Forêts, 2015). The model is most extensively used to study molecular outflows in young stellar objects and star-forming regions (*e.g.* Louvet *et al.* 2016, Gusdorf *et al.* 2015, Tram *et al.* 2018, Benedettini *et al.* 2017), but it is also appropriate to analyze the emission of slow ($v_{\rm s} = 5-60$ km s^{-1}) molecular shocks in evolved SNR shells interacting with molecular clouds (*e.g.* Gusdorf *et al.* 2012, Anderl *et al.* 2014).

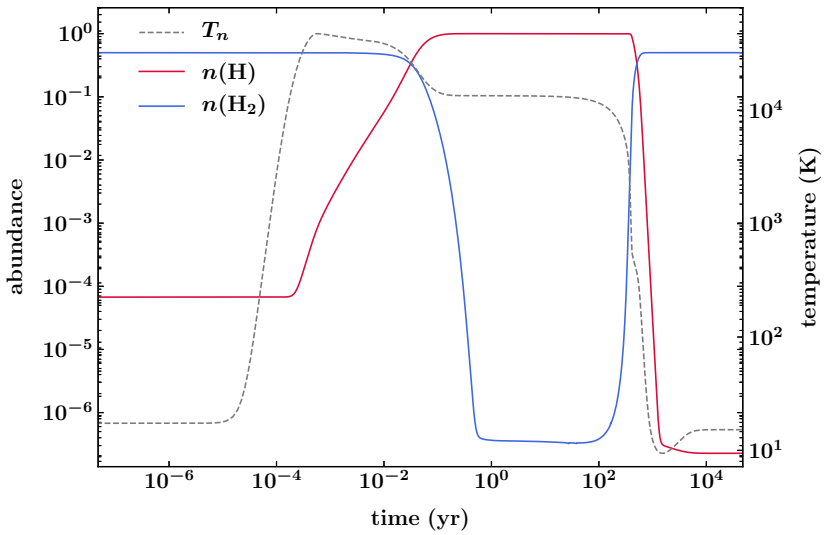

Figure 1.19 Neutral temperature ($T_{\rm n}$) and abundances of H (n(H)) and H_2 ($n(H_2)$) profiles through a J-type shockwave of speed $v_{\rm s} = 30$ km s^{-1}, preshock density $n = n$(H)+ $2n(H_2) = 10^4$ cm^{-3}, assuming a cosmic-ray ionization rate of hydrogen $\xi = 5 \times 10^{-17}$ s^{-1}. Model produced with the current version of the Paris Durham shock model (Flower and Pineau des Forêts, 2015).

H_2 emission, cooling, destruction and formation in molecular shocks H_2 is the most abundant molecule and it plays a crucial role both in chemistry (since it participates in many reactions) and in the excitation of other species (since it is an important collider). Finally, it is also an important

[8] G_0 is the 'Habing field': $G_0 = 1$ corresponds to a UV field intensity $\int_{0.09\ \mu{\rm m}}^{0.24\ \mu{\rm m}} J_\lambda {\rm d}\lambda$, where J_λ is the local interstellar radiation field, Habing (1968).

cooler. Overall, the H_2 emission lines carry the signature of the type and conditions of shocks in a given region. The excitation of H_2 rovibrational lines in J-type and C-type shocks was studied by Flower (1998), Flower and Pineau des Forêts (1999), Wilgenbus *et al.* (2000), Le Bourlot *et al.* (2002), Flower *et al.* (2003) (see also references therein). Shockwaves with velocity higher than 20 km s^{-1} collisionaly dissociate H_2 (Kwan *et al.* 1977, London *et al.* 1977), but the molecule can be formed again in the postshock gas. Figure 1.19 shows the destruction and subsequent reformation of H_2 in a fast J-type shock with velocity v_s = 30 km s^{-1}, together with the evolution of the temperature.

The formation of H_2 is the product of a catalytic reaction on the surface of interstellar dust grains (see Wakelam *et al.* 2017 for a review of H_2 formation processes), hence its efficiency also depends on the survival of dust grains in fast shocks. The formation of H_2 greatly affects the cooling time of the gas, as a consequence it plays a significant role in the thermal balance of shocks (H_2, CO and H_2O are the main coolants, Neufeld and Kaufman 1993). This is the reason why the temperature falls rapidly when H_2 is formed (see Figure 1.19, between $t = 10^2$ and $t = 10^3$ yr). Le Bourlot *et al.* (1999) computed the radiative losses of a cooling layer of H_2 collisionaly excited by H, He and H_2, including the collisional processes that modify the steady-state ortho-to-para ratio. They found that the ortho-to-para ratio can be greater than 3 in a low-density environment.

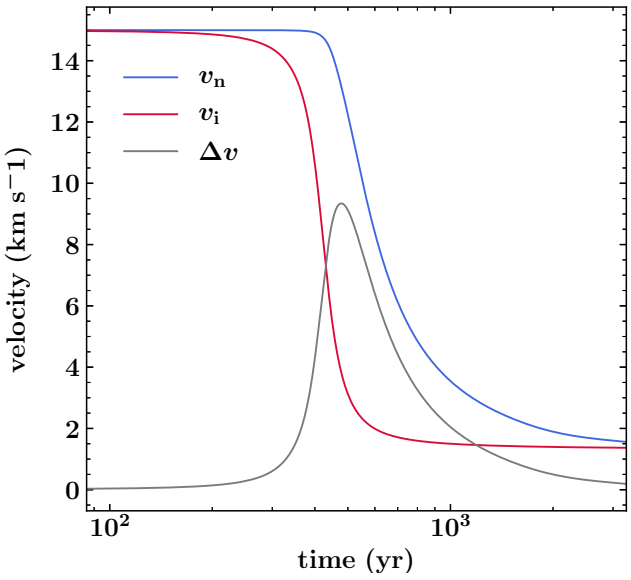

Figure 1.20 Neutral (v_n), ionic (v_i) and neutral-ion drift (Δv) velocity profiles through a C-type shockwave of speed v_s = 15 km s^{-1}, preshock density $n = n(H) + 2n(H_2) = 10^4$ cm^{-3} and magnetic field B = 100 μG; the fractional abundance of PAH is $n_{PAH}/n_H = 1.0 \times 10^{-6}$ and the rate of cosmic ray ionization of hydrogen is $\xi = 5 \times 10^{-17}$ s^{-1}. The independent variable, t, is the flow time of the neutral fluid (in years). Model produced with the current version of the Paris Durham shock model (Flower and Pineau des Forêts, 2015).

C-type molecular shocks: maximum velocity, gas-grain dynamics and sputtering Since H_2 is the main coolant, its dissociation in fast shocks causes a rapid increase in the kinetic temperature of the gas, resulting in a feedback loop and ultimately the development of a sonic point in the flow. In addition to the magnetosonic velocity value limit, this is another limit to the maximum velocity that a C-type shock can attain before it dissociates H_2 and transitions into a J-type shock. Draine *et al.* (1983) initially predicted a maximum velocity of 50 km s^{-1} for C-type shocks, but Le Bourlot *et al.* (2002) showed that the maximum speed of C-type shocks can be much higher, up to 70 – 80 km s^{-1} in low-density environments ($n \sim 10^3 - 10^4$ cm^{-3}), since the dissociation time can be higher than the flow time.

Flower and Pineau des Forêts (2003) studied the gas-grain interactions in C-type shocks, in particular the influence of the dust grains on the dynamics of the flow and shattering of interstellar

dust grains in dark molecular clouds. Charged dust grains are expected to be coupled to the magnetic field (Draine and Sutin 1987, Guillet *et al.* 2007, Guillet *et al.* 2011). In C-type shocks, a ion-neutral drift occurs because of the difference between the flow velocities of the charged (v_i) and neutral particles (v_n) (see Figure 1.20). Therefore, *via* a different mechanism than in J-type shocks (Jones *et al.* 1994, Tielens *et al.* 1994) dust grains can be shattered in C-type shocks as well. In this case, the shattering is a consequence of the collisions between neutrals and charged grains, which can be viewed as two fluids with distinct dynamics. For example, in a C-type shock of velocity $v_s = 20$ km s^{-1} the ion-neutral drift velocity can be $\Delta v = 14$ km s^{-1}, corresponding to a kinetic energy $\mu\Delta v^2/2$, where μ is the reduced mass. Assuming a single carbon bond energy $E_B = 3.6$ eV (Jones *et al.*, 1990), a relative collision speed $\Delta v = 7.5$ km s^{-1} is sufficient to shatter a grain by disrupting half of its single bonds.

Schilke *et al.* (1997) studied the sputtering of Si-bearing dust grains by neutral particle impact on charged grains in C-type shocks and showed that the production of SiO is a tracer of shocks around $v_s \sim 25$ km s^{-1}, and May *et al.* (2000) studied the sputtering of Mg- and Fe-bearing silicates. For a shock speed greater than 40 km s^{-1}, they found that up to 50% of dust grains can be destroyed in C-type shocks. The Si elements embedded in the silicate matrices of dust mantles and cores are released by the destruction of dust grains, and then associate with the oxygen to form SiO:

$$O_2 + Si \rightarrow SiO + O \tag{1.38}$$

$$OH + Si \rightarrow SiO + H \tag{1.39}$$

Hence, assuming that all Si is initially contained in dust grain cores, SiO was considered a tracer of the propagation of fast ($v_s \geq 25$ km s^{-1}) C-type shocks (Schilke *et al.* 1997, Gusdorf *et al.* 2008a) and J-type shocks (Guillet *et al.*, 2009). However, Gusdorf *et al.* (2008b) showed that this assumption and scenario was not compatible with the C-type shock dynamical timescales, and that non stationary shocks are best-suited to simultaneously reproduce both the emission of H_2 and SiO lines. In that case, the assumption that all Si is initially in dust grain cores is dropped, and it is assumed that the region of interest has already been processed by shocks, allowing to have $1-10\%$ of free Si in the pre-shock gas phase. For example, Louvet *et al.* (2016) reported the observations of SiO associated with low-velocity shocks ($v_s = 7-12$ km s^{-1}) in shocks associated with cloud-cloud collisions in the W43-MM1 ridge.

1.2.3.1 Irradiated and radiative molecular shocks

Externally irradiated slow molecular shocks ($v_s < 25$ km s^{-1}) There are disagreements between observations of molecular shocks in SNRs and the luminosity of non irradiated shock models (Snell *et al.* 2005, Hewitt *et al.* 2009b). In a variety of environments (protostellar shocks, diffuse media), one has to include both the effect of the shocks and UV photons emitted by external sources (such as protostars). In the IC443 supernova remnant, in addition to the direct impact of the SN blast, UV photons can be injected by massive protostars and/or X-ray decay.

Godard *et al.* (2019) implemented several new physico-chemical processes in the Paris-Durham shock model to study slow ($5-25$ km s^{-1}) molecular shocks in environments illuminated by an external UV field ($G_0 = 0 - 10^4$). They found that a strong external UV field can modify the structure of the shock itself and boost the efficiency in producing bright molecular lines. On the

other hand, several molecules (such as H_2, CO, OH, H_2O) are found to be destroyed too quickly by UV photons to be efficiently produced in irradiated shocks. Assuming a standard magnetic field strength ($B_0 = 1 \times (\frac{n_H}{1 cm^{-3}})^{1/2}$ µG, Godard *et al.* 2019), irradiated shock models show that only low-velocity C-type shocks ($v_s \leq 5$ km s^{-1}) can exist in the diffuse ISM ($n_H \sim 30$ cm^{-3}, $G_0 \sim 1$). Higher-velocity shocks are either C* or CJ[9] ($5 \leq v_s \leq 25$ km s^{-1}), or J ($v_s \geq 25$ km s^{-1}). In fact, the exact velocity at which a C-type shock can exist depends on the combined effect of several parameters (most importantly the local density n_0, magnetic field B_0 and radiation field G_0, see Fig. 1.21).

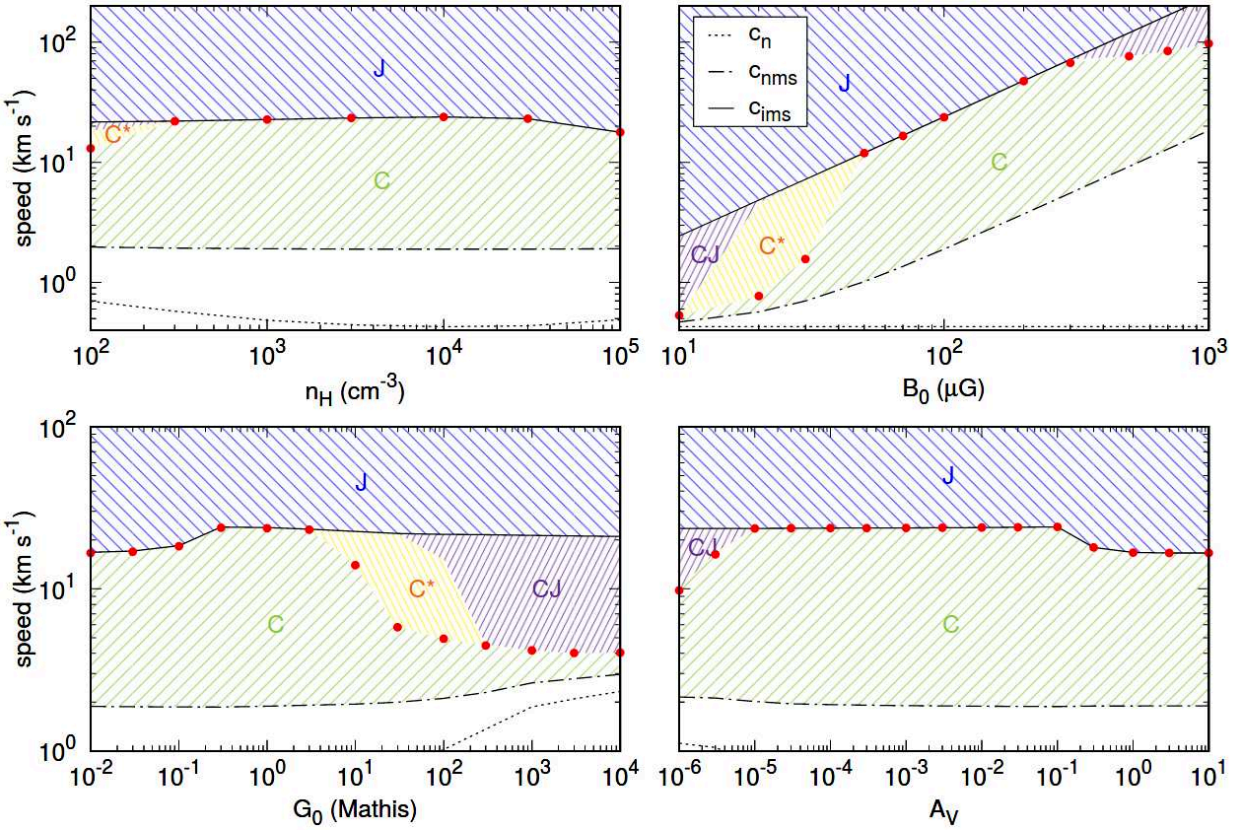

Figure 1.21 Neutral sound speed (dotted) and neutral (dot-dashed) and ion (solid) magnetosonic speeds as functions of the density (upper left panel), transverse magnetic field intensity (upper right panel), UV radiation field intensity (lower left panel), and visual extinction (lower right panel). All the non-varying parameters are set to their standard values (see Godard *et al.* 2019), and the standard value of the buffer visual extinction is set to $A_V^0 = 10^{-2}$. The critical velocities above which C-type shocks cannot exist are shown with red points, while colored areas highlight the range of velocities at which C- (green), C*- (yellow), CJ- (violet), and J-type (blue) shocks develop. Figure reproduced from Godard *et al.* (2019).

Radiative (self-irradiated) molecular shocks (30 kms^{-1} $< v_s <$ 60 **km s^{-1}**) Lehmann *et al.* (2020) updated the Paris-Durham shock model to include stationary J-type radiative molecular shocks in weakly magnetized environments ($v_s = 25 - 60$ km s^{-1}). Above $v_s = 30$ km s^{-1} (and assuming $n_H = 10^4$ cm^{-3}), the shock generates Lyman-α and Lyman-β emission with an intensity

[9]Stationary two-fluids shocks are called C*-type or CJ-type depending on whether the sonic point is crossed continuously or not. They should not be confused with non-stationary CJ-type shocks (Chieze *et al.*, 1998).

greater than the standard interstellar radiation field (ISRF, Mathis *et al.* 1983). The self-generated UV radiation field escapes into the preshock gas where it heats the gas up to ~ 100 K on a length ~ 0.03 pc. Similarly to low-velocity irradiated shocks, self-irradiated shocks have their atomic fine structure emission lines boosted by the radiation field (in particular, the O(62.3μm) and S(25.2μm) fine-structure lines).

1.2.3.2 Shock chemistry, models and observations in evolved SNRs

Molecular shock studies in SNRs Low-velocity shocks models (v_s < 60 km s^{-1}) represent a key tool to interpret observations in evolved SNRs. Self-irradiated, externally irradiated, J-type, C-type shock models are all required to study the emission in molecular SNR shells and molecular clouds interacting with SNR blasts. Reach *et al.* (2005) reported IR and sub-millimeter observations of shocked molecular gas in the W28 and W44 SNRs. In these remnants, bright and clumpy H_2 structures trace the interaction of the blastwave with the molecular environment. The location of the H_2 shock fronts follows closely the rim of the bright radio shells in these two SNRs. They showed that a clear distinction can be made between the preshock and shocked gas in the CO and CS J=2–1 spectra, and that the emission is consistent with the propagation of nondissociative shocks in media of density $10^3 - 10^4$ cm^{-3}.

Hewitt *et al.* (2009b) reported the observation of shocked H_2 in six SNRs (Kes 69, 3C 396, Kes 17, G346.6-0.2, G348.5-0.0, and G349.7+0.2) using *Spitzer*-IRS. They interpreted the bright H_2 S(0)-S(7) emission lines as the signature of radiative cooling from the shocks interacting with cold, quiescent dense clouds in the SNR environment. Using the C-type Paris-Durham shock models updated by Wilgenbus *et al.* (2000) and Le Bourlot *et al.* (2002), they found that the excitation of H_2 in these SNRs can be described using two nondissociative shock components: *i.)* a slow ~ 10 km s^{-1} C-type shock propagating in molecular clumps of density ~ 10^6 cm^{-3}, and *ii.)* a faster 40-70 km s^{-1} C-type shock propagating in a more diffuse medium (~ 10^4 cm^{-3}). Gusdorf *et al.* (2012) presented APEX (Atacama Pathfinder EXperiment) and SOFIA (Stratospheric Observatory For Infrared Astronomy) observations of higher J transitions of ^{12}CO in the SNR W28, towards the F knot. Their comparison with shock models indicate that C-type shocks of velocity up to 25 km s^{-1} propagating in a medium of density ~ 10^4 cm^{-3} and magnetic field 45 – 100 μG can reproduce both the ^{12}CO observations and H_2 emission detected with *Spitzer* observations of the remnant. Anderl *et al.* (2014) mapped two regions in the SNR W44 with the APEX telescope and compared the observations with a grid of models. They found that CO line emission is compatible with non-stationary shocks, a pre-shock density of 10^4 cm^{-3} and a shock age ~ 1 – 3 kyr.

Neufeld *et al.* (2014) investigated the water abundance in the W28 and 3C391 SNRs, based on *Herschel* observations of the remnants. They found that nondissociative shock models can reproduce H_2O line fluxes. Similarly, we will see in the next chapter that the IC443 SNR constitutes an exceptional candidate to test shock models (*e.g.* Burton *et al.* 1990, van Dishoeck *et al.* 1993, Cesarsky *et al.* 1999, Snell *et al.* 2005, Reach *et al.* 2019).

1.3 | Supernova remnants and star formation

Supernova remnants are tied to star formation in many ways. It has often been suggested that SNRs can trigger star formation in nearby molecular clouds (*e.g* Desai *et al.* 2010) but most im-

Figure 1.22 *Upper panel (5 × 6 mosaic):* optical sample of 30 young stellar objects, as imaged by *Hubble* in the Orion Nebula. *Bottom panel (1 × 3 mosaic):* from left to right, the young stellar objects CoKu Tau 1, IRAS 04248+2612 and IRAS 04302+2247, as imaged by *Hubble*. Credit: NASA/ESA and L. Ricci (ESO), D. Padgett (IPAC/Caltech), W. Brandner (IPAC) and K. Stapelfeldt (JPL).

portantly they regulate the rate of star formation through mechanical feedback, turbulence and energy injection, and conversely the CCSN rate is regulated by the high-mass star formation efficiency. Before moving on to the description of the intertwined studies of cosmic star formation history and SN/SNR rate and feedback, we will provide a short description of the current knowledge of star formation. For a complete description of the state of the art, we redirect to the seminal review by Shu *et al.* (1987) and a comprehensive review by Krumholz (2014), along with reviews focusing on isolated low-mass (Andre *et al.* 2000) and high-mass star formation (Zinnecker and Yorke 2007, Motte *et al.* 2018), and the origin of the initial mass function (Kroupa *et al.* 2013, Offner *et al.* 2014, Lee *et al.* 2020).

1.3.1 Elements of star formation theory

From gas to stars: gravitational collapse of molecular clouds Stars are born in cold molecular clouds (Larson 1981, Blitz 1993, Williams and Myers 2000) where a sufficient amount of mass is available to reach densities that allow gravitational collapse to overcome all possible supporting agents (rotation, turbulent, radiative and thermal pressure, magnetic field, Myers *et al.* 1995, Larson 1981, Longmore *et al.* 2014). The standard mechanisms of star formation are not well understood, in particular the first stages of the collapse process are still uncertain.

Minus the considerations on the magnetic field and the theory of subcritical and supercritical regimes, the discussion by Shu *et al.* (1987) remains correct for the formation of isolated, low-mass stars (Crutcher, 2012). Stars can also form in clusters: the gravitational collapse of a cloud is in fact hierarchical and leads to fragmentation of the parental molecular cloud into a collection of star forming clumps (*e.g.* Efremov and Elmegreen 1998, Hopkins 2013, Vázquez-Semadeni *et al.* 2019).

Originally, Larson (1969) identified distinct, successive stages in the formation of individual protostars: *i.)* firstly, a molecular cloud fragments and collapses into a number of gravitationally bound cores, supported against gravity by thermal, magnetic and turbulent pressures; *ii.)* At $T = 2000$ K, the endothermal dissociation of H_2 causes a drop of the thermal pressure, the core becomes gravitationally unstable and quickly collapses further to form an hydrostatic protostellar core; *iii.)* the new hydrostatic core accretes matter from a surrounding infalling envelope until it reaches its main sequence mass. The accretion phase is accompanied by the ejection of bipolar outflows that evacuate the angular momentum of the rotating protostar (Snell *et al.* 1980, Snell *et al.* 1988, Bontemps *et al.* 1996). Assuming a self-gravitating cloud without considering the effect of rotation nor magnetic field, the duration of the protostellar phase is given by solving the following equation of motion:

$$\frac{d^2r}{dt^2} = -\frac{4\pi G\rho_0 a^3}{3r^2} \tag{1.40}$$

Where r is the radius of a cloud of initial density ρ_0 and radius a. The solution of this equation is the so-called free fall time $t_{\rm ff}$ (Spitzer, 1978):

$$t_{\rm ff} = \sqrt{\frac{3\pi}{32G\rho_0}} \tag{1.41}$$

Where ρ_0 is the initial density of the envelope, and G is the gravitational constant. Assuming $\rho_0 \simeq 4 \times 10^{19}$ g cm^{-3} (*i.e.* $n_{\rm H_2} = 10^5$ cm^{-3}) this time is $t_{\rm ff} \sim 10^5$ yr.

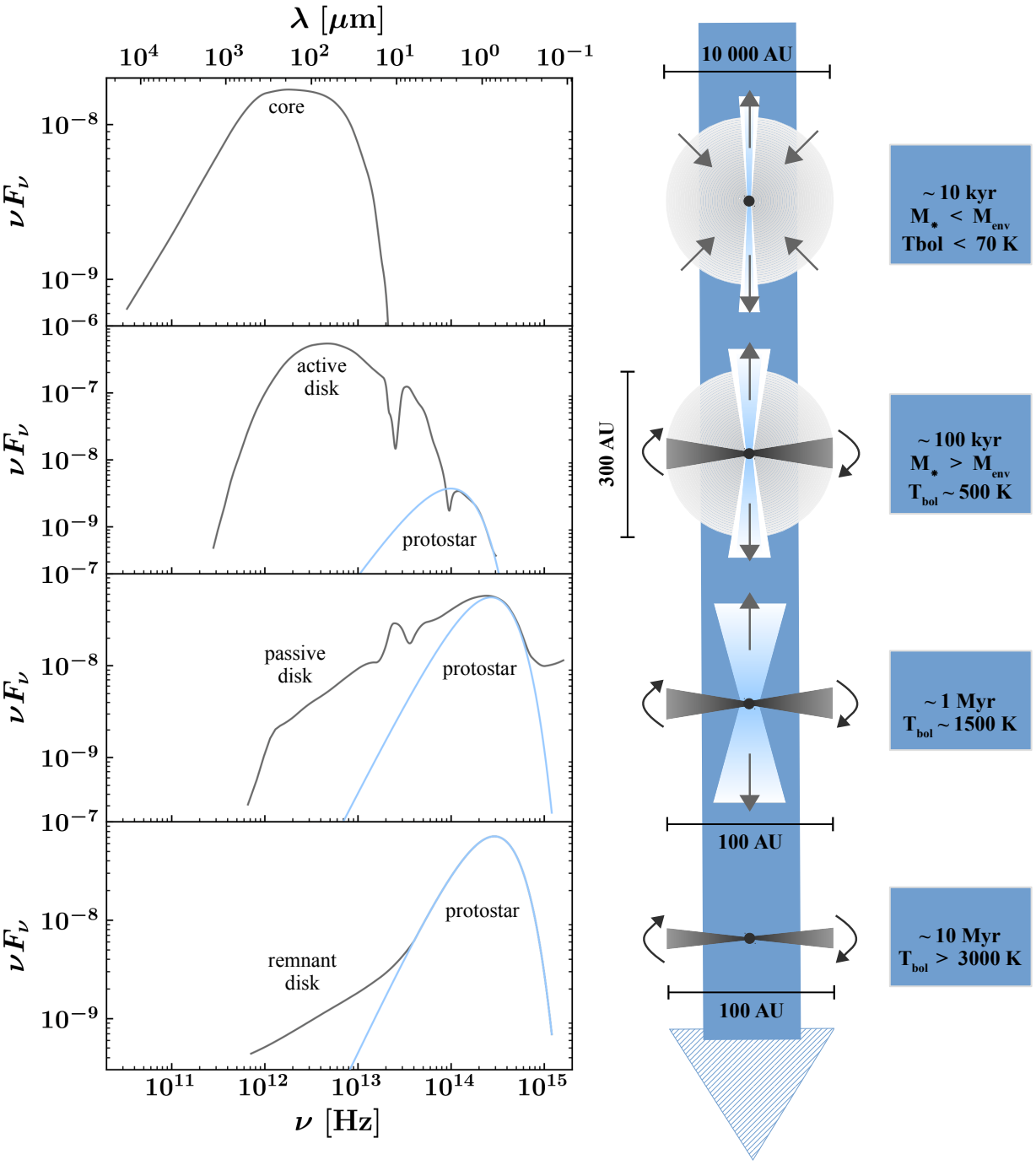

Figure 1.23 Spectral energy distribution (left) and schematic representation of each corresponding class of protostars (right). This sequence holds for low-mass, isolated star formation. At a given evolutionary stage (progressing from top to bottom), the black curves represent the total flux of a young stellar object (infrared excess of the disk and envelope + luminosity of the protostar) and the light blue curves represent the black body radiation from the central protostar. The envelopes (light gray), bipolar jets, outflows (light blue) and accretion disks (dark gray) are represented, and the typical age and bolometric temperature $T_{\rm bol}$ are indicated for class 0-III protostars. $M_\star$ and $M_{\rm env}$ account respectively for the protostar and envelope masses. Based on the description by André (1994). A sample of real Class I-III protostars is shown in figure 1.22, as imaged by *Hubble*.

Gravitational instability and supporting agents The stability of a non-magnetized molecular cloud is determined by the Virial theorem (established by Clausius in 1870 and Poincaré in 1911):

$$\langle E_{\rm kin} \rangle = \frac{1}{2} \langle |E_{\rm p}| \rangle \tag{1.42}$$

If the average of the absolute value of the potential energy $E_{\rm p}$ is greater than twice the average kinetic energy $E_{\rm kin}$, then the system is out of equilibrium and the molecular cloud collapses (McKee, 1999). Assuming a spherical, homogeneous cloud of radius R, temperature T and mass M, we have:

$$E_{\rm kin} = \frac{3}{2} k_{\rm B} T \frac{M}{\mu m_{\rm H}} \tag{1.43}$$

$$E_{\rm p} = -\frac{3}{5} \frac{GM^2}{R} \tag{1.44}$$

Equations 1.42, 1.43 and 1.44 allow to define the critical Jeans mass and length:

$$M_{\rm J} = \left(\frac{5 k_{\rm B} T}{G \mu m_{\rm H}} \right)^{3/2} \times \sqrt{\frac{3}{4\pi\rho}} \tag{1.45}$$

$$L_{\rm J} = \left(\frac{\pi k_{\rm B} T}{G \mu m_{\rm H} \rho} \right)^{1/2} \tag{1.46}$$

These two quantities define the stability conditions of an idealized, non magnetized, isolated molecular cloud. If a molecular cloud exceeds the Jeans mass $M_{\rm J}$, the system starts to collapse as result of its own gravity unless it is sufficiently supported by rotation, turbulence or magnetic field. Similarly, the Jeans length shows that the system remains stable for any perturbation of wavelength $\lambda \leq L_{\rm J}$. Therefore, for star formation to occur an initial "kick" is required to disrupt the Virial equilibrium and cause the collapse of stable molecular clouds. On a galactic scale for example, the rotation of spiral arms can provide a perturbation pressure strong enough to trigger collapse (as suggested by Roberts 1969), but it is likely that SNe dominate the regulation of star formation at lower scales by injecting energy, turbulent motions and thermal pressure (Norman and Ferrara, 1996).

In fact, molecular clouds are observed to have masses far superior to the Jeans mass $M_{\rm J}$ due to the effect of magnetic and turbulent support (Mac Low and Klessen 2004, Heiles *et al.* 1993, Crutcher 1999). Spectral observations of molecular line widths towards molecular clouds are indicative of highly supersonic motions (*e.g.* Falgarone *et al.* 1998). Both turbulence and the magnetic field act as nonthermal, macroscopic pressures that support self-gravitating clouds (Lizano and Shu, 1989). Hence, turbulent energy has to be dissipated on small scales (<0.1 pc) for star formation to occur (Nakano 1998, Williams *et al.* 2000), as well as magnetic field *via* ambipolar diffusion (Mac Low and Klessen, 2004).

Evolutionary stages of a low-mass protostar An empirical evolutionary sequence of young stellar objects (YSO) was established based on the slope of the spectral energy distribution of protostars (Lada and Wilking 1984, Lada 1987):

$$\alpha = \frac{d \ln(\lambda F)}{d \ln \lambda} \tag{1.47}$$

The measurement of α allows to attribute an evolutionary stage to a given YSO (see Fig. 1.23, based on the description by André 1994 and references below). *Caution*: the sign of the slope is inverted between Eq. 1.47 (defined with respect to the wavelength λ) and Fig. 1.23 (represented with respect to the frequency ν). The 'α' index cannot be measured for Class 0 protostars, since these sources do not emit in infrared (see Fig. 1.23). Class I, II and III protostars can be identified based on the slope of their SED:

- ◇ **Class I** ($\alpha > 0$, *i.e.* a negative slope of the spectral energy distribution in Fig. 1.23, *e.g.* Wilking *et al.* 1989): these are relatively evolved protostars (100 – 200 kyr, Greene *et al.* 1994) surrounded both by a disk and low mass envelope. These objects are observed in close association with molecular gas (Myers *et al.*, 1987).

- ◇ **Class II** ($-1.5 < \alpha < 0$, *i.e.* a flat/positive slope of the spectral energy distribution in Fig. 1.23): Classical T Tauri stars, which are pre-main sequence stars (age $\sim$ 1 Myr) still undergoing gravitational contraction. These young stars have accreted their entire envelope but still have an accretion disk (Andre and Montmerle, 1994).

- ◇ **Class III** ($\alpha < -1.5$, *i.e.* a strictly positive slope of the spectral energy distribution in Fig. 1.23): weak T Tauri stars (age $\sim$ 10 Myr), in which the accretion disk is either weak or entirely absent (Beckwith *et al.*, 1990).

Class I-III protostars are warm enough for their blackbody radiation to be observed in infrared, but there are younger and colder protostellar objects. **Class 0** YSOs are short-lived (a few 10 kyr, close to 100 kyr, Maury *et al.* 2019), young protostars that can only be seen in FIR/millimeter observations towards dark molecular cloud cores. These embedded, compact protostellar condensations are completely invisible at $\lambda < 25$ µm. One can use the ratio of the sub-millimeter to bolometric luminosities $L_{\rm sub-mm}/L_{\rm bol}$ to track the mass ratio of envelope to stellar mass $M_{\rm env}/M_{\rm star}$ and use it as a quantitative evolutionary indicator (Andre *et al.*, 1993). There is a strong link between accretion and ejection (Konigl and Pudritz, 2000). Bipolar structures are required to remove the angular momentum from young stellar objects (Lada 1985, Shu *et al.* 1994):

- – Bipolar jets are fast (200 km s^{-1} to 350 km s^{-1} terminal speeds), collimated (from 20° – 30° initially to a few degrees beyond 50 AU of the source) accretion-powered, centrifugally-driven ejections of mass produced by protostars (*e.g.* Mundt and Fried 1983, Cabrit 2007). Jets carve a cavity in their environment on a parsec scale, and can be traced by forbidden line emission from atomic species (*e.g.* O I, Fe II, C II).

- – Bipolar molecular outflows are the products of the interaction of jets with their environment. Outflows are traced by molecular species such as CO, SiO, H_2 and H_2O (*e.g.* Bally and Lada 1983, Cabrit and Bertout 1986, Snell *et al.* 1988, Bally 2016).

Class 0 protostars drive bipolar, powerful "jet-like" CO molecular outflows (*e.g.* Bachiller 1996, Richer *et al.* 2000, see Fig. 1.26) much more powerful and collimated than the outflows observed in Class I-II protostars. It has been suggested that the decline of the outflow and jet power reflects the decline of the infall and accretion rate of the protostar (Andre *et al.*, 2000). Class 0 protostars are born in prestellar cores, the smallest molecular cloud units (Bergin and Tafalla, 2007). A dense prestellar core may be defined as a molecular cloud fragment that can potentially form

an individual star or small multiple system by gravitational collapse, but is not yet observed to host any protostars. Historically, prestellar cores were first observed and described as "Bok" dark globules seen in extinction (Bok and Reilly, 1947).

The elusive high-mass star formation mechanisms High-mass ($M > 10$ M$_\odot$) star formation is not well known in comparison to isolated, lower mass star formation. In contrast to the "core accretion model" which was initially proposed by McKee and Tan (2002), high-mass star formation cannot simply be a scaled up version of low-mass star formation because of lifetime constraints and because of the strength of radiation pressure produced by massive protostars (which prevents gravitational collapse). Therefore, star formation has to be bimodal (Andre *et al.*, 2000). The formation of massive stars is regulated by fragmentation and competitive accretion in clustered environments ('competitive accretion model', Bonnell *et al.* 2001, Bonnell *et al.* 2004, Bonnell *et al.* 2007). There is no firmly established evolutionary sequence for the formation of high-mass protostars, although scenarios have been suggested (*e.g.* Motte *et al.* 2018).

Nonetheless, these scenarios are descriptive but not predictive, which constitutes a weakness in our current knowledge of massive star formation. According to these empirical scenarios, massive clusters of stars are formed in giant molecular complexes, where massive, filamentary clumps called ridges account for the preferred sites of high-mass star formation (*e.g.* Schneider *et al.* 2010). The particular property of massive protostellar embryos is that they strongly heat and eventually ionize the gas of their surrounding envelope, creating a compact H II region that expands into their parental cloud (Spitzer, 1978). Because their lifetime is short ($\sim 10^4$ yr, Tigé *et al.* 2017), detections of high-mass prestellar cores are very sparse in comparison to their lower mass counterparts. Although there have been several surveys in massive molecular complexes (*e.g.* in W43, Motte *et al.* 1998, Motte *et al.* 2018; in Cygnus X, Motte *et al.* 2007; in the Rosette, Schneider *et al.* 2012) only a few prestellar core candidates with $M \gg 10$ M$_\odot$ are currently known (Bontemps *et al.* 2010, Wang *et al.* 2014, Cyganowski *et al.* 2014, Nony *et al.* 2018, Molet *et al.* 2019). The quest for high-mass prestellar cores is still an effort in progress, with the assistance of the high-resolution potential of the Atacama Large Millimeter/submillimeter Array (ALMA).

1.3.2 Mass functions

The initial mass function The initial mass function (IMF) is a statistically determined stellar mass spectrum, *i.e.* it represents the number of stars with a given mass at birth. Measuring it and understanding it is a central issue of star formation, and it also has implications on galactic structure and evolution, stellar nucleosynthesis and even the formation of planetary systems. The IMF determines the number of stars per mass category, therefore it allows to evaluate the stellar feedback on the ISM, which is a key parameter in simulations of the evolution of galaxies. The first definition of the IMF was given by Salpeter (1955):

$$dN \propto M^{-\alpha} dM \tag{1.48}$$

Based on observations of star populations, Salpeter (1955) determined the "canonical" value $\alpha = 2.35$, and this value is still considered standard and universal for stars with $M > 1$ M$_\odot$ (although the slope of the IMF is sometimes claimed to be steeper at higher masses, *e.g.* Scalo 1986). For lower mass stars ($M < 1$ M$_\odot$) there is break of the $\alpha = 2.35$ slope (Miller and Scalo, 1979), and

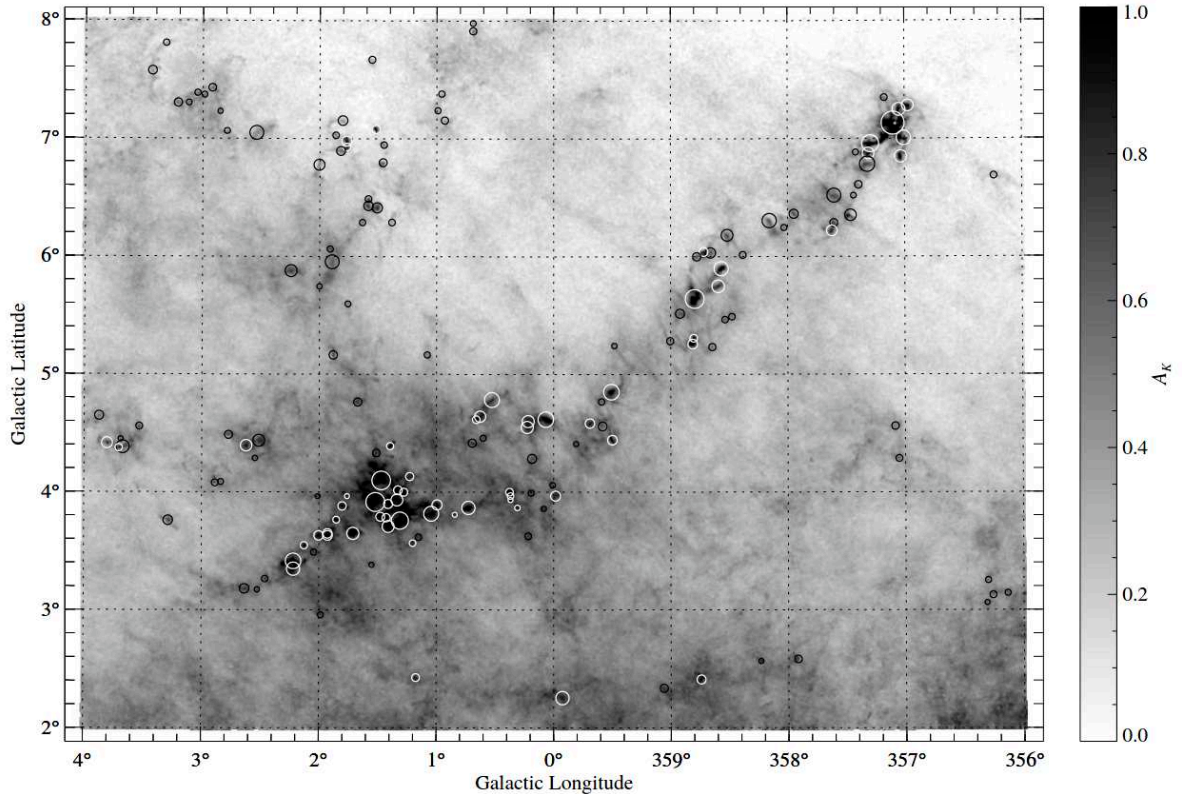

Figure 1.24 Dust extinction map of the nearby Pipe nebula molecular complex from Lombardi *et al.* (2006). This map was constructed from near-infrared 2MASS observations of about 4 million stars in the background of the complex. Based on wavelet transform analysis (Langer *et al.* 1993, Williams *et al.* 1994) approximately 160 individual cores are identified within the cloud and are marked by an open circle proportional to the core radius. Most of these cores appear as distinct, well separated entities. Figure reproduced from Alves *et al.* (2007).

more modern forms often adopt a log-normal distribution at low masses and then a power law above solar masses (Chabrier, 2003). Sometimes, the IMF can also be written:

$$N(M) = \frac{dN}{d\ln(M)} \propto M^{\Gamma} \tag{1.49}$$

Where $\Gamma = 1-\alpha = -1.35$. The IMF has a great importance for the study of SNRs, since the amount of CCSN progenitors expected to form in a galaxy is directly determined by the distribution of high-mass stars.

Universality of the IMF From an observational point of view, the empirical IMF is determined by measuring the luminosities of a population of stars in a given region and using a mass-magnitude relationship to convert it into a present day mass function (PDMF). Then, the PDMF is corrected for star formation history (depending on the redshift z) to obtain the IMF. Although these steps introduce several biases and systematic uncertainties, the universality of the IMF has been established by abundant statistical studies in a wide range of near (Galactic), distant (up to $z = 2$), quiet and active regions (see the reviews by Kroupa *et al.* 2013, Offner *et al.* 2014, Chabrier 2005). In their review, Bastian *et al.* (2010) show that the IMF universality holds both in the local and distant universe, up to $z \sim 2$. In the Milky way, even in extreme Galactic star-forming

regions, no strong variations of the IMF have been found so far, as well as in nearby galaxies (the Large Magellanic Cloud and Small Magellanic Cloud) and starburst galaxies. There have been attempts at finding cosmological IMF variations, but no conclusive evidence were found, although extragalactic detections are known to be biased towards higher mass at higher redshifts (Davé, 2008).

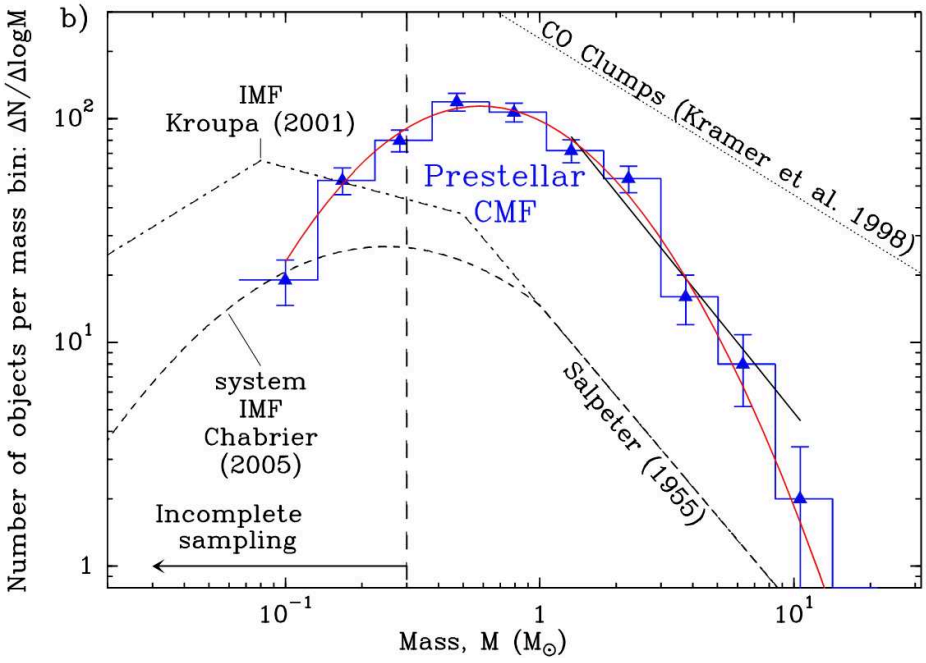

Figure 1.25 Core mass function (blue histogram with error bars) of the ~ 500 candidate prestellar cores identified with *Herschel* in Aquila (Könyves *et al.* 2010, André *et al.* 2010). The IMF of single stars (corrected for binaries, *e.g.* Kroupa 2001), the IMF of multiple systems (*e.g.* Chabrier 2005), and the typical mass spectrum of CO clumps (*e.g.* Kramer *et al.* 1998) are shown for comparison. A log-normal fit to the observed CMF is superimposed (red curve); it peaks at ~ 0.6 $M_\odot$, close to the Jeans mass within marginally critical filaments at $T \sim 10$ K. Figure reproduced from André *et al.* (2010).

The core mass function The efforts to understand the origin of the IMF have led to study the formation of prestellar cores in star-forming regions *via* wide field surveys in sub-millimeter, in order to build the mass function of the previous evolutionary stage: the so-called "core mass function". Motte *et al.* (1998) reported the results of a 1.3 mm, ~ 480 arcmin^2 survey towards the main ρ-Oph cloud (d = 150 pc). They identified 100 compact condensations with angular scales ~ 15″ – 30″ (2500 – 5000 AU), and observed that their mass distribution is a scaled-down version of the IMF (characterized by the same slope in the > 1$M_\odot$ regime, which was then confirmed by Johnstone *et al.* 2000). Testi and Sargent (1998) came to the same conclusion in the more distant and more massive Serpens molecular cloud (d = 200 pc) where they found 26 protostellar condensations. The resemblance between the mass spectrum of prestellar cores and and the IMF strongly suggests that these condensations are the direct progenitors of individual stars. Following these findings, several surveys were performed to constrain the so-called core mass function (CMF, *e.g.* Könyves *et al.* 2010, André *et al.* 2010, Alves *et al.* 2007 see Fig. 1.24 and Fig. 1.25).

This understanding (until 2018) of the CMF was biased towards lower mass star formation, because most surveys were performed in the solar neighborhood (at a distance $d < 500$ pc), which only forms stars of mass $0.1-5\ M_\odot$ (*e.g.* Enoch *et al.* 2006, André *et al.* 2014). These CMF studies were restricted to the solar neighborhood (typically the Gould belt) because of angular resolution constraints. In order to correct this bias, the large program ALMA-IMF (Motte et al. 2017) aims to benefit from the high-resolution of ALMA in order to study high-mass star formation in distant massive molecular complexes (up to $2-5$ kpc) such as W43 (Motte *et al.*, 2003) and Cygnus-X (Motte *et al.*, 2007). For the first time, in W43 Motte *et al.* (2018) found a CMF which has a slope shallower than the IMF (*i.e.*, with an unexpectedly large proportion of high-mass protostars).

These new surveys will contribute to fill the gap between low-mass and high-mass star formation and constrain the origin of the high-mass IMF. The IMF might be spatially invariant, but observations of the core populations in the Galactic ministarbursts W43 and W51 (Ginsburg *et al.*, 2017) suggest the existence of a temporal variability: clusters would be underpopulated with low-mass protostars in the first $\sim 10^5$ years and then converge to the canonical IMF once H II regions have formed.

On the origin of the IMF and its relation to the CMF The origin of the IMF is one of the most central questions in star formation (Offner *et al.*, 2014). There are two approaches to interpret the IMF (Kroupa *et al.*, 2013): either *i.)* the origin of the IMF is stochastic (it is a probabilistic distribution that can be understood by studying dynamical interactions and stochastic accretion of stars competing for gas) or *ii.)* the IMF is self-regulated and deterministic. In the first case, the similarity between the IMF and the CMF is coincidental and in fact the two distributions are completely independent (*e.g.* Bonnell *et al.* 2001, Bate *et al.* 2003, Clark *et al.* 2007). In the second case, there is a truly direct mapping between the CMF and the IMF, because the stellar masses are inherited from the mass distribution of the parental cores (*e.g.* Padoan and Nordlund 2002, Hennebelle and Chabrier 2008).

The link between the IMF and CMF is not trivial, and several conditions must be met for the IMF to be a direct mapping of the CMF: *i.)* all the observed cores must be truly prestellar (*i.e.* they must be destined to condense into stars); *ii.)* the cores must not alter their mass by merging with other massive structures or accreting mass, or they have to do it in a self-similar fashion; *iii.)* cores of different mass must have the same star formation efficiency; *iv.)* finally the eventual fragmentation of cores has to be self-similar. In addition, Louvet *et al.* (2021) has shown that the angular resolution has an effect on the measured sizes and masses of the so-called isolated prestellar cores. The relationship between the IMF and CMF was studied with hydrodynamical and magneto-hydrodynamical simulations (*e.g.* Padoan *et al.* 2007, Hennebelle and Chabrier 2008, Schmidt *et al.* 2010). The approaches based on the turbulent collapse of a molecular cloud reproduce well the observed IMF. However, reproducing the top-heavy CMF found by ALMA-IMF represents a new challenge for simulations.

1.3.3 Supernova remnant feedback in star forming regions

Stellar feedback mechanisms There are several stellar feedback mechanisms by which the star formation rate can be altered (Elmegreen, 1998). Stellar outflows and high-velocity winds produce a continuous dynamic input into molecular clouds (Norman and Silk, 1980), shaping the environ-

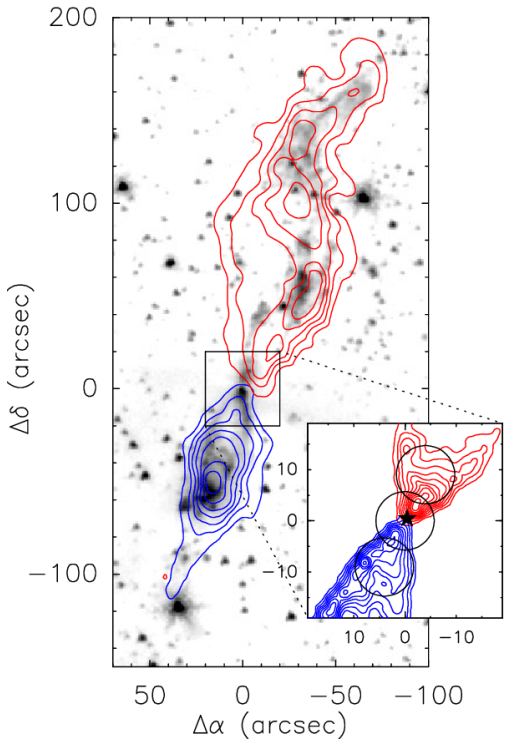

Figure 1.26 Large-scale view of the parsec-scale L1157 bipolar outflow in Cepheus. The main frame shows a superposition of the IRAM-30m CO(2 → 1) map from Bachiller *et al.* (2001) (blue contours: -20 to 2.7 km s^{-1}, red contours: 2.7 to 28 km s^{-1}) and the 3.6 µm *Spitzer*-IRAC image from Looney *et al.* (2007). The inset shows the inner outflow according to the interferometric CO(2 → 1) map of Jørgensen *et al.* (2007) obtained with the sub-millimeter array (SMA). The star symbol represents the Class 0 protostar L1157-mm (Gueth *et al.*, 1997). Figure reproduced from Tafalla *et al.* (2015).

ment and individually limiting the mass accretion onto forming stars (Li and Nakamura, 2006). The energy deposited by outflows can reach 10^{47} – 10^{48} erg (*e.g.* Garden *et al.* 1991, *e.g.* Fig. 1.26). Negative feedback has often been blamed for the long-standing problem of the low star formation efficiencies in molecular clouds (Solomon *et al.*, 1979) but the feedback can also enhance or even trigger the formation of new stars. Expanding H II regions around OB associations drive shocks in molecular clouds that can trigger star formation (Elmegreen and Lada 1977, Thompson *et al.* 2012). In this section we will focus on the feedback exerted by supernova remnants on their environment, *via* the propagation of shocks, emission of photons and diffusion of cosmic rays.

Can we observe SNR-triggered star formation? Opik (1953) was the first to suggest that the death of one star in a supernova explosion may lead to the birth of a great number of new stars. According to the anomalously high ^{60}Ni abundance found in old meteorites, our own solar system could have formed at a site where a recent SN explosion had occurred (Vanhala and Boss 2002, Tachibana *et al.* 2006). The assumption that the solar system was born in an interstellar cloud that collapsed due to a nearby SN allows to account for most isotopic anomalies and traces of extinct radioactivities (Cameron and Truran, 1977).

As a matter of fact, star formation is frequently observed near SNRs (*e.g.*, Montmerle 1979b, Koo *et al.* 2008b, Gouliermis *et al.* 2008). However, a physical association does not necessarily indicate a causal relationship. In their review of a total of 67 observational studies, Dale *et al.* (2015) conclude that one should be very careful about any claim of "triggered star formation", since a robust observational evidence is hard to come by. In fact, since massive stars are born in clusters and evolve much faster than their low-mass siblings, it is entirely possible to observe a SNR interacting with YSOs that actually belong to the same generation of stars as the progenitor of the SN explosion. Due to lifetime constraints, one cannot expect to observe evidence of SNR-triggered low-mass evolved protostars (Class I-III) in ∼ 10 kyr old SNRs, but at best Class 0 protostars, and more likely prestellar condensations. Even a 10 $M_\odot$ pre-main sequence star has a

formation time scale ~ 0.1 Myr (Beech and Mitalas, 1994), hence it would be required to observe very old SNRs to find positive evidence of triggered star formation.

1.3.3.1 Shock feedback

Positive feedback: Shock-induced star formation According to the theory of turbulent fragmentation, prestellar cores are expected to form at the convergence of large-scale flows or in shells swept-up by expanding H II region or SNRs (Klessen 2001, Hennebelle and Teyssier 2008). As we saw in the previous section, a good mean to induce star formation in an initially stable cloud is to increase the external pressure in order to disrupt the Jeans stability conditions. Shock-generated density fluctuations can provide the required input to trigger the fragmentation of molecular structures. Once the gas density in swept-up shells reaches a critical value, the shells become gravitationally unstable, leading to their fragmentation and collapse.

Mueller and Arnett (1976) described a galactic propagating star-forming mechanism with a sequential numerical model in which high-mass stars produce spherical shock waves that induce formation of new high-mass stars which, in turn, produce new shock waves, *etc*. Elmegreen and Elmegreen (1978) proposed a theoretical description of the gravitational instabilities and star formation triggering mechanisms in a shock-compressed layer. Collapse and fragmentation of a nearby molecular cloud can be triggered by the ram pressure caused by low-velocity shocks ($v_s < 50$ km s^{-1}, Boss 1995) but faster shocks might destroy the clouds (Vanhala and Cameron, 1998).

Hence, old SNRs (in which *i.)* the shocks have slowed down, *ii.)* the gas temperature has decreased *via* radiative losses so that gravity overcomes the thermal pressure, and *iii.)* YSOs had enough time to form) interacting with molecular clouds are good candidates for SNR-triggered star formation. This represents an observational challenge, since the best candidates for SNR-triggered star formation are the most difficult SNRs to observe, as they are in the phase during which they merge with the ISM.

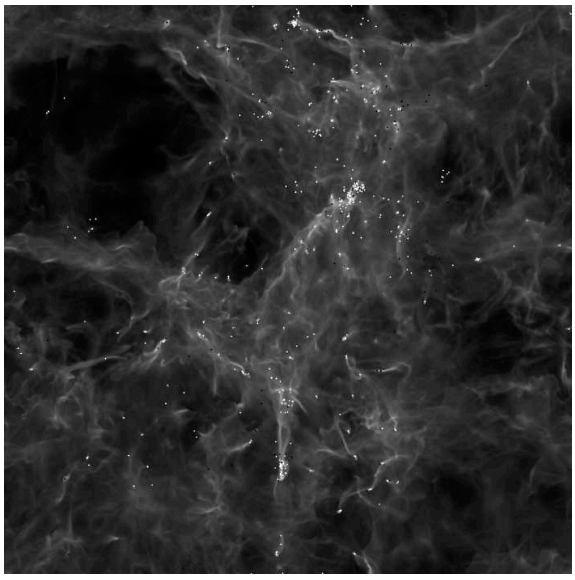

Figure 1.27 Collapsing cores in a driven, supersonic, self-gravitating, MHD turbulence numerical simulation (Padoan and Nordlund, 2011). The logarithm of projected density is represented from a snapshot of an exploratory $1{,}000^3$ run with a ratio of mean gas pressure to mean magnetic pressure $\beta_0 = 22.2$, rms sonic Mach number $\mathcal{M}_{S,} = 18$, and virial parameter $\alpha_{\rm vir} = 0.9$, at a time when approximately 10% of the mass has been converted into stars. Bright dots show the positions of the stars (sink particles), while black dots are for brown dwarfs (some of which are still accreting and may later grow to stellar masses).

Negative feedback: Turbulence injection Numerical simulations of driven, supersonic, self-gravitating, magneto-hydrodynamic turbulence show that the star formation rate is primarily con-

trolled by interstellar turbulence (*e.g.* Padoan and Nordlund 2011, Federrath and Klessen 2012, see Fig. 1.27). The simulated star formation rate is shown to decrease with stronger turbulence, as predicted by numerical models of accretion and turbulent support (Mac Low and Klessen, 2004). Turbulence decays on the timescale of the free-fall time (Stone *et al.* 1998, Mac Low 1999) thus it has to be continuously regenerated to have an effective impact on star formation. As we saw earlier (see Fig. 1.8) SNRs are a primary source of turbulence injection and allow the turbulence to be constantly driven over large volumes of the ISM. Supernova-driven turbulence simulations allow to predict a star formation rate that is consistent with measurements in nearby molecular clouds (Padoan *et al.*, 2017).

Observational evidence in individual SNRs and supershells One the first observational pieces of evidence of SNR-triggered star formation was brought up by Herbst and Assousa (1977) towards the Canis Major R1 (CMa R1) association where a SN explosion occurred about ~ 0.5 Myr ago. They found an expanding H I shell associated with a ring of optical and radio emission. The CMa R1 association is located on the outer edge of the shell, and its age is in close agreement with the estimated SNR age. Desai *et al.* (2010) reported the analysis of a sample of 45 SNRs in the Large Magellanic Cloud (LMC). They found 10 SNRs associated with YSOs, but could not establish any evidence of SNR-triggered star formation. In their study of the young SNR G54.1+0.3, Koo *et al.* (2008b) found YSOs associated with the remnant and located along a loop. They proposed that the star formation could be triggered by the expansion of the H II region associated with the progenitor of the SNe, rather than the SNR itself.

Sano *et al.* (2010) studied the young ($\sim$ 1600 yr) TeV SNR RX J1713.7-3946 interacting with a molecular cloud. Sub-millimeter and FIR observations towards RX J1713.7-3946 show strong signs of active star formation (outflows, embedded protostellar sources) within the dense molecular clumps seen in ^{13}CO. They presented a scenario in which one of the densest molecular cores survived the blast and is currently shock-compressed by the SNR blast. All these studies are limited by the fact that it is difficult to determine if star formation was triggered either by the SN/SNR blast or by the stellar wind of the progenitor (Xu *et al.*, 2011).

Supershells (size $\sim 10^2$ pc) are spherical molecular structures created by clusters of SNRs that merged into a single, larger entity (McCray and Kafatos 1987, Tenorio-Tagle and Bodenheimer 1988). There is a widespread evidence of supershells in 21 cm line surveys, and these structures are expected to form sequentially around OB associations (Tomisaka *et al.*, 1981). When a supershell becomes gravitationally unstable (typically after $\sim$ 10 Myr) it fragments and forms new molecular clouds (see Fig. 1.10) where star formation will eventually occur. This triggering mechanism of star formation was identified towards the supergiant shells N44 (Chen *et al.*, 2009) and LMC-4 (Yamaguchi *et al.*, 2001), where supershells expand into molecular clouds.

1.3.3.2 Cosmic-ray feedback

Ionization and injection of free electrons Low-energy cosmic rays (below $\sim$ 100 MeV) are the primary agent of ionization and heating in molecular clouds, in which UV photons are attenuated (see section 1.4.2.1, Grenier *et al.* 2015b, Neufeld and Wolfire 2017). Therefore, they influence the chemical, thermal and dynamical evolution of molecular clouds (*e.g.* Padovani *et al.* 2009). Since it controls the abundance of free electrons and ions, the CR ionization rate determines the degree of coupling of the interstellar gas with the magnetic field, which in turn controls the star formation

efficiency of a molecular region through magnetic support (Padovani *et al.*, 2013). Hence, *via* the injection and acceleration of the bulk of low-energy CRs (see section 1.4), SNRs regulate the ionization rate and gravitational stability of nearby molecular clouds (*e.g.* Indriolo and McCall 2013, Padovani *et al.* 2020).

Effective cosmic-ray pressure Cosmic rays also regulate the star formation rate by contributing to the nonthermal pressure of the ISM. Numerical treatments and simulations of the nonthermal pressure contribution associated with CRs indicate that they reduce the star formation efficiency (*e.g.* Booth *et al.* 2013, Salem and Bryan 2014). CR streaming drives powerful and sustained winds on the scale of galaxies, which expel a large fraction of the baryons and suppress the star formation rate by a factor of ~ 5 (Uhlig *et al.*, 2012) by providing a significant pressure support in the ISM. Thus, like the SN explosions that produce them, CRs represent a fundamental feedback parameter that controls the star formation rate. A detailed description of this strong feedback mechanism is crucial to solve the problem of star formation regulation in models of galaxy formation (Jubelgas *et al.* 2008, Naab and Ostriker 2017).

1.3.3.3 Radiative feedback (photons)

It is uncertain whether photons have a positive or negative feedback on star formation. Elmegreen and Lada (1977) proposed that OB associations drive ionization and shock fronts into molecular clouds, causing the external layers to become gravitationally unstable, and therefore triggering new cycles of star formation. However, radiative feedback is also thought to play a role in limiting the star formation efficiency of molecular clouds by removing material *via* the photo-ionization by UV photons (*e.g.* Schneider *et al.* 2020).

Based on hydrodynamic simulations, Walch *et al.* (2012) studied how the feedback of massive stars controls the evolution of molecular clouds. The authors found that in the short term the feedback is positive: star formation occurs more quickly. However, they found that in the long term the feedback is negative, since the cloud is dispersed at a rate of 10^{-2} $M_\odot$ yr^{-1}, and as a consequence the triggered star formation is limited to a few percent of the total mass of the cloud.

Observations of expanding H II regions suggest that the radiative feedback is positive, such as in RCW49 (Tiwari *et al.*, 2021) and RCW120 (Zavagno *et al.* 2007, Luisi *et al.* 2021). For example, in RCW120 Zavagno *et al.* (2007) found that the layer of gas and dust accumulated along the shell has collapsed into a total of 8 dense fragments that are potential sites of star formation, and they also detected Class I and Class II protostars all over the region.

In the IC443 supernova remnant, energetic photons (from UV to γ-rays) are detected. In particular, the cavity is filled with X-rays which are likely to decay into UV photons and interact with the shell of the remnant (see Chapter 2). Therefore, radiative feedback is expected to play a role in the star formation efficiency of the SNR shell.

1.3.4 Cosmic star formation history

Observational constraints on the star formation rate history The cosmic history of the star formation rate is one of the most fundamental observables in cosmology (Madau and Dickinson, 2014). The star formation rate used to be much greater in the past: stars were formed at a rate nearly 10 times higher than what is measured today. It is established that the star formation rate

peaked around ~ 3.5 Gyr after the Big Bang ($z = 2$, see Fig. 1.28). A consequence of this finding is that the star formation used to take place in environments affected by a much stronger stellar and SNR feedback, where the impact of energy injection, shocks, photons and CRs was more important than what is measured in our Galaxy. Hence, observations towards supernova remnants represent a unique opportunity to study the mechanisms of star formation in environments similar to the $z = 2$ universe, since they represent a snapshot of SNR-feedback driven star formation.

In a single SNR, the timescale on which all these feedback mechanisms play a role is very small compared to the timescale of star formation. However, in the region where we observe a SNR, there are probably other SNe that have exploded over tens or even hundred of thousand years before, providing continuous feedback on timescales that are significant with respect to the timescale of star formation.

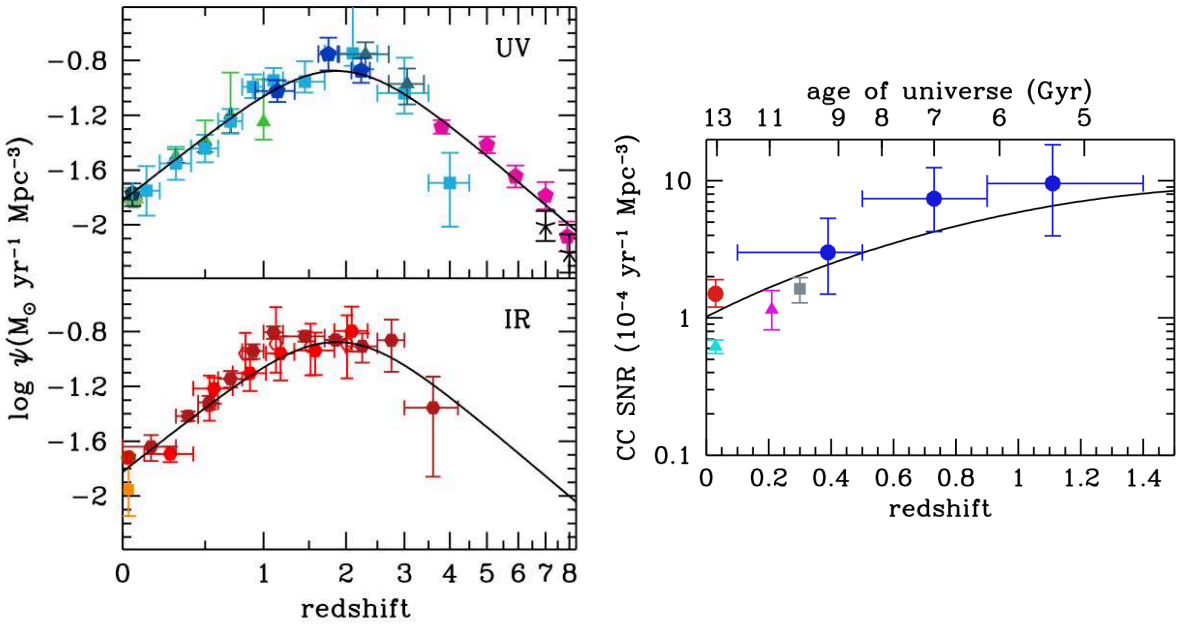

Figure 1.28 *Left:*. The history of cosmic star formation from FUV (top panel) and IR (bottom panel) measurements. The data points with symbols are given in Madau and Dickinson (2014). The solid curve represents the best-fit star formation rate density. *Right:* The cosmic CCSN rate. The data points are taken from Li *et al.* (2011) (cyan triangle), Mattila *et al.* (2012) (red dot), Botticella *et al.* (2008) (magenta triangle), Bazin *et al.* (2009) (gray square), and Dahlen *et al.* (2012) (blue dots). The solid line shows the rates predicted from a fit to the cosmic star-formation history. Figure reproduced from Madau and Dickinson (2014).

The intertwined SN rate, IMF and star formation rate On one hand, the rate of CCSNe should reflect ongoing star formation, since it is directly linked to the formation of massive, short-lived stars. On the other hand, the CCSN rate directly depends on the IMF. Madau *et al.* (1998) proposed a numerical computation of the CCSN rate based on the IMF $\phi(m)$ and star formation rate ψ at a time t:

$$\mathrm{SNR_{II}} = \psi(t)\frac{\int_8^{125} dm\phi(m)}{\int_{0.1}^{125} dm\phi(m)} \tag{1.50}$$

Where it is assumed that stars with a mass $8 < m < 125$ (where m is in solar mass unit) evolve into CCSNe (or Type II SNe). This equation shows that the frequency of CCSNe is largely dependent on the IMF $\phi(m)$. The computation of the SNIa rate requires more assumptions, but it can be estimated from the sum of the explosions of all the binary white dwarfs produced in the past that have not had the time to explode yet (Madau *et al.*, 1998):

$$\mathrm{SNR_{Ia}} = \frac{\eta \int_0^t \psi(t')dt' \int_{m_c}^{m_{\max}} \exp(-\frac{t-t'-t_m}{\tau})\phi(m)dm}{\tau \int \phi(m)dm} \tag{1.51}$$

Where $m_c = \max[m_{\min}, m(t')]$, $m(t') = (10\ \mathrm{Gyr}/t')^{0.4}$ is the minimum mass of a star that reaches the white dwarf phase at a time t', and $m = 10\ \mathrm{Gyr}/m^{2.5}$ is the standard lifetime of a star of mass m. For a fixed initial mass m, the frequency of SNIa peaks at an epoch that reflects an "effective" delay $\Delta t = \tau + t_m$ from stellar birth. This second equation shows as well that the computation depends a lot on the assumption that the IMF is universal.

In this thesis, we aim to study the impact of SNR feedback on the intertwined physical processes that shape the IMF and star formation rate, in order to shed light on the conditions that correspond to the $z = 2$ universe. The problem is two-fold: *i.)* the SNR feedback needs to be measured precisely to determine the evolution of the cosmic star formation rate; *ii.)* the assumption that the IMF is universal must be verified in SNR-driven environments, since it has important implications on the SN rate.

1.4 | γ-ray production in evolved supernova remnants

Context. **The quest for the origin of cosmic rays** As early as the 20$^{\text{th}}$ century, evidence of a highly penetrating radiation was observed in electroscope experiments (an electroscope is a sealed device that measures the rate of ion production in a finite volume). In 1912, Victor Hess showed *via* balloon-born electroscope measurements that the rate of ionizing radiation increases with altitude, suggesting that the source must be from above the atmosphere. The term "cosmic rays" (CRs) was later coined by Robert Millikan once it was established that CRs were originating from outer space (Millikan and Cameron, 1928). Originally thought by Millikan to be electromagnetic radiation, CRs are in fact high-energy charged particles (protons, electrons, nuclei) traveling through space at relativistic speeds and reaching our planet as a steady and isotropic flux. The production site of CRs cannot be observed directly, since they are scattered by the interstellar magnetic field. As a consequence, the quest for their exact origin is a long standing problem in astrophysics. The bulk of mid-energy CRs ($E <$ PeV, see Fig. 1.29) has to originate from a Galactic source, because they cannot survive inverse Compton losses (from the interaction with cosmic microwave background photons) throughout the intergalactic space.

However, higher energy CRs ($E >$ PeV) are extragalactic. As early as 1934, W. Baade and F. Zwicky proposed that supernova remnants could accelerate particles into cosmic rays (Baade and Zwicky, 1934). To this day, SNRs are still the strongest candidates for the production of the bulk of CRs (Bloemen, 1987). For a complete review on the origin of cosmic rays and their role in the ISM, the reader is directed to Blasi (2013), Grenier *et al.* (2015b) (overall reviews), Tatischeff and Gabici (2018), Bykov *et al.* (2018) (CRs accelerated by SNe), Aharonian *et al.* (2006), HESS Collaboration *et al.* (2016) and Gaggero *et al.* (2017) (on the discovery and interpretation of high-energy CRs from the Galactic center) and Padovani *et al.* (2020) (impact of CRs on star formation).

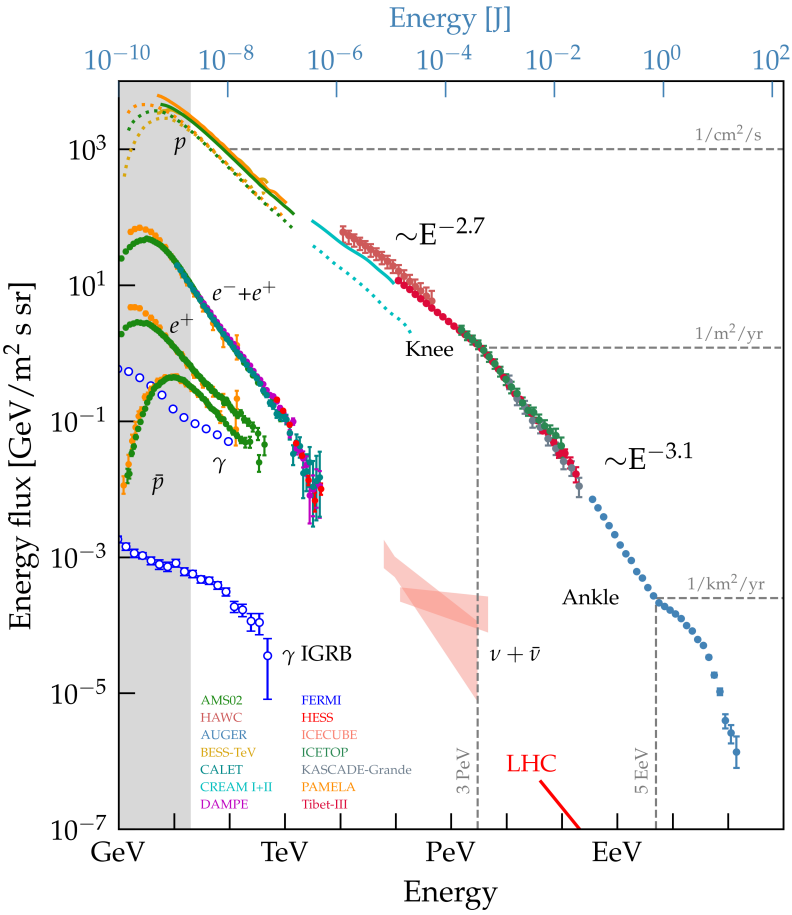

Figure 1.29 Compilation of the cosmic-ray energy spectrum measured by fourteen different experiments performed after 2000 (AMS-02, AUGER, BESS-TeV, CALET, CREAM, DAMPE, FERMI, HAWC, HESS, ICECUBE, ICETOP, KASKADE-GRANDE, PAMELA, TIBET-III). The energy of the sum of all particles is shown, as well as individual energy distributions: p, $\overline{p}$, e^-, e^+, γ, γ-IGRB, ν and $\overline{\nu}$ stand respectively for protons, antiprotons, electrons, positrons, γ-ray photons, the isotropic diffuse γ-ray background, neutrinos and antineutrinos. The positions of the "knee" and "ankle" are indicated by labels, as well as the slope Γ of the energy spectrum (energy flux $\propto E^{-\Gamma}$, $\Gamma = 2.7 - 3.1$). Figure reproduced from Evoli (2018) (see references therein).

The cosmic-ray energy spectrum The particle flux as a function of kinetic energy (*i.e.* the CR energy spectrum) spans a dozen of magnitudes in energy, and $\sim$ 10 magnitudes in energy flux (see Fig. 1.29). Particles on the high-energy end of the spectrum have higher energies than the maximum energies attained in particle accelerators such as the Large Hadron Collider. The CR energy spectrum can be described by a power-law distribution from $\sim 10^{10}$ eV to $\sim 10^{21}$ eV:

$$\frac{d\Phi}{dE} \propto E^{-\Gamma} \tag{1.52}$$

With $\Gamma = 2.7 - 3.1$ (see Fig. 1.29). At lower energies (tens of GeV and up to PeV) the power law is described by $\Gamma \sim 2.7$, with a steepening around $\sim 10^{6.5}$ GeV where the power law goes from $\Gamma \sim 2.7$ to $\Gamma \sim 3.1$ (referred to as the "knee"). At higher energies (EeV) a second break is referred to as the "ankle". At lower energies ($E < 10^{10}$ eV) the spectrum is difficult to measure due to deflections by the solar wind and magnetic field. However, since 2012 the Voyager 1 probe has been observing the local ISM spectrum down to $\sim$ 3 MeV (Cummings *et al.*, 2016).

1.4.1 Cosmic-rays acceleration, composition and diffusion in supernova remnants

Cosmic rays are believed to be accelerated by diffusive shock acceleration (DSA). Fermi (1949) proposed that CRs might be accelerated by scattering off the random motions of magnetized, turbulent gas, but this mechanism is now referred to as "second order Fermi acceleration". First order

Fermi acceleration is expected in collisionless shock waves (which are distinct from the shocks described in section 1.2), in which charged particles repeatedly bounce off Alfvén waves between the shock front and postshock region and sequentially gain energy before they escape from the shock (Axford *et al.* 1977, Bell 1978, Blandford and Ostriker 1978). The DSA mechanism allows the kinetic energy of a fast flow to be converted into cosmic-ray energy and naturally leads to a power-law population of relativistic charged particles.

Acceleration mechanism and maximum CR energy in SNRs: diffusive shock acceleration constraints and observations Supernova explosions can provide the conditions for the acceleration of CRs in shockwaves *via* DSA (*e.g.* in Cas A, Scott and Chevalier 1975). The detailed process of DSA is still a matter of debate, but SNR-cloud interactions are thought to be a significant source of high-energy CR ions and electrons below the knee ($\sim 10^{15}$ eV). Kinetic energy, magnetic field and a significant ionization fraction are the required ingredients for the acceleration of particles.

The maximum energy that a CR can be accelerated to depends on the shock speed, hence the bulk of very high-energy CRs ($E > 1$ TeV) are produced in young SNRs, in which fast shocks are propagating ($v_s = 10^3 - 10^4$ km s^{-1}). Significant magnetic field amplification (up to factors 10-100) is required to accelerate protons up to observed Galactic values, since the magnetic field required to confine the CRs in the vicinity of the shocks is much higher than the mean interstellar magnetic field (Schure *et al.*, 2012).

Evidence that cosmic rays are accelerated in supernova remnants The first suggestion that SNRs could be a significant source of Galactic cosmic rays was based on an energy budget argument (Baade and Zwicky, 1934). About 10% of the energy available in SNRs is enough to replenish the observed CRs flux against their loss. The detection of γ-rays produced *via* pion decay (see section 1.4.2.2) is a direct signature of high-energy protons. After the first detection of $E > 70$ MeV γ-rays towards the Galactic plane by the Orbiting Solar Observatory 3 (OSO-3, Clark *et al.* 1968), Montmerle (1979a) proposed that SNRs could generate observable γ-rays, an assumption that was then confirmed by statistical studies (Sturner and Dermer, 1995).

The physical association between γ-ray production, CR acceleration and SNRs sustained an active debate for a long time before next-generation γ-ray observatories entered service. The bulk of CRs up to 100 TeV are thought to be accelerated by first order Fermi mechanism at supernova shocks (Gaisser *et al.*, 1998). Esposito *et al.* (1996) presented γ-ray observations in the IC443 and γ-Cygni SNRs with the Energetic Gamma Ray Experiment Telescope (EGRET), suggesting that these two radio-bright SNRs are sites of CR acceleration.

Ackermann *et al.* (2013) reported on the detection of the characteristic spectral feature of pion decay in the two SNRs IC443 and W44 (see Fig. 1.30) with *Fermi*-LAT. The "pion decay bump" is a steep rise below 200 MeV that directly indicates the existence of accelerated protons towards a target, hence this observation strongly supports the role of SNRs as powerful hadronic accelerators. Aharonian (2013) concluded from the results of Galactic-plane γ-ray surveys that SNRs are very likely to be the main sites of CR acceleration, since a number of very-high-energy γ-ray sources are associated with young and middle-aged SNRs. SNRs are now commonly accepted as the most likely accelerators below the so-called "knee" of the energy distribution of CRs: there is no doubt that SNRs are sites of cosmic-ray acceleration up to TeV energies. Nowadays, the

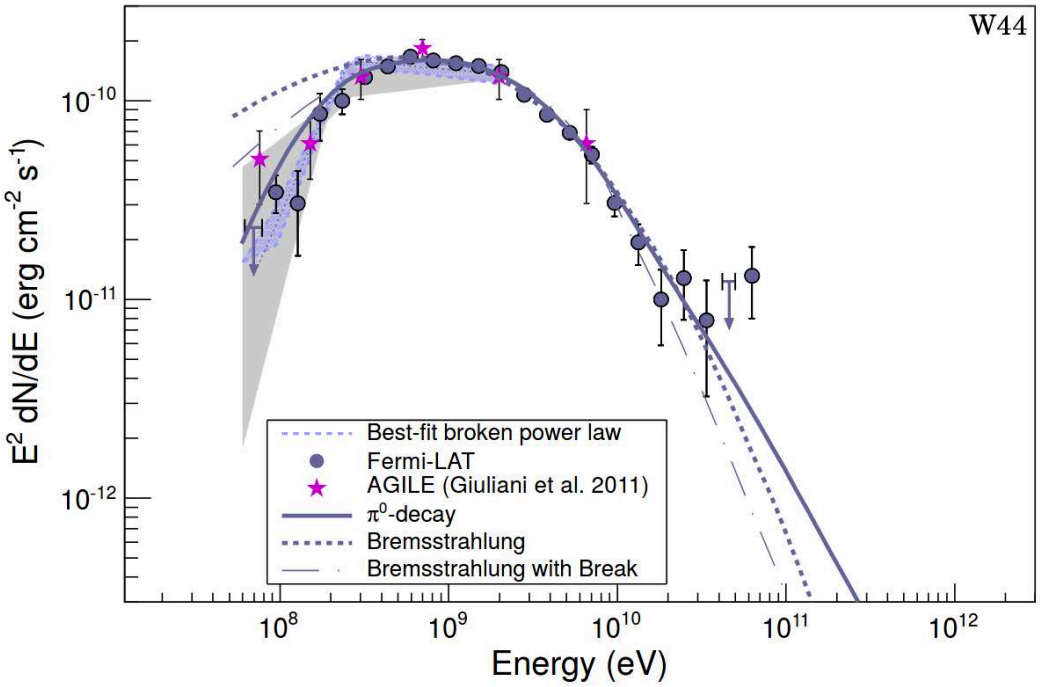

Figure 1.30 γ-ray spectrum of the W44 SNR as measured with the *Fermi*-LAT. Color-shaded areas bound by dashed lines denote the best-fit broadband smooth broken power law (60 MeV to 2 GeV), gray-shaded bands show systematic errors below 2 GeV due mainly to imperfect modeling of the Galactic diffuse emission. Solid lines denote the best-fit pion-decay γ-ray spectrum, dashed lines denote the best-fit bremsstrahlung spectrum, and dash-dotted lines denote the best-fit bremsstrahlung spectrum when including an ad hoc low-energy break at 300 MeV in the electron spectrum. Magenta stars denote measurements from the AGILE satellite. Figure reproduced from Ackermann *et al.* (2013).

subject of debate is whether all CRs are accelerated in SNRs, and in which evolutionary phase (Blasi 2013, Grenier *et al.* 2015b, Tatischeff and Gabici 2018, Bykov *et al.* 2018).

Cosmic-ray composition: leptonic and hadronic scenarios The hadron *vs.* lepton distribution of CRs accelerated in SNRs remains weakly constrained, because the knowledge of key parameters is lacking (mass, density, ionization fraction, magnetic field, interstellar radiation field). These environmental factors determine which of the two competing processes (leptonic or hadronic) dominate the distribution (Bykov *et al.*, 2018).

In hadronic models, pion decay is the dominant mechanism of γ-ray production, whereas the inverse Compton scattering drives the high-energy spectrum of γ-rays in leptonic models (see section 1.4.2.2). The fact that a statistically significant proportion of TeV sources are associated with molecular clouds favors hadronic scenarios, because these clouds provide dense targets for inelastic proton-proton interactions (*i.e.* pion decay, Tatischeff and Gabici 2018). Numerical simulation of shock-cloud interactions support a hadronic origin in SNRs where molecular clouds are illuminated by CRs (see section 1.4.3, Inoue *et al.* 2012). However, hadronic models still have issues, and in many cases leptonic models are more adequate to describe the observed γ-ray energy spectrum (Aharonian, 2013). For example, in the young SNR RX J1713.7-3946, broadband γ-ray observations with the *Fermi*-LAT are consistent with a leptonic origin as a dominant mechanism.

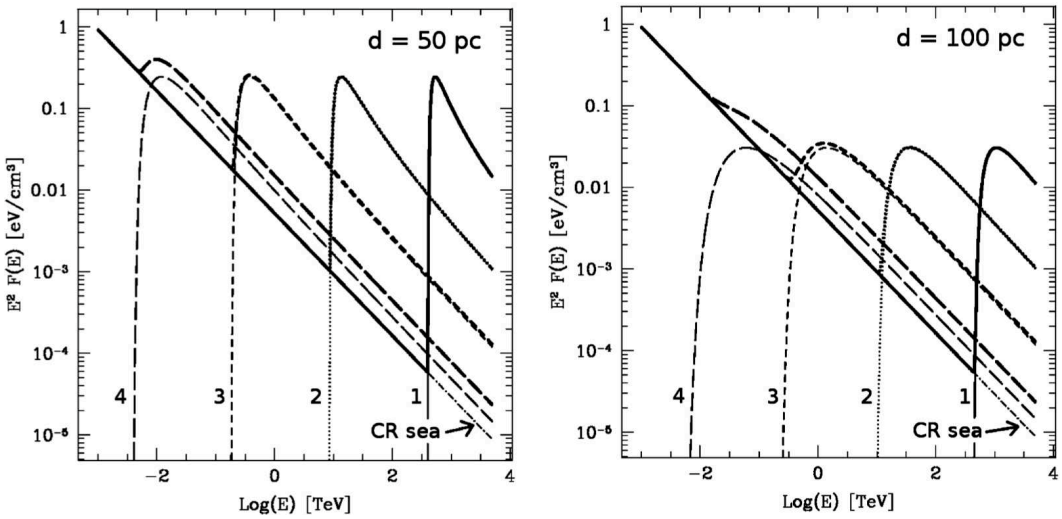

Figure 1.31 Spectrum of CRs at the location of the molecular cloud. The cloud is located at 50 pc (left-hand panel) and 100 pc (right-hand panel) from a SNR. The thin dot-dashed line shows the Galactic CR spectrum, while the thin solid (curve 1), dotted (2), short-dashed (3) and long-dashed (4) lines represent the spectrum of CRs coming from the SNR for 500, 2000, 8000 and 32 000 years after the supernova explosion, respectively. The thick lines show the total CR spectrum at the cloud location. Figure reproduced from Gabici *et al.* (2009b).

Cosmic-ray maximum energy, diffusion and escape Young SNRs are likely to be PeVatrons (Gabici and Aharonian, 2007), although very high-energy CRs accelerated in the early stages of a SN explosion escape rapidly from the remnant. The energy of CRs accelerated by a SNR decreases with time, as the remnant grows in size and starts to interact with the dense ISM (which causes energy losses by friction). The energy distribution of escaping CRs at any distance R from the SNR and at any time t is given by Gabici *et al.* (2009b):

$$f(t,R,E) = \frac{\eta E_{\rm SN}}{\pi^{3/2}\ln(E_{\rm MAX}/E_{\rm MIN})}\frac{e^{-(R/R_{\rm d})^2}}{R_{\rm d}^3}E^{-2} \tag{1.53}$$

where $E_{\rm SN}$ is the total SN explosion energy, η is the fraction of such energy converted into CRs, and $E_{\rm MAX}$, $E_{\rm MIN}$ are respectively the maximum and minimum energies of CRs accelerated during the Sedov phase ($E_{\rm MIN}$ = 1 GeV and $E_{\rm MAX}$ = 5 PeV, Gabici *et al.* 2009b). $R_{\rm d}$ is the diffusion distance, given by:

$$R_{\rm d}(E) = \sqrt{4D(E)[t-\chi(E)]} \tag{1.54}$$

Where $D(E)$ is the diffusion coefficient and $\chi(E) = t_{\rm Sedov}\,(E/E_{\rm MAX})^{-1/\delta}$ (with $\delta = 2.48$, Gabici *et al.* 2009b). If cosmic rays were not able to escape from the shock front, it would require to wait for the shock to dissipate before they can propagate in the ISM. In fact, the sharp synchrotron rims observed in young SNRs suggest that a strong diffusion barrier is associated with the fast expanding blastwave (Achterberg *et al.*, 1994). The localized magnetic field amplification inhibits the forward propagation of CRs, which are scattered back towards the shock (Bell *et al.*, 2013). Ultimately, the observed CR energy spectrum is determined by the escape efficiency at different energies ($D(E)$ in Eq. 1.54), since it corresponds to the distribution of runaway particles (Ohira *et al.*, 2010). Drury (2011) presented a careful description of the escape mechanism in the DSA framework. Using a box model, they showed that the bulk of low-energy CRs are produced and

released in the late stages of SNR evolution (typically during the snowplow phase), whereas the higher energy CRs (~PeV) escape early on.

Alternative candidates for cosmic-ray acceleration Currently, SNRs seem to be the best candidates for cosmic-ray acceleration, but there are no reasons to believe that only SNR accelerate particles since the DSA mechanisms can take place in any type of shock. Young stellar objects represent additional candidates for the origin of cosmic rays. Padovani *et al.* (2015) found that protostellar jets and surface shocks can be strong accelerators of protons *via* the DSA mechanism, and showed that this model can explain the high ionization rate observed near protostellar sources. At jet shocks, protons can be injected from the thermal plasma and accelerated up to relativistic energies (up to 10-13 GeV and 26-37 GeV respectively for jet acceleration and protostellar surface shock acceleration in lower-mass stars). Fast jets ($v_s \sim 10^3$ km s^{-1}) from high-mass protostars might produce cosmic rays up to TeV energies (Padovani *et al.*, 2016).

In addition, cosmic rays could also be accelerated in H II regions (Padovani *et al.*, 2019), massive star clusters (Aharonian *et al.*, 2019), superbubbles (Ackermann *et al.* 2011, Bykov *et al.* 2020), Fermi bubbles (Grenier *et al.*, 2015b) and in the Galactic center (Gaggero *et al.*, 2017).

1.4.2 Interaction of cosmic rays with the interstellar medium

1.4.2.1 Physical and chemical impact of cosmic rays

Lower-energy (< 100 MeV) cosmic rays are a key element of astrochemistry, as well as the thermal and dynamical evolution of molecular clouds (Iglesias 1977, Padovani *et al.* 2009). Most importantly, CRs drive interstellar chemistry *via* ionization, but they also heat the interstellar medium, produce light element isotopes and generate internal UV photons in cold cores through the Lyman and Werner band excitation of H_2 (Prasad and Tarafdar, 1983). The average ISM energy density of CRs is $\sim$ 1 eV cm^{-3}, hence they represent a large source of energy and feedback.

***i.)* Ionization** Interstellar gas phase chemistry is driven by fast ion-neutral reactions (Indriolo and McCall, 2013) hence the ionization rate is fundamental. In non-diffuse regions ($n_H \gg 1$ cm^{-3}), photons with $E > 13.6$ eV are quickly absorbed by the abundant interstellar atomic hydrogen. As a consequence, photoionization is only efficient for species with ionization potential below that of hydrogen (*e.g.* Si, C) and there is a lack of ionizing radiation for other species (He, O, N, H_2, D). In environments where ionizing radiation cannot penetrate due to self-shielding, low-energy CRs can be the main agent of ionization (McKee, 1989). Hence, the CR ionization rate is a key parameter for hydrogen, oxygen and deuterium chemistry, and more generally in chemical models and calculations of molecular abundances. For example, CRs are a driver of cold core chemistry *via*:

$$H_2 + CR \longrightarrow H_2^+ + e^- \tag{1.55}$$

followed by

$$H_2^+ + H_2 \longrightarrow H_3^+ + H \tag{1.56}$$

The ion-molecule reactions initiated by H_3^+ are fundamental in the subsequent formation of many other species (*e.g.* Geballe and Oka 1996) hence CRs can induce and enhance chemistry in molecular regions. The CR ionization rate has been claimed to be measured using the DCO^+/HCO^+ratio: *e.g.* Ceccarelli *et al.* (2011) found a CR ionization rate $\sim$ 100 times larger than the standard value in a molecular cloud near the W51C SNR, associated with a TeV γ-ray source, see also Vaupré *et al.* (2014) in the W28 SNR.

According to these studies, the CR ionization rate can be estimated using the DCO^+/HCO^+ ratio, which is a tracer of the electron fraction $x(e^-) = n(e^-)/n(\mathrm{H})$. However, the chemical models used in these highly dynamical regions did not include any shock modelization. In addition, Shingledecker *et al.* (2016) demonstrated that these results are sensitive to small deviations of the ortho-to-para ratio of molecular hydrogen. CRs can also drive ionization in protostellar disks, which in turn controls their magnetic properties (Dolginov and Stepinski 1994, Cleeves *et al.* 2015, Padovani *et al.* 2018).

***ii.)* Spallation** Cosmic rays can fragment heavy nuclei (carbon, nitrogen, oxygen) into smaller pieces (a process referred to as *spallation*) resulting in different isotopes of lighter elements (Matteucci, 2012). As a matter of fact, ^{6}Li, ^{9}Be and ^{10}B are believed to form only *via* CR spallation (Meneguzzi *et al.*, 1971).

***iii.)* Dust charging** In the diffuse ISM, interstellar dust grains are subject to two primary electric charging processes: collisions with the plasma of thermal electrons and the photoelectric effect. Ivlev *et al.* (2015) studied the effects of CRs on dust charging in cold, shielded molecular clouds. They showed that the photoelectric emission of grains due to the UV radiation field generated by CRs dominates the electric charging process in molecular environments. Dust charging has important consequences on the chemical and dynamical evolution of molecular clouds. In particular, the Coulomb repulsion might modify the rate of coagulation of dust grains. Shingledecker *et al.* (2018) presented the results of models illustrating the effects of cosmic-ray driven grain chemistry.

***iv.)* Grain sputtering** In shielded environments (interstellar dense clouds), the bombardment of ice mantles by low-energy CRs is the primary source of fast ions (keV-MeV). These ions play a role in a rich chemistry of complex organic molecules (Palumbo *et al.*, 2008). The flux of CRs on icy mantles affects the structure of grains and may induce cosmic ray sputtering, amorphisation, desorption of molecules and radicals (*e.g.* Dartois *et al.* 2013, Dartois *et al.* 2015a, Dartois *et al.* 2015b Dartois *et al.* 2018). These effects are of uttermost importance for astrophysical models to constrain the chemical evolution of the dense phase of the ISM.

1.4.2.2 γ-ray production

Cosmic rays are not detected directly (at least not the low-energy CRs), but only by the γ-rays that they produce: these γ-rays are their signature. The advantage of working with detected photons rather than charged particles is that it is possible to localize the source of the photons, in contrast to CRs that interact with the magnetic fields they encounter on their way.

There are four primary channels for the production of γ-rays *via* the interaction of cosmic rays with the ISM (see Fig. 1.32). The corresponding mechanisms are described in the four following paragraphs and represented in the formulas 1.58, 1.59, 1.60 and 1.61:

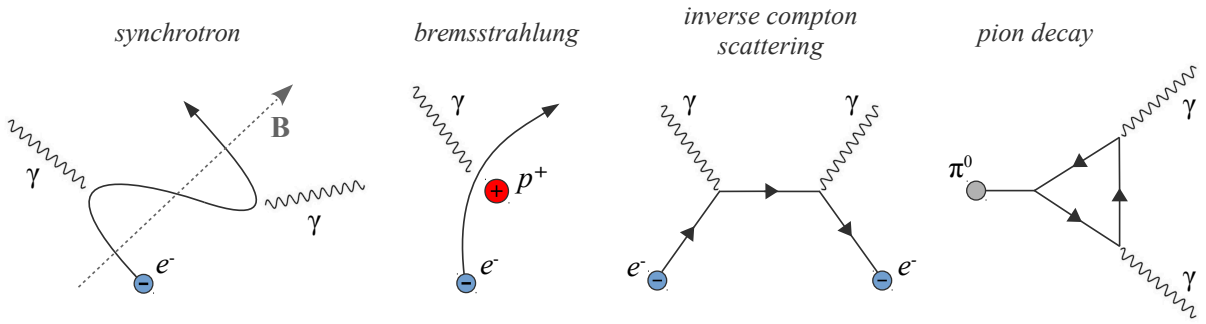

Figure 1.32 Schematic representation of the four main channels for γ-ray production, from left to right: synchrotron radiation, bremsstrahlung, inverse Compton scattering and pion decay. The symbols e^-, p^+, π^0 and γ account respectively for electrons, protons, neutral pions and photons.

***i.)* Pion decay** Neutral pions are subatomic particles made either of the combination $u\bar{u}$ (*"up"* quark and antiquark) or $d\bar{d}$ (*"down"* quark and antiquark). Neutral pions can be produced in high-energy proton-proton collisions if the colliding proton has a kinetic energy above the threshold $\sim$ 280 MeV:

$$\tilde{p} + p \longrightarrow p + p + \pi^0 \tag{1.57}$$

Where $\tilde{p}$, p and π^0 respectively account for a high-energy proton, rest proton and neutral pion. The neutral pion then spontaneously decays into two γ-ray photons (neutral pions have a lifetime $\sim 8.5 \times 10^{-17}$ s, Zyla *et al.* 2020) with an energy $m_{\pi^0}c^2/2 = 67.5$ MeV in the rest frame of the neutral pion:

$$\pi^0 \longrightarrow 2\gamma \tag{1.58}$$

Pions decay into photons that carry a typical energy that represents $\sim$ 10% of the kinetic energy of the colliding proton (additionally to the 67.5 MeV rest frame energy).

***ii.)* Inverse Compton scattering** High-energy photons can also be produced *via* inverse Compton inelastic scattering, a process in which an electron transfers a part of its energy to a scattered photon:

$$e^- + \gamma \longrightarrow e^- + \gamma' \tag{1.59}$$

Where γ corresponds to an incident photon of energy $h\nu$, and γ' a scattered photon of energy $h\nu'$, with $\nu' > \nu$ ($\Delta\nu = \nu' - \nu$ is referred to as the *Compton shift* of frequency).

***iii.)* Bremsstrahlung** Bremsstrahlung[10] is a free-free process in which electromagnetic radiation is produced by the interaction between a decelerating electron and a proton:

$$e^- + p \longrightarrow e^- + p + \gamma \tag{1.60}$$

[10]In german, *bremsen* means "to brake" and *strahlung* means "radiation", *i.e.* "braking radiation".

***iv.)* Synchrotron** Charged particles (most generally electrons) gyrating around magnetic field lines produce electromagnetic radiation referred to as synchrotron radiation:

$$e^- \longrightarrow e^- + \gamma \tag{1.61}$$

In SNRs, synchrotron radiation is typically observed from radio shells where relativistic electrons interact with the turbulence-enhanced magnetic field, and also in X-rays (Chevalier, 1982b).

Among the four X-ray/γ-ray production mechanisms presented above, three processes involve electrons, and one process involves protons. Therefore, disentangling the contribution of these mechanisms to the total X-ray/γ-ray luminosity allows to constrain the electron/nuclei proportion in CRs.

Interstellar ingredients for γ-ray production in supernova remnants The aforementioned four mechanisms of interaction between CRs and the ISM underline how γ-ray studies require to know the ISM contents of SNRs with great accuracy. It is possible to constrain the relative contributions of each mechanism (bremsstrahlung, pion decay, inverse Compton, synchrotron) from the analysis of the energy spectrum of γ-rays measured in SNRs. The local magnetic field, radiation field, ionization fraction and mass all are key parameters to model and constrain the γ-ray energy spectrum, CRs composition and dominant acceleration mechanisms.

The high-energy γ-ray flux produced *via* nucleus-nucleus interaction leading to pion decay depends both on the energy density of CRs *and* the density of the ambient medium that provides the nuclei to interact with (Drury *et al.*, 1994). Similarly, constraining the inverse Compton radiation requires to have an accurate knowledge of the infrared and optical energy distribution of the radiation field in the remnant (Mastichiadis 1996, Gaisser *et al.* 1998).

In this thesis, we aim to work towards the establishment of precise measurements of these "ISM parameters" in the IC443 SNR (in particular, the gas mass and radiation field). Measuring these parameters is required to interpret future γ-ray observations and to constrain the exact emission mechanisms which drive the γ-ray production in IC443. Formerly, the *Fermi* observations of IC443 have been interpreted by Abdo *et al.* (2010) and Ackermann *et al.* (2013). In these studies, the authors modeled the γ-ray spectra with approximate descriptions of the interstellar medium: they considered a molecular mass of 10^4 $M_\odot$, and adopted a local density of 10^4 cm^{-3} based on the detection of OH masers (Frail *et al.*, 1996). Because their constraints on the ISM contents of the region are rough, their best-fit models are degenerate, and the authors cannot positively conclude on the nature of the emission mechanisms (leptonic and hadronic: pion-decay, bremsstrahllung, inverse Compton scattering, synchrotron, *etc*). We aim to fill this gap and bring the required interstellar measurements which were missing in these studies, in order to produce thorough γ-ray spectrum models and identify the nature of the interactions between the ISM and CRs in IC443.

1.4.3 Supernova remnants interacting with molecular clouds

SNRs are efficient particle accelerators, hence they represent a strong source of X-ray to γ-ray emission due to the CR-ISM interactions (although X-ray and γ-ray peaks are likely to be located in distinct places, since they trace different energies and different processes). Electrons reach higher energies in the interclump shocks, which are likely to be the dominant site of γ-ray and radio to X-ray synchrotron emission. Evidence of electron acceleration in SNRs first came from radio

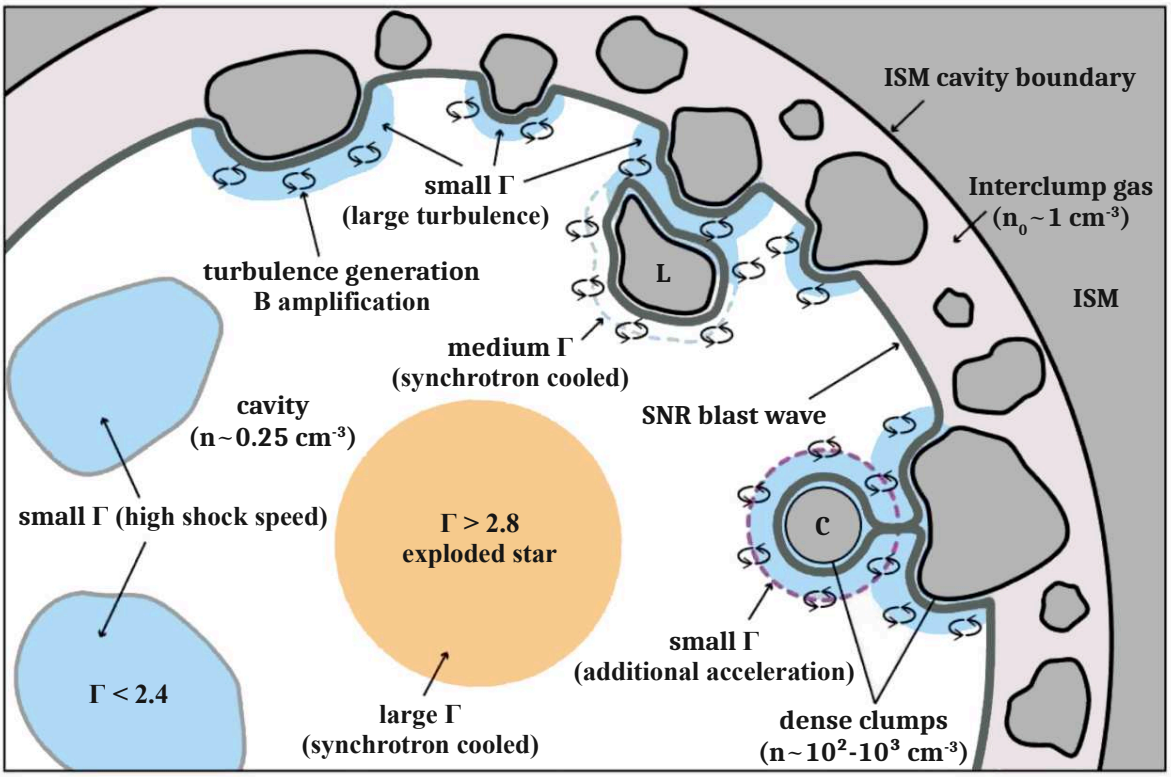

Figure 1.33 Schematic image of the efficient cosmic-ray acceleration in turbulent cells towards RX J1713.7-3946, with the positions of clumps C and L indicated by labels. The SNR shock waves travel through the cavity (gas density $n \sim 0.25$ cm^{-3}), where cosmic-ray acceleration is working by DSA scheme and the shock speed is not much decelerated in lower density. Propagated shock waves are stalled toward the dense clumps, and are traveling in the interclump space. Shock-cloud interaction generates the turbulence ($\eta \sim 1$) and enhances the magnetic field around the dense clumps. The accelerated particles in the innermost cavity and some of the clumps are already cooled down due to the synchrotron cooling. The additional acceleration is induced due to the high turbulence and strong magnetic fields around the some of the dense clumps. Γ is the spectral index of the synchrotron X-ray radiation. Figure reproduced from Sano *et al.* (2015).

synchrotron radiation, before the observations of nonthermal X-ray radiation in SN1006 by ASCA provided evidence for electron acceleration up to 100 TeV (Koyama *et al.*, 1995). Reynolds (1998) presented a model of synchrotron radiation for the Sedov-Taylor phase of SNRs that predicts the acceleration of electrons up to 1 TeV in shockwaves, and the subsequent emission of X-ray radiation by electrons within the shell.

Molecular clumps interacting with moderately fast radiative shocks are expected to be sources of hard X-rays and MeV γ-rays (Torres *et al.*, 2003). Bykov *et al.* (2000) proposed a model of nonthermal emission in evolved SNRs interacting with MCs based on the acceleration of electrons in the shocks associated with the SNR blastwave. The W51C, W44, IC443 and W28 SNRs are resolved by *Fermi*-LAT observations, and are all interacting with MCs (*e.g.* Abdo *et al.* 2009), hence they represent a unique opportunity to study the high-energy contents of particle accelerators interacting with dense molecular gas.

The nonthermal, multi-wavelength emission produced by SNR/cloud interaction is described thoroughly by Gabici *et al.* (2009b), including the effect of distance between the SNR and the cloud, the age of the remnant, the total mass of the cloud and the local magnetic field. Uchiyama *et al.* (2010) studied the synchrotron and γ-ray emission in 'GeV-bright' SNRs (W51C, W44, IC443) based on a model in which the GeV signal is enhanced through pion decay towards crushed clouds. In their 3D MHD simulations, Inoue *et al.* (2012) studied the interaction of a SNR blast with interstellar clouds. Interstellar clouds are formed as complex of clumps fragmented by the thermal instability (Hennebelle *et al.*, 2008), hence the SNR blast is interacting with a clumpy medium. The shock is stalled within the dense clouds, but remains fast in the diffuse interclump medium. Around the envelopes of molecular clumps interacting with the blast, the shock-generated turbulence amplifies the local magnetic field (up to $\sim$ 1 mG for a shock velocity $v_s = 10^3$ km s^{-1}). The high-energy radiation in the shell-type SNR RX J1713.7-3946 (aged $\sim$ 1600 yr) is a remarkable example of this mechanism. Sano *et al.* (2015) presented an analysis of *Suzaku* 0.4-12 keV observations of this very high-energy SNR (one of the highest energy γ-ray source, Aharonian *et al.* 2004). In this SNR, protons and electrons are respectively accelerated up to 10-800 TeV and 1-40 TeV. The X-ray flux in RX J1713.7-3946 shows enhancement towards the dense clumps, in agreement with the magneto-turbulent cells model of Inoue *et al.* (2012) (see Fig. 1.33).

The discovery of X-ray variability in RX J1713.7-3946 provided a strong evidence of CR acceleration in young SNRs. Uchiyama *et al.* (2007) reported *Chandra* observations of the brightening and decay of X-ray filaments and knots towards the remnant shell on a time scale $\sim$ 1 yr. This rapid variability can be interpreted as fast synchrotron cooling towards active sites of acceleration and magnetic field amplification, suggesting that we witness real-time CR acceleration (Uchiyama and Aharonian, 2008).

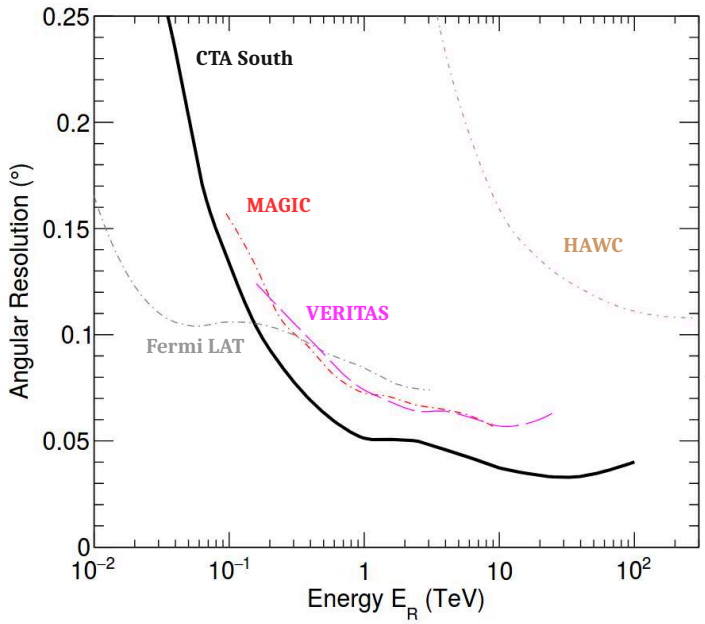

Figure 1.34 Comparisons of the angular resolution with respect to energy (from 10 GeV to 300 TeV) for CTA and a selected sample of existing γ-ray instruments (the *Fermi*-LAT curve corresponds to the Pass 8 data release). The angular resolution is expressed as the 68% containment radius of reconstructed γ-ray emission (the resolution for CTA-North is similar). Figure reproduced from Cherenkov Telescope Array Consortium *et al.* (2019). For the latest CTA performance plots, see `https://www.cta-observatory.org/science/cta-performance`.

γ-ray observations: future prospects The Cherenkov Telescope Array (CTA, Cherenkov Telescope Array Consortium *et al.* 2019) will be operating between 20 GeV and 300 TeV and will constitute a major ground based observatory in the next decade. CTA has a wider field of view

than previous observatories, improved sensitivity and will reach ∼ 1 arcmin resolution at high energies (see Fig. 1.34). CTA will allow to determine the sites of very high-energy (> 100 TeV) particle acceleration, increase the statistics of γ-ray observations towards a large number of SNRs and over a broad range of energies, and promises breakthrough regarding the identification of the acceleration and γ-ray production mechanisms (Aharonian, 2013).

Finding out if SNRs are indeed the dominant accelerators of CRs is a major science goal of CTA. In Galactic SNRs such as IC443, the unprecedented resolution offered by CTA will allow to precisely pinpoint the origin of the γ-ray emission and work towards accurate interpretations based on multi-λ studies. A major goal of this thesis is to prepare such a task by building an accurate description of the ISM contents of the IC443G region, where the γ-ray peak has been detected by the Very Energetic Radiation Imaging Telescope Array System (VERITAS) and *Fermi* (Humensky and VERITAS Collaboration, 2015).

1.5 | Questions and scientific goals

In this thesis, we aim to simultaneously tackle questions related to several intertwined aspects of the impact of evolved supernova remnants on the interstellar medium of galaxies.

Why *evolved* supernova remnants? Why the IC443 supernova remnant? We aim to study evolved supernova remnants (age ≫ 1 kyr) in order to determine the total energetic and chemical impact of SNRs over large volumes of the ISM and within the major part of their lifespan. The IC443 supernova remnant is an ideal candidate to pursue these scientific goals:

– IC443 is an evolved SNR (∼ 25 kyr, *e.g.* Chevalier 1999), hence the volume in which energy has been injected by shocks, energetic photons and cosmic rays into the environment is large (∼ 20 pc diameter).

– In addition, IC443 is a typical case of a SNR interacting with a molecular cloud, and it is a strong GeV-TeV source (*e.g.* Abdo *et al.* 2009). Therefore, it allows to study the interaction of CRs accelerated by a SNR with the ISM and the mechanisms of γ-ray production in such an object.

– IC443 is nearby: it is located at a distance 1.8 ± 0.2 kpc (Ambrocio-Cruz *et al.* 2017, Yu *et al.* 2019). Therefore, the remnant can be mapped with a high spatial resolution (10″ corresponds to ∼ 0.1 parsec towards IC443). In addition, IC443 has been intensively surveyed both in the radio range and by γ-ray observatories, and it is a well-known object (as of September 2021, there are a total of 310 ADS[11] items that contain the keyword 'IC443' in their title). In Chapter 2, we present a review of previous studies in the IC443 SNR.

We want to quantify and understand the physical and chemical impacts and the energy injection mechanisms taking place in the regions in which the IC443 SNR is interacting with its environment, including the dense molecular gas phase and the dust phase.

To this day, the high-energy emission characteristics of IC443 are well constrained in the radio, X-ray and γ-ray ranges (*e.g.* Castelletti *et al.* 2011, Troja *et al.* 2006, Troja *et al.* 2008). We

[11]This research has made use of NASA's Astrophysics Data System.

aim to fill the gap in the far-infrared to millimeter range to study the dense molecular phase (both quiescent and perturbed by the SNR) and dust phase of the SNR (gas-phase chemical abundances, total mass, local density, grain properties, *etc*). In addition, we want to characterize all stages of star formation and study their causal relation to the SNR. Accurate interstellar measurements, and in particular constraints on the total mass and interstellar radiation field are essential parameters to understand the cosmic-ray electron *vs.* nuclei distribution, the γ-ray production and to connect the 'interstellar medium' and 'very high-energy' studies (since these parameters are required to constrain the relative contributions of the pion decay, inverse Compton scattering and Bremsstrahlung to the γ-ray spectrum, see section 1.4.2.2).

Questions on the intertwined issues of evolved supernova remnants, cosmic rays, γ-rays and star formation The work presented in this manuscript revolves around the following issues:

- In the IC443 supernova remnant, can we identify conspicuous interstellar and/or stellar features (dense molecular clumps, H II regions, young stellar associations, *etc*) that could be targets of interaction with the SNR blast and with cosmic rays?

- What are the physical conditions: local density, total mass, kinetic temperature of the gas and dust phases, kinematics (turbulent velocity dispersion, kinetic energy, systemic velocity), interstellar radiation field, ionization fraction, *etc* in the SNR? What can we learn from these measurements about *i.)* the energetic impact of the SNR on its surroundings and *ii.)* the interaction of cosmic rays with the interstellar medium (*i.e.* the interpretation of γ-ray spectra)?

- What is the status of star formation in the regions interacting with the SNR blast? Can we find evidence of SNR-induced star formation? What is the impact of cosmic rays and shock feedback on the star-forming efficiency?

- How can we update the interpretation of γ-ray observations in the IC443 SNR based on our analysis of its interstellar contents? Can protostars contribute to the injection of energetic particles? What are the dominant sources and mechanisms of cosmic ray injection, acceleration and interaction with interstellar matter in the SNR? Are γ-rays produced *via* the interaction of the SNR with CRs accelerated in the early stages of the SN explosion, or with freshly accelerated CRs? Can we lift the electrons/nuclei degeneracy in the cosmic ray population?

Working towards a clear picture of these issues will also allow to better understand the star-forming conditions in $z = 2$ galaxies, in which the SN rate is higher (see section 1.3.4). In fact, the ISM environment of evolved supernova remnants such as the IC443 SNR should be reminiscent of the conditions found in these active galaxies, and thus our study might contribute to constrain the impact of the paramount shock and CR feedback on the evolution of galaxies.

Methodology and plan To pursue these scientific goals and tackle these questions, we have focused our efforts on a $10' \times 10'$ field of observations located in the IC443 SNR (the 'extended G region', see Fig. 2.20). In this area of the SNR where the centroid of γ-ray emission has been located by high-energy observations (Humensky and VERITAS Collaboration 2015, see also

Fig. 2.15, Fig. 2.20), we performed new spectral-line and continuum observations in order to characterize as much as possible the interstellar and stellar contents of the SNR and its environment. With this new study of IC443, we want to prepare the upcoming delivery of new γ-ray observations with CTA, and to introduce a detailed picture of the local ISM into future interpretation of the high-energy processes that occur in SNRs. With a $\sim 1'$ CTA angular resolution, our measurements will allow to accurately interpret the γ-ray spectra in the $10' \times 10'$ region of IC443 where CRs interact with the ISM.

The methods used in this study of IC443 are presented in Chapter 3 (detection methods), Chapter 4 (radiative transfer analysis of molecular lines) and Chapter 5 (dust thermal emission models). Our new observations include ^{12}CO, ^{13}CO and C^{18}O hyperspectral and continuum submillimeter/millimeter observations with the IRAM 30m and APEX telescopes (respectively presented in Chapter 6, Chapter 7). We have performed both LTE and non-LTE radiative transfer analyses of H_2 and ^{12}CO, ^{13}CO and C^{18}O pure rotational lines to estimate the total molecular mass in the $10' \times 10'$ 'extended G region' (Chapter 8). We then studied the dust contents of the SNR with both archival continuum data (*Spitzer*/MIPS, WISE, AKARI, LABOCA) and new NIKA2 observations at 1.15 mm and 2.0 mm, which we analyzed using two state of the art Bayesian inference models for dust thermal emission (`PPMAP` and `HerBIE`/THEMIS, Chapter 9). Finally, we produced a catalog of candidate protostars from a standard color-color filtering analysis of WISE, 2MASS and Gaia point sources and compared our findings with multi-wavelength measurements (Chapter 10).

Chapter 2 | The IC443 supernova remnant: a preliminary review

Contents

2.1 | Discovery, age and distance

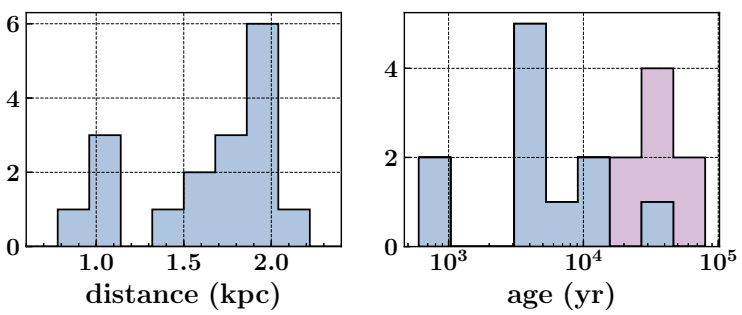

Figure 2.1 Distance (*left*) and age (*right*) measurements for the supernova remnant IC443. On the right panel, two colors are used to distinguish estimates from X-ray studies (in blue) from other methods of measurements (in pink).

Distance (pc)	Reference
800	Radhakrishnan (1960)
800-1200	Harris (1962)
> 1000	Malina *et al.* (1976)
700-1500	Lozinskaya (1981)
1400	Kargaltsev *et al.* (2017)
1500	Sharpless (1965)
1500	Welsh and Sallmen (2003)
1729^{+116}_{-94}	Yu *et al.* (2019)
1500-2000	Milne (1970)
1500-2000	Fesen and Kirshner (1980)
1900	Milne (1979)
1900	Ambrocio-Cruz *et al.* (2017)
2000	Minkowski (1959)
2000	van der Laan (1962a)
2000	Parker (1963)
2000	Ilovaisky and Lequeux (1972)
> 2200	Dickel (1973)

Age (yr)	Reference
1000	Wang *et al.* (1992)†
1000	Asaoka and Aschenbach (1994)†
2800-3400	Petre *et al.* (1988)†
3400	Winkler and Clark (1974)†
4000^{+2500}_{-1800}	Malina *et al.* (1976)†
4000	Troja *et al.* (2008)†
4500	Hnatyk and Petruk (1998)†
5000	Mufson *et al.* (1986)†
8000	Ustamujic *et al.* (2021)†
12 700	Parkes *et al.* (1977)
13 000	Gulliford (1974)†
20 000	Lee *et al.* (2008)
25 000	Lozinskaia (1975)
30 000	Chevalier (1999)
30 000	Olbert *et al.* (2001a)†
30 000	Ambrocio-Cruz *et al.* (2017)
48 000	Welsh and Sallmen (2003)
60 000	Lozinskaya (1969)
< 100 000	Minkowski (1959)

Table 2.1 Distance and age measurements for the supernova remnant IC443. Age measurements based on X-ray observations are marked by a '†'. The measurements listed in these two tables are also represented in Fig. 2.1.

IC443's first reference on ADS is in a list of 'photographic nebulosities and star clusters connected with the Milky Way' compiled by Barnard (1894). The next reference is another compilation of 'new emission nebulae' by Minkowski (1946), where it was listed as a 'diffuse and peculiar nebulosity' located in Gemini. In the 1950s, the idea that a class of interstellar emission nebulae might be related to the remnants of SN explosions (Minkowski, 1942; Baade, 1943) was firmly established. Shajn and Gaze (1954) and Shklovsky (1954) suggested that IC443[1] could be the remnant of the historical supernova 837AD, a guest star recorded by Chinese astronomers in the Xin-Tang-Shu (New History of the Tang Dynasty, Ouyang and Song 1061) and Wen-Xiang-Tong-Kao (Historical Investigation of Public Affairs, Ma 1254). 837AD was also mentioned in the records of Biot (1864), Williams (1871), Lundmark (1921), Ho (1962) and Xi and Bo (1965). The Chinese records indicate that the guest star was visible for a duration of 22 days in Gemini, although Xi (1955) and Green and Stephenson (2003) argued against this association, and claimed that there is a confusion between 837AD and the Halley's Comet (this is discussed in Wang *et al.* 1992 and Wilson 2003).

Minkowski (1959) classified IC443 in the same category as the Cygnus loop, with bright filaments composing an incomplete expanding shell whose momentum could only be driven by a type II SN. Minkowski also posited an age lower than 10^5 years, and an interaction with interstellar regions of various densities. A few years later, IC443 was still referred to as a possible supernova remnant by Harris (1962), who inferred a constant spectral index between 86 MHz and

[1]IC443 is also often referred to as the G189.1+3.0 SNR (Green catalog, *e.g.* Green 2019). The identifiers '3C157', 'Sh2-248' and 'Jellyfish Nebula' are also used.

1.42 GHz, and provided an estimate of 0.8 − 1.2 kpc for its distance, based on the interpretation of the observed radio emission as entirely originating from synchrotron radiation. Parker (1963, 1964) also classified IC443 as a possible SNR and concluded that the physical conditions inferred from spectrophotometric observations in its individual filaments were reminiscent of what can be expected behind a shock wave. Howard and Dickel (1963) categorized IC443 as a SNR more firmly, based on the lack of variation of its spectral index with frequency between 38 MHz and 8 GHz. From this moment on, the idea that IC443 is indeed a SNR interacting with the local ISM seems definitely accepted (e.g., Hogg 1964).

Hogg (1964) also provided references for an estimate of the distance of the SNR, between 0.8 and 2 kpc, highlighting the important uncertainty spread resulting from the various, themselves uncertain measurement techniques. He also identified a faint nebulosity associated with an H II region stretching to the north and the east of the object. Sharpless (1965) first made the assumption of an association of IC443 with the neighboring S249 H II region, hence a similar distance for both objects, 1.5 kpc. This was in agreement with the theoretical $\Sigma - d$ relation for SNRs (*e.g.* Woltjer 1972). Dickel (1973) then used 21-cm line absorption measurements to infer a distance probably greater than 2.2 kpc and qualitatively wiped off the assumption of an association between the H II region and the SNR. On the other hand, Fesen and Kirshner (1980) and Fesen (1984) used the interaction of IC443 with an [H I] cloud discovered by Denoyer (1977) (as opposed to the [H I] condensations observed within the remnant at negative velocities, Denoyer 1978) and related to the H II region S249 to constrain the distance to IC443 in the 1.5-2.0 kpc range (see discussions therein).

The distance of the Gem OB1 association is ∼ 1.51 kpc (Humphreys, 1978). Based on [Na I] and [Ca II] absorption lines observed towards four early-type stars in the line-of-sight towards IC443, Welsh and Sallmen (2003) confirmed the value of 1.5 kpc. Most recently, Ambrocio-Cruz *et al.* (2017) used a scanning Fabry-Pérot interferometer to measure a kinematic distance of 1.9 kpc from the Sun, while with the same technique the S249 H II region was found to be located 0.6 kpc in front of the SNR. Using 3D interstellar dust extinction maps, Yu *et al.* (2019) provided new distance estimates of four SNRs interacting with molecular clouds, including IC443. From the analysis of two molecular cloud features, they measured the respective distances 1729^{+116}_{-94} pc and 1865^{+174}_{-116} pc, and they adopted the first one. It should be noted that Kargaltsev *et al.* (2017) proposed a distance 1.4 kpc in their study, but their estimate is based on the assumption that IC443 is physically associated with the PWN G189.23+2.90 (see next section). Based on the recent studies of Ambrocio-Cruz *et al.* (2017) and Yu *et al.* (2019), we will adopt a value of 1.8 ± 0.2 kpc in the analysis of our own measurements.

The age of IC443 is also a matter of debate. After the first very rough estimate by Minkowski (1959), Lozinskaya (1969) constrained the value of 60 kyr, with [Hα] Fabry-Perot observations allowing to measure an expansion velocity of 65 km s^{-1}, based on the distance and radius assumptions of 1.5 kpc and 10 pc (80 kyr adopting 1.9 kpc and 13 pc for these values). Lozinskaia (1975) later identified faster moving filaments in IC443 and deduced an age of 25 kyr. Simultaneously, a lower estimate was inferred from the interpretation of X-ray data: 3.4-6 kyr for Winkler and Clark (1974) and 4000^{+2500}_{-1800} yr for Malina *et al.* (1976). Since these early times, the literature contains these two kinds of value (∼3 and ∼30 kyr, see Fig. 2.1 and Tab. 2.1), depending on the kind of data that is analyzed. We attempt to point to this in the following developments.

2.2 | The origin of IC443: SNIa or CCSN?

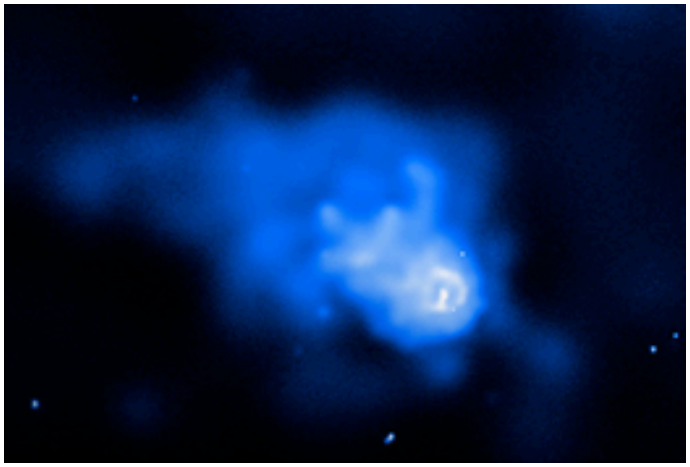

Figure 2.2 X-ray intensity image of the hard X-ray cometary feature ($E > 2.1$ keV) towards the southern edge of IC443, mapped by the *Chandra* observatory (Olbert *et al.* 2001a, Swartz *et al.* 2015). The comet-like shape of the pulsar wind nebula G189.22+2.90 suggests that the neutron star CXOU J061705.3+222127 is moving away from the center of the supernova remnant. Credit: `https://chandra.harvard.edu`, NASA/CXC/MSFC/D.Swartz *et al.*

The PSR 0611+22 pulsar was discovered 0.6° west of IC443's center by Davies *et al.* (1972) at 408 MHz with the Jodrell Bank Mark IA radio telescope, and tentatively associated with the remnant based on the close similarity between its spindown age (60 kyr) and the one estimated for the remnant at this stage (Lozinskaya, 1969). However the younger age of IC443 inferred from X-ray observations (*e.g.* Winkler and Clark 1974, Malina *et al.* 1976) and by Lozinskaia (1975) casted doubt on this association (additionally, with such an age the implied runaway velocity is unreasonably large: $\geq$ 5000 km s^{-1}, Keohane *et al.* 1997, Chevalier 1999), especially since the pulsar's spindown time was brought up to 189 kyr by Graham and Hunt (1973). Later X-ray observations did not detect emission from the pulsar (Levine *et al.*, 1979).

A hard, non-thermal, X-ray source was discovered in the southern portion of IC443 by Keohane *et al.* (1997) with the Advanced Satellite for Cosmology and Astrophysics (ASCA; these authors identified possible sites of CR acceleration in IC443 based on this finding). This discovery was confirmed by Bocchino and Bykov (2000) (with BeppoSAX, interpreting it as a possible shocked molecular clump), Bocchino and Bykov (2001b) (with the X-ray Multi-Mirror Mission, *i.e.* XMM-Newton, categorizing it as a plerion nebula). In 2001, Olbert *et al.* (2001a) confirmed the discovery of the runaway neutron star CXOU J061705.3+222127 and Pulsar Wind Nebula (PWN) G189.23+2.90 in IC443 based on *Chandra* X-ray observatory and Very Large Array (VLA) images, in the form of a comet-shaped nebula of hard emission with a softer point source at its apex (see Fig. 2.2). Its morphology was found to be in agreement with a supersonic motion of the neutron star of ~250 km s^{-1}, consistent with an age of 30 kyr for the SN event and subsequent neutron star formation in a core-collapse scenario. Gaensler *et al.* (2006) studied the structure of the pulsar bowshock based on deep observations with the *Chandra* X-Ray Observatory. They separated a 'tongue' of emission close to the neutron star from a larger, fainter 'tail'. Their interpretation of the aforementioned morphology supported a physical association with IC443. They also confirmed the velocity of the neutron star, about 230 km s^{-1}, independent of the assumed distance. Finally Swartz *et al.* (2015) globally confirmed all these findings with deep *Chandra* Advanced CCD Imaging Spectrometer (ACIS) observations, slightly modifying the coordinates of the pulsar, and questioning (without giving answers) the association with IC443. Straal and van Leeuwen (2019) could not find a radio counterpart to this pulsar in their search with the LOw Frequency ARray (LOFAR) around 150 MHz (see references therein for other unsuccessful searches

at radio frequencies).

By tracing back the cometary tail of the PWN, Dincel *et al.* (2016) found a potential pre-supernova companion of the progenitor of IC443. HD 254577 is an OB B0II/III type runaway star with a proper motion that is significantly larger than the other members of the GEM OB1 association ($v = 37 \pm 7$ km s^{-1} at 1.5 kpc). In his PhD thesis, Dincel (2017) suggested that the neutron star CXOU J061705.3+222127 and HD 254577 might have a common origin (*i.e.* binary supernova disruption). The explosion center suggested by this association is located $\sim 12'$ away from the geometrical center, but an asymmetrical SN explosion in an inhomogeneous medium could still be consistent with that scenario (see Fig. 2.3).

It is worth noting that also based on Chandra observations, Bykov *et al.* (2005) identified an isolated hard X-ray source, XMMU J061804.3+222732, composed of a few bright clumps in a $30''$ region, that they interpreted as either an ejecta fragment interacting with the dense ambient medium or a PWN (associated either to IC443 or the companion SNR G189.6+3.3, Asaoka and Aschenbach (1994), see section 2.3.6). In view of these pieces of observational evidence, we assume that IC443 is the remnant of a CCSN.

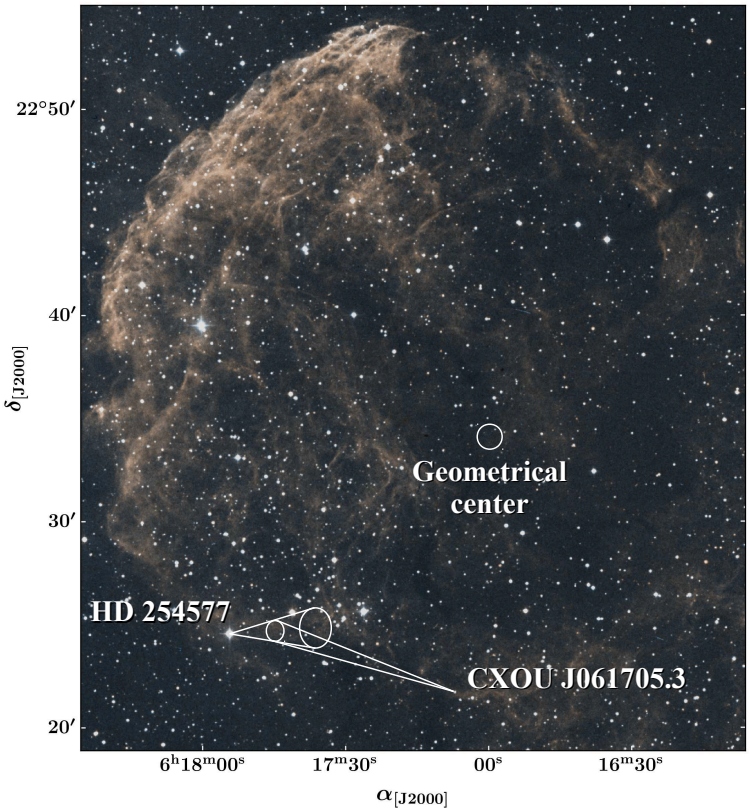

Figure 2.3 Color composite image of IC443. DSS (R-band) image is in yellow and DSS (B-band) in blue. The white circle shows the geometrical center of the supernova remnant if we take into account the subshells A and B (see section 2.3.1). The possible OB runaway - neutron star system is indicated in the bottom area of the figure. The error cone of the proper motion tracing back to the massive star HD 254577, for 30 and 60 kyr, is shown in white. The proper motion of the neutron star derived here, for 30 kyr elapsed time, is $\mu_\alpha = -16.1 \pm 1.1$ mas yr^{-1}, $\mu_\delta = -5.1 \pm 1.9$ mas yr^{-1}, consistent with the measured value for CXOU J061705.3+222127. Figure reproduced from Dincel (2017).

2.3 | Observational studies

2.3.1 The shell morphology and interstellar environment of IC443 from H I, H_2 and ^{12}CO studies

The first [H I] map of the environment of IC443 was presented by Locke *et al.* (1964), with the Dominion Radio Astrophysical Observatory (beam size $\sim 36'$). These early observations allowed

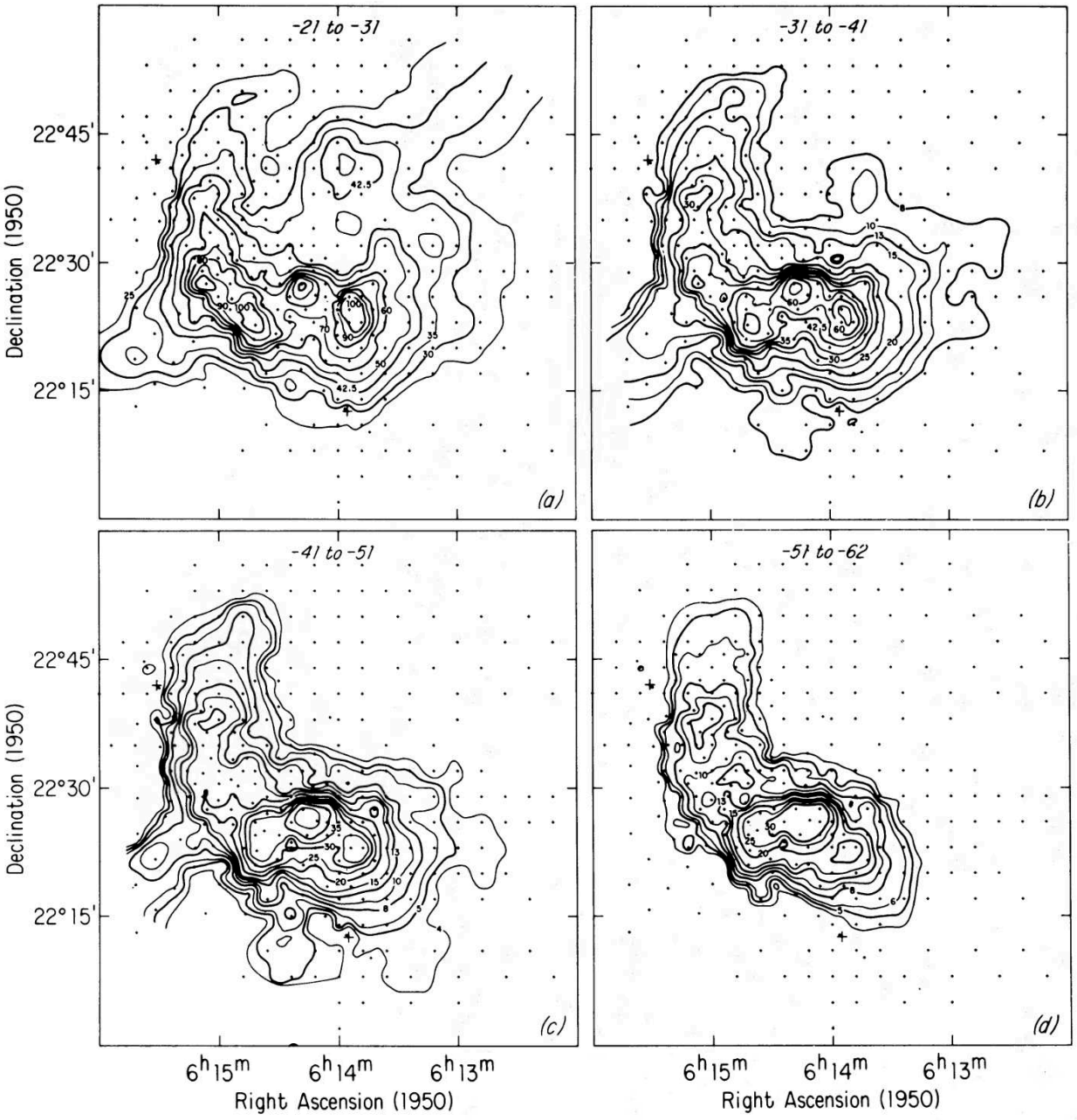

Figure 2.4 Channel maps of [H I] towards the IC443 supernova remnant. The observations were carried out at the Arecibo Observatory with the 305m telescope: each panel represents the antenna temperature integrated over the velocity range specified by the upper labels (*e.g.* -21 km s^{-1} to -31 km s^{-1} for the top-left panel)). Dots mark the sampling points. Figure reproduced from Giovanelli and Haynes (1979).

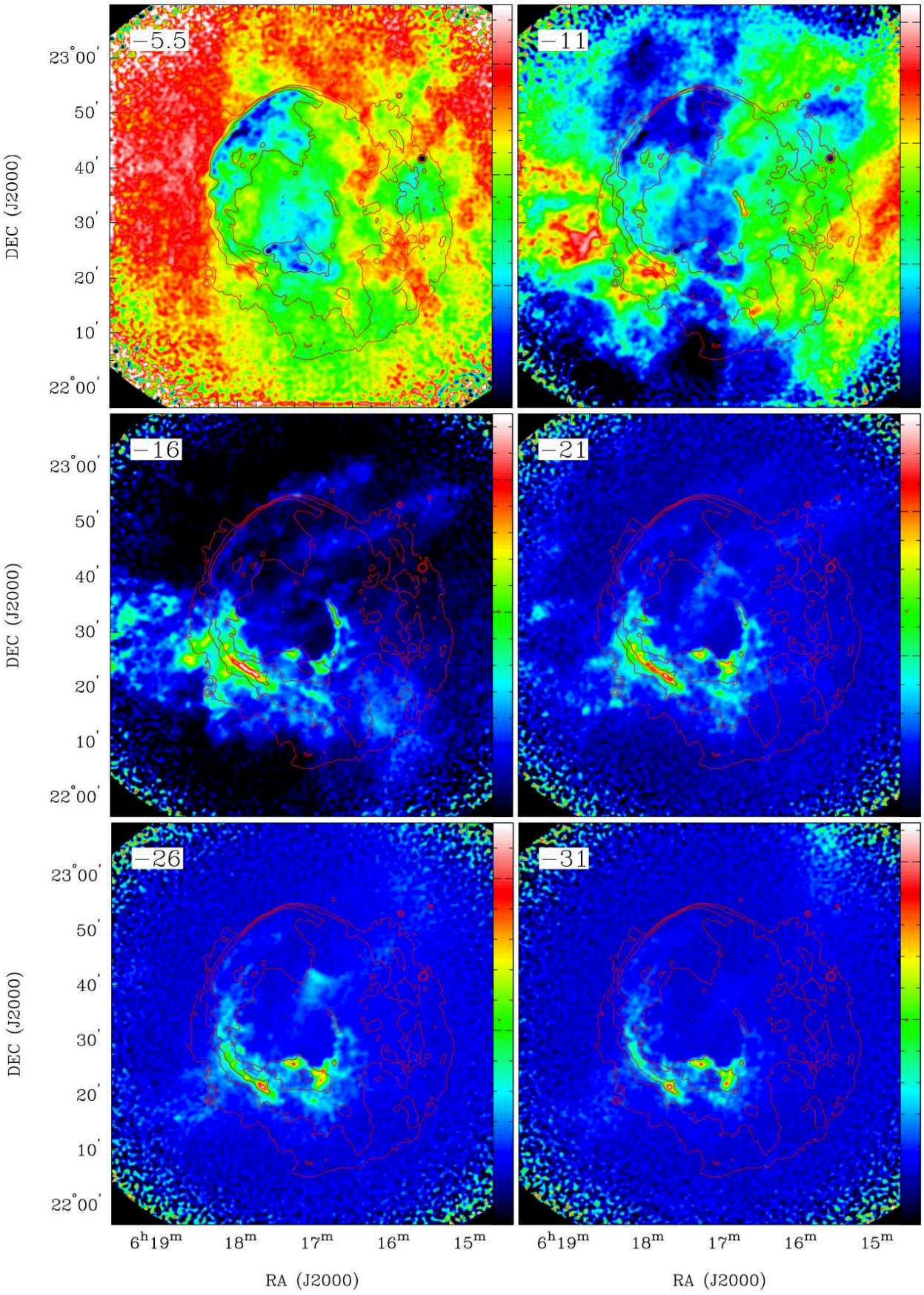

Figure 2.5 [H I] 21 cm line channel maps (VLA & Arecibo) of IC443 with a radio continuum contour overlaid. The units for the image are Jy/beam. Contour levels are 10, 20, 40 mJy/beam. Figure reproduced from Lee *et al.* (2008).

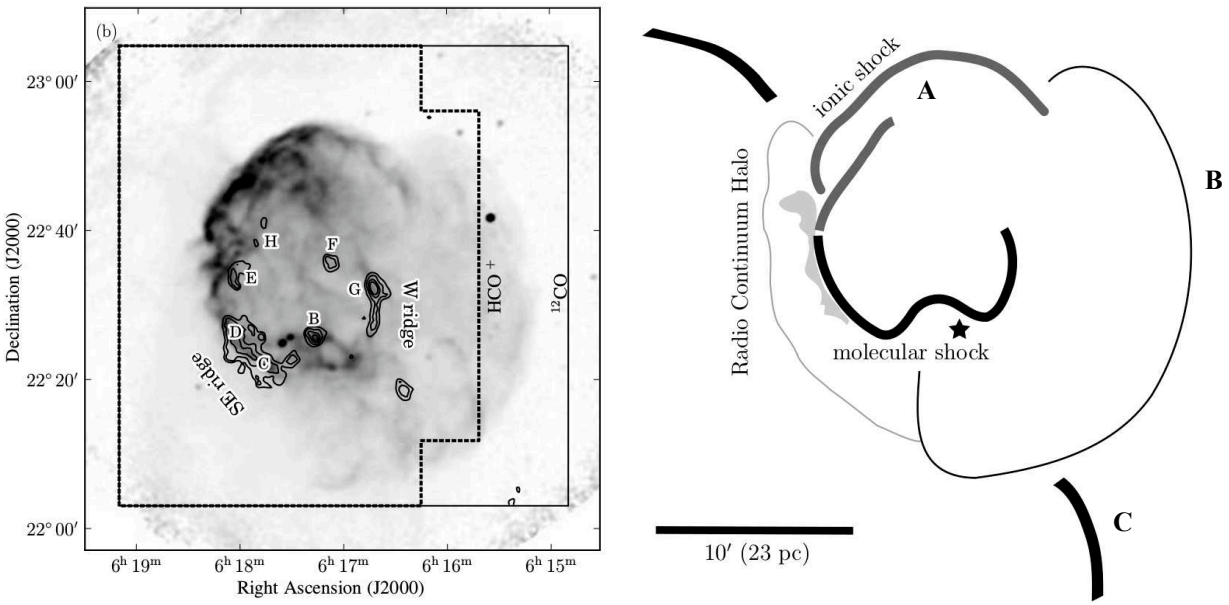

Figure 2.6 *Left*: VLA 21 cm radio continuum image of IC443 (Lee *et al.*, 2008). The black contours represent the distribution of shocked molecular gas, detected via FCRAO observations of the transition ^{12}CO J=1–0. The labels and locations of the different molecular clumps identified by Denoyer (1979a) and Dickman *et al.* (1992) are indicated in capital letters (B, C, D, E, F, G, H). *Right:* schematic view of the overall morphology of IC443, with the nomenclatures of the shells (A, B, C) and shock fronts (molecular, ionic) overlaid. The asterisk indicates the position of the pulsar detected by Olbert *et al.* (2001a). Figures reproduced from Lee *et al.* (2012). *Caution:* the structures 'B' and 'C' in the right panel (SNR shells) are unrelated to the structures 'B' and 'C' in the left panel (molecular clumps).

to identify an atomic cloud with a mean velocity of approximately -2 km s^{-1} towards the SNR. The detection of the [H I] cloud was confirmed by Akabane (1966) with the 24m spherical dish of the Tokyo Astronomical Observatory. Without regard to further investigations, the association of this cloud with IC443 was a reasonable assumption based on its proper motion. Since only positive velocities are permitted by Galactic rotation in the direction of IC443, it would be very unlikely that this H I cloud is not associated to the remnant (Denoyer, 1978). Using a distance $\sim$ 1 kpc (following the IC443's distance measurement by Harris (1962)), Akabane (1966) inferred a cloud diameter of 40-70 pc and a density $n_{\rm H} = 10-20$ cm^{-3}. Thereafter, several studies of [H I] emission were carried out to characterize the cloud in the vicinity of IC443 with increasing precision (*e.g.* Duin and van der Laan 1975, Denoyer 1977, Denoyer 1978, Giovanelli and Haynes 1979). In total, the neutral hydrogen mass associated with the shell is $\sim$ 700 M$_\odot$ (Giovanelli and Haynes, 1979). Braun and Strom (1986) better constrained the geometry of the atomic gas contents of the SNR using Westerbork Synthesis Radio Telescope (WSRT) data. At negative velocities, the [H I] brightness distribution shows a semi-circular arc coincident with the optical filaments in the eastern part of the remnant, and a compact cloud in the south (see Fig. 2.4, 2.5).

Braun and Strom (1986) produced a classification of the radio and [H I] structures observed in the region of IC443: three interconnected subshells (labeled A, B and C, see Fig. 2.6) corresponding respectively to two relatively smaller eastern and western subshells (radii $\sim$ 10 pc), and a larger third subshell (radius $\sim$ 20 pc) with a centroid that is significantly displaced with respect to the A+B subshells system. The shells A and B define the usually assumed boundaries of IC443, while

the subshell C extends towards the northeastern and southwestern perimeter of the IC443 complex (these 'A', 'B' and 'C' shells will be referred to throughout this review, *e.g.* in section 2.3.5). They proposed that the morphology of this system of asymmetrical subshells might be explained by the interaction of the SNR with three pre-existing wind-blown cavities and their high-density shells. This system would have been formed by stellar wind driven bubbles generated by the members of the Gem OB1 association evolving in an inhomogeneous medium (they proposed the stars HD 44139, AGK3+22685 and AGK3+22686 as powering candidates for the excavation of subshell C, and a single type O star for subshells A and B).

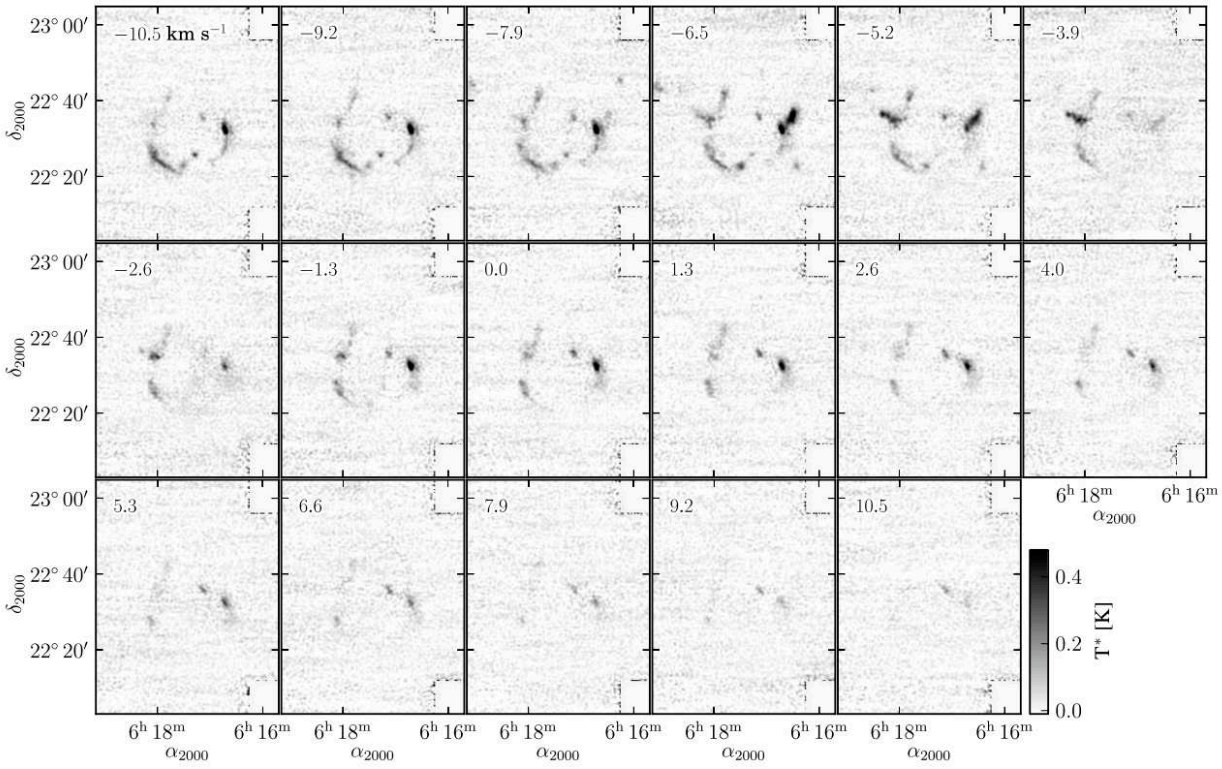

Figure 2.7 HCO^+ channel maps for velocities between -10 km s^{-1} and +10 km s^{-1} corresponding to the observations by Lee *et al.* (2012) using the FCRAO 14m telescope. The emission is predominantly from shocked molecular gas.

Lee *et al.* (2008) produced high resolution maps of both the [H I] line and continuum flux at 21 cm with the VLA and Arecibo Observatory. Their findings support the scenario of a breakout of the SN within a less dense medium towards the western part of the remnant, which is consistent with its asymmetrical two-shell morphology. They detected [H I] emission from −50 km s^{-1} to +100 km s^{-1} that is spatially and kinematically associated with optical radiative filaments in the north-eastern part of the remnant, suggesting that this emission corresponds to the recombination of [H I] within the shocks. Several studies of the dense, molecular phase followed the description of the [H I] structure of IC443, using ^{12}CO as a tracer (*e.g.* Cornett *et al.* 1977, Dickman *et al.* 1992). The shell system described by Braun and Strom (1986) is at the rear of a ^{12}CO cloud that lies diagonally across the center of the SNR (v_{LSR}[2] between −3 km s^{-1} and 4 km s^{-1}, Cornett *et al.* 1977). The subshell A is in contact with the ^{12}CO cloud in the several locations of the remnant, but subshells B and C are bounded with more diffuse gas.

[2] 'LSR ' stands for 'Local standard of rest'.

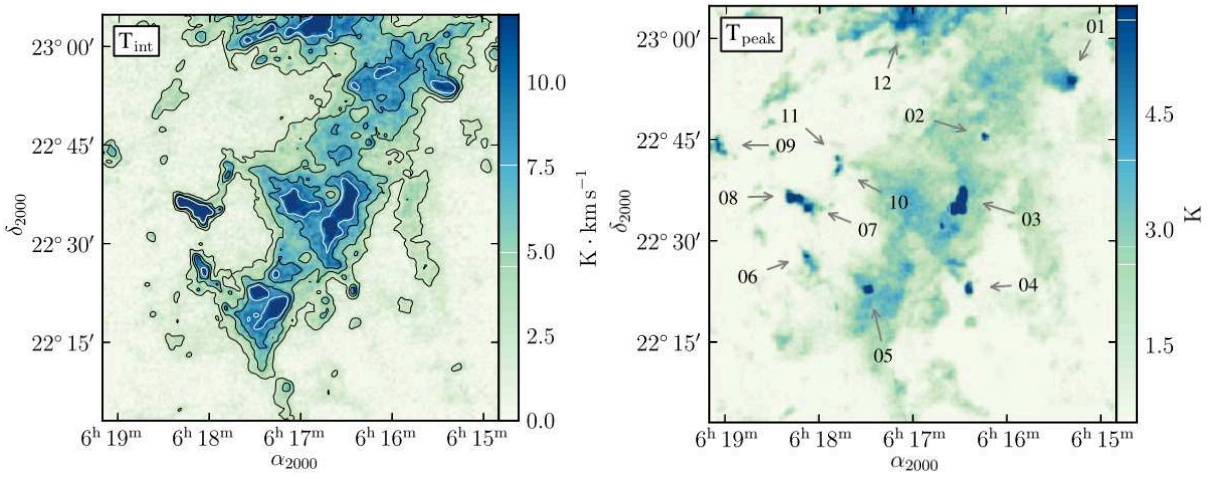

Figure 2.8 *Left panel*: ^{12}CO integrated temperature map in velocity range of -10 to 0 km s^{-1}, mostly tracing the ambient gas (Lee *et al.*, 2012). *Right panel*: ^{12}CO peak temperature map over the same velocity interval. The numbers denote the labels and location of small molecular clumps identified by the authors.

The most up-to-date and complete description of the structure and kinematics of the dense molecular environment of IC443 was offered by Lee *et al.* (2012) (see Fig. 2.7, Fig. 2.8). With the 14m dish of the Five College Radio Astronomy Observatory (FCRAO) they obtained $\sim 1^\circ \times 1^\circ$ maps of ^{12}CO and HCO$^+$ J=1-0 rotational transitions that allowed to identify the molecular structures interacting with the SNR shockwave within the inner molecular shell. The authors found two main molecular structures along the northwest-southeast and northeast-southwest axes, respectively at -3 km s^{-1} and $+6$ km s^{-1}, and suggested that the second is not interacting with the SNR shocks. They also identified 12 bright small clouds that they interpret as the residual cores of the molecular clouds that were exposed to the stellar wind of the progenitor. Some of these residual cloud cores are currently interacting with the SNR shocks (see Fig. 2.8, Fig. 2.6). Lastly, they proposed an age 2×10^4 yr for IC443, based on a dynamical model of the SNR breakout. Finally, the analysis of absorption lines in the spectra of background stars brought further refinements in the description of the gas interacting with the remnant (*e.g.* Welsh and Sallmen 2003, Hirschauer *et al.* 2009). Most interestingly, the line intensity gradient between the positive and negative velocity components of these absorption features seems to indicate that the dense medium is one-sided, between the explosion center and the observer (Dincel, 2017).

2.3.2 Nonthermal radio emission in IC443

The radio emission in IC443 is partly correlated with the molecular shell, and also reveals a secondary shell towards the southwestern part of the SNR, associated with the atomic shell B. Hogg (1964) reported a bright radio shell on the eastern part of the remnant mapped at 40, 21 and 10 cm with the National Radio Astronomy Observatory (NRAO). The average spectral index measured in IC443 is $\alpha = -0.36$ ($S_\nu \propto \nu^\alpha$), but it is not uniform within the remnant, in particular towards the NE optical filaments where the detection of nonthermal emission was reported (*e.g.* Hill 1972, Green 1986). Duin and van der Laan (1975) proposed that the nonthermal features of the radio spectrum could arise from synchrotron emission of relativistic electrons gyrating in the compressed magnetic shell (van der Laan 1962a, van der Laan 1962b).

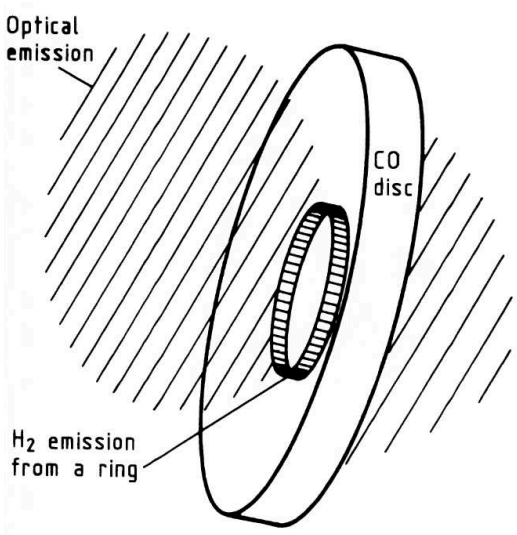

Figure 2.9 Schematic diagram of a model of IC443 proposed by Burton *et al.* (1988). This is a side view, looking at a plane through the molecular disc and optical shell. The SN has exploded within the remnant of a molecular disc left over from the formation of the pre-SN star. The H_2 line emission originates in a narrow ring where the blast wave is interacting with the clumpy molecular disc. Behind the shock lies accelerated molecular and atomic gas, the atomic gas being dissociated H_2. The optical emission (mainly Hα) results from the expansion of the blast wave above and below the disc into lower-density neutral gas. A cavity filled with hot low-density material is left behind and emits X-rays.

In the last two decades, high-resolution maps of IC443 were obtained at various frequency ranges. Leahy (2004) presented wide field ($\sim 2^\circ \times 2^\circ$) observations of the IC443/G189.6+3.3/S249 region at 408 MHz and 1420 MHz with the Dominion Radio Astrophysical Observatory (DRAO). He suggested that the PWN found by Olbert *et al.* (2001a) is more likely to be associated with the companion SNR G189.6+3.3 rather than IC443, based on the estimated pulsar age ($\sim$ 30 kyr) and the velocity of the pulsar (pointing back roughly to the center of G189.6+3.3). However, this argument holds only for the lower-end age estimates of IC443, and this association cannot be ruled out for higher age estimates (*e.g.* Chevalier 1999).

Lee *et al.* (2008) provided continuum and spectral maps of the emission at 1420 MHz obtained with VLA and the Arecibo Observatory and showed that the two shells have distinct radial velocities (see Fig. 2.5). The low-frequency radio emission was scrutinized and compared with multi-wavelength data by Castelletti *et al.* (2011) using the VLA at 74 and 330 MHz. They interpreted the correlation between eastern flattest spectrum features and NIR ionic lines as the signature of the passage of a fast dissociating J-type shock. The Sardinia Radio Telescope (SRT) permitted to map the high and very high radio frequency contents of IC443 at 7 GHz (Egron *et al.*, 2017) and 21.4 GHz (Loru *et al.*, 2019). The latter proposed a spinning dust mechanism to interpret the 20-70 GHz radio spectrum bump.

2.3.3 Molecular shocks in IC443: H_2 and ^{12}CO observations

Over the past decades, the interaction of IC443 with the interstellar medium was confirmed *via* three different paths: *i.)* detections of OH masers tracing SNR-cloud interaction (*e.g.* Frail *et al.* 1996, Hewitt *et al.* 2006), *ii.)* detections and studies of 'shock excited' molecular lines towards the shell (OH, ^{12}CO, H_2, SiO: *e.g.* van Dishoeck *et al.* 1993, Richter *et al.* 1995b, Cesarsky *et al.* 1999), *iii.)* detections of atomic species tracing an expanding tenuous gas from -200 km s^{-1} to $+250$ km s^{-1} (21 cm [H I] line, [Hα], [N II], *e.g.* Braun and Strom 1986, Meaburn *et al.* 1990). In this section, we focus on the second type of studies. IC443 has strong molecular emission that makes it a clear case of interaction between a SN and a molecular cloud.

Molecular hydrogen was observed in IC443 first with the detection of $v = 1 - 0$ transitions

(Treffers 1979, Graham *et al.* 1987, Moorhouse *et al.* 1991). These observations were interpreted as the result of the excitation of H_2 by the SNR blast wave and confirmed that line emission is a primary cooling mechanism of the shocked gas within the remnant radiative shell. Along the southern ridge of the SNR, the distribution of the molecular hydrogen is similar to that of [H I], suggesting partial dissociation. From the analysis of $v = 1 - 0$ S(1) observations with the United Kingdom Infrared Telescope (UKIRT), Burton *et al.* (1988) suggested that the H_2 ring found in the southern ridge is tilted with respect to the line of sight, and Dickman *et al.* (1992) estimated that the tilt is ∼50° (see Fig. 2.9).

The first detection of a pure rotational transition of H_2 in IC443 was presented by Richter *et al.* (1995c) using the NASA Infrared Telescope Facility (IRTF) to image the $v = 0{-}0$ S(2) line towards clump C. They noted that the emission has a knotty appearance, unlike the filamentary morphology of the optical shock fronts. Thereafter, the interpretation of the molecular line strengths was the subject of many endeavors. In the effort to study molecular shocks, larger systematic studies of H_2 pure rotational transitions were performed, starting with the mapping of a 3′×3′ field within the clump G by ISOCAM on board of the Infrared Space Observatory (ISO) (Cesarsky *et al.*, 1999). The authors found that from 5 μm to 14 μm the flux is dominated by H_2 $v = 0-0$ lines S(2) to S(8) whose intensity can be reproduced by non-stationary shock models characterized by a velocity of 30 km s^{-1}, pre-shock density of 10^4 cm^{-3} and evolutionary times spanning from 1000 yr to 2000 yr (*warning:* this is a constraint on the age of the shock, not the age of the remnant). The shock models used in these studies were in general identical to the models used to analyze the emission of protostellar outflows.

Clumps C and G were also observed by *Spitzer*-IRS (InfraRed Spectrograph) between 5.2 μm and 37 μm, providing 1′×1′ maps of H_2 lines S(0) to S(7) (see Neufeld *et al.* 2007 for clump C). They proposed that the emission is produced by non dissociative slow ($v_s = 10 - 20$ km s^{-1}) shocks driven by the overpressure within the SNR cavity. The molecular clumps B, C and G were also observed by *Akari* between 2.5 μm and 5 μm, leading to the detection of shocked H_2 throughout the molecular ridges of the SNR (Shinn *et al.*, 2011). They described H_2 population levels with a two-n(H_2) power-law admixture model since the emission could not be reproduced by LTE models. The Stratospheric Observatory for Infrared Astronomy (SOFIA) laid a milestone in the study of molecular hydrogen in SNR shocks, as the first spectrally resolved ($\Delta v = 4.5$ km s^{-1}) measurement of the velocity profile of an H_2 line was reported by Reach *et al.* (2019). These authors compared their observations of the pure rotational line S(5) towards clumps B, C and G with Paris-Durham shock models (Flower and Pineau des Forêts 2003, 2015, Lesaffre *et al.* 2013, Tram *et al.* 2018, Godard *et al.* 2019) and concluded that the emission of H_2 arises from a layer of 60-2000 AU behind a mixture of shocks with stratified physical conditions. All these studies were carried out in small fields (typically $\approx 1' \times 1'$) and allowed to put constraints on the characteristics of the molecular shocks in the southern ridge.

Kokusho *et al.* (2020) presented a map of the H_2 1-0 S(1) and H_2 2-1 S(1) lines covering the entire remnant ($\sim 30' \times 35'$) with the IRSF/SIRIUS (Infrared Survey Facility / Simultaneous Infrared Imager for Unbiased Survey). Their $\sim 1''$-resolution map shows a clumpy morphology of the southern ridge, and no substantial emission in the rest of IC443 where faster shocks are propagating (see Fig. 2.10). In regards to the γ-ray hadronic scenario, they argued that the clumpiness of the molecular clouds suggested by their observations would allow the CRs to interact with a large amount of protons.

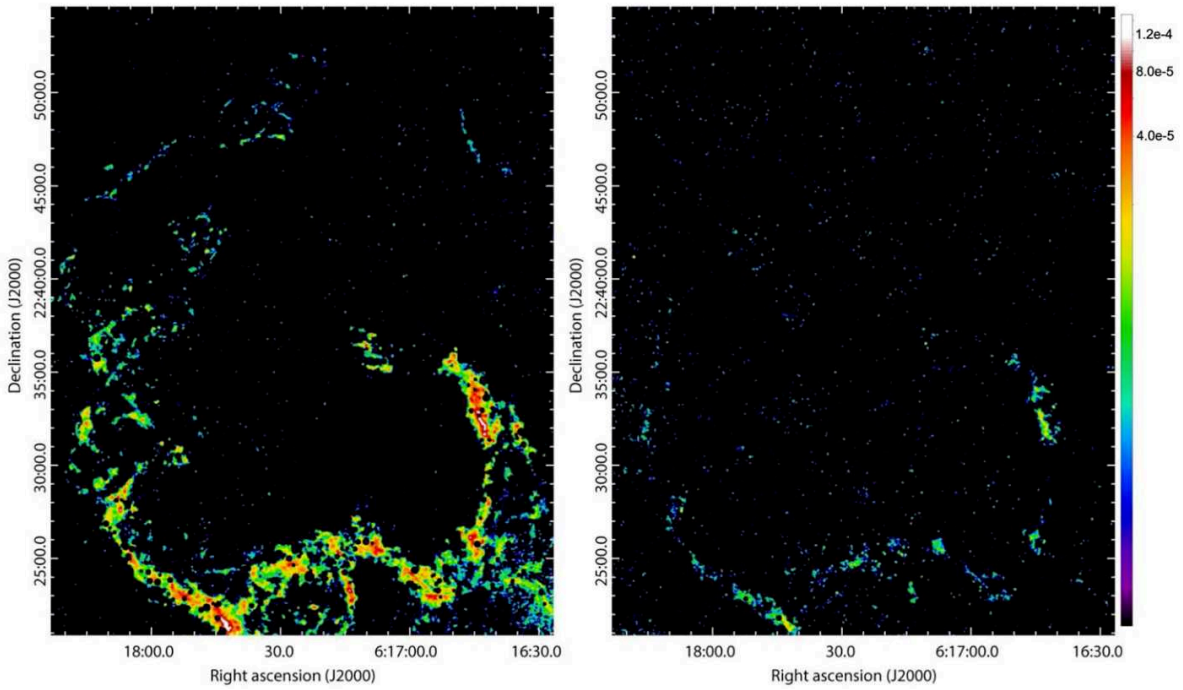

Figure 2.10 IRSF/SIRIUS H2 1–0 S(1) (left) and 2–1 S(1)(right) line-intensity maps of the southern molecular shell and subshell A, where point sources are removed. The maps are smoothed with a Gaussian kernel of 2.″3 in sigma. The color levels are given in units of erg s^{-1} cm^{-2} sr^{-1}. Figure reproduced from Kokusho *et al.* (2020).

CO emission was systematically surveyed in IC443 for the first time by Scoville *et al.* (1977) and Cornett *et al.* (1977) in order to trace the molecular contents of the SNR. The latter produced a $\sim 1^\circ \times 0.5^\circ$ under-sampled raster map of the J=1–0 transition and revealed a local CO molecular cloud displaying a hole within the northeastern optical filaments. Denoyer (1979b) followed up on the discovery of three shocked CO clumps (size $\sim$ 1 pc) along the southern molecular ridge (labeled A, B, C) displaying linewidths of 20 km s^{-1} using the NRAO 11m dish.

Systematic pointed observations of CO(1–0) over a 50′×50′ field were performed with the FCRAO 14m dish (Huang *et al.* 1986, Dickman *et al.* 1992). Their detections of new areas of shock-cloud interaction allowed to identify 5 previously unknown CO clumps (size $\sim$ 1 pc), extending the classification started by Denoyer (1979b) and providing the first mention of the clump G. From J=1–0 ^{12}CO and HCO^+ emission, Dickman *et al.* (1992) estimated that a total mass of 500-2000 $M_\odot$ is perturbed by the SNR (corresponding to 5%-10% of the SN energy considering that the average velocity of the clumps is 25 km s^{-1}). They measured the masses of all these clumps, and found they are ranging between 3.9 $M_\odot$ and 41.6 $M_\odot$ (41.6 $M_\odot$ for the shocked clump ‘G’). Zhang *et al.* (2010) showed that two distinct structures are resolved in the region G, labeling G1 the strongest ^{13}CO peak and G2 the previously mentioned shocked clump.

Using a CO-to-H_2 conversion factor (Dame *et al.*, 2001), Lee *et al.* (2012) measured a mass of 57.7±0.9 $M_\odot$ for the clump G. Oddly, Xu *et al.* (2011) measured a mass of $2.06\times10^3 M_\odot$ for the ‘cloud G’, which is $\sim$ 40 times higher than the previous estimates. These discrepancies can be partly explained by *i.)* the confusion between the G1 and G2 clumps at lower spatial resolution observations, and *ii.)* different decisions regarding the assumption that the ^{12}CO lines are optically thin (Dickman *et al.* 1992 assumed that the ^{12}CO J=1–0 line is optically thin and that it possesses

an excitation temperature T_{ex} = 50 K; Xu *et al.* (2011) estimated the mass from the ^{12}CO J=3–2 line, assuming an optical depth τ = 3.1, given by Braun and Strom (1986) and assuming that $T_{ex} = 16.6/\ln[1 + 1/(T_{mb}/16.6 + 0.0024)]$, where T_{mb} is the corrected main beam temperature; Lee *et al.* (2012) assumed that the ^{12}CO J=1–0 line is optically thin and adopted the canonical conversion factor $N_{H_2} / \int T(^{12}\mathrm{CO})dv \simeq 2 \times 10^{20}$ cm^{-2} K^{-1} km^{-1} s).

Several molecular shocks were mapped within the SNR by White *et al.* (1987) using CO J=1–0 as a tracer with the Nobeyama 45m (down to an angular resolution of 15″). The authors resolved shocked clumps of typical size 0.1-0.3 pc ($\simeq 10'' - 30''$) spatially correlated with shocked H_2 and proposed that they are by-products of the fragmentation of the molecular cloud interacting with the SNR. High resolution observations ($3'' - 5''$) of the transition J=2–1 of CO were performed by Wang and Scoville (1992) towards clumps A, B and C with the Owens Valley Radio Observatory (OVRO) and Caltech Submillimeter Observatory (CSO). The authors found the signature of gas ablation and suggested that the molecular clumps are accelerated at high velocities by the ram pressure of the SNR. They proposed a model based on a J-type shock for the high-velocity component and C shock for the low-velocity component of the line emissions observed within the shocked CO clumps. van Dishoeck *et al.* (1993) presented observations of the rotational transition J=3–2 of CO obtained with CSO along the shocked molecular ring and offered a complete characterization of the kinematics and morphology of clumps B, F, E and G at a spatial resolution of 20″-30″.

Zhang *et al.* (2010) presented the first 45′×40′ map of ^{13}CO(1–0) towards the SNR with the Purple Mountain Observatory (PMO). They proposed to label G1 and G2 the two distinct clumps in IC443G. Two complete, fully sampled maps of IC443 at 2.6 mm were performed in the last ten years (Lee *et al.* 2012, see previous paragraph and Su *et al.* 2014). The latter performed a 1.5°×1.5° map of the SNR of the transition J=1–0 for the isotopologs ^{12}CO, ^{13}CO and C^{18}O at a spatial resolution of 54″ with PMO. Their observations show a half-ring structure with a radius of 26′ beyond the northern part of the radio shell that could be a partial molecular shell formed by the stellar wind of the progenitor.

Millimeter and sub-millimeter observations of IC443 were performed to characterize the enhanced chemistry of many species detected towards the shocked molecular gas, such as SiO, SO, H_2CO, HCO^+, N_2H^+, CS, OCS, HCN, OH (Denoyer and Frerking 1981, White *et al.* 1987). Observations of clumps B and G with the FCRAO 14m performed by Ziurys *et al.* (1989) revealed a hundredfold enhancement of the SiO abundance with respect to the abundance expected in a cold dark cloud. At this time, this was interpreted as the signature of high-temperature chemistry in the hot and dense shocked clumps. High-resolution interferometric observations of HCO^+ towards clumps B and G carried out with BIMA (Berkeley Illinois Maryland Array) revealed a clumpy distribution of shocked gas, suggestive of ablation of the gas around the clump cores (Turner *et al.* 1992, Tauber *et al.* 1994). To this day, the work presented by van Dishoeck *et al.* (1993) is the most complete sub-millimeter spectral survey of an evolved SNR. Their characterization of the chemistry allowed to put several constraints on the physical conditions and nature of shocks in IC443 (global kinematics, velocity of shocked gas, column density, molecular abundances, *etc*). Snell *et al.* (2005) detected the ground state of shocked ortho-H_2O towards clumps B, C and G using SWAS (Submillimeter Wave Astronomy Satellite) at 557 GHz. They estimated an ortho-H_2O/CO abundance of 10^{-4}-10^{-3} and proposed the combination of J- and C-type shocks to reproduce their measurements.

2.3.4 Infrared surveys towards IC443: warm dust and shocked gas

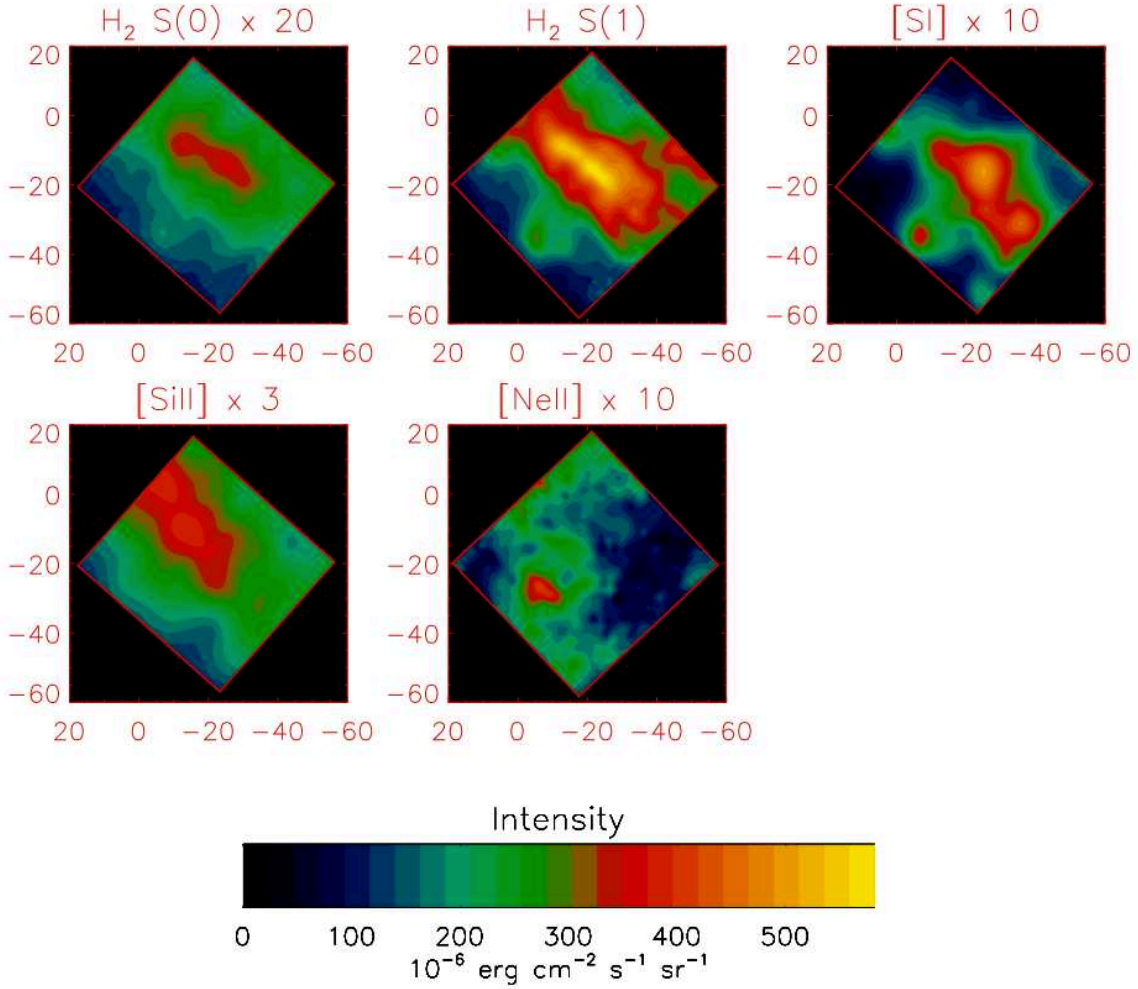

Figure 2.11 H_2 S(0), H_2 S(1), [S I], [Si II], and [Ne II] emission line intensities observed towards IC443C. The inset boxes delimit the regions within which each transition was mapped. The horizontal and vertical axes show the R.A. ($\Delta\alpha\ \cos\delta$) and declination ($\Delta\delta$) offsets in arcsec relative to $\alpha = 06^{\rm h}17^{\rm m}44.^{\rm s}2$, $\delta = +22°21'49''$ (J2000). Figure reproduced from Neufeld *et al.* (2007).

The first complete near-infrared coverage of IC443 was performed by 2MASS (Two-Micron All-Sky Survey) and presented by Rho *et al.* (2001). They reported that the shell-morphology is observed in the J, H, K bands with different features across the remnant. The sheet-like, filamentary structure of the NE shell, arising from atomic fine structure transitions contrasts with the clumpy morphology of the southern ridge, where rovibrational lines of H_2 dominate the flux. Neufeld *et al.* (2007) reported the detection of 15 fine structure transitions with *Spitzer*-IRS in the range 5.2-37 μm, as well as hydrogen deuteride and PAH (Polycyclic Aromatic Hydrocarbon) emission towards a 1′×1′ field of observations in IC443C (see Fig. 2.11). Based on principal component analysis, they found that the observed emission lines fall in five distinct groups that are associated with distinct spatial distributions (in addition, lines in 'group 1' originate in molecular material subject to a slow, nondissociative shock and lines in 'groups 3 − 5' are primarily associated with faster dissociative shocks).

The infrared and far-infrared contents of IC443 were unveiled by IRAS (InfraRed Astronom-

ical Satellite, Neugebauer *et al.* 1984) at 12, 25, 60 and 100 µm, revealing the loop-like, shell-morphology of the remnant at these wavelengths. Oliva *et al.* (1999) reported ISO-SWS (Short Wave Spectrometer) spectral observations towards IC443 and showed that the emission of [Fe II] and [Ne II] dominates the 12 and 25 µm IRAS bands, challenging the standard interpretation involving thermal emission of dust grains. Burton *et al.* (1990) observed [O I] ($^3P_1 \rightarrow ^3P_2$ emission line at 63.18 μm) with the Kuiper Airborne Observatory (KAO, the predecessor of SOFIA), performing the first far-infrared line emission observations towards a SNR. The authors found that the [O I] emission is correlated to shocked H_2, and estimated that the 60 µm flux is dominated at 40-75% by [O I], thereby reducing the relative contribution of the thermal emission from warm dust grains. Excitation by shocks was suggested as the most likely scenario by these different studies, instead of X-ray or FUV mechanisms. [O I] was also observed by ISO towards several positions across the remnant by Rho *et al.* (2001). Their comparison with shock models favored a fast J-type shock (~100 km s^{-1}) in the NE shell, and a C shock (v_s ~30 km s^{-1}) propagating in the southern ridge.

In the 2010s, the infrared scientific material available for IC443 was greatly upgraded thanks to *Spitzer* and WISE (Wide-field Infrared Survey Explorer, Wright *et al.* 2010). IC443 was fully mapped by *Spitzer*-MIPS (Multi-Band Imaging Photometer) at 24, 70 and 160 µm, providing the most up-to-date, high-resolution observations of the remnant at far-infrared wavelengths (Pinheiro Gonçalves *et al.* 2011, Noriega-Crespo *et al.* 2009). WISE also delivered observations of IC443 at 3.4, 4.6, 12 and 22 µm with unprecedented resolution and coverage, completing the already vast amount of infrared data obtained towards the environment of the SNR. It should be noted that a complementary approach to the study of molecular and atomic IR emission lines is the analysis of absorption lines of background stars (*e.g.* Welsh and Sallmen 2003, Hirschauer *et al.* 2009, Taylor *et al.* 2012). Most recently, Ritchey *et al.* (2020) presented a thorough investigation of *Hubble* FUV spectra from IC443's background stars. Towards the molecular and atomic regions that IC443 is interacting with, the authors found high-velocity absorption lines with evidence of significantly reduced dust grain depletion and enhanced thermal pressure. Ultimately, infrared studies in the IC443 SNR have shown that the shocks propagating in the shell can be reproduced using the same models as in protostellar outflows (*e.g.* Gusdorf *et al.* 2011).

2.3.5 The bright, filamentary optical features in IC443

Optical observations of IC443 display a strong correlation with radio and [H I] features, reproducing shells A and B (see section 2.3.1). Additional faint filaments ~ 15′ east of the main optical shell are likely to trace the shell C, and were studied by Fesen (1984). Since he measured the same emission-line intensity ratio as in the main SNR filamentary structures for several atomic species, he suggested that these faint filaments are physically associated with IC443. The bright optical filaments towards the northeastern part of the SNR were the object of many studies. Parker (1964) performed spectrophotometric observations of several bright filaments located both in the molecular and secondary optical shell with the Mount Wilson 60-inch telescope. He concluded from the observation of Balmer, [S II], [N II] and [O II] lines that the filaments are collisionally excited by the SNR shockwave.

Lozinskaya (1969) measured the Doppler shifts of the [Hα] line with a Fabry Perot interferometer and estimated an expansion velocity of 65 km s^{-1} and a velocity dispersion of 50 km s^{-1}

within bright filaments. Six locations (four in the NE shell, two in the SE shells) throughout the remnant were analyzed by Fesen and Kirshner (1980) using spectrophotometric scans with the 1.3m McGraw-Hill Observatory. They measured temperatures up to 24 000 K from [O III] lines and interpreted the detection of [Ca II] as a possible consequence of dust grain destruction. The authors found a good agreement between their data and shock models (by Dopita *et al.* 1977, Shull and McKee 1979, Raymond 1979) corresponding to a velocity 65-100 km s^{-1} and preshock density 10-20 cm^{-3}. Narrow-band imagery of [Hα], [N II] and [S II] was also obtained towards the NE bright filaments by Fesen and Kirshner (1980) with the 4m telescope at Kitt Peak. These optical structures were characterized as the product of shock compression of dense clumps driven by the SNR blast propagating in an inhomogeneous medium by Mufson *et al.* (1986) and Dickel *et al.* (1989). The apparent filamentary morphology and localized high-speed motions measured by long-slit spectroscopy of [Hα] and [N II] lines towards the NE optical shell were interpreted by Meaburn *et al.* (1990) as the products of a wavy, thin sheet of emitting gas (Hester, 1987).

IC443 was fully mapped by the Sloan Digital Sky Survey (SDSS, York and SDSS Collaboration 2000). Ambrocio-Cruz *et al.* (2017) estimated an age of ~30 000 yr and an energy $7.2{\times}10^{51}$ erg injected in the environment by the SNR from the comparison of new observations of [Hα] with SNR models (Chevalier, 1974). Alarie and Drissen (2019) obtained maps of the NE bright filaments at an unprecedented spatial and spectral resolution with the CFHT (Canada-France-Hawaii Telescope) imaging spectrograph SITELLE. The authors compared their data with the MAPPINGS shock models library and estimated shock velocities from 20 km s^{-1} to 150 km s^{-1} and preshock densities 20-60 cm^{-3} across the different resolved filamentary structures.

2.3.6 The 0.1-100 keV view of IC443: shock-heated plasma, stellar ejecta and a pulsar wind nebula

The shell-like structure of IC443 in radio, centrally filled in X-rays puts the remnant into the category of mixed-morphology SNRs (Rho and Petre, 1998). IC443 was referenced as an X-ray source first by Giacconi *et al.* (1974) in the third catalog of sources observed with the Uhuru X-ray observatory (Giacconi *et al.*, 1971). Winkler and Clark (1974) positively identified the remnant as the source of X-rays with much more confidence from OSO-7 (Orbiting Solar Observatory) detection in the 1-10 keV energy band. Using a thermal bremsstrahlung model they provided an estimate of the electron temperature of $\sim 10^7$ K. A similar temperature was measured by Parkes *et al.* (1977) who reported on observations of Ariel V in the range 1.1-7.5 keV.

The remnant was mapped in the 0.2-3.1 keV by the Einstein Observatory (Petre *et al.*, 1988). The soft X-ray morphology is partially correlated to the radio and optical features and fills the remnant, with an inhomogeneous aspect due to variations of the absorption by the ambient molecular clouds. Asaoka and Aschenbach (1994) determined that IC443 is overlapping with the companion SNR G189.6+3.3 based on the results of the X-ray sky-survey performed with ROSAT (Röntgen-satellit) at 0.5-0.7 and 1.7-2.2 keV.

ROSAT unveiled the subshell C in X-rays for the first time, allowing to recover the three subshell morphology seen in radio and IR observations. The ROSAT observations show that subshell C is in fact a complete, spherical shell (radius $\sim$ 20 pc) that is partially overlapping with IC443, and its X-ray spectrum suggests that it is a separate $\sim 10^5$ yr old SNR (hereafter G189.6+3.3). The absorption analysis shows that the two SNRs are separated by a molecular

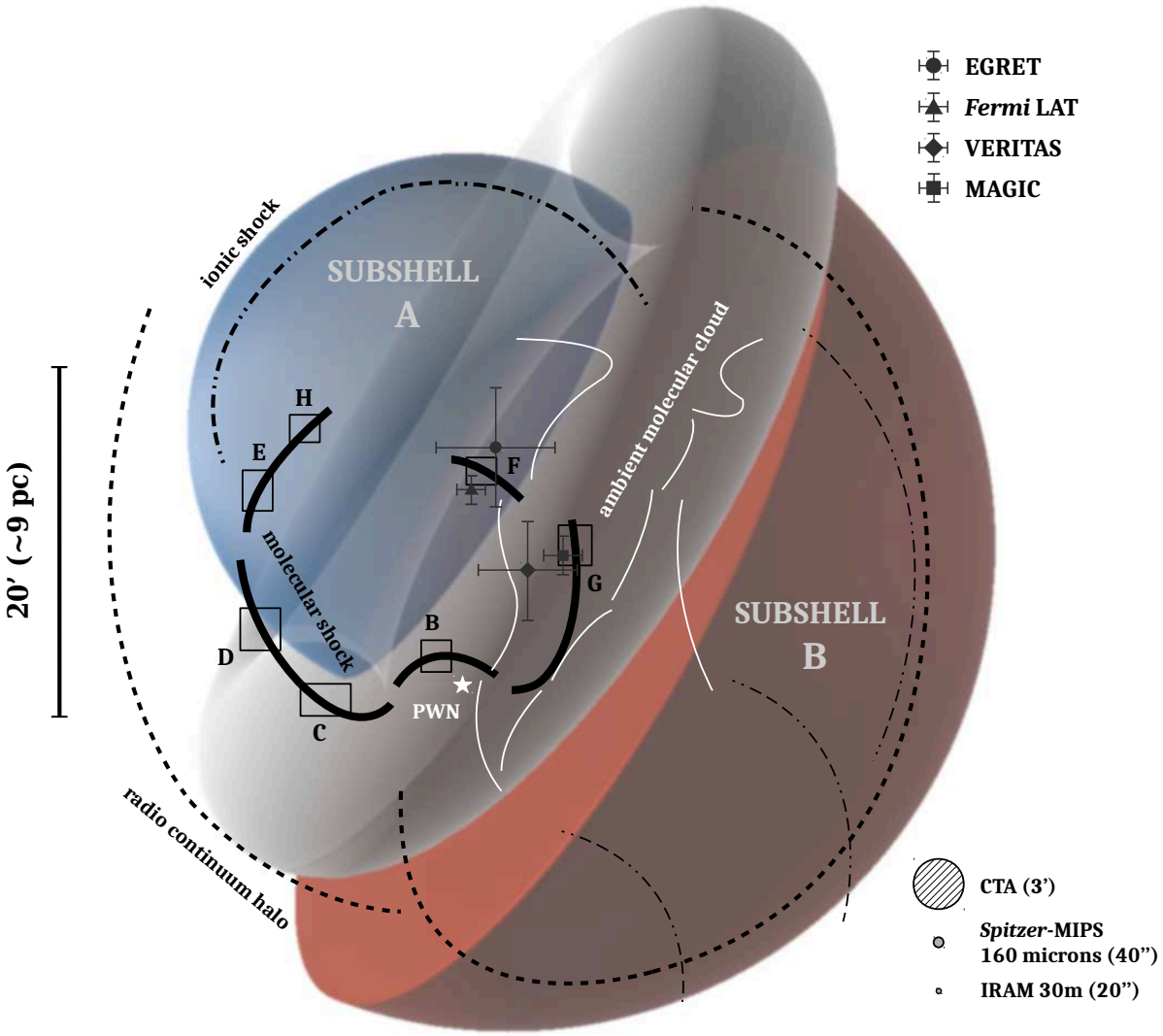

Figure 2.12 Schematic overview of the morphology of the supernova remnant IC443. The two-shell model proposed by Troja *et al.* (2006) is shown as a background colored image: the gray torus represents the molecular cloud discovered by Cornett *et al.* (1977), with the most condensed areas represented by white curved lines based on the higher resolution observations by Lee *et al.* (2012). The blue hemisphere, labeled as subshell A, represents the shock front in the eastern region. In the northeast, where it has been confined by the encounter with the neutral H I cloud of Denoyer (1978), the ionic shock front is traced by optical, infrared and very soft X-ray emission (dashed-dotted black lines). In the southern region the thick, black curved lines represent the areas of interaction with the molecular cloud and the shocked H_2 ridges of Burton *et al.* (1988). The labels and positions of the different molecular clumps identified by Denoyer (1979a) and Dickman *et al.* (1992) are indicated in capital letters (B, C, D, E, F, G, H). The red hemisphere, labeled as subshell B, represents the shock front in the western region, where it is expanding in a homogeneous and less dense medium. The position of the PWN discovered by Olbert *et al.* (2001a) is indicated by a white star. The extension of the radio continuum halo is shown by dashed black lines (Lee *et al.*, 2008). Locations and extensions of the four gamma-ray sources are indicated: EGRET centroid (○), MAGIC centroid (□), VERITAS centroid (◇), and Fermi LAT centroid (△), respectively measured by Esposito *et al.* (1996), Albert *et al.* (2007), Acciari *et al.* (2009) and Abdo *et al.* (2010). The respective localization errors are shown as crosses of size 0.5 σ. The sizes of typical instrumental beams are indicated in the bottom-right corner of the figure.

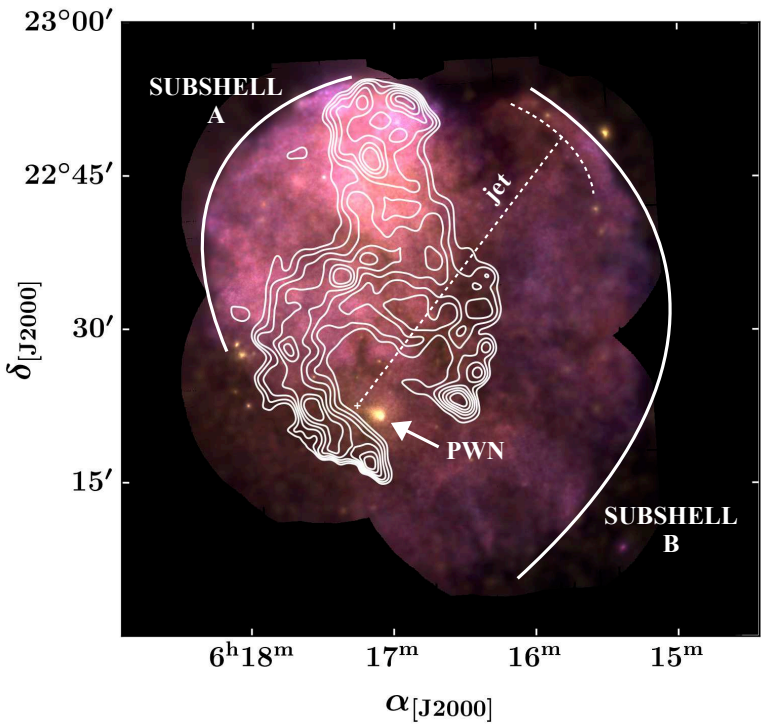

Figure 2.13 Composite image (see section 2.7, Fig. 2.17) of XMM-Newton observations in the IC443 SNR (1.4 – 5 keV). The sum of the equivalent width images of [Si XIII] + [Si XIV] and [S XV] + [S XVI] lines are represented by a set of contours, indicating the location of stellar ejecta. The position of the PWN is indicated by an arrow. The solid lines represent the boundaries of the SNR (subshells A and B). The dashed lines represents the jet-like structure studied by Greco *et al.* (2018). Data reproduced from Troja *et al.* (2008).

cloud (described in details by Lee *et al.* 2012), with G189.6+3.3 in the front position, and IC443 behind the cloud. Asaoka and Aschenbach (1994) suggested that the progenitors of both SNRs might have been members of the Gem OB1 association, which would account for their proximity. In that scenario, the aforementioned molecular cloud complex would encompass the parental cloud of the two progenitors.

The hard X-ray contents ($E > 10$ keV) of IC443 were mapped by the Advanced Satellite for Cosmology and Astrophysics (ASCA) up to 12 keV (Keohane *et al.*, 1997), by *Ginga* up to 20 keV (Wang *et al.*, 1992) and by BeppoSAX up to 100 keV (Bocchino and Bykov, 2000). The authors of these hard X-ray studies reported that the structures detected in this energy range are correlated with bright molecular emission regions and soft X-ray counterparts, and in some cases shifted towards the remnant interior. They proposed that the hard X-ray emission arises from shock-heated plasma in the southwestern and western regions, where the remnant shocks interact with molecular structures. Wang *et al.* (1992) proposed an unusually short estimate of the age of IC443 ($\sim$ 1000 yr) based on evidence for gas with a temperature $\geq 10^8$ K, and argued that the X-ray data is in agreement with the old assumption that IC443 is the remnant of the 837AD supernova (Shajn and Gaze 1954, Shklovsky 1954).

Keohane *et al.* (1997) reported that the hard X-ray emission is highly localized and found a hard X-ray ridge in the southern region of the remnant, along the rim of the radio shell. Most generally, the isolated, hard X-ray sources in IC443 can be interpreted as fragments of SNR ejecta (*e.g.* Zhang *et al.* 2018). An other interpretation is the existence of a PWN powering the hard X-ray emission. Based on evidence of enhanced particle acceleration (up to $\sim$ 10 TeV), Keohane *et al.* (1997) suggested that the hard-X-ray southern ridge could be associated with a plerion, which was soon to be confirmed. In fact, the *Chandra* X-ray observatory revealed a synchrotron bright, comet-shaped nebula within IC443, identified as a PWN powered by a young neutron star (Olbert *et al.* 2001a, Gaensler *et al.* 2006). In this scenario, the synchrotron emission provides a more consistent explanation of the hard X-ray emission than the 'high-temperature plasma scenario',

thus the main argument for the small age of the remnant is dismissed (hence, the age proposed by Wang *et al.* 1992 can be considered an outlier in X-ray studies of the IC443 SNR).

Kawasaki *et al.* (2002) presented the results of ASCA observations in the energy range 0.7-10 keV. The authors found that the softness-ratio map ($F_{0.7-1.5\ \mathrm{keV}}/F_{1.5-10\ \mathrm{keV}}$) is correlated to the shell morphology of the SNR and reported evidence of plasma overionization inside the remnant. XMM-Newton mapped IC443 in the ranges 0.3-0.5 keV and 1.4-5.0 keV with an unprecedented field of view and spatial resolution (Bocchino and Bykov, 2003). From this new data delivery, Troja *et al.* (2006) introduced a two-shell morphological model of IC443 destined to better interpret X-ray observations (see Fig. 2.12): *i.)* in the NE region, subshell A has been confined by the neutral [H I] described by Denoyer (1978), Giovanelli and Haynes (1979) and Lee *et al.* (2008); *ii.)* in the SW region, subshell B is expanding, unimpeded by the inhomogeneous and less dense medium; *iii.)* a toroidal molecular cloud (Cornett *et al.* 1977, Lee *et al.* 2012) is located below the spherical cap formed by subshell A. They proposed that the torus-shaped molecular cloud is interacting with the southern remnant molecular shocks (Burton *et al.*, 1988) and partly absorbing soft X-rays. They also emphasized the excellent correlation between the bright optical/radio NE filaments and the soft 0.3-0.5 keV features.

Troja *et al.* (2008) reported the detection of a ring-shaped stellar ejecta encircling the PWN, associated with a hot metal rich plasma (Si, S, Mg) which abundances are in agreement with a core-collapse scenario (see Fig. 2.13). Lastly, the northern part of IC443 was mapped by the *Suzaku* satellite at 1.75-6.0 keV, leading to the first detection of radiative recombination continuum in a SNR (Yamaguchi *et al.*, 2009). A collimated, Mg-rich jet-like structure associated with overionized plasma was discovered by Greco *et al.* (2018) from a new analysis of XMM-Newton observations. Based on the direction of the jet towards the remnant interior and the expected initial position of the PWN, their findings support the association of the SNR with the neutron star, hence a core-collapse scenario.

Based on the model of inhomogeneous ambient gas introduced by Troja *et al.* (2006), Ustamujic *et al.* (2021) studied the X-ray morphology of IC443 with 3D hydrodynamical simulations and synthesized X-ray maps that can be compared to XMM-Newton observations. The authors found that the asymmetric and centrally-peaked morphology can be reproduced if the origin of the explosion is set at the initial position of the PWN and assuming an age of $\sim$ 8000 yr for the remnant.

2.3.7 γ-ray observations towards IC443: anatomy of a TeVatron

The CR and high-energy contents of IC443 have been inspected by multiple γ-ray observatories from MeV to TeV energies. γ-ray emission ($E > 100$ MeV) from a source spatially associated with IC443 was first observed by the Energetic Gamma Ray Experiment Telescope (EGRET) on the Compton Gamma Ray Observatory (CGRO, Esposito *et al.* 1996). They determined a power-law spectral index that is consistent with shock acceleration of CRs by the SN shock wave, and inferred from the γ-ray flux intensity that approximately 10% of the energy released by the SN was converted in the acceleration of CRs.

The detection of this γ-ray source was confirmed by the Major Atmospheric Gamma Imaging Cherenkov Telescopes (MAGIC) in the very high-energy (VHE, $E \geq 100$ GeV) band (Albert *et al.*, 2007), allowing to reject its association with the PWN discovered by Olbert *et al.* (2001a)

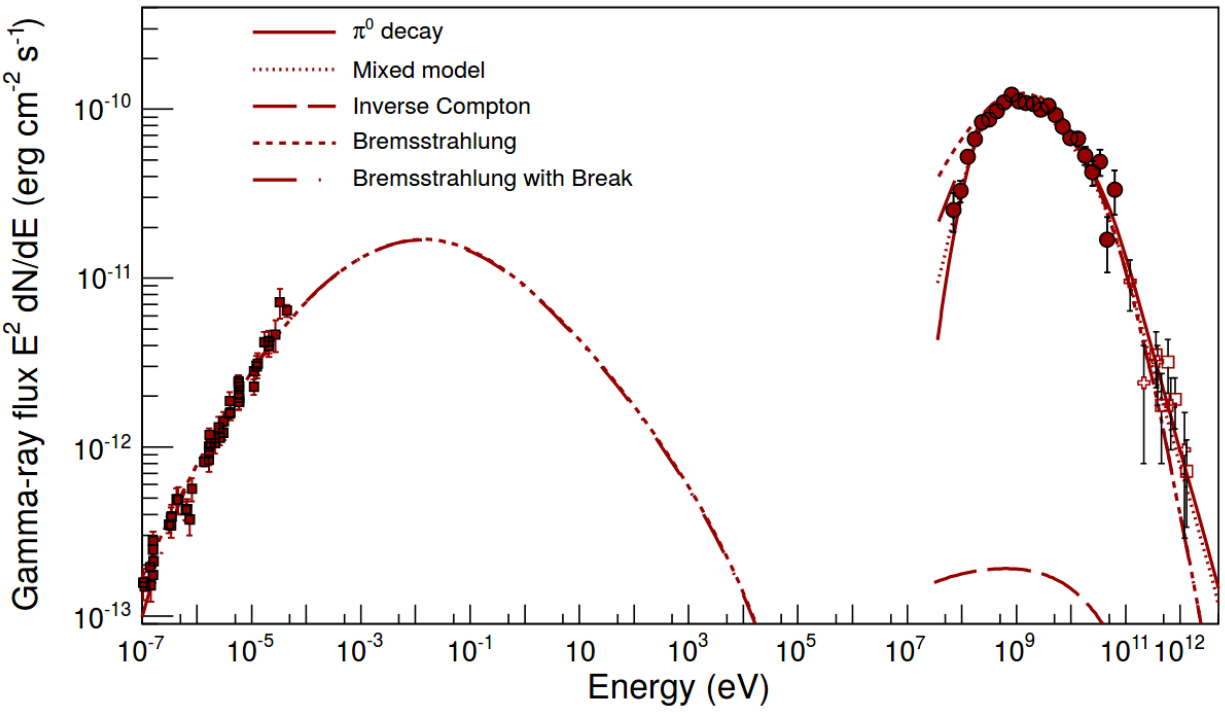

Figure 2.14 The observed spectral energy distribution of IC443 compared with various models. In the γ-ray domain, the SED data is found to be consistent with several models, including electron bremsstrahlung (dashed and dash-dotted lines) and pion-decay (solid line). In the radio band the dominant radiation process is synchrotron emission. The parameters used in the calculation for the models are $p_{\rm br} = 10$ GeV c^{-1} (break proton momentum), $B = 50\,\mu$G, and $n_{\rm H} = 300$ cm^{-3}. The dotted line shows a combined bremsstrahlung and pion-decay model to demonstrate that such a model is also consistent with the data. Radio data are taken from Castelletti *et al.* (2011). Figure reproduced from Ackermann *et al.* (2013).

due to a significant spatial separation of the respective centroids. Instead, they proposed a pion decay scenario to tie the VHE emission to the interaction of CRs with the dense molecular cloud associated with IC443.

Acciari *et al.* (2009) reported the detection of this γ-ray source in the VHE band of the Very Energetic Radiation Imaging Telescope Array System (VERITAS) and revealed that the source is extended (the updated VERITAS skymap of IC443 is shown in Fig 2.15). They examined two scenarii for the production of these γ-rays: *i.* interaction of the CRs accelerated in the early phase of the SNR (Torres *et al.*, 2003) with the molecular clouds such as the G clump, that is separated by 0°.03 from the centroid; *ii.* inverse Compton scattering and synchrotron radiation of the CRs accelerated by the PWN, since the spatial offset measured between the γ-ray emission and the PWN position is comparable with the offset found in HESS J1825-137 (Aharonian *et al.*, 2006).

IC443 was also observed by the *Fermi* Gamma-ray Large Area Telescope (LAT) that detected an extended γ-ray source in the 200 MeV - 50 GeV energy band (Abdo *et al.* 2010, Ackermann *et al.* 2013). The aforementioned authors established that the spectrum is well reproduced by the decay of neutral pions (see Fig. 2.14), observed that the clouds B, C, D, F and G are included in the extended γ-ray emission and discarded the PWN as a major contributor to the γ-ray flux. Tavani *et al.* (2010) reported the detection of γ-ray enhancement towards the NE shell in the 100 MeV - GeV range observed by the Astro-Rivelatore Gamma a Immagini Leggero (AGILE). They

proposed a hadronic model in which the cloud 'E' is the suggested target for the interaction with CRs. Re-acceleration of pre-existing Galactic CRs is an additional plausible scenario to account for the observed γ-ray emission in IC443 (Uchiyama *et al.*, 2010).

Indriolo *et al.* (2010) measured the CR ionization rate in IC443 based on H_3^+ observations ($\xi = 2 \times 10^{-15}$ s^{-1}) and suggested that IC443 is accelerating a large population of low-energy, ionizing CRs. Interestingly, the location of the γ-ray peak differs between the lower energy emission (*Fermi*, EGRET) and the VHE emission (VERITAS, MAGIC). This tendency is also verified by Tavani *et al.* (2010) who located the 100 MeV γ-ray peak close to the *Fermi*/EGRET position and further towards NE. Torres *et al.* (2008) presented a model in which the displacement between the EGRET and MAGIC sources can be physically explained. They proposed that the MAGIC observations can be accounted for as 'delayed TeV emission'. In that scenario, the CRs accelerated by the SNR are now diffusing and interacting with the $\sim$ 8000 $M_\odot$ molecular cloud of Cornett *et al.* (1977) and Lee *et al.* (2012), at a distance of 20 pc in the foreground of the remnant. In that case, the discrepancy between the lower energy and VHE emission would be related to different properties of the proton spectrum at different locations of the IC443 complex.

Recently, Humensky and VERITAS Collaboration (2015) presented an updated *Fermi* map where the position of the peak was shifted and consistent with VERITAS. These discrepancies and revisions are suggestive of an intrinsic uncertainty related to the localization of the peak from the analysis of γ-ray data, and are also caused by the two following intertwined issues: *i.)* there is a great variety of possible interpretations of the γ-ray spectrum (leptonic *vs.* hadronic scenarios); and *ii.)* we are lacking an accurate knowledge of the interstellar contents of the region (total mass of protons, ionization fraction, interstellar radiation field, *etc*).

In regard to the exact localization of the γ-ray peak, future observations with CTA might bring surprising new results. Nonetheless, the choice of the region studied in this thesis is justified by the VHE γ-ray significance map from Humensky and VERITAS Collaboration (2015) (VERITAS and *Fermi* centroids), which supports the clump G as a likely target of high-energy CR interaction with dense molecular gas (see also Fig. 2.15).

2.4 | The polarization and magnetic field in IC443

Explicit magnetic field studies towards IC443 are scarce. Polarized observations at 2700 MHz were performed first by Milne (1971) with the Australian National Radio Astronomy Observatory (ANRAO). From these observations, Milne concluded that the magnetic field is mostly radial throughout the remnant, and found that the maximum polarization temperatures and fractions are located away from the radio continuum peaks. Kundu and Velusamy (1972) presented polarized observations at 2.8 cm and found no evidence for radial magnetic field in IC443. Based on their average Faraday rotation measurements, they estimated $\langle N_e B_{11} \rangle = 0.09$ μG cm^{-3} (where N_e is the electron density and B_{11} the longitudinal component of the magnetic field). Dickel and Milne (1976) performed polarimetric observations at 2.7 and 5 GHz in a total of 20 SNRs including IC443. They confirmed the results obtained by Kundu and Velusamy (1972), although the authors found a smaller Faraday rotation throughout the remnant.

Wood *et al.* (1991) presented 6.1 cm polarimetric observations of the filamentary structure of the northeast rim of IC443. The authors found that the local magnetic field is rather correlated with the rim structure, but with no clear orientation (*i.e.* parallel or perpendicular) to it. They

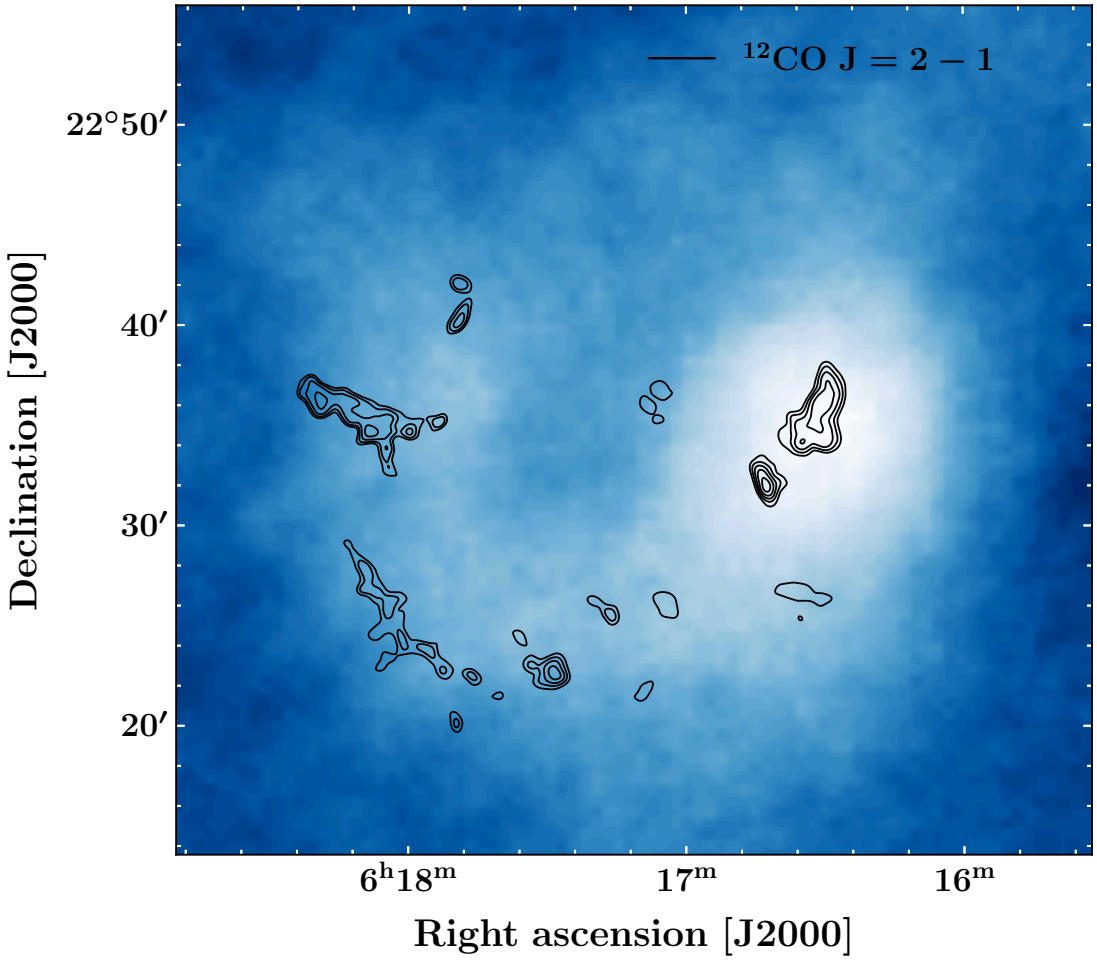

Figure 2.15 VERITAS skymap of IC443 ($E > 200$ GeV), showing resolved emission over the full extent of the supernova remnant. The VERITAS data is reproduced from Holder (2017). Black contours represent the emission of the ^{12}CO J=2–1 line (mapped with the IRAM 30m, see also Fig. 2.20).

associated polarized brightness detected beyond the rim to the outer shock of the SN explosion. Koo *et al.* (2010) measured Zeeman splitting of [H I] with the Arecibo telescope to constrain the strength of the magnetic field in IC443, and derived upper limits that are lower than expected from a dense shocked cloud (100-150 μG towards clumps B, C and E). Since then, only Hezareh *et al.* (2013) conducted an explicit polarization study in the G knot of IC443. They observed circular and linear polarization of the CO (1–0) and (2–1) lines with the IRAM-30m telescope, and linear polarization maps from the dust continuum with APEX. They showed that their observations were compatible with a scenario in which non-Zeeman CO circular polarization is due to a linear to circular polarization conversion. They attributed this conversion to an anisotropic resonant scattering effect affecting incident background photons before they escape the cloud (Houde *et al.*, 2013). Their study constitute a crucial step towards the characterization of the interaction of CRs with the magnetic field towards clump G.

2.5 | Shock-induced star formation in IC443

Star formation in IC443 was the focus of a few studies. The fundamental idea supporting the study of star formation in the vicinity of SNRs is that the compression and subsequent cooling caused by the passage of a shock wave create favorable conditions for star formation to take place at some point after the SN explosion (*e.g.* Elmegreen 1998 and Dubner and Giacani 2015 and references therein for more developments). Odenwald and Shivanandan (1985) studied the possible association of the northern component of IC443 with forming stars based on Far Infrared Sky Survey Experiment at 20, 27, and 93 μm and VLA observations at 2, 6, and 20 cm and concluded that the young stellar candidates had probably been formed before the SN explosion.

Huang *et al.* (1986) studied the correlation of point sources observed with the Infrared Astronomical Satellite (IRAS) and CO (1–0) observations performed with the FCRAO. They extended Denoyer (1979b)'s initial alphabetical classification (A, B, C) of molecular clumps from D to H. More interestingly, the authors found associations between IRAS point sources and some of the identified shocked CO clumps, and attributed them either to protostars or to a new class of infrared objects. Xu *et al.* (2011) then went one step beyond. They used color criteria for the point sources of IRAS and the Two Micron All Sky Survey (2MASS) to identify protostellar objects and Young Stellar Object (YSO) candidates (including Classical T-Tauri Stars, CTTSs and Herbig Ae/Be stars). Based on CO J=2–1 and J=3–2 maps from the Kölner Observatorium for Submillimeter Astronomy (KOSMA), they showed that their YSO candidates are spatially associated with shocked molecular regions along the molecular shell, including clump G. Based on the lifetime of the protostellar candidates and the estimated SNR age, they concluded that the formation of newly formed stars had not been triggered by the SNR, but rather by the stellar winds of its progenitor.

Su *et al.* (2014) confirmed the shell-like pattern of the spatial distribution of YSO candidates using a selection method based on color-color diagrams inferred from WISE (band 1, 2 and 3) and 2MASS (band K) photometric measurements towards point sources. It is unlikely that the spatial correlation between the YSO candidates and the molecular shell exposed by Xu *et al.* (2011) and Su *et al.* (2014) is accidental. In fact, star formation is expected to be triggered by the stellar wind feedback from a massive progenitor (*e.g.* Koo *et al.* 2008b). Therefore, all of the aforementioned evidence is consistent with a scenario of star formation induced by a massive progenitor, but does not constitute conclusive evidence for 'SNR-induced ' star formation.

2.6 | Maser studies

There is a long history of maser studies in IC443. Goss (1968) surveyed four OH absorption lines, at 1612, 1665, 1667, and 1720 MHz in the northern hemisphere radio sources, with the aim of discussing Galactic structure (based on velocity considerations) and to infer physical conditions (they discussed the equation of transfer and the determination of the excitation temperature of the OH Λ doublet). They detected only the 1667 MHz line in IC443, at -3.5 and -12.5 km s^{-1} with the Hat Creek Telescope of the University of California at a resolution of 10 kHz ($\sim$1.8 km s^{-1}).

Denoyer (1979a) was able to infer a OH/H I ratio (between 6×10^{-7} and 4×10^{-6} in the shocked material, that is an enhancement factor of about 100 compared with unshocked clouds) by means of observations of the OH 1665, 1667, and 1720 MHz lines (at eight positions of IC443) with the National Radio Astronomy Observatory. She characterized the OH emission as 'shocked'

based on the line profiles she obtained (velocity widths $\sim$ 40 km s^{-1}, at 1.5 km s^{-1} resolution) and on its spatial distribution, which she found to be coincident with shocked [H I] absorption profiles and distribution. She also noted that the 1720 MHz line was inverted. After Elitzur (1976) demonstrated that the 1720 MHz line could be inverted by collisional processes (bypassing the need for an infrared continuum to achieve radiative pumping), Turner (1982) showed that indeed the OH 1720 MHz maser in IC443 was not associated with an IR continuum source, with an upper limit of 5 mJy for such a continuum observed at 6 and 18 cm with the VLA.

Green (1989) then searched for the OH line at 1667 MHz with the Dominion Radio Astrophysical Observatory. He found absorption at three positions in IC443, with broad profiles indicative of shock excitation. At this stage, the idea that OH masers were tracing the interaction between SNRs and adjacent clouds was beginning to be established. Although IC443 (along with W28 and W44) was excluded from his first list, Frail *et al.* (1996) surveyed the OH 1720 MHz line in 66 Galactic SNRs, and demonstrated that this line was proving a powerful new diagnostic for the classification of SNRs interacting with molecular clouds.

The observations of IC443, W28 and W44 with the VLA at arcsecond resolution were the focus of a dedicated publication by Claussen *et al.* (1997b): they identified 6 masing spots in IC443, all located in the 'G' region delineated by Huang *et al.* (1986), provided a collisional excitation model for this line in shocks, and also pinpointed that OH masers spots could be promising candidates for high-energy searches for the sites of CR acceleration. Importantly, since their observations were performed in full Stokes polarimetric mode, they were also able to constrain the line-of-sight strength of the magnetic field within a factor of three of 0.2 mG at all locations in W28 and W44. However, they did not observe an S-shape (characteristic of Zeeman splitting) in the Stokes V profile in IC443 and hence could not constrain this value in this SNR.

Lockett *et al.* (1999) quickly improved the modelling of the shock origin for the OH 1720 MHz maser line, associated with moderate temperatures (50-125 K), local densities ($\sim 10^5$ cm^{-3}) and OH column densities of the order of 10^{16} cm^{-2}. Lockett *et al.* (1999) also claimed that these conditions could only be found in C-type shocks, constituting their most powerful indicator. Wardle (1999) added the effect of the dissociation of molecules by far ultraviolet (FUV) photons generated by the de-excitation of H_2 subsequent to its collisional excitation by the energetic electrons produced by CR and X-ray ionization in molecular clouds. Yusef-Zadeh *et al.* (2003) demonstrated the significance of this effect by highlighting the strong correlation between the maser emission and the mixed-morphology aspect of SNRs such as IC443 (center-filled thermal X-ray emission surrounded by a shell of radio emission).

Wardle and Yusef-Zadeh (2002) then reviewed the science made possible by the observation of the OH 1720 MHz maser line. Hoffman *et al.* (2003) re-observed the G region where Claussen *et al.* (1997b) had found 6 OH maser spots at 1720 MHz. They used both the VLA at a much improved angular resolution of 12 mas, and the MERLIN radio telescope with a 160 mas resolution. With MERLIN they detected three of the six masers spots, resolving one of them into two spots. With their new VLA observations, they resolved one of these two 'sub'-sources into three spots. The MERLIN data yielded deconvolved sizes for the sources in the range 90-180 mas (135-270 AU at 1.5 kpc), while the VLA data showed compact emitting cores of 15-55 mas size. Hewitt *et al.* (2006) observed OH in the whole remnant with the Green Bank Telescope (GBT) at 1667, 1665, 1612, and 1720 MHz. The authors found three other spots of weak, extended (with typical sizes of $10' \times 7'$) maser emission with absorption in the other lines in the B, D, and G

clumps, all coinciding with molecular clumps ridges of H_2 emission. With the physical properties they measured, they concluded that OH emission was clearly enhanced by the passage of the SNR shock. They generalized their GBT observations and slightly refined this analysis for IC443 in Hewitt *et al.* (2008), showing that extended weak 1720 MHz maser emission is common in evolved SNRs.

Hewitt *et al.* (2009a) finally studied the association between γ-ray and maser emission in SNRs, concluding that the local CR ionization rates could explain the production of OH molecules behind C-type shock waves propagating in these regions. To our knowledge, the quest for excited-state OH masers was unsuccessful in IC443. Searches were performed at 4.7, 7.8, and 23.8 GHz by Pihlström *et al.* (2008) (with the VLA), and at 6 GHz by Fish *et al.* (2007) (with the Effelsberg telescope) and McDonnell *et al.* (2008) (with the Parkes 64-m radio telescope). Pihlström *et al.* (2008) found their non detection consistent with C-type shock models, while McDonnell *et al.* (2008) noted a discrepancy between their upper limits on OH column density and values measured earlier from absorption studies, specially in IC443; they attributed this discrepancy to a possible lower velocity coherence for 6049 MHz masers than for 1720-MHz ones. To finish this section on masers, it should be noted that no H_2O masers were detected in IC443, despite searches with the VLA (Claussen *et al.*, 1999), and with the Very Long Baseline Array (VLBA, Claussen *et al.* 1999), placing further constraints on post-shock densities and consistent with density limits fixed by molecular observations and OH 1720 MHz maser observations. CH_3OH masers were also searched for in vain in SNRs (at 44 GHz with the Onsala Space Observatory by Litovchenko *et al.* 2011 and at 36 and 44 GHz with the VLA by Pihlström *et al.* 2014).

2.7 | Multi-λ visual summary of the IC443 supernova remnant

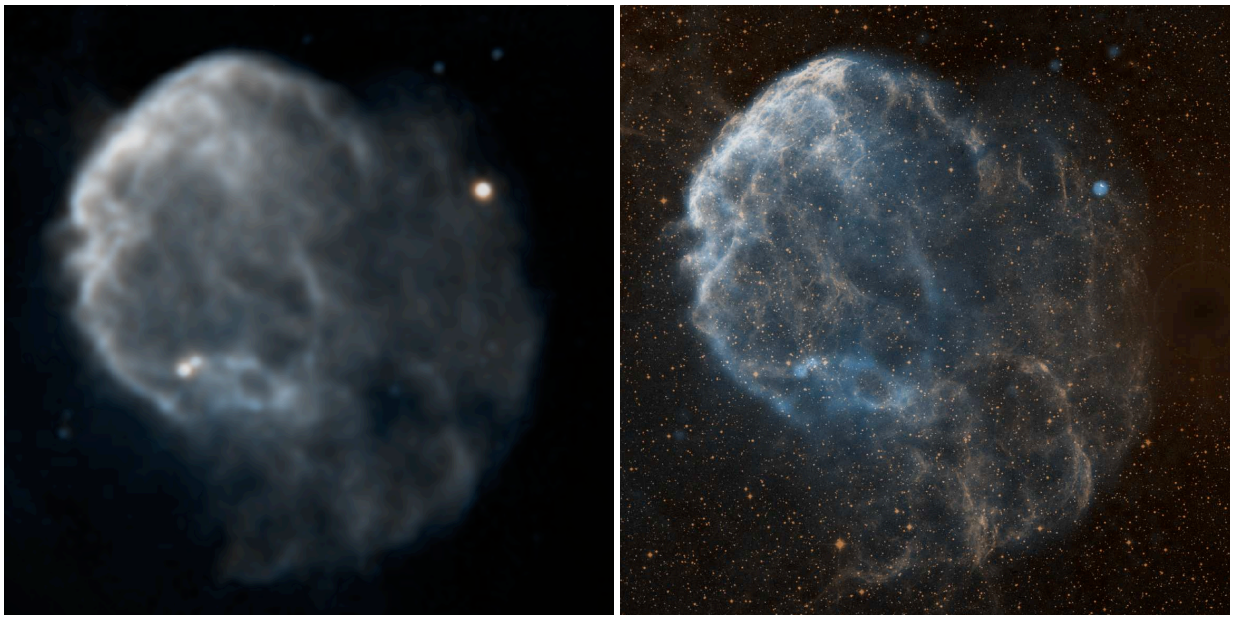

Figure 2.16 Composite images of IC443. *Left:* VLA observations. *Yellow:* VLA 330 MHz ($\sim$ 1 m), *Blue:* VLA 21 cm continuum (Lee *et al.*, 2008). *Right:* DSS and VLA observations. *Yellow:* DSS (optical), *Blue:* VLA 21 cm continuum.

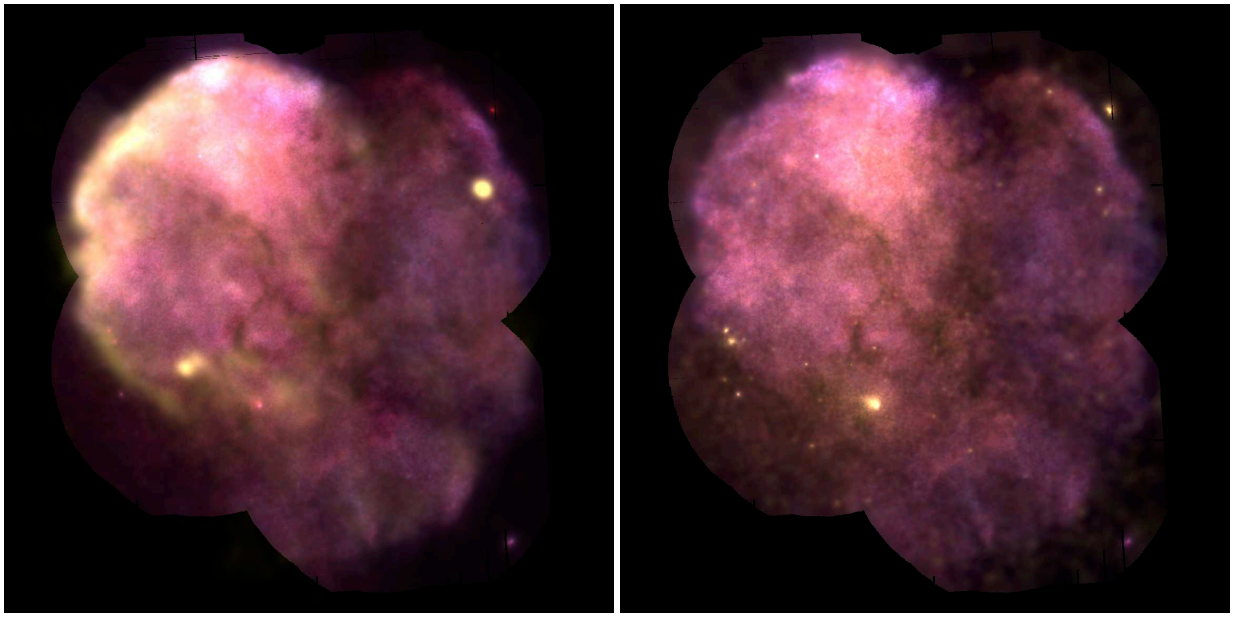

Figure 2.17 Composite images of IC443. *Left:* XMM-Newton and VLA observations. *Red:* 0.75-1.3 keV, *yellow:* 330 MHz, *blue:* 0.4-0.75 keV. *Right:* XMM-Newton observations (Bocchino and Bykov, 2003). *Red:* 0.75-1.3 keV, *yellow:* 2-7.2 keV, *blue:* 0.4-0.75 keV.

The radiation from supernova remnants is driven by a broad range of distinct physical processes (see Chapter 1). In this regard, IC443 is a unique example of how complex a mixed-morphology SNR can be. During this work, we gathered a large amount of wide-field data from MHz frequencies to TeV energies. In this section, we illustrate the striking morphological discrepancies and similarities of the IC443 SNR between its high-energy and μm to millimeter contents.

Composite images. Using `Python`[3], we produced RGB-like color images from 2D data of the IC443 SNR. We used the standard process for creating color images from monochrome data: using three different arrays ($a_i = a_1, a_2, a_3$) of intensity data (for example, one could use *Spitzer*-MIPS 24 μm $\rightarrow a_1$, 70 μm $\rightarrow a_2$, 160 μm $\rightarrow a_3$) we build a RGB-like array where in each pixel, the values of the three color channels are determined by the rescaled intensity of the corresponding pixel in the arrays a_i. The a_i data arrays are systematically rescaled so that the intensity of each pixel is in the interval [0, 1], so that the values in the resulting RGB-like array are in the interval [0, 255]. As a consequence, the relative intensities of the different images represented in the composite image are not conserved by the process. Hence, the composites images shown in this section are *entirely qualitative*, and serve only to illustrate the morphology of the SNR at different wavelengths. As a matter of fact, in some cases we applied the function $x \mapsto x^\alpha$, $\alpha = 0.5 - 2$ (where x is the integrated intensity of the map) to the data in order to enhance the contrast.

Usually, the standard colors used to build RGB images are [255, 0, 0] (red), [0, 255, 0] (green) and [0, 0, 255] (blue). Composite images produced with these "pure" colors are not always the most pleasing, hence we used two slightly modified color schemes: *i.*) [204, 20, 20] (red), [230, 220, 100] (yellow) and [86, 122, 255] (blue); *ii.*) [169, 104, 54] (yellow) and [54, 119, 169] (blue).

[3]To a large extent, the results presented in this manuscript were obtained with `Python` (Van Rossum and Drake 2009; a dynamic, open source programming language: `https://www.python.org/`). In particular, we frequently used the modules `numpy` (van der Walt *et al.*, 2011), `scipy` (Jones *et al.*, 2001), `matplotlib` (Hunter, 2007) and `astropy` (Astropy Collaboration *et al.* 2013, Astropy Collaboration *et al.* 2018).

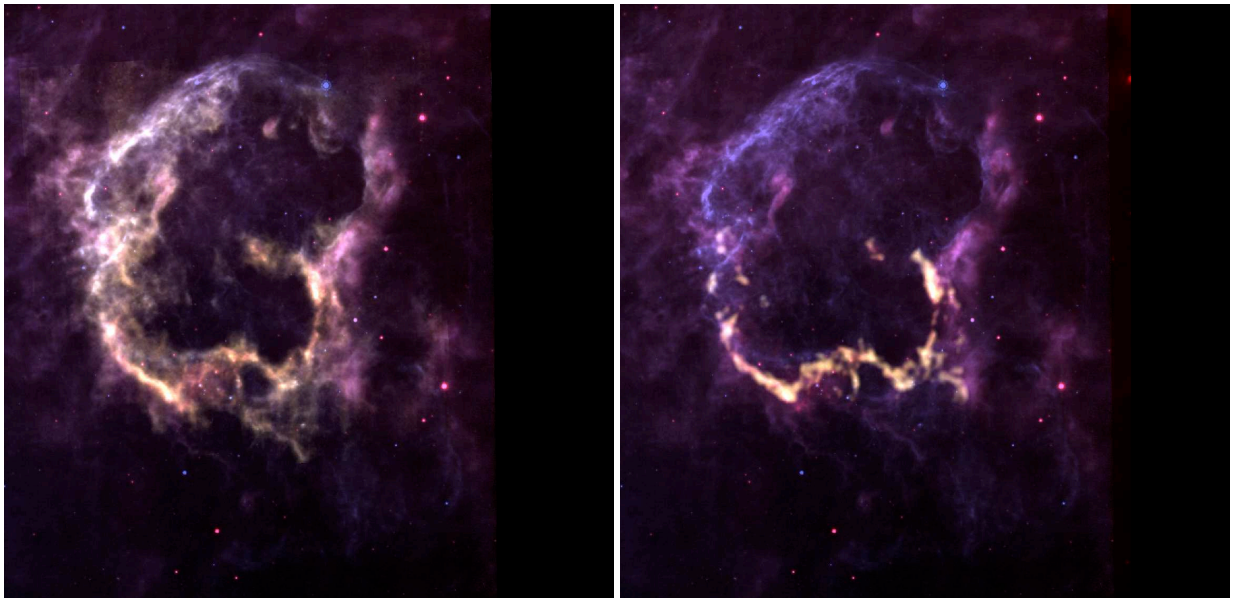

Figure 2.18 Composite images of IC443. *Left: Spitzer*-MIPS and WISE observations (Pinheiro Gonçalves *et al.*, 2011). *Red:* 12 μm, *yellow:* 70 μm, *blue:* 24 μm. *Right: Spitzer*-MIPS, WISE and IRSF/SIRIUS observations (Kokusho *et al.* 2020, see also Fig. 2.10). *Red:* 12 μm, *yellow:* H_2 v =1–0 S(1) (17 μm), *blue:* 24 μm.

We made sure that this choice of colors does not alter the possibility to distinguish the different components of a composite image.

In order to allow cross-comparisons between the different sets of composites images, we systematically represented the data corresponding to the boundaries [6^h:14^m:30^s; 6^h:19^m:00^s] (in right ascension) and [22°; 23°] (in declination). This $\sim 1° \times 1°$ field of view contains the entire remnant and its two main shells (A and B). Naturally, the available data does not systematically cover the entire $\sim 1° \times 1°$ field of view (*e.g. Spitzer*-MIPS mapped around 80% of that area) so there might be dark patches in our images where the data is missing (*e.g.* Fig. 2.18). The composite images presented in the following paragraphs are reproduced next to each other in Fig. A.1 in order to have all of them on the same page of the manuscript (for cross-comparison purposes).

***i.)* Radio and optical observations: the two-shell morphology** We produced two composite images (see Fig. 2.16) of IC443 based on VLA observations at 330 MHz and 21 cm (Lee *et al.*, 2008) and DSS optical observations. Both the optical and radio maps display a two-shell morphology (shells A and B, Braun and Strom 1986). The two bright 330 MHz point-like sources in the southern ridge are extragalactic sources. There is an excellent correlation between the intensity distribution in radio and the bright optical filamentary features (see right panel). Towards these filamentary shock fronts, the optical emission arises from recombination lines of ionic species, and the radio emission is driven by enhanced synchrotron radiation due to local magnetic field amplification (Vink, 2012). The left panel shows that the emission at 330 MHz ($\sim$ 1 m) and 21 cm is very similar, although some differences can be noticed by the color variation across the remnant. In fact, the variations of the radio spectral index (α, $S_\nu \propto \nu^\alpha$) can be visualized on this figure. Since the 330 MHz is coded in yellow, and the 21 cm in blue, it follows that the 'yellow' areas have a lower spectral index than the 'blue' areas (*i.e.* the spectrum is flat, and the emission is nonthermal). As it could be expected, the nonthermal emission is more important towards the NE

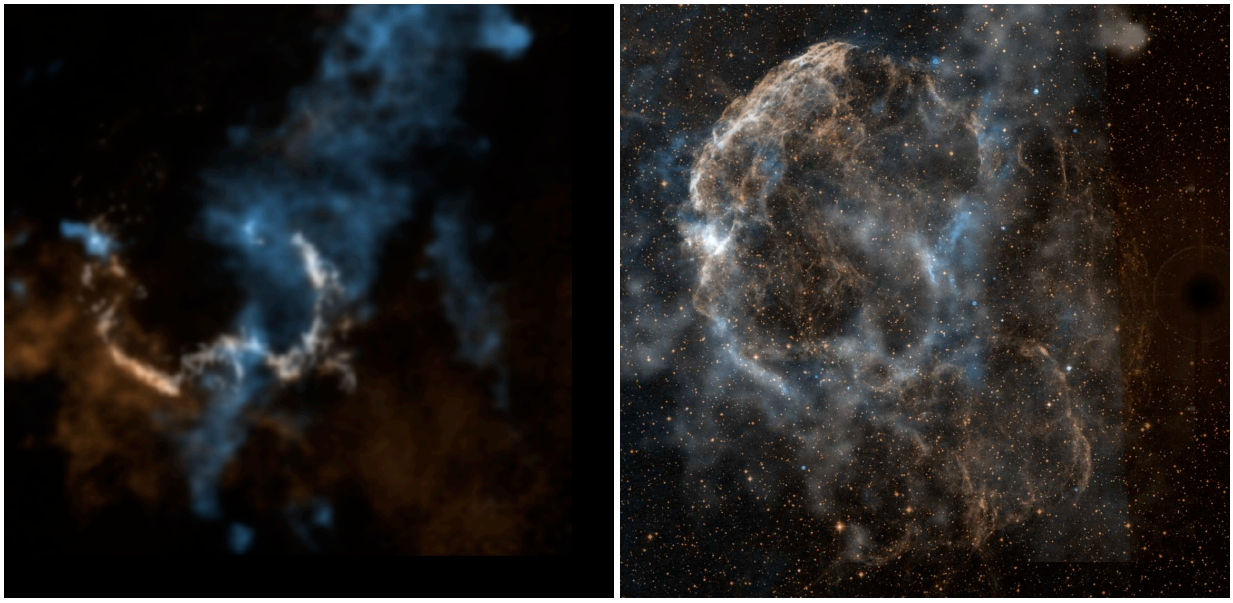

Figure 2.19 Composite images of IC443. *Left:* Observations of the atomic and molecular phases. *Yellow:* 21 cm [H I] velocity-integrated map from $v_{\rm LSR} = -18.3$ km s^{-1} to $v_{\rm LSR} = -10.7$ km s^{-1} (Lee *et al.*, 2008), *blue:* ^{12}CO J=1–0 slice at $v_{\rm LSR} = -3.79$ km s^{-1} ($\Delta v = 0.5$ km s^{-1}, Lee *et al.* 2012), *white:* H_2 v =1–0 S(1) (Kokusho *et al.*, 2020). *Right:* MIPS, DSS and molecular-phase observations. *Yellow:* optical (DSS), *blue:* 24 μm, *white:* 21 cm [H I] velocity-integrated map + ^{12}CO J=1–0 slice at $v_{\rm LSR} = -3.79$ km s^{-1}.

shell, where fast shocks are propagating (up to $v_{\rm s} \sim 150$ km s^{-1}, *e.g.* Alarie and Drissen 2019).

ii.) **High-energy emission: XMM-Newton and VLA observations** We produced two composite images (see Fig. 2.17) of IC443 based on XMM-Newton (0.4-7.2 keV) and VLA (330 MHz) archival data. The X-ray emission fills the entire remnant, and it appears to be confined by the radio shells (it is particularly visible within the eastern front). The X-ray emission can be attributed to thermal bremsstrahlung emission from a hot plasma (electron temperature $T \sim 10^7$ K, *e.g.* Parkes *et al.* 1977). The soft bands 0.4-075 keV and 0.75-1.3 keV are well correlated, but the hard 2-7.2 keV band presents isolated, strong sources with limited soft counterparts. On the right panel, the bright, condensed yellow spot in the southern center of the remnant corresponds to the PWN found by Olbert *et al.* (2001a). Absorption of the X-ray radiation along the line of sight can be seen along several filamentary structures towards the interior of the remnant (visible as dark, brownish lanes). Along the NW-SE axis, some of these patches of absorbing areas are likely to be physically associated with the molecular cloud described by Cornett *et al.* (1977) and Lee *et al.* (2012) (see Fig. 2.19), but it is also possible that they are further away along the line of sight.

Overall, the morphology in soft X-ray is inhomogeneous and quite complex, with a significant brightness gradient towards the NE shell, and a particularly bright spot in the northern part of the remnant. Fig. 2.13 shows that this bright northern area of X-ray emission is correlated with the (Mg, Si, S)-enhanced stellar ejecta found by Troja *et al.* (2008). It can be challenging to interpret the X-ray data of IC443, and one is appealed to assume that we are observing more than a single energetic event in this region. However, Ustamujic *et al.* (2021) managed to reproduce a non-uniform and asymmetric morphology with hydrodynamical simulations of a single SN

event occurring in an inhomogeneous ambient medium (based on the descriptive model of the inhomogeneous environment by Troja *et al.* 2006).

***iii.)* Infrared emission from warm dust and shocked gas: *Spitzer*-MIPS, WISE and H_2 observations** We produced two composite images (see Fig. 2.18) of IC443 based on *Spitzer*-MIPS and WISE archival data, as well as IRSF/SIRIUS data reproduced from Kokusho *et al.* (2020). The infrared emission morphology is unexpectedly different from the radio and optical brightness distribution. The infrared counterpart of the shell B is nowhere to be found, although the shell A is bright and well defined (except in the NW corner of the remnant). The higher spatial resolution of infrared instruments permits to see how clumpy the shell really is. These two panels (Fig. 2.18) also allow to visualize the different emission mechanisms at play in different locations of the remnant. On the right panel, we represent the emission from warm, shocked H_2 detected by IRSF/SIRIUS (Kokusho *et al.*, 2020) in yellow, together with the emission at 12 μm (WISE, in red) and 24 μm (MIPS, in blue).

This composite image shows that towards the southern ridge the continuum IR data is highly contaminated by H_2 rovibrational lines. It is likely that the IR emission in the northern part of the shell is also contaminated by atomic and ionized species (*e.g.* Fe II, Ne II, O I, Oliva *et al.* 1999, Burton *et al.* 1990) but thermal emission from warm dust grains should also contribute to the flux. Interestingly, the 12 μm and 24 μm emission patterns are uniformly correlated (pink hue) except towards the NE shell where the 24 μm flux seems to be more important (violet hue). This variation in the IR energy spectrum is likely to be related to different emission mechanisms towards the NE ionic shock fronts. Indeed, the NE shell is likely to be dominated by ionic and atomic lines, in contrast to the rest of the shell where there is probably a more important contribution from dust thermal emission and H_2 lines.

***iv.)* The ambient gas: atomic and molecular observations** We produced two composite images (see Fig. 2.19) of IC443 based on H I (Lee *et al.*, 2008), ^{12}CO (Lee *et al.*, 2012), H_2 (Kokusho *et al.*, 2020), *Spitzer*-MIPS and DSS data. The aim of this two-panel figure is to show the ambient medium in which the IC443 SNR is embedded, and how the asymmetric morphology of the shell is related to the inhomogeneous distribution of gas. The left panel focuses on the atomic (H I) and molecular (^{12}CO, H_2) contents of the region. The large molecular cloud described by Cornett *et al.* (1977) is represented by a slice of the ^{12}CO J=1–0 observations presented by Lee *et al.* (2012), coded in blue. It crosses the middle of the SNR along a NW-SE axis, and connects to a region of H I emission in the southeastern region of the remnant (also a data slice, in yellow).

The southern ridge of shocked H_2 gas described by Burton *et al.* (1988) is spatially correlated with both structures, suggesting that it encompasses regions of interaction between the SNR shocks and the ambient medium. Interestingly, the bright, filamentary optical structures towards the NE arc of shell A (right panel) are anti-correlated to the distribution of dense ambient gas in the NE section of the remnant. It is likely that the fast shocks propagating in this area have cleared most of the diffuse atomic gas by shock-driven ionization. In fact, the NE filaments are correlated with faint H I emission, interpreted by Lee *et al.* (2008) as recombined hydrogen, but this emission is too dim to be visible on the left panel.

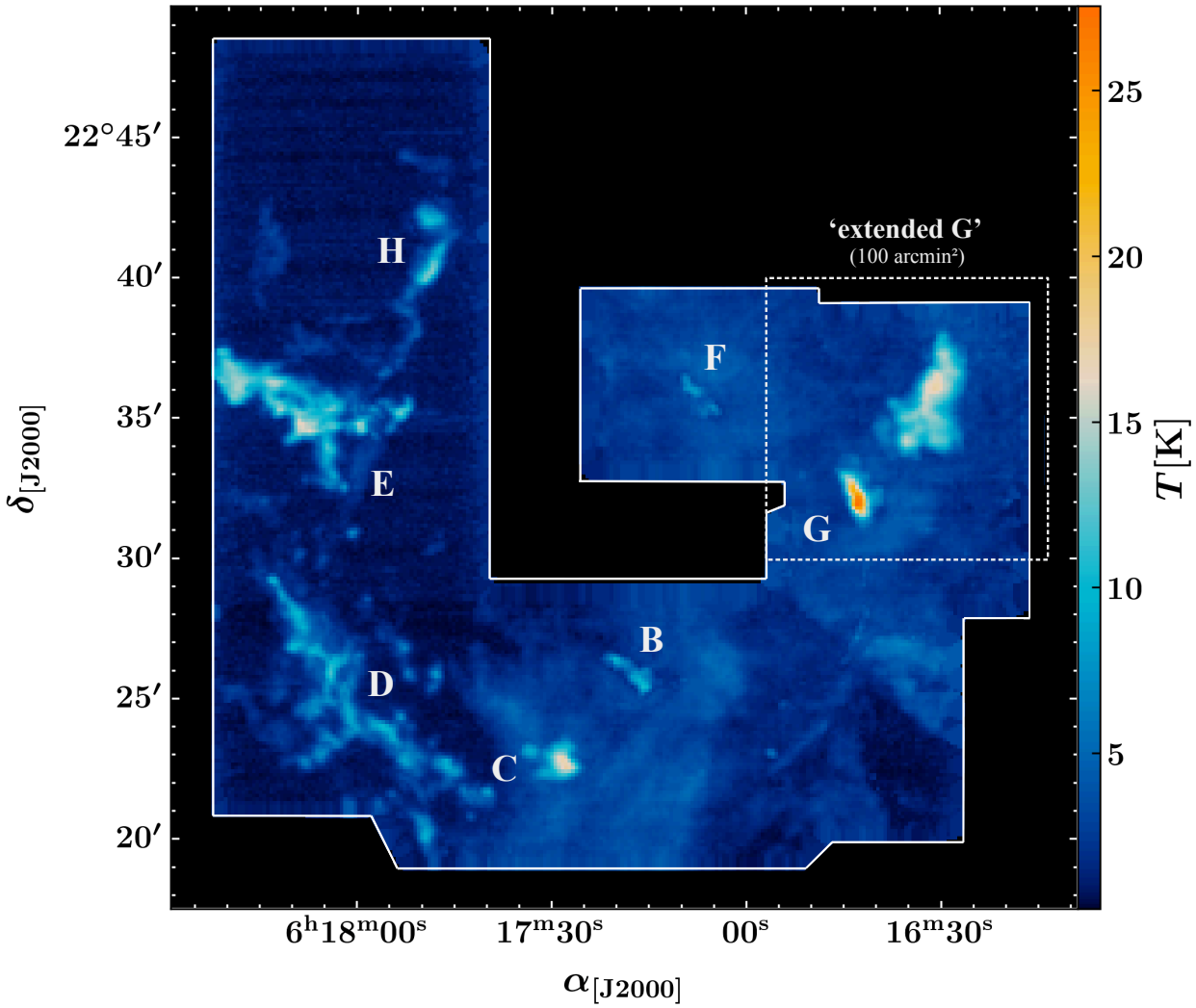

Figure 2.20 ^{12}CO J=2–1 map of the IC443 supernova remnant obtained with the IRAM 30m telescope. The quantity shown is the peak main beam temperature (K). The positions of the 'B', 'C', 'D', 'E', 'F', 'G', 'H' molecular clumps are indicated. The white dashed box indicates the $10' \times 10'$ area studied in this work, referred to as the 'extended G region' (see Chapter 6).

^{12}CO observations of the SNR In Fig. 2.20, we present earlier observations of the ^{12}CO J=2–1 pure rotational line obtained with the IRAM 30m telescope (provided by A. Gusdorf). In this peak temperature map, the molecular contents of the SNR are visible with a 11.2″ resolution. In addition to the faint, extended emission of the cloud of Cornett *et al.* (1977), several bright clumps are located along the shell (the 'B', 'C', 'D', 'E', 'F', 'G', 'H' molecular clumps, see section 2.3.3 and Fig. 2.12). These bright structures trace regions of interaction of the SNR blastwave with the fragmented molecular shell. In Chapter 6, we present new IRAM 30m and APEX observations of ^{12}CO, ^{13}CO and C^{18}O in the 'extended G region' (indicated by a white dashed box in Fig. 2.20).

Part II : Methods

Chapter 3 | Detection methods

Contents

While it is usually possible for a physicist to engage with experimental results obtained in controlled environments with fine-tuned parameters, we, astronomers, are located *inside* the experiment. There are many practical consequences to this critical constraint. Most importantly, the majority of our possibilities of investigation are restricted to the observation of photons emitted by distant regions of interest. As a matter of fact, almost everything that we learned about the Universe comes from the detection of electromagnetic radiation. However, this paradigm is shifting nowadays with multi-messenger astronomy: in addition to studies of cosmic rays, comets, *in situ* measurements and the analysis of extraterrestrial material returned by spacecrafts (*e.g.* the Hayabusa mission, Nakamura *et al.* 2011), the recent possibility to detect neutrinos and gravitational waves has opened novel windows on the Universe (*e.g.* Punturo *et al.* 2010, Abbott *et al.* 2018, Ahlers and Halzen 2018, Cherenkov Telescope Array Consortium *et al.* 2019).

The possibilities offered observations of electromagnetic radiation are restricted. Not only are there physical constraints, but the available data are limited by technology as well. As in any experimental science, interpretation of the data requires to carefully characterize the response of the instruments (sensitivity, receiver noise, absolute flux calibration, point spread function, efficiencies, gain, *etc*: see *e.g.* section 9.1). From the region in space where it is emitted to the data product in which it is ultimately saved into numerical values, the information carried by a bundle of photons undergoes a long sequence of alterations. Most generally, the flux measured on a detector is the product of a complex interaction between the 'true' brightness of the source and a combination of instrumental and line-of-sight effects (extinction by interstellar dust, atmospheric absorption, zodiacal light contamination, *etc*). Correctly calibrated observations hold a wealth of information (morphology, kinematics) and offer the possibility to infer measurements of physical and chemical quantities (*e.g.* column densities, local temperature, ionization fraction) using a few assumptions (see chapter 4).

Until recently, the only method used to examine the universe was through observations performed at optical wavelengths. For thousands of years, only visible light could be scrutinized by astronomers, hence the sky remained 'invisible' except for a tiny fraction of the energy spectrum (see Fig. 3.1). This changed radically during the 20th century. The radio and infrared windows respectively became the object of thorough investigations around the 1930s (*e.g.* Jansky 1933) and 1980s (launch of the InfraRed Astronomical Satellite in 1983, Neugebauer *et al.* 1984). In 1970, the first observations of the pure rotational transitions of ^{12}CO (at 115 GHz), representing the birth of millimeter-wave radio astronomy, were made by a group from Bell Laboratories using a specially designed receiver mounted on the NRAO (Blundell and Tong, 1992). Since these pioneer days, the sensitivity, spatial and spectral resolution have continuously increased. The data products analyzed in this thesis were obtained with the most capable infrared, submillimeter and millimeter observatories that are currently at disposal.

In this chapter, we aim to provide a description of the infrared and (sub)millimeter detection methods and corresponding instruments used in this work. In section 3.1, we present the characteristics of three infrared observatories (*Spitzer*, WISE, 2MASS, 1 µm - 160 µm). In section 3.2, we describe the heterodyne detection method and its application to sub-millimeter and millimeter observations (IRAM 30m, APEX, NOEMA, 0.8 mm - 3 mm).

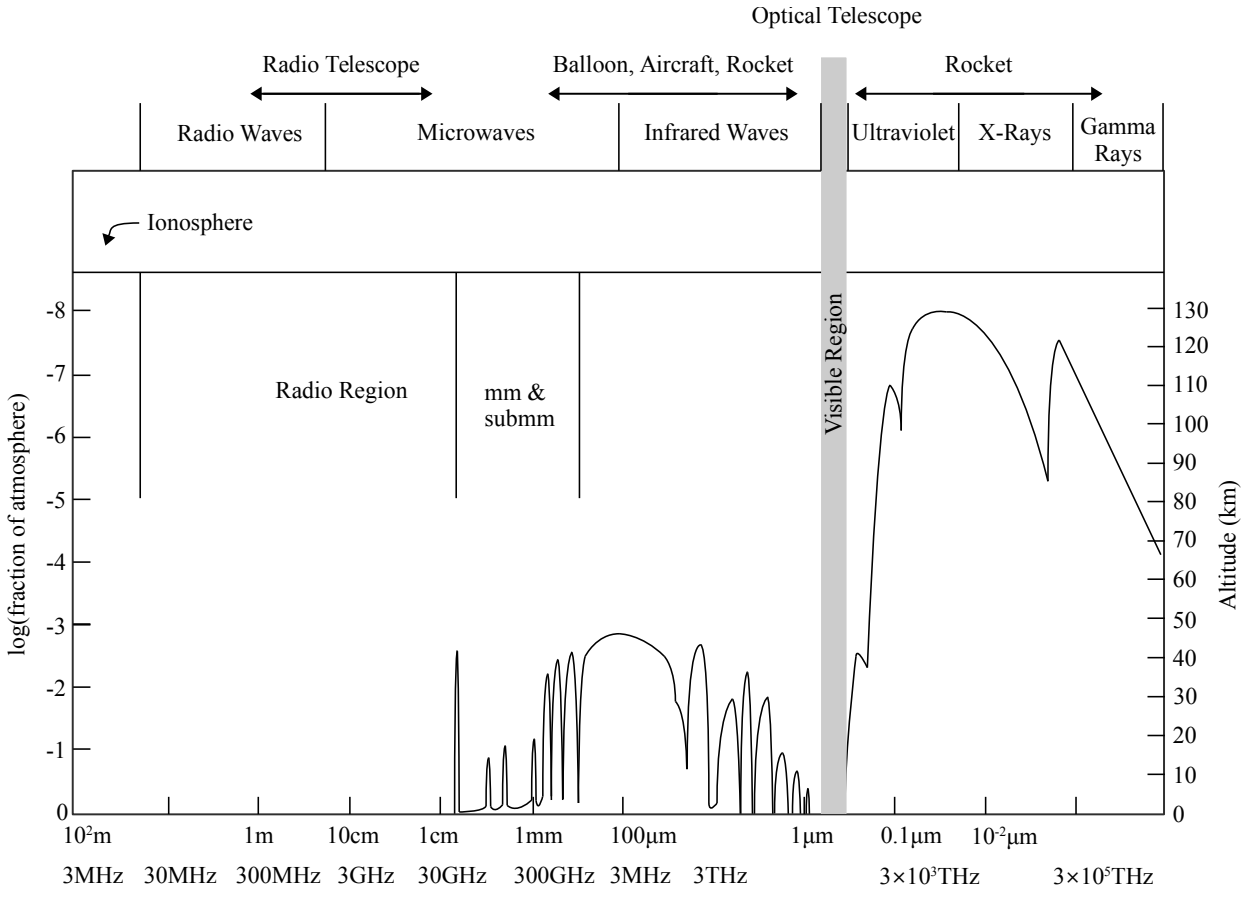

Figure 3.1 The transmission of the Earth's atmosphere for electromagnetic radiation. The diagram gives the height in the atmosphere at which the radiation is attenuated by a factor 1/2. Figure reproduced from Wilson *et al.* (2009).

3.1 | Infrared observations

The techniques of infrared detection are not distinct from the ones used in classical optical reflectors. A detector sensitive to infrared wavelengths, cooled to cryogenic temperatures and located in the focal plane of a primary mirror constitutes the core building block of an infrared telescope. Cooling is required to minimize the intrinsic thermal radiation of the telescope structure, and to reach the optimum operating point of sensors. Silicon (Si), germanium (Ge), gallium-doped silicon (Si:Ga) and arsenic-doped silicon (Si:As) are some examples of materials used to build arrays of infrared photoconductors.

A critical difference between optical and infrared astronomy is the transparency of the atmosphere (see Fig. 3.1). The primary molecules that are responsible for the majority of the infrared atmospheric absorption are water vapor (H_2O, very strong absorber with several bands in the $\sim 1 - 10$ μm range and for $\lambda > 20$ μm, variable in time and space since it depends on the local weather) and carbon dioxide (CO_2, mid and far-infrared absorber). There are different approaches to solve the problem of atmospheric absorption. Airborne observatories, such as the Stratospheric Observatory For Infrared Astronomy (SOFIA) and its predecessors, operate at high altitude where the rarefaction of molecules allows to reach a satisfying transmission of the atmosphere. The second approach is to simply send the instruments in space. Airborne observatories are more versatile than space observatories, because they can easily be modified and upgraded with new receivers over time.

Instrument/band	λ (μm)	Array type	$\lambda/\Delta\lambda$	FoV	Pixel size ($''$)	$1.22\lambda/D$ ($''$)
IRS [SL]	5.2-14.7	Si:As	64-128	$3.7'' \times 57''$	1.8	1.5-4.4
IRS [SH]	9.9-19.5	Si:As	~ 600	$4.7'' \times 11.3''$	2.3	2.9-5.8
IRS [LL]	14.3-35.1	Si:Sb	64-128	$10.6'' \times 168''$	5.1	4.2-10.4
IRS [LH]	18.9-37.0	Si:Sb	~ 600	$11.1'' \times 22.3''$	4.5	5.6-11.0
MIPS-1	24	Si:As	5	$5.4' \times 5.4'$	2.55	7.1
MIPS-2	70	Ge:Ga	4	$2.7' \times 1.4'$	5.20	20.7
MIPS-3	160	Ge:Ga	5	$0.53' \times 5.33'$	16×18	47.4

Table 3.1 Spitzer instrumentation summary for the IRS and MIPS modules. λ is the nominal wavelength, $\lambda/\Delta\lambda$ is the spectral resolution, 'FoV' refers to the field of view and the pixel sizes of the detectors are given in arcseconds. Columns 1-6 are reproduced from Tab. 3.2 in the *Spitzer* telescope handbook. In the last column, we indicate the size of the diffraction-limited PSF.

3.1.1 *Spitzer* Space Telescope

The *Spitzer* Space Telescope began its life as the 'Shuttle Infrared Telescope Facility' (SIRTF) before it was renamed to honor Lyman Spitzer, Jr (Werner *et al.*, 2004). Launched in 2003, it functionned until 2020 when it was finally decommissioned. The 'cryogenic mission' ($T \sim 5.6$ K) ended in 2009, but according to the *Spitzer* Space Telescope Handbook, the sensitivity and image quality of the short-wavelength IRAC channels remained the same during the 'warm mission' ($T \sim 27.5$ K). The *Spitzer* telescope and its three focal-plane instruments were cooled to their operating temperature using liquid helium cryogen ($T_{\rm cryo} = 1.2$ K) under the pumping action of space, and high-pressure nitrogen was used to control the spacecraft *via* a reaction control system

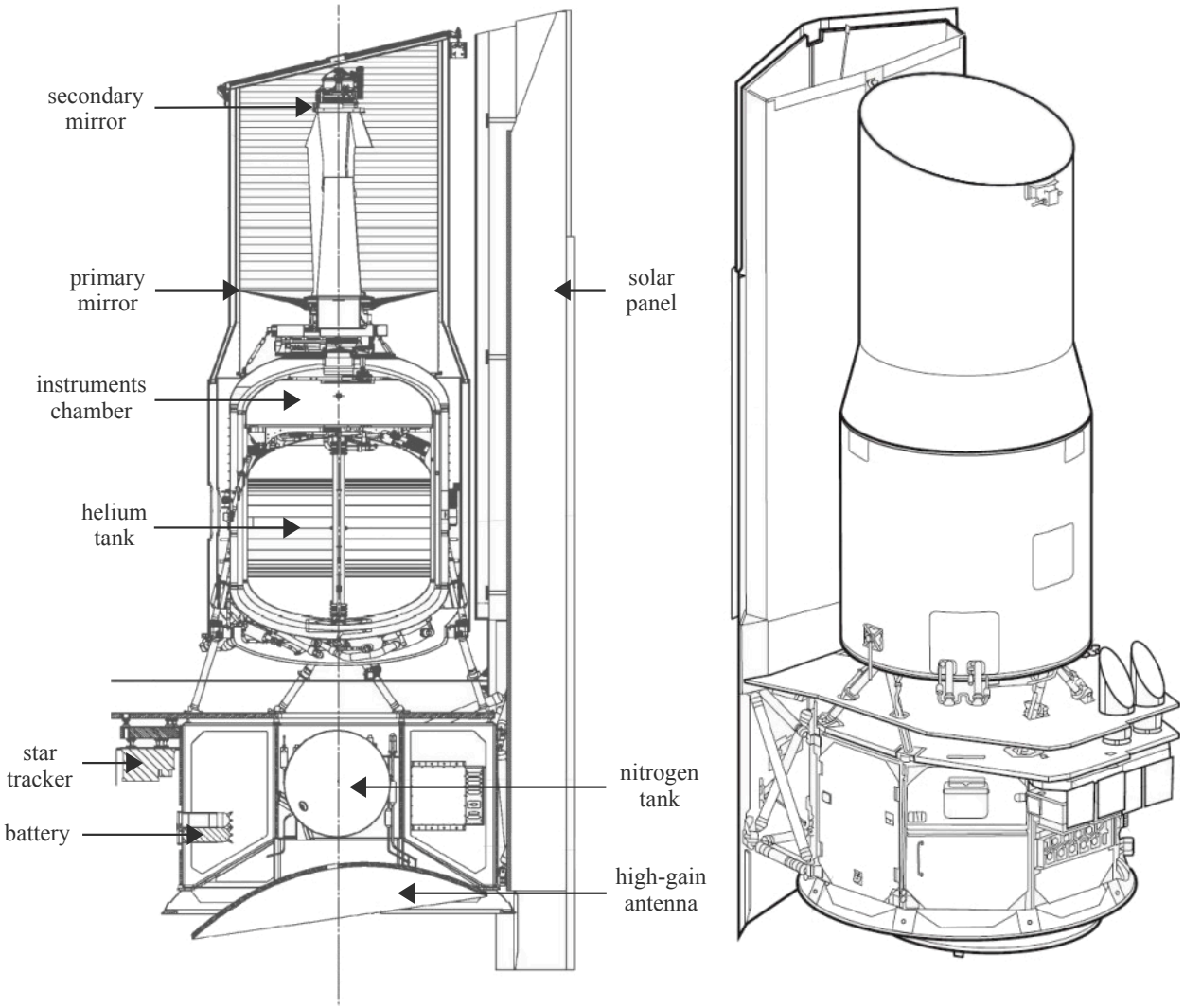

Figure 3.2 Schematic representation of the *Spitzer* Space Telescope (Gehrz *et al.*, 2007).

(see Fig. 3.2). The Ritchey-Chrétien design of the primary mirror (D_{primary} = 85 cm) minimized spherical aberration and coma over the field of view of the telescope (FoV = 32′). A complete technical description of the *Spitzer* space telescope and its instrument package is given in the corresponding handbooks of the '*Spitzer* Heritage Archive Documentation'[1]. In the following sections, we provide a short description of the two instruments that we used in this work.

3.1.1.1 The Multiband Imaging Photometer for *Spitzer* (MIPS)

The Multiband Imaging Photometer (hereafter MIPS, Rieke *et al.* 2004) is the diffraction-limited broadband imaging instrument of the *Spitzer* space telescope. MIPS has three broad photometric bands (24 μm, 70 μm and 160 μm, see Fig. 3.3) related to three distinct arrays of detectors. The 24 μm array of detectors (using Si:As impurity band detection, see Tab. 3.1) has accurate photometric properties (rms relative error ∼ 1%) . Since there are no silicon dopants that meet the requirements to detect such low-energy photons, the 70 μm and 160 μm were built using Ge:Ga photoconductors, which have a relatively poor photometric stability. As a consequence, the rms

[1] https://irsa.ipac.caltech.edu/data/SPITZER/docs/sitemap/

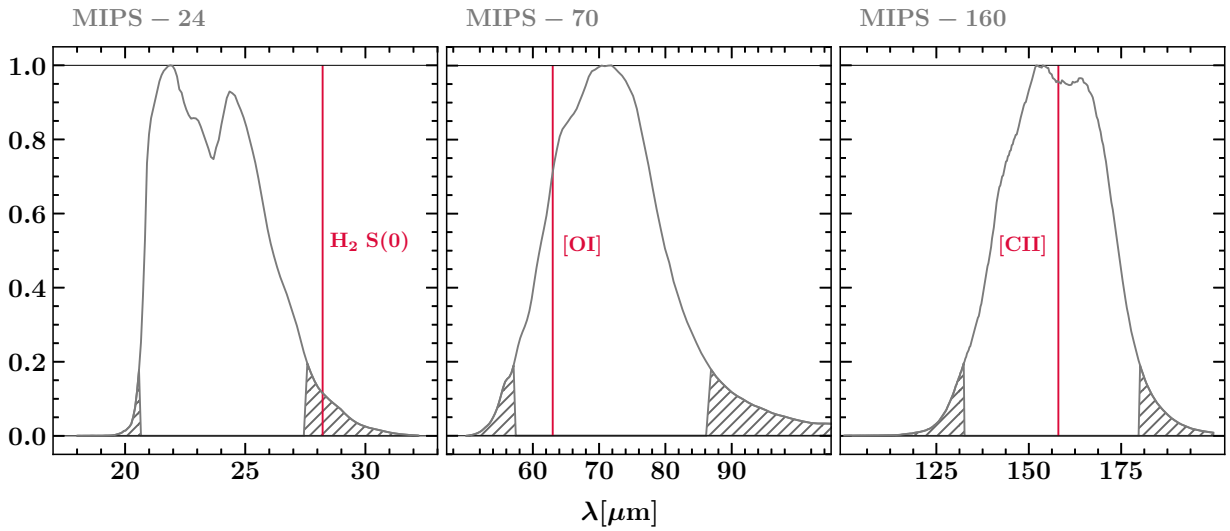

Figure 3.3 Normalized spectral bandpasses of the *Spitzer*-MIPS instrument. *Left:* band 1 (24 μm); *center:* band 2 (70 μm); *right:* band 3 (160 μm). In red, we indicate the atomic and molecular lines that are the most likely to significantly contribute to the measurements performed by MIPS (H_2 S(0): $\lambda = 28.22$ μm, [O I]: $\lambda = 63.18$ μm, [C II]: $\lambda = 157.74$ μm). The hatched areas represent the wavelengths at which the normalized transmission of the bands are lower than 20%. See also Fig. 9.1.

relative error of the 70 μm and 160 μm arrays is ∼ 10%.

Most generally, the flux measured by a broadband receiver is the sum of the contributions from continuum emission (thermal emission from dust grains) and spectral line emission (recombination, fine-structure, rovibrational lines, *etc*, see also Fig. 5.1). Each *Spitzer*/MIPS band is subject to contamination by atomic and molecular lines:

– The 24 μm band is sensitive to the H_2 0 − 0 S(0) pure rotational line ($\lambda = 28.22$ μm), [Si I] ($^3P_1 - ^3P_2$, $\lambda = 25.25$ μm) and [Fe II] ($^6D_{7/2} - ^6D_{9/2}$, $\lambda = 25.99$ μm). *e.g.* Neufeld *et al.* (2007), Neufeld *et al.* (2009).

– The 70 μm band is sensitive to [O I] ($^3P_1 - ^3P_2$, $\lambda = 63.18$ μm) and [Si I] ($^3P_2 - ^3P_1$, $\lambda = 68.47$ μm).

– The 160 μm band is sensitive to [C II] ($^2P_{3/2} - ^2P_{1/2}$, $\lambda = 157.74$ μm).

These lines are significant sources of contamination, since they trace various components of the ISM in the regions studied and/or along the line of sight.

In scan mode, MIPS has efficient mapping capabilities (all three arrays view the sky simultaneously, and a scan mirror moves at a constant rate to produce a mosaic of sub-fields). A single scan pass provides multiple redundancy at 24 μm and 70 μm, but only a single redundancy at 160 μm at the slow and medium scan rates. Using the fast scan rate, the 160 μm map is not even fully sampled in a single scan.

3.1.1.2 The Infrared Spectrograph (IRS)

The Infrared Spectrograph (hereafter IRS) is the diffraction-limited spectral instrument of the *Spitzer* space telescope (Houck *et al.*, 2004). IRS includes four distinct sub-modules: the short-

low (SL), short-high (SH), long-low (LL) and long-high (LH) spectrographs (see Tab. 3.1). The terms 'short' and 'long' refer to the length of the slit, and the terms 'low' and 'high' refer to the spectral resolution $\lambda/\Delta\lambda$ (where λ is the nominal wavelength and $\Delta\lambda$ is an element of spectral resolution). Naturally, a longer slit results in a greater field of view (see Tab. 3.1). The four separate spectrograph modules cover a wavelength range from 5.3 to 38 µm. The low spectral resolution modules (SL, LL, $\lambda = 5.2 - 35.1$ µm, $\lambda/\Delta\lambda = 64 - 128$) are grating spectrographs, whereas the high spectral resolution modules (SH, LH, $\lambda = 9.9 - 37.0$ µm, $\lambda/\Delta\lambda \sim 600$) are cross-dispersed echelle spectrographs.

Mapping mode spectroscopy IRS can be used in mapping mode to produce a mosaic of spectroscopic observations. In mapping mode, the submodules of the spectrograph can be used simultaneously to perform a raster map by moving the slits around a central target position. The Cube Builder for IRS Spectral Mapping (CUBISM) tool then allows to reduce the data and build a full spectral cube from a collection of single slit spectra (Smith *et al.*, 2007), including flux calibration, pixel rejection and masking processes.

***Spitzer* data products** The *Spitzer* data products can be downloaded *via* the *Spitzer* heritage archive (SHA) web interface[2]. A search query using a source name and/or sky coordinates allows to track the 'basic calibrated data' available in a defined region of the sky. Basic calibrated data (BCD) corresponds to reduced data that has been pushed through the pipelines, hence it offers the most reliable data products produced by automated processing. Automated processing includes operations such as correction of photometric response, flat-field, dark current, gain, application of pixel masks, *etc.* (a complete description of the pipeline processing is given in the handbooks of each instrument). MIPS BCD products can be directly used as scientific data products, and IRS BCD products can be used as input to the CUBISM software to produce spectral cubes.

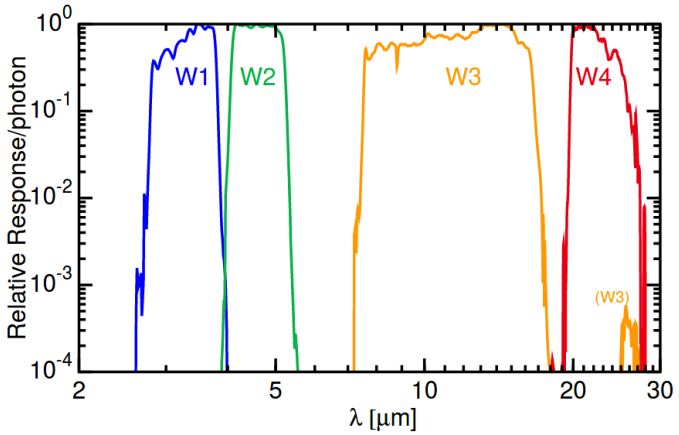

Figure 3.4 The weighted mean WISE relative spectral response functions for the bands W_1 (in blue), W_2 (in green), W_3 (in yellow) and W_4 (in red) after normalizing to a peak value of unity, on a logarithmic scale. Figure reproduced from Wright *et al.* (2010). See also Fig. 9.1.

3.1.2 Sky surveys

In Chapters 9 (dust thermal emission analysis) and 10 (infrared point source census), we study the near-infrared and mid-infrared continuum emission in the IC443 SNR using the full-sky surveys

[2] https://sha.ipac.caltech.edu/applications/Spitzer/SHA/

Instrument/band	λ (µm)	Array type	FoV	Pixel size ($''$)	FWHM ($''$)
W_1	3.4	HgCdTe	$47' \times 74'$	2.75	6.1
W_2	4.6	HgCdTe	$47' \times 74'$	2.75	6.4
W_3	20	Si:As	$47' \times 74'$	2.75	6.5
W_4	22	Si:As	$47' \times 74'$	5.5	12.0

Table 3.2 WISE instrumentation summary. λ is the nominal wavelength, 'FoV' refers to the field of view and the pixel sizes of the detectors are given in arcseconds. The 'FWHM' is the full width at half maximum in the final images.

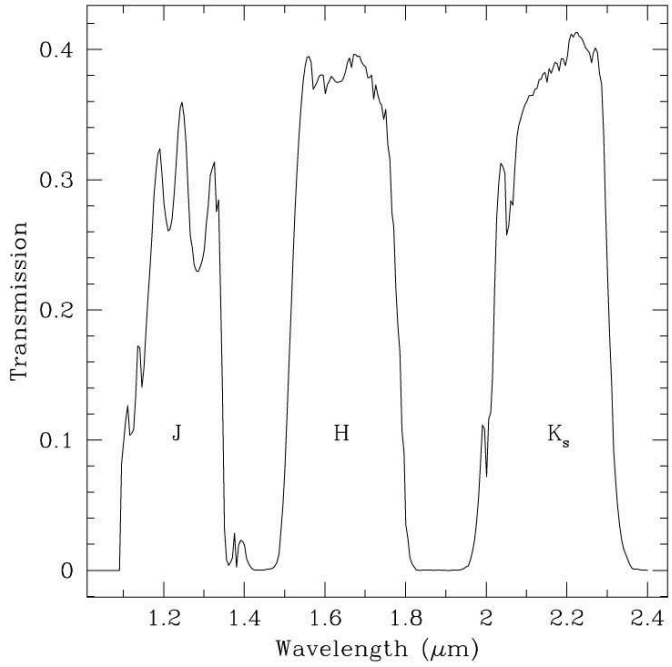

Figure 3.5 2MASS bandpasses for the J, H and K photometric bands. The curve represents calculated total transmission as a function of wavelength including the atmosphere (modeled with a precipitable water of 5 mm), telescope optics, camera optics, and array quantum efficiency. This composite transmission is derived from witness measurements of mirror, dichroic, lens coating efficiency, and quantum efficiency measurements of similar arrays. Figure reproduced from Skrutskie *et al.* (2006). See also Fig. 9.1.

performed by the Wide-field Infrared Survey Explorer (hereafter WISE) and the Two-Micron All-Sky Survey (hereafter 2MASS). In the following subsections, we briefly present the characteristics of these two observatories.

3.1.2.1 Wide-field Infrared Survey Explorer (WISE)

The Wide-field Infrared Survey Explorer is a space observatory which has completed a mid-infrared survey of the entire sky between 3.4 µm and 22 µm (Wright *et al.*, 2010). WISE mapped the sky at 3.4 µm (W_1), 4.6 µm (W_2), 12 µm (W_3) and 22 µm (W_4) using a 40 cm telescope feeding Mercury cadmium telluride (HgCdTe) and Si:As photodetector arrays with a total of 4 million pixels (see Tab. 3.2, Larsen and Schick 2005). The relative responses of the WISE photometric bands are shown in Fig. 3.4.

WISE data products The WISE data releases offer position and photometry measurements for 7 337 642 955 objects and 18 240 Atlas `FITS` images (four bands intensity and uncertainty maps). WISE data products can be downloaded from the NASA/IPAC infrared science archive web interface in `FITS` format, and the point source catalogs can be queried using the source coordinates and a search radius. However, the Atlas images downloaded from the archive are not calibrated

in flux, hence users have to perform their own absolute flux calibrations (we perform the WISE absolute flux calibration in section 9.1.2).

Instrument/band	λ (µm)	Array type	FoV	Pixel size ($''$)	FWHM ($''$)
J	1.235	HgCdTe	$8.'5 \times 8.'5$	2.0	2.5
H	1.662	HgCdTe	$8.'5 \times 8.'5$	2.0	2.5
K	2.159	HgCdTe	$8.'5 \times 8.'5$	2.0	2.5

Table 3.3 2MASS instrumentation summary. λ is the nominal wavelength, 'FoV' refers to the field of view and the pixel sizes of the detectors are given in arcseconds. The 'FWHM' is the full width at half maximum in the final images.

3.1.2.2 Two-Micron All-Sky Survey (2MASS)

The Two-Micron All-Sky Survey has completed a near-infrared survey of the entire sky between 1.2 µm and 2.2 µm (Skrutskie *et al.*, 2006). 2MASS mapped the sky at 1.235 µm (J band), 1.662 µm (H band) and 2.159 µm (K band) using two 1.3m Cassegrain ground telescopes feeding 256×256 HgCdTe photodetector arrays (see Tab. 3.3). Two telescopes, one in each hemisphere were used to observe the entire celestial sphere (one at Mount Hopkins, Arizona and one at Cerro Tololo, Chile). The J, H, K photometric bands used by 2MASS correspond to the classical bands defined by Johnson *et al.* (1962), with the exception that the 2MASS K band excludes wavelengths greater than 2.31 µm to reduce thermal background and airglow, and extends down to 2.00 µm to maximize bandwidth. The 2MASS photometric bands are shown in Fig. 3.5. In contrast to WISE, 2MASS is not diffraction-limited since it is a ground telescope: the angular resolution is $2''.5$ under the best seeing conditions.

2MASS data products The 2MASS All-Sky Data Release offers a point source catalog containing 470 992 970 sources and an extended source catalog that contains 1 647 599 objects, in addition to 4 121 439 near-IR maps covering 99.998% of the sky (Skrutskie *et al.*, 2006). Photometric fluxes are measured with a $\sim$ 5% uncertainty, and the positional accuracy is $\sim 0''.5$. Data products can be downloaded from the NASA/IPAC infrared science archive web interface in `FITS` format, and the point source catalogs can be queried using the source coordinates and a search radius.

3.2 | (Sub)millimeter observations

Radio astronomy has come a long way since the first reports of the detection of a 20.5 MHz (λ = 14.6 m) extraterrestrial radiation source by Jansky in 1931 (Jansky, 1933). Radio astronomy has a critical advantage over infrared astronomy: the atmosphere is semi-transparent to radio waves between 15 MHz (20 m) and 1.5 THz (0.2 mm). At the junction of the infrared and radio domains (see Fig. 3.1), millimeter and submillimeter radio astronomy (0.1-3 mm) occupies a frequency range that is crucial for the observation of interstellar molecular lines, *e.g.* ^{12}CO (115 GHz, 2.6 mm), CH_3OH (86.6 GHz, 3.5 mm), HNC (90.7 GHz, 3.3 mm), ^{13}CS (92.5 GHz, 3.2 mm), SiO (86.8 GHz, 3.5 mm). Unfortunately, it follows that atmospheric molecules (O_2 and H_2O) can

also absorb radiation before it reaches a ground telescope. O_2 and H_2O are respectively responsible for partial transparency of the atmosphere at 1.63 mm (water vapor) and 5 mm (dioxygen). To address this problem, millimeter/sub-millimeter ground observatories are located in high-altitude (to minimize the length of atmosphere) and dry environments (*i.e.* low-precipitation areas such as the Atacama Desert).

Preliminary remarks: brightness temperature In radio astronomy, specific intensities I_ν (in Jansky) are commonly expressed by the brightness temperature T_b (in Kelvin). Specific intensities can be directly converted into brightness temperatures, and conversely. The Planck's law describes the spectral density of electromagnetic radiation (in erg $\mathrm{s^{-1}}$ $\mathrm{cm^{-2}}$ $\mathrm{Hz^{-1}}$ $\mathrm{sr^{-1}}$):

$$B_\nu(T) = \frac{2h\nu^3}{c^2} \frac{1}{\exp\left(\frac{h\nu}{k_\mathrm{B}T}\right) - 1} \tag{3.1}$$

where k_B is the Boltzmann constant, h is the Planck constant, ν the frequency of the signal and c the speed of light. Eq. 3.1 can be further simplified under the condition $h\nu \ll k_\mathrm{B}T$, although the following expression of the brightness temperature is frequently used whether or not this condition is satisfied. If we consider the ^{12}CO J=1–0 pure rotational line for example, we have a frequency $\nu = 115.27$ GHz. Assuming a typical kinetic temperature of 30 K, we have $h\nu/k_\mathrm{B}T = 0.18$. A Taylor expansion of Planck's law (using $\lim_{u\to 0} \mathrm{e}^u = 1 + u$) yields the Rayleigh-Jeans approximation:

$$B_{RJ}(\nu, T) = \frac{2\nu^2}{c^2} k_\mathrm{B}T \tag{3.2}$$

With this relation a given intensity I_ν (Jy) can be related to a brightness temperature T_b (K). The brightness temperature corresponds to the temperature of a blackbody that would emit a specific intensity $I_\nu = B_\nu(T_\mathrm{b})$:

$$T_\mathrm{b}\ [\mathrm{K}] = \frac{\lambda^2}{2k_\mathrm{B}} I_\nu\ [\mathrm{erg\ s^{-1}\ cm^{-2}\ Hz^{-1}\ sr^{-1}}] \tag{3.3}$$

Therefore, we denote an additional quantity, the effective radiation temperature $J_\nu(T_\mathrm{b})$, given by the following relation:

$$J_\nu(T_\mathrm{b}) = \frac{c^2}{2k_\mathrm{B}\nu^2} B_\nu(T_\mathrm{b}) \tag{3.4}$$

The effective radiation temperature is equal to the brightness temperature ($J_\nu(T_\mathrm{b}) = T_\mathrm{b}$) only when the Rayleigh-Jeans approximation is satisfied.

In addition, it is possible to convert the integrated quantity $\int T_\mathrm{b} dv$ (velocity-integrated temperature brightness) to $\int I_\nu \mathrm{d}\nu$ (frequency-integrated specific intensity) by considering the following identity (Doppler effect):

$$\frac{dv}{c} = -\frac{\mathrm{d}\nu}{\nu} \tag{3.5}$$

Hence, following Eq. 3.3 and Eq. 3.5 we have:

$$\int T_\mathrm{b} dv = \frac{\lambda^3}{2k_\mathrm{B}} \int I_\nu \mathrm{d}\nu \tag{3.6}$$

Need for signal amplification Radio frequency (RF) signals are weak. For example, consider a typical ^{12}CO J=1–0 line with a peak brightness temperature $T_\mathrm{b} = 30$ K. Following Eq. 3.6, the specific intensity measured in a velocity channel $\Delta v = 1$ km s^{-1} is $10^3 \times (2k_\mathrm{B}/\lambda^3)T_\mathrm{b}$ (W m^{-2} sr^{-1}). Assuming $\lambda = 2.6$ mm and $T_\mathrm{b} = 30$ K, we obtain 4.7×10^{-11} W m^{-2} sr^{-1}, *i.e.* 5.1×10^{-15} W m^{-2} in the 22.5″ beam of the IRAM 30m telescope (see section 3.2.2). As a consequence, the weakness of typical RF electromagnetic radiation amplitudes requires to amplify the signal to a level suitable for processing by spectrometers. In section 3.2.1.2, we will present the principles of heterodyne detection and amplification of the RF signal.

3.2.1 Introduction to single dish observations

Methods of detection in radio astronomy are radically different from the methods used in optical and infrared astronomy, in particular in regards to the receivers. Heterodyne receivers, bolometers and kinetic inductance detectors are based on distinct principles from the quantum well infrared photodetectors mentioned in section 3.1 (which are also used in optical cameras). Before we characterize heterodyne receivers in section 3.2.1.2, we will begin with a preliminary description of antenna theory in the upcoming section (3.2.1.1), in order to introduce the concept of antenna temperature, its relation to the RF electromagnetic signal and to the voltage measured in the receivers. We redirect the interested reader to Wilson *et al.* (2009) and Blundell and Tong (1992) for more details.

3.2.1.1 Fundamentals of antenna theory

Johnson-Nyquist thermal noise and antenna temperature Based on the Johnson-Nyquist theorem, the definition of *antenna temperature*, T_a, relates the output of the antenna to the electrical power P_ν of a matched resistor:

$$P_\nu = k_\mathrm{B} T_\mathrm{a} \tag{3.7}$$

where k_B is the Boltzmann constant. This equation (satisfied in thermal equilibrium) expresses that the thermal motion of the electrons in the resistor will produce a current that is determined by the physical temperature. In classical radio receivers, the RF electromagnetic radiation is converted into a voltage signal by a cooled Schottky diode mixer receiver (see section 3.2.1.2).

System temperature and receiver calibrations The temperature corresponding to the voltage measured by real receivers is not directly equal to the antenna temperature. The *system temperature* of a radio telescope is defined by:

$$T_\mathrm{sys} = \sum T_i \tag{3.8}$$

where T_i includes the contributions from source, atmosphere, ground and receiver. As a matter of fact, in the most general case Eq. 3.7 should be rewritten as $P_\nu = k_\mathrm{B}(T_\mathrm{a} + T_\mathrm{r})$ where T_r corresponds to the receiver temperature. To separate these two terms, a receiver can be switched periodically between the sky input (T_a) and a resistive load at a known thermodynamic temperature T_ref. An absorber immersed in a liquid bath of cold nitrogen or helium can provide an ideal reference (T_ref needs to be close to T_a in order to minimize the noise induced by the calibration

procedure). Following Eq. 3.8, the power per unit bandwidth entering the receiver of a radio telescope can be characterized by the sum of the receiver temperature $T_{\rm r}$ and antenna temperature $T_{\rm a}$. However, the antenna temperature is not exactly equal to the brightness temperature of the sky source $T_{\rm b}$. In the following paragraphs, we describe the relations between the antenna temperature and the source brightness temperature.

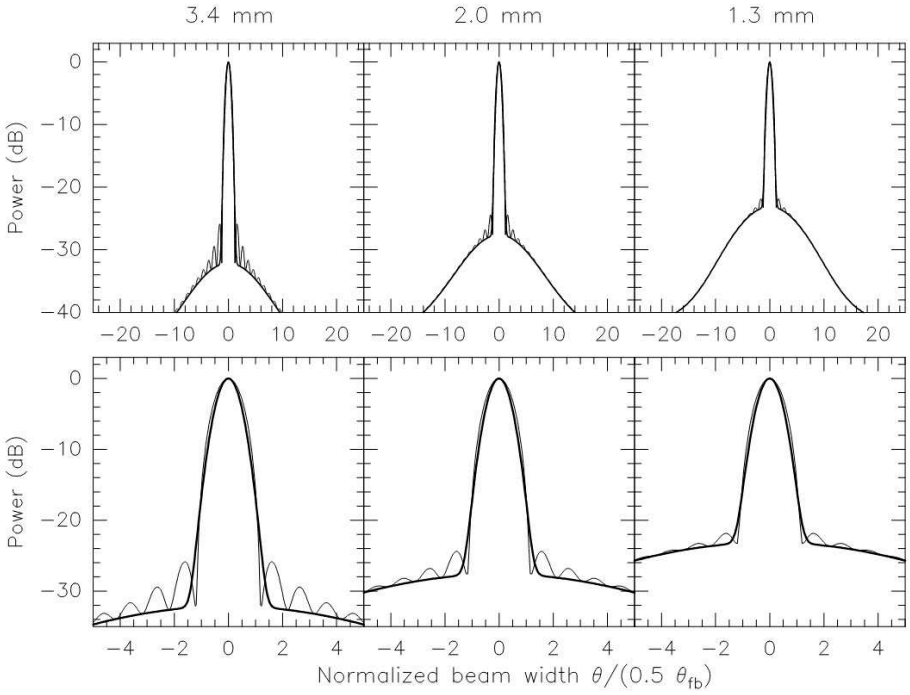

Figure 3.6 IRAM 30m telescope beam pattern, including the side lobes (Greve *et al.*, 1998). The heavy lines show the case of a Gaussian approximation of the main beam. The accuracy of the profiles is ±1 dB beyond the main beam area. The beam patterns are shown on logarithmic scale (dB). For each wavelength the profile is normalized to 1/2 width of the full beam.

Power pattern, 'main beam' The power pattern of a filled aperture antenna corresponds to the sensitivity of the antenna to directions in space (see *e.g.* Fig. 3.6). The normalized power pattern is defined by:

$$P_n(\theta,\varphi) = \frac{1}{P_{\rm max}} P(\theta,\varphi) \tag{3.9}$$

where $P_{\rm max} = \max(P(\theta,\varphi))$. Practically, the power pattern can be measured thanks to the reciprocity theorem. The reciprocity theorem indicates that the capacity to receive electromagnetic radiation is equivalent to the capacity to emit radiation, hence it is possible to determine the power pattern by using the antenna as an emitter. The beam solid angle of an antenna is given by:

$$\Omega_{\rm a} = \int_0^{2\pi}\int_0^{\pi} P_n(\theta,\varphi)\sin(\theta)d\theta d\varphi \tag{3.10}$$

The antenna temperature measured *via* Eq. 3.7 is the convolution of the brightness temperature $T_{\rm b}(\theta,\varphi)$ with the beam pattern $P_n(\theta,\varphi)$ of the telescope:

$$T_{\rm a}(\theta_0,\varphi_0) = \frac{\int T_{\rm b}(\theta,\varphi)P_n(\theta-\theta_0,\varphi-\varphi_0)\sin(\theta)d\theta d\varphi}{\int P_n(\theta,\varphi)d\Omega} \tag{3.11}$$

Hereafter, we introduce a distinction between the *main beam temperature* $T_{\rm mb}$ and the *antenna temperature* $T_{\rm a}$. The main beam temperature measures what is emitted by the source (*i.e.* it is more intrinsic than the antenna temperature, which is sensitive to several directions including the error beams, or 'side lobes', see Fig. 3.6). The main beam solid angle is given by:

$$\Omega_{\rm mb} = \iint_{\rm mb} P_n(\theta,\varphi)d\Omega \tag{3.12}$$

where the 'mb' in place of the interval of integration means that the power pattern is integrated over the main beam. The beam efficiency corresponds to the relative proportion of the antenna and main beam solid angles (respectively given by Eq. 3.10 and Eq. 3.12):

$$\eta_{\rm mb} = \frac{\Omega_{\rm mb}}{\Omega_{\rm a}} \tag{3.13}$$

The main beam efficiency allows to correct the antenna temperature for the power pattern, *i.e.* to convert from the antenna temperature $T_{\rm a}$ to the main beam temperature $T_{\rm mb} = \eta_{\rm mb}T_{\rm a}$, $\eta_{\rm mb} \leq 1$. For example, at 230 GHz the main beam efficiency of the APEX telescope varied between $\eta_{\rm mb} = 0.6$ and $\eta_{\rm mb} = 0.71$ in 2021[3]. Additionally, for a ground based radio telescope, the expression $T_{\rm a}$ in Eq. 3.11 actually corresponds to $T'_{\rm a}$, *i.e.* an antenna temperature corrected for aperture efficiency *and* atmospheric losses. In the next paragraph, we describe the calibrations that allow to perform this correction.

Chopper wheel calibration At millimeter wavelengths, the Earth's atmosphere is only partially transparent, and the transmission varies on relatively short time scales (∼10 min) as the weather modifies the water contents of the atmosphere above the telescope. The antenna temperature $T_{\rm a}$ is related to the true temperature brightness of the source $T_{\rm b}$ by the following relation:

$$T_{\rm a}(s) = T_{\rm b}(0)\mathrm{e}^{-\tau_\nu(0)} + T_{\rm atm}(1-\mathrm{e}^{-\tau_\nu(0)}) \tag{3.14}$$

where s is the geometric path length along the line of sight ($s = 0$ at the upper edge of the atmosphere), $T_{\rm atm}$ is the emission of the atmosphere and $\tau_\nu(0)$ is the total opacity of the atmosphere at a frequency ν. The total opacity is defined by:

$$\tau_\nu(s) = \int \kappa_\nu(s)ds \tag{3.15}$$

where κ_ν is the volume absorption coefficient. Frequent calibrations of the atmospheric absorption must be performed to take into account the time variations of $\tau_\nu(0)$ during the observations. The chopper wheel method (Kutner and Ulich 1981, Downes 1989) is the standard calibration procedure in spectral line millimeter astronomy. The procedure consists in the two following (consecutive) measurements: *i.)* the measurement of the receiver output when an ambient temperature 'chopper' load is placed before the feed horn ($T_{\rm amb}$), *ii.)* the measurement of the receiver

[3] https://www.apex-telescope.org/telescope/efficiency/

output when the feed horn is directed toward cold sky background ($T_{\rm sky}$). The first measurement yields:

$$V_{\rm amb} = G(T_{\rm amb} + T_{\rm r}) \tag{3.16}$$

where G is the antenna gain and $T_{\rm r}$ is the receiver temperature. Then, the second measurement (towards the sky background) yields:

$$V_{\rm sky} = G(\eta_{\rm forward} T_{\rm sky} + (1 - \eta_{\rm forward}) T_{\rm ground} + T_{\rm r}) \tag{3.17}$$

where $\eta_{\rm forward}$ is the forward efficiency (corresponding to the fraction of power in the forward beam of the feed) and $T_{\rm ground}$ is the ground temperature brightness. Hence, the calibration is given by the voltage difference $\Delta V_{\rm cal} = V_{\rm amb} - V_{\rm sky} = G\eta_{\rm forward} T_{\rm amb} {\rm e}^{-\tau_\nu}$ (see Eq. 3.14) where τ_ν is the atmospheric absorption at a frequency ν. The same procedure applied to the signal received from the radio source (instead of the sky) yields $\Delta V_{\rm source} = GT'_{\rm a}{\rm e}^{-\tau_\nu}$, where $T'_{\rm a}$ is the antenna temperature of the source outside the atmosphere (referred to as the *corrected antenna temperature*). Thus, the antenna temperature $T'_{\rm a}$ is determined by:

$$T'_{\rm a} = \frac{\Delta V_{\rm source}}{\Delta V_{\rm cal}} \eta_{\rm forward} T_{\rm amb} \tag{3.18}$$

Defining the *forward beam temperature* $T^*_{\rm a} = T'_{\rm a}/\eta_{\rm forward}$ and $\eta = \eta_{\rm mb}/\eta_{\rm forward}$, then we have $T_{\rm mb} = \eta T^*_{\rm a}$. Hence, η allows to correct the antenna temperature measurement $T^*_{\rm a}$ for the beam pattern efficiency *and* forward efficiency of the telescope. The efficiency η can be measured on calibrators of different sizes (*e.g.* Uranus, Jupiter, Mars) at the start of any observing session. Examples of efficiencies are given in Tab. 6.1 and Tab. 6.2.

3.2.1.2 Heterodyne detection

The purpose of the frontend receivers is to collect the signal at the focal point of the antenna and to amplify it to a level suitable for further processing by the backends (*e.g.* spectrometers, continuum detectors). The transition between the astronomical signal propagating in free space and the signal transmitted to the receivers occurs at a *feedhorn* coupled with a waveguide. Corrugated feedhorns are commonly used in millimeter parabolic antennas. These cylindrical horns are built with periodic ring structures (characteristic size $\sim \lambda/4$, Love 1976). The signal is then transported by a waveguide to the heterodyne receivers. Classical radio receivers are Schottky junctions, but superconducting tunnel junctions, *i.e.* 'SIS' junctions are more common nowadays. SIS junctions are made of two layers of superconducting metal separated by an insulator. SIS junctions allow photon-assisted tunneling, hence they can function as total power detectors operating at radio frequencies (the current generated per power absorbed can be estimated to be of the order of one electron per photon, *e.g.* Schuster *et al.* 2000).

Frontends: heterodyne receivers Heterodyne detection consists in shifting the output signal frequency using a non-linear device. This process is called mixing or downconversion. The modification of the frequency allows to choose a lower 'working frequency' at which the signal is more easily amplified and further processed, and it also permits to avoid feedback of amplified signals from the backends (autocorrelators) to the frontends (amplifiers, mixers, working at sky

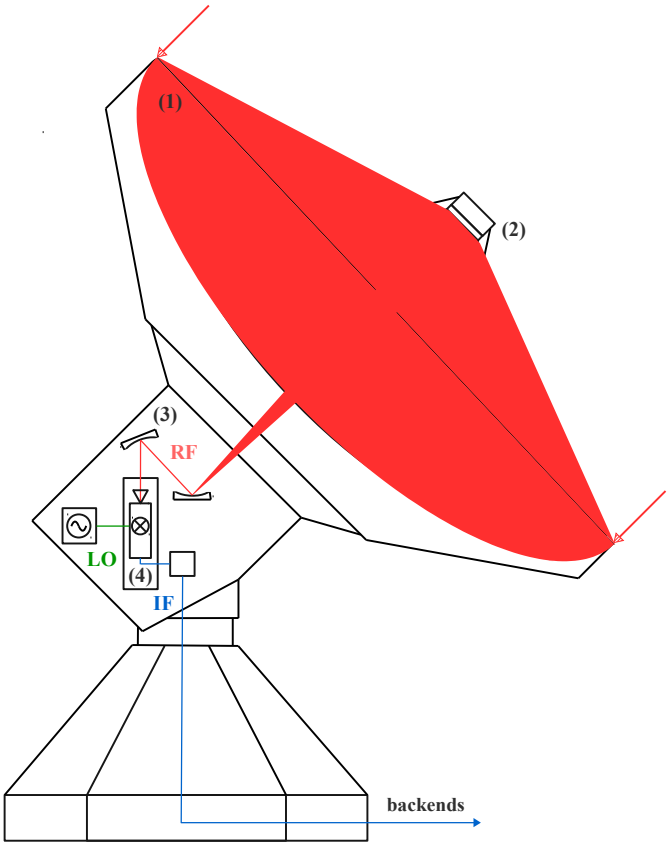

Figure 3.7 Schematic representation of a radio telescope based on the IRAM 30m configuration (see also Fig. 3.12). The path of the radio frequency (RF) electromagnetic wave is represented in light pink: plane waves are collected by the primary reflector (1) and bounce back on the secondary reflector (2) where they are re-directed into the frontend receivers cabin. In the cabin, dichroic mirrors (3) carry the focalized beam into the heterodyne receiver (4) where the RF electromagnetic signal is mixed with the local oscillator (LO) signal to produce an intermediate frequency (IF) voltage ouput that can be further processed by the backends ($\nu_{\rm IF} \ll \nu_{\rm RF}$). Fig. 3.8 (directly below) shows a more detailed description of the processing steps applied to the input RF signal by the heterodyne receivers.

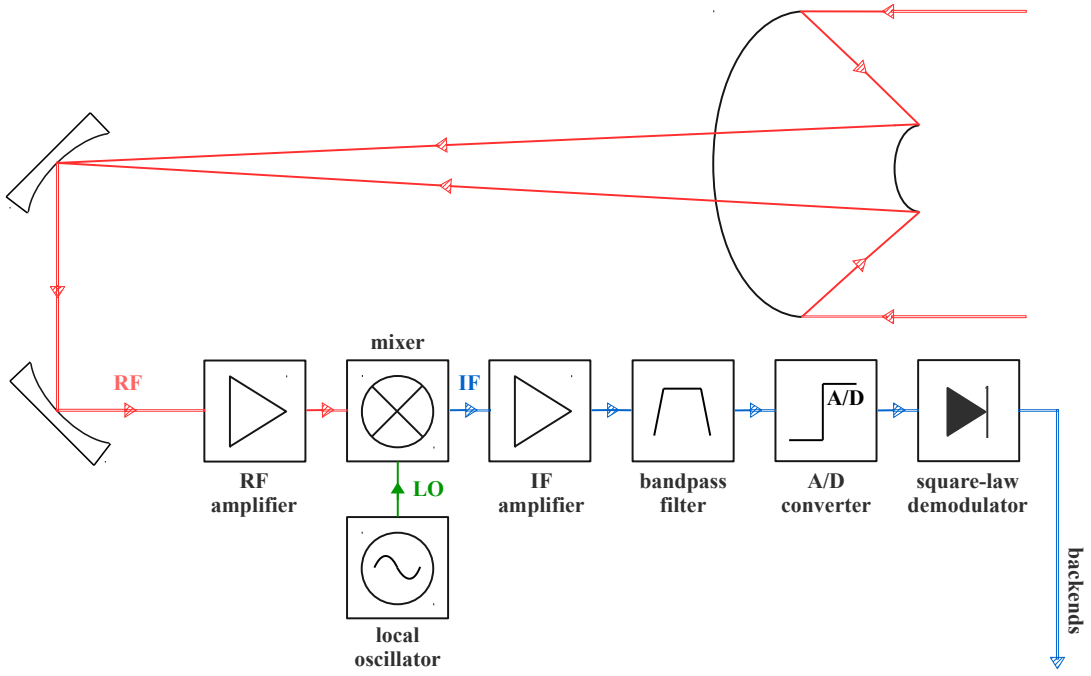

Figure 3.8 Schematic representation of an heterodyne receiver (see text). 'RF', 'LO' and 'IF' stand respectively for the radio frequency, local oscillator and intermediate frequency signals.

frequency). The frequency-shift is performed by mixing the signal with a monochromatic signal produced by a local oscillator (hereafter 'LO'). Applying both a sky frequency signal (ν_S) and the local oscillator signal (ν_{LO}) to a mixer (*e.g.* a Schottky junction) yields the following sum of voltages:

$$\begin{aligned}
&\alpha[E\sin(2\pi\nu_S t + \delta_S) + V\sin(2\pi\nu_{LO} t + \delta_{LO})]^2 \\
&= \frac{1}{2}\alpha(E^2 + V^2) && \text{(DC component)} \\
&- \frac{1}{2}\alpha E^2 \sin(4\pi\nu_S t + 2\delta_S + \pi/2) && (2^{\text{nd}} \text{ harmonic of signal}) \\
&- \frac{1}{2}\alpha V^2 \sin(4\pi\nu_{LO} t + 2\delta_{LO} + \pi/2) && (2^{\text{nd}} \text{ harmonic of LO}) \\
&+ \alpha EV\sin[2\pi(\nu_S - \nu_{LO})t + (\delta_S - \delta_{LO} + \pi/2)] && \text{(difference frequency)} \\
&- \alpha EV\sin[2\pi(\nu_S + \nu_{LO})t + (\delta_S + \delta_{LO} + \pi/2)] && \text{(sum frequency)}
\end{aligned} \tag{3.19}$$

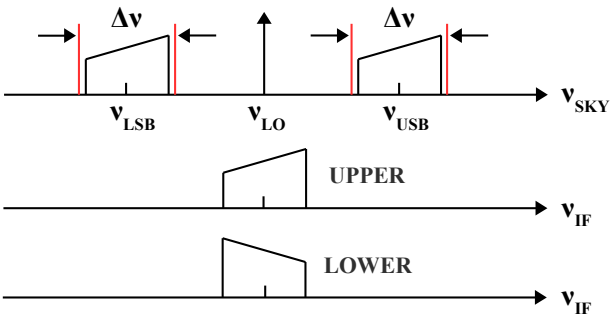

Figure 3.9 Sketch of the frequencies shifted from the sky frequency (*top*) to the output (*lower*) of a double sideband mixer ($\nu_{IF} = \nu_S - \nu_{LO}$ is the intermediate frequency). The slanted boxes represent the lower side (LSB) and upper side (USB) passbands, the direction of the slant in the boxes indicate the upper and lower edges of bandpass in frequency. Figure reproduced from Wilson *et al.* (2009).

where α is a constant that depends on the mixer, E and V are respectively the amplitudes of the output and local oscillator signals and δ_S, δ_{LO} are their phases. Using an appropriate bandpass filter, all the undesired components of this equation can be removed, and the final product of the (mixer + bandpass filter) device is an output at the intermediate frequency (IF) $\nu_{IF} = \nu_S - \nu_{LO}$. Hence, the output of the mixer contains two signals corresponding to two distinct frequency bands above and below the local oscillator frequency, separated by the intermediate frequency (see Fig. 3.9). These two sidebands correspond to the radio frequencies (RF) $\nu_{USB} = \nu_{LO} + \nu_{IF}$ (upper side band, 'USB') and $\nu_{LSB} = \nu_{LO} - \nu_{IF}$ (lower side band, 'LSB'). Thus, in standard double sideband mixers, two distinct RF signals occupy the same IF frequency domain. The scientific target is referred to as the 'signal frequency' while the other one is called the 'image frequency'. In single sideband mixers, the response from the image band is suppressed. Sideband separating mixers are the most convenient: they allow to separate the mixing products from the USB and LSB into two distinct IF channels. See sections 3.2.2 (IRAM 30m) and 3.2.3 (APEX) for examples of LSB/USB channel sizes and resolutions.

Backends: autocorrelators and Fourier spectrometers Until now, we have described radio receivers as electronic devices that are sensitive to the specific intensity of a radio source *via* the measurement of the voltage at a Schottky junction fed by the RF signal (the voltage signal is related to the brightness temperature T_b of the astronomical object, following the Johnson-Nyquist theorem, Eq. 3.7). In the frontends, a feedhorn collects the signal and transmits it to a mixer where

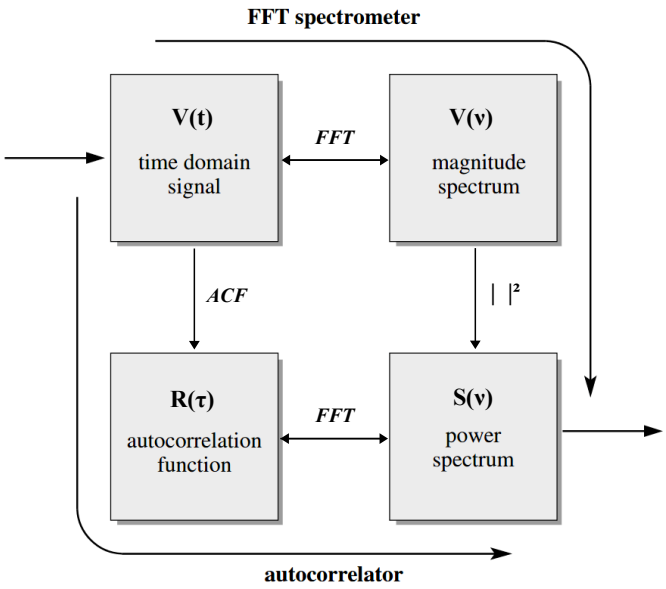

Figure 3.10 Sketch of the relation between the voltage input as a function of time, $V(t)$, and frequency, $V(\nu)$, with the autocorrelation function, $R(\tau)$ and corresponding power spectral density, $S(\nu)$ (Wiener-Khinchin theorem). The two-headed arrows represent reversible processes. The two distinct paths corresponding to FFT spectrometers and autocorrelators are indicated by arrows. 'FFT' stands for Fast Fourier Transform. Figure reproduced from Klein *et al.* (2006).

the frequency of the voltage signal is shifted into two sidebands using a local oscillator. Thereafter, the signal undergoes a series of modifications (see Fig. 3.8): *i.)* it is amplified by a low-noise high electronic mobility transistor (HEMT); *ii.)* then it passes through a bandpass filter that defines the spectral range of the receiver; *iii.)* a square-law detector produces a signal proportional to the average power in the reception band and *iv.)* an averager determines the time response of the output. Thus, the final products of the frontend receivers are two voltage signals $V_{\rm USB}(t)$ and $V_{\rm LSB}(t)$.

In the context of spectral line observations we aim to measure the spectrum of an astronomical object, *i.e.* the power spectral density of the RF signal. Backend spectrometers are devices that transform the IF voltage measurement in time $V(t)$ into a measurement of the power spectral density $S(\nu)$. The Wiener-Khinchin theorem states that the voltage measurement in time $V(t)$, the voltage in frequency $V(\nu)$, the power spectral density $S(\nu)$ and the autocorrelation function in time delay $R(\tau)$ are Fourier transform pairs (see Fig. 3.10):

$$S(\nu) = |\mathrm{FT}[V(t)]|^2, \; S(\nu) = \mathrm{FT}[R(\tau)] \tag{3.20}$$

where 'FT' refers to the Fourier transform. The Wiener-Khinchin theorem indicates two paths to determine the power spectral density from a measurement of $V(t)$, hence there are two different types of spectrometers. One method is to apply a Fast Fourier transform (FFT) algorithm to the input voltage and then square the signal (*e.g.* Klein *et al.* 2006). This type of backend device is referred to as 'Fourier spectrometers'. An other method is to determine the autocorrelation function of the input signal, and then apply a FFT algorithm (Weinreb *et al.*, 1963). The autocorrelation function is measured by a multiplication of the input voltage $V(t)$ with a sample delayed by τ: $V(t + \tau)$, an operation that can be performed both by analog and digital devices. These spectrometers are referred to as 'autocorrelators' or 'autocorrelation spectrometers'. Autocorrelators require less computational power, because it is possible to accumulate the autocorrelation function before the Fourier transform produces the final power spectrum. However, Fourier spectrometers offer more bandwidth. Both the IRAM 30m and APEX telescopes use Fourier spectrometers (see sections 3.2.2, 3.2.3).

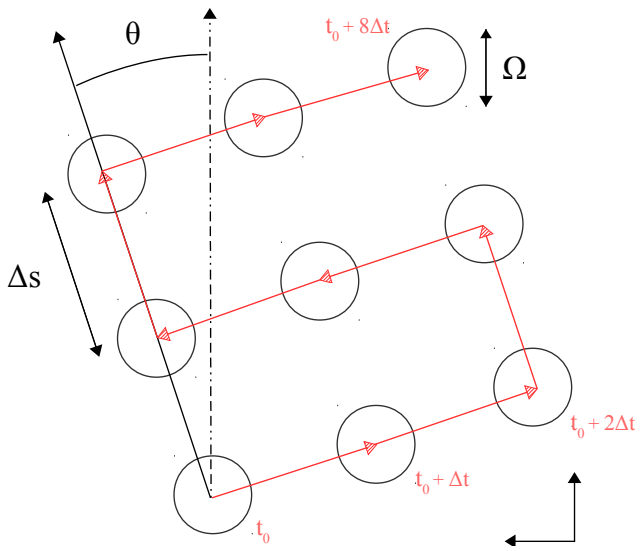

Figure 3.11 Schematic representation of the On-The-Fly mapping technique (in this example, the map is undersampled). The red arrows indicate the path of the telescope beam on the sky. At each step, the location of the beam is shown by a black circle of diameter Ω (FWHM). Δs is the step between each successive sample. The time at which each position is reached by the telescope is indicated in red, next to the black circles. The antenna scans the sky at a velocity $\Delta s/\Delta t$. 'θ' is an arbitrary position angle defined with respect to the North axis (the reference axis can vary depending on the telescope).

3.2.1.3 On-The-Fly mapping (spectral observations)

In the previous sections, we have described the instrumental processes by which the signal collected by the antenna can be processed into a spectrum of the source $S(\nu)$ in the frequency channel offered by the receiver (which will usually contain one or several spectral lines of interest). The most basic application of a radio telescope is to point the antenna at an astronomical object and tune the local oscillator at a chosen frequency corresponding to a line of interest (*e.g.* ^{12}CO J=1–0, at 115 GHz). After an integration time t on the sky, a spectrum corresponding to a single line of sight is obtained. These measurements are referred to as 'pointed observations'. In chapter 6, we will present spectral-line *maps* of ^{12}CO, ^{13}CO and C^{18}O. These maps are obtained by performing an adequate amount of pointed observations within the field of observations, either by using the 'raster' or 'On-The-Fly' mapping technique. The raster mapping technique is the most basic procedure: it consists in manually sampling the map with an arbitrary sequence of pointed observations.

The On-The-Fly (OTF) mapping is an observing technique in which the telescope antenna scans the field of observation at a constant speed while data and antenna position informations are recorded continuously (*e.g.* Ungerechts *et al.* 2000, Mangum *et al.* 2007). In comparison to the raster mapping technique ('step-and-integrate' observation of discrete positions), OTF mapping allows to minimize telescope overheads, hence it is more time efficient (*i.e.* more sensitive in the same timespan).

Sampling The On-The-Fly mapping technique is illustrated in Fig. 3.11. The telescope antenna scans the sky at a constant velocity $\Delta s/\Delta t$, where Δt (s) is the integration time and Δs ($''$) the angular distance between two measurements ($1/\Delta t$ is the amount of samples per second). The Shannon-Nyquist sampling criterion indicates that the condition $\Delta s \leq \Omega/2$ should be verified, where Ω is the full width at half maximum of the instrumental beam. Otherwise, the map is undersampled. If $\Delta s \leq \Omega/2$, then the positions of the beams in Fig. 3.11 are overlapping, and the map is 'fully sampled' (as it stands, the schematic shown in Fig. 3.11 shows an undersampled map):

the spatial frequencies which can be sampled by the telescope resolution are entirely recovered in the final data products.

3.2.1.4 Observing routine

In this section, we describe the procedures followed in millimeter/sub-millimeter radio astronomy for the observation and mapping of spectral lines. We base our description on the techniques used at the IRAM 30m telescope (see next section, 3.2.2). The first step is connect the receivers to the antenna feed and tune the local oscillator at a chosen frequency to select a sky frequency that contains the spectral lines of interest. Thereafter, the pointing and focus of the telescope must be calibrated.

Pointing, focus The pointing of the telescope is calibrated on a bright, unresolved source (such as a quasar) that is spatially close to the astronomical source of interest. The pointing correction depends on the sky longitude and latitude (since the mechanical stress strongly depends on the orientation of the antenna), hence it is important to minimize the distance between the pointing calibrator and the source. The calibration is performed by scanning the area around the coordinates of the source in On-The-Fly mode, using continuum receivers to maximize the signal-to-noise ratio. The gaussian pattern of the resulting map allows to determine the required corrections in azimuth and altitude. Once the pointing corrections are registered, the antenna focus is calibrated by measuring the continuum flux of a bright source (*e.g.* a planet) with respect to the distance between the primary and secondary reflectors. Pointing and focus corrections must respectively be updated approximately every two hours and four hours. Additionally, the focus and pointing calibrations must be reinitialized after sunrise and sunset to correct the impact of temperature variations on the mechanical structure.

Calibrations, off-position references Every $\sim$ 15 minutes, chopper wheel receiver calibrations are performed on the hot and cold loads to measure the receiver gain fluctuations ($T_{\rm r} \sim 50$ K at 3mm). In between calibrations, On-The-Fly mapping subscans are only interrupted by regular off-position reference observations. It is recommended to perform off-position reference measurements approximately every two minutes in order to sample the time variations of the atmospheric absorption and sky emission ($T_{\rm sky} \sim 30$ K at 3mm).

3.2.2 The IRAM 30m telescope

The IRAM 30m telescope (also referred to as the 'MRT': Millimeter Radio Telescope) is a millimeter/sub-millimeter-observing ground-based facility (see Fig. 3.1) that was commissioned in 1984 by the IRAM (Institut de Radio Astronomie Millimétrique). In this section, we provide a general description of the telescope (based on Baars *et al.* 1987), followed by a description of the frontend receivers (Carter *et al.*, 2012) and backends (Klein *et al.*, 2012b) used in this work.

Telescope and receiver cabin configuration The IRAM 30m telescope is located on the Pico Veleta in the Spanish Sierra Nevada, at an altitude $h = 2870$ m. The average precipitable water

vapor[4] (pwv) is ∼ 4 mm in summer, and ∼ 2 mm in winter. The telescope has a 30 m diameter paraboloidal main reflector (420 concentric aluminum panels with a surface accuracy ∼ 26 µm rms) placed on an azimuth mounting (see Fig. 3.12). The telescope is diffraction limited, hence it has a beam width $\sim 25.2'' \times (100/f[\mathrm{GHz}])$. The beam pattern is shown on Fig. 3.6.

The telescope operates in a Nasmyth configuration: after reflection on the secondary reflector, the beam is redirected to a room that contains the receiver systems in between the elevation bearings. In the receiver cabin, a system of flat mirrors, polarization splitter and dichroic mirror creates several focus location, allowing to use up to three receivers simultaneously. Calibrations of the antenna temperature scale are performed using two 'hot' an 'cold' loads that can be inserted in the beampath between the second Nasmyth mirror and the polarization splitter: a radio-frequency absorbing material at room temperature (293 K) and liquid nitrogen (77 K). The ambient load is built as a rotating 'chopper wheel' that allows to quickly switch between sky and load.

Local oscillator The IRAM 30m telescope local oscillator (LO) signal is generated by a commercial Gunn oscillator (Carter *et al.*, 2012). A Gunn diode is a semiconductor device with negative dynamic resistance (dV/dI, where V is the voltage and I the current) over a range of frequencies. The Gunn local oscillator used at the IRAM 30m telescope provides a 60-120 GHz monochromatic signal that can be coupled with a varactor multiplier (variable capacitance diode offering a ×2, ×3 or ×4 frequency multiplying factor) and carried by a waveguide to the mixers for heterodyne frequency conversion (see next paragraph).

EMIR band	RF coverage (GHz)	mixer type	polarization	$\Delta\nu_{\mathrm{IF}}$ (GHz)	T_{r} (K)	G_{im} (dB)
E0	73-117	2SB	H/V	8	50	> 10
E1	125-184	2SB	H/V	8	50	> 10
E2	202-274	2SB	H/V	8	80	> 10
E3	277-350	2SB	H/V	8	80	> 10

Table 3.4 EMIR parameters of the bands E0, E1, E2 and E3. Radio frequency (RF) coverages are given for the centers of the outer, respectively inner, 4 GHz intermediate frequency (IF) bands. '2SB' accounts for dual sideband mixers, H/V refers to horizontal and vertical polarizations, T_{r} is the receiver temperature in single sideband observations and G_{im} is the image band rejection.

***Frontends:* The Eight MIxer Receiver (EMIR)** The Eight MIxer Receiver (EMIR) is the multiband, dual polarization heterodyne receiver of the IRAM 30m telescope operating between 75 GHz and 350 GHz (commissioned in 2009). EMIR offers the possibility to observe four $\Delta\nu_{\mathrm{IF}} = 8$ GHz frequency bands with distinct radio frequency coverages shown in Tab. 3.4. EMIR uses dual sideband mixers, hence it is able to separate the lower and upper sidebands into two distinct intermediate frequency (IF) outputs. This is done by exploiting the fact that the lower and upper sidebands have distinct phase shifts (see Eq. 3.19). Horizontal and vertical polarizations are also separated using a gold plated tungsten wire grid with a pitch of 100 µm. Using dichroic mirrors, EMIR allows to observe up to two frequency bands simultaneously with minimal power

[4]The total amount of precipitable water (usually measured in mm) above an altitude h_0 is an integral of the density of water along the line of sight.

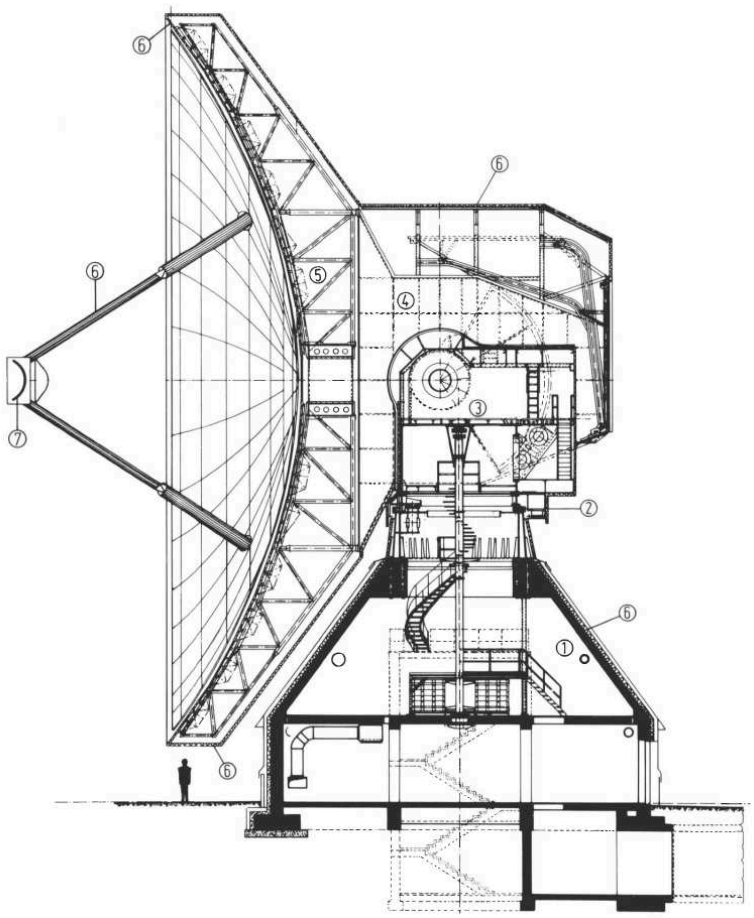

Figure 3.12 Cross section of the IRAM 30m telescope. A concrete pedestal (1) carries a 5 meter diameter azimuth bearing (2). A two-storey cabin (3) contains all drive systems on the lower floor and the radio astronomy receivers in the upper part between the elevation bearings. The yoke and conesection (4) is supported at the elevation bearings and carries the reflector structure (5). Thermal insulation (6) covers the outside of the telescope and is also present between reflector surface and its support structure. The quadrupod and prime focus cabin are also insulated. The reference antenna for radio-holography is mounted in the prime-focus cabin (7). Figure reproduced from Baars *et al.* (1987).

loss (< 3%, Carter *et al.* 2012). The possible band combinations are E0+E1, E0+E2 and E1+E3 (see Fig. 3.13).

EMIR performs heterodyne down-conversion of the radio frequency (millimeter wave) signal to the intermediate frequency (microwave, $\sim 4 - 12$ GHz, Carter *et al.* 2012), and amplifies the IF signal after separation of the sidebands. All EMIR mixers are based on superconducting tunnel junctions (see section 3.2.1.2), or 'SIS' junctions (in this case, Niobium superconducting layers separated by a few nanometers of Aluminum oxide insulator). The EMIR mixers are fed with the LO+RF input by a waveguide probe and an RF choke only lets pass the IF output signal to the backends. EMIR mixers are cooled down to $T \sim 4.2$ K (boiling temperature of He) in order to reach the optimum performance temperature of the SIS junctions. The output signal of the mixer (in the intermediate frequency IF) is then amplified to a level suitable for further processing by a cryogenic low noise amplifier that provides a gain ~ 35 dB, with a noise temperature ~ 4 K.

***Backends:* The Fast Fourier Transform Spectrometer (FFTS)** After heterodyne downconversion and amplification, the output signal of the EMIR frontends is transmitted from the receivers cabin to the backends room inside the IRAM 30m main building (see Fig. 3.7). There are several backends for EMIR, such as the Wideband Line Multiple Autocorrelator (WILMA), the high spectral resolution Versatile SPectrometer Array (VESPA), and the Broad Band Continuum backends (BBC) that fully exploit the 8 GHz bandwidths of EMIR. We focus on the description of the Fast Fourier Transform Spectrometer (FFTS, commissioned in 2011, Klein *et al.* 2012b), on which our ^{12}CO, ^{13}CO and C^{18}O rotational line observations relied.

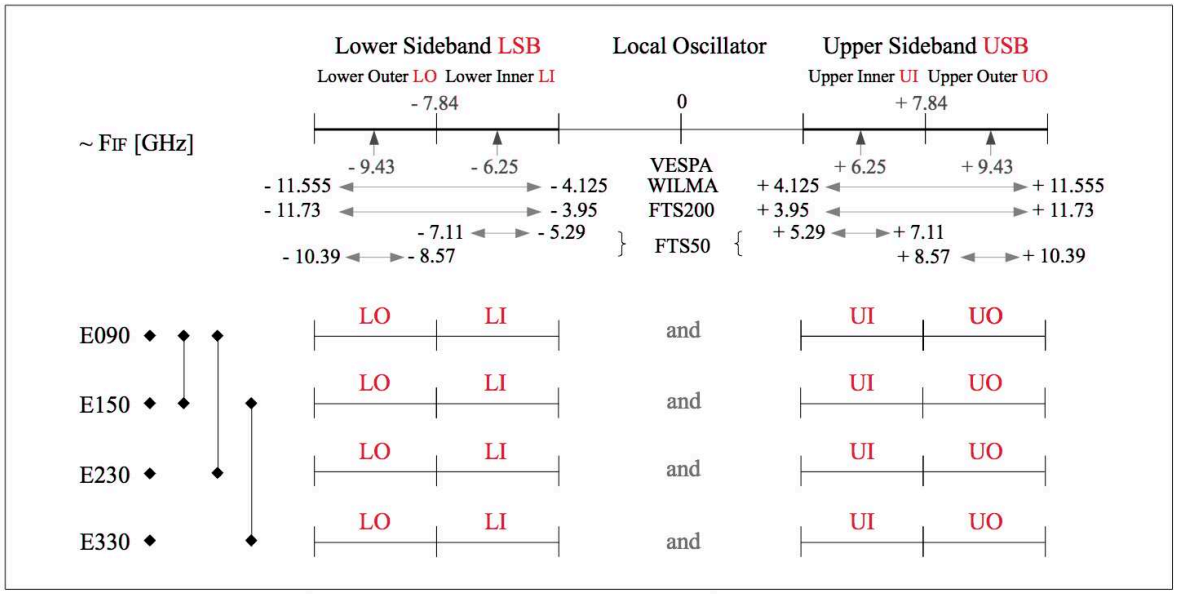

Figure 3.13 Overview of EMIR band combinations and frequencies which are available after the EMIR upgrade and commissioning in September/October 2013. Central frequencies of the (sub-)bands refer to VESPA, and the band edge frequencies are given for WILMA and the FTS backends in the two resolution presets (respectively $\Delta\nu$ = 50 kHz and $\Delta\nu$ = 200 kHz). Frequency edges are taken from the list provided by G.Paubert. Possible band combinations are indicated on the left. The 32 GHz IF transport system allows the selection of a total of 8 sub-bands of 4 GHz bandwidth, within limitations. Figure reproduced from the IRAM wiki webpages.

The full 32 GHz of EMIR bandwidth are covered by an array of 24 FFTS working at either 50 kHz or 200 kHz resolution (respectively corresponding to $\Delta v \sim 0.1$ km s^{-1} and $\Delta v \sim 0.5$ km s^{-1} at 115 GHz). An IF spectrum-slicer allows to observe either four parts of the IF bands with 200 kHz resolution and 8 GHz bandwidth each, or eight parts of the IF bands with 50 kHz resolution and $\sim$ 1.8 GHz bandwidth each.

***Continuum frontends*: The New IRAM Kids Array-2 (NIKA2)** Continuum observations rely on instrumental and processing techniques that are distinct from the heterodyne detection technique presented in section 3.2.1.2. The New IRAM Kids Array-2 (hereafter NIKA2, Calvo *et al.* 2016, Adam *et al.* 2018, see also Monfardini *et al.* 2011) is the millimeter continuum camera at the IRAM 30m telescope. NIKA2 has a 6.5′ × 6.5′ field of view and operates at 1.15 mm and 2.0 mm employing a total of around 2900 kinetic inductance detectors (hereafter KID). KIDs are superconducting pair breaking detectors with multiplexing capabilities, in which the kinetic inductance increases upon photon detection (Gao 2008, Baselmans 2012). KIDs represent an innovative alternative to bolometers in the millimeter range (*e.g.* LiteBIRD, Matsumura *et al.* 2014). In the NIKA2 instrument, the KIDs are cooled down to 150 mK by two pulse tubes and a dilution refrigerator in order to reach the optimal working temperature. The NIKA2 1.15 mm (260 GHz) and 2.0 mm (150 GHz) bandpasses are shown in Fig. 3.14.

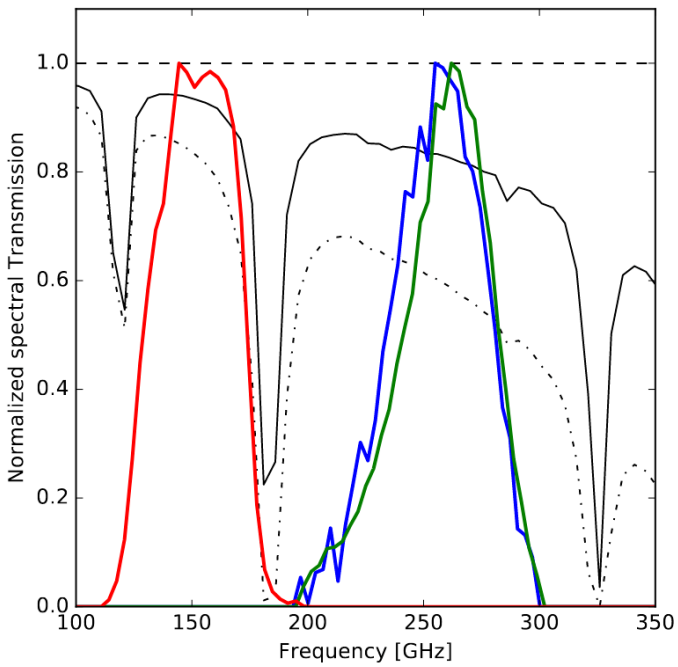

Figure 3.14 NIKA2 spectral characterization for the two 260 GHz arrays: horizontal polarization (blue) and vertical polarization (green) measured in the NIKA2 cryostat, and for the 150 GHz array (red) measured in a test cryostat equipped with exact copies of the NIKA2 band-defining filters. The band transmissions are not corrected for Rayleigh-Jeans spectrum of the input source. For comparison, black curves represent the atmospheric transmission (Pardo *et al.*, 2002) assuming 2 mm of precipitable water vapour (PWV), that is, very good conditions, and 6 mm PWV, that is, average conditions. Figure reproduced from Adam *et al.* (2018). See also Fig. 9.1.

3.2.3 The Atacama Pathfinder EXperiment (APEX)

The Atacama Pathfinder EXperiment (APEX) 12m telescope is located at an altitude of 5107m on Llano de Chajnantor in the Chilean High Andes (Güsten *et al.*, 2006). This location offers an exceptional transmission of the atmosphere (see Fig. 3.15), with a median column of precipitable water $\sim$ 1.2 mm (according to the ALMA site characterization data base, 1995-2004). During winter, the median drops by a factor 2-3 (pwv$\sim$ 0.3 – 0.6 mm). APEX was designed to be a prototype for the Atacama Large Millimeter Array (ALMA), a millimeter/submillimeter interferometer (Wootten and Thompson, 2009). APEX was commissioned in 2005 by a collaboration between the Max-Planck-Institut für Radioastronomie (MPIfR), the Onsala Space Observatory (OSO) and the European Southern Observatory (ESO).

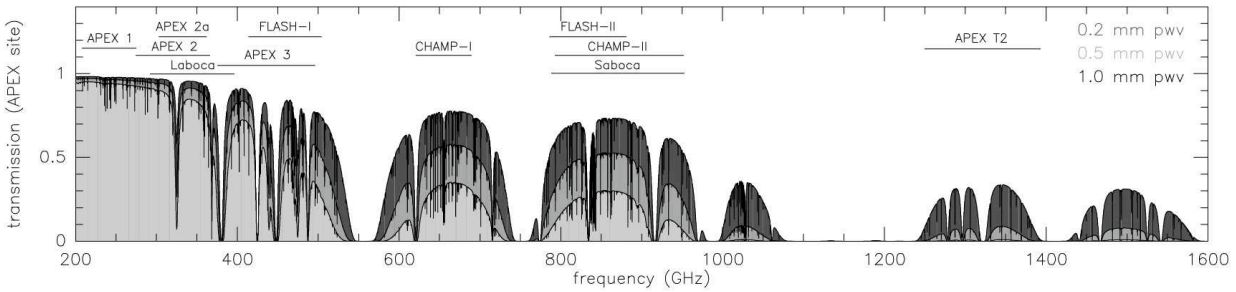

Figure 3.15 Zenith transmission of the atmosphere above Llano de Chajnantor at submillimeter wavelengths. The frequency coverage of the APEX facility and PI receivers are superimposed (corresponding to the situation in 2006). Figure reproduced from Güsten *et al.* (2006).

Telescope and receiver cabin configuration APEX has a 12m diameter paraboloidal reflector (264 aluminum panels with a surface accuracy $\sim$ 15 µm rms) mounted on an alt-azimuthal mount. The telescope is diffraction limited, hence it has a beam width $\sim$ $15.6'' \times (400/f[\mathrm{GHz}])$. The

telescope is a modified ALMA prototype with two Nasmyth cabins and one Cassegrain cabin where distinct heterodyne and continuum receivers are stored. A mirror system installed on a rotary support allows to select between the cabins.

Spectral line observations: **The Principal Investigator (PI)230 and the First Light APEX Submillimeter Heterodyne (FLASH) receivers** The APEX receiver cabins host several instruments that cover a broad range of frequencies. Our ^{12}CO, ^{13}CO and C^{18}O J=2–1, J=3–2 observations were performed with the PI230 (commissioned in 2015, Nasmyth-B cabin) and FLASH (commissioned in 2012, Nasmyth-A cabin) receivers. The PI230 receiver is a dual polarization, sideband separating 230 GHz heterodyne system built by the MPIfR. PI230 offers 32 GHz of bandwidth in the frequency range 195-270 GHz, with a spectral resolution of $\sim$ 60 kHz (corresponding to $\sim$ 0.08 km s^{-1} at 230 GHz).

FLASH (Heyminck *et al.* 2006, Klein *et al.* 2014) is a dual channel sideband separating SIS mixer (parallel observation at ν_1 = 345 GHz and ν_2 = 460 GHz) provided by the IRAM and NAOJ (National Astronomical Observatory of Japan). The mixers are fed with the signal of a solid-state local oscillator (ν_{LO} = 10.2 – 14.2 GHz, coupled with a ×27 multiplier at 345 GHz and a ×36 multiplier at 460 GHz). FLASH provides a 4-8 GHz bandwidth in the frequency ranges 268-374 GHz and 374-515 GHz, and it is coupled with FFT based spectrometers which sample 2.5 GHz of instantaneous bandwidth with a resolution $\sim$ 40 kHz at 345 GHz and $\sim$ 80 kHz at 460 GHz (respectively corresponding to $\sim$ 0.04 km s^{-1} and $\sim$ 0.05 km s^{-1}).

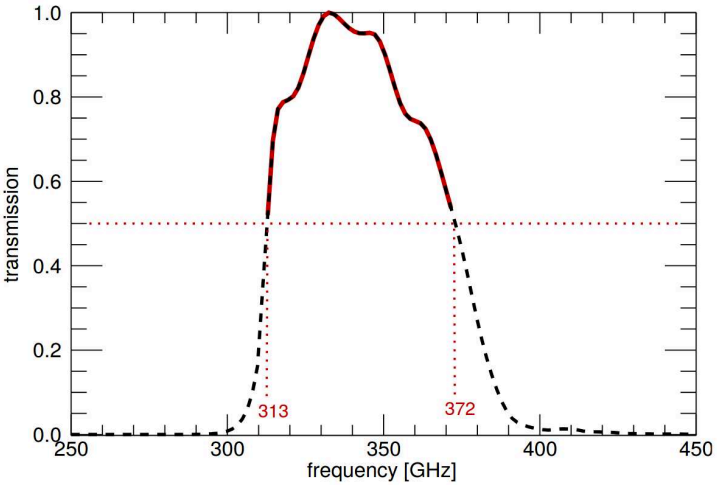

Figure 3.16 Spectral response of the Large APEX BOlometer CAmera (LABOCA). The transmission is normalized with respect to the maximum. The central frequency is 345 GHz (corresponding to a wavelength λ = 870 μm), and the portion with 50% or more transmission is between 313 GHz and 372 GHz (indicated in red). Figure reproduced from Siringo *et al.* (2009). See also Fig. 9.1.

Continuum observations: **The Large APEX BOlometer CAmera (LABOCA)** The Large APEX BOlometer CAmera (hereafter LABOCA) is the continuum receiver at the APEX telescope (Siringo *et al.*, 2009). Bolometers absorb incoming radiation power and convert it into heat, which can then be evaluated with a sensitive resistive thermometer (Low 1961, Mather 1984). LABOCA is an array of 295 semiconducting bolometers operating at 345 GHz (neutron-transmutation doped germanium semiconducting chips, Haller *et al.* 1982). In order to reach optimal sensitivity, the bolometer array is cooled down to 285 mK by a cryogenic system using liquid nitrogen and liquid helium. The LABOCA bandpass is shown in Fig. 3.16.

Chapter 4 | Radiative transfer analysis of molecular lines

Contents

4.1 | Introduction to radiative transfer

In the paragraphs that follow, we aim to present basic material for radiative transfer analysis. The quantities defined in this section will be necessary to describe the methods presented in the sections 4.2.4 and 4.3. For an advanced description of radiative transfer in astrophysics, the reader is redirected to Dullemond (2013) and Rybicki and Lightman (1979).

Specific intensity, brightness temperature and beam dilution The specific intensity I_ν of a spectral line is defined by the following conserved quantity:

$$I_\nu = \frac{dE}{d\nu dA dt d\Omega} \tag{4.1}$$

where dE, $d\nu$, dt, dA and $d\Omega$ respectively correspond to the energy, frequency, time, surface and solid angle. Specific intensities are usually given in erg s^{-1} Hz^{-1} sr^{-1} cm^{-2} (1 Jy = 10^{-23} erg s^{-1} cm^{-2} Hz^{-1}). This equation relates the energy dE emitted by a source of angular size $d\Omega$ to the specific intensity measured by an observer per unit bandwidth $d\nu$, during an observing time dt, on a collecting surface dA (normal to the path).

In chapter 3, we have shown that the specific intensity I_ν can be rewritten in a form in which it is related to the effective radiation temperature $J_\nu(T_\mathrm{b})$ (see Eq. 3.3, Eq. 3.4). If the beam filling factor[1] is equal to 1, then the main beam temperature T_mb is related to the specific intensity by:

$$T_\mathrm{mb}\ [\mathrm{K}] = \frac{\lambda^2}{2k_\mathrm{B}} I_\nu\ [\mathrm{erg}^{-1}\ \mathrm{Hz}^{-1}\ \mathrm{cm}^{-2}\ \mathrm{s}^{-1}\ \mathrm{sr}^{-1}] \tag{4.2}$$

where λ is the radiation wavelength and k_B the Boltzmann constant. Specific intensities and brightness temperatures can be converted into each other independently of the satisfaction of the Rayleigh-Jeans approximation. If the source is not resolved, then $\lambda^2 I_\nu / 2k_\mathrm{B}$ is a lower limit of the actual brightness temperature of the source (in fact, it corresponds to the *average* specific intensity over the solid angle of the beam). The beam dilution can be corrected if the filling factor is known.

Equation of radiative transfer The specific intensity measured by an observer is the result of emission, absorption and scattering processes occurring along the line of sight. For a given frequency, the variation of the specific intensity along an infinitesimal path ds is given by:

$$\frac{dI_\nu}{ds} = j_\nu - \alpha_\nu I_\nu \tag{4.3}$$

where j_ν is a volumic source term that represents the emission (erg $^{-1}$ Hz^{-1} cm^{-3} s^{-1} sr^{-1}), and α_ν is the absorption coefficient (cm^{-1}). By definition, the optical depth of a line is related to the absorption coefficient by $d\tau_\nu = \alpha_\nu ds$, hence we have:

$$\tau_\nu = \int_{s_0}^{s} \alpha_\nu(s')ds' \tag{4.4}$$

The equations above are valid for any type of emission (continuum, spectral lines, *etc*). In the case of spectral-line observations, the determination of the source term j_ν depends on the considered line. Assuming a transition $u \rightarrow l$ (between an upper level 'u' and a lower level 'l') associated with a probability of spontaneous de-excitation A_ul (also referred to as the Einstein coefficient for spontaneous emission, see section 4.2), we have:

$$j_\nu = \frac{h\nu_\mathrm{ul}}{4\pi} n_u A_\mathrm{ul} \phi(\nu) \tag{4.5}$$

where the term 4π was introduced because we assume that the emission is isotropic, n_u is the population density of the upper level (in cm^{-3}), ν_ul is the frequency of the transition, h is the Planck constant and $\phi(\nu)$ describes the line profile. For a Maxwellian distribution of particle velocities, the line profile is a Gaussian, but in all rigor a Voigt profile should be adopted to take into account collisional broadening effects (that is, the convolution of a gaussian profile with a Lorentzian profile, *e.g.* Armstrong 1967). The most simple approximation of $\phi(\nu)$ is a rectangle of height $1/\Delta\nu$ and width $\Delta\nu$ centered on $\nu = \nu_\mathrm{ul}$. Similarly, the absorption coefficient can be written:

$$\alpha_\nu = \frac{h\nu_\mathrm{ul}}{4\pi} \left[n_\mathrm{l} B_\mathrm{lu} \varphi(\nu) - n_\mathrm{u} B_\mathrm{ul} \chi(\nu) \right] \tag{4.6}$$

[1]The filling factor represents the ratio $\Delta\Omega_\mathrm{b}/\Delta\Omega_\mathrm{s}$, where $\Delta\Omega_\mathrm{b}$ is the angular size of the beam, and $\Delta\Omega_\mathrm{s}$ is the angular size of the source.

where $B_{\rm lu}$ and $B_{\rm ul}$ are respectively the stimulated excitation and de-excitation rates (also referred to as the Einstein coefficients for photon absorption and induced emission), $n_{\rm l}$ is the density of the lower level and $\varphi(\nu)$ and $\chi(\nu)$ are the line profiles for absorption and stimulated emission (counted as negative absorption in Eq. 4.6). We define the source function S_ν by:

$$S_\nu = \frac{j_\nu}{\alpha_\nu} \tag{4.7}$$

By developing the expression S_ν *via* the definitions of j_ν (Eq. 4.5) and α_ν (Eq. 4.6) and using the Einstein relations, it can be shown that the source function takes the form $S_\nu = B_\nu(T_{\rm ex})$, where B_ν is the black body radiation and $T_{\rm ex}$ is the excitation temperature, defined relatively to the population of upper and lower energy levels for any transition (Rybicki and Lightman 1979, see also Eq. 4.21):

$$T_{\rm ex} = \frac{E_{\rm ul}/k_{\rm B}}{\ln(\frac{n_{\rm l}/g_{\rm l}}{n_{\rm u}/g_{\rm u}})} \tag{4.8}$$

where $E_{\rm ul} = E_{\rm u} - E_{\rm l}$ is the energy of the transition, $k_{\rm B}$ is the Boltzmann constant and $g_{\rm u}$, $g_{\rm l}$ are the degeneracies[2] of the upper and lower energy levels. At thermal equilibrium, $T_{\rm ex} = T_{\rm kin}$ (where $T_{\rm kin}$ is the kinetic temperature of the gas, see section 4.2.3). Using $d\tau_\nu = \alpha_\nu ds$ and $S_\nu = j_\nu/\alpha_\nu$, we can rewrite Eq. 4.3 in the form:

$$\frac{dI_\nu}{d\tau_\nu} = -I_\nu + S_\nu \tag{4.9}$$

The general solution (valid both for continuum radiation and spectral lines) of this first-order, ordinary differential equation of I_ν is:

$$I_\nu(\tau_\nu) = I_\nu(0)\mathrm{e}^{-\tau_\nu} + \int_0^{\tau_\nu} \mathrm{e}^{-(\tau_\nu - \tau'_\nu)} S_\nu(\tau'_\nu) d\tau'_\nu \tag{4.10}$$

In this equation, $I_\nu(\tau_\nu)$ corresponds to the specific intensity measured by an observer, $I_\nu(0)$ is the specific intensity emitted by a background source, and the product of the integral is the sum of the emission contributed by the source function S_ν along the line of sight.

Using $S_\nu = B_\nu(T_{\rm ex})$ (spectral line observations), the solution of Eq. 4.9 in an homogeneous medium illuminated by a background radiation $I_\nu^{\rm bg}$ is:

$$I_\nu = B_\nu(T_{\rm ex})(1 - \mathrm{e}^{-\tau_\nu}) + I_\nu^{\rm bg}\mathrm{e}^{-\tau_\nu} \tag{4.11}$$

Hence, in the optically thick regime ($\tau_\nu \gg 1$) we have $I_\nu = B_\nu(T_{\rm ex})$. *Under the Rayleigh-Jeans approximation* ($h\nu_{\rm ul} \ll k_{\rm B}T$) and at thermal equilibrium, the brightness temperature of an optically thick spectral line is $T_{\rm mb} = T_{\rm kin}$ (where $T_{\rm kin}$ is the kinetic temperature of the gas).

4.2 | Rovibrational molecular spectroscopy

In the following section, we aim to give a quick rundown of the basics of rovibrational molecular spectroscopy in order to prepare the next sections and chapters. For a complete and detailed description, the interested reader is redirected to Tennyson (2019), Draine (2011), Bransden and Joachain (2003) and Mangum and Shirley (2015).

[2]The degeneracy g_i represents the amount of quantum states that can occupy the same energy level E_i.

4.2.1 Diatomic molecules

Rotational energy levels of diatomic molecules Additionally to their electronic state, the energy level structure of molecules includes a vibration-rotation spectrum. Diatomic molecules (*e.g.* H_2, ^{12}CO, OH) can either vibrate along their internuclear axis or rotate around their center of mass. The vibrational and rotational energy levels of molecules are quantized: *i.)* the vibrational number $v = 0,\ 1,\ 2,\ ...$ represent the number of nodes in the vibrational wave function and *ii.)* the rotational number $J = 0,\ 1,\ 2,\ ...$ represents the quantized angular momentum $J\hbar$ (where $\hbar$ is the reduced Planck constant, $\hbar = h/2\pi$). Following Tennyson (2019), the energy $E(v, J)$ of a level can be described by:

$$E(v, J) = V(r_0) + h\nu_0\left(v + \frac{1}{2}\right) + B_v J(J + 1) \tag{4.12}$$

$$\nu_0 = \frac{\omega_0}{2\pi} \tag{4.13}$$

$$B_v = \frac{\hbar^2}{2m_r r_0^2} \tag{4.14}$$

where $V(r)$ is the effective internuclear potential, r_0 the nuclear separation that minimizes $V(r_0)$ and ν_0 the frequency of the harmonic oscillator modelling the vibrational motions of the molecule:

$$\omega_0 = (k/m_r)^{1/2} \tag{4.15}$$

where k is the spring constant (closely related to the strength of the chemical bond) and $m_r = m_1 m_2/(m_1 + m_2)$ the reduced mass of the spring system. The constant B_v in Eq. 4.12 is the 'rotation constant' for a vibrational level v (B_v depends on the nuclear separation r_0), derived from the moment of inertia of the molecule $I = m_r r_0^2$. In the following sections, the energies $E(v, J)$ will be expressed in Kelvin through division by the Boltzmann constant k_B.

Pure rotational transitions Non-electronic molecular energy transitions are identified by indicating the upper and lower rovibrational states. 'Pure rotational transitions' correspond to the transitions in which only the rotational energy changes (*e.g.* in the transition $J : 1 \rightarrow 0$, or 'J=1–0', $J_u = 1$ and $J_l = 0$ are respectively the upper and lower energy levels). Transitions will change J by ± 1 (dipolar transitions) or ± 2 (quadrupolar transitions).

De-excitation pure rotational transitions ($\Delta J = -1,\ -2$) are accompanied by the emission of a photon of energy $h\nu = E_{ul}$, where $E_{ul} = E(v, J_u) - E(v, J_l)$ is the energy shift between the upper and lower energy levels. The process of spontaneous de-excitation is governed by the Einstein coefficient A_{ul} of the transition, that describes the probability of spontaneous de-excitation (s^{-1}). For dipolar transitions, $A_{ul} \propto \mu^2 E_{ul}^3$ where μ is the dipole moment, and for quadrupolar transitions $A_{ul} \propto E_{ul}^5$ (Draine, 2011).

Rotational, vibrational and electronic energy levels involve different magnitudes of energy separations. For example, for H_2 the $J = 2$ rotational energy level is 510 K above the $J = 0$ energy level, the $v = 1$ vibrational energy level is 6000 K above the $v = 0$ energy level, and the first excited electronic level $B^1\Sigma_u^+$ is 140 000 K (12 eV) above the electronic ground state $X^1\Sigma_g^+$. In chapter 8, we study the emission of H_2, ^{12}CO, ^{13}CO and $C^{18}O$ pure rotational lines in the IC443 SNR. The specific characteristics of these lines are described in the next paragraphs.

line	J_u	λ_{ul} (micron)	A_{ul} (s^{-1})	g_u	E_u (K)
H_2 0–0 S(0)	2	28.219	2.9493×10^{-11}	5	509.85
H_2 0–0 S(1)	3	17.035	4.7716×10^{-10}	21	1015.2
H_2 0–0 S(2)	4	12.278	2.7607×10^{-9}	9	1681.7
H_2 0–0 S(3)	5	9.6645	9.8574×10^{-9}	33	2503.9
H_2 0–0 S(4)	6	8.0255	2.6489×10^{-8}	13	3474.4
H_2 0–0 S(5)	7	6.9089	5.8923×10^{-8}	45	4586.4
H_2 0–0 S(6)	8	6.1086	1.1444×10^{-7}	17	5829.8
H_2 0–0 S(7)	9	5.5112	2.0058×10^{-7}	57	7197.0

Table 4.1 Spectroscopic parameters corresponding of H_2 pure rotational lines. J_u is the rotational quantum number of the upper level, λ_{ul} and A_{ul} are respectively the wavelength and the Einstein coefficient of the transitions. E_u and g_u are respectively the energy and degeneracy corresponding to the upper level. The values given are taken from the Cologne Database for Molecular Spectroscopy (Müller *et al.* 2001, Müller *et al.* 2005, Endres *et al.* 2016) and Jet Propulsion Laboratory database (Pickett *et al.*, 1998), and are the numeric values used in this work.

H_2 pure rotational transitions For reference, the rovibrational energy spectrum of H_2 is shown in Fig. 4.1. H_2 is a homonuclear diatomic molecule, hence it has no permanent dipole moment. As a consequence, dipolar transitions are forbidden and only quadrupolar transitions can occur ($\Delta J = \pm 2$, *e.g.* $J : 3 \rightarrow 1$). The rotational transitions of H_2 are labeled S(0) (J=2–0), S(1) (J=3–1), ... , *etc*, where the letter 'S' means $\Delta J = J_u - J_l = +2$. Pure rotational transitions $J \rightarrow J - 2$ have an energy $h\nu = E(0, J) - E(0, J - 2) = 2B_0(2J - 1)$ (see Eq. 4.12).

The internuclear distance of the H_2 molecule is $r = 7.416 \times 10^{-11}$ m (0.74 Å, *e.g.* Field *et al.* 1966). The reduced mass is $m_r = (1 \times 1/2) = 0.5$ atomic mass unit. Thus, the energy of the upper level $J_u = 2$ is $6B_0/k_B = 510$ K, and the wavelength of the radiated photon for the transition $J : 2 \rightarrow 0$ is $hc/6B_0 = 28$ µm. For higher J, the energy of upper levels grows as $J(J + 1)$ (510 K, 1015 K, 1681 K, ...) and the wavelength of the radiated photons decreases as $1/(2J - 1)$ (28.2 µm, 17.0 µm, 12.3 µm, ...).

For reference, Tab. 4.1 contains the spectroscopic parameters of the H_2 S(0) to S(7) lines. We can already conclude from the relatively high energies of H_2 upper levels that the rotational excitation of H_2 lines requires high temperatures (since the energy of the $J_u = 2$ level is $E_2 = 510$ K). For example, at a temperature $T_{kin} = 20$ K (typical temperature of a cold molecular cloud), the partition function is given by Eq. 4.19 (see section 4.2.3): $Z_{H_2}(20\ \mathrm{K}) = 1.0018$. Therefore, at this temperature 99.82% of H_2 is in the ground state (since $(1.0018)^{-1} = 0.9982$, see Eq. 4.20).

^{12}CO, ^{13}CO and C^{18}O pure rotational transitions CO isotopologs are heteronuclear diatomic molecules, hence they have a permanent dipole moment. As a consequence, dipolar transitions are allowed ($\Delta J = \pm 1$). Pure rotational transitions $J \rightarrow J-1$ have an energy $h\nu = E(0, J)-E(0, J-1) = 2B_0J$ (see Eq. 4.12).

The internuclear distance of the ^{12}CO molecule is $r_0 = 1.1306 \times 10^{-10}$ m (1.13 Å, *e.g.* Plyler *et al.* 1955). The reduced mass is $m_r = (12 \times 16/28) = 6.86$ atomic mass unit. Hence, the energy of the upper level $J_u = 1$ is $2B_0/k_B = 5.5$ K, and the frequency of the radiated photon for the transition $J : 1 \rightarrow 0$ is $2B_0/h = 115$ GHz. For higher J, the energy of upper levels grows as $J(J + 1)$ (5.5 K, 16.6 K, 33.2 K, ...) and the frequency of the radiated photons grows as J (115

species	J_u	ν_{ul} (GHz)	A_{ul} (s^{-1})	g_u	E_u (K)
^{12}CO	1	115.2712018	7.203×10^{-8}	3	5.53
^{12}CO	2	230.5380000	6.910×10^{-7}	5	16.6
^{12}CO	3	345.7959899	2.497×10^{-6}	7	33.19
^{13}CO	1	110.2013543	6.294×10^{-8}	3	5.29
^{13}CO	2	220.3986841	6.038×10^{-7}	5	15.87
^{13}CO	3	330.5879652	2.181×10^{-6}	7	31.73
C^{18}O	1	109.7821734	6.266×10^{-8}	3	5.27
C^{18}O	2	219.5603541	6.011×10^{-7}	5	15.81

Table 4.2 Spectroscopic parameters of ^{12}CO, ^{13}CO and C^{18}O lines. J_u is the rotational quantum number of the upper level, ν_{ul} and A_{ul} are respectively the frequency and the Einstein coefficient of the transitions. E_u and g_u are respectively the energy and degeneracy corresponding to the upper level. The values given are taken from the Cologne Database for Molecular Spectroscopy (Müller *et al.* 2001, Müller *et al.* 2005, Endres *et al.* 2016) and Jet Propulsion Laboratory database (Pickett *et al.*, 1998), and are the numeric values used in this work.

GHz, 230.5 GHz, 345 GHz, ...). Small corrections of the internuclear distance r_0 and reduced mass m_r cause the energy and frequency of the ^{13}CO and C^{18}O transitions to be slightly different (*e.g.* from 115 GHz for ^{12}CO to 110 GHz for ^{13}CO). For reference, Tab. 4.2 contains the spectroscopic parameters of ^{12}CO, ^{13}CO and C^{18}O.

4.2.2 Collisional excitation

So far, we have described the energy level structure and de-excitation processes of diatomic molecules without regard to the collisional mechanisms that lead to their prior excitation (we only presented the excitation mechanism which involves the absorption of photons). In the ISM, inelastic collisions produce most of the excitations of molecules that ultimately result in the emission of photons. The probability to populate higher energy levels *via* collisions is determined by collisional rates (collision partners can be H_2 molecules, H and He atoms.). Similarly to the Einstein coefficient A_{ul} (describing the spontaneous de-excitation rate per second), the collisional excitation rate coefficient $\langle \sigma v \rangle_{ul}$ describes the probability of collisionally induced excitation per second, per particle in a unit volume (cm^3 s^{-1}):

$$\langle \sigma v \rangle_{ul} = \int_0^\infty \sigma(v) v f_v dv \tag{4.16}$$

where $\sigma(v)$ is the reaction cross section and $f_v dv$ is the probability that the projectile and target molecule have relative speed v in dv. In thermal equilibrium at temperature T, this probability is determined by a Maxwellian velocity distribution:

$$f_v dv = 4\pi \left(\frac{m_r}{2\pi k_B T} \right)^{3/2} e^{-m_r v^2 / 2 k_B T} v^2 dv \tag{4.17}$$

where m_r is the reduced mass of the collision partners. Additionally to collisional excitation, de-excitation can be caused by collisions. For the equilibrium abundances to satisfy the law of

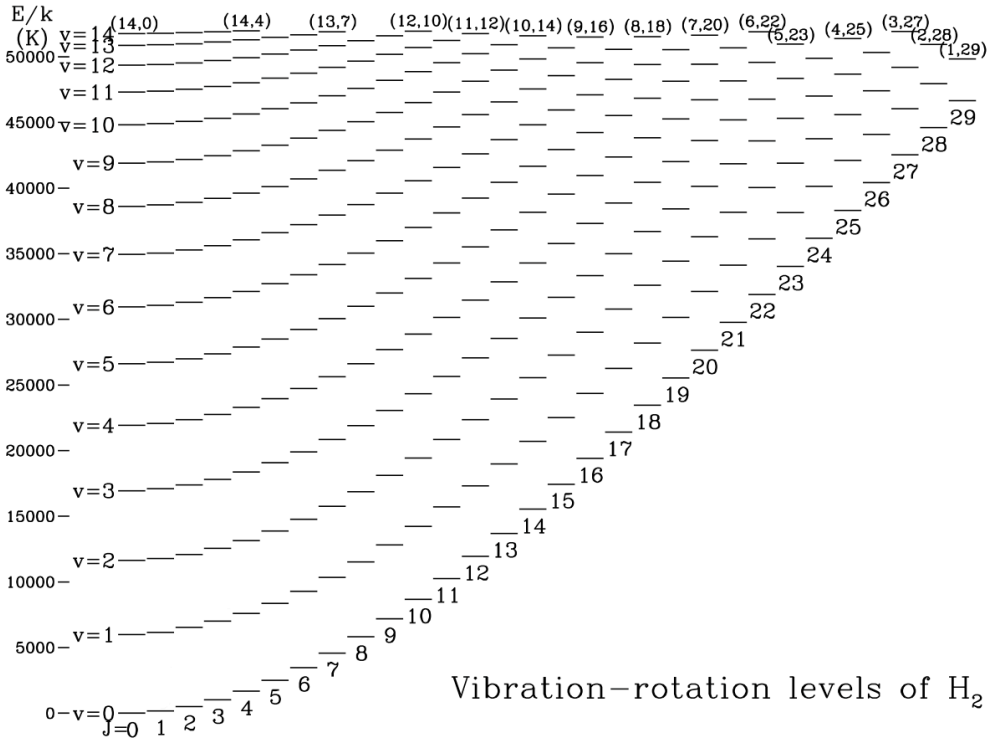

Figure 4.1 Vibration-rotation energy spectrum of the ground electronic state of H_2 for $J \leq 29$. The energy of the levels $E(v, J)/k_B$ is indicated in Kelvin on the left axis. Figure reproduced from Draine (2011).

mass action, the ratio of collisional excitation and de-excitation rate coefficients must satisfy the following condition (see Draine 2011 for a derivation):

$$\langle \sigma v \rangle_{lu} = \frac{g_u}{g_l} e^{-E_{ul}/k_B T} \langle \sigma v \rangle_{ul} \tag{4.18}$$

Hereafter, we will refer to the collisional coefficients $\langle \sigma v \rangle_{ul}$ as 'C_{ul}'. As we have just noted, the calculation of these coefficients requires the determination of reaction cross sections in inelastic collisions between a projectile and a target molecule (see Eq. 4.16). Such calculations require a knowledge of the intermolecular potential, hence it represents a case by case, daunting computational task. Collisional excitation rates depend on the kinetic temperature of the gas (see Eq. 4.17), and they are usually tabulated for a range of temperatures (*e.g.* Flower and Roueff 1998a). Due to their astrophysical importance, the collisional systems of ^{12}CO and H_2 have been studied with the most sophisticated methods. In the following paragraphs, we present the theoretical works that determined the collisional excitation rate coefficients for these two molecules.

Collisional excitation of H_2 Collisional cross sections and rate coefficients were calculated for the rovibrational excitation of H_2 by H (Flower 1997, Flower and Roueff 1998b), He (Flower *et al.*, 1998) and H_2 (Flower and Roueff, 1998a) employing fully quantum mechanical methods with the appropriate interaction potentials (see also Wrathmall *et al.* 2007, Nesterenok *et al.* 2019). We will use these coefficients in chapter 8.

Collisional excitation of ^{12}CO, ^{13}CO and $C^{18}O$ The CO-H_2 collisional system has been the subject of many experiments (see Yang *et al.* 2010 and references therein). The most recent

calculations were performed by Yang *et al.* (2010) for J_u=1–40, based on an approximate potential energy surface. We will use these coefficients for all CO isotopologs in chapter 8.

4.2.3 Local thermodynamic equilibrium

Statistical equilibrium The populations of different energy levels of a diatomic molecule can be described by statistical mechanics. Most generally, for a physical system that presents a collection of s distinct possible states of energies E_s and degeneracy g_s[3], the internal partition function at a temperature T is defined by the following sum over all distinct possible states of the system:

$$Z(T) = \sum_s g_s e^{-E_s/k_B T} \tag{4.19}$$

where k_B is the Boltzmann constant. The partition function $Z(T)$ allows to determine the distribution of column densities N_s (cm^{-2}) of each state at thermal equilibrium:

$$N_s(T) = \frac{N_{tot}}{Z(T)} g_s e^{-E_s/k_B T} \tag{4.20}$$

where N_{tot} is the total column density. In a system that is at local thermodynamic equilibrium (hereafter LTE), the Boltzmann distribution (Eq. 4.20) is locally verified. A system that verifies this relation is also said to be 'thermalized', and/or to follow a thermal distribution. We have written Eq. 4.20 for the column densities N_s, N_{tot} (cm^{-2}), but it can also be applied to volume densities n_s, n_{tot} (cm^{-3}). Eq. 4.20 also allows to determine the population ratio n_u/n_l between an upper and a lower energy level, which can be useful (see next paragraph):

$$\frac{n_u}{n_l} = \frac{g_u}{g_l} e^{-E_{ul}/k_B T} \tag{4.21}$$

where g_u, g_l are the upper and lower level degeneracies and $E_{ul} = E_u - E_l$ is the energy of the $u \rightarrow l$ transition.

Critical density If we consider the general case of a transition between two levels[4] (an upper level u and a lower level l), the time evolution of the population n_u (cm^{-3}) is given by:

$$\frac{dn_u}{dt} = n_c n_l C_{lu} - n_c n_u C_{ul} - n_u A ul \tag{4.22}$$

where n_c is the density of collision partners, and C_{ul}, C_{lu}, A_{ul} are respectively the collisional excitation, de-excitation and spontaneous de-excitation rate coefficients. For the sake of simplicity, we have neglected optical pumping and chemical formation of the species in an excited state (*e.g.* Godard and Cernicharo 2013). The steady state solution of this equation ($dn_u/dt = 0$) is:

$$\frac{n_u}{n_l} = \frac{n_c C_{lu}}{n_c C_{ul} + A_{ul}} \tag{4.23}$$

[3]The degeneracy g_s refers to the number of distinct quantum states that share the same energy level.

[4]In a real system, a sum of transitions should be taken into account, depending on the number of transitions allowed by quantum selection rules, *e.g.* Godard and Cernicharo (2013).

It is convenient to re-organize this relation in the following manner:

$$\frac{n_{\rm u}}{n_{\rm l}} = \frac{C_{\rm lu}/C_{\rm ul}}{1 + A_{\rm ul}/n_{\rm c}C_{\rm ul}} \tag{4.24}$$

We can see from this equation that for $n_{\rm c} \to \infty$, we have $n_{\rm u}/n_{\rm l} \to C_{\rm lu}/C_{\rm ul}$. In virtue of Eq. 4.18 (corollary of the law of mass action), it follows that:

$$\lim_{n_{\rm c}\to\infty} \frac{n_{\rm u}}{n_{\rm l}} = \frac{g_{\rm u}}{g_{\rm l}} {\rm e}^{-E_{\rm ul}/k_{\rm B}T} \tag{4.25}$$

Which is asymptotically identical to Eq. 4.21. Hence, we have shown that for a sufficiently high density $n_{\rm c}$ of collision partners, the energy levels above the ground state are collisionally populated such that the system follows a thermal distribution. In our derivation, we have ignored photoabsorption and stimulated emission, and we adopted a simplified two-level system. These additional processes would be accounted for by additional terms in Eq. 4.22. In a gas illuminated by a strong radiation field, radiative pumping can compete with collisional excitation, and the population levels might deviate significantly from the thermal distribution corresponding to the kinetic temperature of the gas. As long as we neglect photoabsorption and stimulated emission, we can define the critical density as the density for which collisional de-excitation is equal to spontaneous de-excitation ($n_{\rm crit}C_{\rm ul} = A_{\rm ul}$):

$$n_{\rm crit} = \frac{A_{\rm ul}}{C_{\rm ul}}\ ({\rm cm}^{-3}) \tag{4.26}$$

The population levels in a gas that satisfies $n_{\rm c} \geq n_{\rm crit}$ are expected to have marginal deviations from a thermal distribution. If $n_{\rm c} \ll n_{\rm crit}$ and/or if there are competing radiative excitation processes, then the population distribution is not characterized by the kinetic temperature of the gas (it is either 'subthermal' or tracing the temperature of the radiation field), and in that case the temperature in Eq. 4.21 is referred to as the 'excitation temperature' $T_{\rm ex}$ (instead of the kinetic temperature of the gas, $T_{\rm kin}$).

The critical density is a very convenient quantity to predict if a gas in a region of known density can be assumed to be thermalized. In chapter 8, we will estimate the critical densities of H_2 and CO lines for different kinetic temperatures in order to confirm the validity of LTE assumptions in the IC443G region. We show the critical densities of H_2 transitions computed at 1000 K, 2000 K and 4500 K in Tab. 4.3, and the critical densities of ^{12}CO transitions computed at 10 K, 30 K and 150 K in Tab. 4.4.

4.2.4 Population diagram analysis

Now that we have introduced the rotational energy level structure and statistical equilibrium characteristics of diatomic gases, we will describe a method to infer the excitation temperature and total column density of H_2 and CO isotopologs. Goldsmith and Langer (1999) presented the first detailed description of the population diagram. The population diagram is also sometimes referred to as the 'rotation diagram', 'excitation diagram' or 'Boltzmann plot', Blake *et al.* (1987), Helmich *et al.* (1994). In all rigor, these distinct names relate to different contexts:

line	J_u	n_{crit}(1000 K) (cm^{-3})	n_{crit}(2000 K) (cm^{-3})	n_{crit}(4500 K) (cm^{-3})
H_2 0–0 S(0)	2	5×10^0	2×10^0	8×10^{-1}
H_2 0–0 S(1)	3	7.6×10^1	2.8×10^1	1×10^1
H_2 0–0 S(2)	4	5.9×10^2	2.0×10^2	6.1×10^2
H_2 0–0 S(3)	5	3.3×10^3	9.0×10^2	2.5×10^2
H_2 0–0 S(4)	6	1.5×10^4	3.2×10^3	7.8×10^2
H_2 0–0 S(5)	7	5.4×10^4	1.0×10^4	2.1×10^3
H_2 0–0 S(6)	8	1.6×10^5	2.7×10^4	5.0×10^3
H_2 0–0 S(7)	9	4.3×10^5	6.4×10^4	1.1×10^4

Table 4.3 Two-level critical densities of H_2 pure rotational lines (see Eq. 4.26). J_u is the rotational quantum number of the upper level, and $n_{crit}(T)$ is the critical density at a temperature T. The values of A_{ul} are taken from Tab. 4.1, and the values of $C_{ul}(T)$ are taken from Flower and Roueff (1998a).

line	J_u	n_{crit}(10 K) (cm^{-3})	n_{crit}(30 K) (cm^{-3})	n_{crit}(150 K) (cm^{-3})
^{12}CO J=1–0	1	2.2×10^3	2.2×10^3	2.1×10^3
^{12}CO J=2–1	2	9.7×10^3	1.1×10^4	9.9×10^3
^{12}CO J=3–2	3	3.1×10^4	3.7×10^4	3.0×10^4

Table 4.4 Two-level critical densities of ^{12}CO pure rotational lines (see Eq. 4.26). J_u is the rotational quantum number of the upper level, and $n_{crit}(T)$ is the critical density at a temperature T. The values of A_{ul} are taken from Tab. 4.1, and the values of $C_{ul}(T)$ are taken from Yang *et al.* (2010).

- In spectroscopy, the 'Boltzmann plot' or 'excitation diagram' is the most general version of the method (applied to any type of transitions).
- In molecular spectroscopy, the 'rotation diagram' or 'population diagram' usually applies to rotational transitions of molecules (in addition, the 'population diagram' is corrected for opacity, but the 'rotation diagram' is not).

The idea of the population diagram is to analyze the populations of each energy level relatively to the ground state.

Equation of the population diagram In this section, we consider a thermalized gas of diatomic molecules with upper energy levels (E_u, g_u). In the most general case, the distribution of populations N_u follows the Boltzmann distribution (Eq. 4.20) with $T = T_{ex}$. Applying the Neperian logarithm to Eq. 4.20 yields:

$$\ln\left(\frac{N_u}{g_u}\right) = \ln\left(\frac{N_{tot}}{Z(T_{ex})}\right) - \frac{E_u}{k_B T_{ex}} \tag{4.27}$$

where $Z(T_{ex})$ is the partition function of the diatomic molecule at $T = T_{ex}$. This equation can be re-written as $y = ax + b$, with $y = \ln(N_u/g_u)$, $a = -1/k_B T_{ex}$, $x = E_u$ and $b = \ln(N_{tot}/Z(T_{ex}))$. Hence, it is possible to infer the total column density N_{tot} and excitation temperature T_{ex} from a simple linear fit of the data points $\ln(N_u/g_u)$ as a function of energy E_u. For a measurement of the

parameters a, b of the linear fit, we have:

$$N_{\rm tot} = Z(T_{\rm ex})\mathrm{e}^{b} \tag{4.28}$$

$$T_{\rm ex} = -\frac{1}{k_{\rm B}a} \tag{4.29}$$

$\mathbf{N_u}$ measurement (optically thin regime) We have just seen that under some assumptions, the total column density and excitation temperature can be derived from upper level column density measurements ($N_{\rm u}$). But what we actually measure is a flux of photons on a detector for different transitions. De-excitation photons are emitted at a rate $N_{\rm u}A_{\rm ul}$, where $A_{\rm ul}$ is the spontaneous de-excitation coefficient (s^{-1}), hence in an optically thin regime we have (see also Eq. 4.5):

$$\sum I_\nu \Delta\nu = \frac{h\nu_{\rm ul}}{4\pi} N_{\rm u}A_{\rm ul} \tag{4.30}$$

where I_ν is the specific intensity (erg s^{-1} cm^{-2} sr^{-1} Hz^{-1}), $\Delta\nu$ is a finite frequency channel, h is the Planck constant and $\nu_{\rm ul}$ the frequency of the photon ($h\nu_{\rm ul} = E_{\rm ul}$, where $E_{\rm ul} = E_{\rm u} - E_{\rm l}$ is the energy of the transition). This relation is convenient for specific intensity measurements, such as *Spitzer*-IRS H_2 spectral-line maps, but for millimeter observations we will use the 'radioastronomer equivalent version' of Eq. 4.30:

$$\sum T_a \Delta v = \frac{hc^3 A_{\rm ul} N_{\rm u}}{8\pi k_{\rm B} \nu_{\rm ul}^2} \tag{4.31}$$

where T_a is the antenna temperature (in Kelvin, see chapter 3), Δv is a finite velocity channel and $k_{\rm B}$ is the Boltzmann constant. In both cases (Eq. 4.30 and Eq. 4.31), the observed source must fill the beam of the instrument, otherwise a filling factor correction has to be applied. If $\Delta\Omega_s$ and $\Delta\Omega_b$ are respectively the source and instrumental beam solid angles, then the filling factor is $ff = \Delta\Omega_s/\Delta\Omega_b$.

$\mathbf{N_u}$ measurement (optically thick regime) If the emission of the observed transition is optically thick ($\tau \gg 1$, see section 4.1), then the following correction factor has to be applied to the $N_{\rm u}$ measurements (Surdej 1977, Goldsmith and Langer 1999, see also section 4.3):

$$C_\tau = \frac{\tau}{1 - \mathrm{e}^{-\tau}} \tag{4.32}$$

where τ is the optical depth. The optical depth can be estimated from the comparison with the lines of a lower-abundance isotopolog. For instance, in chapter 8 we will infer the opacity of ^{12}CO lines from the emission of ^{13}CO and C^{18}O. The corrected upper level column densities $N_{\rm u}^*$ are given by:

$$N_{\rm u}^* = N_{\rm u} C_\tau \tag{4.33}$$

where $N_{\rm u}$ is the upper level column density deduced from Eq. 4.30 or Eq. 4.31 (depending on the type of observations used). The effect of optical depth correction on the population diagram can be interpreted by writing Eq. 4.27 for $N_{\rm u}^*$:

$$\ln\left(\frac{N_\mathrm{u}}{g_\mathrm{u}}\right) + \ln\left(C_\tau\right) = \ln\left(\frac{N_\mathrm{tot}}{Z(T_\mathrm{ex})}\right) - \frac{E_\mathrm{u}}{k_\mathrm{B}T_\mathrm{ex}} \tag{4.34}$$

Since $C_\tau \geq 0$, the additional term $\ln(C_\tau)$ shifts the ordinates upwards in the population diagram, hence it increases the inferred total column density. If C_τ is different for distinct levels, then the slope might also vary, hence the inferred excitation temperature will be modified as well.

Algorithm 1: Total column density and excitation temperature estimate from a population diagram analysis of upper levels 1, ..., J. Bold variables are arrays or functions, and non-bold variables are scalars. The function **curvefit** refers to the module `scipy.optimize.curve_fit` in `Python`.

Data: $\mathbf{N_u}$:$[N_1, \ldots, N_J]$ upper level column densities (rotational transitions $1 \rightarrow 0$ to $J \rightarrow J-1$), $\mathbf{E_u}$ (upper level energies, dimension $1 \times J_\mathrm{max}$) and $\mathbf{g_u}$ (upper level degeneracies, dimension $1 \times J_\mathrm{max}$) tabulated up to $J_\mathrm{max} \gg J$.
Result: N_tot (column density), T_ex (excitation temperature)
$\mathbf{Y} = \ln(\mathbf{N_u}/\mathbf{g_u}[:\mathbf{J}])$;
$\mathbf{X} = \mathbf{E_u}[:\mathbf{J}]$;
a, b = **curvefit**$(\mathbf{x} \mapsto \mathbf{ax} + \mathbf{b},\ \mathbf{X},\ \mathbf{Y})$;
$T_\mathrm{ex} = -1/(ak_\mathrm{B})$;
initialize Z;
for *j in* $(1 \rightarrow J_\mathrm{max})$ **do**
  $Z = Z + g_j \exp(-E_j/k_\mathrm{B}T_\mathrm{ex})$;
end
$N_\mathrm{tot} = Z\exp(b)$;
return $(N_\mathrm{tot}, T_\mathrm{ex})$

Summary: standard LTE method for the analysis of molecular lines In this section, we have presented results of statistical mechanics, radiative transfer and rovibrational spectroscopy that allow to infer the total column density and kinetic temperature of a molecular gas from the observation of rotational lines. If one has a sample of data points for any number of rotational transitions of a molecule, then it should be possible to experiment with this method. The only requirement is the knowledge of A_ul, ν_ul and the list of g_u, E_u for a large number of transitions (typically the $\sim 10^2$ first energy levels). The following steps must be carefully applied:

1. Verify using Eq. 4.26 ($n_\mathrm{crit} = A_\mathrm{ul}/C_\mathrm{ul}$) that all the observed transitions are thermalized.
2. Estimate the filling factor $\Delta\Omega_s/\Delta\Omega_b$.
3. Estimate the opacity of the lines using lower-abundance isotopologs (see section 8.2.3).
4. Infer N_u from the measured specific intensity (Eq. 4.30) or antenna temperature (Eq. 4.31), using a filling factor correction if required (based on higher resolution observations).
5. Plot the opacity-corrected population diagram (defined by Eq. 4.27).
6. Perform a linear fit of the data points. Deduce the excitation temperature from Eq. 4.29, then compute the partition function $Z(T = T_\mathrm{ex})$ from Eq. 4.19 and finally infer the total column density from Eq. 4.28.

Steps 1–4 are a case by case problem, and represent the most delicate task. In chapter 8 we describe the detailed procedure to analyze H_2, ^{12}CO, ^{13}CO and $C^{18}O$ lines. A general-purpose pseudo-code describing the steps 5–6 is presented in the algorithm 1.

4.3 | Statistical equilibrium radiative transfer

In the previous section, we have presented a total column density measurement method that relies on the critical assumption that the lines are thermalized. In the interstellar medium, most generally the local density is not sufficient to reach LTE ($n \ll n_{\rm crit}$, see Eq. 4.26). In that case, more advanced methods must be employed. Hereafter, we present the basic principles of non-LTE statistical equilibrium calculations under the Large Velocity Gradient assumption (hereafter LVG, see section 4.3.1) and then we briefly describe the non-LTE radiative transfer code `RADEX` (section 4.3.2).

The LVG assumption is based on the existence of large velocity gradients in most parts of a molecular structure, which enables the velocity component along any line of sight to change by more than the thermal line width on a short distance (Sobolev, 1960). *Example:* for ^{13}CO, at 10 K the thermal width is $\sigma \simeq 75$ m s^{-1}. Therefore, a velocity gradient ∇v that satisfies $l \times \nabla v \gg 0.1$ km s^{-1} (where l is a characteristic length) is required to satisfy the LVG assumption for a ^{13}CO line.

4.3.1 Large Velocity Gradient approximation

Statistical equilibrium equations In this section, we consider an arbitrary set of population levels connected by energy transitions $i \leftrightarrow j$. The time variation of the density n_i (cm^{-3}) of any population level is given by:

$$\frac{dn_i}{dt} = \sum_{i \neq j} n_j \Gamma_{ji} - n_i \sum_{i \neq j} \Gamma_{ij} \tag{4.35}$$

where the variable n_j corresponds to the density of distinct population levels ($i < j$ for higher energy levels and $i > j$ for lower energy levels). Γ_{ji} and Γ_{ij} are respectively the formation and destruction rates of the level i, defined by the following system of equations:

$$\Gamma_{ij} = \begin{cases} A_{ij} + B_{ij}\overline{J_\nu} + C_{ij} & (i > j) \\ B_{ij}\overline{J_\nu} + C_{ij} & (i < j) \end{cases}$$

where $A_{\rm ij}$, $B_{\rm ij}(i > j)$ and $B_{\rm ij}(i < j)$ are respectively the spontaneous de-excitation, stimulated de-excitation and absorption rates. Similarly, $C_{\rm ij}(i > j)$ and $C_{\rm ij}(i < j)$ are the collisional de-excitation and excitation rates. The introduction of $C_{\rm ij}$ in our system of equations implies that statistical equilibrium calculations require an accurate knowledge of the collisional rates, whereas LTE calculations required only spectroscopic data ($A_{\rm ul}$, $\nu_{\rm ul}$). $\overline{J_\nu}$ corresponds to the specific intensity I_ν averaged over the whole 4π steradian and integrated over the line profile $\phi(\nu)$:

$$\overline{J_\nu} = \frac{1}{4\pi} \iint I_\nu \phi(\nu) d\nu d\Omega \tag{4.36}$$

Assuming statistical equilibrium, we have $dn_i/dt = 0$ (steady state), hence Eq. 4.35 is an algebraic system of equations on the level populations (densities n_i) and local radiation field $\overline{J_\nu}$.

The difficulty in solving this system of equations is that the level populations and the radiative transfer calculations are coupled (due to the definition of the term Γ_{ij}).

The Sobolev approximation Statistical equilibrium calculations can be solved by introducing a geometrically averaged escape probability $0 \leq \beta \leq 1$. The escape probability describes the probability that a photon will escape from the medium in which it was emitted. By definition, the expression of β depends only on the optical depth τ. The so-called Sobolev solution corresponds to the expression of the escape probability in an expanding spherical shell (Sobolev, 1960):

$$\beta = \frac{1 - \mathrm{e}^{-\tau}}{\tau} \tag{4.37}$$

The calculations are presented in details by Surdej (1977). The inverse of this expression is used to correct the upper level populations for opacity (see Eq. 4.32 in section 4.2.4). The main idea behind the calculations is that a photon emitted at some point in the envelope of a spherical shell is either absorbed in the immediate vicinity or escapes entirely due to Doppler shifts across the medium. The Sobolev approximation is also referred to as the *Large Velocity Gradient* approximation (hereafter LVG), because the calculations are based on the assumption that there is a large enough velocity gradient along the line of sight to allow significant Doppler shifts (such that the total line width, measured by the full width at half maximum Δv, satisfies the condition $\Delta v \gg \sigma$, where σ is the thermal line width). Under this assumption, the optical depth is controlled by the ratio of the column density and total line width: $\tau \propto N/\Delta v$ (see Eq. 4.39).

There are other expressions of β for distinct geometries (*e.g.* the plane-parallel slab model, de Jong *et al.* 1975). Ignoring background radiation (for the sake of simplicity), Eq. 4.36 becomes $\overline{J_\nu} = S_\nu(1-\beta)$ (see Eq. 4.10). For a spectral line, the source function $S_{\nu_{\mathrm{ul}}} = j_\nu/\alpha_\nu$ can be developed using the expressions of j_ν (see Eq. 4.5) and α_ν (see Eq. 4.6):

$$S_{\nu_{ul}} = \frac{n_{\mathrm{u}} A_{\mathrm{ul}}}{n_{\mathrm{l}} B_{\mathrm{lu}} - n_{\mathrm{u}} B_{\mathrm{ul}}} \tag{4.38}$$

Thus, we can express $\overline{J_\nu}$ in terms of A_{ul}, B_{ul}, B_{lu}, n_{u}, n_{l} and β (*i.e.* τ). If we inject this expression into the statistical equilibrium system of equations (Eq. 4.35) then we have decoupled the level populations and radiation field, and the equations can be solved separately.

4.3.2 Description of the radiative transfer code RADEX

Description of the program `RADEX` is a one-dimensional non-LTE radiative transfer code that uses the escape probability formulation (Eq. 4.37) to solve statistical equilibrium in an isothermal, homogeneous medium. For a detailed description of the program, see van der Tak *et al.* (2007). For a homogeneous medium with no global velocity field, the optical depth τ at the center of a gaussian line of full width at half maximum Δv (in velocity units) is given by:

$$\tau = \frac{c^3}{8\pi\nu_{\mathrm{ul}}^3} \frac{A_{\mathrm{ul}} N_{\mathrm{tot}}}{1.064\Delta v} \left[x_{\mathrm{l}} \frac{g_{\mathrm{u}}}{g_{\mathrm{l}}} - x_{\mathrm{u}} \right] \tag{4.39}$$

where N_{tot} is the total column density, g_{u}, g_{l} are the upper and lower level degeneracies and x_{u}, x_{l} are the upper and lower level fractional populations. This relation shows that the results

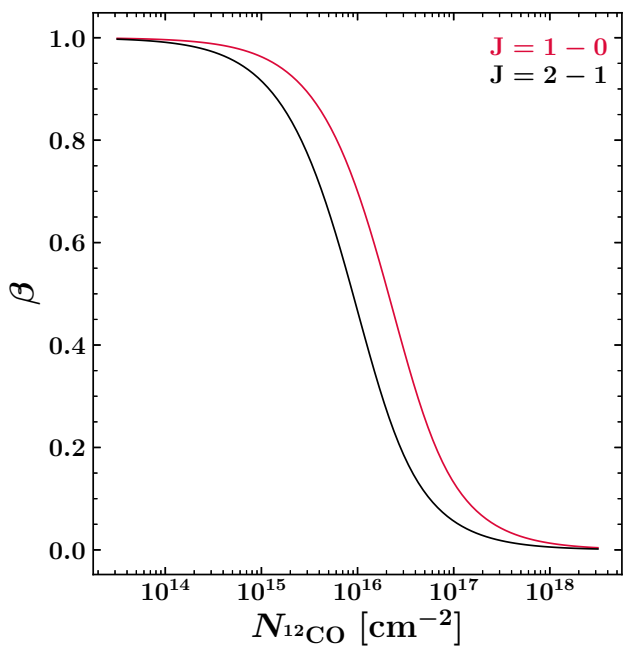

Figure 4.2 Variation of the escape probability $\beta_{\rm ul} = (1 - {\rm e}^{-\tau_{\rm ul}})/\tau_{\rm ul}$ (where $\tau_{\rm ul}$ is the optical depth) with respect to the total column density of ^{12}CO for the J=1–0 (in red) and J=2–1 (in black) pure rotational transitions. The curves were produced using $n = 100$ distinct `RADEX` radiative transfer models with logarithmically spaced values of the column density parameter $N_{^{12}{\rm CO}}$ between 5×10^{13} cm^{-2} and 5×10^{18} cm^{-2}. The other parameters remain fixed: $T_{\rm kin} = 15$ K, $\Delta v = 1$ km s^{-1}, $T_{\rm bg} = 2.7$ K (cosmic microwave background), $n_{\rm H_2} = 10^6$ cm^{-3}. For the ^{12}CO J=1–0 line, the escape probability is equal to 0.5 for $N_{^{12}{\rm CO}} = 2 \times 10^{16}$ cm^{-2} (corresponding to $\tau_{10} \simeq 1.6$).

obtained with `RADEX` are mostly determined by the quantity $N_{\rm tot}/\Delta v$, which controls the value of the escape probability β (see Eq. 4.37). `RADEX` can take into account up to seven collisional partners and produce synthetic intensities for an arbitrary number of transitions if the collisional and spectroscopic data is provided.

The program iteratively solves the statistical equilibrium system of equations (Eq. 4.35) assuming that the line profiles are gaussian. `RADEX` starts from an initial calculation based on the assumption that the emission is optically thin ($\beta = 1$), and then updates the estimate of the optical depth (*i.e.* of $\beta = (1 - {\rm e}^{-\tau})/\tau$) until it converges to a solution. In Fig. 4.2, we presents the results of `RADEX` calculations of the escape probability for ^{12}CO pure rotational lines.

Description of the input parameters The `RADEX` radiative transfer code is shipped with an executable program that can be launched in a shell environment. There are also `Python` wrappers that interact directly with `RADEX`, such as the package `SpectralRadex` (Holdship *et al.*, 2021). Launching a model requires to supply the following parameters:

– **Molecular data file.** Solving the statistical equilibrium system of equations requires to know the collisional and spectroscopic parameters $C_{\rm ul}$ (collisional rates), $A_{\rm ul}$, $B_{\rm ul}$ (Einstein coefficients), $\nu_{\rm ul}$ (transition frequency), E_i, g_i, (level energies and degeneracies), *etc* (see previous section). Molecular data files are ordered tables that contain these parameters for a number of transitions.

– **Minimum and maximum output frequencies.** `RADEX` will solve the statistical equilibrium system of equations and return the results only for an arbitrary number of transitions specified by the frequency boundaries $\nu_{\rm min}$, $\nu_{\rm max}$ (in GHz). For example, selection of a spectral range characterized by $\nu_{\rm min} = 100$ GHz and $\nu_{\rm max} = 200$ GHz for ^{12}CO will restrict the output to the J=1–0 pure rotational line only ($\nu_{10} = 115.27$ GHz, see Tab. 4.2).

- **Kinetic temperature.** The choice of the kinetic temperature of the gas $T_{\rm kin}$ (K) affects the values of the collisional rates $C_{\rm ul}$ and $C_{\rm lu} = g_{\rm u}/g_{\rm l} e^{-h\nu_{\rm ul}/k_B T_{\rm kin}}$ (see also Eq. 4.18).

- **Collision partners.** `RADEX` allows to select up to seven distinct collision partners. H_2 is the primary collision partner in the molecular medium, and its collisional data is well constrained both for ortho-H_2 and para-H_2 (Flower and Roueff 1998a, Wrathmall *et al.* 2007, Nesterenok *et al.* 2019). The access to distinct collision partners is limited by the progress on the determination of the spectroscopic and collisional data for complex molecules.

- **Density of collision partners.** The choice of the collision partner density n (cm^{-3}) affects the probability of collisional de-excitations and excitations per second ($nC_{\rm ul}$, $nC_{\rm lu}$, see section 4.2.2). At high densities ($n \gg n_{\rm crit}$) the level populations converge to the LTE distribution.

- **Background temperature.** The background temperature correspond to the equivalent blackbody temperature of the background radiation term $I_\nu^{\rm bg}$ in Eq. 4.11. It is usually set to 2.7 K, *i.e.* the temperature of the cosmic microwave background (Fixsen and Mather, 2002).

- **Column density.** The total column density (cm^{-2}) of the modelled molecule is one of the two parameters that characterize the value of the optical depth at the center of the line τ (see Eq. 4.39). It is usually the physical parameter that we aim to constrain using `RADEX` models (by finding a model that best reproduces the observations).

- **Line width.** The full width at half maximum of the line (Δv, in km s^{-1}) is the second parameter that characterizes the optical depth at the center of the line τ (see Eq. 4.39). The line widths are assumed to be the same for all lines (which are assumed to have a gaussian profile).

Output If the parameters listed above are supplied, `RADEX` returns the calculated excitation temperature $T_{\rm ex}$ (K), optical depth τ, level populations $N_{\rm u}$, $N_{\rm l}$ (cm^{-2}) and flux (both in K km s^{-1} and erg cm^{-2} s^{-1}) for all specified transitions. The program also returns the quantity $T_{\rm R}$ (K), which corresponds to the peak main beam temperature $T_{\rm mb}$ (see section 3.2.1) that would be measured with a telescope (assuming a unit filling factor).

Column density measurements using RADEX The most basic applications of the radiative transfer code `RADEX` are *i.)* to model the velocity integrated intensity of an arbitrary number of lines and constrain the total column density using χ^2 statistics (*e.g.* Leurini *et al.* 2004), or *ii.)* merely to check that a given set of physical conditions (local density, column density, temperature) satisfies the LTE approximation and/or the assumption that a line is optically thin. Building a grid of models with varying input parameters ($N_{\rm tot}$, $T_{\rm kin}$), one can determine the parameters that minimize χ^2 and constrain the column density and kinetic temperature of the gas. In some applications, it is also possible to constrain the local density, although most of the time only a lower bound can be determined (because for $n \geq n_{\rm crit}$ the models converge to the LTE distribution). In environments where the thermalization assumption does not hold, `RADEX` offers an excellent alternative to the population diagram method presented in section 4.2.4. In chapter 8, we present an analysis of ^{12}CO and ^{13}CO lines using `RADEX`.

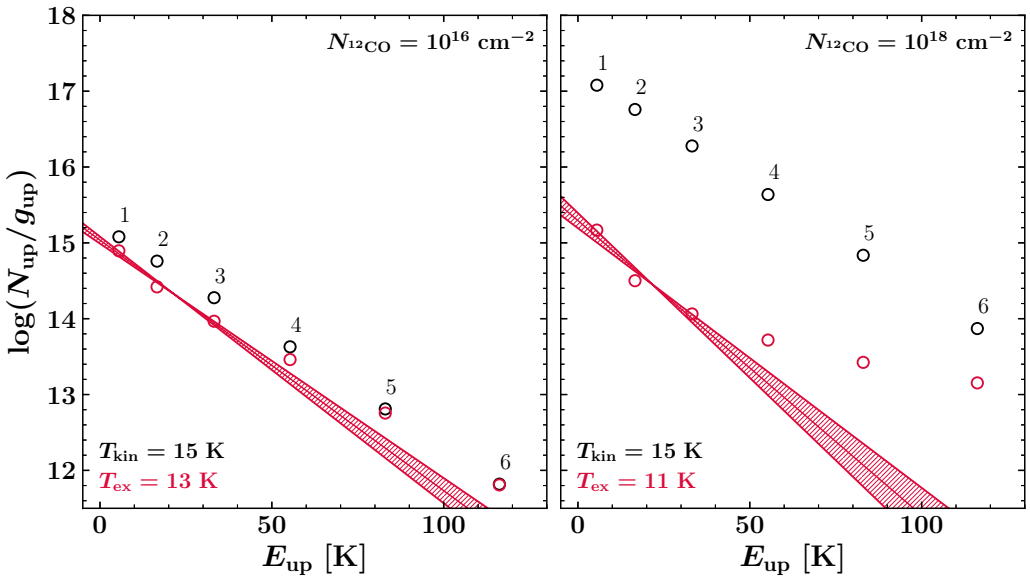

Figure 4.3 Synthetic population diagrams produced with RADEX using distinct total ^{12}CO column densities in the input. *Left:* $N_{^{12}CO} = 10^{16}$ cm^{-2}. *Right:* $N_{^{12}CO} = 10^{18}$cm^{-2}. The other parameters remain fixed: $T_{kin} = 15$ K, $\Delta v = 1$ km s^{-1}, $T_{bg} = 2.7$ K, $n_{H_2} = 10^6$ cm^{-3}. The black data points correspond to the exact values of the upper level populations for $J_u = 1 - 6$, whereas the red data points correspond to the upper level populations inferred from the modelled intensities of the transitions (*via* Eq. 4.30, *i.e.* not corrected for line opacity). We indicate the excitation temperature inferred from a linear fit of the level populations $J_u = 1 - 3$.

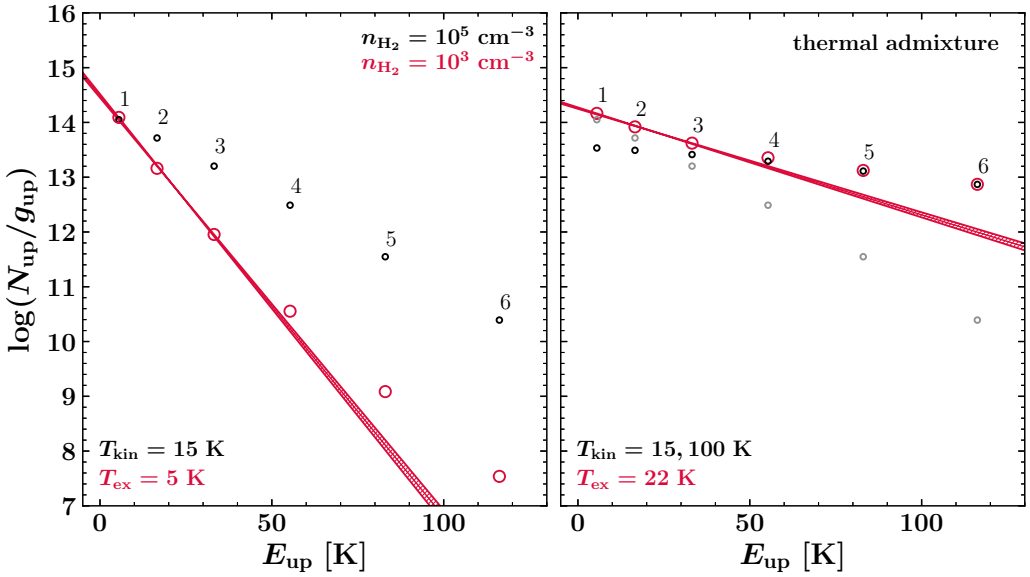

Figure 4.4 Synthetic population diagrams produced with RADEX using distinct input parameters. *Left:* $n_{H_2} = 10^5$ cm^{-3} (black data points) and $n_{H_2} = 10^3$ cm^{-3} (red data points). The other parameters remain fixed: $N_{^{12}CO} = 10^{15}$, $T_{kin} = 15$ K, $\Delta v = 1$ km s^{-1}, $T_{bg} = 2.7$ K. *Right:* thermal admixture model produced with a sum of two components: *i.)* $N_{^{12}CO} = 10^{15}$cm^{-2}, $T_{kin} = 15$ K (gray data points); *ii.)* $N_{^{12}CO} = 10^{14}$cm^{-2}, $T_{kin} = 100$ K (black data points). The sum of the two components is represented by red data points. The other parameters remain fixed: $\Delta v = 1$ km s^{-1}, $T_{bg} = 2.7$ K, $n_{H_2} = 10^6$ cm^{-3}. We indicate the excitation temperatures inferred from linear fits of the level populations $J_u = 1 - 3$.

Synthetic population diagrams with RADEX In order to illustrate the impact of the different RADEX input parameters and to demonstrate the value and limitations of the population diagram analysis, we produced several synthetic population diagrams of ^{12}CO with the radiative transfer code (see Fig. 4.3, Fig. 4.4). In each case, we modelled the $J_u = 1 - 6$ level populations of ^{12}CO (N_u) and studied distinct input parameters separately.

1. *Total column density variations: line opacity caveats*. In Fig. 4.3, we study the impact of the line opacity τ_{ul}. We produced two models with distinct total column densities (left diagram: $N_{^{12}CO} = 10^{16}$ cm^{-2}, right diagram: $N_{^{12}CO} = 10^{18}$ cm^{-2}). Following Eq. 4.39, the optical depth increases with the column density if the line width Δv (km s^{-1}) remains constant. In each diagram, we represent the true level populations (in black) and the level populations inferred from the line fluxes with Eq. 4.31 (in red). Using Eq. 4.31 to estimate the upper level populations signifies that we are ignoring the impact of the optical depth.

   The population diagrams show that the saturation of the lines causes the N_u measurements to decouple from the true distribution as the optical depth increases. Additionally, the excitation temperature inferred from the linear fit of the $J_u = 1 - 3$ data points deviates from the kinetic temperature, because the opacity of the J=2–1 and J=3–2 lines are higher than the opacity of the J=1–0 line. This simple test shows that it is mandatory to correct the opacity of the lines (using Eq. 4.32 and Eq. 4.33) to recover the total column density and not to introduce a bias in the excitation temperature estimate.

2. *Local density variations: deviations from LTE*. In Fig. 4.4 (left panel), we study the impact of the density of collisional partners. We produced two models with $n_{H_2} = 10^5$ cm^{-3} and $n_{H_2} = 10^3$ cm^{-3}. These densities should be compared with the critical densities of ^{12}CO lines (see Tab. 4.4). Our population diagram analysis shows that the excitation temperature inferred from the lower density model leads to a lower estimate of the kinetic temperature of the gas ($T_{ex} = 5$ K *v.s.* $T_{kin} = 15$ K). This discrepancy is due to the limitations of the population diagram analysis when assumptions are not met: at $n_{H_2} = 10^3$ cm^{-3}, the ^{12}CO lines are significantly subthermal. We experimented with various densities to estimate the impact of the local density on the thermalization of the lines. Even for $n_{H_2} = 10^4$ cm^{-3} the lines are not fully thermalized and the inferred excitation temperature is $T_{ex} = 9$ K. These tests show that the excitation temperature measurement should be interpreted with caution.

3. *Thermal admixture*. In Fig. 4.4 (right panel) we experimented with a 2-temperature model in order to illustrate the effects of temperature stratification along the line of sight. We produced a model based on the sum of two ^{12}CO components: a 'cold' component with $N_{^{12}CO} = 10^{15}$cm^{-2}, $T_{kin} = 15$ K and a 'warm' component with $N_{^{12}CO} = 10^{14}$cm^{-2}, $T_{kin} = 100$ K. The population diagram shows that the $J_u = 4-6$ level populations are dominated by the warm component, and the $J_u = 1$ level population is dominated by the cold component. In this case, the linear fit of the $J_u = 1 - 3$ levels suggests an excitation temperature $T_{ex} = 22$ K, which is a kind of average measurement of the two components.

Chapter 5 | Interstellar dust continuum emission

Contents

Interstellar dust Interstellar dust grains are solid particles of size 0.3 nm $\leq r \leq$ 0.3 µm. Their exact chemical composition is still under scrutiny, but a substantial fraction of dust grains falls into two broad categories: silicates and carbonaceous grains (*e.g.* Min *et al.* 2007, Jones *et al.* 1990). A short list of candidate materials for the bulk of interstellar dust grains includes silicates (pyroxenes, olivine), oxides of silicon, magnesium, iron (SiO_2, MgO, Fe_3O_4), carbon solids (graphite, amorphous carbon, diamond), hydrocarbons, carbides and metallic Fe (Draine, 2011). Dust grains represent less than 1% of the total mass in the ISM, but they account for ~30% of the total infrared luminosity, and they play an important role as catalysts for chemical reactions, including the formation of H_2 (Gould and Salpeter, 1963).

In this chapter, we will rather focus on the modelling of thermal dust emission than on a detailed description of dust characteristics such as chemical composition, structure, shape, size, charging, polarization, *etc* (for a review, the reader is redirected to Draine 2003 and Li 2020). We aim to describe the methods used in Chapter 9 (analysis of continuum emission in the IC443 SNR). In section 5.1, we present the Modified Black Body model (hereafter MBB), and the Bayesian MBB fitting algorithm `PPMAP`. In section 5.2, we present a 'full dust model' approach based on the hierarchical Bayesian algorithm `HerBIE` combined with the THEMIS[1] dust model. In section 5.3, we discuss the gas-to-dust mass ratio.

[1] https://www.ias.u-psud.fr/themis/THEMIS_model.html

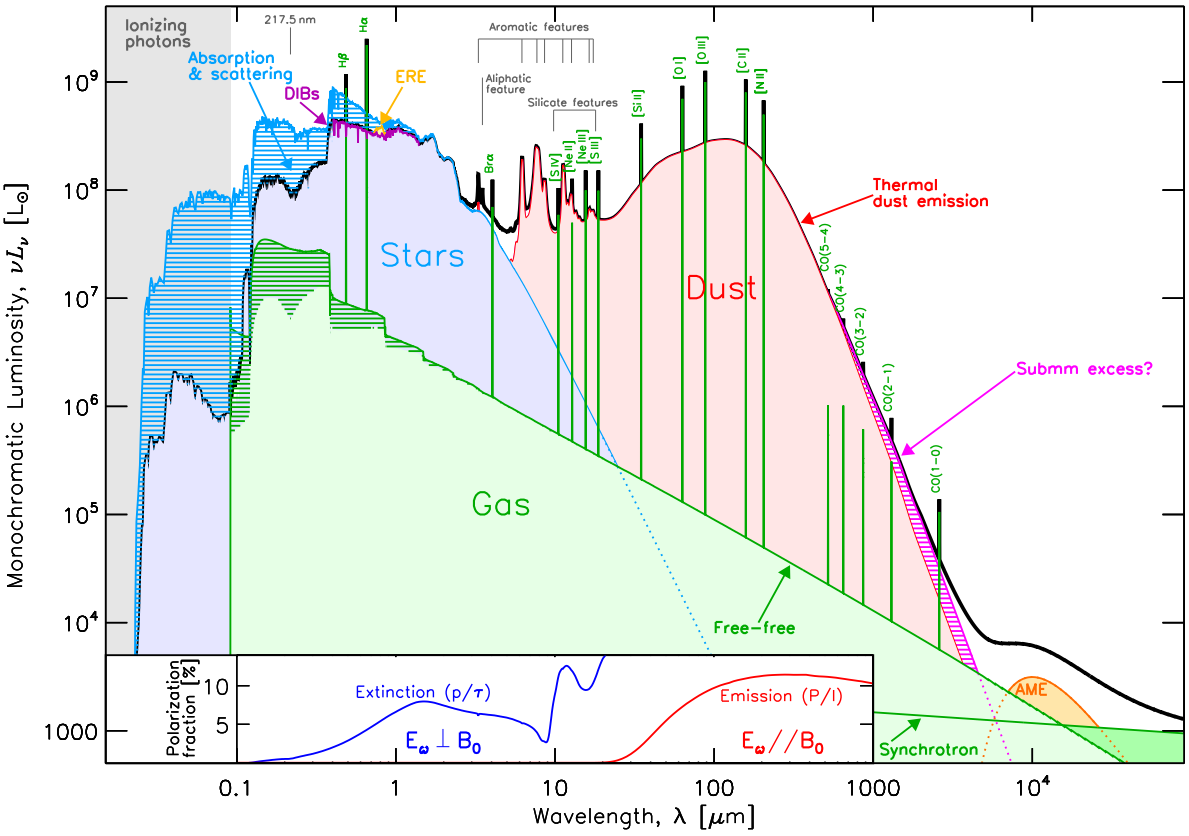

Figure 5.1 Spectral energy distribution of a typical late-type galaxy. The blue hatched area shows the power absorbed by dust. Figure reproduced from Galliano *et al.* (2018). DIBS, ERE and AME respectively stands for Diffuse Interstellar Bands, Extended Red Emission and Anomalous Microwave Emission.

5.1 | Modified Black Body models (MBB)

5.1.1 Spectral energy distribution of dust thermal emission

Heating and cooling of dust grains When an optical or UV photon (*e.g.* from ambient starlight) is absorbed by a dust grain, an electron is raised in an excited electronic state. Electronically excited states deexcite nonradiatively with the energy going into several vibrational modes, which results in increasing the heat content of the grain. The heat accumulated by dust grains is removed mainly *via* radiative cooling (although chemical and photoelectric cooling can be non-negligible), in the form of near-infrared to millimeter radiation. The energy gain of a grain following absorption is given by (*e.g.* Draine 2011):

$$E_{\rm abs} = \int_0^\infty \underbrace{4\pi a^2}_{\text{grain surface}} \quad \underbrace{Q_{\rm abs}(\nu)\pi\frac{cu_\nu}{4\pi}}_{\text{energy absorbed (erg cm}^{-2}\text{ Hz}^{-1})} \quad {\rm d}\nu \tag{5.1}$$

where u_ν is the local energy density of the radiation field, a is the dust grain radius and $Q_{\rm abs}(\nu)$ is the absorption efficiency at the frequency ν. $Q_{\rm abs}(\nu)$ can be approximated as a power law in frequency (Draine, 2011):

$$Q_{\rm abs}(\nu) = Q_0(\nu/\nu_0)^\beta = Q_0(\lambda/\lambda_0)^{-\beta} \tag{5.2}$$

where 'β' is referred to as the opacity index. As said above, grains lose energy *via* infrared emission. The energy loss by emission can be written as follows:

$$E_{\rm em} = \int_0^\infty \underbrace{4\pi a^2}_{\text{grain surface}} \underbrace{Q_{\rm abs}(\nu)\pi B_\nu(T_{\rm d})}_{\text{power emitted (erg cm}^{-2}\text{ Hz}^{-1})} \, {\rm d}\nu \tag{5.3}$$

where $B_\nu(T_{\rm d})$ is the blackbody emission at the temperature of the grain $T_{\rm d}$. Fig. 5.1 shows a generic spectral energy distribution (SED) corresponding to a typical late-type galaxy, in which the thermal contribution of dust is shown in red. Two distinct heating regimes are required to describe two different domains of the spectral energy distribution, which are related to distinct populations of interstellar dust grains. These two distinct dust heating regimes are the following:

i.) **Thermal equilibrium (large grains)** Dust grains with large radii ($r \geq 0.02$ μm) have a greater enthalpy than the mean energy of photons that they absorb. Thus, a single photon absorption event does not significantly alter their temperature and their thermal energy can be considered nearly constant, *i.e.* the assumption that $E_{\rm abs} = E_{\rm em}$ holds at any time. Under this assumption, the 'steady state' thermal emission of equilibrium dust grains is characterized by the Planck function $B_\nu(T_{\rm d})$, where $T_{\rm d}$ is the dust temperature (see Eq. 5.1 and Eq. 5.3):

$$B_\nu(T_{\rm d}) = \frac{2h\nu^3}{c^2} \frac{1}{\exp\left(\dfrac{h\nu}{k_{\rm B}T_{\rm d}}\right) - 1} \tag{5.4}$$

where h is the Planck constant, ν the radiation frequency, c the light speed and $k_{\rm B}$ the Boltzmann constant. In Fig. 5.1, this cooling regime produces the characteristic black body radiation between 10^2 μm and 10^4 μm.

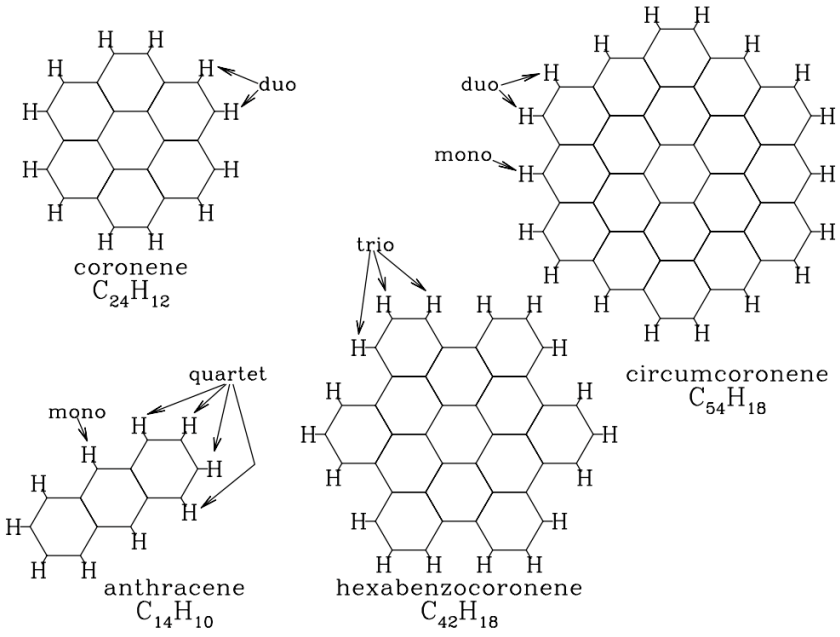

Figure 5.2 Structure of four PAHs. Examples of singlet, doublet, trio and quartet H atoms are indicated. Figure reproduced from Draine (2011).

***ii.)* Stochastic heating (small grains)** On the opposite, stochastic heating refers to the regime that applies to small grains ($r \leq 0.02$ μm). Because they have smaller cross sections, small grains are less likely to interact with photons. However, a single photon will cause a significant temperature spike (a few hundred Kelvin) when absorbed by a small dust grain, hence this population is out of equilibrium due to transient heating (Draine and Anderson, 1985). In this case, the temperature of grains is a fluctuating quantity, and to calculate the emission from small, stochastically heated grains requires to take into account the probability distribution function of the temperature dP/dT, where $P(T)$ is the probability that a grain will have a temperature less than or equal to T (therefore, the dust thermal emission is not characterized by a plain Planck function at a single temperature $B_\nu(T_\mathrm{d})$).

In Fig. 5.1, thermal emission from out-of-equilibrium dust grains is confined in the $\lambda \leq 10^2$ μm part of the spectral energy distribution, in addition to the contribution from polycyclic hydrocarbons (hereafter PAHs, see Fig. 5.2). Conspicuous features at 3.3 μm, 6.2 μm, 7.7 μm, 8.6 μm, 11.3 μm, and 12.7 μm correspond to the vibrational spectrum of a collection of aromatic bonds in a hydrocarbon matrix. In fact, the observed aromatic features are likely to arise from a statistical mixing of PAHs of different sizes and structures (Duley and Williams 1981, Leger and Puget 1984).

It follows that studying the thermal emission of dust grains for $\lambda \leq 10^2$ μm requires to adopt a stochastic heating model and to include the contribution of PAHs. In the current section, we will restrict our analysis to the emission of large dust grains, for which the emission is characterized by a trivial modified black body radiation (in IC443, we aim to measure the mass of dust grains, which is primarily traced by the emission of large equilibrium grains). In section 5.2, we present a model that accounts for the emission of small grains.

5.1.2 Standard analysis of thermal emission from large dust grains

The modified black body approximation The modified black body (MBB) is the most widely used approximation for the analysis of thermal emission from dust grains at $\lambda \geq 10^2$ μm. Under the MBB approximation, the IR luminosity $L_\nu(\lambda)$ produced by a population of large dust grains is given by (*e.g.* Galliano *et al.* 2018):

$$L_\nu(\lambda) = M_\mathrm{d}\kappa(\lambda_0)\left(\frac{\lambda_0}{\lambda}\right)^\beta 4\pi B_\nu(\lambda, T_\mathrm{d}) \tag{5.5}$$

where M_d is the total dust mass, T_d is the dust temperature and B_ν is the Planck function (see also Eq. 5.4). $\kappa(\lambda_0)$ is the reference dust mass absorption coefficient (cm^2 g^{-1}) at $\lambda = \lambda_0$ (see Eq. 5.1, Eq. 5.2). The parametric opacity $\kappa(\lambda) = \kappa(\lambda_0)(\lambda_0/\lambda)^\beta$ allows to take into account variation of the absorption coefficient with respect to the wavelength. In Eq. 5.5, T_d provides a constraint on the physical condition of the grains, and the parameter β of the power law provides a constraint on their composition, since different materials can have different β.

Limitations (assumptions) Using Eq. 5.5 to model dust emission relies on strong assumptions. Eq. 5.5 assumes that the emission comes from identical grains (single value of β), at a single temperature T_d, with a power-law dust mass absorption coefficient. A gradient of temperature along the line of sight will broaden the spectral energy distribution, hence a mixing of physical conditions would bias the estimate obtained under this approximation (*e.g.* Hunt *et al.* 2015).

In addition, there is an inverse correlation between the emissivity spectral index and dust temperature (Paradis *et al.*, 2010), and unexpected variations in the FIR dust emissivity (500 µm excess, Paradis *et al.* 2012). Malinen *et al.* (2011) also showed that line-of-sight temperature variations can lead to underestimates in mass, and Planck Collaboration *et al.* (2014b) reported an increase of the dust opacity at 353 GHz from the diffuse to the denser ISM. Finally, this approximation is only valid for large dust grains (*i.e.* for $\lambda \geq 10^2$ µm), since it cannot reproduce the emission from stochastically heated small dust grains nor PAH features.

Standard procedure for pixel-per-pixel SED fitting Assuming that one has a sample of mapped observations at $\lambda \geq 10^2$ µm, the standard MBB fitting procedure is the following (*e.g.* Könyves *et al.* 2010, Peretto *et al.* 2010, Bernard *et al.* 2010):

1. First smooth the maps to a common resolution (*i.e.* to the coarsest resolution available). This is done by convolving the maps with a suitable gaussian kernel, which causes the information carried by spatial frequencies lower than the coarsest resolution to be lost. A variant of this technique relies on spatial filtering to restore spatial resolution (Palmeirim *et al.* 2013, Marsh *et al.* 2015).

2. Then in each spatial bin of the map (pixel), determine the best-fit parameters M_d, β and T_d (see Eq. 5.5) with respect to the data points. At least three data points at distinct frequencies are required to constrain these parameters.

5.1.3 Point Process Mapping (PPMAP)

5.1.3.1 Description of the algorithm

The *Point process mapping* procedure (hereafter PPMAP, Marsh *et al.* 2015, Marsh *et al.* 2017) is an iterative Bayesian fitting algorithm that allows to account for mixing of physical conditions along the line of sight (both dust temperature gradients and variations of the opacity index β). PPMAP is based on the point process formalism (Richardson and Marsh 1987, Richardson and Marsh 1992). In contrast to regular modified blackbody fitting procedures, PPMAP does not require to degrade the set of input observations to the poorest common resolution. Given a set of observational data of dust continuum emission with different instrumental resolutions, PPMAP produces resolution-optimized maps of the dust column density and temperature, taking into account line of sight temperature variations and knowledge of the point spread function (hereafter PSF) of the instruments that were used to perform the observations.

Point process The point process formalism is described in details by Marsh *et al.* (2015). It allows to represent any real astrophysical system by a collection of primitive components (or 'objects'), each corresponding to a set of physical parameters. The entire system is represented by a distribution of points in a suitably defined state space: position on the sky (x, y), dust temperature T_d, opacity index β and dust optical depth $\tau_\mathrm{d}(\lambda)$ (*i.e.* the dimensions corresponding to the properties of the system). For each 'object', the state space is divided into a grid of N cells corresponding to the total number of states, in which a vector $\mathbf{\Gamma}$ defines the position of each component, *i.e.* their respective physical state, since the coordinates of the points define their physical properties. PPMAP is built such that each 'object' is defined to have a unit column density and a gaussian

spatial profile (with a full width at half maximum of 2 pixels), so that the local density of points corresponds to the local optical depth of dust with a given sky position, temperature and opacity index. In other words, the column density in any cell is defined by the occupation number. Thus, the total measurement model is defined by:

$$\mathbf{d} = \mathbf{A\Gamma} + \mu \tag{5.6}$$

where $\mathbf{d}$ is the measurement vector. The m^{th} component of $\mathbf{d}$ represents the pixel value at the location (x_m, y_m) in the observed image at wavelength λ_m, and μ is the adopted measurement noise (assumed to be gaussian). Finally, $\mathbf{A}$ is the system response matrix. In the response matrix, the mn^{th} element corresponds to the response of the m^{th} measurement to an 'object' which occupies the n^{th} cell in the state space (spatial position x_n, y_n, temperature T_n). The response matrix contains the thermal emission approximation used by `PPMAP`.

Multi-temperature MBB emission modelling `PPMAP` assumes that the radiation emitted by dust at all observed wavelengths is optically thin, such that the system response matrix $\mathbf{A}$ is given by the following MBB approximation:

$$A_{mn} = H_{\lambda_m}(x_m - x_n, y_m - y_n) K_{\lambda_m}(T_n) B_{\lambda_m}(T_n) \kappa(\lambda_m) \Delta\Omega_m \tag{5.7}$$

where H_λ is the convolution of the PSF at wavelength λ, $K_\lambda(T)$ a possible color correction (taking into account the finite bandwidth of the observations), $B_\lambda(T)$ the Planck function, $\kappa(\lambda)$ the dust opacity law and $\Delta\Omega$ the solid angle corresponding to a given pixel of the output map. H_λ is the parameter that allows `PPMAP` to work without degrading the spatial resolution of input maps, and to inform model estimation through high fidelity beam profiles. Following Eq. 5.5, the wavelength variation of the `PPMAP` dust opacity law is parametrized by the opacity index β:

$$\beta = -\frac{d\ln(\kappa_\lambda)}{d\ln(\lambda)} \tag{5.8}$$

Hence, for any λ the dust opacity law κ_λ can be written:

$$\kappa(\lambda) = \kappa_{300} \left(\frac{\lambda}{300\ \mu\text{m}} \right)^{-\beta} \tag{5.9}$$

where β is the opacity power-law index and $\kappa_{300} = 0.1\ \text{cm}^2\text{g}^{-1}$ the reference opacity (measured at $\lambda_0 = 300\ \mu$m) corresponding to the total mass (dust *and* gas). The value of the dust absorption coefficient used by `PPMAP` ($\kappa_{300} = 0.1\ \text{cm}^2\text{g}^{-1}$) is consistent with a gas-to-dust mass ratio of 100 (Hildebrand, 1983).

Iterative minimization In Eq. 5.7, the physical parameters that we aim to minimize using `PPMAP` are the dust temperature T_n and the dust absorption coefficient $\kappa(\lambda_m)$ (*i.e.* the opacity power-law index β_n). Firstly, `PPMAP` initializes a uniform array of small column density quanta, and then generates the corresponding synthetic map, which can be compared with the real maps (using synthetic noise). Throughout the fitting procedure and in each pixel of the maps, `PPMAP` minimizes the reduced-χ^2 derived from the sums of squares of deviations between the response matrix $\mathbf{A}$ components and the corresponding observations. Using a Bayesian process (described in

details by Marsh *et al.* 2015, section 2.3), the distribution of points in the state space is iteratively updated until the model converges to the observations.

5.1.3.2 Practical aspects

`PPMAP` can be downloaded on the Github page of A. Howard[2] and built from source. The program is shipped with two executables (`premap` and `ppmap`) that require the compiler `ifortran` (for parallel computing). In the next paragraphs, we provide a quick, practical description of the program and basic user guidelines.

Input files `PPMAP` requires two sets of input `FITS` files:

1. The intensity measurement maps at wavelengths λ_1, ... λ_i (in MJy/sr). For example, one could use *Herschel* maps at 70 µm, 160 µm, 250 µm, 350 µm and 500 µm (*e.g.* Howard *et al.* 2019).

2. The instrumental PSF associated with the intensity measurements at wavelengths λ_1, ... λ_i. If the exact instrumental PSFs are not known, gaussian profile synthetic PSFs can be used as an approximation.

Algorithm 2: Example of `PPMAP` input parameters (`premap.inp` file).

94.181	<gloncent> ; gal. lon. (or RA) at centre [deg];
22.567	<glatcent> ; gal. lat. (or Dec) at centre [deg];
0.35 0.35	<fieldsize>; field of view dimensions [deg];
15.	<pixel> ; output sampling interval [arcsec];
0.3	<dilution> ; a priori dilution ;
500	<maxiterat>; max no. of integration steps;
1800.	<distance> ; [pc];
0.1	<kappa300> ; reference opacity [cm2/g];
5	<nbeta> ; number of opacity law index values;
1.6 1.7 1.8 1.9 2.	<betagrid> ; opacity law index values;
2. 0.25	<betaprior>; a priori mean and sigma of beta;
40	<ncells> ; nominal size of subfield;
20	<noverlap> ; size of subfield overlap;
3	<Nt> ; number of temperatures;
12. 22.	<temprange>; range of temperatures [K];
7	<nbands> ; number of bands;
70. 90. 140. 160. 870. 1150. 2000.	<wavelen> ; wavelengths [microns];
0.65 0.8 1.84 1.9 0.6 0.17 0.021	<sigobs>;
<obsimages>; list of FITS files follows;	
70.fits;	
90.fits;	
140.fits;	
160.fits;	
870.fits;	
1150.fits;	
2000.fits;	

[2] https://github.com/ahoward-cf/ppmap

Input parameters PPMAP input parameters are set by multiple entries in a plain text file (`premap.inp`, see the example shown in the 'algorithm 2'):

- **Input observations.** The input files that PPMAP works with are set *via* the entries `nbands`, `wavelen`, `sigobs` and `obsimages`. `nbands` is the total number of input maps, `obsimages` is a list of the FITS files names and `sigobs` is a list of measurement uncertainties. `wavelen` contains a list of the corresponding wavelengths. The input PSF FITS files should be named after the `wavelen` list in order to be correctly read by PPMAP (*e.g.* in our example: `psf_0070.fits`, ... `psf_02000.fits`).

- **Assumptions.** The `distance` parameter corresponds to the distance of the astronomical object (in parsecs), and `kappa300` is the reference dust opacity at 300 μm (in $\mathrm{cm^2\ g^{-1}}$).

- **Definition of the field** `gloncent` and `glatcent` are the coordinates at the center of the field, and `fieldsize` defines the size of the field along the 'RA' and 'Dec' axes ($0.35^\circ \times 0.35^\circ$ in the example).

- **Spatial sampling and definition of the mosaic** In order to reduce computation time, PPMAP can perform the calculations on sub-fields, and rebuild the entire image at the end of the process. The input parameter `pixel` defines the size of the map spatial bins (in arcseconds), and `ncells` sets the size of a sub-field in units of spatial bins. In our example, we use $15''$ pixels and $40 \times 15 = 600''$ sub-fields. The size of sub-fields determines the number of fields in the mosaic, hence the computation time. `noverlap` is the size of the overlaps between sub-fields. With `noverlap` = 0.5 `ncells` (which is the recommended value) and $600''$ sub-fields, a 3×3 mosaic is required to map the $0.35^\circ \times 0.35^\circ$ field.

- **Opacity index grid.** The input parameters `nbeta`, `betagrid` and `betaprior` respectively define the number of elements in the β grid of parameters, the list of β and the *a priori* values of $\overline{\beta}$ and σ_β (mean and rms).

- **Temperature grid.** The input parameters `Nt` and `temprange` respectively define the number of elements in the T_d grid of parameters and the boundaries (T_min, T_max) of the adopted dust temperature. PPMAP adopts a set of `Nt` logarithmically spaced temperatures between T_min and T_max (in our example: T_d = 12 K, 16.25 K, 22 K).

- **Minimization parameters.** `maxiterat` is the maximum number of integration steps allowed in each sub-field. PPMAP interrupts the calculations when `maxiterat` is reached. The `dilution` input parameter characterizes the degree to which the procedure is forced to represent the data with the least number of 'objects' (*e.g.* with the least number of MBB components with distinct dust temperatures T_d). Values in the range 0.01-1 are recommended.

General guidelines for PPMAP modelling Once PPMAP is installed, calculations are performed by applying the following steps[3]:

[3]Before we started the analysis of dust thermal emission in IC443, we benchmarked the use of PPMAP on a distinct project in collaboration with members of the ALMA-IMF consortium. We have performed the analysis of *Herschel*, SABOCA, LABOCA and ALMA observations of the massive star-forming region W43 (Motte *et al.*, 2018).

1. Gather mapped observations (FITS files) of continuum emission ($\lambda \geq 10^2$ μm) in units of MJy/sr in a working directory (*e.g.* 'IC443'), and the corresponding PSF FITS files in the same directory as the premap and ppmap executables.

2. Set up a suitable input parameter table based on the template provided in the 'algorithm' 2.

3. In a UNIX shell environment in which the ifortran compiler is installed, run the premap executable by typing *e.g.* '`./premap IC443`' (assuming that the input parameters file is named '`IC443_premap.inp`'). The premap program will prepare the mosaic and the corresponding '`ppmap.inp`' file.

4. In a UNIX shell environment, run the ppmap executable by typing *e.g.* '`./ppmap IC443 1 9 mosaic`' (assuming that the premap has prepared a 3×3 mosaic).

PPMAP prints the values of χ^2 as it progresses through the iterative steps, allowing to monitor the calculations for each sub-field. At the end of the computations, PPMAP prints both the global value of χ^2 and the total mass (in units of $M_\odot$), and saves the output files in the working directory.

output FITS file	physical quantity	definition	unit	data format
cdens	tot. column density	$N_{\rm tot}$	10^{20} cm^{-2}	$N_x \times N_y$
tdenscube	diff. column density	$N(T_{\rm d},\beta)$	10^{20} cm^{-2}	$N_x \times N_y \times N_{T_{\rm d}} \times N_\beta$
sigtdenscube	uncertainty	$\sigma[N(T_{\rm d},\beta)]$	10^{20} cm^{-2}	$N_x \times N_y \times N_{T_{\rm d}} \times N_\beta$
temp	dust temperature	$T_{\rm d}$	Kelvin	$N_x \times N_y$
tvar	temperature variance	$\frac{1}{N-1}\sum_{k=1}^{N}(T_{{\rm d},k}-\overline{T_{\rm d}})^2$	Kelvin	$N_x \times N_y$
tskew	temperature skewness	$\frac{1}{N}\sum_{k=1}^{N}\left[(T_{{\rm d},k}-\overline{T_{\rm d}})/\sigma\right]^3$	dimensionless	$N_x \times N_y$
tkurt	temperature kurtosis	$\left\{\frac{1}{N}\sum_{k=1}^{N}\left[(T_{{\rm d},k}-\overline{T_{\rm d}})/\sigma\right]^4\right\}-3$	dimensionless	$N_x \times N_y$
beta	opacity index	β	dimensionless	$N_x \times N_y$
rchisq	reduced χ^2	χ^2	dimensionless	$N_x \times N_y$

Notes. In the mathematical definitions of the dust temperature skewness and kurtosis, σ stands for the square root of the dust temperature variance: $\sigma = \sqrt{\frac{1}{N-1}\sum_{k=1}^{N}(T_{\rm d,k}-\overline{T_{\rm d}})^2}$.

Table 5.1 PPMAP output files.

Output files At the end of the calculations, PPMAP returns a total of 9 FITS files, presented in Tab. 5.1. If PPMAP is given a grid of N dust temperatures and M opacity indices, the program returns a differential column density cube of dimensions $N_x \times N_y \times N \times M$, where N_x and N_y are the spatial dimensions. The total column density map $N_{\rm tot}$ is the sum over all the 'objects' stored in the differential column density cube $N_(T_{\rm d},\beta)$:

$$N_{\rm tot} = \sum_{k=1}^{N}\sum_{l=1}^{M} N(T_{{\rm d},k},\beta_l) \tag{5.10}$$

Similarly, the dust temperature and opacity index maps are defined by the following average quantities, with respect to the differential column density cube:

We have obtained dust temperature maps of the W43-MM1 and W43-MM2 ridges. Our results will be presented in Motte *et al.*, in prep and Pouteau *et al.*, in prep.

$$T_{\rm d} = \frac{1}{N_{\rm tot}} \sum_{k=1}^{N} \sum_{l=1}^{M} \{T_{{\rm d},k} N(T_{{\rm d},k}, \beta_l)\} \tag{5.11}$$

$$\beta = \frac{1}{N_{\rm tot}} \sum_{k=1}^{N} \sum_{l=1}^{M} \{\beta_l N(T_{{\rm d},k}, \beta_l)\} \tag{5.12}$$

Finally, in virtue of Eq. 5.7, the `PPMAP` synthetic intensity at wavelength λ in any pixel is defined by the following double sum:

$$I_\lambda = \sum_{k=1}^{N} \sum_{l=1}^{M} \left\{ \left(\frac{N(T_{{\rm d},k}, \beta_l)}{2.1 \times 10^{24}\ {\rm cm}^{-2}} \right) \left(\frac{\lambda}{300\ \mu{\rm m}} \right)^{-\beta_l} B_\lambda(T_{{\rm d},k}) \right\} \tag{5.13}$$

where $N(T_{{\rm d},k}, \beta_l)/2.1 \times 10^{24}\ {\rm cm}^{-2} = \tau_{300}$ is the optical depth at 300 μm assuming a dust opacity $\kappa_{300} = 10\ {\rm cm}^2\ {\rm g}^{-1}$, fractional abundance by mass of hydrogen and molecular hydrogen $X_{\rm H} = 0.7$, $X_{\rm H_2} = 1$, and fractional abundance by mass of dust $Z_{\rm D} = 0.01$ (Howard *et al.* 2019, Howard *et al.* 2021). This equation allows to produce synthetic intensity maps and/or synthetic spectral energy distributions from the '`tdenscube.fits`' output returned by `PPMAP`. The equation can also be applied to the '`sigtdenscube.fits`' output in order to obtain the uncertainties on I_λ.

Remarks on the temperature 'skewness' and 'kurtosis' The dust temperature skewness and kurtosis are respectively the third and fourth moments of the dust temperature, defined in the third column of Tab. 5.1. These quantities are nondimensional, and only characterize the shape of the distribution of temperatures in each pixel.

In statistics, the skewness characterizes the degree of asymmetry of a distribution around its mean. In this context, a positive value of skewness corresponds to a distribution with an asymmetric tail extending towards more positive temperatures, and a negative value signifies a distribution whose tail extends towards more negative temperatures. The kurtosis measures the relative peakedness or flatness of the temperature distribution relative to a normal distribution (hence the normalization constant '-3' in the definition). In this context, a positive value of kurtosis corresponds to a *leptokurtic* distribution (relatively peaked), and a negative value traces a *platykurtic* distribution (relatively flat).

5.2 | Introduction to an accurate interstellar dust emission model

In the previous section, we described the MBB approximation, which is valid for $\lambda \geq 10^2$ μm. In order to study lower wavelength dust continuum emission, 'full dust models' with stochastic heating and accurate description of dust grains are required (see Fig. 5.1). A model for interstellar dust must specify the composition, geometry and mixture conditions of the dust particles (chemical composition, structure, icy mantles, shape, size, abundance relative to gas, *etc*).

5.2.1 The Heterogeneous dust Evolution Model for Interstellar Solids (THEMIS)

The Heterogeneous dust Evolution Model for Interstellar Solids[4] (hereafter THEMIS) is an interstellar dust modelling framework (see Jones *et al.* 2017 and references therein). THEMIS takes into account the dust structure, composition and evolution in response to the local physical conditions in the ambient medium: density, radiation field intensity and hardness, gas dynamics, *etc* (Jones *et al.* 2013, Köhler *et al.* 2014, Jones *et al.* 2014, Köhler *et al.* 2015, Ysard *et al.* 2015, Jones and Ysard 2019). THEMIS was initially oriented towards diffuse ISM studies, but the model was extended in order to explore the evolution of the dust optical properties in denser molecular regions by including accurate treatments of dust coagulation and accretion processes (Köhler *et al.* 2012, Köhler *et al.* 2015).

Scattering cross sections The dust chemical composition and structure directly affects dust optical properties (the complex indices of refraction $m = n + ik$). THEMIS is built upon laboratory measurements of dust optical properties on interstellar dust analogue materials (amorphous hydrocarbon materials, amorphous olivine-type and pyroxene-type silicates with iron and iron sulphide nano-inclusions). The optical constants are used to derive the dust cross-sections for extinction (i = ext), absorption (i = abs) and scattering (i = sca):

$$C_i(a, \phi, \xi, \lambda) = \pi a^2 Q_i(a, \phi, \xi, \lambda) \tag{5.14}$$

where Q is the absorption efficiency (see also Eq. 5.1), a is the particle radius, λ the wavelength and (ϕ, ξ) are indices referring to the dust grain material and structure. Hence, a dust mixture with distinct chemical compositions, sizes and structures is characterized by a combination of different extinction, absorption and scattering cross sections.

Dust grain structure, size and composition distributions The THEMIS diffuse ISM dust model provides the following grain structure and composition distributions[5]

- A power-law distribution of a-C nano-particles ($a < 20$ nm) with strongly size-dependent optical properties and a size distribution that is sensitive to the local radiation field.
- A log-normal distribution ($a \sim 160$ nm) of large a-C(:H) core/mantle grains with a-C mantles (depth ~ 20 nm) surrounding a-C:H cores.
- A log-normal distribution ($a \sim 140$ nm) of large a-Sil(Fe,FeS) grains with a-C mantles (depth $\sim 5 - 10$ nm) formed by carbon accretion and the coagulation of a-C nano-particles onto their surfaces.

In order to study dense regions, the core diffuse ISM model is updated by sequentially accreting carbon from the gas to form secondary a-C:H mantles, coagulating the dust grains into aggregate particles and then accreting ice mantles.

[4] https://www.ias.u-psud.fr/themis/THEMIS_model.html
[5] see also https://www.ias.u-psud.fr/themis/

5.2.2 Hierarchical Bayesian Inference for dust Emission (HERBIE)

HerBIE is hierarchical Bayesian inference code (see section 5.2.2.2 for a basic description of Bayesian inference) developed by F. Galliano (Galliano, 2018). In contrast to MBB codes (*e.g.* PPMAP, see section 5.1.3, see also Juvela *et al.* 2013, Veneziani *et al.* 2013), HerBIE works with 'full dust models' such as THEMIS, hence it can use several types of grains, accurate optical properties, size distributions, stochastic heating and mixing of physical conditions.

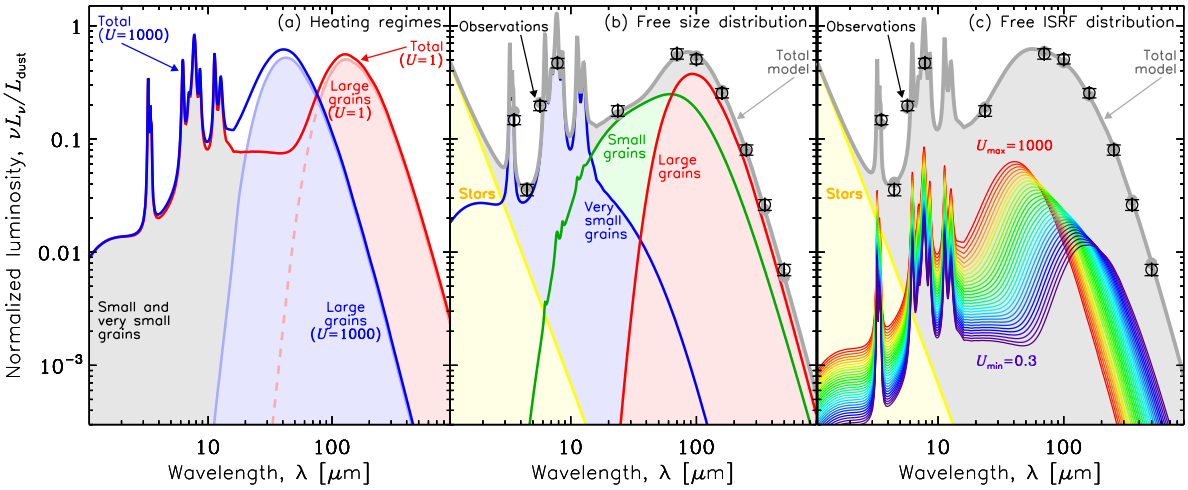

Figure 5.3 Phenomenological SED modelling. *(a)* Dust emission model of the Milky Way (Jones *et al.*, 2017), heated by the ISRF of the diffuse ISM ($U = 1$; red) and a thousandfold larger ISRF ($U = 1000$; blue). It demonstrates that the shape of the SED of small, out-of-equilibrium grains (grey), is independent of U. On the contrary, the shape of the SED of large grains, which are at equilibrium with the ISRF, shifts to shorter wavelengths when U increases, as their equilibrium temperature increases. *(b)* Simulated broadband observations (black), fitted by varying the mass fractions of very small (0.35 nm $\leq r <$ 1.5 nm; blue), small (1.5 nm $\leq r <$ 20 nm; green) and large (0.02 μm $\leq r <$ 0.3 μm; red) grains, with a single $U = 8$ (fitted). *(c)* Same simulated observations as in panel *(b)*, alternatively fitted with a starlight intensity distribution ($\propto U^{-\alpha}$; rainbow curves). Figure reproduced from Galliano *et al.* (2018).

5.2.2.1 Emission components

In order to reproduce input observations, HerBIE fits a linear combination of SED models components to a set of n sources (pixels) observed through m frequencies (see Fig. 5.3). In this section, we provide a summary of the model components available with HerBIE, following the description by Galliano (2018).

Modified Black Body (MBB) HerBIE can use the widely adopted MBB approximation (see also Eq. 5.5) to model large dust grains. The monochromatic MBB luminosity of a source s_i at frequency ν_j is:

$$L_\nu^{\rm mod}(\nu_j, M_i, T_i, \beta_i) = M_i 4\pi\kappa(\nu_0)\left(\frac{\nu_j}{\nu_0}\right)^{\beta_i} B_\nu(T_i, \nu_j) \tag{5.15}$$

where M_i is the dust mass, T_i the dust temperature and β_i the opacity index. B_ν is the Planck function (see Eq. 5.4), and $\kappa(\nu_0)$ is the reference dust opacity. `HerBIE` uses a dust opacity at reference wavelength $\lambda_0 = 160$ µm, fixed to $\kappa_{160} = 1.4$ m^{2}kg^{-1}. `HerBIE` can also use a refinement of the MBB approximation: the broken emissivity MBB introduced by Gordon *et al.* (2014), accounting for a change of the emissivity slope β at long wavelengths (β_1 for $\nu > \nu_{\rm break}$ and β_2 for $\nu \leq \nu_{\rm break}$, *e.g.* $\lambda_{\rm break} \simeq 480$ µm, Lamperti *et al.* 2019).

Equilibrium dust grains This component is similar to the MBB approximation (see also Eq. 5.3), except that it uses an accurate absorption efficiency $Q_{\rm abs}$ measured in the laboratory instead of using an empirically calibrated power law for the dust absorption coefficient κ. The monochromatic luminosity of a source s_i at frequency ν_j is expressed as:

$$L_\nu^{\rm mod}(\nu_j, M_i, T_i) = M_i \frac{3\pi}{a\rho} Q_{\rm abs}(a, \nu_j) B_\nu(T_i, \nu_j) \tag{5.16}$$

where a is the dust grain radius and ρ the mass density of the material. Since $Q_{\rm abs}/a$ is quasi constant with respect to a in the IR-millimeter range, a is arbitrarily set to 30 nm. $Q_{\rm abs}$ can be chosen in a large database of optical properties (*e.g.* from the THEMIS dust grain model, see Eq. 5.14).

Illuminated dust mixture This component corresponds to an accurate 'full dust model' (more advanced than the MBB approximation). `HerBIE` can use a mixture of grains with different compositions (silicates, amorphous carbons, PAHs, *etc.*) and sizes by implementing the THEMIS distributions (see section 5.2.1) or distributions from other dust models (*e.g.* Zubko *et al.* 2004, Compiègne *et al.* 2011, Galliano *et al.* 2011). The 'illuminated dust mixture' component represents a full ISM dust mixture heated by an interstellar radiation field (hereafter ISRF) with intensity U. The quantity 'U' is a scaling parameter defined such that $J_\nu(\nu) = U J_\nu^\odot(\nu)$, where J_ν is the local intensity of the radiation field, and $J_\nu^\odot$ represents a reference intensity measured in the solar neighborhood (Mathis *et al.*, 1983). The 'illuminated dust mixture' monochromatic luminosity of a source s_i at frequency ν_j is given by:

$$\begin{aligned} L_\nu^{\rm mod}(\nu_j, M_i, U_i, q_i^{\rm PAH}, f_i^+) = M_i [& q_i^{\rm PAH} f_i^+ l_\nu^{\rm PAH^+}(U_i, \nu_j) \\ & + q_i^{\rm PAH}(1 - f_i^+) l_\nu^{\rm PAH^0}(U_i, \nu_j) \\ & + (1 - q_i^{\rm PAH}) l_\nu^{\rm non-PAH}(U_i, \nu_j)] \end{aligned} \tag{5.17}$$

where $q_i^{\rm PAH}$ is the PAH mass fraction (which controls the strength of aromatic features) and f_i^+ is a control parameter that characterizes the ratio between C–C and C–H bands. The terms $l_\nu^{\rm PAH}$, $l_\nu^{\rm PAH^+}$ and $l_\nu^{\rm non-PAH}$ correspond to the monochromatic luminosities of neutral PAH, charged PAH and non-PAH dust grains, which are computed with a stochastic heating method for the adopted distribution of grains (Guhathakurta and Draine, 1989). `HerBIE` can work either with uniformly illuminated (*i.e.* assuming single value of U) or non-uniformly illuminated dust mixtures (*i.e.* assuming a mixing of excitation conditions along the line-of-sight and in the instrumental beam), using a power-law distribution for the radiation field intensity in the latter case (see Fig. 5.3, right-panel).

Near-IR stellar continuum `HerBIE` is able to fit pixels contaminated by starlight using a near-IR stellar continuum component. This component is modelled by assuming a black body emission corresponding to a temperature $T_\star = 50\,000$ K, and adjusting the stellar bolometric luminosity $L_i^\star$ to match the observations of a source s_i at frequency ν_j:

$$L_\nu^{\rm mod}(\nu_j, L_i^\star) = L_i^\star \frac{\pi}{\sigma T_\star^4} B_\nu(T_\star, \nu_j) \tag{5.18}$$

where σ is the Stefan-Boltzmann constant ($\sigma = 5.670 \times 10^{-8}$ W m^{-2} K^{-4}).

Free-free and synchrotron radio continua Finally, an additional component allows to model the millimeter continuum excess produced by free-free and synchrotron emission. This component is based on a linear combination of two power laws:

$$L_\nu^{\rm mod}(\nu_j, L_{1,i}, f_{{\rm FF},i}, \alpha_{s,i}) = \frac{L_{1,i}}{\nu_1} \left(f_{{\rm FF},i} \left(\frac{\nu_j}{\nu_1} \right)^{-0.1} + (1 - f_{{\rm FF},i}) \left(\frac{\nu_j}{\nu_1} \right)^{-\alpha_{s,i}} \right) \tag{5.19}$$

where $L_{1,i}$ is the luminosity at $\lambda = 1$ cm (at $\nu = \nu_1$), $f_{{\rm FF},i}$ is the fraction of free-free emission at $\lambda = 1$ cm and $\alpha_{s,i}$ is the index of the synchrotron power law.

5.2.2.2 Hierarchical Bayesian SED fitting

`HerBIE` is built upon hierarchical Bayesian inference. Traditional non-hierarchical approaches (based on χ^2 minimization) are subject to a strong degeneracy between the dust temperature $T_{\rm d}$ and opacity index β, as they produce a noise-induced false anti-correlation between these two parameters (Shetty *et al.*, 2009). Kelly *et al.* (2012) showed that hierarchical Bayesian analytical MBB models can solve these problems. Hierarchical Bayesian inference is a "*multi-level*" approach in which the dust parameters (mass, temperature, *etc*) are defined by hyper-parameters that control their distributions (it is called a *multi-level* approach for that reason). For example, hyper-parameters such as the average and covariance matrix of the parameter vector {parameter 1, parameter 2, ..., parameter N} can be used (see following developments). In this way, the information on the distribution of parameters has an impact on the likelihood of individual sources (individual sources can be a collection of point sources, or a number of pixels in a map).

Introduction to Bayesian formalism Ignoring systematic uncertainties, the observed spectral energy distribution of a source s at a frequency ν_j ($L_\nu^{\rm obs}(\nu_j)$) is given by the sum of the `HerBIE` emission model $L_\nu^{\rm mod}(\nu_j)$ and a random deviation produced by the noise $\sigma_\nu^{\rm noise}(\nu_j)$:

$$L_\nu^{\rm obs}(\nu_j) = L_\nu^{\rm mod}(\nu_j, \overrightarrow{x}) + \epsilon(\nu_j)\, \sigma_\nu^{\rm noise}(\nu_j) \tag{5.20}$$

where $\epsilon(\nu_j)$ is a random variable with mean $\langle\epsilon\rangle = 0$ and standard deviation $\sigma(\epsilon) = 1$, and $\overrightarrow{x}$ is the corresponding set of input parameters (*e.g.* the mass M, dust temperature T, opacity index β, *etc*). The likelihood that a sample of observed luminosities $\overrightarrow{L}_\nu^{\rm obs} = \left\{ L_\nu^{\rm obs}(\nu_1), \ldots, L_\nu^{\rm obs}(\nu_m) \right\}$ is associated with a set of input parameters $\overrightarrow{x}$ is given by the following conditional probability:

$$p(\overrightarrow{L}_\nu^{\rm obs} | \overrightarrow{x}) = \prod_{j=1}^{m} p(\epsilon(\nu_j, \overrightarrow{x})) \tag{5.21}$$

Assuming a gaussian distribution of the errors on the luminosity measurements, finding the maximum of this likelihood is equivalent to a traditional χ^2 minimization. Bayes' theorem states that:

$$p(\overrightarrow{x}|\overrightarrow{L}_\nu^{\rm obs}) = \frac{p(\overrightarrow{L}_\nu^{\rm obs}|\overrightarrow{x})p(\overrightarrow{x})}{p(\overrightarrow{L}_\nu^{\rm obs})} \tag{5.22}$$

Since $p(\overrightarrow{L}_\nu^{\rm obs})$ is a constant (it is independent of the parameters), it can be treated as a normalization factor, and the above equation can be re-written:

$$\underbrace{p(\overrightarrow{x}|\overrightarrow{L}_\nu^{\rm obs})}_{\text{posterior distribution}} \propto \underbrace{p(\overrightarrow{L}_\nu^{\rm obs}|\overrightarrow{x})}_{\text{likelihood}} \underbrace{p(\overrightarrow{x})}_{\text{prior distribution}} \tag{5.23}$$

In the equation above, the definition of the *posterior* and *prior* distributions are indicated by braces. The prior represents the intrinsic distribution of parameters. Usually, the condition $p(\overrightarrow{x}) = 1$ is satisfied over a physical range of parameters. Bayesian inference consists in sampling the likelihood by populating the posterior distribution. The most common approach is to use a Markov Chain Monte-Carlo algorithm to randomly draw parameter values from the posterior and then estimate confidence intervals, standard deviations, parameter averages, *etc*.

Hierarchical Bayesian inference When working with a sample of sources $s_1, \ldots, s_N$ (*e.g.* an image that contains $N \geq 1$ pixels) one can perform hierarchical Bayesian inference. In this case, a generalization of Eq. 5.23 yields:

$$\underbrace{p(\overrightarrow{x_1}, \ldots, \overrightarrow{x_N}|\overrightarrow{L}_\nu^{\rm obs,1}, \ldots, \overrightarrow{L}_\nu^{\rm obs,N})}_{\text{posterior of the whole image}} \propto \prod_{i=1}^{N} \underbrace{p(\overrightarrow{L}_\nu^{\rm obs,i}|\overrightarrow{x_i})}_{\text{i}^{\text{th}}\text{ likelihood}} \underbrace{p(\overrightarrow{x_1}, \ldots, \overrightarrow{x_N})}_{\text{global prior}} \tag{5.24}$$

The shape and position of the global prior distribution is parametrized and controlled by hyperparameters (average and covariance matrix of $\overrightarrow{x_1}, \ldots, \overrightarrow{x_N}$). There is only one common set of hyperparameters for the N sources, hence it holds information that relate the likelihoods of individual sources to a shared distribution of parameters, which makes the method more robust than standard, non-hierarchical inference.

5.2.2.3 Practical aspects

Required inputs `HerBIE` requires two sets of input `FITS` files:

1. A cube of dimensions $N_x \times N_y \times M$ that contains M intensity maps of dimensions $N_x \times N_y$, each corresponding to a frequency ν_j ($j = 1, \ldots, M$). This cube contains the measurements $L_\nu^{\rm obs}(\nu_j)$ (W m^{-2} Hz^{-1} s^{-1}).

2. In the same data format (cube of dimensions $N_x \times N_y \times M$), the uncertainties associated with the measurements $\sigma_\nu^{\rm noise}$ (W m^{-2} Hz^{-1} s^{-1}). In contrast to PPMAP, uncertainties are treated pixel-per-pixel based on the noise maps. In section 9.1, we present our treatment of uncertainties for the analysis of dust emission in the IC443 SNR.

Pre-processing Real sets of observations are rarely uniform in angular resolution and sensitivity. In contrast to `PPMAP`, `HerBIE` requires to first convolve all maps to the same angular resolution (*i.e.* the coarsest) and spatially resample the maps on the same grid. In chapter 9, we will describe how to perform these pre-processing procedures using `Python`.

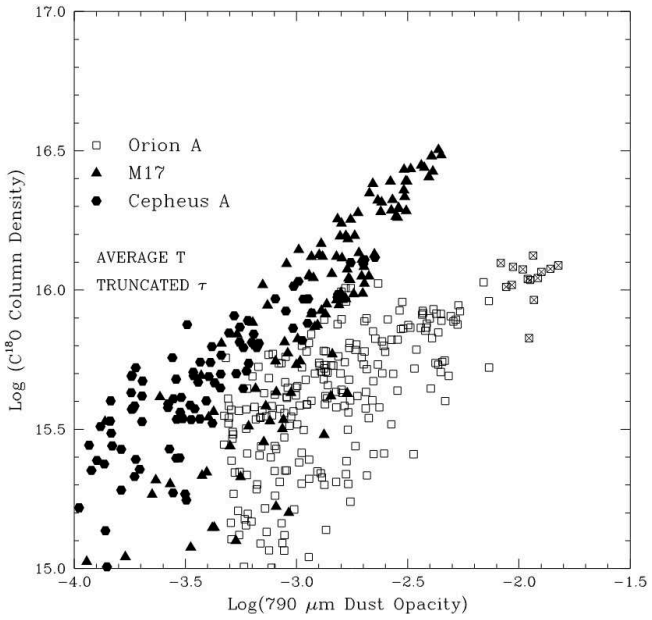

Figure 5.4 Study of the gas-to-dust mass ratio in dense molecular gas (Goldsmith *et al.*, 1997). This figure represents the correlation of $C^{18}O$ column density with dust optical depth at 790 µm on a position-by-position basis in three giant molecular cloud cores located in our galaxy (Orion A, M17 and Cepheus A). Data points in the central portion of the Orion ridge are denoted by a cross, in order to note the impact of embedded heating sources. Figure reproduced from Goldsmith *et al.* (1997).

5.3 | Gas-to-dust mass ratio

Dust is a tracer of total gas column density (Savage and Mathis 1979, Hildebrand 1983). Hence, measurements of the dust column density can be used to infer the gas mass, based on the following relation:

$$\Sigma_D \times \mathrm{GDR} = \Sigma_{H_I} + \Sigma_{H_2} \tag{5.25}$$

where Σ_D is the dust mass surface density, and Σ_{H_I} and Σ_{H_2} are respectively the atomic and molecular gas mass surface densities. The 'GDR' is the gas-to-dust mass ratio. Therefore, adopting an expected value of the 'GDR' allows to directly convert the total dust mass into the total gas mass, based on the following assumptions:

– Dust and gas are well mixed.

– The gas-to-dust mass ratio is uniform across the considered object.

While still object to its own systematic uncertainties, this mass measurement technique relies on a different set of assumptions than those presented in Chapter 4 (radiative transfer analysis of molecular lines). Therefore, it allows us to obtain an additional, independent measurement of the total mass in the IC443 SNR (see Chapter 9).

The gas-to-dust ratio has been extensively studied and calibrated in various environments. For example, Goldsmith *et al.* (1997) studied the gas column density to dust optical depth ratio $N(C^{18}O)/\tau_{790\ \mu m}$ in giant molecular cloud cores in the Milky Way (Orion A, M17, Cepheus A,

see Fig. 5.4). Draine *et al.* (2007) studied the gas-to-dust ratio in the SINGS Galaxy Sample, and Sandstrom *et al.* (2013) studied both the CO-to-H_2 and gas-to-dust ratios in 26 nearby star-forming galaxies. These studies confirmed the correlation between dust mass and gas mass, in addition to variations with respect to the metallicity of the environments and local radiation field. Estimates of the gas-to-dust ratio vary around 10^2. In this work we adopt GDR = 10^2, with a $\pm$30% uncertainty.

Part III : Observations

Chapter 6 | IRAM 30m and APEX 10′×10′ spectral cubes

Contents

In chapter 1, we have explained our motive to study the molecular contents in the evolved supernova remnant IC443, in particular in the vicinity of the 'G' clump (see Fig. 2.20), where the peak of high-energy γ-ray emission is located by Humensky and VERITAS Collaboration (2015) (see Fig. 2.15).

Between September 2018 and February 2019, we achieved a series of observations with the IRAM 30m and the APEX telescopes towards the IC443G clump. The preparation of the APEX observing runs was handled by A. Gusdorf one month before my PhD began, but I was given the responsibility to prepare and execute the observations with the IRAM 30m in February. In this chapter, we present our ^{12}CO, ^{13}CO and C^{18}O observations of pure rotational lines performed with the IRAM 30m and APEX telescopes (see chapter 3 for a detailed description of the telescopes and receivers). In the first section, we describe the receiver setup and mapping strategy. In the second section, we present the data products that we obtained and discuss the results.

6.1 | Setup, mapping strategy, observations

We used the On-The-Fly spectral-line mapping technique with both telescopes to cover a $10' \times 10'$ region centered on the position $\alpha_{[J2000]}$=6^{h}16^{m}37.5^s, $\delta_{[J2000]}$=+22°35′00″ (see Fig 6.1, Fig. 6.2). Hereafter, we refer to this field of observations as the 'extended G region'. For practical purposes, we subdivided the field of observations in four $5' \times 5'$ subfields (labeled G1, G2, G3, G4). This allowed an individual subfield to be mapped in roughly 80 minutes by the IRAM 30m (~ 30 min with APEX), enabling regular pointing and focus procedures. We sampled our maps at 1/3rd of

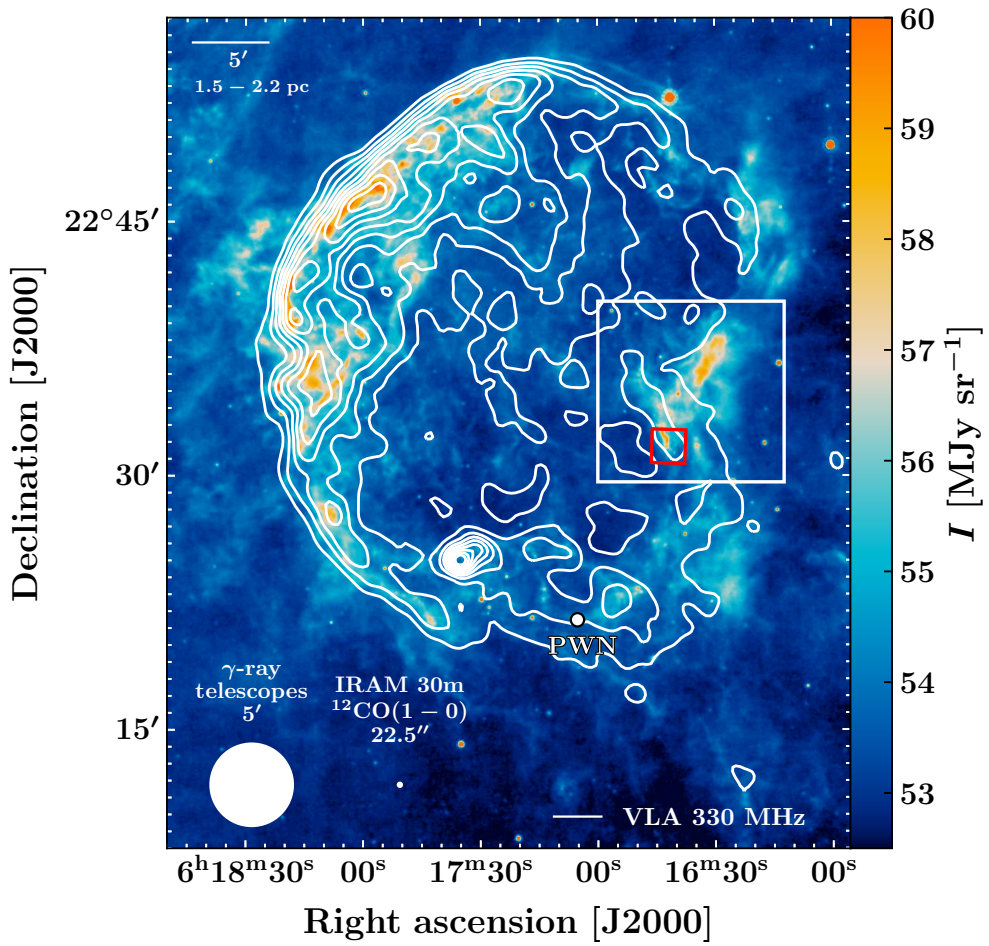

Figure 6.1 *Spitzer*-MIPS map (colors) of IC443 at 24 μm (Noriega-Crespo *et al.* 2009, Pinheiro Gonçalves *et al.* 2011). In contours, the Very Large Array (VLA) emission map displays the morphology of the synchrotron emission at 330 MHz (Claussen *et al.*, 1997a). The white dot marks the position of the pulsar wind nebula (Olbert *et al.*, 2001b). The red box represents one of the fields observed by *Spitzer*-IRS (Neufeld *et al.*, 2004), corresponding roughly to the G region defined by Huang *et al.* (1986). The white box represents the 10′×10′ field of our observations, that we name 'the extended G region' (see text). The IRAM 30m instrumental beam diameter corresponding to the ^{12}CO J=1–0 transition and the size of the typical PSF of γ-ray telescopes (5′) are indicated by white disks in the lower left corner of the figure.

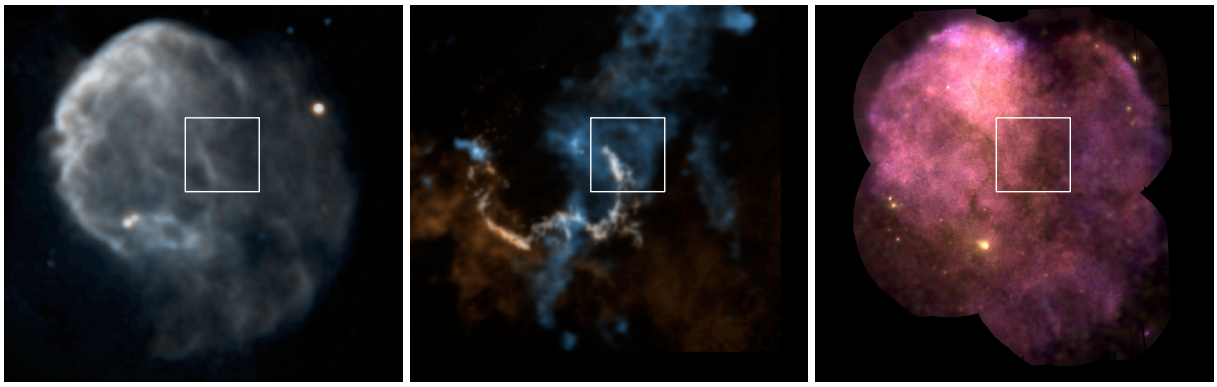

Figure 6.2 Reproduction of the figures 2.16 (left: radio observations), 2.19 (center: ^{12}CO, H I and H_2 observations) and 2.17 (right: X-ray observations). The white box represents the $10' \times 10'$ field of observations of our IRAM 30m and APEX observations.

Table 6.1 IRAM 30m observations summary: ν_{ul} is the frequency of the transition, FWHM corresponds to the full width at half maximum of the instrumental beam, $\eta_{\rm forward}$ is the forward efficiency and $\eta_{\rm mb}$ the beam efficiency of the dish. 'E090' and 'E230' respectively stand for the first and third bands of the EMIR receiver ($\Delta\nu_{\rm E090}$ = 73 – 117 GHz, $\Delta\nu_{\rm E230}$ = 202 – 274 GHz). $\overline{T_{\rm sys}}$ is the average system noise temperature and Δv the nominal spectral resolution. The 'pwv' line indicates the precipitable water vapor, and 'r.m.s' refers to the standard deviation measured on the baseline (at the native spectral resolution Δv = 0.5 km s^{-1} offered by the FTS200 backends at 3mm).

species	^{12}CO	^{12}CO	^{13}CO	C^{18}O
line	J = 1–0	J = 2–1	J = 1–0	J = 1–0
ν_{ul} (GHz)	115.271	230.538	110.201	109.782
FWHM (″)	22.5	11.2	23.5	23.6
sampling (″)	3.5	3.5	3.5	3.5
receiver	E090	E230	E090	E090
backend	FTS	FTS	FTS	FTS
$\eta_{\rm forward}$	0.94	0.92	0.91	0.94
$\eta_{\rm mb}$	0.78	0.59	0.51	0.78
$\overline{T_{\rm sys}}$ (K)	172	321	118	118
Δv (km s^{-1})	0.5	0.25	0.5	0.5
r.m.s (K)	0.035	0.039	0.025	0.022
pwv (mm)	0.3-3.8	0.3-3.8	0.3-3.8	0.3-3.8

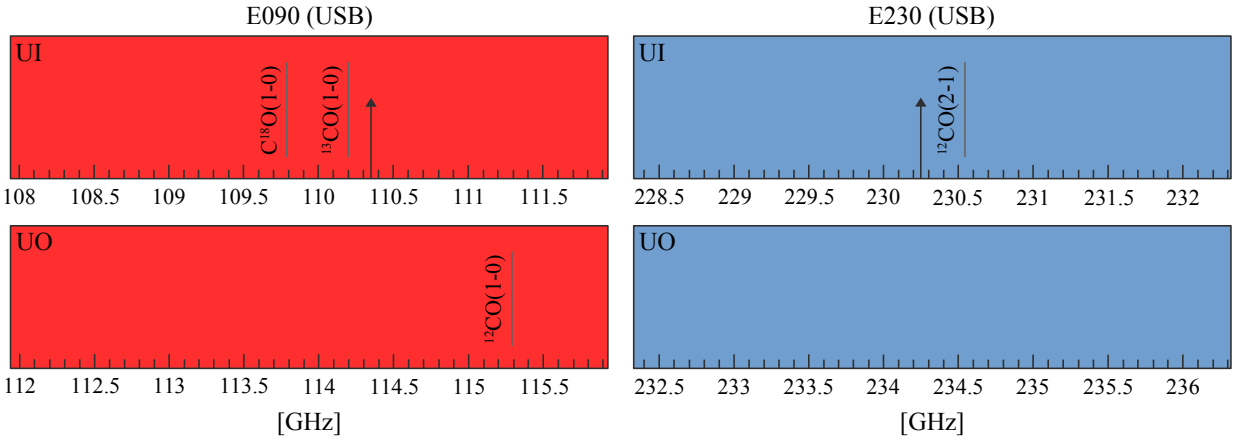

Figure 6.3 Spectral setup of the EMIR receivers and FTS backends. The upper sidebands of the E090 (left) and E230 (right) receivers are represented by two blocks (corresponding to the inner sideband, 'UI', and the outer sideband 'UO'). The local oscillator frequency is indicated by a black arrow. The ^{12}CO, ^{13}CO and C^{18}O rotational lines are indicated by vertical lines (see Tab. 6.1 for the exact frequencies).

the beam size (3.5″ for IRAM observations, and 6″ for APEX observations, see Tab. 6.1 and Tab. 6.2) in order to satisfy the Nyquist-Shannon sampling criterion.

6.1.1 IRAM 30m observations

Receiver setup The IRAM 30m[1] observations towards the extended G region were conducted during one week, from February 20, 2019 to February 24, 2019. The heterodyne receiver EMIR (Eight MIxer Receiver, Carter *et al.* 2012), operating at 115 GHz and 230 GHz simultaneously, was used in combination with the FTS200 ($\Delta\nu$ = 200 kHz, corresponding to $\Delta v \sim$ 0.5 km s^{-1} at 3mm) and VESPA backends ($\Delta\nu$ = 80 kHz, corresponding to $\Delta v \sim$ 0.2 km s^{-1} at 3mm). The local oscillator frequency was tuned in order to be able to observe simultaneously the transitions

[1]This thesis is based on data acquired under project number 169-18 with the IRAM 30m telescope. IRAM is supported by INSU/CNRS (France), MPG (Germany) and IGN (Spain).

J=1–0 for ^{12}CO, ^{13}CO, C^{18}O and J=2–1 for ^{12}CO (see Fig. 6.3 and Tab. 6.1 for the corresponding observing setup). The VESPA backends were not particularly useful to achieve our goals, with a limited bandwidth of 480 MHz (*vs.* 4 GHz for the FTS backends) but they could be added in parallel with no cost in bandwidth or sensitivity.

Algorithm 3: On-The-Fly horizontal submap (paKo).

```
1: SWTOTAL;
2: /TPHASE 0.5;
3: CALIBRATE /DEFAULT;
4: START;
5: OTFMAP -156.25 -156.25 -156.25 9.35;
6: /CROLOOP ROOOOOOR;
7: /NOTF 35;
8: /REFERENCE +651.0 +44.0;
9: /STEP 3.6 0;
10: /SYSTEM projection;
11: /TOTF 22.7;
12: /TREFERENCE 15;
13: /ZIGZAG;
14: START;
```

Description of the code: these paKo commands allow to perform an horizontal On-The-Fly submap (size $\sim 2.5' \times 2'$, excluding overlaps). NOTF and TOTF respectively refer to the number of rows and duration of the individual horizontal OTF crossings. Lines 3-4 send a request to perform a preliminary calibration of the receivers. The telescope moves in zigzag in the spatial range defined in line 5 ($x_{\rm min}$ $y_{\rm min}$ $x_{\rm max}$ $y_{\rm max}$), progressing by 3.6″ horizontal steps (line 9) every 0.5s (line 2). Lines 6 & 8 request the telescope to observe the reference target (+651.0, +44.0 are the coordinates in arcseconds with respect to the field center at the coordinates 0, 0) for 15 seconds (line 12) every 6×22.7s $\simeq$ 2.3 minutes (line 6: in 'ROOOOOOR', 'R' refers to reference, and 'O' refers to an OTF crossing).

Observations The observations were performed in position-switching/on-the-fly mode. The weather was excellent during the observations (pwv$\sim$ 0.3 − 3.8). The off-position used for calibrations was $\alpha_{\rm [J2000]}$=6$^{\rm h}$17$^{\rm m}$54$^{\rm s}$, $\delta_{\rm [J2000]}$=+22°47′40″, in the northeastern ionized region of the SNR where no molecular line emission is expected. We checked the pointing of the telescope every $\sim$ 1.5 hours, and the focus every $\sim$ 4 hours during the observing sessions on several bright sources. The pointing accuracy was better than $\sim$3″ rms. The telescope was controlled *via* paKo, the observer's user interface at the IRAM 30m telescope. A fragment of our On-The-Fly (OTF) mapping routine is shown in the algorithm 3, as an example. We used four distinct routines (corresponding to the subfields G1, G2, G3, G4) that were strictly identical except for the relative position of the off-reference (shifted with respect to the absolute position of the subfield center). Further subdivision of the $5' \times 5'$ subfields was necessary to allow a receiver calibration every 15 minutes, hence the routines were made of six blocks (four $2.5' \times 2'$, $\sim$ 15 minutes blocks similar to the algorithm 3, and two $2.5' \times 1'$, $\sim$ 7.5 minutes blocks).

6.1.2 APEX observations

Receiver setup APEX[2] observations towards IC443G were conducted on September 11, 2018. The heterodyne receivers PI230 and FLASH345 (First Light APEX Submillimeter Heterodyne receiver, Heyminck *et al.* 2006, Klein *et al.* 2014), operating at 230 GHz and 345 GHz respectively, were used in combination with the FFTS4G and the MPIfR fast Fourier transform spectrometer

[2]This thesis is based on data acquired under project M9508A_102 with the Atacama Pathfinder EXperiment (APEX). APEX is a collaboration between the Max-Planck-Institut für Radioastronomie (MPIfR), the European Southern Observatory, and the Onsala Space Observatory.

species	^{12}CO	^{12}CO	^{13}CO	^{13}CO	C^{18}O
line	J = 2–1	J = 3–2	J = 2–1	J = 3–2	J = 2–1
ν_{ul} (GHz)	230.538	345.796	220.399	330.588	219.560
FWHM (″)	28.7	19.2	30.1	20.0	30.2
sampling (″)	6	6	6	6	6
receiver	PI230	FLASH345	PI230	FLASH345	PI230
backend	FFTS4G	XFFTS	FFTS4G	XFFTS	FFTS4G
$\eta_{\rm forward}$	0.95	0.95	0.95	0.95	0.95
$\eta_{\rm mb}$	0.73	0.63	0.73	0.63	0.73
$\overline{T_{\rm sys}}$ (K)	146	291	129	330	129
Δv (km s^{-1})	0.1	0.1	0.1	0.1	0.1
r.m.s (K)	0.069	0.066	0.084	0.080	0.130
pwv (mm)	0.7-0.8	0.7-0.8	0.7-0.8	0.7-0.8	0.7-0.8

Table 6.2 APEX observations summary: ν_{ul} is the frequency of the transition, FWHM corresponds to the full width at half maximum of the instrumental beam, $\eta_{\rm forward}$ is the forward efficiency and $\eta_{\rm mb}$ the beam efficiency of the dish. 'PI230' and 'FLASH345' refer to the APEX receiver ($\Delta\nu_{\rm PI230}$ = 195 – 270 GHz, $\Delta\nu_{\rm FLASH345}$ = 268 – 374 GHz). $\overline{T_{\rm sys}}$ is the average system noise temperature and Δv the nominal spectral resolution. The 'pwv' line indicates the local precipitable water vapor measured during the observations, and 'r.m.s' refers to the standard deviation measured on the baseline. We applied a $\times\sqrt{5}^{-1}$ multiplication factor to the r.m.s in order to allow direct comparison with the IRAM 30m observations (*i.e.* we converted from the native spectral resolution Δv = 0.1 km s^{-1} of the FFTS4G and XFFTS backends to a spectral resolution Δv = 0.5 km s^{-1}).

backends (XFFTS, Klein *et al.* 2012a). Both XFFTS and FFTS4G offer a spectral resolution $\Delta v \sim 0.1$ km s^{-1}. The local oscillator frequency was tuned in order to observe simultaneously the transitions J=2–1 for ^{12}CO, ^{13}CO, C^{18}O and J=3–2 for ^{12}CO and ^{13}CO. The corresponding observing setups are indicated in Tab 6.2.

Observations The observations were performed in position-switching/on-the-fly mode using the APECS software (Muders *et al.*, 2006). The off-position used for calibrations was $\alpha_{\rm [J2000]}$=6$^{\rm h}$17$^{\rm m}$35.8$^{\rm s}$, $\delta_{\rm [J2000]}$=+22°33′00.8″, in the inner region of the SNR. We checked the focus during the observing session on the stars IK Tau and R Dor. We checked the pointing of the telescope every hour locally on V370 Aur, Y Tau, IK Tau and R Dor. The pointing accuracy was better than ∼3″ rms, regardless of which receiver we used. The absolute flux density scale was also calibrated on these sources.

6.1.3 Data reduction

We have performed observations of the ^{12}CO, ^{13}CO (J=1–0, J=2–1, J=3–2) and C^{18}O (J=1–0, J=2–1) lines with the IRAM 30m and APEX telescopes. The primary data products consist in a list of spectra (referred to as 'scans') obtained at different lines of sight for each receiver. For example, the 'FTS201902.30m' file contains a total of 513 741 scans (4.2 Go, hence each FTS spectrum weighs ∼ 8 ko). In order to produce spectral-line maps, it is required to build a mosaic of observations from these lists of raw scans.

We used the GILDAS[3] package to perform calibrations and build mosaics from our primary data products (Pety, 2005). GILDAS is maintained by the IRAM, but it can also be used to reduce APEX lists of scans, since the data format is the same. Calibrations include the correction of the main beam efficiency and forward efficiency of the telescope (conversion from T_a^* to T_{mb}) as well as baseline subtractions, spatial and spectral resampling of the raw list of scans and gridding into spectral-line cubes through a convolution with a Gaussian kernel. This data reduction is performed using the module CLASS (Continuum and Line Analysis Single-dish Software). In the next paragraphs, we describe these steps with basic examples of codes.

Baseline subtraction and spectral resampling of individual scans The first step in reducing the data is to perform baseline subtraction and spectral resampling of the scans. Our baselines were excellent, hence we applied a simple 1st order baseline subtraction. We present an example of CLASS code used to reduce the data in the algorithm 4. This example is applied to IRAM data, which is quite similar to the APEX data reduction. We implemented additional tweaks to our APEX raw data: *i.)* using the command 'fft' (enabling Fast Fourier Transform analysis), we removed some spurious harmonics, *ii.)* using the command 'drop', we also removed a dozen of noisy scans.

In order to match the spectral resolution of our APEX and IRAM data, we resampled all spectra to a spectral resolution $\Delta v = 0.5$ km s^{-1}, *i.e.* to the nominal resolution of our IRAM data (limited by the FTS channel resolution of 200 kHz). This resampling causes a five-fold reduction of the APEX spectra resolution, but it also increases the signal-to-noise ratio by averaging velocity channels.

Algorithm 4: Baseline subtraction and spectral resampling of a scan list of ^{12}CO J=1–0 spectra (CLASS).

```
1: file in FTS201902.30m;
2: file out IC443G1-12CO10.30m;
3: set tel 30ME0*UO*;
4: set sou IC443G1;
5: find;
6: for i 1 to found;
7:     get n ;
8:     modify frequency 115.2712;
9:     set unit v f;
10:    set mode x -100 100;
11:    set window -60 40;
12:    base 1;
13:    resample 200 91 -4.5 0.5 velo;
14:    write;
15:    next;
```

Description of the code: this CLASS code performs a systematic baseline subtraction followed by spectral resampling of individual scans contained in a list. Lines 1-2 define the input and output files. Line 3 allows to select the receiver and sub-band that contains the ^{12}CO J=1–0 line (E0, UO, see Fig. 6.3). Line 4 defines the target sub-field (IC443G1). Once these filters are selected, the command 'find' (line 5) queries the list of corresponding scans. The command in line 6 allows to parse (for loop) the list of scans. We modify the origin in frequency (line 8) and define a window on which we estimate the best-fit linear model of the baseline (lines 10-12). Finally, we resample the spectra on 200 channels centered on the velocity $v_{LSR} = -4.5$ km s^{-1}, with a channel size $\Delta v = 0.5$ km s^{-1} (line 13).

Once the individual scans were correctly reduced and resampled for each submap (G1, G2,

[3]The Grenoble Image and Line Data Analysis Software is developed and maintained by IRAM to reduce and analyze data obtained with the 30m telescope and Plateau de Bure interferometer. See www.iram.fr/IRAMFR/GILDAS

G3, G4) and all lines (^{12}CO J=1–0, ^{12}CO J=2–1, *etc.*), we spatially re-calibrated all scans onto the central position of the 10′ × 10′ field of observations using the command 'modify position', and we merged the individual subfield files into a single, larger file. Then, we spatially resampled the data and built the mosaic using CLASS (see algorithm 5).

Algorithm 5: Spatial resampling of a scan list of ^{12}CO J=1–0 spectra and construction of the mosaic (CLASS).

```
1: file in IC443G-12CO10.30m;
2: find;
3: set unit v;
4: set wei s ;
5: let map reso 30 ;
6: table IC443G-12CO10.tab new;
7: xy_map IC443G-12CO10;
```

Description of the code: this code *i.)* performs spatial resampling of the scans, *ii.)* produces a spectral-line cube (Position-Position-Velocity mosaic). The command in line 3 sets up a velocity scale, and line 4 forces the algorithm to average the scans based on their individual r.m.s. (measured on the baseline). Line 5 defines the spatial resolution of the output (30″ in this example, applied using a gaussian kernel with $\sigma_{\rm kernel}$ = (FWHM^2+(1/3×FWHM)^2)$^{1/2}$, *i.e.* 31.6″). Lines 6-7 produce the XY-table and corresponding lmv spectra cube.

6.2 | Data products

The results of the reduction process described in the previous section are fully-sampled position-position-velocity (PPV) cubes of the rotational lines indicated in Tab. 6.1 and Tab. 6.2. In this section, we inspect the data and discuss the morphology and kinematics of ^{12}CO, ^{13}CO and C^{18}O lines.

We produced several figures to visualize the great amount of information contained in our 9 distinct 10′ × 10′ PPV cubes. Channel maps are convenient 2D representations of PPV cubes, in which an arbitrary sample of slices is shown. Each slice corresponds to the line emission in a velocity range $v_{\rm min}$, $v_{\rm max}$. We present several channel maps of our observations of ^{12}CO and ^{13}CO rotational lines:

1. ^{12}CO J=1–0 (IRAM 30m telescope, Fig. 6.4)
2. ^{13}CO J=1–0 (IRAM 30m telescope, Fig. 6.5)
3. ^{12}CO J=2–1 (IRAM 30m telescope, Fig. 6.6)
4. ^{12}CO J=2–1 (APEX telescope, Fig. 6.7)
5. ^{12}CO J=3–2 (APEX telescope, Fig. 6.8)

We also produced integrated maps (*i.e.* 0$^{\rm th}$-order moment map, $\int T_{\rm mb} dv$) and peak temperature maps ($T_{\rm peak}$ = max($T_{\rm mb}$)) for each isotopolog (see Fig. 6.9, 6.10, 6.11, 6.12). We have two PPV cubes of the ^{12}CO J=2–1 (obtained with the IRAM 30m and APEX telescopes). The IRAM 30m PPV cube has the better spatial resolution, and the APEX PPV cube has the better spectral resolution. We have checked the intercalibration of both data cubes (results are presented in section 8.2.1).

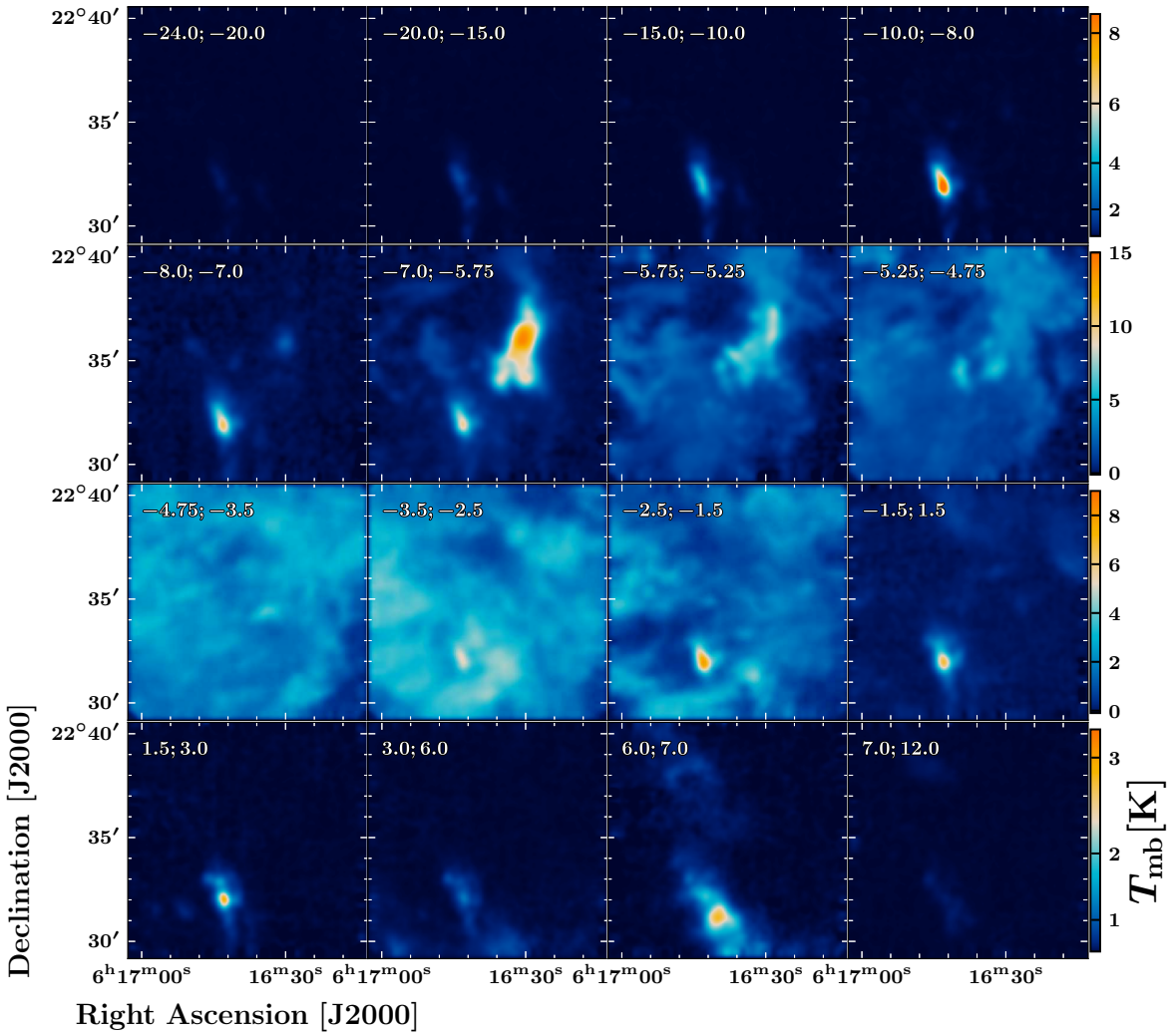

Figure 6.4 Channel maps of our **^{12}CO J=1–0 PPV cube**. The 10′ × 10′ field observed with the IRAM 30m telescope is entirely displayed. Each panel represents the velocity-integrated emission towards the same area, between −24 km s^{-1} and 12 km s^{-1}. The boundaries of the velocity intervals (in km s^{-1}) are indicated in the top left corner of each panel. Note that the colorscale varies between rows. The angular resolution is 22.5″.

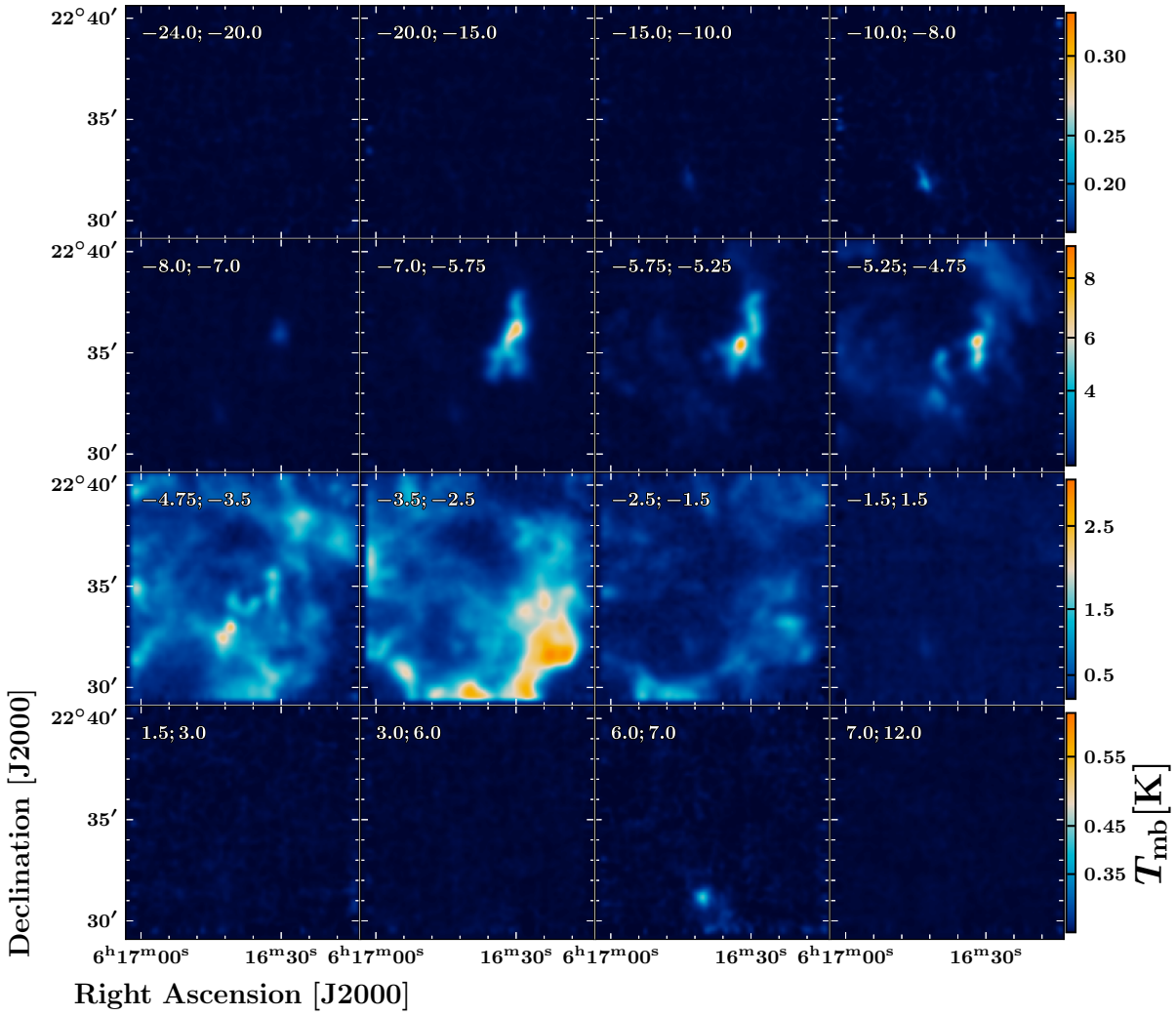

Figure 6.5 Channel maps of our **^{13}CO J=1–0 PPV cube**. The 10′ × 10′ field observed with the IRAM 30m telescope is entirely displayed. Each panel represents the velocity-integrated emission towards the same area, between −24 km s^{-1} and 12 km s^{-1}. The boundaries of the velocity intervals (in km s^{-1}) are indicated in the top left corner of each panel. Note that the colorscale varies between rows. The angular resolution is 23.5″.

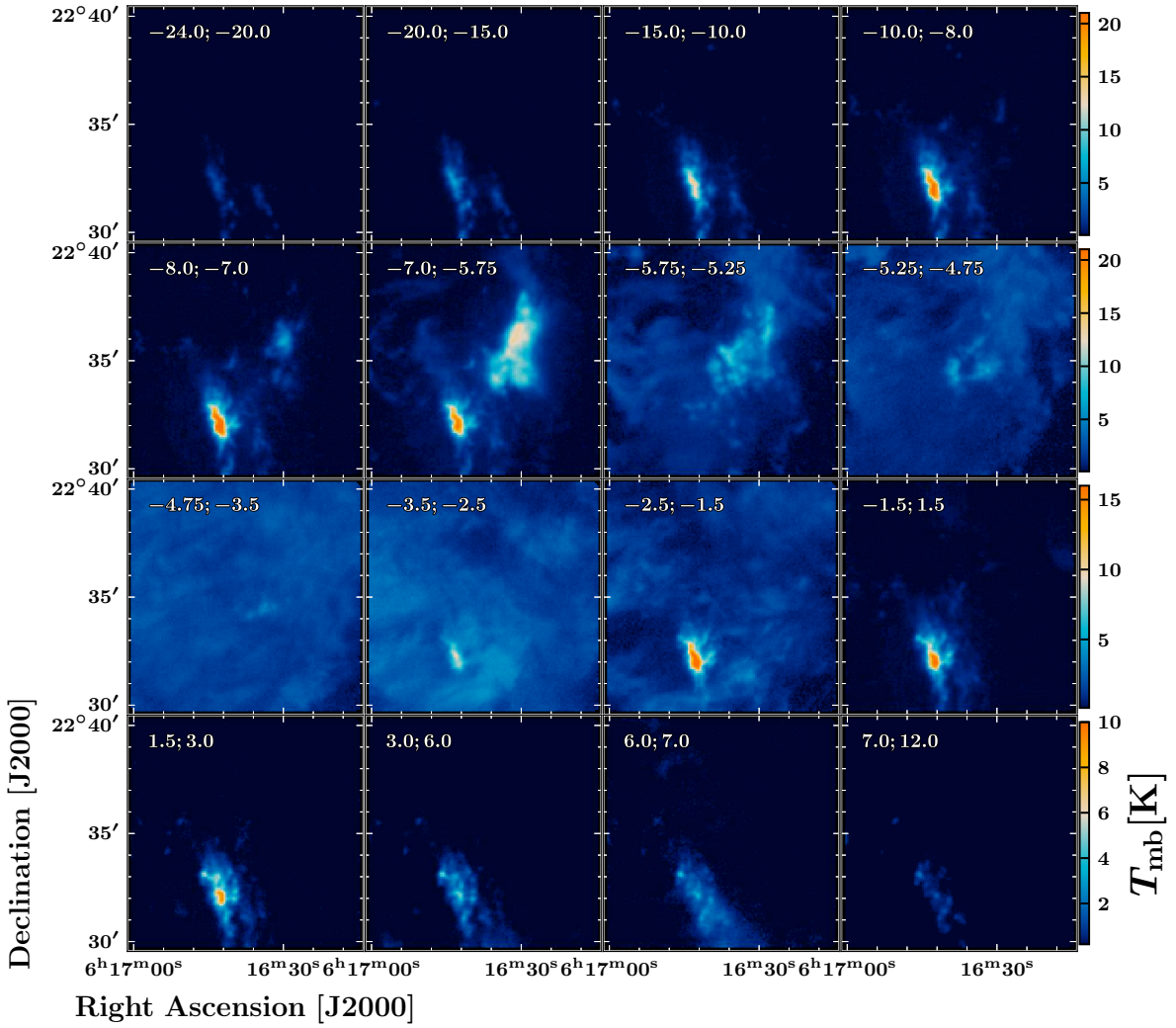

Figure 6.6 Channel maps of our **^{12}CO J=2–1 PPV cube**. The 10′ × 10′ field observed with the IRAM 30m telescope is entirely displayed. Each panel represents the velocity-integrated emission towards the same area, between −24 km s^{-1} and 12 km s^{-1}. The boundaries of the velocity intervals (in km s^{-1}) are indicated in the top left corner of each panel. Note that the colorscale varies between rows. The angular resolution is 11.2″.

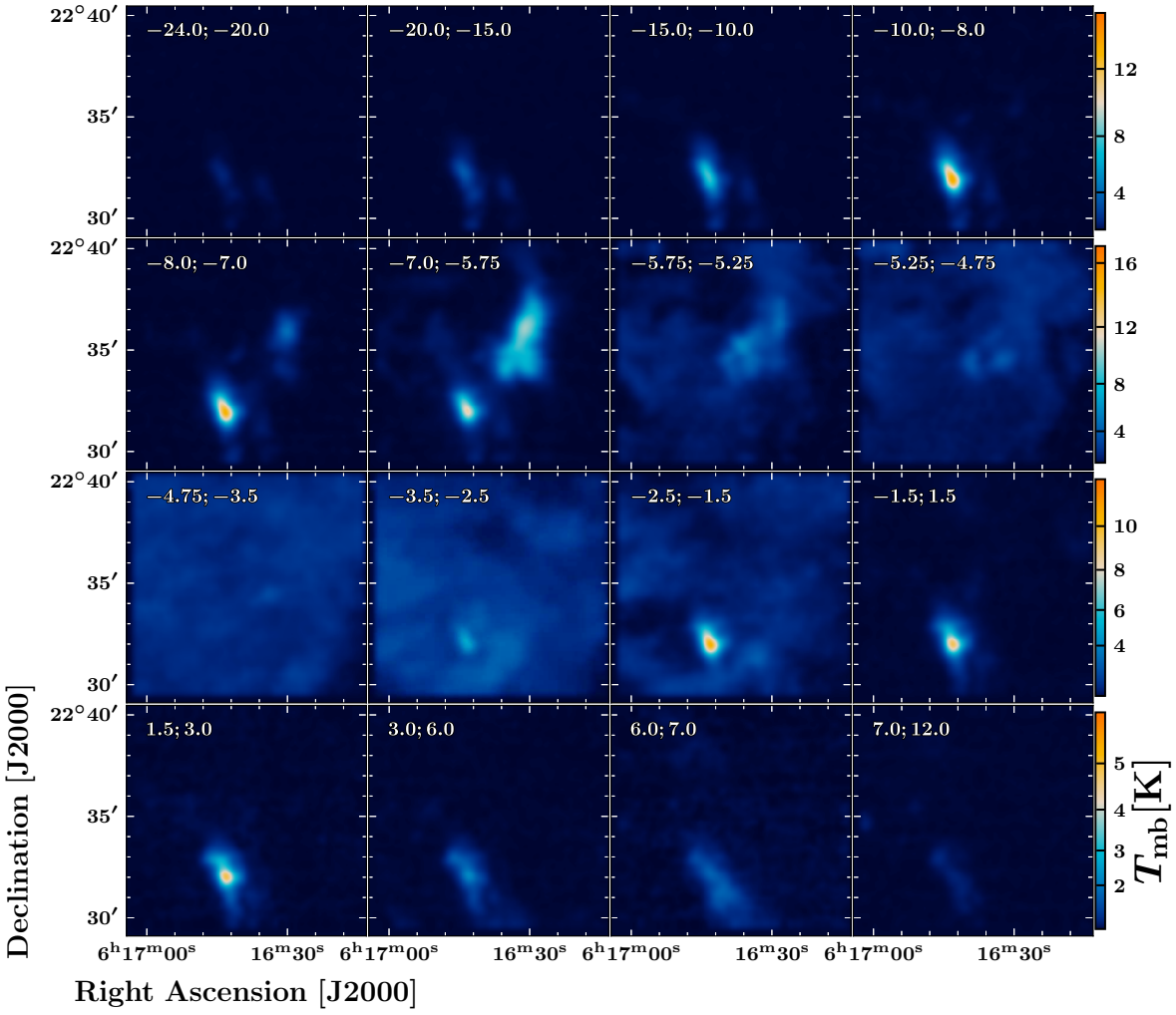

Figure 6.7 Channel maps of our **^{12}CO J=2–1 PPV cube**. The 10′ × 10′ field observed with the APEX telescope is entirely displayed. Each panel represents the velocity-integrated emission towards the same area, between −24 km s^{-1} and 12 km s^{-1}. The boundaries of the velocity intervals (in km s^{-1}) are indicated in the top left corner of each panel. Note that the colorscale varies between rows. The angular resolution is 28.7″.

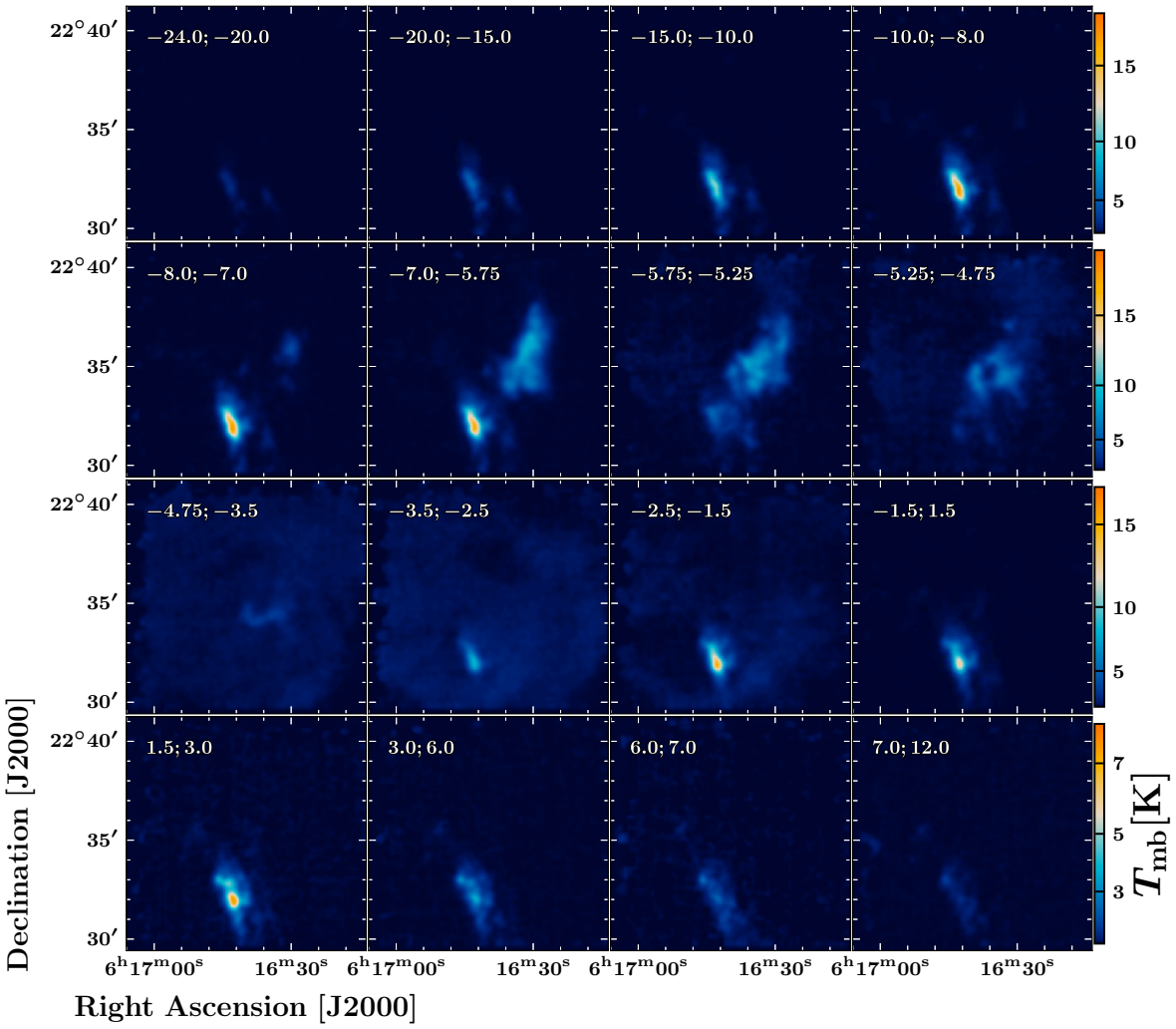

Figure 6.8 Channel maps of our **^{12}CO J=3–2 PPV cube**. The 10′ × 10′ field observed with the APEX telescope is entirely displayed. Each panel represents the velocity-integrated emission towards the same area, between −24 km s^{-1} and 12 km s^{-1}. The boundaries of the velocity intervals (in km s^{-1}) are indicated in the top left corner of each panel. Note that the colorscale varies between rows. The angular resolution is 19.2″.

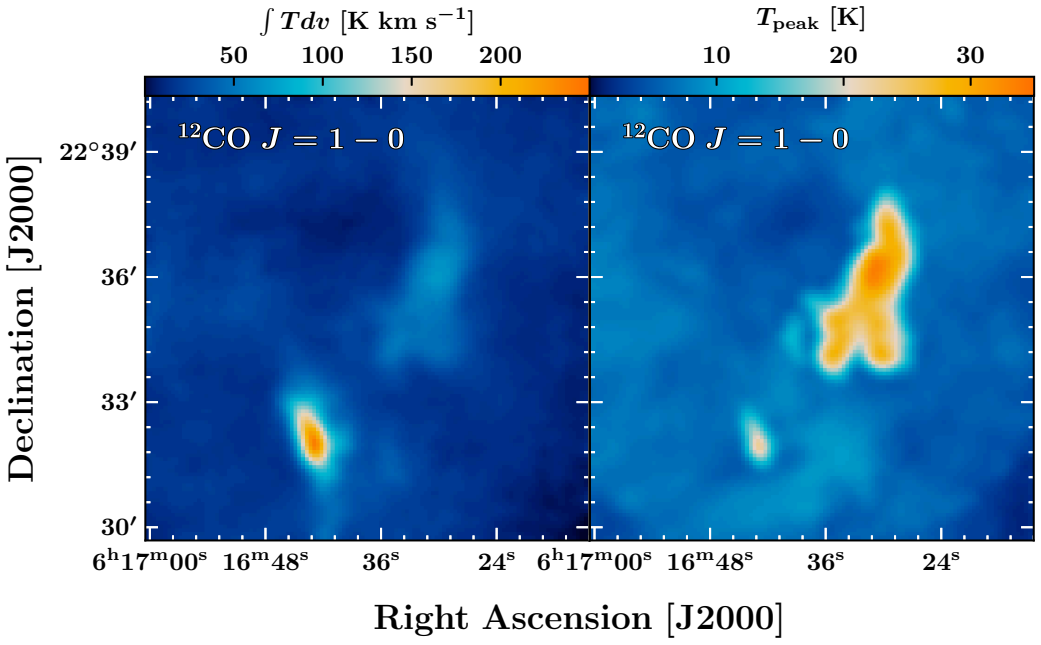

Figure 6.9 *Left:* 0$^{\rm th}$-order moment (velocity-integrated map) of our ^{12}CO J=1–0 PPV cube. *Right:* Map of the 'peak main beam temperature' max($T_{\rm mb}$) of our ^{12}CO J=1–0 PPV cube. The 10′ × 10′ field observed with the IRAM 30m telescope is entirely displayed. The angular resolution is 22.5″.

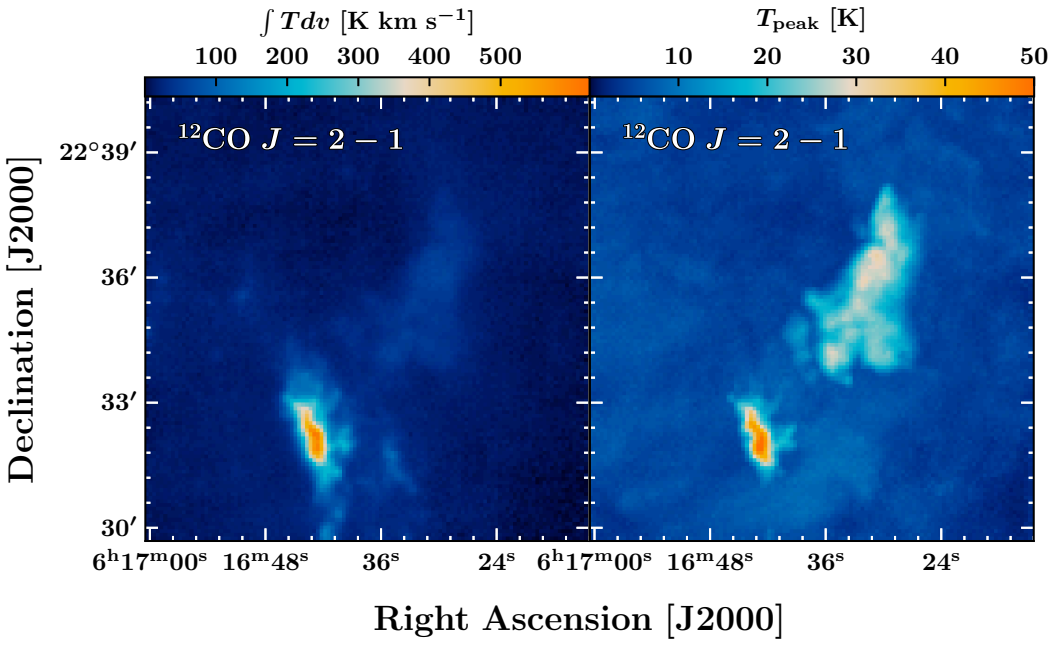

Figure 6.10 *Left:* 0$^{\rm th}$-order moment (velocity-integrated map) of our ^{12}CO J=2–1 PPV cube. *Right:* Map of the 'peak main beam temperature' max($T_{\rm mb}$) of our ^{12}CO J=2–1 PPV cube. The 10′×10′ field observed with the IRAM 30m telescope is entirely displayed. The angular resolution is 11.2″.

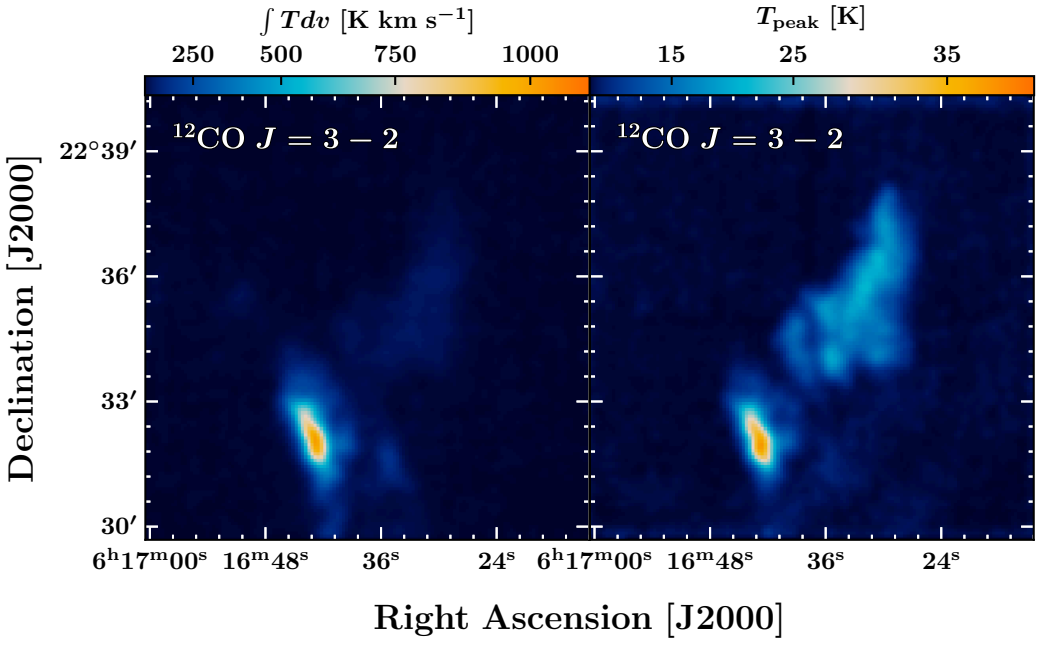

Figure 6.11 *Left:* 0$^{\rm th}$-order moment (velocity-integrated map) of our ^{12}CO J=3–2 PPV cube. *Right:* Map of the 'peak main beam temperature' max($T_{\rm mb}$) of our ^{12}CO J=3–2 PPV cube. The 10′ × 10′ field observed with the APEX telescope is entirely displayed. The angular resolution is 19.2″.

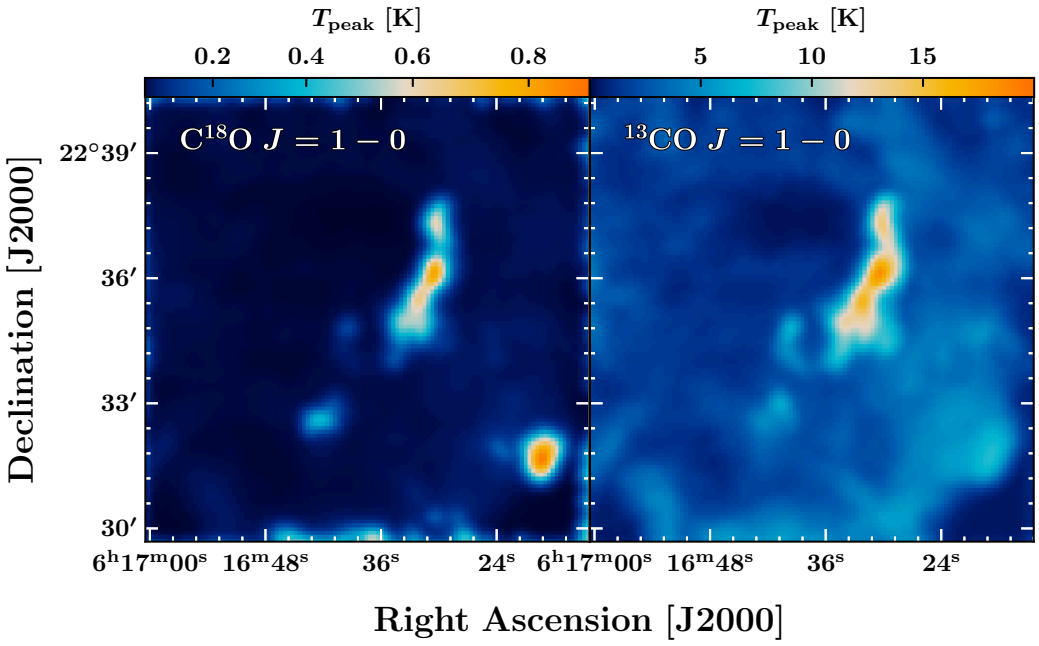

Figure 6.12 *Left:* Map of the 'peak main beam temperature' max($T_{\rm mb}$) of our C^{18}O J=1–0 PPV cube. *Right:* Map of the 'peak main beam temperature' max($T_{\rm mb}$) of our ^{13}CO J=1–0 PPV cube. The 10′ × 10′ field observed with the IRAM 30m telescope is entirely displayed. The angular resolutions are 23.5″ and 23.6″ respectively for the ^{13}CO and C^{18}O maps.

6.2.1 Morphology

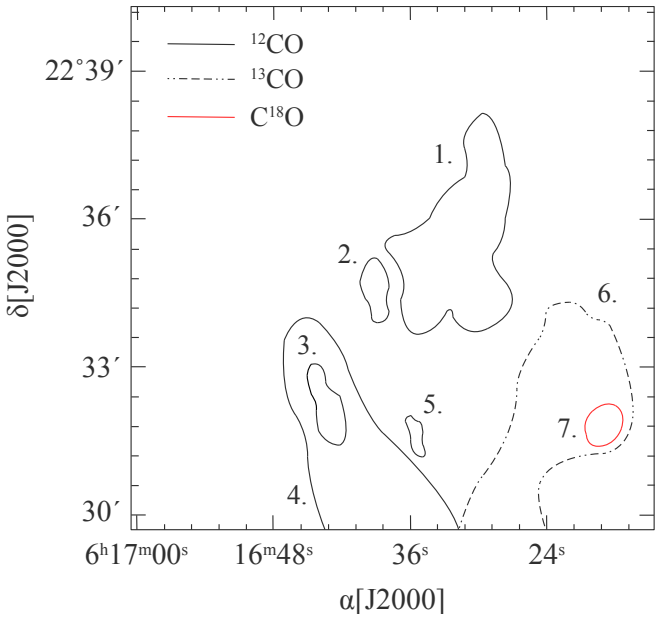

Figure 6.13 Schematic drawing of the morphology of the dense gas in the extended G region (based on ^{12}CO J=2–1 observations, see Fig. 6.10). The structures which are regularly referred to in the text are indicated by numeric labels: *(1.)* & *(2.)* encompass the 'quiescent cloudlet' and 'ring-like structure'; *(3.)* is the 'shocked clump'; *(4.)* the 'NE-SW arm' seen at $v_{\rm LSR}$ = 6.5 km s^{-1} (see Fig. 6.6 and Fig. 6.4, last row, third column); *(5.)* the 'secondary shocked clump'; and *(6.)* & *(7.)* encompass the 'dense region' seen in ^{13}CO and C^{18}O at $v_{\rm LSR}$ = 3 km s^{-1} (see Fig. 6.5, third row, second column). Structures are represented in a line style and color corresponding to the isotopolog in which they are the most visible.

Our 10′×10′, ∼10-30″ resolution maps of ^{12}CO and ^{13}CO emission in the extended G region provide a detailed picture of the morphology of the molecular phase. The IRAM 30m observations of the J=2–1 line offer the best spatial resolution, allowing to map structures at an angular scale of ∼ 11.2″ with the beam of the telescope (∼ 0.1 pc at a distance of 1.8 kpc). Fig. 6.10 (left panel) shows the 0$^{\rm th}$-order moment map of our IRAM 30m ^{12}CO J=2–1 observations (integration between v = −40.0 km s^{-1} and v = +30 km s^{-1}). This wide interval of velocity includes all the components of the signal that are detected in our observations of the extended G region. The right panel of Fig. 6.10 shows the ^{12}CO J=2–1 peak temperature map, corresponding to the maximum brightness temperature measurement towards each line of sight.

In addition to several smaller and/or fainter structures that will be described in the following developments, the peak temperature maps shown in Fig. 6.9, Fig. 6.10 and Fig. 6.11 reveal two bright molecular structures that are spatially separated. The first structure (bottom-center in Fig. 6.10) has a peak integrated intensity of 578 K km s^{-1}, one order of magnitude higher than the peak integrated intensity of the second structure (top-right in Fig. 6.10) that is around 63 K km s^{-1}. The first structure is associated with bright infrared filamentary structures mapped by *Spitzer* (see Fig. 6.19, box 'C') and presents high-velocity ^{12}CO line wings (∼ 20 km s^{-1}, see Fig. 6.21). The second one has no obvious counterpart in the infrared range probed by *Spitzer*, and it does not seem to be associated with high-velocity line emission (the line width is ∼ 2 km s^{-1}, see section 6.2.2).

Hereafter, these two structures will be referred to as the 'shocked clump' and 'quiescent cloudlet' (see Fig. 6.13, labels '1' and '3'). We justify these identifiers in the rest of this chapter, based on the morphology and kinematic analysis of our data products (in this section, as well as in section 6.2.2 and section 6.2.3).

These two structures stand out with respect to a complex background. Several faint and sparse knots are detected over all the field of observations, especially around the systemic ve-

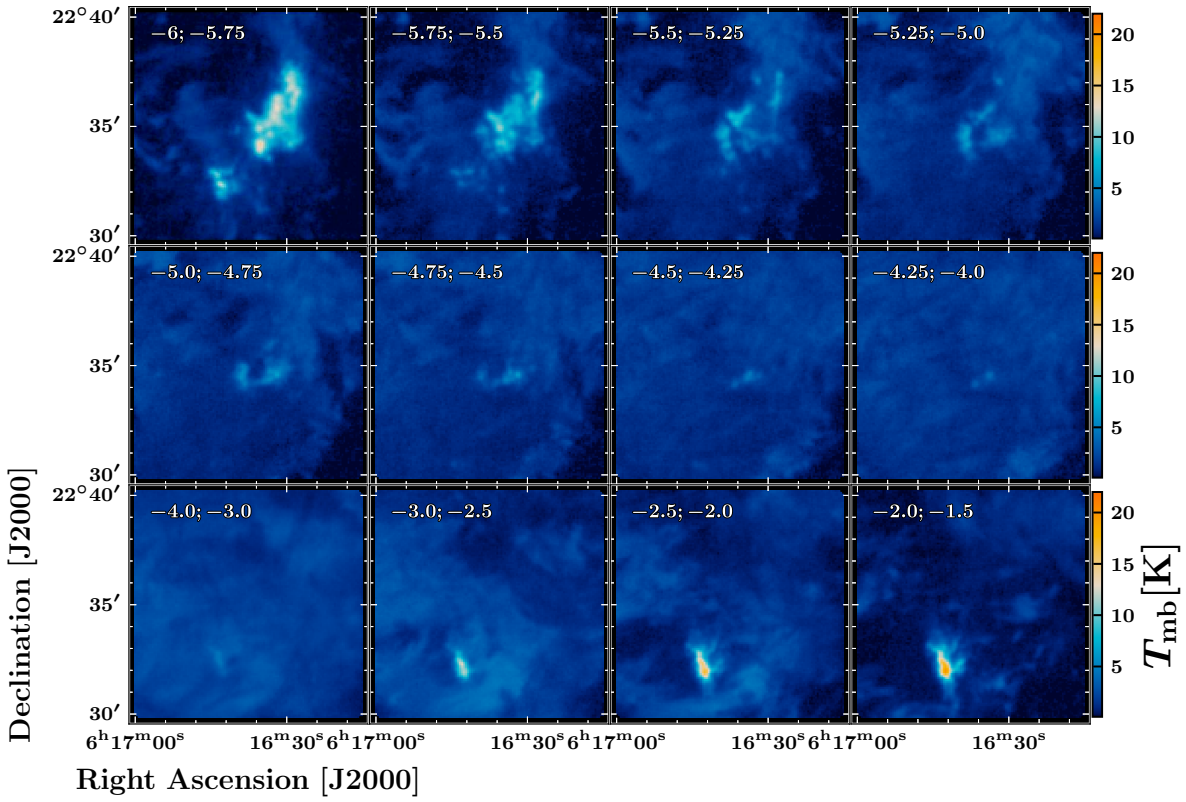

Figure 6.14 Channel maps of our IRAM 30m ^{12}CO J=2–1 observations between −6 km s^{-1} and −1.5 km s^{-1} (see also Fig. 6.6). Each panel represents the velocity-integrated emission within a velocity channel of width Δv = 0.5 km s^{-1} or Δv = 0.25 km s^{-1}. The boundaries of the velocity intervals (in km s^{-1}) are indicated in the top left corner of each panel.

locity of IC443 ($v_{\rm LSR}$ = −4.5 km s^{-1}, Hewitt *et al.* 2006). This diffuse gas, noticeable between v = −7.5 km s^{-1} and v = −1.5 km s^{-1} (see Fig. 6.14) appears to correspond to the ambient gas associated with the NW-SE molecular cloud in which IC443G is embedded (Cornett *et al.* 1977, Lee *et al.* 2012). Between v = −5 km s^{-1} and v = −3 km s^{-1} the emission is extended and quasi-uniform over the field of view. Around the velocity at which the quiescent cloudlet appears (around v = −5.5 km s^{-1}, see Fig. 6.14) the ambient, diffuse gas seems to connect with the structure, indicating that it might be physically related to the ambient cloud.

The velocity and spatial correlation of the shocked clump with the rest of the ambient gas suggests that a fraction of the extended, diffuse gas could correspond to a slice of turbulent medium driven by the SN shockwave. Apart from these remarks on the extended emission seen between v = −7.5 km s^{-1} and v = −1.5 km s^{-1}, the description of the region probed by our observations can be divided into six distinct, clearly bounded structures (see Fig. 6.13):

***i.)* Quiescent cloudlet** In the upper part of the field we observe a large (∼ 5′ × 2′, *i.e.* ∼2.8 pc × 1.1 pc) elongated cloudlet detected between v = −7.0 km s^{-1} and v = −5.5 km s^{-1} (indicated by the label '1' on Fig. 6.13), detected in ^{12}CO J=1–0, J=2–1 and J=3–2. This structure was labeled 'G1' by Zhang *et al.* (2010), as part of what they call the 'double peaked morphology' of the extended G region. The ^{13}CO J=1–0 counterpart of this quiescent structure is much brighter

than the other main structures in the field of observations, and it is also detected in the transitions J=2–1 and J=3–2, as well as in $C^{18}O$ J=1–0 and J=2–1.

This structure was also presented and characterized by Lee *et al.* (2012) who proposed the label 'SC 03', among a total of 12 small clouds (SCs, of size ∼1') found in IC443. Interestingly, the spatial resolution of the J=2–1 IRAM 30m map shows a remarkable clumpiness at $v = -5.5$ km s^{-1} (Fig. 6.14, first row. Also Fig. 6.6, second row, third column). The clumps are not resolved by the 11.2″ beam of the telescope (∼ 0.1 pc at distance of 1.8 kpc).

***ii.)* Ring-like structure** A ring-like structure seemingly lying in the center of the field (the position is indicated by the label '2' on Fig. 6.13), appearing between $v = -5.5$ km s^{-1} and $v = -4.5$ km s^{-1} in ^{12}CO J=1–0, J=2–1 and J=3–2. It has a semi-major axis of 1.5′, or 0.8 pc. This structure might be coincidental and is likely to be physically connected to the elongated cloudlet as both are spatially contiguous and their emission lines are spectrally close. Actually, the ring is hardly visible in the peak temperature map (Fig. 6.10) although it can consistently be found in the channel maps around $v = -5$ km s^{-1} (Fig. 6.4, 6.6, 6.8). The ring-like structure is partially detected as well in our observations of ^{13}CO J=1–0, J=2–1 and J=3–2, and also has a faint, partial counterpart in $C^{18}O$ J=1–0 and J=2–1. Remarkably, this structure is also found in higher-J observations of ^{12}CO, up to J=7–6 (archival APEX data of A. Gusdorf).

To understand the nature of this potentially mysterious region of our maps we searched for counterparts in *Spitzer*-MIPS, WISE, DSS, XMM-Newton, as well as in near-infrared and optical point source catalogs, without success. Due to projection effects, this apparent circular shape could also be explained by an unresolved and clumpy distribution of gas.

***iii.)* Shocked clump** In the lower part of the field we identify a very bright clump emitting between $v = -31.0$ km s^{-1} and $v = 16$ km s^{-1} (3σ detection). This structure of size $\sim 2' \times 0.75'$ (∼ 1.1 pc ×0.4 pc), which is detected in ^{12}CO J=1–0, J=2–1 and J=3–2, belongs to the southwestern ridge of the molecular shell of the SNR and has been described as a shocked molecular structure by several previous studies (van Dishoeck *et al.* 1993, Cesarsky *et al.* 1999, Snell *et al.* 2005, Shinn *et al.* 2011, Zhang *et al.* 2010). The structure is clearly correlated to a bright infrared source seen in *Spitzer*-MIPS, *Spitzer*-IRS and *Spitzer*-IRAC observations of the region (see Fig. 6.19). The core of the shocked clump (indicated by the label '3' on Fig. 6.13) is also detected in ^{13}CO in the transitions J=1–0, J=2–1 and J=3–2, as well as in $C^{18}O$ J=1–0 and J=2–1. The shocked clump disappears in the velocity range of the cloud of Cornett *et al.* (1977) (between $v = -5.5$ km s^{-1} and $v = -3.5$ km s^{-1}), where the emission is absorbed by cold ambient gas along the line of sight.

Interestingly, the morphology of the shocked clump is slightly different between the two high-velocity wings separated by the v_{LSR} of the ambient cloud ($v = -4.5$ km s^{-1}). The shocked clump exhibits several clumpy sub-structures, suggesting a complex morphology unresolved by our 11.2″ beam. The clumpy morphology of the shocked clump is also visible in observations of this region at higher resolutions (*e.g.* DSS, WISE, MIPS, *etc*).

***iv.)* NE-SW quiescent arm** At the same position as the shocked clump and extending in south-west direction, we find a faint, elongated clump emitting between $v = 5.0$ km s^{-1} and $v = 7.5$ km s^{-1}. This structure (indicated by the symbol '4' on Fig. 6.13) is spatially coinciding with the shocked clump, yet the peak velocity is not the exact same (also see below developments

on the kinematics of the region in the next section). The structure has a faint counterpart in ^{13}CO J=1–0. Observations of the ambient molecular cloud by Lee *et al.* (2012) indicate that this structure belongs to a faint NE-SW complex of molecular gas in the velocity range +3 km s^{-1} < $v_{\rm LSR}$ < +10 km s^{-1}, that would be unrelated to the shocked clump.

v.) **Shocked knot** An additional shocked molecular structure (indicated by the letter '5' on Fig. 6.13) is also detected to the west of the previously described 'shocked clump', between $v = -31$ km s^{-1} and $v = 11$ km s^{-1}. This fainter and smaller structure ($\sim 1' \times 0.5'$, *i.e.* $\sim$ 0.5 pc ×0.3 pc) is spatially separated from the main shocked clump. We hypothesize that this structure is either a residual clump interacting with the SNR blast (Lee *et al.*, 2012), or a bow shock associated with a protostar.

vi.) **Dense southwestern region** Finally, the ^{13}CO J=1–0 map (Fig. 6.5 and Fig. 6.12) indicates a large clump of gas extending from the bottom-center to the right end of the field, with a bright knot in the bottom-right corner of the field of observations (labels '6' and '7' on Fig. 6.13). However, this structure has no bright, well-defined counterpart in any of the ^{12}CO transitions maps. This structure is spatially and kinematically correlated with the faint and extended ^{12}CO J=1–0 and J=2–1 emission seen in the velocity range −5.5 km s^{-1} < $v_{\rm LSR}$ < −2 km s^{-1}. From the comparison with the ^{12}CO observations of Lee *et al.* (2012) and ^{13}CO observations of Su *et al.* (2014) towards the SNR, we conclude that this structure is part of the western molecular complex observed in the velocity range −10 km s^{-1} < $v_{\rm LSR}$ < 0 km s^{-1}.

6.2.2 Kinematics

In this section, we aim to describe the kinematics of the gas revealed by ^{12}CO lines. The IRAM 30m ^{12}CO J=2–1 PPV cube offers the combination of the best spatial resolution (11.2″) with a spectral resolution of 0.25 km s^{-1} (not as good as the spectral resolution of APEX observations: $\Delta v = 0.1$ km s^{-1}). We produced the first and second moment maps corresponding to this PPV cube using two different methods (see Fig. 6.15, 6.16) described in the next section. We also produced the moment maps of the IRAM 30m ^{13}CO J=1–0 PPV cube (see Fig. 6.17).

6.2.2.1 Moment maps

Standard moment maps We have already presented the 0$^{\rm th}$-order moment maps of our ^{12}CO, ^{13}CO and C^{18}O PPV cubes (Fig. 6.9-6.12). While the 0$^{\rm th}$-order moment traces the sum of the brightness temperature along a line of sight, the first and second moment maps hold the kinematic information. The first moment map is defined by:

$$\mathcal{M}_1(x,y) = \frac{\int T_{\rm mb}(x,y,v)\, v\, dv}{\int T_{\rm mb}(x,y,v)\, dv} \tag{6.1}$$

where (x, y) are the coordinates of a pixel, and the denominator could be written as $\mathcal{M}_0(x, y)$ (0$^{\rm th}$-order moment map). The quantity $\mathcal{M}_1$ can be interpreted as the 'brightness temperature averaged' velocity, hence it represents the systemic velocity of the gas probed by the ^{12}CO line. Hereafter, we will refer to $\mathcal{M}_1$ as '$v_{\rm sys}$'. The second moment map is defined by:

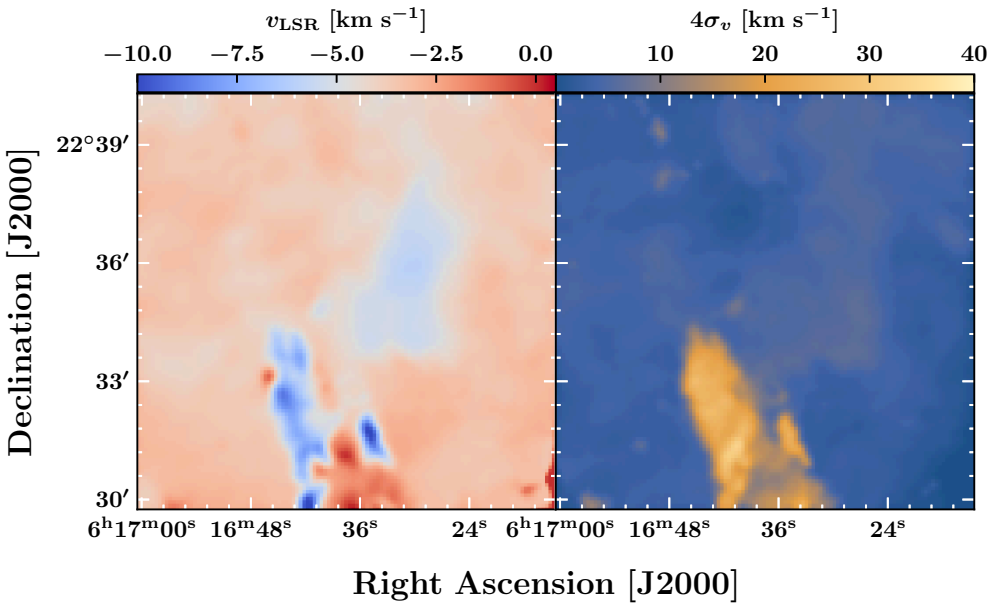

Figure 6.15 'Standard' moment maps (see text). *Left:* first moment map of the IRAM 30m ^{12}CO J=2–1 data cube. *Right:* second moment map. The colorbar of the 1$^{\rm st}$ moment map is centered on the velocity of IC443 in the local standard of rest, $v_{\rm LSR} = -4.5$ km s^{-1}.

$$\mathcal{M}_2(x,y) = \frac{\int T_{\rm mb}(x,y,v)(v - v_{\rm sys}(x,y))^2\, dv}{\int T_{\rm mb}(x,y,v)\, dv} \tag{6.2}$$

where $v_{\rm sys}(x,y) = \mathcal{M}_1(x,y)$ is the systemic velocity inferred from Eq. 6.1. The quantity $\mathcal{M}_2$ can be interpreted as the 'brightness temperature averaged' variance of the velocity with respect to $v_{\rm sys}$. Hence, $\sigma_v = \sqrt{\mathcal{M}_2}$ is the velocity standard deviation associated with the ^{12}CO line. For a gaussian line profile, $2.355\sigma_v$ corresponds to the full width at half maximum of the line, and $4\sigma_v$ is the 'gaussian beam' of the line, which represents the full extent of the line from the tip of the blueshifted wing to the tip of the redshifted wing (zero baseline width).

Using a `Python` code, we applied these formulas (Eq. 6.1 and 6.2) in each line of sight (*i.e.*, in each pixel) of our PPV cube where the signal is larger than 3σ. The results are shown in Fig. 6.15 for ^{12}CO J=2–1, and in Fig. 6.17 for ^{13}CO J=1–0. The problem with this approach is the self-absorption within the shocked clump between $v = -5.5$ km s^{-1} and $v = -3.5$ km s^{-1} for the ^{12}CO J=2–1 PPV cube (see Fig. 6.21), where the emission is absorbed by cold ambient gas along the line of sight. The asymmetric line profile caused by the absorption feature centered on $v_{\rm LSR} \sim -4.5$ km s^{-1} might produce a bias in the measurement of the systemic velocity. As a consequence, the ^{12}CO J=2–1 first moment map is unlikely to be correctly representing the systemic velocity of the shocked clump. However, the ^{13}CO J=1–0 first moment map seems to be unaffected, hence it correctly represents the systemic velocity.

Gaussian model To improve the treatment of our first moment map, we produced a model of the emission in each line of sight. Our model needs to account for the self-absorption feature, hence we started with a 'bi-gaussian' model:

$$T_{\rm mb}(x,y,v) = \mathcal{G}_1(x,y,v) - \mathcal{G}_2(x,y,v) \tag{6.3}$$

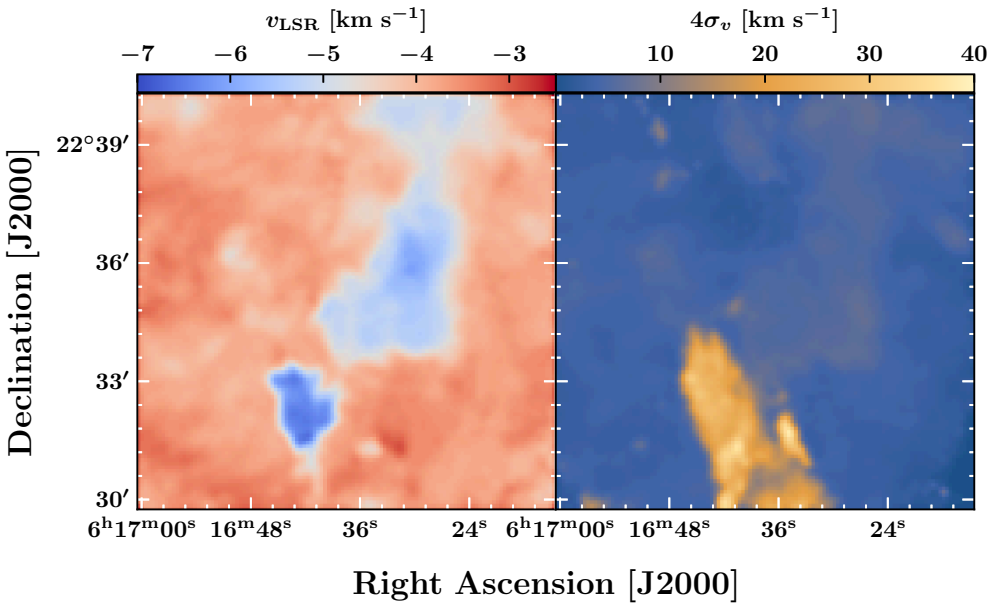

Figure 6.16 Moment maps calculated with our gaussian model (see the description of the model in the text). *Left:* first moment map of the IRAM 30m ^{12}CO J=2–1 data cube. *Right:* second moment map. The second moment map is calculated by injecting the centroid of our gaussian model into Eq. 6.2. The colorbar of the 1$^{\rm st}$ moment map is centered on the velocity of IC443 in the local standard of rest, $v_{\rm LSR} = -4.5$ km s^{-1}.

where $\mathcal{G}_1$ and $\mathcal{G}_2$ are two gaussian functions with positive amplitudes:

$$\mathcal{G}_i(v) = |A_i(x,y)|\exp\left(-\frac{(v - v_i(x,y))^2}{2\sigma_i(x,y)^2}\right) \tag{6.4}$$

$\mathcal{G}_1$ and $\mathcal{G}_2$ are respectively supposed to model the emission and absorption features. Using the `Python` module `curve_fit`, we performed a least squares fitting test to find the best fit in each pixel of our ^{12}CO J=2–1 PPV cube. We found that this model fails to reproduce the high-velocity wings towards the shocked clump, which seems to require an additional lower amplitude, higher standard deviation gaussian function. We updated our model as follows:

$$T_{\rm mb}(x,y,v) = \mathcal{G}_1(x,y,v) + \mathcal{G}_2(x,y,v) - \mathcal{G}_3(x,y,v) \tag{6.5}$$

where $\mathcal{G}_1$, $\mathcal{G}_2$ and $\mathcal{G}_3$ are three gaussian functions with positive amplitudes, and $\sigma_1 < \sigma_2$. After an additional least squares fitting test, we added a fourth gaussian of low, positive amplitude to reproduce the emission of the NE-SW quiescent arm. This model reproduces the observations at a satisfying level: across the map, the median of the relative difference between our fit and the observations is $\sim 2.7\%$. Since the component $\mathcal{G}_1$ reproduces the bulk of the line, we adopt v_1 (see Eq. 6.4) as the systemic velocity corresponding to the line of sight in each pixel of the map. The result is shown on Fig. 6.16 (left panel). Then, we re-calculate the second moment map *via* the application of Eq. 6.2 to the data, using the systemic velocity corresponding to $\mathcal{G}_1$ (the quantity v_i in Eq. 6.4). The result is shown on Fig. 6.16 (right panel).

The second moment map is very similar for both methods (compare Fig. 6.15 with Fig. 6.16). However, the first moment map is significantly modified towards the shocked clump, which ap-

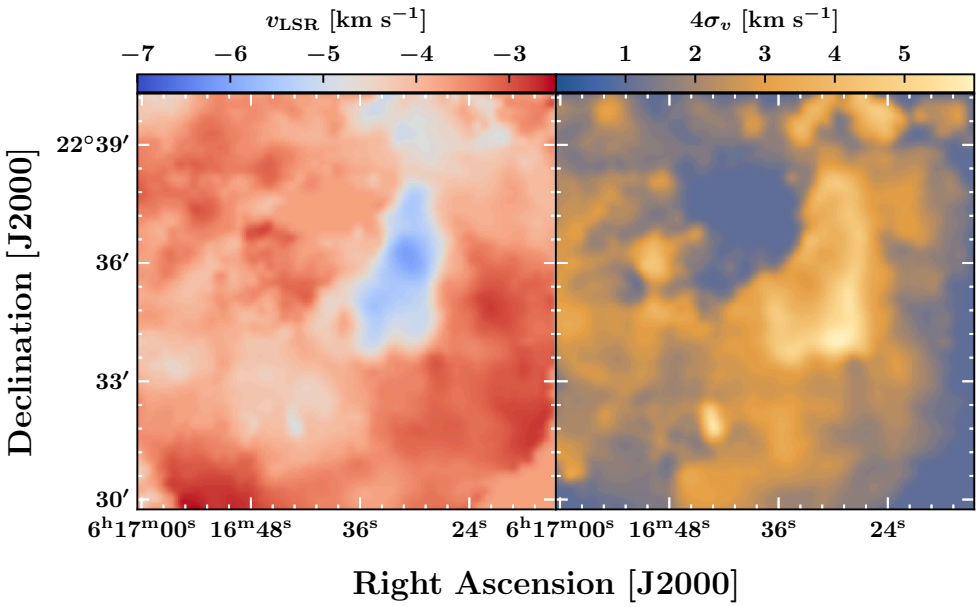

Figure 6.17 'Standard' moment maps (see text). *Left:* first moment map of the IRAM 30m ^{13}CO J=1–0 data cube. *Right:* second moment map. The colorbar of the 1$^{\rm st}$ moment map is centered on the velocity of IC443 in the local standard of rest, $v_{\rm LSR} = -4.5$ km s^{-1}.

pears more compact and homogeneous with our gaussian model. In addition, our results indicate that the systemic velocities of the shocked clump and quiescent cloudlet are closer to each other than what was previously found (compare Fig. 6.15 with Fig. 6.16). Therefore, the assumption that these two molecular structures are physically associated is strengthened.

We note that even with the gaussian fit, the first moment maps of ^{12}CO and ^{13}CO remain significantly different, in particular towards the shocked clump. This discrepancy could be caused by different geometries of the two isotopologs in distinct density regimes (Bron *et al.*, 2018), or by the asymmetry of the ^{12}CO line wings (which may bias the estimate of the centroid velocity).

6.2.2.2 Discussion

***i.)* Quiescent cloudlet** The cloudlet has a mean velocity $v_{\rm LSR} = -5.5$ km s^{-1} that is remarkably uniform throughout the structure. Using a single-gaussian model, we measured $v_{\rm LSR} = -5.7 \pm 0.3$ km s^{-1} from the centroid of the ^{13}CO lines, contrasting with the velocity of IC443 in the local standard of rest by more than 1 km s^{-1}. This discrepancy between the velocities of the cloudlet and IC443 can be interpreted in two manners:

– Either the velocity shift traces a slightly distinct proper motion of the cloudlet with respect to the rest of the molecular gas in the extended G region (as a matter of fact, the velocity wings of the ^{12}CO lines are still within the velocity range of the maser source in IC443G). Lee *et al.* (2012) found that although there are discrepancies of order $\Delta v \sim 1$ km s^{-1} between the proper motions of the small clouds and the systemic velocity of IC443, they are likely to be at the same distance as the remnant.

– Or the velocity shift is caused by distance. If that is the case, a shift $\Delta v = 1$ km s^{-1} would correspond to a maximum displacement of the kinematic distance $\Delta d \approx 300$ pc (following

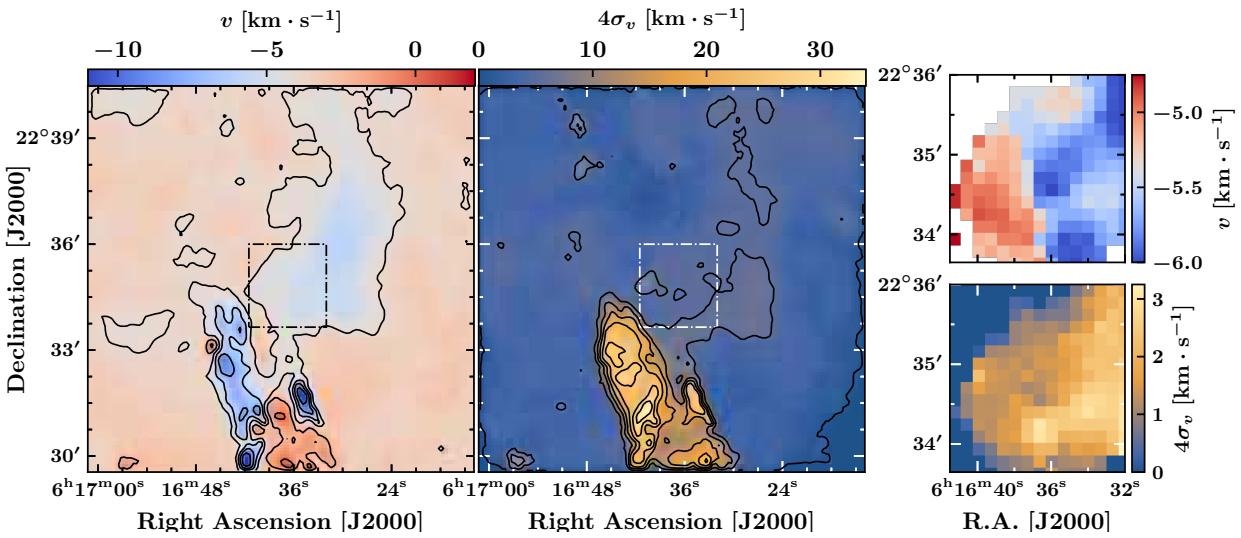

Figure 6.18 Moment maps calculated with Eq. 6.1 and Eq. 6.2. *Left:* first moment map of the IRAM 30m ^{12}CO J=2–1 data cube. *Center:* second moment map. *Right:* zoom into the ring-like structure of the first (top) and second (bottom) moment maps of the J=3–2 data cube (indicated by the box on the left and center panels). The colorbar of the 1st moment map is centered on the velocity of IC443 in the local standard of rest, $v_{\rm LSR} = -4.5$ km s^{-1}.

Wenger *et al.* 2018).

The second moment map reveals a much lower velocity dispersion within the cloudlet than for the shocked clump. The velocity dispersion varies between ∼5 km s^{-1} and ∼7 km s^{-1}, which is slightly higher than the velocity dispersion across the background field, around ∼ 4 km s^{-1}.

***ii.)* Ring-like structure** The apparent ring-like structure is further analyzed in Fig. 6.18 (right panels) where the first and second moment maps are determined for the ^{12}CO J=3–2 data cube obtained with APEX. The superior spectral resolution of the APEX data cube offers a better precision in the determination of the moment maps, at the cost of a lower spatial resolution (see Tab. 6.2). In the first moment map the mean velocity gradient within the ring is suggesting that the structure is rotating or expanding non-isotropically, since the mean velocity field varies between $v_{\rm LSR} = -4.7$ km s^{-1} and $v_{\rm LSR} = -5.8$ km s^{-1} from the western to the eastern arc of the ring. This apparent velocity gradient could be also due to systematic velocity variations between two or more distinct sub-clumps that are not well resolved by our J=3–2 observations ($\theta = 19.2''$, ∼0.2 pc). The velocity dispersion measured within the ring-like structure varies between 1 km s^{-1} and 3 km s^{-1}, with a positive gradient from the eastern part to the western part of the structure where it spatially connects to the cloudlet.

***iii.)* Shocked clump** According to Fig. 6.15, the shocked clump has a systemic velocity varying between $v_{\rm LSR} = -6$ km s^{-1} and $v_{\rm LSR} = -8.5$ km s^{-1} throughout its structure. These mean velocities are subject to caution as the self-absorption and asymmetric wings characterizing the line emissions of ^{12}CO might bias the value of the centroid. According to Fig. 6.16, the shocked clump has a systematic velocity $v_{\rm LSR} = -6.5$ km s^{-1} that is remarkably constant across the structure.

Careful measurement of the centroid of ^{13}CO lines using a single gaussian function favors a velocity centroid of -4.4 ± 0.2 km s^{-1} for the shocked clump, which is consistent with the velocity

of the maser in IC443G, $v_{LSR} = -4.5$ km s^{-1} (Hewitt *et al.*, 2006). The discrepancy between the centroid estimated from ^{13}CO lines and the centroid inferred from the second moment map might be caused by a non-gaussian profile of the ^{12}CO lines (*i.e.* the high-velocity wings are asymmetric), or it could be caused by distinct spatial distribution of the emission of each isotopolog (Bron *et al.*, 2018). The second moment map displays important velocity dispersions, spanning from ∼15 km s^{-1} and up to ∼36 km s^{-1} within the shocked gas, increasing towards the center of the clump. These high velocity dispersions confirm the nature of the 'shocked clump'.

***iv.)* Shocked knot** According to Fig. 6.15 (left panel), the shocked knot has a systemic velocity $v = -9$ km s^{-1}, that is slightly shifted with respect to the shocked clump. The second moment map shows a uniform velocity dispersion of $25 - 30$ km s^{-1}, similar to the dispersion measured within the main shocked molecular structure.

Background The rest of the field of observation has a quasi-uniform mean velocity of approximately -4.1 km s^{-1} to -2.8 km s^{-1}, which is slightly different from the mean velocity of IC443G in the local standard of rest but consistent with the systemic velocity of the ambient NW-SE molecular cloud in which IC443G is embedded (Lee *et al.*, 2012). The velocity dispersion of the ambient gas is spanning from < 1 km s^{-1} to ~ 10 km s^{-1} in a few areas where the velocity dispersion is locally enhanced, with an average value ∼4 km s^{-1}.

Excluding the contribution of the shocked structures and localized high-velocity dispersion knots, velocity dispersions measured from the ^{12}CO J=2–1 line in the extended G field span a range of r.m.s velocity $\sigma_v = 0.4$ to 1.3 km s^{-1} in the ambient (background) gas, and $\sigma_v = 1.2$ to 1.8 km s^{-1} towards the cloudlet. At a temperature of 10 K, the thermal contribution is $\sigma_v = 0.32$ km s^{-1} and it is likely that small-scale motions within the complex of molecular gas contribute to the measured dispersion, hence the ambient cloud is mostly quiescent, with turbulent motions smaller than 1 km s^{-1}.

The velocity dispersion measured towards the cloudlet with the ^{13}CO lines is $\sigma_v = 0.8 \pm 0.1$ km s^{-1}, which is consistent with typical molecular condensations (Larson, 1981). According to these measurements of the velocity dispersion traced by ^{12}CO and ^{13}CO lines, we dot not find any kinematic signature of interaction of the cloudlet nor the ambient cloud with the SNR shocks in the extended G region, except for a few localized high-velocity dispersion knots. Thus, our findings indicate that the ambient cloud of Cornett *et al.* (1977) and Lee *et al.* (2012) is currently not perturbed by the SNR.

6.2.3 Spectral features

In this section, we aim to describe the main spectral features found in our PPV cubes. We defined spatial boundaries enclosing the structures described in section 6.2.1 and independently studied the spectral data corresponding to each sub-region of the field. The spatial boxes defined for the quiescent cloudlet (A), ring-like structure (B), shocked clump (C) and secondary shocked knot (D) are shown in Fig. 6.19, and the average spectra obtained in these boxes are presented in the Fig. 6.20 and Fig. 6.21 for each ^{12}CO, ^{13}CO and C^{18}O line observed with the IRAM 30m and APEX telescopes. Where applicable, we chose to present the APEX spectra (*e.g.* for the J=2–1 line), because they offer a better spectral resolution ($\Delta v = 0.1$ km s^{-1}). Beforehand, we checked

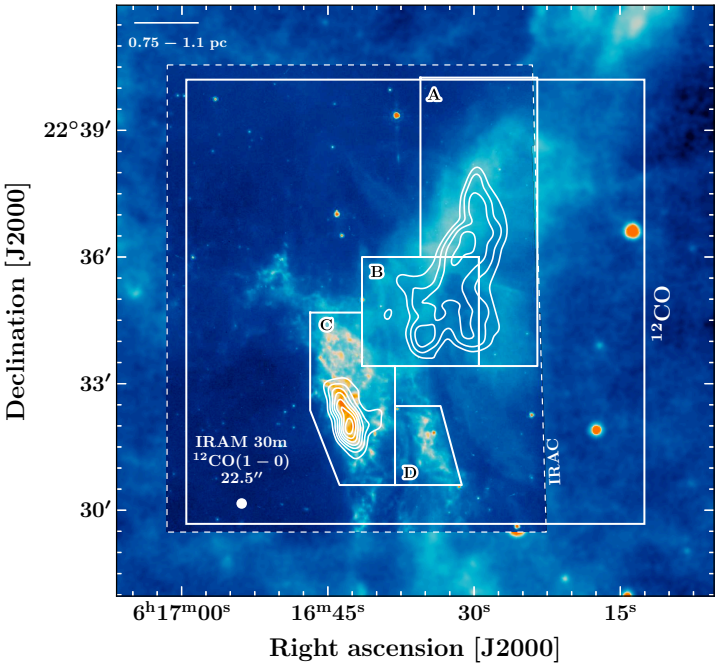

Figure 6.19 *Background: Spitzer*-MIPS (24.0 μm) and *Spitzer*-IRAC (8.0 μm) maps. *White contours:* peak brightness temperature map of the ^{12}CO J=2–1 line observed with the IRAM 30m (see also Fig. 6.10). The white boxes represent the area where the spectra corresponding to each structure (A, B, C, D) are extracted (see text for details on the correspondance of these boxes with the structures shown in Fig. 6.13). The beam diameter of the IRAM 30m observations of ^{12}CO J=1–0 is shown in the bottom-left corner. The 10′ × 10′ field of observations is indicated by a solid white box (indicated by the label '^{12}CO'), and the IRAC field of observation is indicated by a dashed white box (indicated by the label 'IRAC').

that the APEX and IRAM 30m spectra are consistent.

The choice of the boundaries is based on our morphological classification, and we carefully checked that the brightest spectral features are consistent across the different boxes that we defined. We performed that spatial separation manually, as the size of our sample is not large enough to apply robust statistical methods (*e.g.* clustering, see Bron *et al.* 2018). In chapter 8, we will show that the emission of the shocked clump can be strictly separated from the rest of the ^{12}CO features using rotational line ratios, but for now we will use arbitrary boundaries. Based on the analysis of the emission of ^{12}CO, ^{13}CO and C^{18}O spectra, our description of the spectral features found in the extended G region is the following:

i.) **Quiescent cloudlet** Towards box 'A' (Fig. 6.20, left panel), the profiles of the ^{12}CO and ^{13}CO lines are similarly double-peaked, and best modeled by the sum of two gaussian functions centered on the systemic velocities $v_{\rm LSR} = -5.7 \pm 0.3$ km s^{-1} (associated with the cloudlet) and $v_{\rm LSR} = -3.3 \pm 0.1$ km s^{-1} (associated with the ambient cloud of Cornett *et al.* 1977).

ii.) **Ring-like structure** Towards box 'B' (Fig. 6.20, right panel), the ^{12}CO and ^{13}CO lines are double-peaked as well. The use of two gaussian functions to model the line profile yields the systemic velocities $v_{\rm LSR} = -5.6 \pm 0.2$ km s^{-1} (associated with the ring-like structure) and $v_{\rm LSR} = -3.3 \pm 0.1$ km s^{-1} (associated with the ambient cloud of Cornett *et al.* 1977). The gaussian decomposition is very similar to that of the cloudlet, suggesting that the apparent ring-like structure might be incidental.

iii.) **Shocked clump** The spectra corresponding to box 'C' (shocked clump) are shown in Fig. 6.21. Considering the geometry of the SNR and the locally perpendicular direction of propagation of the SNR shockwave (van Dishoeck *et al.*, 1993), the high-velocity emission arises from

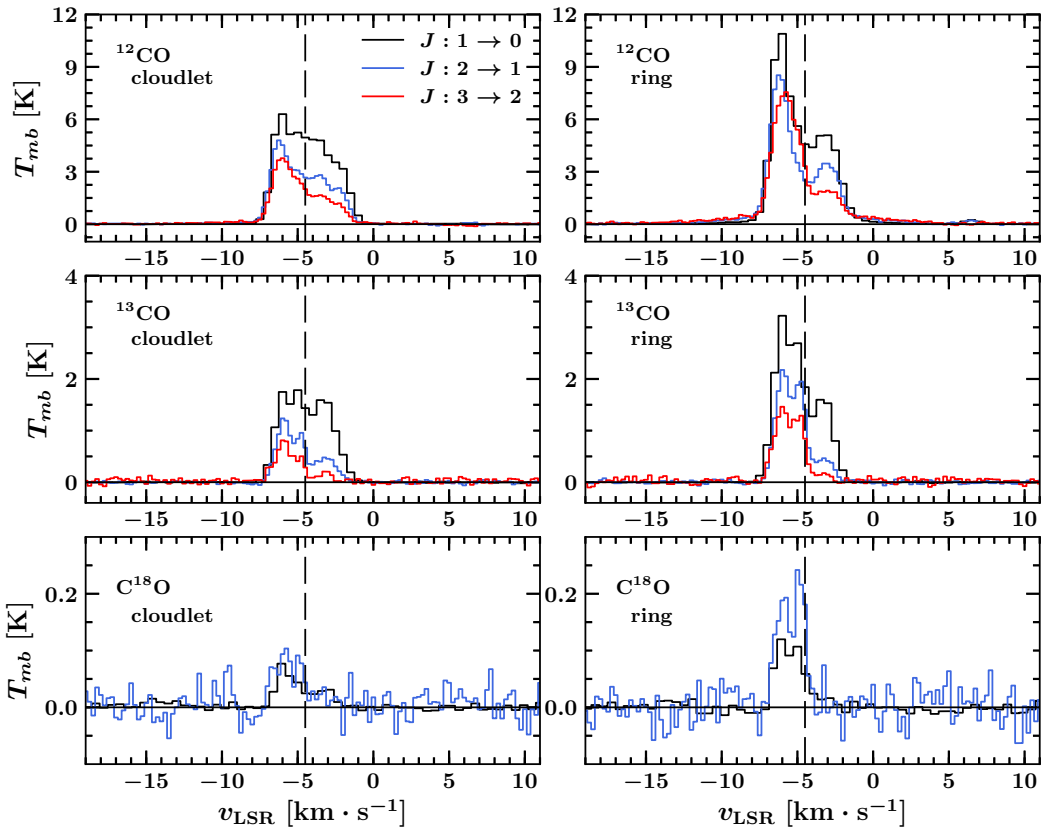

Figure 6.20 Spectra averaged over the boxes enclosing the regions of the quiescent cloudlet (left panels) and ring-like structure (right panels) defined in Fig. 6.19. The following lines are represented: ^{12}CO J=1–0, ^{13}CO J=1–0 and C^{18}O J=1–0 (in black, IRAM 30m observations); ^{12}CO J=2–1, ^{13}CO J=2–1 and C^{18}O J=2–1 (in blue, APEX observations); ^{12}CO J=3–2 and ^{13}CO J=3–2 (in red, APEX observations). Spectral cubes were resampled to allow a direct comparison between the different spectra. Spatial resolutions of all transitions were modified to the nominal resolution of the C^{18}O J=2–1 (which is the coarsest of all), $\theta = 30.2''$. Spectral resolutions were set to 0.5 km s^{-1} for IRAM 30m data and 0.25 km s^{-1} for APEX data. On all panels, the systemic velocity of IC443 is indicated with a vertical dashed line (located at $v_{\rm LSR} = -4.5$ km s^{-1}). The values of the baseline r.m.s are given in Tab. 6.1 and Tab. 6.2.

shock waves propagating in at least two directions, most likely a collection of transverse shocks propagating along the molecular shell. In other words, the projection along the line of sight of several distinct shocked knots and filaments (Fig. 6.19) with distinct systematic velocities could contribute to the broadening of the ^{12}CO lines towards the blueshifted and redshifted velocities. We measure $\Delta v \simeq 27$ km s^{-1} and $\Delta v \simeq 21$ km s^{-1} respectively for the zero baseline width of the blueshifted and redshifted high-velocity wings. At best, these values indicate a rough estimate of the velocity of shocks propagating in the shocked clump.

Except for the J=1–0 spectrum where the emission of the ambient gas contributes to the average spectra, all spectra of ^{12}CO lines exhibit a significant absorption feature around the $v_{\rm LSR}$ of IC443G, suggesting that there is strong self-absorption of the emission lines. Evidence of line absorption is found in the velocity range -6 km s^{-1} $< v_{\rm LSR} < -2$ km s^{-1}, which is where we detect the spatially extended features associated with the NW-SE complex of molecular gas described

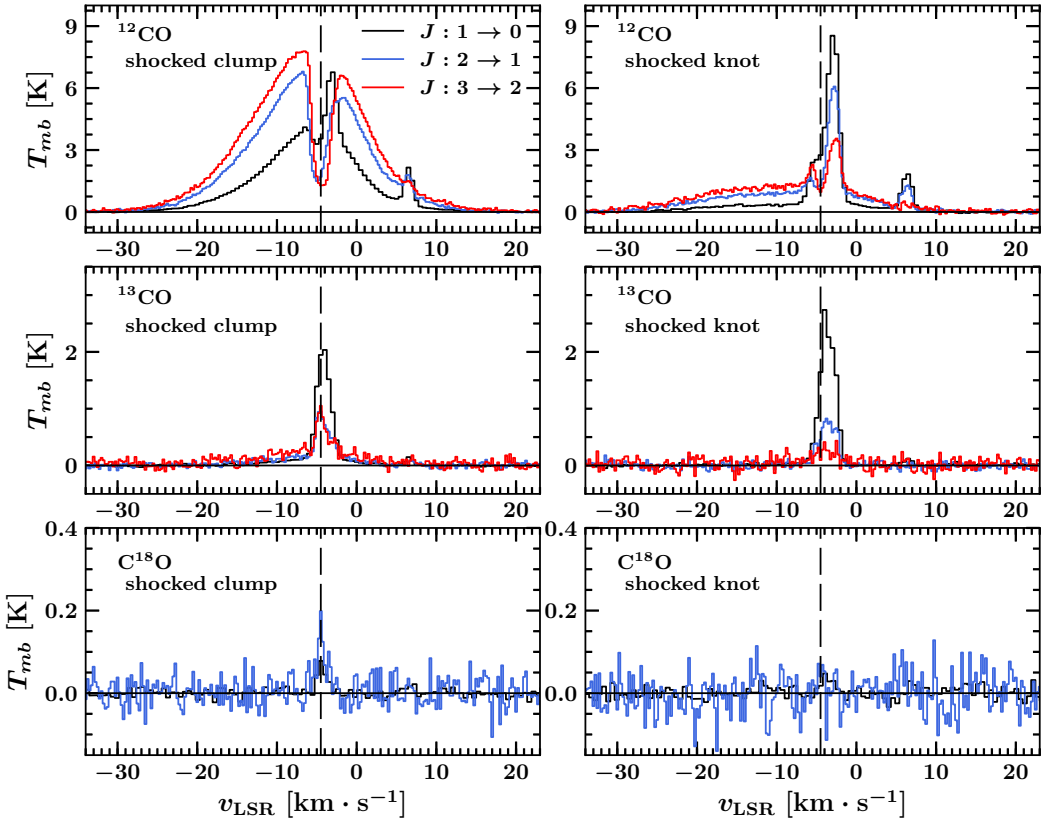

Figure 6.21 Spectra averaged over the boxes enclosing the regions of the main shocked clump (left panels) and secondary shocked knot (right panels) defined in Fig. 6.19. The following lines are represented: ^{12}CO J=1–0, ^{13}CO J=1–0 and C^{18}O J=1–0 (in black, IRAM 30m observations); ^{12}CO J=2–1, ^{13}CO J=2–1 and C^{18}O J=2–1 (in blue, APEX observations); ^{12}CO J=3–2 and ^{13}CO J=3–2 (in red, APEX observations). Spectral cubes were resampled to allow a direct comparison between the different spectra. Spatial resolutions of all transitions were modified to the nominal resolution of the C^{18}O J=2–1 (which is the coarsest of all), $\theta = 30.2''$. Spectral resolutions were set to 0.5 km s^{-1} for IRAM 30m data and 0.25 km s^{-1} for APEX data. On all panels, the systemic velocity of IC443 is indicated with a vertical dashed line (located at $v_{\rm LSR} = -4.5$ km s^{-1}). The values of the baseline r.m.s are given in Tab. 6.1 and Tab. 6.2.

by Lee *et al.* (2012). Hence, it is likely that the foreground cold molecular cloud is causing the absorption of the ^{12}CO J=1–0, J=2–1 and J=3–2 lines. A faint and thin emission line is detected around $v = 6.5$ km s^{-1} both in the ^{12}CO and ^{13}CO spectra. This signal is associated with the NE-SW quiescent arm of molecular gas described in section 6.2.1, which is spatially coincident with the shocked clump, but more extended.

iv.) **Shocked knot** The shock signature of the line contained in box ‘D’ is distinct from the shocked clump. As hinted by the standard moment maps (Fig. 6.15), its fainter high-velocity wings are displaced towards negative velocities. A self-absorption feature is also observed in this structure. Between $v = -5.5$ km s^{-1} and $v = -2$ km s^{-1} a bright and thin feature traces the ambient gas shown in Fig. 6.14, and the contribution of the NE-SW quiescent arm is also detected around $v = 6.5$ km s^{-1}.

^{13}CO line profiles The linewidth measured from the ^{13}CO line profiles when we consider only the spectral component that are physically associated with the quiescent cloudlet and ring-like structure (discarding the contribution of the ambient cloud) are respectively 2.0 ± 0.3 km s^{-1} and 1.6 ± 0.3 km s^{-1}, measured by carefully defining much more constrained spatial boundaries around the structures. From the average spectra presented in this section, there is no spectral evidence for the propagation of molecular shocks and/or outflows within these two structures, except for the faint wings displayed by the ^{12}CO lines in the box associated with the ring-like structure. These extended wings arise from the contamination by the high-velocity emission of the shocked sub-structures that are contained in box 'B' (see Fig. 6.15, 6.16).

Chapter 7 | NIKA2 continuum maps

Contents

One of the conclusions of our investigation of the ^{12}CO, ^{13}CO and C^{18}O lines in the 'IC443 extended G region' was the requirement to perform continuum observations in order to complement the limitations of our molecular analysis with a study of dust thermal emission (Dell'Ova *et al.* 2020, see discussions in section 8.2.6). To this end, we submitted a project to the 'NIKA2 2020 summer call for proposals' which was accepted and rated 'A' by the IRAM program committee. We describe the mapping strategy, observing scripts and data reduction in the next sections.

7.1 | Setup, mapping strategy, observations

7.1.1 Initial mapping strategy

Proposed observations and spatial coverage We proposed to perform continuum observations at 1.15 mm and 2 mm in the extended G region with the NIKA2 camera, in order to work towards the establishment of near-IR to millimeter spectral energy distributions of dust thermal emission (the analysis is presented in Chapter 9). We initially aimed to map the millimeter continuum emission in the same $10' \times 10'$ field of observations that was already mapped in ^{12}CO, ^{13}CO and C^{18}O with the IRAM 30m and APEX telescopes (see Chapter 6). It was recommended by the IRAM technical staff to perform observations with a larger field of view than our spectral-line maps, in order to correctly estimate the background emission during data reduction.

In our proposal, we requested a $12' \times 12'$ mosaic centered on the position $\alpha_{[J2000]}$=6^{h}16^{m}37.5^s, $\delta_{[J2000]}$=+22°35′00″ (see also Fig 6.1), in order to have a fully-sampled map with a quasi-uniform

signal-to-noise ratio across our $10' \times 10'$ area of interest, and to meet the background reduction criteria.

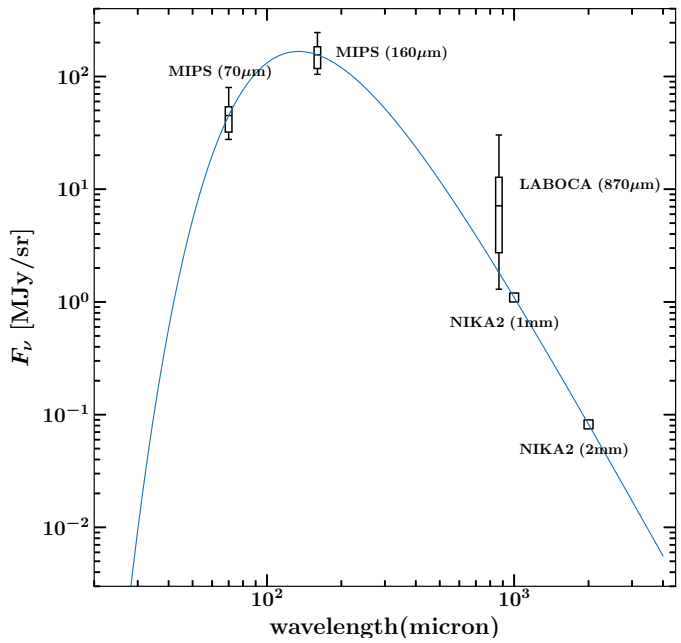

Figure 7.1 Preliminary spectral energy distribution of the IC443 extended G region (spatially averaged). The *Spitzer*/MIPS 70 µm, 160 µm and APEX/LABOCA 870 µm data points represent previous observations of the region, and the NIKA2 1 mm and 2 mm data points are modelled using a single modified black body approximation $S_\nu \sim B_\nu(T_\mathrm{d})\nu^2$ (shown by the blue curve, see text). For each observed continuum data point, statistical indicators are shown. The boundaries of the boxes represent the first and third quartiles ($Q_1 = 0.25$: 25$^{\mathrm{th}}$ percentile, $Q_3 = 0.75$: 75$^{\mathrm{th}}$ percentile). The horizontal bars inside the boxes correspond to the median, and the bottom and top caps represent the 1$^{\mathrm{st}}$ ($p = 0.1$) and 9$^{\mathrm{th}}$ ($p = 0.9$) deciles.

Time estimate Since we did not have prior knowledge of the millimeter continuum fluxes in the extended G region, we based our time estimate on an extrapolation from FIR and sub-millimeter data. The $10' \times 10'$ region was mapped by *Spitzer*/MIPS at 24 µm, 70 µm and 160 µm, and by the APEX/LABOCA continuum camera at 870 µm.

Using the `Python` module `curve_fit`, we determined the best-fit modified black body model $S_\nu \sim B_\nu(T_\mathrm{d})\nu^2$ (MBB, see section 5.1.2) associated with our FIR and sub-millimeter data points. Based on the best fit, we inferred the corresponding millimeter continuum fluxes $S_\nu(1\ \mathrm{mm}) \sim 1.1$ MJy/sr, and $S_\nu(2\ \mathrm{mm}) \sim 0.083$ MJy/sr (see Fig. 7.1). We then used the '`NIKA2_Time_Estimator.py`' `Python` code provided by the IRAM to estimate the time required to perform the observations. Assuming a map size $12' \times 12'$ with a 3σ detection, the code returns a time estimate of ~ 16.3 hours for the 2 mm band, and ~ 14.7 hours for the 1.15 mm band. We adopted an average source elevation of 60°, pwv of 3 mm and the parameters `overhead = 1.5` (telescope overheads: slewing, pointing, focusing, calibration, *i.e.* all telescope time which is not spent on source) and `filter = 1.5` (post-processing noise filtering: values from 1.0 for a point source to 2.0 for extended emission).

7.1.2 Observing scripts

The observations were performed using the On-The-Fly (OTF) mapping technique, with the recommended values for the spacing between OTF lines and scanning speed (20″, 40″ s^{-1}). The telescope was controlled *via* `paKo`, the observer's user interface at the IRAM 30m telescope. We present the scripts used during the first week of observations in the algorithm 6. Our project was observed at the IRAM 30m by pool observers during the second semester of 2020, and then again

during the first semester of 2021. Based on preliminary reductions of the first data delivery and discussions with the IRAM technical staff, we updated our mapping strategy by increasing the field size to $14' \times 14'$ and shifting the center to $\alpha_{[J2000]}=6^h16^m45.5^s$, $\delta_{[J2000]}=+22°33'00''$. Increasing the size and displacing the center of the field towards south-east was a recommendation of R. Zylka (IRAM), in order to correctly map out the extended emission and make the results more reliable.

Algorithm 6: On-The-Fly NIKA2 mapping (paKo script).

```
1: source IC443G;
2: def int Nrounds;
3: let Nrounds 2;
4: for i 1 to Nrounds;
5:    say "Loading round " 'i' "of " 'Nrounds';
6:    @ nkotf 12 12   0 0 20 40 radec;
7:    @ nkotf 12 12 90 0 20 40 radec;
8:    next;
```

Description of the code: these `paKo` commands allow to consecutively perform an horizontal and vertical On-The-Fly map (size $\sim 12' \times 12'$). The commands `nkotf` (lines 6-7) are followed by the map sizes along the two axes (in arcminutes), the angle and inclination of the scanning direction (anti-clockwise, in degrees), the spacing between OTF lines (in arcseconds) and the scanning speed (in arcseconds per second).

7.2 | Data reduction

7.2.1 PIIC pipeline

NIKA2 observations are reduced using the Pointing and Imaging In Continuum software (hereafter `PIIC`) developed by R. Zylka at IRAM. `PIIC` is distributed by IRAM *via* the `GILDAS` pages, it is an extension of the `MOPSIC` data reduction software (Zylka, 2013). `PIIC` works with calibration files (called DAFs) which contain the response of the kinetic inductance detectors (hereafter KIDs) for flux calibration, deleted receiver pixels, frequency files listing the natural resonance frequencies of all KIDs, positions of each KID in the field of view and the atmospheric conditions measured by the observatory's tau-meter during all observing runs.

The DAFs files corresponding to our observations were released in April 2021, approximately five months after our observations, due to a delay caused by issues related to the atmospheric opacity measurements. The essential reductions applied by `PIIC` are the flat field correction, correlation correction, sky subtraction, baseline subtraction, calibration and re-gridding of the final maps. The reduction procedure is an iterative process, during which the source definition and signal-to-noise is improved at each iteration (the noise r.m.s is measured on a user-defined polygon corresponding to a source-free region of sky).

To perform the reduction, we followed the guidelines of the `PIIC` user's guide written by S. Berta and R. Zylka[1]. For an extended object with a complex geometry, it is recommended to use the `PIIC` iterative mode without any a priori definition of the source. We present the `PIIC` script used to reduce the data in the algorithm 7.

[1] https://www.iram.fr/~gildas/dist/piic.pdf

Algorithm 7: `PIIC` reduction script.

```
1: @ mapTPdefs;
2: let nikaBand "1";
3: init inList;
4: init outList;
5: inDir imbfitsDir;
6: outDir reduced;
7: inList "IC443G_a" 'nikaBand';
8: select type m;
9: sort inList;
10: let nrPause 0;
11: let souRmxAS 0;
12: let souRmnAS 0;
13: let souPA 0;
14: let posSeq "6 16 45.5 22 33 00";
15: let eqExtAS 1200.0;
16: let souRAoffAS 0.0;
17: let souDECoffAS 0.0;
18: let blOrderOrig 2;
19: let weakSou yes;
20: let deepField no;
21: let souSign "+";
22: let mxA1toiAvRMS 250.0;
23: let mxA2toiAvRMS 70.0;
24: let mxA3toiAvRMS 190.0;
25: let sbSource "SourceModel.fits";
26: let nIterModel 10;
27: let snrLevel 2.5;
28: let let polZmEq "pol";
29: let polRMSeq "rmspol";
30: @ mapTPfurtherSets;
31: let smModelPar 3.0;
32: exit;
```

Description of the code: The parameter `nikaBand` (line 2) is set either to '1' (1.15 mm band) or '2' (2 mm band). Lines 3-7 define the paths of the working directories and filenames of the NIKA2 observations `FITS` files. Line 8 selects the scans corresponding to mapped observations. Since we do not provide an *a priori* definition of the source, the variables that define the position and size of the source in lines 11-13 are set to 0, as well as the source offsets relative to the map center (lines 16-17). Line 10 disables the interactive pauses between iterations. `posSeq` (line 14) defines the angular position of the center in the final output map, and `eqExtAS` is the size of the final field of view in arcseconds. `blOrderOrig` is the polynomial order of the baseline correction model over individual subscans, set to the default value in this case (2). `weakSou` is set to 'yes' (line 19), which tells `PIIC` that there is faint extended emission in the field of observations, but we set `deepField` to 'no' (line 20), which is adapted to blank fields with very faint point-like sources. We set `souSign` to '+' (it can be set to '-' to study negative signals caused by the Sunyaev-Zeldovich effect towards galaxy clusters). The lines 22-24 define thresholds (in mJy/beam per sampling rate) used to reject maps from the dataset (in case of unstable sky conditions), we used the default values recommended by the NIKA2 team. Line 25 defines the source model (see text). `snrLevel` (line 27) determines the signal-to-noise threshold that defines the source during the iterative process, and `nIterModel` is the number of iterations. `polZmEq` (line 28) and `polRMSeq` (line 29) are respectively the user-defined polygons that determine the area in which the signal-to-noise ratio is optimized by the iterative model, and the source-free area in which the r.m.s is measured. Line 30 calls a script that contains additional fine-tuning parameters that we did not modify. Line 31 applies a smoothing algorithm in order to improve the detection of source pixels.

7.2.2 Iteration residuals

We performed a total of 20 iterations both for the 1.15 mm and 2 mm maps. With a total of 140 Gb of raw NIKA2 data, the `PIIC` reduction costs a significant computation time. The reduction was performed on a regular laptop (Intel Core i7-8650U CPU: 8×1.9 GHz with 15.5 Gb of random access memory) hence it required $\sim$ 40 hours for the 2 mm map, and $\sim$ 120 hours for the 1.15 mm map. We made a first round with 10 iterations which was insufficient (see Fig. 7.2), and then continued with 10 more iterations. The line 25 in algorithm 7 allows to continue the `PIIC`

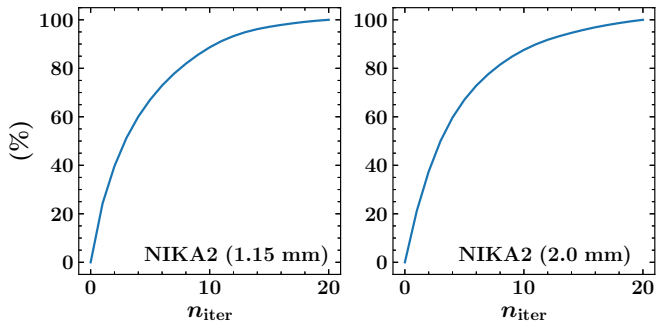

Figure 7.2 Total flux recovery with respect to the iteration number $n_{\rm iter}$ (in percent relative to the total flux difference between the 20$^{\rm th}$ and 0$^{\rm th}$ iteration maps) for the NIKA2 1.15 mm (left panel) and 2 mm (right panel) continuum maps.

reduction where it was interrupted, by introducing the output source model of the first round (at iteration $n = 10$) as the initial source model ($n = 0$) of a new PIIC reduction round.

In Fig. 7.2, we show the evolution of the total flux measured in the continuum maps with respect to the number of PIIC iterations. We have reached a satisfying convergence, although more iterations ($n \gg 30$) might increase the total flux by a few percent, in particular at 2 mm. The PIIC user's guide states that if the average difference across the field is a small fraction of percent of typical sources' flux, then the number of iterations is sufficient. The average difference between our $n = 19$ and $n = 20$ iteration maps represents 0.17% and 0.10% of the median flux respectively at 1.15 mm and 2 mm.

7.3 | Data products

7.3.1 Continuum maps

Intensity and noise maps We have obtained continuum mapped observations of the extended G region at 1.15 mm and 2 mm with NIKA2. The intensity and noise maps are shown in Fig. 7.4. We produced the noise maps by rescaling the weight maps to the r.m.s, following the steps indicated in the PIIC manual. By iteratively updating the source model, PIIC removed most of the negative signal present in the raw frames, although there are still absorption patches on the outer edges of the shocked clump (with negative intensities $|F_\nu| \ll 0.1\sigma$, where σ is the r.m.s, hence negligible).

Continuum observations of the region trace the same spatial structures as in our ^{12}CO observations: the bright molecular shocked clump G and quiescent molecular cloudlet (see section 6.2.1). Since our NIKA2 maps are more extended, we also mapped the shocked molecular clump F, in the northeastern area of the field of observations (see also Fig. 2.20). The NIKA2 continuum maps also reveal the continuity between the bright shocked clump G and the rest of the molecular shell that extends towards the south, and the diffuse emission that connects the shocked clump to the quiescent cloudlet.

7.3.2 Investigation of the '2 mm / 1.15 mm' continuum flux ratio

We produced a map of the flux ratio between our 2 mm and 1.15 mm maps (see Fig. 7.3). Using a gaussian convolution kernel, we convolved the maps to the same resolution and then measured the ratio F_ν[2 mm]/F_ν[1.15 mm] in each pixel, where F_ν[2 mm] and F_ν[1.15 mm] were converted from Jy/beam to Jy/sr, using the following formula:

$$F_\nu[\mathrm{Jy/sr}] = F_\nu[\mathrm{Jy/beam}]\frac{4\ln(2)}{\pi\Omega^2} \tag{7.1}$$

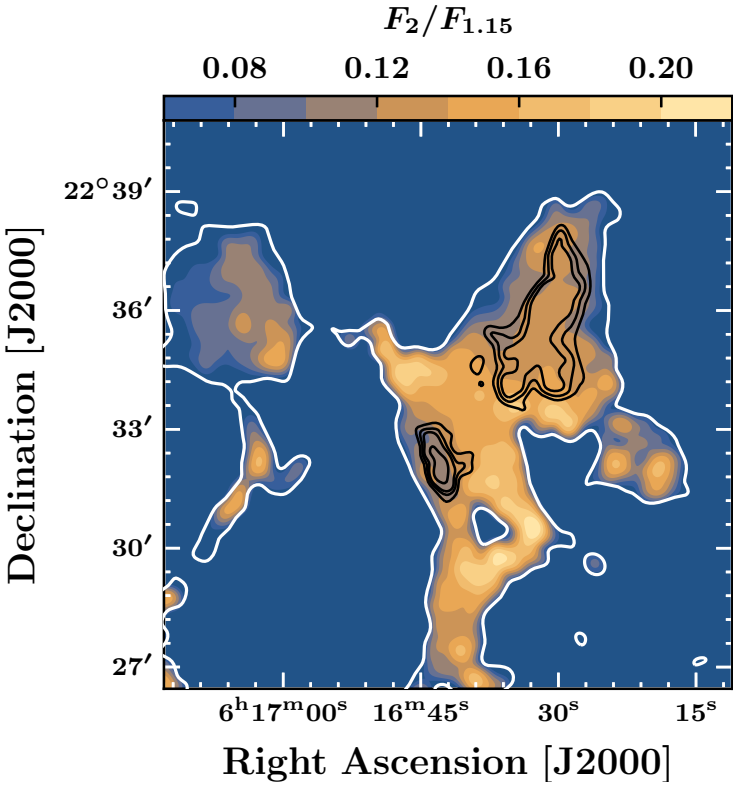

Figure 7.3 Flux ratio between the NIKA2 continuum maps at 2 mm and 1.15 mm. The quantity represented in colors is the pixel-per-pixel ratio F_ν[2 mm]/F_ν[1.15 mm] (both converted in MJy/sr). White contours indicate the area in which F_ν[1.15 mm] $\geq \sigma$, where σ is the r.m.s of the 1.15 mm map. The black contours correspond to the IRAM 30m ^{12}CO J=2–1 peak map shown in Fig. 6.10 (contour levels: 0.25, 0.35, 0.45 and 0.75 times the maximum value across the map).

where Ω is the beam size (in radian). We find that the '2 mm / 1.15 mm' ratio varies between $\sim$ 0.06 and $\sim$ 0.2 across the map, with significant local variations. In addition to dust temperature and opacity index variations, two physical processes can produce variations of the ratio:

– Contribution of bright ^{12}CO lines to the NIKA2 broadband maps can lower the [2 mm / 1.15 mm] ratio, since the 1.15 mm band is sensitive to the J=2–1 line although the 2 mm band is not sensitive to the J=1–0 line (see section 9.1.4 , Fig. 9.1).

– Contribution of free-free and synchrotron continua can enhance the [2 mm / 1.15 mm] ratio (see Fig. 5.1).

Therefore, Fig. 7.3 suggests that *i.)* the continuum emission towards the molecular clumps is contaminated by bright ^{12}CO lines, or that *ii.)* synchrotron and radio continua contribute to the continuum emission within the rest of the molecular shell without penetrating into the molecular clumps, or *iii.)* a combination of both. Our ^{12}CO observations support the first assumption (see *e.g.* Fig. 6.10), and radio observations at 330 MHz by Castelletti *et al.* (2011) also show that radio continua can contribute to the flux at 2 mm along the molecular shell. In fact, Fig. 7.3 shows that the [2 mm / 1.15 mm] ratio is lower in the shocked clump and quiescent cloudlet than in the rest of the SNR shell, which confirms that the areas of higher [2 mm / 1.15 mm] ratio ($\sim$ 0.2) trace free-free/synchrotron emission.

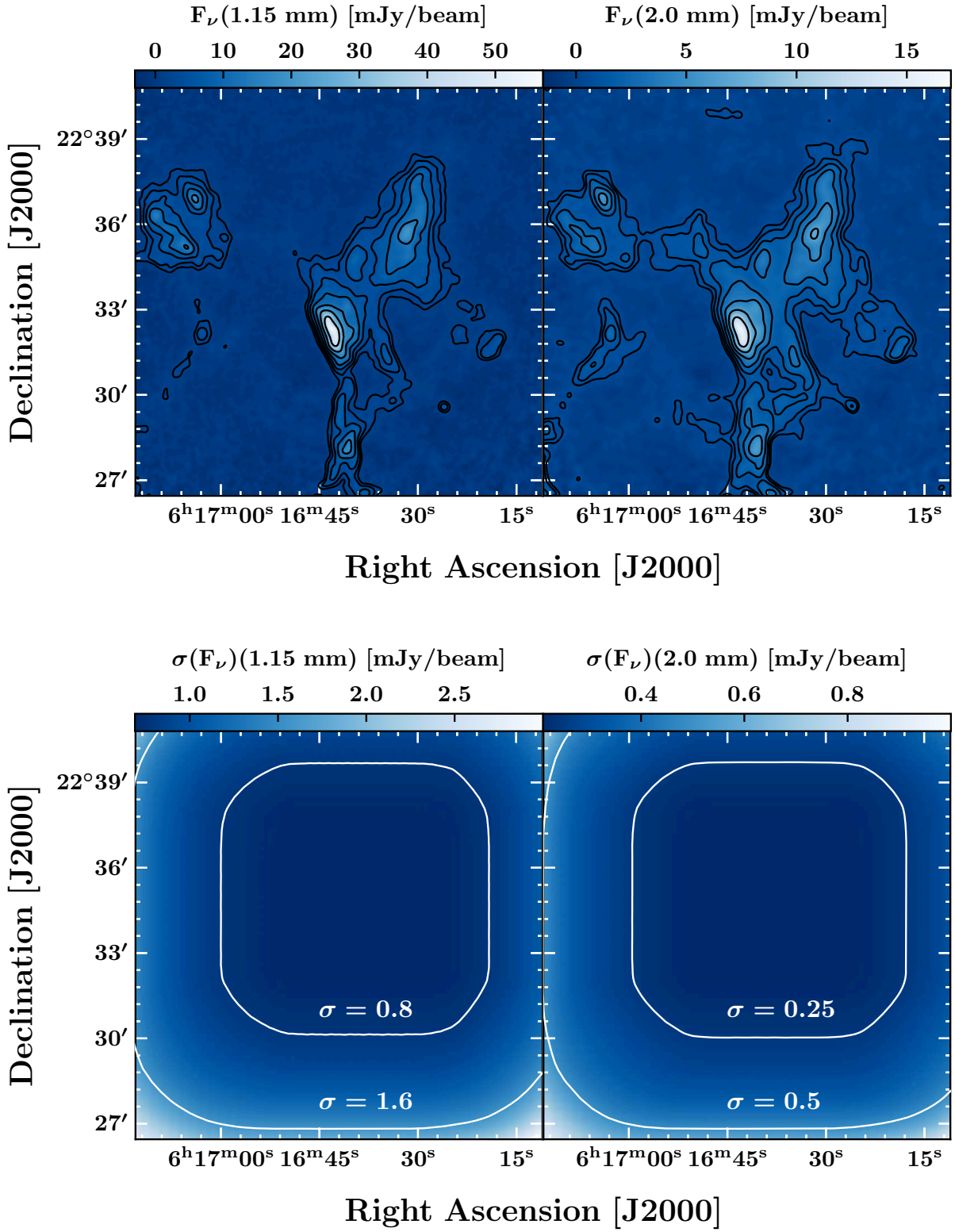

Figure 7.4 *Top row:* NIKA2 continuum maps at 1.15 mm (left panel) and 2 mm (right panel) produced with 20 PIIC iterations. Between 3σ and $\max(F_\nu(x, y))$, eight logarithmically spaced contour levels are drawn (in black). *Bottom row:* NIKA2 noise maps at 1.15 mm (left panel) and 2 mm (right panel) produced with 20 PIIC iterations. The numerical values of σ indicated on the noise maps are in mJy/beam.

Part IV :
Data analysis

Chapter 8 | Radiative transfer analysis of H_2 and ^{12}CO pure rotational lines

Contents

Introduction We have seen in chapter 1 that the interpretation and modelling of γ-ray spectra requires an accurate knowledge of the 'ISM contents' of the emitting region. More precisely, hadronic models require to estimate the amount of protons that the CRs can interact with. In the IC443 SNR, the peak of γ-ray emission is located towards the 'G' clump (Humensky and VERITAS Collaboration 2015, see also Fig. 2.15). Hence, the high-energy data indicates that the bulk of the interactions between the CRs propagating in the SNR and the ISM seems to be located in this region of the remnant.

In this chapter, we aim to work towards the establishment of precise mass measurements in the region IC443G from the analysis of molecular emission. In a first section, we present results obtained from the analysis of molecular hydrogen (H_2) pure rotational lines in a $\sim 2' \times 2'$ region centered on a shocked clump interacting with the SNR blast. In a second section, we analyze our own ^{12}CO, ^{13}CO and $C^{18}O$ $10' \times 10'$ dataset obtained with the IRAM 30m and APEX telescopes. Hereafter, we will be referring to the $10' \times 10'$ field of observations as the 'extended G region'. The location of the $\sim 2' \times 2'$ field of H_2 observations (with respect to the extended G region) is shown on Fig. 8.1.

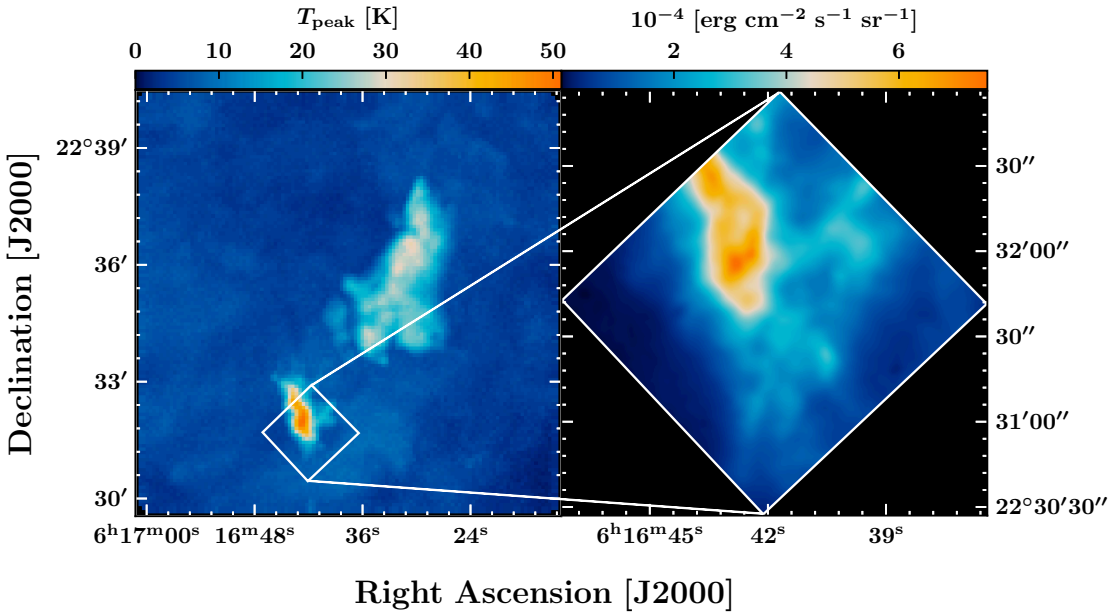

Figure 8.1 *Left:* ^{12}CO J=2–1 $10' \times 10'$ map of the peak temperature obtained with the IRAM 30m telescope. *Right:* H_2 $v = 0-0$ S(1) map of the integrated line intensity obtained with *Spitzer*-IRS.

H_2 and ^{12}CO as tracers of the molecular mass H_2 and ^{12}CO are respectively the most and second most abundant molecules in our universe. These two molecules are unmatched tracers of the dense, molecular phase of the ISM, since they are formed in cold dark clouds where the shielding from UV photons is sufficiently large. Despite that it is $\sim 10^4$ times less abundant than H_2, ^{12}CO is a more convenient molecule for observational purposes. In fact, H_2 is a homonuclear (*i.e.* highly symmetric) molecule with no permanent dipole moment, thus only quadrupole rotational transitions can occur ($\Delta J = \pm 2$, $\Delta J = 0$). As a consequence, the rotational and vibrational states of H_2 radiate weakly, only *via* the perturbations of the electric quadrupole moment when the molecule rotates or vibrates (*e.g.* Le Bourlot *et al.* 1999).

An additional consequence is that there are no allowed transitions from J_u=1 (the J=1–0 transition is forbidden, for it would violate the rule $\Delta J = \pm 2$), hence the two lowest energy levels cannot be directly traced by observations. Moreover, the pure rotational transitions ($v = 0$) of H_2 occur between $\sim$ 5 and $\sim$ 28 microns, a wavelength range in which the Earth's atmosphere is at best only partly transparent. Lastly, the energies of the excited H_2 rotational levels are relatively high, *e.g.* $\sim$ 509 K, $\sim$ 1015 K and $\sim$ 1681 K respectively for the levels probed by the S(0), S(1) and S(2) lines (see Tab. 8.1). As a consequence, the bulk of the cold molecular hydrogen ($\ll T = 10^2$ K) remains invisible, because high kinetic temperatures and/or intense FUV radiation are required to populate the upper levels of H_2 (*e.g.* Habart *et al.* 2005).

On the contrary, ^{12}CO (and its isotopologs, *e.g.* ^{13}CO) is an excellent tracer of the dense, cold molecular phase (*e.g.* Dame *et al.* 2001). Its first three pure rotational lines (J=1–0, J=2–1, J=3–2) trace relatively low-energy upper levels (respectively $\sim$ 5.5 K, $\sim$ 17 K and $\sim$ 33 K, see Tab. 8.4). Additionally, the sub-millimeter/millimeter ^{12}CO lines can be observed from ground-based observatories, such as the IRAM 30m telescope. However, ^{12}CO lines are likely to be optically thick and not correctly thermalized, and their use as a tracer of total molecular mass requires to

know the $^{12}CO/H_2$ abundance. Ultimately, there are no perfect tracers of the dense molecular phase.

line	J_u	λ_{ul} (micron)	A_{ul} (s^{-1})	g_u	E_u (K)
H_2 0–0 S(0)	2	28.219	2.9493×10^{-11}	5	509.85
H_2 0–0 S(1)	3	17.035	4.7716×10^{-10}	21	1015.2
H_2 0–0 S(2)	4	12.278	2.7607×10^{-9}	9	1681.7
H_2 0–0 S(3)	5	9.6645	9.8574×10^{-9}	33	2503.9
H_2 0–0 S(4)	6	8.0255	2.6489×10^{-8}	13	3474.4
H_2 0–0 S(5)	7	6.9089	5.8923×10^{-8}	45	4586.4
H_2 0–0 S(6)	8	6.1086	1.1444×10^{-7}	17	5829.8
H_2 0–0 S(7)	9	5.5112	2.0058×10^{-7}	57	7197.0

Table 8.1 Spectroscopic parameters corresponding to the observed lines. J_u is the rotational quantum number of the upper level, λ_{ul} and A_{ul} are respectively the wavelength and the Einstein coefficient of the pure rotational transition ($v = 0$ where v is the vibrational quantum number). E_u and g_u are respectively the energy and degeneracy corresponding to the upper level. The values given are taken from the Cologne Database for Molecular Spectroscopy (Müller *et al.* 2001, Müller *et al.* 2005, Endres *et al.* 2016) and Jet Propulsion Laboratory database (Pickett *et al.*, 1998), and are the numeric values used in this work.

8.1 | Molecular hydrogen (H_2)

8.1.1 Presentation of *Spitzer*-IRS spectral-line maps

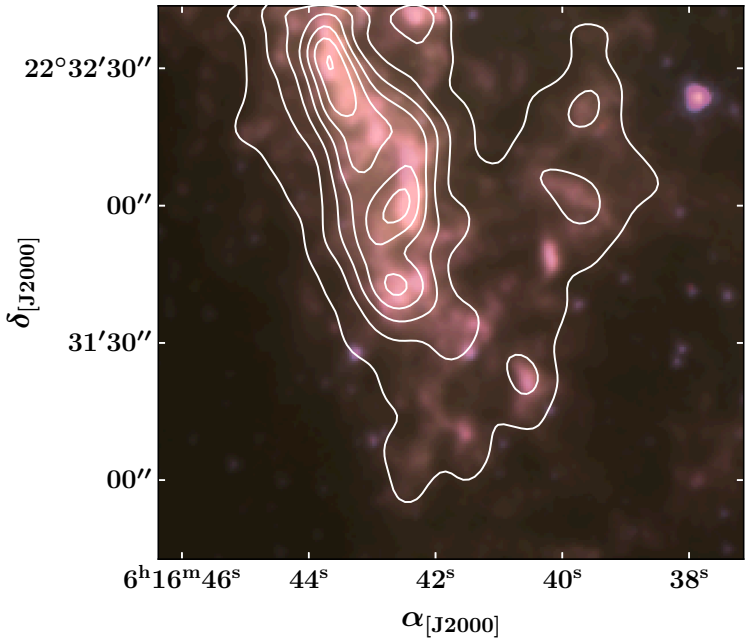

Figure 8.2 *Background:* composite RGB-like image produced from IRAC observations towards the IC443G clump (red: 4.5 µm, yellow: 8 µm, blue: 3.6 µm, see section 2.7 for the production process of RGB-like composite images). *White contours:* H_2 $v = 0 - 0$ S(3) spectral-line map from *Spitzer*-IRS observations (Neufeld *et al.*, 2004).

Origin of the data The IC443G clump was mapped with *Spitzer*-IRS by D.A. Neufeld *et al.* in 2007. In their initial proposal, Neufeld *et al.* (2004) aimed to perform spectral-line mapping

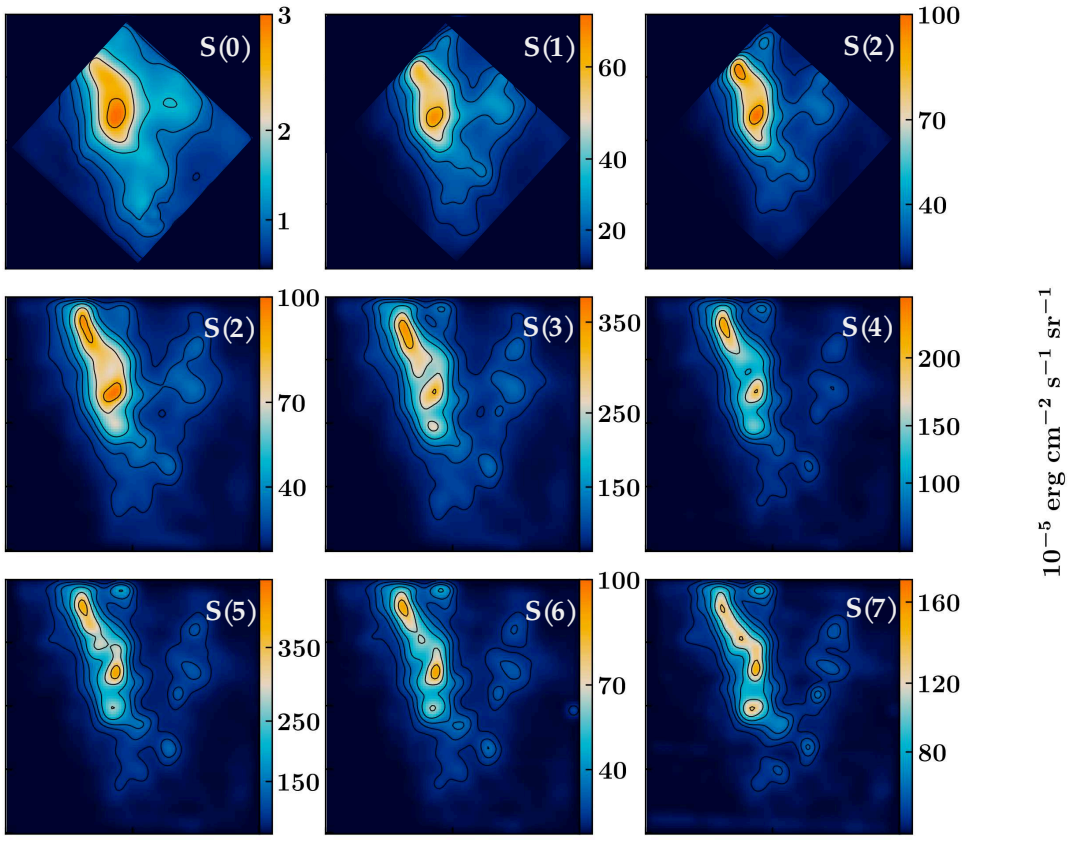

Figure 8.3 H_2 $v = 0 - 0$ S(0) to S(7) pre-processed maps obtained with *Spitzer*-IRS towards the region IC443G (Neufeld *et al.*, 2004). The S(2) line was mapped both by the SH ('short-high', top row) and SL ('short-low', second row) modules. The coordinates of the field of observations are indicated on Fig. 8.1. See also Fig. A.2.

towards four SNRs (IC443, 3C391, W28 and W44) to constrain the molecular shock waves parameters in these regions. The analysis of the IC443C clump was published by Neufeld *et al.* (2007), although the data towards IC443G was never presented. One reason might be that a fraction of this dataset is affected by significant systematic noise. In fact, the maps obtained with the SL ('short-low') module present several stripe-like artifacts and patterns. We present our method for the correction of these artifacts in the following developments.

Morphology The maps of the spectral emission from lines S(0) to S(7) are represented on Fig. 8.3. The $2' \times 2'$ region is centered on a shocked molecular clump interacting with the SNR blast (Dickman *et al.*, 1992). The spatial correlation between the different H_2 lines is significant: the bright, shocked structure along the NW-SE axis is found on each panel, albeit with slightly varying structures at the smallest available scales. This shocked clump is encompassed by the southern H_2 ridge described by Burton *et al.* (1988), along the shell A. The higher spatial resolution and sensitivity to higher temperatures offered by the spectral-line maps S(4) to S(7) show that the apparent extended emission in the S(0) map resolves into several knots of shocked gas to the west of the main structure. It is likely that higher-resolution observations would reveal that these structures are even more clumpy, as it is hinted by *Spitzer*-IRAC observations of this region at 3.6 μm (see Fig. 8.2.).

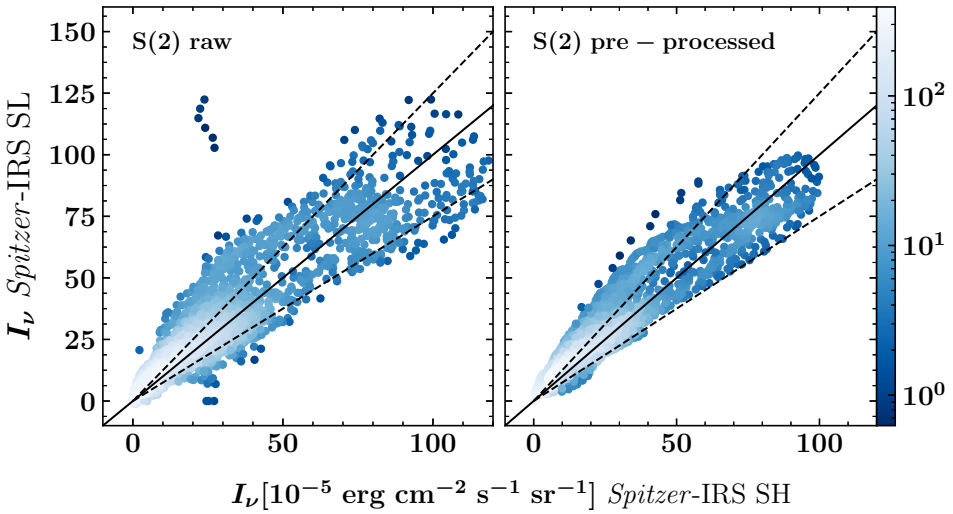

Figure 8.4 pixel-per-pixel comparison of the spectral-line S(2) maps measured by the *Spitzer*-IRS SH and SL modules, before (left panel) and after pre-processing (right panel). The color shows the density of counts (between 1 and $\sim 10^2$). The solid line represents the 1:1 relation expected if the SH and SL data arrays were identical, and the dashed lines represent the ±25% relative errors.

S(2) maps	slope a	offset b [erg cm^{-2} s^{-1} sr^{-1}]	standard deviation [erg cm^{-2} s^{-1} sr^{-1}]
raw	0.902	4.22×10^{-5}	8.51×10^{-5}
pre-processed	0.950	3.60×10^{-5}	5.85×10^{-5}

Table 8.2 Parameters of the linear fit for the $I_\nu^{\rm SL} = f(I_\nu^{SH})$ relationship (see Fig. 8.4).

***Spitzer*-IRS SH *vs.* SL map comparison** It is very convenient that the S(2) line was mapped both by the SH and SL modules, because it allows us to quantitatively estimate the uncertainty introduced by the strong vertical stripe (see Fig. A.2). The relative difference between the total flux of the S(2)[SH] and S(2)[SL] maps is $\sim$ 5.5%, hence *for an average measurement* the systematic uncertainty introduced by the stripe would be lower than $\sim$ 5.5% of the flux. However, this uncertainty is unevenly distributed across the map. In the next paragraph, we describe the processes that we applied to the IRS data to mitigate these systematic artifacts as much as possible.

We performed a pixel-per-pixel comparison of the S(2) spectral-line maps to estimate the uncertainty associated with the data (see Fig. 8.4). The left panel displays a small number of obvious outliers in the SL map (for $I_\nu^{\rm SL} = 100-125$ and $I_\nu^{\rm SH} = 15-35$) that are related to the bright vertical stripe. These outliers are removed by the pre-processing steps that we apply to the SL data (see next paragraph, and right panel of Fig. 8.4). We performed a statistical analysis of the raw and pre-processed data to estimate the systematic and random uncertainties:

1. First, we model the sample of data points $I_\nu^{\rm SL} = f(I_\nu^{\rm SH})$ data by a linear function $x \mapsto ax + b$.

2. Then, we compute the standard deviation between the model $I_\nu^{\rm mod}$ and the SL data points $I_\nu^{\rm SL}$. The standard deviation is given by:

$$\mathrm{std}^2 = \sum (I_\nu^{\rm mod} - I_\nu^{\rm SL})^2 / N \tag{8.1}$$

where N is the number of data points.

Results: the results of this analysis are presented in Tab. 8.2. Firstly, this inquiry shows that the pre-processing has enhanced the signal-to-noise ratio and reduced the systematic uncertainties: *i.)* the relationship between $I_\nu^{\rm SL}$ and $I_\nu^{\rm SH}$ is closer to 1:1 in the pre-processed map than in the raw map, *ii.)* the standard deviation between the linear fit and the data points has decreased. The measurements in Tab. 8.2 also allow us to estimate the uncertainty associated with the *Spitzer-IRS* data. If we consider the second row, we have a systematic uncertainty that represents 5% ($a = 0.950$) of the flux, in addition to two additive terms ($\sigma_b = 3.60 \times 10^{-5}$ and $\sigma_{\rm std} = 5.85 \times 10^{-5}$ erg cm^{-2} s^{-1} sr^{-1}). Thus, for a pixel of intensity I_ν in the pre-processed S(2) maps, the total uncertainty is given by:

$$\sigma_{\rm unc} = \Lambda I_\nu + \Gamma \tag{8.2}$$

where $\Lambda = 0.05$ and $\Gamma = \sqrt{\sigma_{\rm std}^2 + \sigma_b^2} \sim 7 \times 10^{-5}$ erg cm^{-2} s^{-1} sr^{-1}. This uncertainty estimate is only valid for the S(2) maps, but we can infer an estimate of the uncertainty for the other *Spitzer*-IRS maps using some assumptions. We assume that *i.)* the systematic uncertainty ($\Lambda = 0.05$) measured from the SH/SL comparison represents an upper bound of the systematic uncertainty of all spectral-line maps, *ii.)* for any spectral-line map S^i the additive term Γ can be rescaled by the factor $\max(S^i)/\max(S^2)$, where S^2 is the S(2) spectral-line map.

Description of the pre-processing: systematic noise reduction and smoothing

1. The S(0) spectral-line map is strongly affected by the continuum emission of two stars at $\alpha_{\rm [J2000]} = 6^{\rm h}16^{\rm m}41^{\rm s}$, $\delta_{\rm [J2000]} = 22°30'58''$ and $\alpha_{\rm [J2000]} = 6^{\rm h}16^{\rm m}44^{\rm s}.5$, $\delta_{\rm [J2000]} = 22°31'33''$. We used two 2D Gaussian functions (G_1, G_2, re-normalized between 0 and 1) and the S(1) map as an emission model to remove these components in the pixels (x, y):

$$S^0(x,y) = S^0(x,y)\left[1 - (G_1(x,y) + G_2(x,y))\right] + \Lambda \times S^1(x,y)\left[G_1(x,y) + G_2(x,y)\right] \tag{8.3}$$

   where S^0 and S^1 are respectively the S(0) and S(1) maps, and $\Lambda = \text{median}(S^0/S^1)$ is a rescaling factor.

2. The S(6) spectral-line map has the most severe horizontal stripes (see Fig. A.2). We used the S(5) map as an emission model to isolate the emission from the stripes and generate a noise model $N(x, y)$ from a data array initially filled with zeros:

$$\alpha(x,y) = \left[S^6(x,y)/\max(S^6) - S^5(x,y)/\max(S^5)\right] \tag{8.4}$$

$$N(x,y) = S^6(x,y) \text{ where } \alpha(x,y) > \alpha_{\rm treshold} \tag{8.5}$$

   where S^6 and S^5 are respectively the S(6) and S(5) maps, and $\alpha_{\rm treshold}$ is an arbitrary threshold that optimizes the separation between the signal and the systematic stripes. The pre-processed S(6) map is then given by $S^6(x,y) = S^6(x,y) - N(x,y)$.

3. All the SL maps (*i.e.* S(2) to S(7)) systematically present a strong vertical stripe. This stripe is located in columns 52 and 53 of the data arrays. To correct this artifact we performed the

following interpolation:

$$S^i(52, y) = \frac{1}{2}\left(S^i(51, y) + S^i(54, y)\right),\ i = 0,\ \ldots, 7 \tag{8.6}$$

$$S^i(53, y) = \frac{1}{2}\left(S^i(51, y) + S^i(54, y)\right),\ i = 0,\ \ldots, 7 \tag{8.7}$$

4. We convolved each map with a Gaussian kernel of standard deviation $\sigma = 3''$ to smooth out the data. This is particularly useful towards the area where we corrected the vertical stripe (columns 52-53) since it is undersampled as a consequence of the interpolation.

The results of these pre-processing steps are presented in Fig. 8.3 and Fig. A.2. The removal of the systematic vertical stripe is satisfying, as well as the removal of the horizontal stripes in the S(6) map. The average total flux variation between the raw and pre-processed images is $\sim 1.02\%$, hence it should not significantly modify the results, and it is lower than the relative difference between the raw S(2)[SH] and S(2)[SL] maps ($\sim 5.5\%$). Since the *Spitzer*/IRS data products were shared by D. Neufeld with physical units (erg cm^{-2} s^{-1} sr^{-1}), these pre-processed maps are ready to be used for scientific purposes.

8.1.2 Model 1: H_2 standard population diagrams (single T_{ex})

Aim We aim to produce maps of the column density and excitation temperature of H_2. The S(0) to S(7) spectral-line maps are natively projected on 100×100 grids (pixel size: $1.6''$) that are spatially calibrated (*i.e.* for any (i, j) a pixel (x_0, y_0) of the S^i map corresponds to the same line of sight as the pixel (x_0, y_0) in the S^j map). In order to produce a map of the column density of H_2, we chose to perform a population diagram analysis (see chapter 4) in each pixel of the maps.

8.1.2.1 Assumptions

***i.)* Line opacity** We assume that the emission of the pure rotational lines S(0) to S(7) is in the optically thin regime (see chapter 4). Given the low spontaneous rate coefficients A_{ul} of the quadrupolar transitions of H_2 (see Tab. 8.1), the emission of H_2 rovibrational transitions should be optically thin for $n_{H_2} < 10^9$ cm^{-3} (*e.g.* Hartwig *et al.* 2015), a condition that is undoubtedly verified towards the IC443G molecular clump.

***ii.)* Thermalization** We assume that the gas is at local thermodynamic equilibrium (LTE). This condition is verified if the local medium is sufficiently dense for a collisional equilibrium to settle, *i.e.* if the following condition on the local density n is satisfied (see Eq. 4.22, Eq. 4.26):

$$n \geq n_{crit} \tag{8.8}$$

$$n_{crit} = \frac{A_{ul}}{C_{ul}} \tag{8.9}$$

where A_{ul} and C_{ul} are respectively the Einstein coefficient of spontaneous emission and collisional de-excitation rate (see chapter 4 for a derivation). Wrathmall *et al.* (2007) presented the results of calculations of the collisional rate coefficients of H_2 for the kinetic temperatures

$T = 1000$ K, $T = 2500$ K and $T = 4500$ K (see Tab. 4.3). To verify our assumption, we combine these calculations of C_{ul} with the A_{ul} coefficients in Tab. 8.1 to estimate the critical density n_{crit} of the H_2 pure rotational lines.

The S(0) ($J : 2 \rightarrow 0$) line is the most likely to be thermalized, hence it should give a lower bound of the critical density required for our assumption to be verified. At $T = 1000$ K, we have $C_{20} = 6.0 \times 10^{-12}$ cm^3 s^{-1} (Wrathmall *et al.*, 2007) hence $n_{crit} \sim 5$ cm^{-3}. On the contrary, the S(7) ($J : 9 \rightarrow 7$) line gives an upper bound of the critical density (it is the 'most difficult ' to thermalize *via* collisional excitation). Depending on the kinetic temperature, the critical density of the S(7) line is $n_{crit} \sim 1 \times 10^4 - 4 \times 10^5$ cm^{-3} ($C_{97}(1000\text{ K}) = 4.6 \times 10^{-13}$ cm^3 s^{-1}; $C_{97}(4500\text{ K}) = 1.9 \times 10^{-11}$ cm^3 s^{-1}). Cesarsky *et al.* (1999) estimated a pre-shock density $\sim 10^4$ cm^{-3} in clump G, thus the low-J H_2 lines are probably thermalized (see also van Dishoeck *et al.* 1993, Shinn *et al.* 2011). A significant deviation to LTE might be possible for higher-J lines if $T \ll 10^4$ K.

***iii.)* Filling factor** We use a unit filling factor ($ff = 1$). The brightness distribution of the spectral-line maps is extended, but Fig. 8.2 shows that the emission from clumpy structures might be unresolved by *Spitzer*-IRS. This is not an issue as long as the value in each pixel of our output map is interpreted as an average measurement of the column density over a spatial bin.

***iv.)* Extinction** The scattering and absorption of incident photons by interstellar dust is expected to cause the extinction of H_2 lines (Draine, 2011). The S(0) to S(7) lines are characterized by $\lambda_{ul} = 5.5 - 28.2$ μm (Tab. 8.1), a wavelength range in which the extinction is non-negligible. If the extinction is not taken into account, the measurement of the H_2 column density would be an underestimate. For a given wavelength λ, the observed intensity I_ν is related to the emitted signal I_ν^0 by the following equation:

$$I_\nu(\lambda) = I_\nu^0(\lambda) \times 10^{(-A_\lambda/2.5)} \tag{8.10}$$

where A_λ is the extinction at wavelength λ. The quantity A_λ/A_v can be found in Lequeux *et al.* (2002) for $\lambda = 4.8,\ 7.0, 9.7,\ 14.3,\ 19,\ 30$ μm. Using `Python`, we performed a bicubic interpolation of this sample of data points to obtain the quantity A_λ/A_v for the exact wavelength corresponding to each H_2 pure rotational line. Following Shinn *et al.* (2011), we adopt a visual extinction $A_v = 10.8$, inferred from $A_{2.12} = 1.3$, obtained by Richter *et al.* (1995a), employing the 'Milky Way, $R_v = 3.1$' extinction curve. With equation 8.10, the interpolated A_λ/A_v values and $A_v = 10.8$, we have all the required information to correct the extinction of the H_2 lines[1].

8.1.2.2 Method

First, using a gaussian kernel we convolved the S(1) to S(7) maps ($\lambda = 5.5 - 17$ μm) to the spatial resolution of the S(0) map (8.3″ at $\lambda = 28.2$ μm). We then applied the following steps in each pixel (x, y) of the maps:

1. For the maps S(0) to S(7), correct the intensity of each pixel for dust extinction.

2. Convert the intensity I_ν into an upper level population N_u.

[1]With $A_v = 10.8$, we found that the correction of the extinction increases the estimated flux of H_2 lines only by a few percent.

Algorithm 8: pixel-per-pixel H_2 population diagrams. Bold variables are arrays or functions, and non-bold variables are scalars. The function **PopulationDiagram** refers to algorithm 1. Functions **CorrectExtinction** and **Conversion**[$\mathbf{I}_\nu \rightarrow \mathbf{N_u}$] refer respectively to Eq. 8.10 and Eq. 4.30.

Data: [$\mathbf{M_1}$, ... , $\mathbf{M_7}$] integrated line intensity arrays (dimensions $I \times J$, H_2 $v = 0-0$ S(0) to S(7)), $\mathbf{E_u}$ (upper level energies), $\mathbf{g_u}$ (upper level degeneracies)
Result: **N** (column density), **T** (excitation temperature) arrays
initialize **N** ($I \times J$);
initialize **T** ($I \times J$);
for *(i, j) in* ($1 \rightarrow I$, $1 \rightarrow J$) **do**
  initialize **List**;
  for M *in* [$\mathbf{M_1}$, ... , $\mathbf{M_7}$] **do**
    $M_{ij} \leftarrow$ **CorrectExtinction**(M_{ij});
    $M_{ij} \leftarrow$ **Conversion**[$\mathbf{I}_\nu \rightarrow \mathbf{N_u}$]($M_{ij}$);
    List $\leftarrow M_{ij}$;
  end
  $N_{ij}, T_{ij} \leftarrow$ **PopulationDiagram**(**List**, $\mathbf{E_u}$, $\mathbf{g_u}$);
  N $\leftarrow N_{ij}$;
  T $\leftarrow T_{ij}$;
end
return (**N**, **T**)

3. Build the population diagram (that is, $\log(N_u/g_u)$ with respect to E_u). Infer the column density and temperature from the linear fit of the data points (see chapter 4).

A pseudo-code describing these steps is presented in the algorithm 8. We used a `Python` program based on this pseudo-code that works with `fits` files of the H_2 spectral-line maps.

8.1.2.3 Results and derived maps

We performed a systematic population diagram analysis in each pixel of the *Spitzer*-IRS spectral-line maps. We performed two separate linear fits of the H_2 energy levels traced by the S(0), S(1), S(2) and S(3), S(4), S(5), S(6), S(7) lines to take into account temperature stratification (see following developments). The results of our analysis are presented in Fig. 8.6, Fig. 8.7, Fig. 8.8 and Fig. A.3.

Population diagrams We extracted nine population diagrams in different locations of the IC443G clump (these locations are indicated on Fig. 8.5). We have selected regions with low signal-to-noise ratios (first column of the mosaic) and regions with higher signal-to-noise ratios (third column of the mosaic). The diagrams are shown on Fig. 8.6. In order to check the quality of the best-fit models, we performed a chi-square test on the data points, defined by:

$$\chi^2 = \frac{1}{N-p} \sum_{J_u=2}^{9} \frac{(N_u - f(E_u))^2}{\sigma(N_u)^2} \tag{8.11}$$

where N_u refers to the data points, f is the adopted linear model (which is distinct for the energy levels traced by the S(0)-S(2) and S(3)-S(7) lines, following our decomposition into two

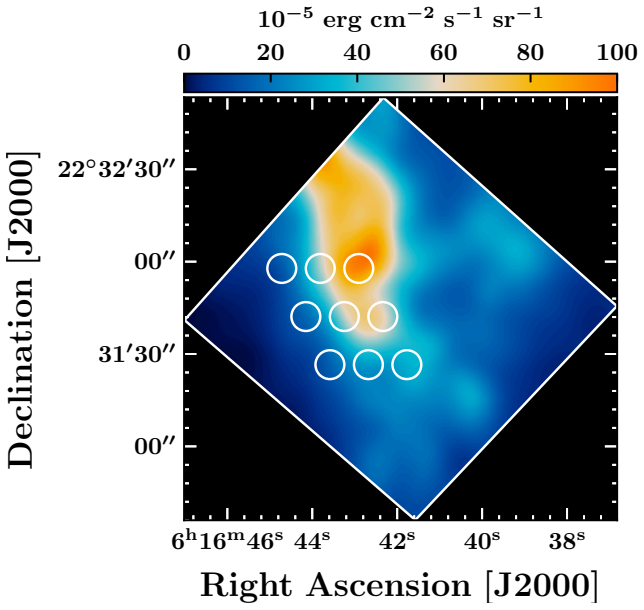

Figure 8.5 Background image: *Spitzer*-IRS S(2)[SL] spectral-line map (see Tab. 8.1). The array of white circles indicates the positions in which we extracted the signals of the S(0) to S(7) spectral-line maps to produce the population diagrams mosaics presented in Fig. 8.6 (model 1: standard LTE approach) and Fig. 8.10 (model 2: H_2 thermal admixture model). The positional order of the population diagrams in Fig. 8.6 and in Fig. 8.10 is the same as the order of white circles in this figure (the size of the circles corresponds to the angular resolution of the S(0) observations, *i.e.* 8.3″ in diameter).

components), $\sigma(N_u)$ is the uncertainty on N_u derived from Eq. 8.2 and $N = 9$ is the number of data points. $p = 4$ is the number of free parameters (the excitation temperature and total column density, both for the warm and col components). The chi-square test allows to estimate the average deviation between the data points and the two-component model, and to compare the magnitude of the deviation to the uncertainty on the data points. In the extracted population diagrams, χ^2 varies between 0.55 and 5.01 (see Fig. 8.6). The χ^2 value in each pixel of the spectral-line maps is shown in Fig. A.3.

The linear fit of the $J_u = 5 - 9$ upper levels (gray curve) systematically fails to reproduce the column density of the population level $J_u = 2$. Conversely, the linear fit of the remaining data points ($J_u = 2 - 4$, red curve) does reproduce the lower energy levels, although it is completely off for higher energy levels. It is clear that at least two excitation temperatures are required to reproduce the H_2 level populations, with a 'cold' component (dominating levels $J_u = 2 - 4$) and a 'warm ' component (dominating levels $J_u = 3 - 9$). Since the slope of the 'cold' component is steeper than the slope inferred from the S(0) to S(7) transitions, it follows that the estimate of the total column density will be higher for this model. Naturally, the total column density is given by the sum of the column densities inferred from each component ('warm' and 'cold').

***i.)* Column density maps** The column density map obtained from the analysis of the S(3) to S(7) transitions is shown on the left panel of Fig. 8.7 ('warm' component). The column density varies between $N \sim 10^{19}$ cm^{-2} and $N \sim 8 \times 10^{20}$ cm^{-2} between the outer edges and the core of clump G. The column density map corresponding to the 'cold' component (S(0) to S(2) transitions) is shown on the left panel of Fig. 8.8. As expected from the inspection of population diagrams, the estimate of the column density is higher, up to $N \sim 2 \times 10^{21}$ cm^{-2}. For both components, the column density distribution is well correlated to the lower-J H_2 spectral-line maps S(0) to S(2), tracing the bulk of the molecular hydrogen.

***ii.)* Temperature maps** The excitation temperature map obtained from the analysis of the S(3) to S(7) transitions is shown on the right panel of Fig. 8.7 ('warm' component). The excitation

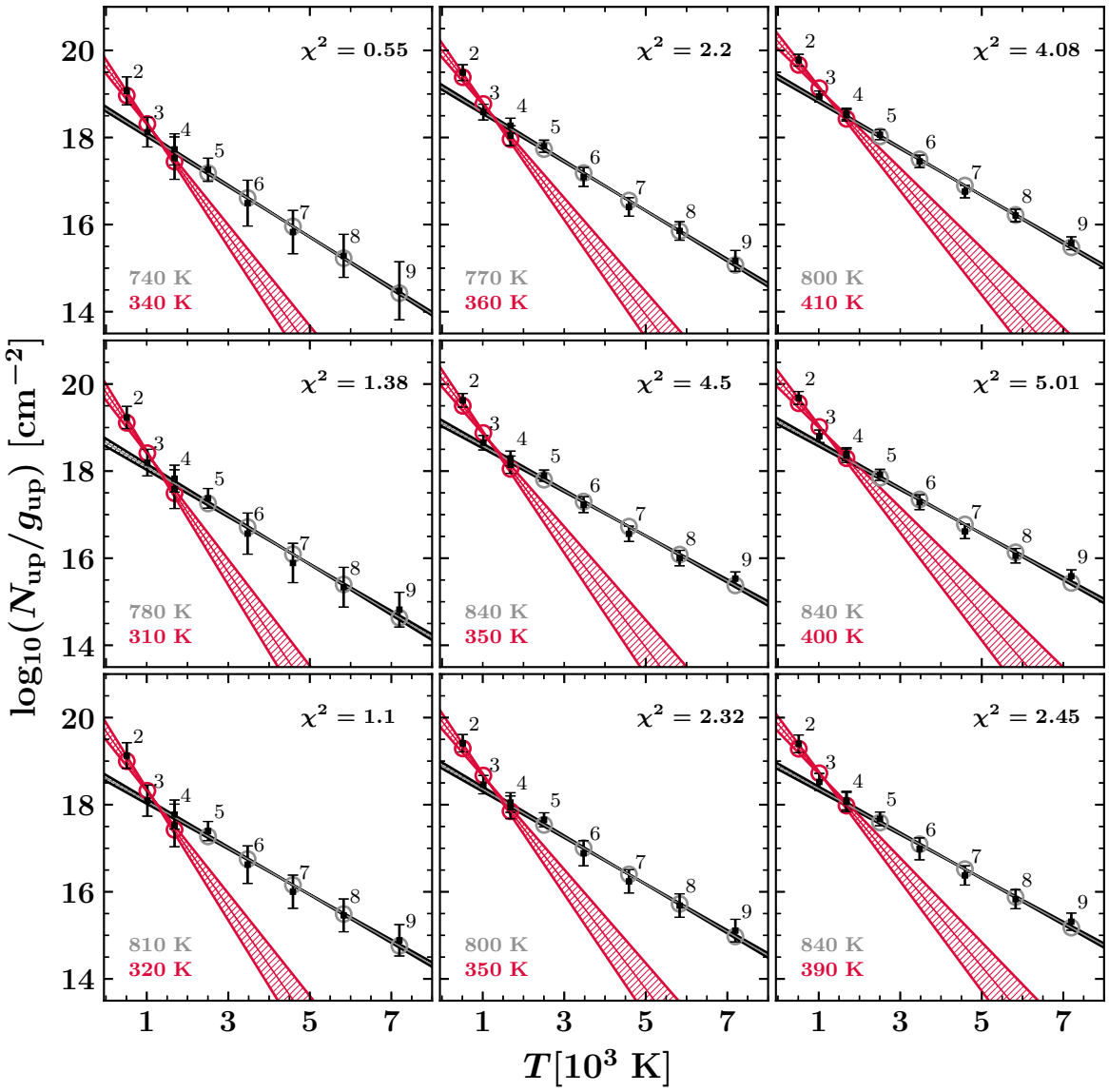

Figure 8.6 Population diagrams extracted from the positions shown in Fig. 8.5. The black data points represent the N_u measurements and their uncertainties. The gray curve and circles represent the linear model obtained for the S(3) to S(7) transitions. The red curve and circles represent the linear model obtained for the S(0) to S(2) transitions. The errors associated with the best linear models are represented by a filled area around the curves. The corresponding excitation temperatures are shown in the bottom-left corner of the diagrams ('cold' component in red, and 'warm' component in gray). The results of the χ^2 test (see text and Eq. 8.11) are presented in the top-right corner of the diagrams. The order of the diagrams (from left to right and top to bottom) is the same as the order of white circles in Fig. 8.5.

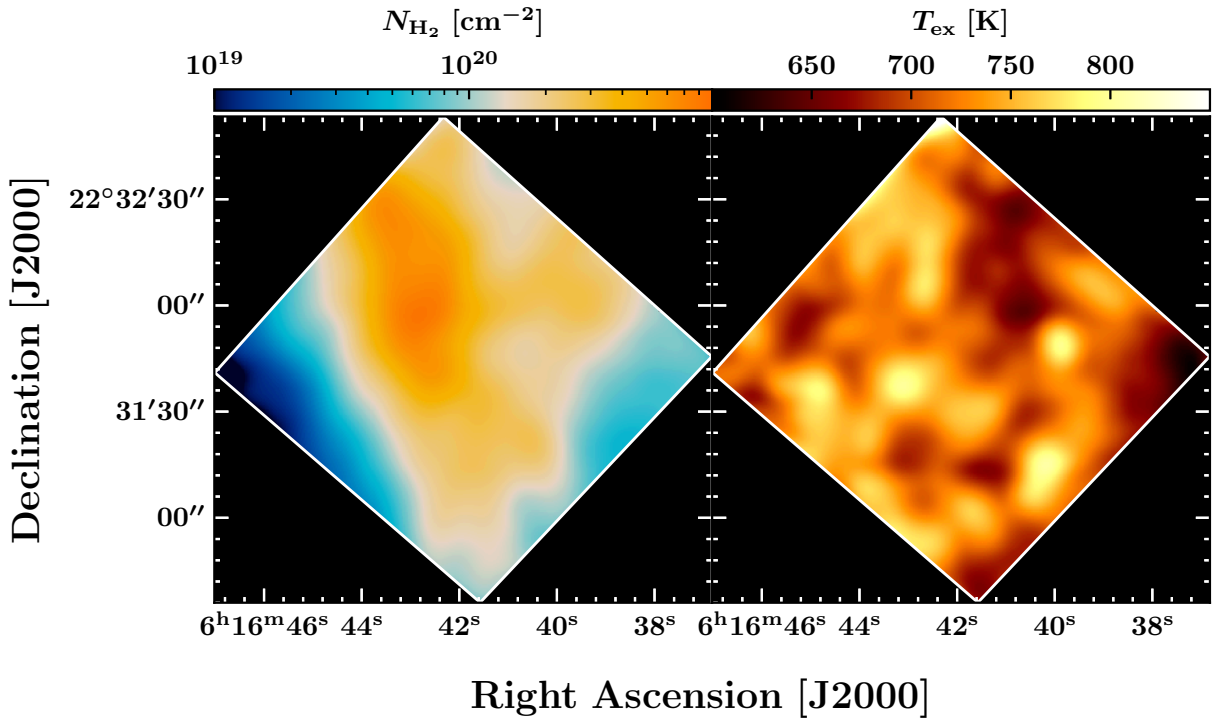

Figure 8.7 Results of the analysis of the S(3) to S(7) H_2 pure rotational lines ('warm component') following the method described in section 8.1.2.2. *Left:* column density map. The maximum value towards the center of clump G is $N = 8 \times 10^{20}$ cm^{-2}. *Right:* excitation temperature map.

temperature varies between $T \sim 600$ K and $T \sim 850$ K. The spatial distribution of the temperature is highly uncorrelated to the column density map or any of the spectral-line maps. Several isolated, localized 'warm spots' are found both within the clump and on the outer edges. Interestingly, the excitation temperature map inferred from the analysis of the 'cold' component (S(0) to S(2) lines) is more correlated to the column density map, and the contribution of the 'warm spots' decreases. This is consistent with the assumption that the 'cold' component traces the bulk of the observable molecular hydrogen.

Discussion We have obtained two maps of the H_2 column density inferred from the emission of the S(0) to S(7) lines. The fit of the S(0), S(1), S(2) (in red in Fig. 8.6) traces the 'cold component' of H_2, and the bulk of the molecular mass. Conversely, the fit of the S(3), S(4), S(5), S(6), S(7) (in gray in Fig. 8.6) traces the 'warm component' of H_2. The transitions of H_2 cannot be reproduced by a single excitation temperature, hence our results indicate that the medium is stratified in temperature.

The energies E_u of the upper levels (J=2 − 9) are 510 − 7200 K (Tab. 8.1). It is unlikely that the result of our analysis yields the total H_2 column density, since even the energy levels traced by the S(0) to S(3) lines might not be thermalized with the first two energy levels of H_2. In fact, the rotational levels J=0 and J=1 are expected to hold the greater part of the 'cold mass' of molecular hydrogen. As shown in section 4.2.1 (third paragraph), assuming that a clump of molecular hydrogen is thermalized at a temperature of 20 K, 99.82% of the molecules are in the ground state.

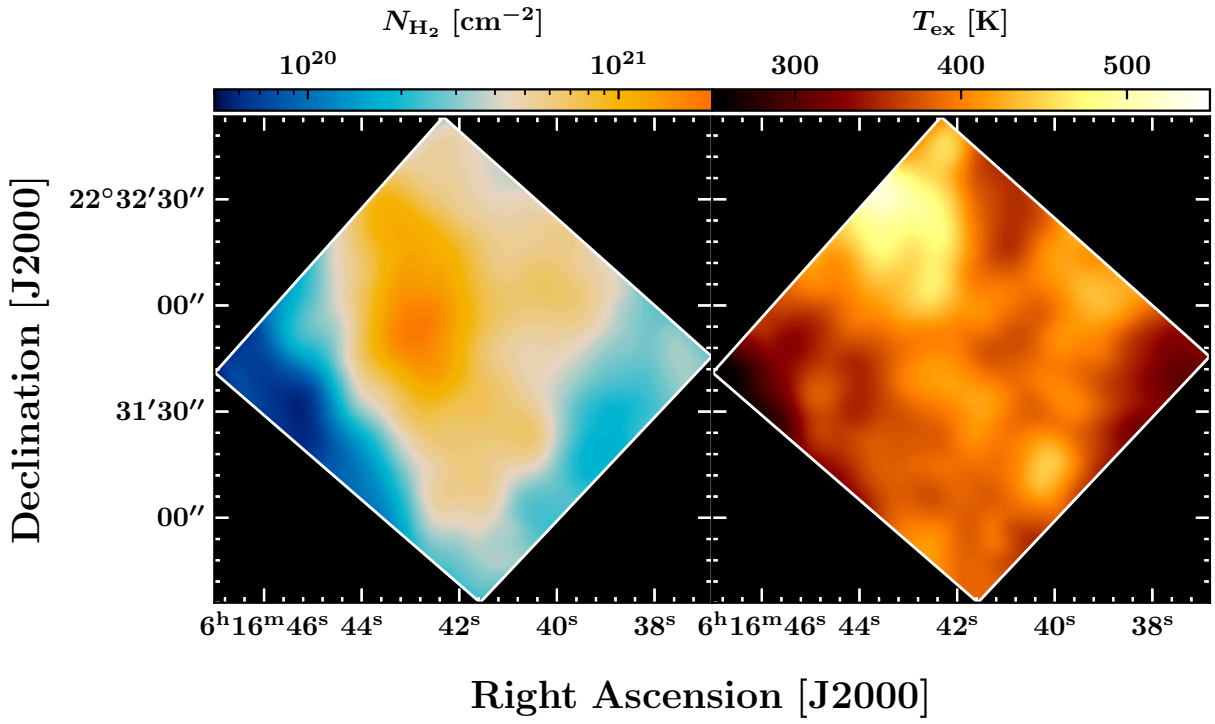

Figure 8.8 Results of the analysis of S(0) to S(2) H_2 pure rotational lines ('cold component') following the method described in section 8.1.2.2. *Left:* column density map. The maximum value towards the center of clump G is $N = 2 \times 10^{21}$ cm^{-2}. *Right:* excitation temperature map.

It is well known that the 'standard' population diagram analysis of H_2 pure rotational lines is a poor method to measure the total column density. Roussel *et al.* (2007) presented results of the analysis of warm H_2 lines in the *Spitzer* SINGS (Spitzer Infrared Nearby Galaxy Survey) galaxy sample. Under a conservative assumption about the distribution of temperatures, they found that the column densities of warm H_2 derived from *Spitzer*-IRS observations amount to between 1% and > 30% of the total mass of H_2. Towards translucent clouds, Ingalls *et al.* (2011) found that the excitation analysis of S(1) and S(2) lines recovers about 2% of the total H_2 column density (inferred *via* the S(0) and S(1) lines). Therefore, it is likely that our estimate of the H_2 column density from the sum of the 'gray' and 'red' fits (Fig. 8.6) lies between 1% and 30% of the 'real' column density.

We can improve our analysis of the population diagram. This first-order analysis has shown that we have made a hidden assumption that was not listed in section 8.1.2.1. We assumed that the molecular hydrogen is thermalized at a uniform temperature T_{ex} along the line of sight. In fact, our population diagrams cannot be modelled by a single excitation temperature, and we should take into account temperature variations within the shocked clump structure. It is likely that the *Spitzer*-IRS observations are better reproduced by a collection of molecular hydrogen layers that are locally thermalized at different temperatures. We build such a model in the next section.

8.1.3 Model 2: H_2 thermal admixture

8.1.3.1 Model description

Following the method presented by Neufeld and Yuan (2008) (referred to as the H_2 thermal admixture model), we assume that the molecular hydrogen probed along a line of sight has a column density that can be described by the following power-law distribution with respect to the kinetic temperature of H_2 (denoted T):

$$dN = \Lambda T^{-\Gamma} dT \tag{8.12}$$

where Λ and Γ are two constants. Γ is the index of the power law, and Λ can be determined by integrating Eq. 8.12 between $T_{\rm min}$ and $T_{\rm max}$:

$$\Lambda = \frac{N_{\rm tot}(T \geq T_{\rm min})(\Gamma - 1)}{T_{\rm min}^{1-\Gamma} - T_{\rm max}^{1-\Gamma}} \tag{8.13}$$

This model is motivated by the fact that the population diagrams shown in Fig. 8.6 are better described by two components than a single $T_{\rm ex}$ (the 'cold' and 'warm' components). Eq. 8.12 is a continuous generalization of this multi-temperature description. In other words, we assume that the emission of H_2 lines is produced by a mixture of gas temperatures (both along the line of sight, and possibly across the plane of sky probed by the beam of *Spitzer*/IRS). Basically, the adopted description (Eq. 8.12) relies on the physical assumption that the medium is stratified in temperature in a way that can be reproduced by a power-law distribution.

The advantage is that if we fix $T_{\rm min}$ and $T_{\rm max}$, we have the same amount of parameters to fit as in the previous section ($a_{\rm lin}$, $b_{\rm lin}$ in the standard population diagram model, and Λ, Γ in this model). Once $T_{\rm min}$ and $T_{\rm max}$ are fixed, the two remaining parameters of this model are the steepness of the distribution (the power-law index Γ) and the total H_2 column density $N_{\rm tot}(T \geq T_{\rm min})$. Based on the excitation temperature maps presented in Fig. 8.7 and Fig. 8.8, we first fixed $T_{\rm max} = 1500$ K. We then verified that higher temperatures do not modify the results (up to $T_{\rm max} = 4000$ K, the temperature at which H_2 is rapidly dissociated, Le Bourlot *et al.* 2002). We fixed the lower boundary of the temperature distribution based on the results of our analysis of ^{12}CO and ^{13}CO lines presented in section 8.2: we set $T_{\rm min} = 25$ K, in accordance with the temperature of the molecular gas determined towards the shocked clump (see Fig. 8.29, Fig. 8.36).

8.1.3.2 Construction of a model grid and chi-square test

We aim to build a model grid of the specific intensity for the S(0) to S(7) lines based on the H_2 thermal admixture model. The H_2 total column density at a temperature $T = T_{\rm layer}$ (referred to as $N_{\rm tot}(T = T_{\rm layer})$) can be determined from Eq. 8.12 and Eq. 8.13. If we adopt the same LTE assumptions as in section 8.1.2.1 for each layer of molecular hydrogen at a temperature $T_{\rm layer}$, then the upper level populations can be derived from Eq. 4.20 applied to $N_{\rm tot}(T = T_{\rm layer})$, and the specific intensity produced by the layer of molecular hydrogen can be inferred from Eq. 4.30. The sum of the specific intensity contributions over the column density distribution yields an estimate of the specific intensity measured along the line of sight. In the following paragraphs, we detail each step of this process.

Discretization of the column density distribution $N(T)$ Discretization of Eq. 8.12 yields:

$$\Delta N = \Lambda T^{-\Gamma} \Delta T \tag{8.14}$$

where $\Delta N = N_{\rm tot}(T = T_{\rm layer})$ is the column density of a layer of molecular hydrogen at temperature T and $\Delta T = (T_{\rm max} - T_{\rm min})/N_{\rm bin}$ is a temperature bin ($N_{\rm bin}$ is the total number of bins). We produced a discretized column density distribution that satisfies the following condition:

$$N_{\rm tot}(T \geq T_{\rm min}) = \sum_{T=T_{\rm min}}^{T_{\rm max}} \Lambda T^{-\Gamma} \Delta T \tag{8.15}$$

$I_\nu(\Lambda, \Gamma)$ **model grid** For a choice of parameter (Γ, $N_{\rm tot}(T \geq T_{\rm min})$), a model of the specific intensities of the S(0) to S(7) lines is produced by performing the following computations:

1. Assuming LTE, we compute the upper level populations of each molecular hydrogen layer, applying Eq. 4.20:

$$N_{\rm u}(T = T_{\rm layer}) = \frac{N_{\rm tot}(T = T_{\rm layer})}{Z(T_{\rm layer})} g_{\rm u} {\rm e}^{-E_{\rm u}/k_{\rm B}T_{\rm layer}} \tag{8.16}$$

   where $Z(T)$ is the partition function, defined by Eq. 4.19.

2. Then, we compute the specific intensities of the S(0) to S(7) lines for each layer, applying Eq. 4.30:

$$I_{\rm ul} = \frac{h\nu_{\rm ul}}{4\pi} N_{\rm u}(T = T_{\rm layer}) A_{\rm ul} \tag{8.17}$$

Finally, the specific intensity of H_2 lines is given by the sum of the contributions from each layer of gas. A model grid is built by applying these steps for a discrete parameter grid (Γ, $N_{\rm tot}(T \geq T_{\rm min})$). To explore the parameter space, we first used parameter grids of dimension 100×100, starting with the parameters $\Gamma = 0.1 - 10$ (linearly spaced) and $N_{\rm tot}(T \geq T_{\rm min}) = 10^{18} - 10^{25}$ cm^{-2} (logarithmically spaced). We then used a more accurate parameter grid of dimension 500×500 (see following developments).

chi-square test Once the model grid is built, we perform a chi-square test to directly compare the observations to the specific intensity models. We measure the following quantity in each cell of the model grid:

$$\chi^2 = \frac{1}{N - p} \sum_{J_{\rm u}=2}^{9} \frac{(s_{\rm J\to J-2} - m_{\rm J\to J-2})^2}{\sigma^2_{J\to J-2}} \tag{8.18}$$

where $s_{\rm J\to J-2}$ is the specific intensity measurement corrected for dust extinction (see previous section), $m_{\rm J\to J-2}$ is the modelled specific intensity (Eq. 8.17), $\sigma_{\rm J\to J-2}$ is the uncertainty (derived *via* Eq. 8.2) and $N = 9$ is the number of data points. $p = 2$ is the number of free parameters (the power law index and total column density). The best fit is then found by locating the minimum χ^2 value in the array resulting from the chi-square test.

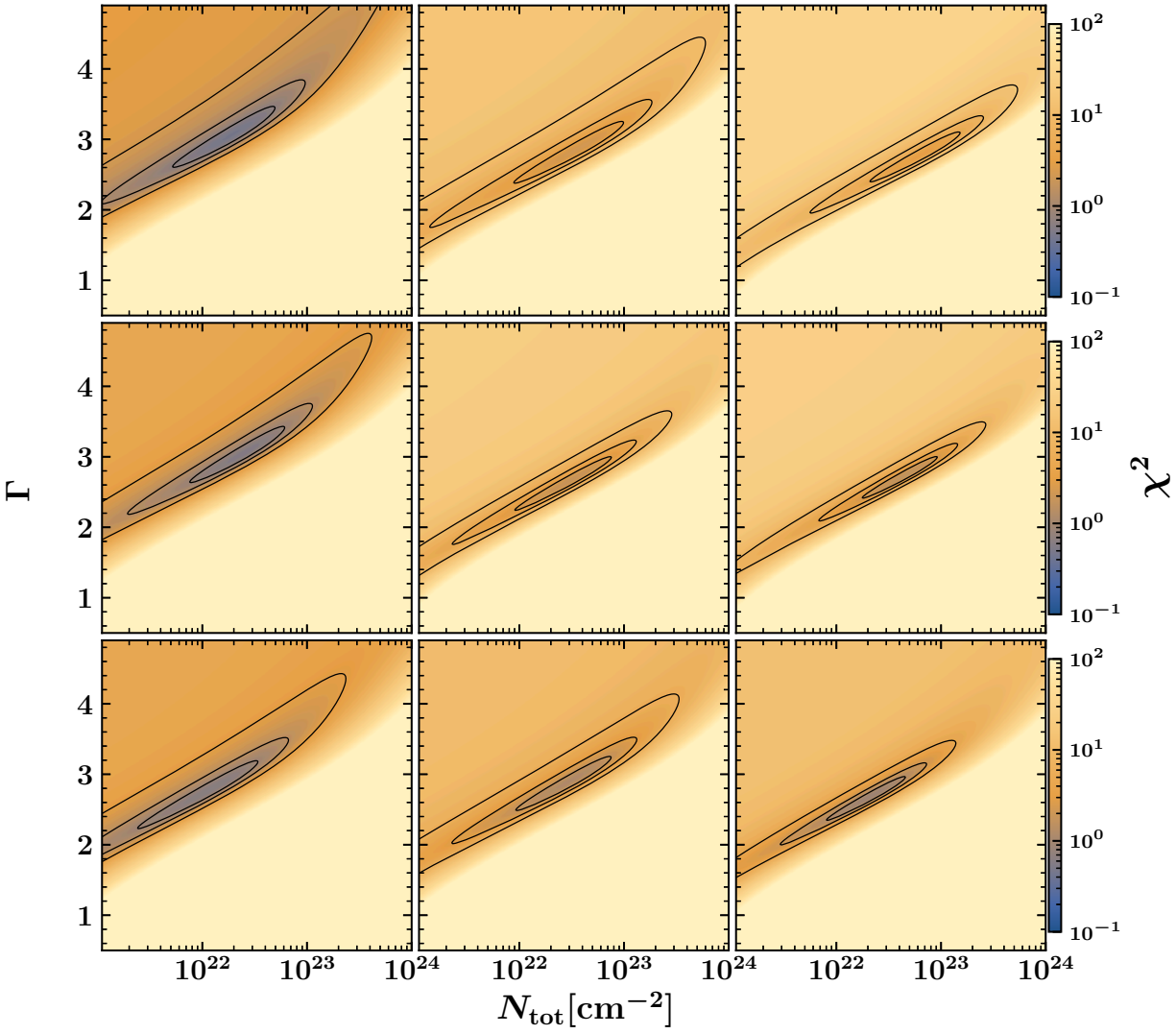

Figure 8.9 Results of the chi-square test applied to our observations and model grid of the specific intensities of the S(0) to S(7) H_2 lines (see Eq. 8.18). Each panel of the mosaic corresponds to the panels shown in Fig. 8.10 (positions indicated on Fig. 8.5). Γ is the power-law index, and N_{tot} is the total column density for $T \geq T_{min} = 25$ K (see Eq. 8.12 and Eq. 8.13). The background color indicates the absolute value of χ^2, and the set of black contours indicate the inner areas corresponding to $\chi^2 \leq [1.5\chi^2_{min},\ 2.5\chi^2_{min},\ 5\chi^2_{min}]$ where χ^2_{min} is the minimum value of χ^2 across the 500×500 grid.

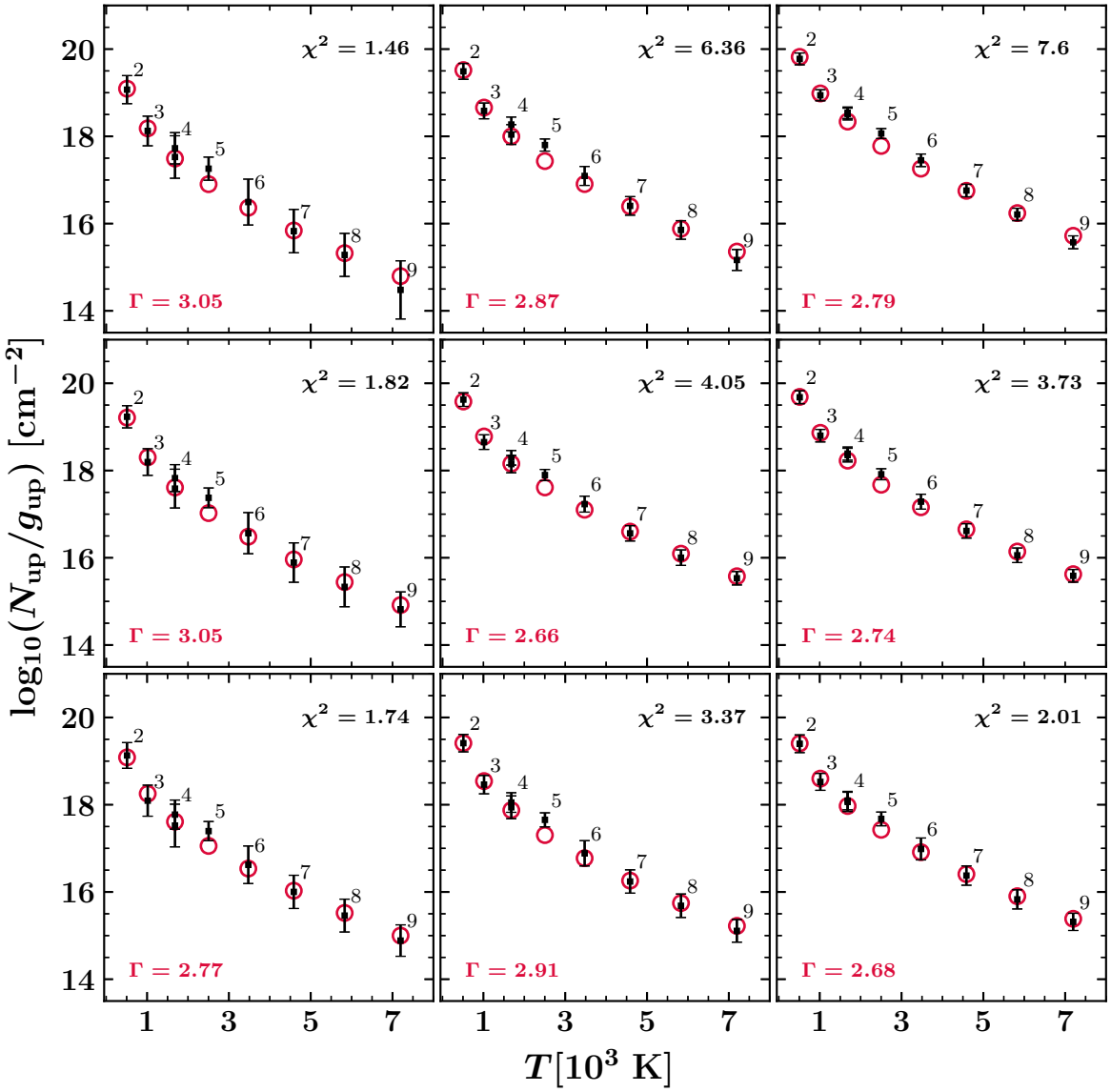

Figure 8.10 Population diagrams extracted from the positions shown in Fig. 8.5 and corresponding to the chi-square test shown on Fig. 8.9. The black data points represent the N_u measurements and their uncertainties. The red circles represent the best-fit model obtained for the S(0) to S(7) transitions. The corresponding power-law indices are shown in red in the bottom-left corner of the diagrams. The results of the χ^2 test (see text) are presented in the top-right corner of the diagrams. The order of the diagrams (from left to right and top to bottom) is the same as the order of white circles in Fig. 8.5.

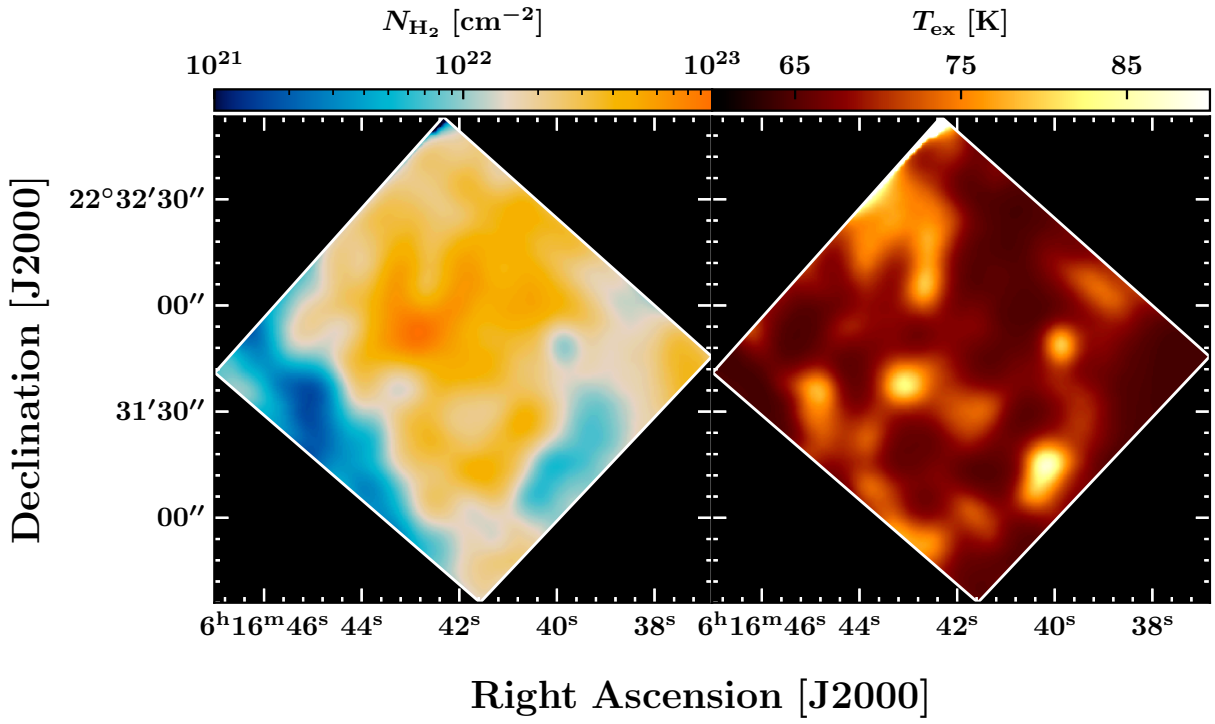

Figure 8.11 Results of the analysis of S(0) to S(7) H_2 pure rotational lines following the method described in section 8.1.3.2. *Left:* column density map. The maximum value towards the center of clump G is $N = 1.0 \times 10^{23}$ cm^{-2}. *Right:* excitation temperature map.

8.1.3.3 Results

We performed a chi-square test based on *Spitzer*-IRS mapping observations of the S(0) to S(7) lines and their comparison with a model grid of dimension 500×500, with parameter boundaries $\Gamma = 0, 5 - 5$ (linearly spaced) and $N_{tot}(T \geq T_{min}) = 10^{21} - 10^{24}$ cm^{-2} (logarithmically spaced). The results are presented in Fig. 8.9, Fig. 8.10, Fig. 8.11 and Fig. A.4.

Chi-square grids In Fig. 8.9, we present the chi-square grids resulting from the application of Eq. 8.18 towards the same locations as presented in Fig. 8.5 and whose first approach analysis is presented in the previous section 8.1.2. This figure illustrates our ability to determine the best-fit parameters (Γ, $N_{tot}(T \geq T_{min})$) based on the areas of the grid where χ^2 is minimized. The chi-square grids shown in the first column of the mosaic display the lowest χ^2 values because they correspond to low signal-to-noise regions of the map, hence $s_{J\rightarrow J-2}/\sigma_{J\rightarrow J-2}$ is systematically lower and so is the product of Eq. 8.18. In all cases, the first black contour level (corresponding to $1.5\chi^2_{min}$, where χ^2_{min} is the minimal value of χ^2 across the 500×500 grid) indicates the values of Γ and N_{tot} that best reproduces the observations. Hence, we find that column densities of order 10^{22} cm^{-2} and power-law indices $\Gamma = 2.6 - 3.1$ reproduce the observations. We discuss the physical interpretation of the power-law index in the conclusions of this section.

Population diagrams Based on our determinations of the best-fit model (Γ, $N_{tot}(T \geq T_{min})$) for each location of the map shown in Fig. 8.5, we built synthetic population diagrams (see Fig. 8.10) to compare our results with the population diagrams presented in the previous section (Fig.

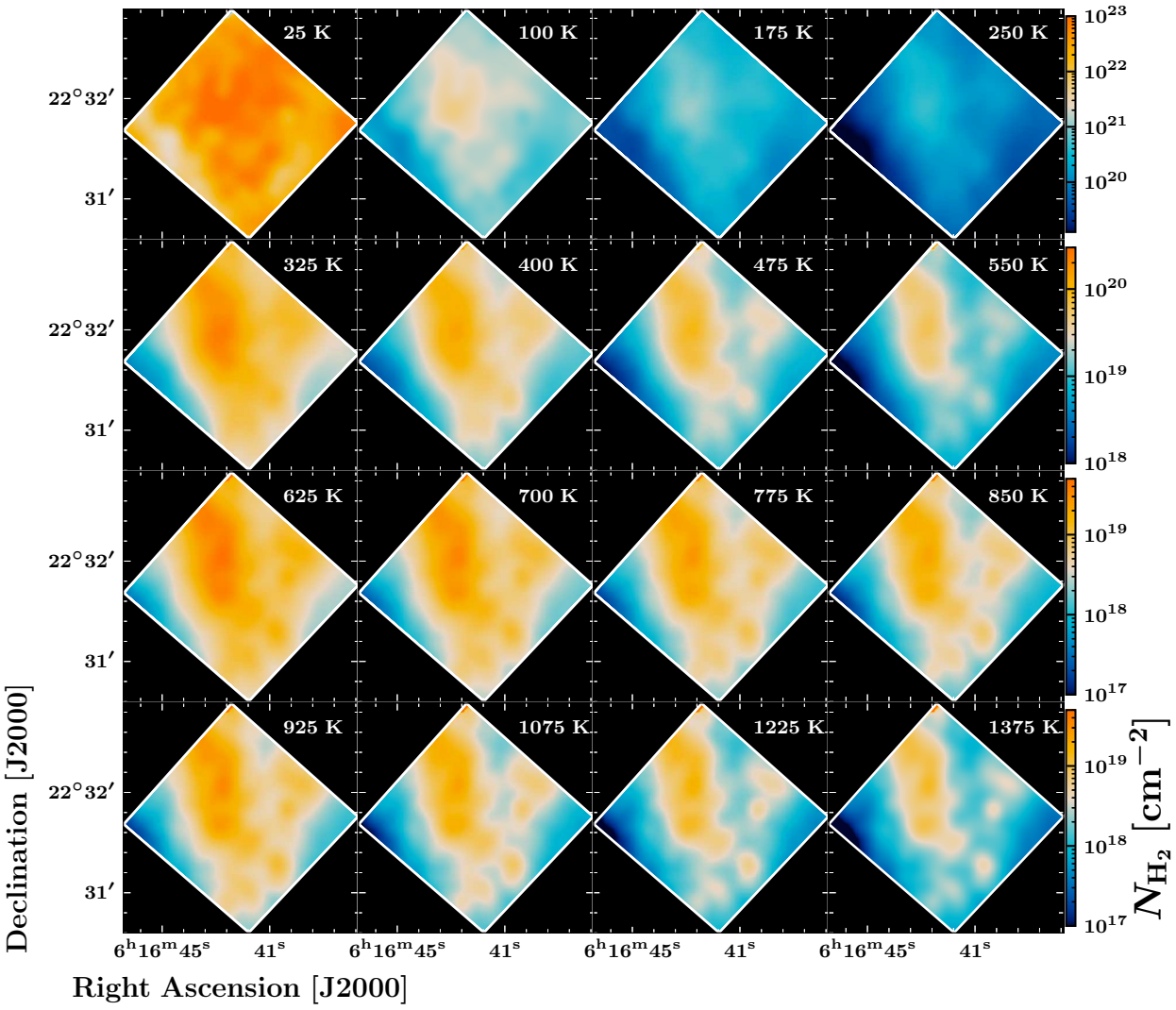

Figure 8.12 Tomographic representation of $N_{H_2}(T)$ produced using the best-fit parameters (Λ, Γ). Each panel represents the partial column density map (defined by Eq. 8.14) corresponding to a temperature bin ΔT (ΔT = 75 K for the first three rows, and ΔT = 150 K for the last row). The temperature T indicated in the top-right corner of each panel is the lower bound of the temperature interval on which the total column density is integrated (the upper bound is $T + \Delta T$). Color scales are different for each row.

8.6). Towards these locations, the minimized χ^2 varies between 1.46 and 7.6. In comparison to the results of the previous section, the best-fit models are in a slightly inferior agreement with the observations, although all data points are reproduced with a single model (instead of two distinct components applied to arbitrary subsets of energy levels). The systematic deviation of the $J_u = 5$ level population above our best-fit model indicates that our power-law distribution might be unable to reproduce the break between the dynamic of the lower-J level populations (tracing cold molecular hydrogen) and the rest of the data points.

Additional tests and remarks: *i.)* We tried to modify the fixed parameter T_{max} from 1500 K to 2000 K, 3000 K and 4000 K to check how the best-fit model is modified. These modifications tend to increase the global χ^2, hence we kept our initial T_{max}; *ii.)* similarly, we tried to adopt a lower value of T_{min} (down to 10 K), which increased the global χ^2 as well; *iii.)* we kept a unit H_2 ortho-to-para ratio ($o/p = 1$) instead of introducing it as an additional parameter, because the deviations between the observations and our model are (for the major part) already in the errorbars.

***i.)* Total column density map** The column density map obtained from the comparison of the S(0) to S(7) transitions with our model grid is shown on the left panel of Fig. 8.11. The column density varies between $N \sim 10^{21}$ cm^{-2} and $N \sim 10^{23}$ cm^{-2} between the outer edges and the core of clump G. The morphology is slightly different (more clumpy) from what was inferred from standard population diagrams with two excitation temperatures (see Fig. 8.7), and the peak column density is approximately fifty times higher.

***ii.)* Average temperature map** The average excitation temperature map obtained from the comparison of the S(0) to S(7) transitions with our model grid is shown on the right panel of Fig. 8.11. The average excitation temperature map is produced by computing the contribution of each layer of molecular hydrogen to the temperature measured along the line of sight and dividing by the total column density:

$$T_{\rm average} = \sum_{T=T_{\rm min}}^{T_{\rm max}} \frac{N_{\rm tot}(T = T_{\rm layer}) T_{\rm layer}}{N_{\rm tot}(T \geq T_{\rm min})} \tag{8.19}$$

The average excitation temperature varies between $T \sim 60$ K and $T \sim 90$ K, hence we succeeded in tracing colder gas. Similarly to our previous results (Fig. 8.7), the spatial distribution of the temperature is highly uncorrelated to the column density map, and several localized 'warm spots' are found both within the clump and on the outer edges.

***iii.)* H_2 temperature tomography** Since we have determined the best-fit parameters (Λ, Γ), Eq. 8.14 allows us to build the partial column density of a layer of molecular hydrogen at any temperature $T_{min} \leq T_{layer} \leq T_{max}$. Using $\Delta T = 75$ K and $\Delta T = 150$ K temperature bins (respectively in the intervals 25 − 925 K and 925 − 1500 K) we built a partial column density map mosaic shown on Fig. 8.12. This figure shows the variation in column density with respect to the excitation temperature of distinct thermalized layers of molecular hydrogen along the line of sight. We can see that the very high temperature molecular hydrogen (fourth row: $T = 925 - 1500$ K) is more clumpy than the warmer molecular hydrogen (second row: $T = 325 - 475$ K). The coldest molecular hydrogen (first row: $T = 25 - 100$ K) is also clumpy, more extended and has a higher column density (up to $N \sim 2 \times 10^{21}$ cm^{-2} in a $\Delta T = 75$ K temperature bin towards the clump core). Hence, these maps confirm that the cold molecular hydrogen holds the bulk of the mass.

Interestingly, we can see that some areas of the map are depleted in cold ($T \sim 25$ K) molecular gas (see first row), corresponding to localized clumpy knots of hot ($T = 925 - 1500$ K) hydrogen (see fourth row). The morphology of the warm gas (second and third rows: $T = 325 - 925$ K) is well correlated to the S(0) to S(2) lines, whereas the clumpy morphology of the hot gas (fourth row: $T = 925 - 1500$ K) is more correlated to the S(3) to S(7) lines (see Fig. 8.3 for comparison). This correlation is quite consistent with the upper level energies of the corresponding lines (respectively $E_u = 509 - 1681$ K and $E_u = 2504 - 7197$ K), thus it demonstrates the sensitivity of the different H_2 lines to distinct excitation temperatures.

8.1.4 Discussion

Summary We have inferred total H_2 column density and excitation temperature maps from the analysis of the S(0) to S(7) pure rotational lines using two distinct models (results are shown in Tab. 8.3). Our second model is slightly better: *i.)* it is based on a continuous description of the temperature stratification along the line of sight and across the plane of sky; *ii.)* the global χ^2 does increase with respect to the first model (from an average $\chi^2 = 2.7$ in Fig. 8.6 to an average $\chi^2 = 3.6$ in Fig. 8.10), but the data is reproduced with a single model instead of two arbitrary components; and *iii.)* it recovers a greater fraction of the 'cold column density' of molecular hydrogen (from a maximum $N \sim 3\times10^{21}$ cm^{-2} to a maximum $N \sim 1\times10^{23}$ cm^{-2}). The comparison between our two models suggests that the "standard" LTE analysis of the *Spitzer*-IRS H_2 lines underestimates the total column density by ~ 97 % in the region IC443G, which is consistent with the conclusions of Roussel *et al.* (2007) in nearby galaxies (they found that between 1% and 30% of the total column density is traced by these transitions).

Local density in IC443G We aim to infer an estimate of the local density from the total H_2 column density. From our ^{12}CO J=2–1 observations (see chapter 6) we propose an approximate geometrical model for the shocked clump (for the sake of simplicity): we describe this structure by a cylinder of length $l = 3'$ and diameter $D = 1'$. At a distance 1.8 kpc (Ambrocio-Cruz *et al.* 2017, Yu *et al.* 2019), this corresponds to $l = 1.5$ pc and $D = 0.5$ pc. Assuming that other sources of emission along the line of sight are negligible, the local density is given by the ratio of the measured column density and the length of shocked clump crossed, hence we have $n_{H_2} = N_{H_2}/D = 1.0 \times 10^{23}/1.5 \times 10^{18} \simeq 7 \times 10^4$ cm^{-3}.

This average estimate is likely to be a lower bound towards the localized knots of H_2 (see Fig. 8.2). In fact, if we assume that in any line of sight, all H_2 molecules are confined in a single quasi-spherical knot of diameter ~ 0.1 pc ($\sim 10''$), then we would have $n_{H_2} \simeq 3.5\times10^5$ cm^{-3}. Assuming $T_{kin} = 1000$ K, our first estimate ($n_{H_2} = 7 \times 10^4$ cm^{-3}) implies that the S(6) and S(7) lines might not be fully thermalized (see Tab. 4.3). The second estimate ($n_{H_2} \sim 3.5 \times 10^5$ cm^{-3}) is consistent with a thermalization of the S(0) to S(6) lines at $T_{kin} = 1000$ K. Thus, our results indicate that the thermalization assumption might be inaccurate for the higher-J lines (in particular the S(6) and S(7) lines).

Gas mass in IC443G We estimate the H_2 molecular gas mass in IC443G by summing up all pixels in our column density map (see Fig. 8.11):

model	N_{tot}^{avg} (cm^{-2})	N_{tot}^{max} (cm^{-2})	n_{H_2} (cm^{-3})	M_{H_2} ($M_\odot$)	T_{ex}^{avg} (K)	χ^2_{avg}
model 1 'warm'	$9.4 \pm 0.5 \times 10^{19}$	$8.3 \pm 0.4 \times 10^{20}$	$0.5 - 2.8 \times 10^3$	2.8 ± 0.6	356	2.5
model 1 'cold'	$2.2 \pm 0.1 \times 10^{20}$	$1.8 \pm 0.1 \times 10^{21}$	$1 - 6 \times 10^3$	7 ± 1	190	2.9
model 2	$2.1 \pm 0.2 \times 10^{22}$	$1.0 \pm 0.1 \times 10^{23}$	$0.7 - 3.5 \times 10^5$	280 ± 60	71	3.6

Table 8.3 Results of our analysis of H_2 S(0) to S(7) pure rotational lines. Models 1 'warm', 1 'cold' and 2 refer respectively to the 'gray' and 'red' linear models in Fig. 8.6 (single T_{ex} models) and the best-fit model in Fig. 8.10 (thermal admixture model). N_{tot}^{avg} and N_{tot}^{max} are the average and peak column densities across the maps, n_{H_2} is the local density inferred for a shocked clump crossing length $l = 0.1 - 0.5$ pc, M_{H_2} is the molecular mass, T_{ex}^{avg} is the average excitation temperature across the map and χ^2_{avg} is the average value returned by the chi-square test across the positions shown in Fig. 8.5.

$$M_{H_2} = 2m_u \sum_{i,j} N_{H_2}[i,j]\Delta s \tag{8.20}$$

where $N_{H_2}[i,j]$ is the column density of a pixel (i,j), $\Delta s[cm^2] \simeq 1.5 \times 10^{10}\ \Delta\Omega[''] d_{kpc}$ is the physical (sky) surface of a pixel and $m_u \simeq 1.66 \times 10^{-27}$ kg is the atomic mass unit. Assuming $d_{kpc} = 1.8 \pm 0.2$ (Ambrocio-Cruz *et al.* 2017, Yu *et al.* 2019) we obtain a mass $M_{H_2} = 280 \pm 60\ M_\odot$ (solar masses). This mass measurement does not correspond to the total mass of the shocked clump, since the *Spitzer*-IRS field of observations does not cover the entire structure (see Fig. 8.1). We can reasonably assume from this result that the total H_2 mass of the shocked clump is in the range $2 - 5 \times 10^2\ M_\odot$. We will discuss this result in relation to our ^{12}CO measurements in the next section.

Conclusions of this section We have analyzed the *Spitzer*-IRS spectral-line maps towards the IC443G region. Our main findings are the following:

(a) The level populations traced by the H_2 S(0) to S(7) pure rotational lines cannot be reproduced by a single excitation temperature: as predicted by any shock model, the shocked clump is stratified in temperature.

(b) A thermal admixture model allows to successfully reproduce the level populations with a power-law index $\Gamma \sim 2.6 - 3.1$ ($\chi^2_{avg} \sim 3.6$). In IC443C, Shinn *et al.* (2011) found variations of Γ over the range $\sim 3 - 6$, with the majority of sight lines in the range $\sim 4 - 5$. In addition, the authors showed that parabolic C-type bow shocks in steady state (Smith and Brand, 1990) would produce a temperature stratification $dN \propto T^{-3.8} dT$ (*i.e.* $\Gamma = 3.8$). In this scenario, spatial variation of Γ across our map would correspond to variations in the distributions of velocities at the head of unresolved bow shocks. Our estimate of Γ is below the value predicted by shock models. We note, however, that more accurate description of shock structures (*e.g.* 3D shock models) could possibly shift the prediction on the temperature distribution in our favor.

(c) The total column density N_{H_2} inferred with two excitation temperatures represents approximately 3% of the total column density deduced from the thermal admixture model. In other words, 97% of the H_2 molecular mass is lost in the 'standard LTE' analysis.

(d) The agreement between the observations and our thermal admixture model suggests that the S(0) to S(7) H_2 lines are thermalized (average global $\chi^2 = 3.6$, see Fig. 8.10).

(e) Assuming that the temperature distribution of H_2 spans the range 25 – 1500 K (based on the determination of the temperature of the cold molecular gas in section 8.2), the total H_2 column density measured in IC443G reaches a maximum $N_{H_2} = 1.0 \times 10^{23}$ cm^{-2} towards the core of the shocked clump.

(f) The local density inferred from our column density measurement is in the range $0.7 - 3.5 \times 10^5$ cm^{-3}, depending on the adopted geometry. At odds with conclusion 'd', this range of local densities is not consistent with a full thermalization of the S(6) and S(7) lines.

(g) Our derived column density maps $N_{H_2}(T)$ (see Fig. 8.12) indicate that both the 'cold' ($T \sim 25 - 100$ K) and 'hot' ($T \sim 800 - 1500$ K) phases of the molecular hydrogen are more clumpy than the 'warm' phase ($T \sim 300 - 600$ K). Local sources of heating might contribute to the localized pockets of hot gas (see Chapter 10).

(h) We measured a mass $M_{H_2} = 280 \pm 60$ M$_\odot$ across the *Spitzer*-IRS field of observations. The total mass of the shocked clump is likely to be in the range $2 - 5 \times 10^2$ M$_\odot$. This measurement represents a lower bound of the mass of protons available for CRs to interact with in IC443G. Additionally, the clumpy structure shown by our maps should allow more CRs to interact with the shocked interstellar material.

8.2 | Carbon monoxide (^{12}CO, ^{13}CO, C^{18}O)

In this section[2], we aim to analyze the emission of ^{12}CO, ^{13}CO and C^{18}O lines mapped with the IRAM 30m and APEX telescopes (see Chapter 6 for a complete description of the observations). The $10' \times 10'$ field of observations is much larger than the *Spitzer-IRS* field of observations studied in the previous section, allowing to completely characterize the region where the γ-ray peak was detected by Albert *et al.* (2007), Acciari *et al.* (2009) and Humensky and VERITAS Collaboration (2015) (see Fig. 8.1, Fig. 8.13). We choose to study such a large region precisely because it is appropriate with respect to the angular resolution of γ-ray telescopes and the uncertainties on the localization of the γ-ray peak in IC443 (*e.g.* Abdo *et al.* 2010).

Tab. 8.4 contains the parameters of the lines observed in the extended G region. The relatively low energies of the first three rotational levels of ^{12}CO ($E_u = 5.5,\ 16.6,\ 33.2$ K) guarantee the possibility to trace the 'cold mass' of the molecular gas, which was lost in the analysis of H_2 lines. We aim to measure the ^{12}CO column density and infer the total mass distribution of the molecular gas in the extended G region, using an assumption on the ^{12}CO/H_2 abundance ratio. In section 8.2.1, we begin with an estimate of the random and systematic uncertainties associated with our data products. In section 8.2.2, we perform a systematic pixel-per-pixel, channel-per-channel comparison of the emission of different isotopologs with LTE radiative transfer models to study the excitation of the lines and isotopic ratios. In section 8.2.3, we measure the opacity of ^{12}CO

[2]This section is a presentation of the paper Dell'Ova *et al.* (2020) (first part).

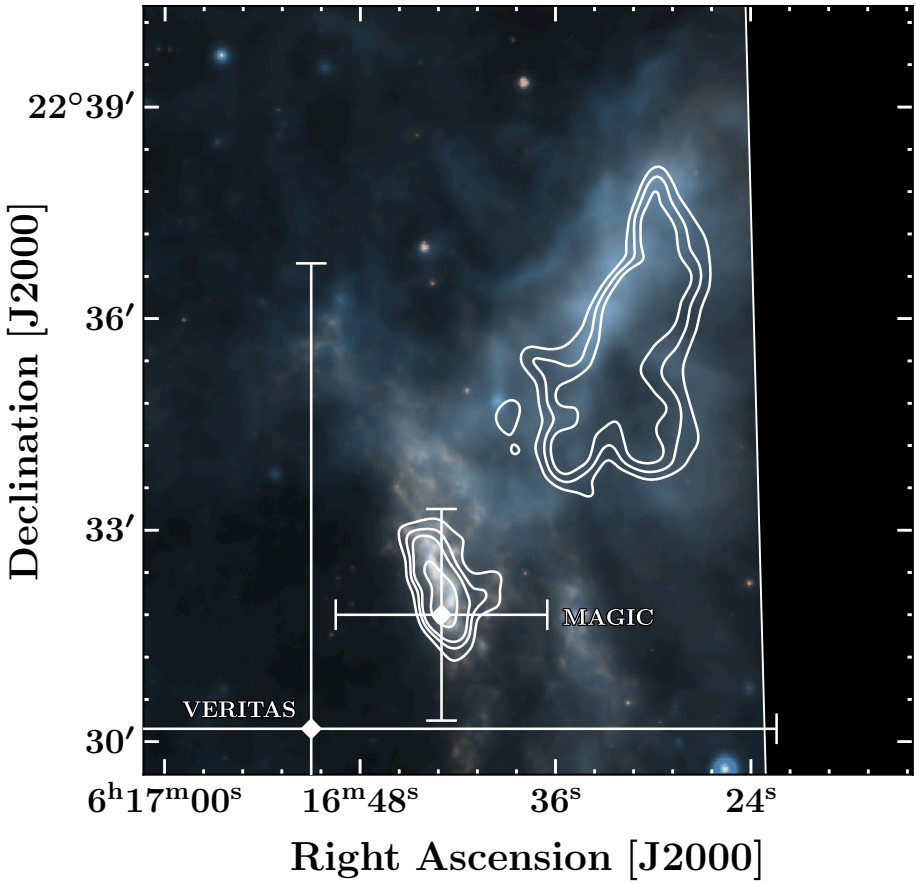

Figure 8.13 *Background:* color composite image of *Spitzer*-IRAC (8 μm, in yellow) and *Spitzer*-MIPS (24 μm, in blue). *Contours:* ^{12}CO J=2–1 IRAM 30m observations of the 'extended G region' (spatial resolution 11.2″). Contour levels are 0.25, 0.35, 0.45 and 0.75 times the maximum value across the map. Markers indicate the locations of the γ-ray centroids found by Albert *et al.* (2007) (MAGIC) and Acciari *et al.* (2009) (VERITAS). The field of observation shown on this figure corresponds to the 10′ × 10′ field observed with the IRAM 30m and APEX telescopes (see chapter 6). There is an empty patch on the right section of the figure because this area was not mapped by *Spitzer*-IRAC.

lines based on the comparison with ^{13}CO and C^{18}O lines. Finally, we measure the ^{12}CO column density using opacity-corrected population diagrams (section 8.2.4) and a statistical equilibrium radiative transfer code (section 8.2.5). We discuss and compare our results in section 8.2.6.

8.2.1 Statistical analysis of uncertainties

In this section, we aim to determine the random *and* systematic errors that characterize our IRAM 30m and APEX observations. The r.m.s values given in Tab. 6.1 and Tab. 6.2 correspond to the measurements of the standard deviation with respect to the baselines, hence they represent a fraction of the total uncertainty associated with our data (*e.g.* absolute flux calibrations, time variations of the atmospheric absorption, receiver gain, *etc*). The uncertainty associated with the brightness temperature measurement must be estimated as accurately as possible, since it will propagate to our column density and mass measurements.

species	J_u	ν_{ul} (GHz)	A_{ul} (s^{-1})	g_u	E_u (K)
^{12}CO	1	115.2712018	7.203×10^{-8}	3	5.53
^{12}CO	2	230.5380000	6.910×10^{-7}	5	16.6
^{12}CO	3	345.7959899	2.497×10^{-6}	7	33.19
^{13}CO	1	110.2013543	6.294×10^{-8}	3	5.29
^{13}CO	2	220.3986841	6.038×10^{-7}	5	15.87
^{13}CO	3	330.5879652	2.181×10^{-6}	7	31.73
$C^{18}O$	1	109.7821734	6.266×10^{-8}	3	5.27
$C^{18}O$	2	219.5603541	6.011×10^{-7}	5	15.81

Table 8.4 Spectroscopic parameters corresponding to the observed lines. J_u is the rotational quantum number, ν_{ul} and A_{ul} are respectively the frequency and the Einstein coefficient of the pure rotational transition ($v = 0$ where v is the vibrational quantum number). E_u and g_u are respectively the energy and degeneracy corresponding to the upper level. The values given are taken from the Cologne Database for Molecular Spectroscopy (Müller *et al.* 2001, Müller *et al.* 2005, Endres *et al.* 2016) and Jet Propulsion Laboratory database (Pickett *et al.*, 1998), and are the numeric values used in this work.

^{12}CO J=2–1 data comparison (IRAM 30m *vs.* APEX) The ^{12}CO J=2–1 line has been observed by both observatories, hence we base our estimate of the systematic uncertainties on the comparison of these two PPV cubes. The two data cubes can be visually compared *via* the channel maps shown in Fig. 6.6 (IRAM 30m telescope) and Fig. 6.7 (APEX telescope). We found no evidence of systematic pointing error between the two data cubes. We performed a quantitative comparison of the two spectral cubes. First, we resampled the data cubes to the same spectral and angular resolutions. The spatial resolution was set to the nominal resolution of APEX ($\theta = 28.7''$) and the spectral resolution was set to the nominal resolution of the IRAM 30m ^{12}CO J=2–1 observations ($\Delta v = 0.25$ km s^{-1}). Then, in each frequency channel and every single pixel of the mosaic we compared the signal detected by the two telescopes where the signal is greater than 3σ.

The results of this complete comparison are represented on a T_{mb}-T_{mb} 2D histogram shown in Fig. 8.14. We determined the best linear fit $x \mapsto a_{lin}x + b_{lin}$ corresponding to the data dispersion between the two telescopes using a threshold of 5σ (168 mK for the APEX telescope, and 98 mK for the IRAM 30m telescope, estimated from the baseline r.m.s) in order to best describe the high signal-to-noise data points. In addition, we excluded the data points located at the borders of the field of observation (by a $1'$ margin) in order to neutralize the effects of spatial resampling. The parameters given by the χ^2-minimization are $a_{lin} = 0.88$, $b_{lin} = -0.35$, indicating a slight overestimate in the measurement of the flux by the IRAM 30m with respect to APEX measurements, at least in the scope of our observations. We then estimated the variance of the data points with respect to our linear model:

$$var = \sum_{i=1}^{N} \frac{(y_i - lin(x_i))^2}{N} \tag{8.21}$$

where y_i and x_i are respectively the APEX and IRAM 30m data points, the function *lin* is our linear model ($a_{lin} = 0.88$, $b_{lin} = -0.35$) and N is the number of data points.

Results Our statistical analysis of the two data cubes shows that:

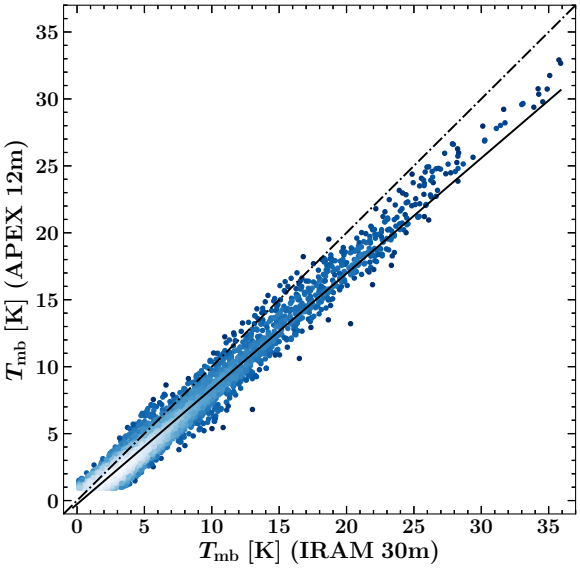

Figure 8.14 Two-dimensional histogram of the systematic comparison between the PPV cubes obtained with the IRAM 30m and APEX telescopes observations of ^{12}CO J=2–1 (each data point in this diagram corresponds to a pair of pixels/velocity channels). The two data cubes were resampled to the same spatial and spectral resolution. The dashed black line represents the 1:1 relation expected between the two spectral cubes if the data points were identical. The solid black line represents the empirical relation measured by determining the best linear fit of the 'extended IC443G region' sample, using a threshold of 5σ to best describe the high signal-to-noise measurements.

1. The lower bound on the systematic errors associated with our data products is approximately 12% of the signal (inferred from $a_{\rm lin} = 0.88$), plus an additive term ($\sigma_b \simeq 350$ mK, inferred from $b_{\rm lin} = -0.35$). This systematic uncertainty could be due to inaccurate correction of telescope efficiencies[3] and/or discrepancies in the observing conditions (absolute flux calibration, focus, off-position references, *etc*).

2. According to the dispersion around the instrumental linear model (measured by Eq. 8.21), our measurements are also affected by a random error characterized by a standard deviation $\sigma_{\rm std} \simeq$550 mK. This estimate of the standard deviation is much larger than the r.m.s measured on the baseline of individual spectra (39 mK and 69 mK respectively for the IRAM 30m and APEX observations, see Tab. 6.1 and Tab. 6.2). This random uncertainty is likely to be caused by several sources of random noise due to varying observing conditions (*e.g.* pwv and weather time-variations).

Thus, this analysis allows us to estimate the uncertainty associated with a measurement of the brightness temperature $T_{\rm mb}$ in a {pixel, velocity channel} data point of our ^{12}CO J=2–1 PPV cube:

$$\sigma_{\rm unc} = \Lambda T_{\rm mb} + \Gamma \tag{8.22}$$

where $\Lambda = 0.12$ and $\Gamma = \sqrt{\sigma_{std}^2 + \sigma_b^2} \sim 650$ mK. We assume that the systematic uncertainty of the ^{12}CO J=2–1 PPV cubes ($\Lambda = 0.12$) represents a lower bound of the uncertainty of the rest of our PPV cubes, hence we adopt this value (12%) as the standard uncertainty in our analysis.

8.2.2 Analysis of ^{12}CO, ^{13}CO and C^{18}O lines ratios

In the next section, we will use assumptions on the excitation of the ^{13}CO and ^{12}CO lines, and on the [^{12}CO / ^{13}CO] isotopic ratio. In general, it is assumed that the three isotopologs (^{12}CO, ^{13}CO

[3]The uncertainty on the beam efficiency at APEX is on the order of 10%, see https://www.apex-telescope.org/telescope/efficiency/index.php.

and C^{18}O) have similar excitation conditions. This assumption makes sense, because the critical densities of the three isotopologs are very similar (approximately 2×10^3 cm^{-3}, see Tab. 4.4) and more generally because their spectroscopic characteristics are similar. A naive assumption is also that relative abundances of these three species are constant in all lines of sight, when in fact different regimes can be observed within a giant molecular cloud (Bron *et al.* 2018, Roueff *et al.* 2021). In this section, we aim to estimate the validity of these assumptions in our observations of the extended G region, by comparing the J=1–0 line intensities of ^{12}CO, ^{13}CO and C^{18}O, and the line intensity ratios of distinct rotational transitions (J=1–0, J=2–1, J=3–2).

8.2.2.1 Description of the histograms

Method We built 2D histograms from the ^{12}CO J=1–0, J=2–1, J=3–2 data cubes, as well as ^{13}CO and C^{18}O J=1–0 data cubes to compare the line intensity from different isotopologs and rotational transitions in each pixel (x, y) and velocity channel Δv. We aim to compare the observations with modified LTE radiative transfer models (following the method presented by Bron *et al.* 2018, see section 8.2.2.2 for the description of the models used to draw the curves on the diagrams presented in this section) in order to estimate isotopic ratios and the excitation conditions of the different lines based on the 'best-fit' models (see next subsection). We examined four different 2D data histograms:

1. J=1–0 line intensity, ^{13}CO *vs.* ^{12}CO (Fig. 8.15, left panel).

2. J=1–0 line intensity, ^{13}CO *vs.* C^{18}O (Fig. 8.16, left panel).

3. J=1–0 line intensity ratio, [^{13}CO/C^{18}O] *vs.* [^{12}CO/^{13}CO] (Fig. 8.16, right panel).

4. ^{12}CO line intensity ratio, [J=3–2]/[J=2–1] *vs.* [J=2–1]/[J=1–0] (Fig. 8.15, right panel).

In order to build the first three data histograms, we convolved all IRAM 30m data cubes to the nominal spatial resolution of C^{18}O J=1–0 (23.6″) and to the nominal spectral resolution of the FTS backend at 3mm (0.5 km s^{-1}). To build the fourth histogram, we resampled IRAM 30m ^{12}CO J=1–0, APEX ^{12}CO J=2–1 and APEX ^{12}CO J=3–2 PPV cubes to the nominal spatial resolution of ^{12}CO J=1–0 (22.5″) and to the nominal spectral resolution given by the FTS backend (0.25 km s^{-1}). We used a threshold of 3σ to select data points where the signal is significantly above the noise level. The resulting 2D data histograms are shown in Fig. A.5 and Fig. A.6.

Using the `scipy.stats.gaussian_kde` module from `Python`, we produced the kernel density estimators of our histograms (Fig. 8.15 and Fig. 8.16). A density estimator is an algorithm which seeks to model the probability distribution that corresponds to a sample of observations. This probability density allows to visualize our distribution of points in a smooth manner. In the next paragraphs, we will be referring to these diagrams as the first (Fig. 8.15, left panel), second (Fig. 8.15, right panel), third (Fig. 8.16, left panel) and fourth (Fig. 8.16, right panel) histograms.

***i.)* ^{13}CO *vs.* ^{12}CO J=1–0** The first histogram (Fig. 8.15, left panel) is characterized by a high signal-to-noise ratio and represents a large statistical sample (n = 20531). The ^{13}CO(1–0) vs ^{12}CO(1–0) relation presents at least two distinct branches. A lower (faint) quasi-horizontal branch traces bright ^{12}CO J=1–0 emission associated with faint ^{13}CO J=1–0 line emission (T_{13} < 1 K

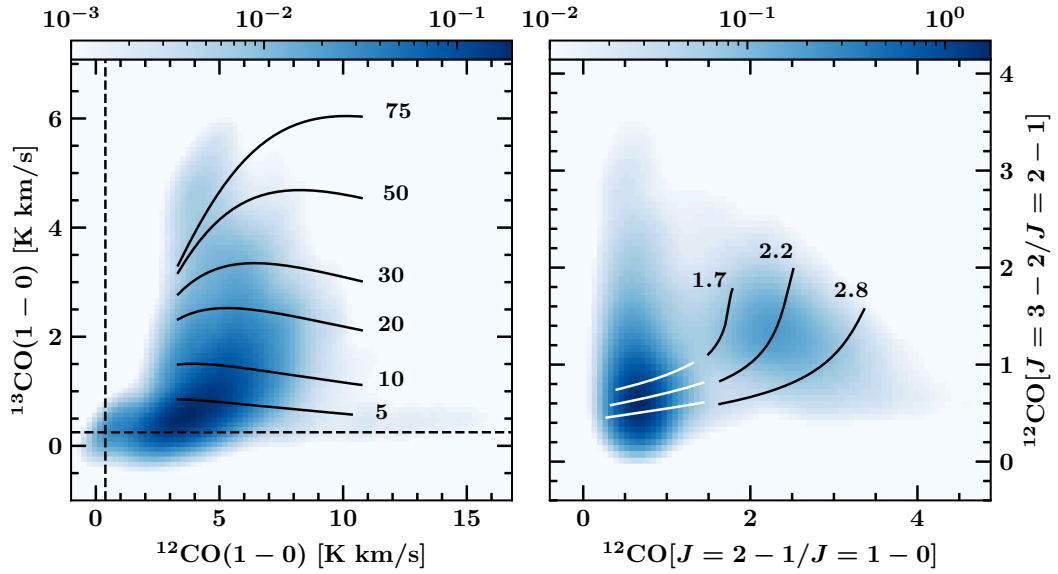

Histogram	$\tau_{^{12}CO}$(20K)	T_{kin} (K)	[^{12}CO/^{13}CO]	[^{13}CO/C^{18}O]	$T_{^{12}CO}$ / $T_{^{13}CO}$	$T_{^{13}CO}$ / $T_{C^{18}O}$
left	[5, 10, 20, 30, 50, 75]	[10-25]	60	30	1	1
Histogram	$\tau_{^{12}CO}$(20K)	T_{kin} (K)	T_{2-1} / T_{1-0}	T_{3-2} / T_{2-1}	τ_{2-1} / τ_{1-0}	τ_{3-2} / τ_{2-1}
right	[5 (white), 40 (black)]	[10-25]	[1.7, 2.2, 2.8]	[1.7, 2.2, 2.8]	0.2	1

Notes. Control parameters of the LTE models: $\tau_{^{12}CO}$ is the list of line opacities used to generate the family of curves, $T_{^{13}CO}$ and $T_{^{12}CO}$ are respectively the ranges of kinetic temperature used for ^{13}CO and ^{12}CO. [^{12}CO/^{13}CO] and [^{13}CO/C^{18}O] are the adopted isotopic ratios. The ratios of excitation temperatures and line opacities for distinct isotopologs or rotational transitions are indicated by the columns T_a/T_b and τ_a/τ_b.

Figure 8.15 *Left:* kernel density estimate of the ^{13}CO *vs.* ^{12}CO J=1–0 histogram. Black curves represent the radiative transfer models obtained for different opacities (indicated by numeric values on the right end of the curves). *Right:* kernel density estimate of the ^{12}CO [J=3–2]/[J=2–1] *vs.* [J=2–1]/[J=1–0] histogram. Black curves (τ = 40) and white curves (τ = 5) represent the radiative transfer models obtained for different T_{2-1}/T_{1-0} ratios (indicated by numeric values on the top end of the curves). The exact parameters of the LTE radiative transfer models are indicated in the table below the two panels. Dashed black lines represent the 3σ threshold. See also Fig. A.5.

km s^{-1}, where T_{13} is the brightness temperature of the ^{13}CO J=1–0 line). This branch is spatially correlated with the shock structure and spectrally correlated with the high-velocity wings of the ^{12}CO line, which have no bright ^{13}CO counterpart because of insufficient integration time. In contrast, the main branch is spatially correlated mainly with the quiescent molecular gas that is found within the cloudlet and ring-like structure, as well as the ambient cloud.

***ii.)* ^{12}CO [J=3–2]/[J=2–1] *vs.* [J=2–1]/[J=1–0]** The second histogram (Fig. 8.15, right panel) is built on a large statistical sample with high signal-to-noise data (n = 9793), as the rotational lines J=1–0, J=2–1 and J=3–2 are well detected in our data cubes. The ^{12}CO [J=3–2]/[J=2–1] vs [J=2–1]/[J=1–0] relationship is clearly bimodal. Indeed, a quasi-vertical branch centered on [J=2–1]/[J=1–0] ≃0.5 can be distinguished from a crescent-shaped branch centered on [J=2–1]/[J=1–0] ≃2 and [J=3–2]/[J=2–1] ≃1.3. The crescent-shaped branch is highly correlated to the

high-velocity wings of the ^{12}CO lines tracing the emission of shocked gas. In contrast, the quasi-vertical branch traces the rest of emission from the cloudlet and ambient gas (see also Fig. 8.19).

It is expected to find an enhanced J=2–1 / J=1–0 ratio in SNRs interacting with molecular clouds (*e.g.* Seta *et al.* 1998 found ratios of up to 1.3-1.7 in regions where the SNR W44 interacts with molecular clouds, and greater than 3 in the high-velocity wings of ^{12}CO lines towards IC443). Seta *et al.* (1998) showed that ^{12}CO J=2–1 / J=1–0 intensity ratios approaching 4 can be produced by optically thin emission from gas thermalized at high excitation temperatures ($T_{ex} > 60$ K).

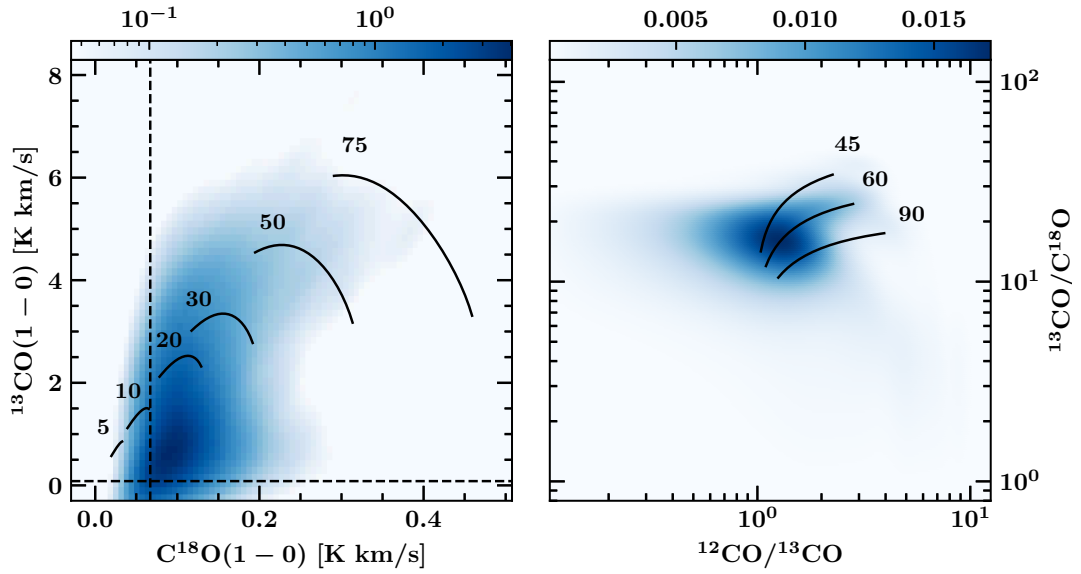

Histogram	$\tau_{^{12}CO}$(20K)	T_{kin} (K)	[$^{12}CO/^{13}CO$]	[$^{13}CO/C^{18}O$]	$T_{^{12}CO}$ / $T_{^{13}CO}$	$T_{^{13}CO}$ / $T_{C^{18}O}$
left	[5, 10, 20, 30, 50, 75]	[10-25]	60	30	1	1
right	40	[10-25]	[45, 60, 90]	30	1	1

Notes. Control parameters of the LTE models: $\tau_{^{12}CO}$ is the list of line opacities used to generate the family of curves, $T_{^{13}CO}$ and $T_{^{12}CO}$ are respectively the ranges of kinetic temperature used for ^{13}CO and ^{12}CO. [$^{12}CO/^{13}CO$] and [$^{13}CO/C^{18}O$] are the adopted isotopic ratios. The ratios of excitation temperatures and line opacities for distinct isotopologs are indicated by the columns T_a/T_b.

Figure 8.16 *Left:* kernel density estimate of the ^{13}CO *vs.* $C^{18}O$ J=1–0 histogram. Black curves represent the radiative transfer models obtained for different opacities (indicated by numeric values on top of the curves). *Right:* kernel density estimate of the [$^{13}CO/C^{18}O$] *vs.* [$^{12}CO/^{13}CO$] (J=1–0) histogram. Black curves represent the radiative transfer models obtained for different $^{12}CO/^{13}CO$ isotopic ratios (indicated by numeric values on the right end of the curves). The parameters of the LTE models are indicated in the table below the two panels. Dashed black lines represent the 3σ threshold. See also Fig. A.6.

***iii.)* ^{13}CO *vs.* $C^{18}O$ J=1–0** The third histogram (Fig. 8.16, left panel) has a much smaller amount of bins determined with a good signal-to-noise ratio ($n = 833$) due to the faint emission of $C^{18}O$ J=1–0 that is hardly detected at a 3σ confidence level within our data cube. The majority of data points seem to fall into the same branch, tracing a single trend for the relationship between ^{13}CO and $C^{18}O$ emission. Therefore, we did not manage to identify any spatial or spectral correlation

with accuracy and certainty based on this diagram.

***iv.)* [^{13}CO/C^{18}O] *vs.* [^{12}CO/^{13}CO] (J=1–0)** The fourth histogram (Fig. 8.16, right panel) has a poor statistical sample for the same reason as the third one (n = 833). If we ignore low signal-to-noise data points ($< 3\sigma$), the [^{13}CO(1–0)] / [C^{18}O(1–0)] *vs.* [^{12}CO(1–0)] / [^{13}CO(1–0)] relationship is localized in an area with little dispersion. Hence, for high signal-to-noise measurements the isotopic ratios are quasi-uniform in the field of observations. Nonetheless, the lower signal-to-noise data bins display a well-defined comet-shaped branch extending from this area. This branch might correspond to distinct physical conditions and/or isotopic ratios for a fraction of the field of observations. The high signal-to-noise ratio area of this branch is spatially correlated with the cloudlet and ring-like structure, whereas the 'tail' of the branch is spatially and spectrally associated with the shocked clump.

8.2.2.2 Comparison with LTE radiative transfer models

In this section, we aim to compare our histograms (Fig. 8.15, Fig. 8.16) with LTE radiative transfer models. We follow the method presented by Bron *et al.* (2018) in their analysis of the J=1–0 rotational lines of ^{12}CO, ^{13}CO and C^{18}O in the Orion B giant molecular cloud.

Description of the model parameters We compared the observational histograms with synthetic families of curves generated using modified LTE radiative transfer models of the observed rotational transition for ^{12}CO, ^{13}CO, and C^{18}O ("modified", because the ratios between the excitation temperatures of distinct isotopologs is treated as a free parameter). Assuming that the gas is at thermal equilibrium, the brightness temperature of the line integrated over an element of spectral resolution (Δv = 0.5 km s $^{-1}$) is given by the following relation:

$$W_\alpha = T_\alpha \Delta v \tag{8.23}$$

where α = 12, 13, 18 or α =1–0, 2–1, 3–2 respectively for the ^{12}CO, ^{13}CO, C^{18}O isotopologs and J=1–0, J=2–1, J=3–2 rotational lines. T_α (K) is the brightness temperature of the line, defined as:

$$T_\alpha = T_\alpha^0 \left[1 - \exp(-\tau_\alpha)\right] \left(\frac{1}{\exp(T_\alpha^0 / T_\alpha^{\rm exc}) - 1} - \frac{1}{\exp(T_\alpha^0 / T_{\rm CMB}) - 1} \right) \tag{8.24}$$

where $T_\alpha^0 = h\nu_{\rm ul}/k_{\rm B}$ is the energy of the transition in temperature unit[4], with $h\nu_{\rm ul} = E_{\rm ul} = E_{\rm u} - E_{\rm l}$ (see in Tab. 8.4 for the corresponding parameters of the studied lines). τ_α is the optical depth of the line, $T_{\rm CMB}$ = 2.7 K is the cosmic microwave background temperature, and $T_\alpha^{\rm exc}$ is the excitation temperature of the line (see Eq. 4.8). The optical depth τ_α and its dependence on the excitation temperature are described by (Bron *et al.*, 2018):

$$\tau_\alpha = \tau_\alpha(T_0) \left(\frac{T_0}{T_\alpha^{\rm exc}} \right) \left(\frac{1 - \exp(T_\alpha^0 / T_\alpha^{\rm exc})}{1 - \exp(T_\alpha^0 / T_0)} \right) \tag{8.25}$$

where $\tau_\alpha(T_0)$ is the optical depth at a kinetic temperature T_0. We use the optical depth at T_0 = 20 K as a reference. In order to explore the excitation conditions of the lines, we made

[4] As in Tab. 8.4 and Tab. 8.4 where the energy levels of H_2 and ^{12}CO are given in Kelvin ($E_{\rm u}/k_{\rm B}$ yields a temperature, where $k_{\rm B}$ is the Boltzmann constant).

the assumption that the excitation temperature of the different isotopologs (T^{12}_{exc}, T^{13}_{exc}, T^{18}_{exc}) and rotational lines (T^{1-0}_{exc}, T^{2-1}_{exc}, T^{3-2}_{exc}) are distinct and controlled their ratios as four supplementary independent parameters of the modified LTE models (Roueff *et al.*, 2021). The opacities of ^{12}CO and $C^{18}O$ isotopologs are determined from the optical depth of ^{13}CO using the corresponding isotopic ratio (assuming that the emission of these isotopologs is co-spatial):

$$\frac{\tau_{12}}{\tau_{13}} = \frac{[^{12}CO]}{[^{13}CO]}, \frac{\tau_{13}}{\tau_{18}} = \frac{[^{13}CO]}{[C^{18}O]} \tag{8.26}$$

Lastly, we assumed a hierarchy in the optical depth of the different rotational lines such that $\tau_{1-0} \geq \tau_{2-1} \geq \tau_{3-2}$. We controlled the opacity ratios as two supplementary parameters of the modified LTE models (Roueff *et al.*, 2021). Hence, there are a total of 9 control parameters that we can tune: the optical depth τ_{13}, the isotopic ratio $[^{12}CO]/[^{13}CO]$, the isotopic ratio $[^{13}CO]/[C^{18}O]$, the temperature ratios $[T_{^{12}CO}/T_{^{13}CO}]$, $[T_{^{13}CO}/T_{C^{18}O}]$, $[T_{3-2}/T_{2-1}]$, $[T_{2-1}/T_{1-0}]$, and optical depth ratios $[\tau_{3-2}/\tau_{2-1}]$, $[\tau_{2-1}/\tau_{1-0}]$.

We used the kinetic temperature of ^{13}CO as a variable of the parametric equation $W_\alpha(T^{13}_{kin})$ to synthesize LTE models that we can plot on top of each 2D data histogram. Each curve in Fig. 8.15 and Fig. 8.16 corresponds to a given set of control parameters, with the kinetic temperature growing linearly along a curve. We produced a family of LTE models with linearly increasing optical depth and a kinetic temperature varying between 10 K and 25 K, corresponding to the typical temperatures of cold molecular clouds. We adopted the isotopic ratio $[^{12}CO]/[^{13}CO]$ and $[^{13}CO]/[C^{18}O]$ that offers the best visual match with our data, and similarly fine-tuned the other control parameters to reproduce the branches observed in each 2D data histogram.

Description of the control parameters All other parameters remaining constants, each control parameter has an effect on the pattern and location of a curve in the histogram space:

1. The minimum and maximum kinetic temperature of ^{13}CO (T^{13}_{kin}) determines the length of the curves and their boundaries in the histograms.

2. The optical depth of ^{12}CO at 20 K ($\tau_{^{12}CO}(20\ K)$) defines the position of a curve in the 'line *vs.* line' diagrams (mostly an upward translation in the first and third histograms). In the 'ratio *vs.* ratio' diagrams, the dependence on the optical depth is decreased, and a single $\tau_{^{12}CO}(20\ K)$ can reproduce most of the observations (*e.g.* in the fourth histogram).

3. An increase in the isotopic ratio $[^{12}CO]/[^{13}CO]$ translates the curves downward in the first histogram and translates the curves rightward in the fourth histogram. It has no effect on the second and third histograms, since the ^{13}CO emission is not studied in the second one, and the ^{12}CO emission is not studied in the third one.

4. An increase in the isotopic ratio $[^{13}CO]/[C^{18}O]$ does not modify the first histogram, but it causes an upward translation of the curves both in the third and fourth histograms.

5. The modification of the excitation temperature ratios alters the shape and orientation of the curves in all the histograms, and it determines the boundaries of the ^{12}CO and $C^{18}O$ curves (since the excitation temperature is shifted with respect to T^{13}_{kin}).

Comparison between the modelled curves and the histograms The LTE models that visually best match our data are presented in Fig. 8.15 and Fig. 8.16 over the data histograms, and their corresponding set of control parameters are summarized in a table below the diagrams. A kinetic temperature in the range 10 − 25 K is sufficient to account for most of the data where the sample is statistically significant. Contrary to Bron *et al.* (2018), we could not constrain the $[T_{^{12}CO}/T_{^{13}CO}]$ and $[T_{^{13}CO}/T_{C^{18}O}]$ ratios based on visual agreement with our data (due to the degeneracy of models), hence we assumed that they are not different from 1. The identity of the excitation conditions for distinct CO isotopologs would suggest that the FUV illumination remains low in the extended G region (in the Orion B giant molecular cloud, Bron *et al.* 2018 and Roueff *et al.* 2021 found a correlation between larger FUV illuminations and excitation temperature discrepancies).

However, the dispersion of the data does not allow to entirely rule out FUV illumination, since LTE models with excitation temperature ratios slightly different from 1 can also fit the data (*e.g.* $T_{^{12}CO}/T_{^{13}CO} = 1.2$). We discuss other signs of FUV illumination in the following developments, based on the histograms shown in Fig. 8.16. In order to obtain a model that accounts for the high [3–2]/[2–1] and [2–1]/[1–0] data bins (second histogram) it was necessary to set their temperature ratios as greater than 1 (see Fig. 8.15), such that we infer an average excitation temperature of up to ∼55 K traced by the J=2–1 lines, and up to ∼120 K for the J=3–2 lines in the high-velocity wings of the ^{12}CO lines. This area of the second histogram also required lower τ_{2-1}/τ_{1-0} and τ_{3-2}/τ_{1-0} ratios, that we set to 0.2 for our models, suggesting that optical depth decreases significantly in the high-velocity wings, where the photons can escape from the cold ambient foreground.

In regards to the fourth histogram, our best models indicate a value of the isotopic ratio $[^{12}CO]/[^{13}CO] = 45 - 90$ and $[^{13}CO]/[C^{18}O] = 20 - 45$ to account for the emission of the different isotopologs observed in the extended G field. As a matter of fact, a large range of isotopic ratios can account for the observed data spread in the fourth histogram, and it is difficult to discriminate between the curves. Additionally, there is some degeneracy between the choice of the isotopic ratios and the excitation temperature ratios (*i.e.* they partially share the same effect on the displacement of the curves in the diagram).

Hence, this analysis does not provide a precise determination of the $[^{12}CO]/[^{13}CO]$ and $[^{13}CO]/[C^{18}O]$ abundance ratios, but the 'best-fit' model seems to favor an isotopic ratio $[^{12}CO]/[^{13}CO] = 60^{+30}_{-15}$. The higher boundary of our $^{12}C/^{13}C$ ratio estimate is anomalous with respect to the local interstellar medium average of 62±4 (Langer and Penzias, 1993). However, this higher bound can be accounted for if we consider the galactic spatial variations of the isotopic ratio. Wilson and Rood (1994) provides an estimate of the elemental abundances based on their distance to the Galactic center (GC):

$$\begin{aligned} ^{12}C/^{13}C &= (7.5 \pm 1.9)D_{GC} + (7.6 \pm 12.9) \\ ^{16}O/^{18}O &= (58.8 \pm 11.8)D_{GC} + (37.1 \pm 82.6) \end{aligned} \tag{8.27}$$

If we adopt the distance of 1.8 kpc for IC443 (Ambrocio-Cruz *et al.* 2017, Yu *et al.* 2019) the SNR is located at a distance of ∼10 kpc from the GC. Hence our estimate of the $^{12}CO/^{13}CO$ ratio is in agreement with the expected abundance of 80±30, but the $^{13}CO/C^{18}O$ indicated by our LTE models remains much higher than the predicted ratio (8±2). If it is real (not a result of systematic uncertainties), such an enhancement of the $^{13}CO/C^{18}O$ ratio might be the product of the fractionation of carbon monoxide isotopologs. The rarefaction of $C^{18}O$ can be caused by isotopolog-selective photodissociation in FUV-illuminated regions (Roueff *et al.*, 2021). The most

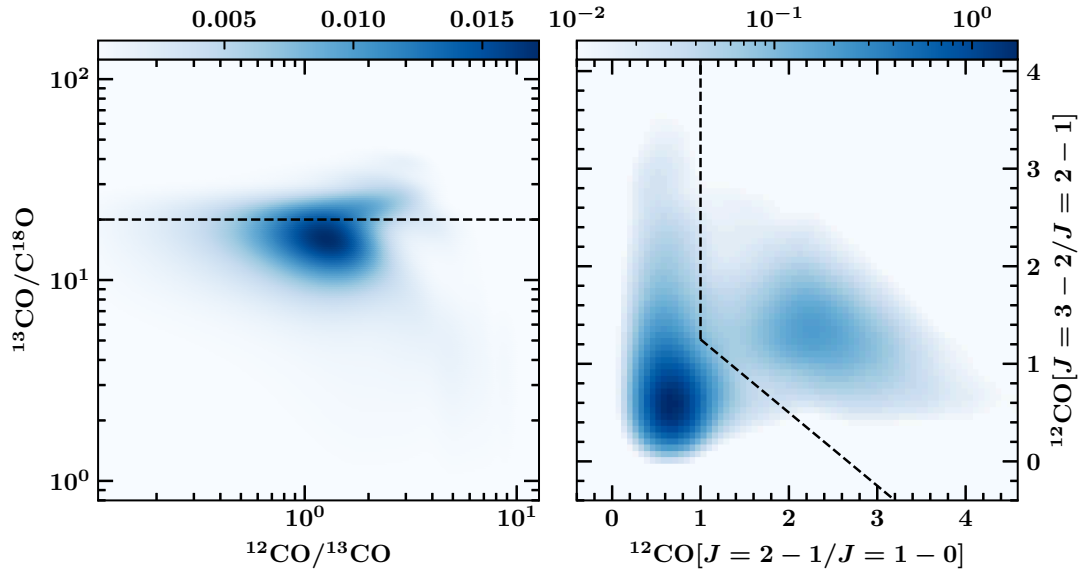

Figure 8.17 *Left:* kernel density estimate of the [^{13}CO/C^{18}O] *vs.* [^{12}CO/^{13}CO] (J=1–0) histogram (see also Fig. 8.16, right panel). *Right:* kernel density estimate of the ^{12}CO [J=3–2]/[J=2–1] *vs.* [J=2–1]/[J=1–0] histogram (see also Fig. 8.15, right panel). The dashed lines represent the arbitrary separation of the data sample into distinct populations (see text). The corresponding maps are shown on Fig. 8.19 (right histogram) and Fig. 8.18 (left histogram).

abundant isotopolog (^{12}CO) is self-shielded, *i.e.* it saturates in absorption, which reduces its rate of photodissociation in comparison to the less abundant isotopologs. Langer *et al.* (1984) and Glassgold *et al.* (1985) provide a physico-chemical mechanism for the rarefaction of C^{18}O and enhancement of the ^{13}CO/C^{18}O ratio with respect to the expected abundance. ^{12}CO and ^{13}CO are chemically coupled by the following reaction:

$$^{13}C^{+} + {}^{12}CO \rightarrow {}^{12}C^{+} + {}^{13}CO + 35\ K \tag{8.28}$$

In contrast, C^{18}O is formed separately, from reactions of ^{18}O with small hydrocarbons (*e.g.* CH, CH_2, C_2H). Hence, ^{13}CO benefits from the self-shielding of ^{12}CO, but not C^{18}O. This fractionation mechanism is expected in translucent layers at the surface of molecular clouds or smaller condensations, where CO and C^+ coexist. In fact, *Herschel*/PACS observations of IC443G (see section 9.1.4) show that C^+ is abundant in the dense molecular shell.

Spatial distributions of distinct branches We checked the spatial distribution of data points corresponding to particular areas of the histograms presented in Fig. 8.15 and Fig. 8.16. To do this, we defined arbitrary boundaries of distinct areas of the diagrams in order to separate populations of data points. In the left panel of Fig. 8.17, we separate the diagram in two regions based on an horizontal boundary corresponding to a J=1–0 line intensity ratio ^{13}CO / C^{18}O= 20. In the right panel of Fig. 8.17, we isolate the low ^{12}CO $[J = 2 - 1]/[J = 1 - 0]$ branch from the high ^{12}CO $[J = 2 - 1]/[J = 1 - 0]$ branch using the (arbitrary) following conditions:

$$W_{2-1}/W_{1-0} \leq 1 \; or \; W_{3-2}/W_{2-1} \leq 2 - 0.75 W_{2-1}/W_{1-0} \tag{8.29}$$

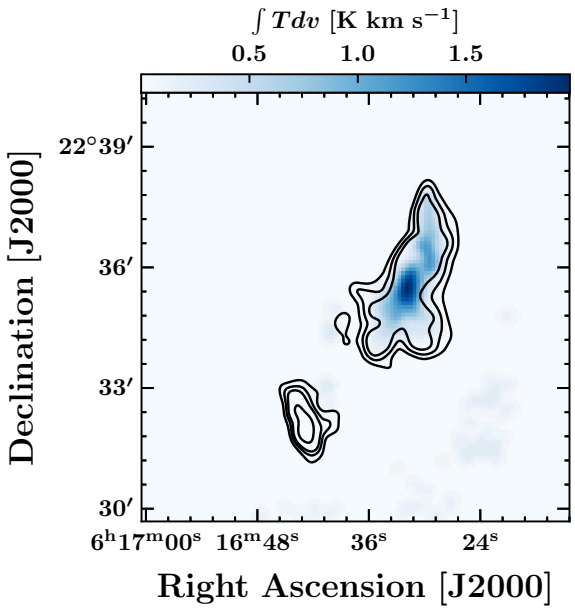

Figure 8.18 0th-order moment map (velocity integrated brightness temperature map) re-built from the separated data samples shown in the left panel of Fig. 8.17. This map corresponds to the 'upper section' of the [^{13}CO/C^{18}O] *vs.* [^{12}CO/^{13}CO] (J=1–0) histogram (tracing a [^{13}CO/C^{18}O] (J=1–0) line intensity ratio higher than 20, as shown by the horizontal dashed line in Fig. 8.17, left panel). Black contours represent the IRAM 30m ^{12}CO J=2–1 peak map shown in Fig. 6.10 (contour levels: 0.25, 0.35, 0.45 and 0.75 times the maximum value across the map).

where W_{2-1}/W_{1-0} and W_{3-2}/W_{2-1} respectively correspond to the ^{12}CO $[J = 2-1]/[J = 1-0]$ and $[J = 3-2]/[J = 2-1]$ line ratios. Using these arbitrary boundaries, we re-build PPV cubes corresponding to the separated sub-samples in order to visualize the spatial distribution of the populations of data points. In Fig. 8.18, we show the spatial distribution corresponding to the higher (> 20) J=1–0 ^{13}CO / C^{18}O line ratio. In Fig. 8.19, we show the spatial distributions corresponding to the lower ^{12}CO $[J = 2-1]/[J = 1-0]$ line ratio (left panel) and higher $[J = 2-1]/[J = 1-0]$ line ratio (right panel).

[^{13}CO/C^{18}O] *vs.* [^{12}CO/^{13}CO] (J=1–0) spatial distributions Interestingly, the data points corresponding to high (≥ 20) J=1–0 ^{13}CO/C^{18}O line ratios are spatially correlated with the quiescent cloudlet only (see Fig. 8.18). More precisely, the population of high J=1–0 ^{13}CO/C^{18}O line ratios data points is confined in the inner core of the quiescent cloudlet, which is the area where most of the C^{18}O J=1–0 signal is detected (see Fig. 6.12). If no protostars are positively identified towards the cloudlet (see chapter 10 for a discussion on the stellar contents of the extended G region), radiative decay from X-ray irradiation seen in the SNR cavity with XMM-Newton might provide a source to account for the isotopolog-selective photodissociation of CO within the cloudlet (Troja *et al.* 2006, Troja *et al.* 2008). This scenario is consistent with the X-ray emission maps (see Fig. 2.17, Fig. 6.2) which show an absorption feature towards the extended G region. As a matter of fact, we found several protostar candidates associated with a local enhancement of the interstellar radiation field to the north-eastern edge of the molecular cloudlet (see Fig. 10.5).

^{12}CO [J=3–2]/[J=2–1] *vs.* [J=2–1]/[J=1–0] spatial distributions Fig. 8.19 (left panel) shows the spatial distribution of the population of data points with lower $[J = 2-1]/[J = 1-0]$ ratio (see Eq. 8.29), while Fig. 8.19 (right panel) shows the distribution of data points with higher $[J = 2-1]/[J = 1-0]$ ratio. The results of the separation in the histogram domain are remarkable: the contribution of the shocked clump is strictly isolated from the rest of the signal. The map on the left panel traces the quiescent phase of the gas, with the contribution of the quiescent cloudlet and ambient cloud of Cornett *et al.* (1977) and Lee *et al.* (2012), and virtually no contribution from

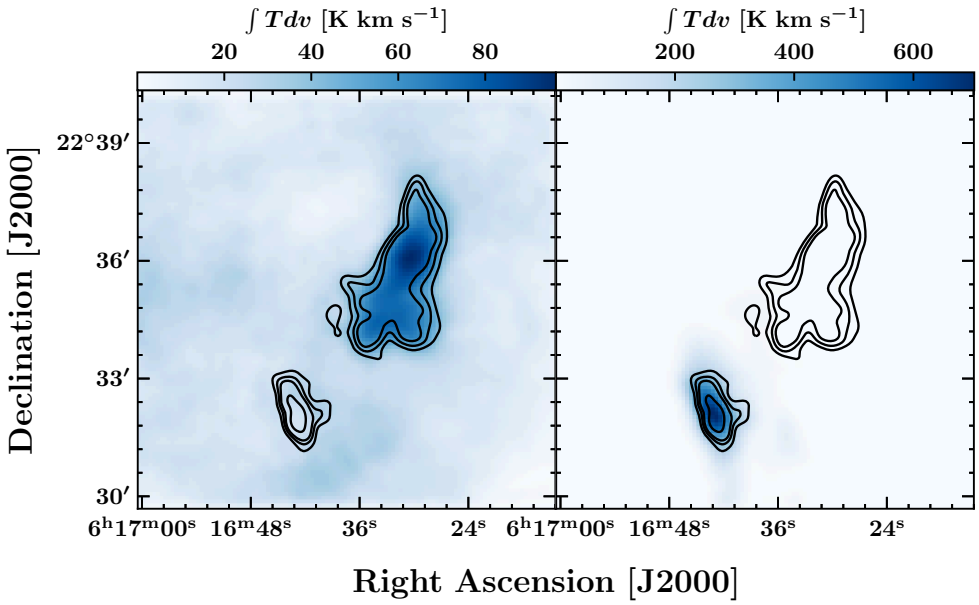

Figure 8.19 0th-order moment maps (velocity integrated brightness temperature maps) re-built from the separated data samples shown in the right panel of Fig. 8.17. *Left:* map corresponding to the 'left section' of the histogram in Fig. 8.17 (lower ^{12}CO [J=2–1]/[J=1–0] ratio). *Right:* map corresponding to the 'right section' of the histogram in Fig. 8.17 (higher ^{12}CO [J=2–1]/[J=1–0] ratio). Black contours represent the IRAM 30m ^{12}CO J=2–1 peak map shown in Fig. 6.10 (contour levels: 25%, 35%, 45% and 75% of the maximum value across the map).

the shocked clump. Conversely, the right panel map traces the emission from the high-velocity wings, where the $[J = 2 - 1]/[J = 1 - 0]$ is higher than normal, hence it is strongly correlated to the shocked clump, with no contributions from the rest of the field of observations. Thus, using arbitrary boundaries in the fourth histogram (Fig. 8.17, right panel) we achieved a separation between the quiescent phase of the gas and the perturbed gas in the extended G region. We will use this result in the next sections.

Additionally, we manually inspected (using hand-selected areas of the histograms) the distribution of the data points corresponding to distinct areas of the crescent-shaped branch. We found that:

– Data points corresponding to high (> 2) $[J = 2 - 1]/[J = 1 - 0]$ and high $[J = 3 - 2]/[J = 2 - 1]$ ratios (top-right section of the crescent) are uniformly correlated with the shocked clump, and spectrally correlated with the high-velocity wings of the molecular line.

– Lower (< 2) $[J = 2 - 1]/[J = 1 - 0]$ and high (> 2) $[J = 3 - 2]/[J = 2 - 1]$ ratios (top-left section of the crescent) are correlated with the eastern front of the shocked clump, within what would be a thin layer of molecular gas. However, this combination of line ratios (low $[J = 2 - 1]/[J = 1 - 0]$ and high $[J = 3 - 2]/[J = 2 - 1]$) is quite unexplainable. We tried to reproduce these line ratios using the radiative transfer code `RADEX` (see chapter 4), but we could not find a set of physical conditions that reproduce this observation. We assume that the line ratios measured in this small sub-sample of data points could be due to an inaccurate registration between the IRAM 30m (J=1–0) and APEX (J=2–1, J=3–2) data sets (either due to pointing errors or inexact re-projection and re-convolution of the data cubes).

8.2.3 Line opacity corrections

In this section, we aim to determine the optical depth of ^{12}CO lines in order to prepare the information required for opacity-corrected column density measurements in section 8.2.4. Assuming a linewidth Δv = 5 km s^{-1}, kinetic temperature $T_{\rm kin}$ = 30 K and local density $n = 10^4$ cm^{-3}, the ^{12}CO J=1–0 line is expected to saturate ($\tau \geq 0.5$) for a column density $N_{^{12}\rm CO} \geq 10^{17}$ cm^{-2}. In the saturated regime, the line intensity of a transition is decoupled from the column density of the upper level population. Therefore, accurate column density measurements require to estimate the opacity of the lines in order to correct the intensities and recover the total column density along the line of sight.

8.2.3.1 Method for optical depth measurement

Under the Sobolev approximation, the optical depth $\tau_{\rm ul}$ of a $J = J_{\rm u} - J_{\rm l}$ line is related to the escape probability of a photon $\beta_{\rm ul}$ by the following equation (see Chapter 4, section 4.3.1):

$$\beta_{\rm ul} = \frac{1 - e^{-\tau_{\rm ul}}}{\tau_{\rm ul}} \tag{8.30}$$

Notice that $\lim_{\tau_{\rm ul}\to 0}(1 - e^{-\tau_{\rm ul}})/\tau_{\rm ul} = 1$ (using the Taylor expansion $\lim_{u\to 0} e^u = 1 + u$). Hence, if the optical depth is negligible ($\tau_{\rm ul} \to 0$) then the medium is transparent ($\beta_{\rm ul} \to 1$) and conversely if $\tau_{\rm ul} \to \infty$ then $\beta_{\rm ul} \to 0$, *i.e.* the line is saturated. Following Eq. 4.31, the brightness temperature $T_{\rm ul}^{12}$ (in a velocity bin Δv) of a J=u–l ^{12}CO rotational line is given by:

$$T_{\rm ul}^{12} = \frac{hc^3 A_{\rm ul}^{12} N_{\rm u}^{12}}{8\pi k_{\rm B} (\nu_{\rm ul}^{12})^2 \Delta v} \beta_{\rm ul}^{12} \tag{8.31}$$

where h is the Planck constant, c the light speed, $A_{\rm ul}$ the probability of spontaneous radiative de-excitation (s^{-1}), $N_{\rm u}^{12}$ the ^{12}CO column density (in a velocity bin Δv), $k_{\rm B}$ the Boltzmann constant and $\nu_{\rm ul}^{12}$ the frequency of the transition. This equation shows that $T_{\rm ul}^{12}$ depends both on $N_{\rm u}^{12}$ and β_{ul}, hence the brightness temperature is not directly coupled to the column density of the upper level if $\beta_{\rm ul} \neq 1$. Thus, we aim to determine as accurately as possible the value of $\beta_{\rm ul}$ (or $\tau_{\rm ul}$, following Eq. 8.30).

Assuming that ^{13}CO lines are optically thin provides a method to determine the value of $\beta_{\rm ul}$. This assumption is reasonable (although with several limitations, see following developments), since the standard [^{12}CO / ^{13}CO] isotopic ratio predicts a $\sim$ 60 factor between the ^{12}CO and ^{13}CO column densities. Additionally, we can verify this assumption using the less abundant C^{18}O isotopolog (see next section). If the ^{13}CO lines are optically thin, then the brightness temperature $T_{\rm ul}^{13}$ is given by:

$$T_{\rm ul}^{13} = \frac{hc^3 A_{\rm ul}^{13} N_{\rm u}^{13}}{8\pi k_{\rm B} (\nu_{\rm ul}^{13})^2 \Delta v} \tag{8.32}$$

where the variables are the same as in Eq. 8.31, with $\beta_{\rm ul} = 1$. Hence, the line ratio (Eq. 8.31 divided by Eq. 8.32) yields:

$$\frac{T_{ul}^{12}}{T_{ul}^{13}} = \frac{A_{ul}^{12}}{A_{ul}^{13}} \left(\frac{\nu_{ul}^{13}}{\nu_{ul}^{12}} \right)^2 [^{12}CO/^{13}CO] \, \beta_{ul}^{12} \tag{8.33}$$

where $A_{ul}^{12}/A_{ul}^{13} \simeq 1$ and $\nu_{ul}^{13}/\nu_{ul}^{12} \simeq 1$ (*e.g.* $A_{10}^{12}/A_{10}^{13} = 1.14$ and $\nu_{10}^{13}/\nu_{10}^{12} = 1.05$, see Tab. 8.4) and $[^{12}CO/^{13}CO]$ is the fixed isotopic ratio. This relation can also be written in an identical way for ^{13}CO and $C^{18}O$. When writing that $N_u^{12}/N_u^{13} = [^{12}CO/^{13}CO]$, we have assumed that the excitation conditions are identical for the rotational transitions of ^{12}CO and ^{13}CO. Under this assumption, this equation allows to deduce the escape probability β_{ul}^{12} from the line ratio T_{ul}^{12}/T_{ul}^{13} (hence the optical depth τ_{ul}^{12}).

8.2.3.2 Assumptions

^{12}CO / ^{13}CO ratio Based on the results presented in section 8.2.2 (see Fig. 8.16), we assume that the $[^{12}CO\,/\,^{13}CO]$ isotopic ratio is uniform across the $10' \times 10'$ field of observations, and equal to 60^{+30}_{-15}. The uncertainty on the isotopic ratio will be propagated to the uncertainty on the optical depth measurements.

Relation between T_{ul}^{12} and T_{ul}^{13} along the line of sight We assume that the ^{12}CO line opacity can be directly traced by ^{13}CO lines as if it was emitted by a homogeneous, unique layer of gas, ignoring the confusion between distinct gas components along the line of sight. As a matter of fact, we know that between $v_{LSR} = -5.5$ km s^{-1} and $v_{LSR} = -3.5$ km s^{-1} there is confusion between the ambient cloud of Cornett *et al.* (1977) and the gas perturbed by the SNR (see Fig. 6.6). The self-absorption of the ^{12}CO lines towards the shocked clump is the signature of a cold, diffuse foreground that is spatially confused with the compact molecular structure. This confusion might cause systematic errors in the measurement of the ^{12}CO line optical depth, because we are measuring a T_{ul}^{12}/T_{ul}^{13} ratio in which each term is the sum of two distinct gas components (possibly with different excitation conditions).

Excitation of the lines In conformity with our previous assumption, we assume that ^{12}CO, ^{13}CO and $C^{18}O$ lines share the same excitation conditions (*i.e.* the excitation temperatures are identical) in each spatial and spectral bin of our PPV cubes. This assumption is supported by our histogram analysis (section 8.2.2, Fig. 8.15, Fig. 8.16) in which we have shown that the data is consistent with LTE models characterized by $T_{^{12}CO}/T_{^{13}CO} = 1$ and $T_{^{13}CO}/T_{C^{18}O} = 1$. However, if take into account the spread of the data points, small deviations are also consistent with our comparisons between histograms and LTE models, hence this is a source of uncertainty.

^{13}CO line opacity We assume that the ^{13}CO line is optically thin. The left panel of Fig. 8.15 (J=1–0 ^{13}CO *vs.* ^{12}CO) and left panel of Fig. 8.16 (J=1–0 ^{13}CO *vs.* $C^{18}O$) are mostly consistent with this assumption: for the bulk of the observations, the control parameters of the LTE curves required to reproduce the data correspond to $\tau_{^{12}CO} \leq 30$. Since $\tau_{13} = [^{13}CO/^{12}CO]\ \tau_{12}$ (see Eq. 8.26), this upper limit would correspond to $\tau_{10}^{13} = 0.5 \pm 0.2$. In order to verify the assumption towards specific positions, we manually extracted the J=1–0 ^{13}CO and $C^{18}O$ line intensities in distinct locations of the $10' \times 10'$ field of observations, within a beam of size $23.6''$.

Assuming an isotopic ratio [^{13}CO/C^{18}O]=10-30 and assuming that the C^{18}O line is optically thin, the line ratios measured towards the shocked clump ($6^h17^m42^s$, $+22°32'39''$) and quiescent cloudlet ($6^h16^m30^s$, $+22°36'12''$) are found to be consistent with an optically thin regime (following Eq. 8.33), hence the data is consistent with our assumption. In addition, we specifically checked the optical depth at the center of ^{13}CO lines in order to verify our assumption on the velocity channels which are the most likely to be optically thick (the quantity shown in Fig. 8.20 is the optical depth at the center of the line, *i.e.* max[τ^{13}_{10}]).

8.2.3.3 Optical depth PPV cubes

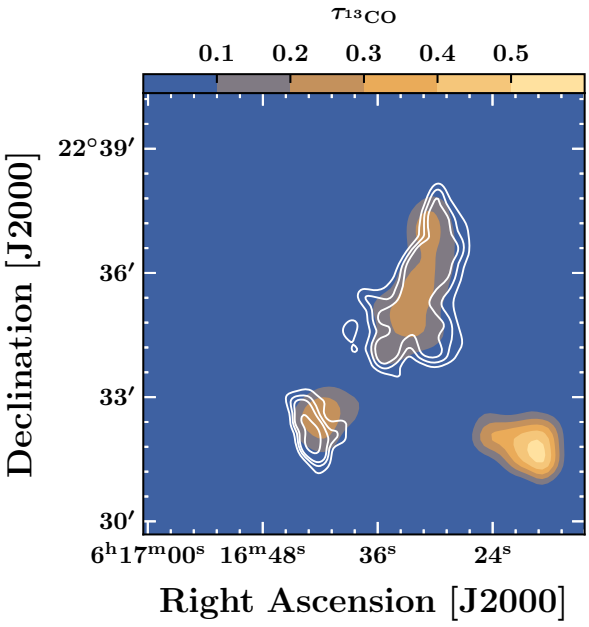

Figure 8.20 *Filled contours:* map of the peak J=1–0 ^{13}CO line opacity inferred from the comparison between the J=1–0 ^{13}CO and C^{18}O lines observed with the IRAM 30m telescope in the extended G region ($10'\times10'$ field of observation). We assumed that the C^{18}O line is optically thin. The quantity shown by the colored filled contours is max[$\tau^{13}_{10}(v_{LSR})$], *i.e.* the optical depth at the center of the ^{13}CO line, corresponding to the maximum line opacity measured in a pixel. *White contours:* IRAM 30m ^{12}CO J=2–1 peak map shown in Fig. 6.10 (contour levels: 0.25, 0.35, 0.45 and 0.75 times the maximum value across the map).

Method: pixel-per-pixel, channel-per-channel measurements We produced optical depth PPV cubes both for the ^{13}CO lines (to verify our assumption in each pixel) and ^{12}CO lines. These data cubes are produced by measuring T^{12}_{ul}/T^{13}_{ul} (respectively T^{13}_{ul}/T^{18}_{ul}) in each pixel/channel data point of our brightness temperature PPV cubes, and then inverting Eq. 8.33 for β^{12}_{ul} (respectively β^{13}_{ul}). Then, τ^{α}_{ul} can be deduced from β^{α}_{ul} by solving Eq. 8.30 (using the `Python` module `fsolve`). We adopted the isotopic ratios [^{12}CO/^{13}CO]=60^{+30}_{-15} to measure the ^{12}CO line opacities (see section 8.2.2), and [^{13}CO/C^{18}O]=8 ± 2 to check our assumption on the opacity of ^{13}CO lines (Wilson and Rood, 1994).

For consistency, we convolved all brightness temperature data cubes to the same spatial resolution, using the nominal resolution of the ^{13}CO J=2–1 observations, such that we have a beam diameter of 30.1″. The spectral resolution was also modified to 2 km s^{-1} in order to increase the signal-to-noise ratio. In order to minimize systematic uncertainties due to the intercalibration of the two telescopes, we used only IRAM 30m data for the J=1–0 measurements, and only APEX data for the J=2–1 and J=3–2 measurements (*i.e.* we did not compare the J=2–1 ^{12}CO IRAM 30m PPV cube with the J=2–1 ^{13}CO APEX PPV cube). We performed the opacity measurements on all velocity channels with a signal greater than 3σ (where σ is the noise measured on the baseline).

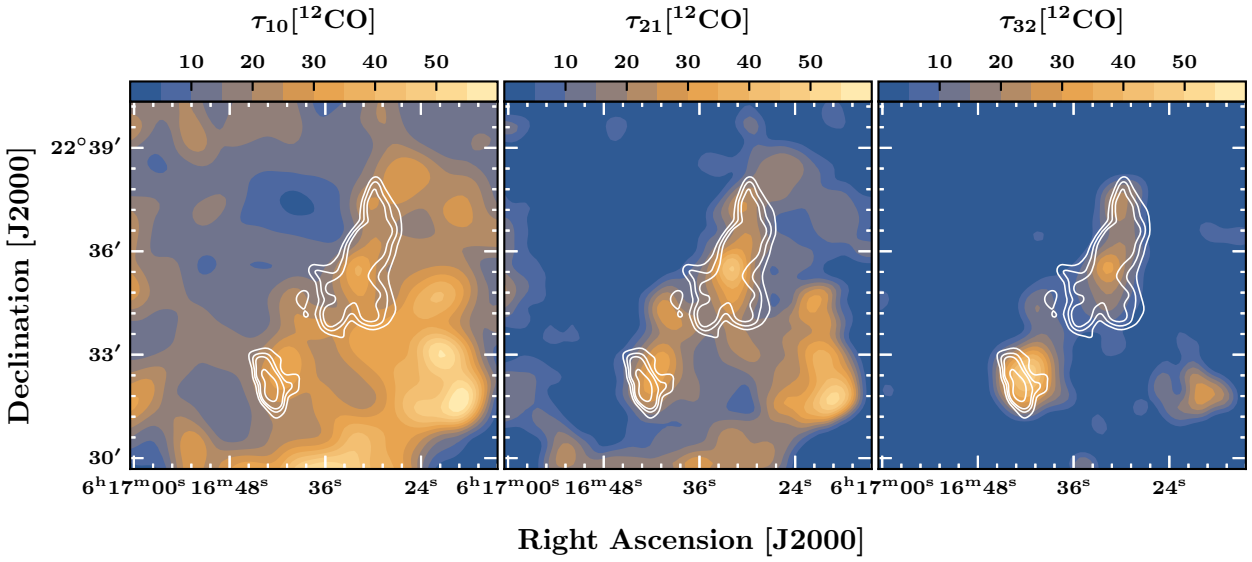

Figure 8.21 *Filled contours:* map of the peak J=1–0 (left panel), J=2–1 (mid panel), J=3–2 (right panel) ^{12}CO line opacity inferred from the comparison between the ^{12}CO and ^{13}CO lines observed with the IRAM 30m and APEX telescope in the extended G region ($10' \times 10'$ field of observation). The quantity shown by the colored filled contours is $\max[\tau_{ul}^{12}(v_{LSR})]$, *i.e.* the optical depth at the center of the ^{12}CO line, corresponding to the maximum line opacity measured in a pixel. *White contours:* IRAM 30m ^{12}CO J=2–1 peak map shown in Fig. 6.10 (contour levels: 0.25, 0.35, 0.45 and 0.75 times the maximum value across the map).

Results We obtained PPV measurements of τ_{10}^{12}, τ_{21}^{12} and τ_{32}^{12} (^{12}CO line opacities) as well as τ_{10}^{13} (^{13}CO line opacity). The map of the peak J=1–0 ^{13}CO line opacity is shown in Fig. 8.20. The ^{13}CO line opacity is lower than 0.3 towards the quiescent cloudlet and shocked clump, and it reaches 0.5 within the SW corner of the field of observations, where a blob of bright C^{18}O emission is detected (see Fig. 6.12, left panel). This region is associated with the western molecular complex described by Lee *et al.* (2012) (see section 6.2.1), hence it is not physically associated with the SNR. Following Eq. 8.30, a line opacity $\tau_{ul} = 0.3$ corresponds to $1-\beta_{ul} \simeq 0.1$, hence the brightness temperature reduction caused by the optical depth of the ^{13}CO lines is within our errorbars (±12%, see section 8.2.1). Thereafter, we consider our assumption to be verified.

The maps of the peak J=1–0, J=2–1 and J=3–2 ^{12}CO line opacities are shown on Fig. 8.21. The J=1–0 ^{12}CO line optical depth (τ_{10}, left panel) is mostly tracing the ambient cloud of Cornett *et al.* (1977), and the contribution of the ambient gas is also visible in J=2–1 (compare with Fig. 6.12). The optical depths of the J=1–0, J=2–1 and J=3–2 lines are high towards the quiescent cloud and shocked clump (up to $\tau_{10} \sim 35$, $\tau_{21} \sim 45$, $\tau_{32} \sim 50$): ^{12}CO lines are heavily saturated in the extended G region.

In Fig. 8.22, we present a statistical summary of the spectral variations of the ^{12}CO line opacity $\tau_{ul}(v_{LSR})$. The top panel shows that towards the shocked clump, the higher measurements of the optical depth ($\tau \gg 10$) are confined in the very center of the lines (around $v_{LSR} \sim -4.5$ km s^{-1}), where the ^{12}CO line is self-absorbed. The opacity deduced from the comparison with the ^{13}CO line should allow to recover a fraction of the signal lost in the self-absorption feature. The optical depth in the high-velocity wings is non-negligible, but it is much lower than in the center of the lines. The bottom panel shows that across the $10' \times 10'$ field of observations, the opacity of the

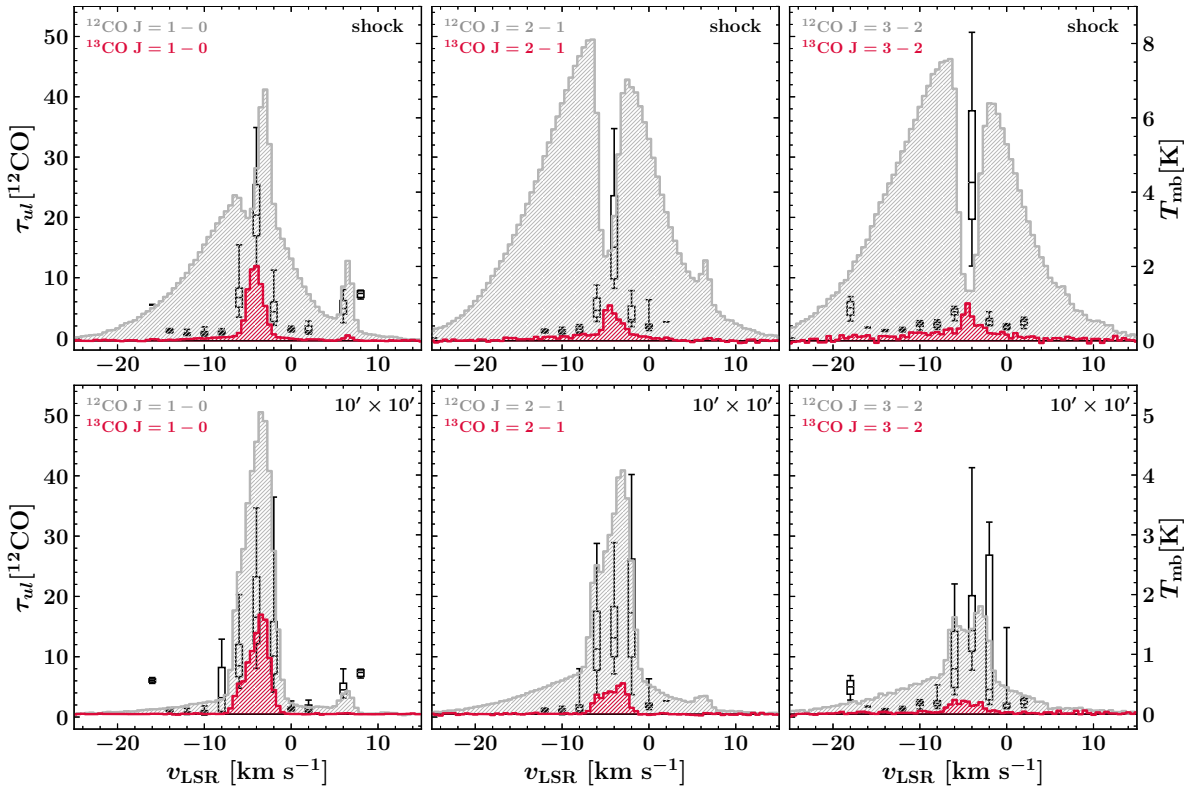

Figure 8.22 Box plot of the PPV line optical depth measurements. Top panels correspond to a sub-sample of data points extracted towards the shocked clump (box 'C', Fig. 6.19, Fig. 8.23). Bottom panels correspond to the entire sample of data points ($10' \times 10'$ field of observations) including the emission of the shocked clumps, quiescent cloudlet, and ambient cloud (background emission). On each panel, the ^{12}CO (in gray) and ^{13}CO (in red) average spectra (over the selected regions) are shown in the background (left panel: J=1–0, mid panel: J=2–1, right panel: J=3–2, all resampled to Δv = 1 km s^{-1}). In each velocity channel Δv, statistical indicators of the sample of τ_{ul} measurements for ^{12}CO lines are shown. The boundaries of the boxes represent the first and third quartiles (Q_1 = 0.25: 25$^{\mathrm{th}}$ percentile, Q_3 = 0.75: 75$^{\mathrm{th}}$ percentile). The horizontal bars inside the boxes correspond to the median. The bottom and top caps represent the 5$^{\mathrm{th}}$ (p = 0.05) and 95$^{\mathrm{th}}$ (p = 0.95) percentiles.

^{12}CO line is far from negligible ($\tau \geq 10$) between $v_{\mathrm{LSR}} = -6$ km s^{-1} and $v_{\mathrm{LSR}} = -2$ km s^{-1}, *i.e.* at the systemic velocities of the quiescent cloudlet and ambient cloud of Cornett *et al.* (1977).

8.2.4 ^{12}CO opacity-corrected population diagrams

Using the ^{12}CO J=1–0, J=2–1 and J=3–2 lines, we aim to determine the physical conditions (column density $N_{^{12}\mathrm{CO}}$, kinetic temperature T_{kin}, local density, total molecular mass) of the cold molecular gas in the extended G region. Using the optical depth PPV measurements determined in the previous section, we performed pixel-per-pixel, channel-per-channel population diagrams in which the opacity of the lines are corrected (Goldsmith and Langer, 1999). The correction of the optical depth allows to recover the total mass of the cold gas traced by the combination of saturated ^{12}CO lines and optically thin ^{13}CO lines.

Summary of the contents of this section. The 'population diagram' was already introduced to study H_2 lines (see section 8.1.2). The only difference for the treatment of ^{12}CO lines is the

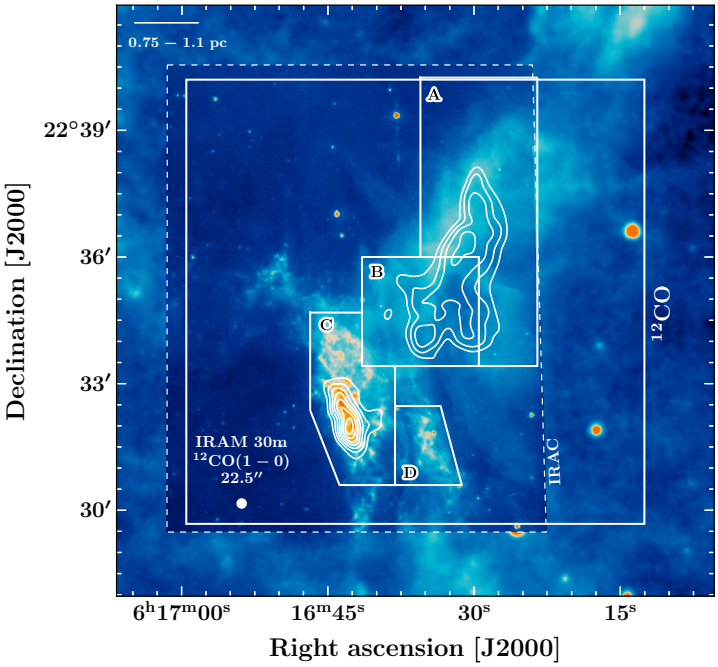

Figure 8.23 *Background: Spitzer*-MIPS (24.0 μm) and *Spitzer*-IRAC (8.0 μm) maps. *White contours:* peak brightness temperature map of the ^{12}CO J=2–1 line observed with the IRAM 30m (see also Fig. 6.10). The white boxes represent the area where the spectra corresponding to each structure (A, B, C, D) are extracted. The beam diameter of the IRAM 30m observations of ^{12}CO J=1–0 is shown in the bottom-left corner. The 10′×10′ field of observations is indicated by a solid white box (indicated by the label '^{12}CO'), and the IRAC field of observation is indicated by a dashed white box (indicated by the label 'IRAC').

correction of optical depth, and the fact that we apply the method to a sample of PPV cubes instead of a sample of 2D maps.

Following the method presented in chapter 4, we measured the upper level column density N_u (hereafter level population) of $J_u = 3$, $J_u = 2$, $J_u = 1$ and built a population diagram for each data point (*i.e.* for each {pixel, channel}) available in our PPV cubes. We systematically used the ^{13}CO line to correct N_u for the effect of optical depth, applying the correction factor $C_{\tau_{ul}}$ (see Eq. 4.32) corresponding to τ_{10}, τ_{21}, τ_{32} (see Fig. 8.21) in each element of spatial resolution (*i.e.* for each of line of sight) and in all velocity channels where a measurement of the optical depth is available.

Hereafter, we study both the pixel-per-pixel, channel-per-channel measurements and the average measurements corresponding to each sub-region of the field of observations (see Fig. 8.23). In section 8.2.4.1, we describe the assumptions adopted to perform the measurement of $N_{^{12}CO}$ from the analysis of population diagrams. In section 8.2.4.2, we provide a detailed description of the method and present the results (population diagrams, column density maps, temperature maps, *etc*).

8.2.4.1 Assumptions

***i.)* ^{12}CO Line opacity** We assume that the emission of the ^{12}CO pure rotational lines J=1–0, J=2–1 and J=3–2 can be corrected using the corresponding ^{13}CO lines. In section 8.2.2, we have shown that the ^{12}CO, ^{13}CO and C^{18}O lines can be assumed to share the same excitation conditions (at least, this assumption cannot be ruled out by the LTE models shown in Fig. 8.15 and Fig. 8.16). In section 8.2.3, we have shown that the ^{13}CO line is optically thin (within errorbars). Assuming that the relative abundance of ^{12}CO and ^{13}CO are uniform across the extended G region, we produced PPV measurements of τ_{10}, τ_{21} and τ_{32} at a spectral resolution of 2 km s^{-1} (see Fig. 8.21). We adopted [^{12}CO/^{13}CO]=60^{+30}_{-15} (see section 8.2.2).

***ii.)* Thermalization** We assume that the molecular gas is at local thermodynamic equilibrium (LTE) across the $10' \times 10'$ field of observations. This condition is verified if the local medium is sufficiently dense for a collisional equilibrium to settle, *i.e.* if the following condition on the local density n is satisfied for all transitions (J=1–0, J=2–1, J=3–2):

$$n \geq n_{\rm crit} \tag{8.34}$$

$$n_{\rm crit} = \frac{A_{\rm ul}}{C_{\rm ul}} \tag{8.35}$$

where $A_{\rm ul}$ and $C_{\rm ul}$ are respectively the Einstein coefficient of spontaneous emission and collisional de-excitation rate (see chapter 4 for a derivation). Yang *et al.* (2010) presented the results of calculations of the collisional rate coefficients of ^{12}CO, ^{13}CO and C^{18}O ($J_{\rm u} = 1 - 40$) at the kinetic temperatures $T = 2 - 3000$ K (see Tab. 4.4 for the values at $T = 10$ K, $T = 30$ K, $T = 150$ K). In order to verify our assumption, we combine these calculations of $C_{\rm ul}$ with the $A_{\rm ul}$ coefficients in Tab. 8.4 to estimate the critical density $n_{\rm crit}$ of the ^{12}CO pure rotational lines. The J=1–0 line is the most likely to be thermalized, hence it should give a lower bound of the critical density required for our assumption to be verified. At $T = 10$ K, we have $C_{10} = 3.3 \times 10^{-11}$ cm^3 s^{-1} (Yang *et al.*, 2010) hence $n_{\rm crit} \sim 2.2 \times 10^3$ cm^{-3}. At the same temperature, we have $C_{21} = 3.0 \times 10^{-11}$ cm^3 s^{-1}, hence the critical density of the J=2–1 line is $n_{\rm crit} \sim 9.7 \times 10^3$ cm^{-3}.

The J=3–2 line gives an upper bound of the critical density (it is the 'most difficult ' to thermalize *via* collisional excitation). The critical density of the J=3–2 line is $n_{\rm crit} \sim 3.1 \times 10^4$ cm^{-3} ($C_{32}(10\ {\rm K}) = 7.2 \times 10^{-13}$ cm^3 s^{-1}). Cesarsky *et al.* (1999) estimated a pre-shock density $\sim 10^4$ cm^{-3} in clump G. In section 8.1 (analysis of H_2 lines), we concluded that $n_{\rm H_2} = 0.7 - 3.5 \times 10^5$ cm^{-3}. Thus, the ^{12}CO J=1–0, J=2–1 and J=3–2 lines are very likely to be correctly thermalized, although a small deviation to LTE might be possible for the ^{12}CO J=3–2 line in more diffuse areas of the ambient cloud. However, in the considerations above we compared the estimate of the density with the two-level critical density of ^{12}CO lines. If we take into account more interactions (*i.e.* a sum of collisional coefficients $C_{\rm ij}$ instead of a single $C_{\rm ul}$ in Eq. 8.35, *e.g.* Godard and Cernicharo 2013) the critical densities would be lowered, hence our assumption on the thermalization would be further strengthened.

***iii.)* Filling factor** We use a unit filling factor ($ff = 1$). The brightness distribution suggested by the channel maps is extended (see *e.g.* Fig. 6.4, Fig. 6.6), but potential clumpy structures of angular size $< 11.2''$ are not resolved by our maps. In section 8.1.2.1, we mentioned that *Spitzer*-IRAC observations at 8 µm suggest the existence of clumpy structures towards the shocked clump (see Fig. 8.2, and also Fig. 8.13). This is not an issue as long as the value in each pixel of our output map is interpreted as an average measurement of the column density towards a given line of sight. Higher resolution observations would likely reveal localized enhancement of the ^{12}CO column density towards unresolved clumpy structures, but the average column density measurement is still correct.

***iv.)* Single excitation temperature** We assume that the ^{12}CO lines can be modelled by a single excitation temperature, *i.e.* we assume that there is a single component of homogeneous molecular gas with a uniform temperature along the line of sight. This assumption can be argued to be unrealistic. Actually, in a line of sight that crosses the extended G field we expect to measure the

sum of the contribution from the gas perturbed by the SNR *and* the ambient gas corresponding to the molecular cloud of Cornett *et al.* (1977), hence there might be more than a single excitation temperature characterizing the confused upper level population measurements.

However, a 'warm' excitation temperature component (*e.g.* $T_{\rm ex} \gg 50$ K) would have a marginal contribution to the level populations $J_{\rm u} = 1$ ($E_1 = 5.5$ K), $J_{\rm u} = 2$ ($E_2 = 16.6$ K) and $J_{\rm u} = 3$ ($E_3 = 33.2$ K). In addition, with only three data points (^{12}CO J=1–0, J=2–1, J=3–2), it is not possible to refine the analysis with two distinct components (*i.e.* four parameters, $N^1_{^{12}\rm CO}$, $T^1_{\rm ex}$, $N^2_{^{12}\rm CO}$, $T^2_{\rm ex}$).

8.2.4.2 Pixel-per-pixel, channel-per-channel opacity-corrected population diagrams of ^{12}CO J=1–0, J=2–1, J=3–2

Method In this section, we describe the treatments applied to each {pixel, channel} data point of our IRAM 30m and APEX PPV cubes. For consistency, we convolved all our PPV cubes to the same spatial resolution, using the nominal resolution of ^{13}CO J=2–1, such that we have a beam diameter of 30.1″. The spectral resolution was also modified and set to 2 km s^{-1} for each transition in order to increase the signal-to-noise ratio. Then, we performed the following measurements in each spatial bin using a `Python` program:

1. In each pixel (x, y), we sigma-clipped the ^{12}CO J=1–0, J=2–1, J=3–2 spectra, using a threshold of 3σ. The data bins with a signal lower than 3σ are set to 'NaN' in order to work with robust detections only.

2. In every single velocity channel Δv remaining after sigma-clipping, we measured the ^{12}CO $N_{J=3}$, $N_{J=2}$ and $N_{J=1}$ level populations using Eq. 4.31 (applied to a single velocity bin Δv).

3. We read the optical depth measurements τ_{3-2}, τ_{2-1} and τ_{1-0} corresponding to each pixel (x, y) and velocity bin Δv in the previously built PPV opacity cubes (see section 8.2.3, Fig. 8.21). *Reminder:* this stage of the measurement is based on the assumption that ^{13}CO lines are optically thin and that the excitation temperatures of the two isotopologs (^{12}CO and ^{13}CO) are approximately equal (see section 8.2.4.1).

4. We correct the measurement of the ^{12}CO level populations ($N_{J=3}$, $N_{J=2}$ and $N_{J=1}$) for optical depth using the correction factor $C_{\tau_{\rm ul}} = \tau_{\rm ul}/(1 - e^{-\tau_{\rm ul}})$ (see Eq. 4.32), such that the corrected column density is given by $N^*_{\rm u} = C_{\tau_{\rm ul}} N_{\rm u}$ (Goldsmith and Langer, 1999).

5. We put the corrected level populations $N^*_{\rm u}$ and their corresponding energies $E_{\rm u} = h\nu_{\rm ul}/k_{\rm B}$ into an opacity-corrected population diagram $\ln(N^*_{\rm u}/g_{\rm u}) = f(E_{\rm u})$. Then, we used a χ^2-minimization algorithm (the `Python` module `scipy.optimize.curve_fit`[5]) to determine the best linear fit of the data points ($\ln(N^*_{\rm u}/g_{\rm u}) = a_{\rm lin} E_{\rm u} + b_{\rm lin}$).

   The excitation temperature $T_{\rm ex}$ is deduced from the slope of the best-fit model ($a_{\rm lin}$), and the total column density $N_{^{12}\rm CO}$ is determined by computing the partition function $Z(T_{\rm ex})$[6] and measuring the offset ($b_{\rm lin}$). For a derivation, see chapter 4.

[5] Based on the Levenberg-Marquardt least square curve fitting algorithm

[6] We computed the partition function taking into account the first 40 upper rotational levels of ^{12}CO taken from the Cologne Database for Molecular Spectroscopy and Jet Propulsion Laboratory database, *i.e.* the Yang *et al.* (2010) calculations. The thermal energy of the 40$^{\rm th}$ level is $E_{40} = 4513$K.

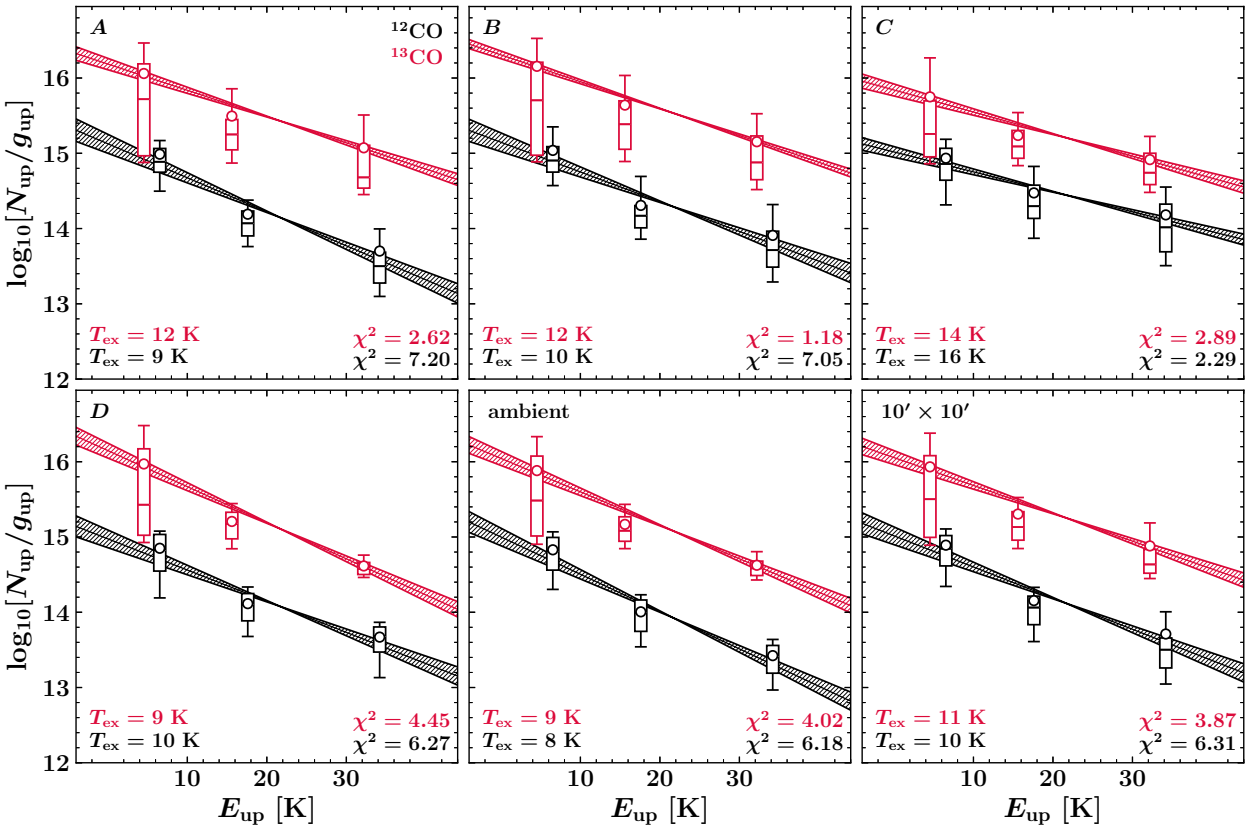

Figure 8.24 Population diagrams (uncorrected for line opacity) of ^{12}CO and ^{13}CO in the extended G region. Each panel corresponds to a different sample of {pixel, velocity channel} data points ('A', 'B', 'C', 'D' corresponding to the spatial boxes shown in Fig. 8.23 and 'ambient' corresponding to $\overline{\mathrm{A}} \cap \overline{\mathrm{B}} \cap \overline{\mathrm{C}} \cap \overline{\mathrm{D}}$). On each panel, two distinct results are shown: in red, the upper level populations of ^{13}CO (multiplied by 60, the adopted ^{12}CO/^{13}CO isotopic ratio). In black, the upper level populations of ^{12}CO. The red and black data points are artificially shifted by ±1 K along the energy axis in order to be able to distinguish them. The errors associated with the best linear models are represented by a filled area around the curves. For each upper level (E_u), statistical indicators of the sample of N_u measurements are shown to represent the dispersion of the sample of {pixel, velocity channel} data points around the average for each spatial box shown in Fig. 8.23 (restricted to 3σ detections). The boundaries of the boxes represent the first and third quartiles (Q_1 = 0.25: 25$^{\mathrm{th}}$ percentile, Q_3 = 0.75: 75$^{\mathrm{th}}$ percentile). The horizontal bars inside the boxes correspond to the median, and the circles represent the average. The bottom and top caps represent the 1$^{\mathrm{st}}$ (p = 0.1) and 9$^{\mathrm{th}}$ (p = 0.9) deciles.

6. Finally, we derived the mass of the molecular gas from the measured total column density $N_{^{12}CO}$, using the expected $[H_2]/[^{12}CO]$ ratio towards dense molecular regions and assuming that the distance of IC443 is 1.8 kpc (Ambrocio-Cruz *et al.* 2017, Yu *et al.* 2019). We adopted 10^4 for the H_2-to-^{12}CO abundance ratio (Gordon and Burton 1976, Frerking *et al.* 1982). The molecular mass in a pixel of the final map is given by $M_{H_2} = (2m_H)\mathcal{A}N_{^{12}CO} \times 10^4$ where $\mathcal{A}$ is the area of a spatial bin (a pixel) and m_H the mass of one hydrogen atom.

Uncertainties The errorbars on the total ^{12}CO column density, molecular mass and kinetic temperature are determined by: *(i.)* instrumental errors (systematic uncertainty on the brightness temperature (±12%, see section 8.2.1); *(ii.)* the quality of the linear fit applied to the population diagram; *(iii.)* systematic errors on the adopted distance of IC443 (1.8±0.2 kpc); *(iv.)* systematic uncertainties on the adopted $[^{12}CO/^{13}CO]$ isotopic ratio (60^{+30}_{-15}, propagated into the uncertainty on the ^{12}CO line opacities), *(v.)* the uncertainty on the adopted H_2-to-^{12}CO abundance ratio (propagated into the uncertainty on the mass measurement).

8.2.4.3 Results

Assuming LTE, we obtained measurements of $N_{^{12}CO}$ and T_{ex} in each {pixel, velocity channel} data point of our PPV cubes (inferred from a total of 10 222 population diagrams). In order to understand the effect of optical depth correction on our measurements, we performed a test run with $\tau_{ul} \ll 1$ (*i.e.* assuming that the ^{12}CO lines are optically thin).

The population diagrams of ^{12}CO and ^{13}CO ($J_u = 1, 2, 3$) are shown in Fig. 8.24 and Fig. 8.25. The maps of upper level populations are shown in Fig. 8.26, and the χ^2 map is shown in Fig. 8.27. The column density and excitation temperature maps are shown in Fig. 8.28 ($\tau_{ul} \ll 1$) and Fig. 8.29 (τ_{ul} estimated with the ^{13}CO lines). We compare the results obtained in Fig. 8.30.

Preliminary test: ^{13}CO *vs.* ^{12}CO population diagrams We produced standard population diagrams (not corrected for optical depth) for ^{12}CO and ^{13}CO (see Fig. 8.24). For consistency, we compare the measurements only in the {pixel, velocity channel} data points where there is a 3σ detection for ^{13}CO lines. Additionally, in order to directly compare the results obtained with ^{12}CO and ^{13}CO lines, we multiplied the upper level populations of ^{13}CO by 60 (the adopted $^{12}CO/^{13}CO$ isotopic ratio). These preliminary diagrams confirm that it is required to correct the opacity of ^{12}CO lines in order to recover the true column density: there is an average ten-fold enhancement of the inferred column densities using ^{13}CO lines.

Opacity-corrected ^{12}CO population diagrams The ^{12}CO opacity-corrected population diagrams shown in Fig. 8.25 allow to visualize the effect of optical depth correction for each upper level population. Since the J=1–0 line opacity is greater than the J=3–2 line opacity across the majority of the lines of sight (see Fig. 8.21), the $N_{J=1}$ population benefits more from the optical depth correction than the $N_{J=3}$ population (this also true, to a lesser extent, for $N_{J=2}$ with respect to $N_{J=1}$). As a consequence, the slope of the opacity-corrected diagram is greater than the slope of the $\tau_{ul} \ll 1$ diagram, hence the excitation temperature decreases, and the total column density increases.

We produced maps of the level populations $N_{J=1}$, $N_{J=2}$ and $N_{J=3}$ in order to precisely visualize the relative spatial distributions of the first three excited pure rotational states of ^{12}CO across the

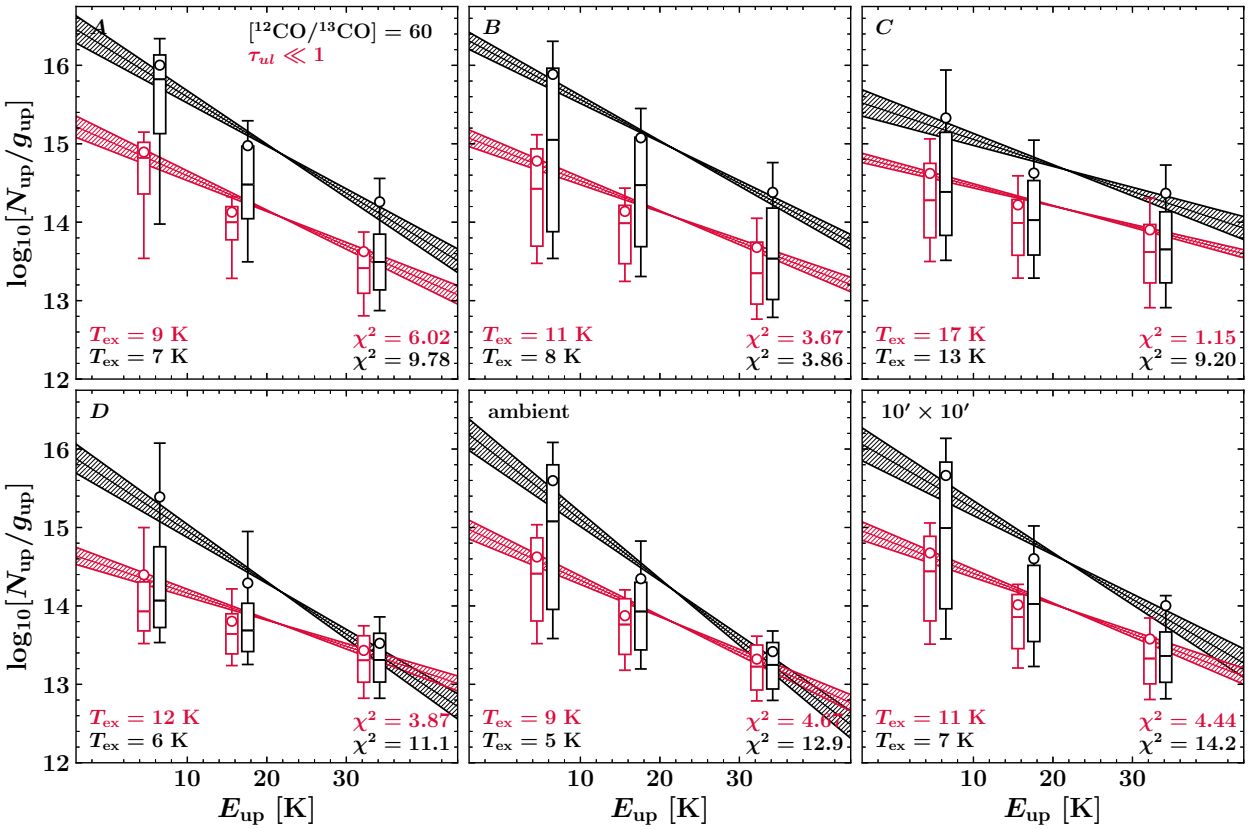

Figure 8.25 Same figure as in Fig. 8.24, but these are the population diagrams of ^{12}CO lines only. On each panel, two distinct results are shown: in red, the upper level populations obtained assuming that $\tau_{\rm ul} \ll 1$ (optically thin ^{12}CO lines). In black, the upper level populations obtained using the opacity measurements shown in Fig. 8.21.

extended G region (see Fig. 8.26). The distinction between the J=1 level (E_1 = 5.5 K) and the J=2 and J=3 levels (E_2 = 16.6 K, E_3 = 33.2 K) is fairly noticeable: the opacity-corrected J=1–0 transition is mostly sensitive to the cold ambient gas associated with the cloud of Cornett *et al.* (1977), whereas the J=2–1 and J=3–2 transitions trace the warmer shocked clump and the quiescent cloudlet. This distinction is a hint that modelling the ^{12}CO lines with a single excitation temperature across the map might be a poor assumption, in particular towards the lines of sight where there is spatial confusion with the ambient gas. In order to evaluate the quality of our linear models of the population diagrams, we performed a χ^2 test, defined by the following quantity:

$$\chi^2 = \frac{1}{N-p} \sum_{J_{\rm u}=1}^{3} \frac{(N_{\rm u} - f(E_{\rm u}))^2}{\sigma(N_{\rm u})^2} \tag{8.36}$$

where $N_{\rm u}$ refers to the *average* of the samples of measurements (both spatially and spectrally averaged), f is the adopted linear model, and $\sigma(N_{\rm u})$ is the uncertainty on $N_{\rm u}$ (set to 12%, *i.e.* the uncertainty on the brightness temperature) and N = 3 is the number of data points. p = 2 is the number of free parameters (the excitation temperature and total column density). We obtain χ^2 = 3.45 – 18.1 without the correction of the optical depth, and χ^2 = 11.6 – 42.6 with the correction. By applying a line opacity correction factor $C_{\tau_{\rm ul}}$, we have introduced an additional uncertainty in the measurement (since [^{12}CO / ^{13}CO]=60^{+30}_{-15}). If we modify the value of $\sigma(N_{\rm u})$ to

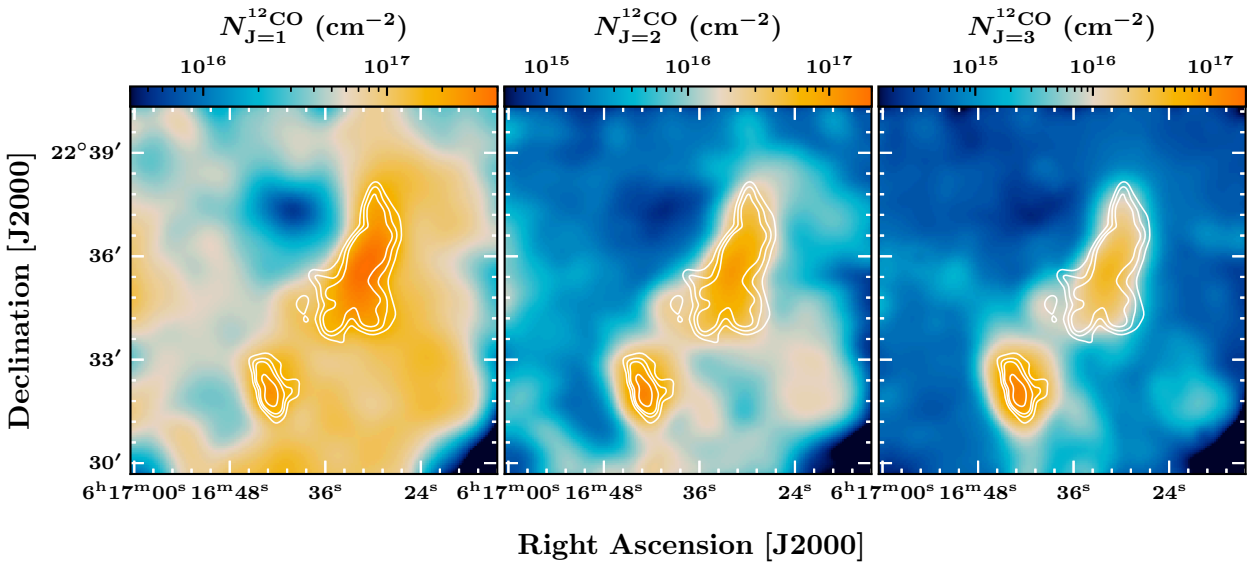

Figure 8.26 J=1, 2, 3 level populations maps of ^{12}CO determined *via* opacity-corrected population diagrams. *White contours:* IRAM 30m ^{12}CO J=2–1 peak map shown in Fig. 6.10 (contour levels: 0.25, 0.35, 0.45 and 0.75 times the maximum value across the map).

take this isotopic uncertainty into account, we obtain $\chi^2 = 1.29 - 4.89$ for the black data points in Fig. 8.25. These values of χ^2 are average indicators, because they correspond to a linear fit applied to the average measurements of $N_{J=1}$, $N_{J=2}$ and $N_{J=3}$ (in which a sample of lines of sight and velocity channels are confused).

Spatial distribution of deviations to LTE Pixel-per-pixel measurements of χ^2 are shown in Fig. 8.27. The left panel of Fig. 8.27 shows the χ^2 map associated with the $\tau_{ul} \ll 1$ test, and the right panel corresponds to the opacity-corrected measurements. The white contour shows the areas where $\chi^2 \leq 3$. This figure shows that the correction of the line optical depths allows to consistently fit the J=1–0, J=2–1 and J=3–2 transitions with our assumptions (for the most part of the field of observations, including the shocked clump, quiescent cloudlet and ring-like structure). In contrast, the left panel displays mostly large deviations ($\chi^2 \geq 3$) to the LTE models, except towards the main and secondary shocked clumps. This is expected, since the correction of the optical depth displaces the upper level column densities in the population diagram, and the correction is not identical for all transitions hence the relative distribution of the levels can be modified (see Fig. 8.21). The variation in χ^2 shows that the opacity-corrected population diagrams tend to reconcile the upper level populations with the LTE distribution.

Interestingly, the lowest deviations with respect to LTE ($\chi^2 \leq 0.1$) are found towards the C^{18}O bright region in the SW corner of the $10' \times 10'$ field of observations (see Fig. 6.12). This is consistent with the assumption that this area of the map corresponds to a dense region of the molecular cloud of Cornett *et al.* (1977). In conclusion, the opacity-corrected ^{12}CO lines are predominantly consistent with the assumption that the molecular gas is thermalized, except in the eastern and northeastern areas of the $10' \times 10'$ field of observations where significant deviations are found. These deviations could be due to systematic errors in the correction of the optical depth, or they could be real if the density of the gas is too low in the ambient cloud ($n \ll 10^4$ cm^{-3}).

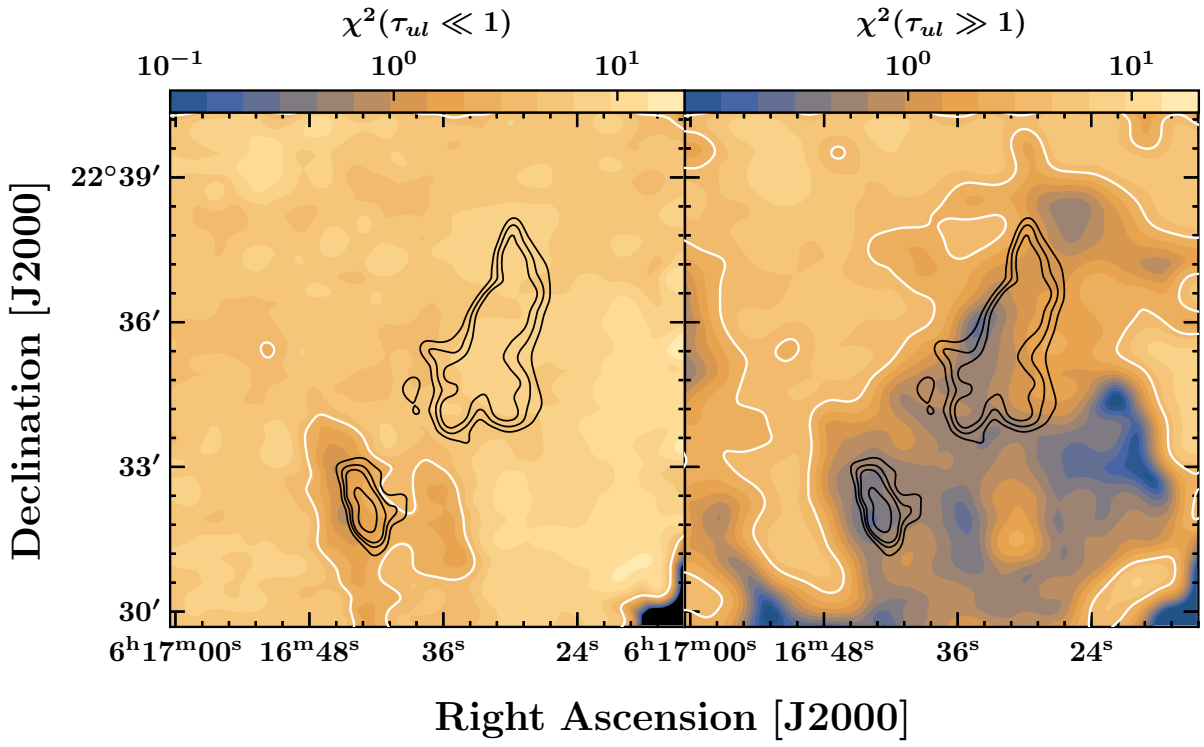

Figure 8.27 Average χ^2 maps (see Eq. 8.36). *Left:* χ^2 map associated with the ^{12}CO $J_u = 1, 2, 3$ population diagrams built assuming that $\tau_{ul} \ll 1$ (no correction of the optical depth). *Right:* χ^2 map associated with the ^{12}CO $J_u = 1, 2, 3$ opacity-corrected population diagrams. The white contour traces the area delimited by $\chi^2 = 3$. The black contours correspond to the IRAM 30m ^{12}CO J=2–1 peak map shown in Fig. 6.10 (contour levels: 0.25, 0.35, 0.45 and 0.75 times the maximum value across the map).

Column density maps The resulting column density maps are shown in Fig. 8.28 left panel (for $\tau_{ul} \ll 1$) and Fig. 8.29 left panel (opacity-corrected population diagrams). Without the optical depth corrections, the column density peaks at $\sim 3 \times 10^{17}$ cm^{-2} towards the shocked clump, and $\sim 6 \times 10^{16}$ cm^{-2} towards the quiescent cloudlet. The column density of the ambient molecular gas is of the order $\sim 10^{16}$ cm^{-2}.

The column density measurements inferred from the opacity-corrected population diagrams (Fig. 8.29, left panel) are greatly enhanced (more than a ten-fold enhancement towards the quiescent cloudlet). The peak column density increases up to $\sim 1.2 \times 10^{18}$ cm^{-2} towards the shocked clump, and $\sim 1 \times 10^{18}$ cm^{-2} within the quiescent cloudlet. The mass measured in the ambient cloud of Cornett *et al.* (1977) also benefits greatly from the optical depth corrections, in particular in the SW corner of the field of observations where the column density reaches $\sim 3 \times 10^{17}$ cm^{-2}.

Clarification remark. An inquisitive reader might be surprised when comparing the column density maps with the results shown in the population diagrams (Fig. 8.25). Indeed, the column densities inferred from the population diagrams reach $\sim 1.2 \times 10^{18}$ cm^{-2} towards the shocked clump, but the black curve intersects the origin at $y \simeq 15.5$ in the first row, third column diagram (box 'C', corresponding to the shocked clump). Since the partition function of ^{12}CO at $T_{ex} = 13$ K is $Z(13\ \mathrm{K}) \simeq 4$, we would have $N_{^{12}\mathrm{CO}} = 4 \times 10^{15.5} \simeq 1.3 \times 10^{16}$ cm^{-2}, which is far lower than the value read from the column density map in Fig. 8.29 (left panel).

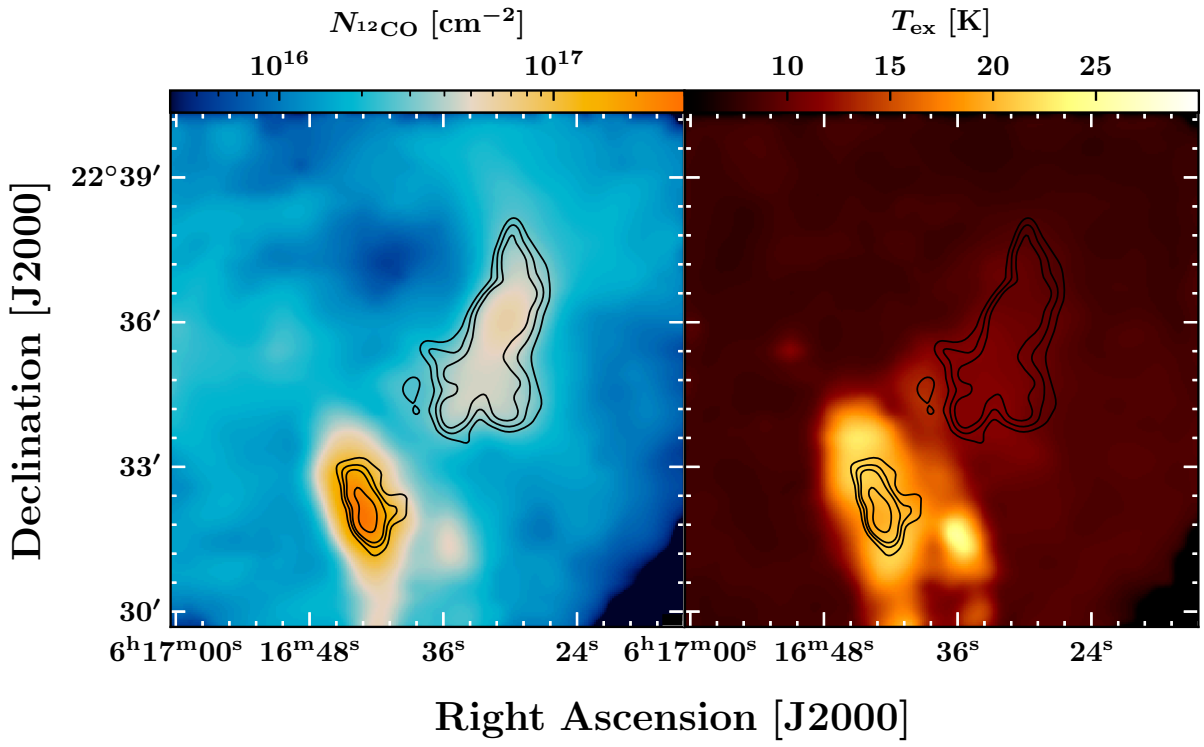

Figure 8.28 Results of the $\tau_{ul} \ll 1$ population diagram analysis of ^{12}CO pure rotational lines. *Left:* ^{12}CO column density map. The maximum value towards the shocked clump is $N_{^{12}CO} \sim 3 \times 10^{17}$ cm^{-2}. *Right:* excitation temperature map. The black contours correspond to the IRAM 30m ^{12}CO J=2–1 peak map shown in Fig. 6.10 (contour levels: 0.25, 0.35, 0.45 and 0.75 times the maximum value across the map).

Similarly, the maximum excitation temperatures that can be read at the center of the shocked clump in Fig. 8.29 and Fig. 8.28 are greater than the excitation temperatures indicated in the population diagrams (Fig. 8.25). This apparent discrepancy is due to two dilution factors: *i.)* the upper level populations shown in Fig. 8.25 correspond to *average* measurements over the spatial boxes shown in Fig. 8.23; *ii.)* the column density map displays the *total* ^{12}CO column density (summed over all the velocity channels), in contrast to the population diagrams in which we present the samples of {pixel, velocity channel} data points.

Temperature maps The resulting excitation temperature maps are shown in Fig. 8.28 right panel (for $\tau_{ul} \ll 1$) and Fig. 8.29 right panel (opacity-corrected population diagrams). The quantity shown is the average T_{ex} (along N velocity channels) weighted by the column density:

$$\overline{T_{ex}(x,y)} = \frac{1}{N_{^{12}CO}(x,y)} \sum T_{ex}(x,y,\Delta v) N_{^{12}CO}(x,y,\Delta v) \tag{8.37}$$

The excitation temperature inferred from the $\tau_{ul} \ll 1$ population diagrams varies between $T_{ex} = 8$ K and $T_{ex} = 27.5$ K across the extended G region. Lower temperatures are confined in the regions of the field of observations corresponding to the ambient cloud, in contrast to the shocked clump where the excitation temperature increases, reflecting the heating of the gas by the passage of the shock wave. The spatial distribution of the higher excitation temperatures is correlated with

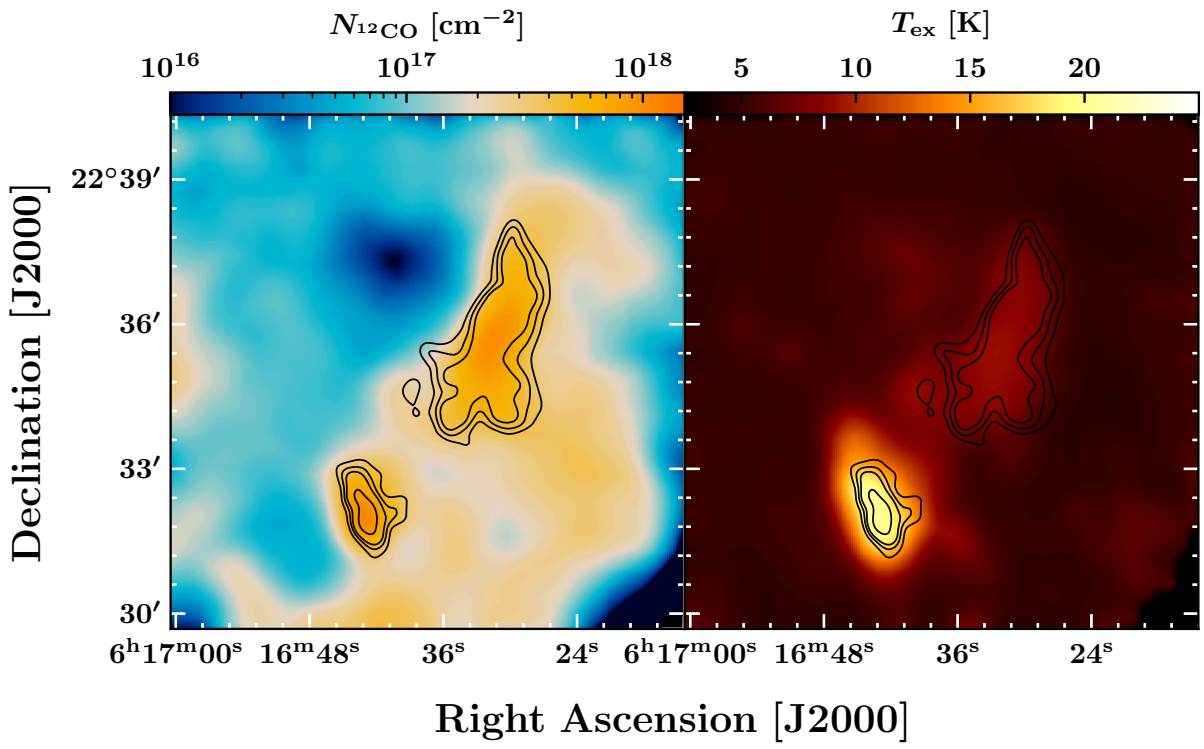

Figure 8.29 Results of the opacity-corrected population diagram analysis of ^{12}CO pure rotational lines. *Left:* ^{12}CO column density map. The maximum value towards the shocked clump is $N_{^{12}CO} \sim 1.2 \times 10^{18}$ cm^{-2}. *Right:* excitation temperature map. The black contours correspond to the IRAM 30m ^{12}CO J=2–1 peak map shown in Fig. 6.10 (contour levels: 0.25, 0.35, 0.45 and 0.75 times the maximum value across the map). *Caution:* the boundaries of the color scale used in this figure are different from the boundaries adopted in Fig. 8.28.

the larger ^{12}CO line widths (see second moments maps: Fig. 6.15, Fig. 6.16), tracing the warm shocked molecular gas.

The excitation temperature measured within the quiescent cloudlet is $\sim 9-10$ K. The excitation temperatures measured with the opacity-corrected population diagrams (Fig. 8.29, right panel) are systematically lower. The excitation temperature probed across the ambient molecular gas decreases down to $T_{ex} \sim 5$ K, and $T_{ex} \sim 8-9$ K within the quiescent cloudlet. We discuss these findings in the next paragraph.

Quantitative results (mass measurements) In Tab. 8.5, we provide a quantitative summary of the measurements performed in the extended G region using opacity-corrected population diagrams for ^{12}CO lines. We indicate the total molecular mass inferred from the adopted H_2-to-^{12}CO abundance ratio (10^4, following Gordon and Burton 1976, Frerking *et al.* 1982). In order to compare our mass measurements with a reference, we produced rough estimates of the mass using the ^{12}CO J=1–0 conversion factor X_{CO} (Dame *et al.* 2001, Bolatto *et al.* 2013). This '^{12}CO J=1–0 to M_{H_2}' conversion factor is a highly idealized, simplified relation in which all variations of environment, geometry and excitation are ignored, hence it represent the most approximate mass measurement available with our ^{12}CO observations. In the Milky Way, X_{CO} has been empirically calibrated in different ways: *i.)* employing virial masses of molecular clouds, *ii.) via* optically

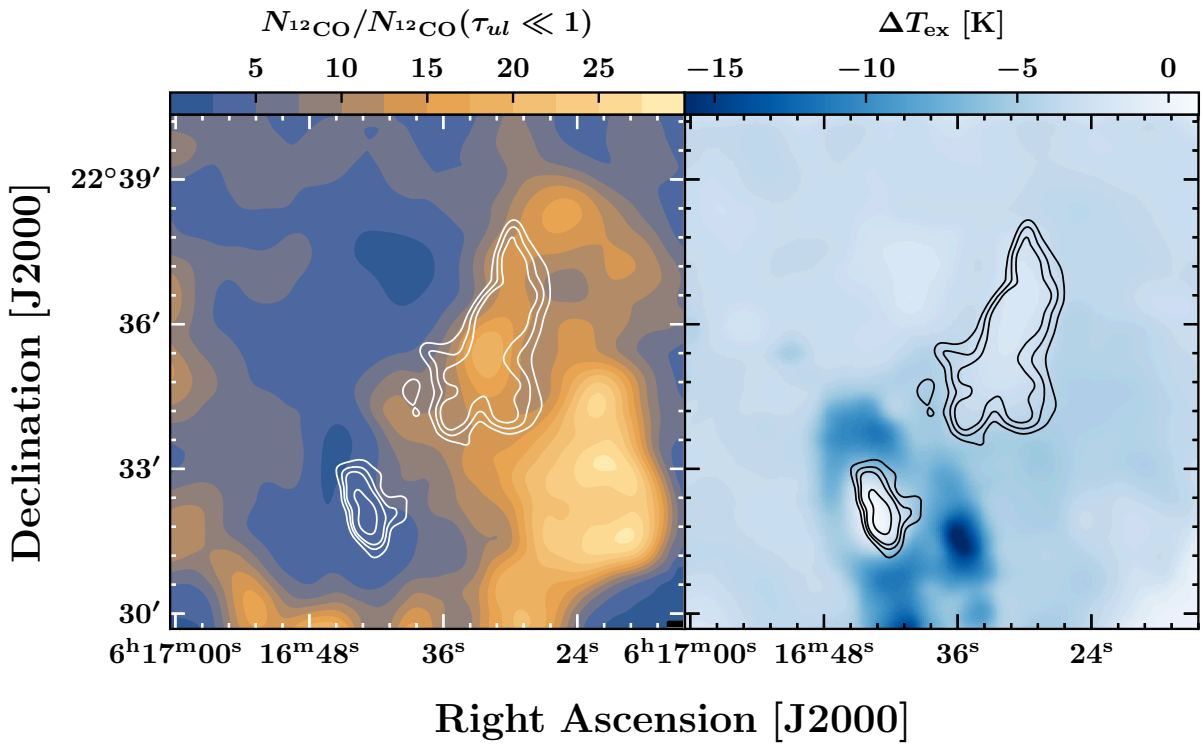

Figure 8.30 Direct comparison between the ^{12}CO column density and excitation temperature maps shown in Fig. 8.28 and Fig. 8.29. *Left:* comparison of the column density measurements (Fig. 8.29 left panel divided by Fig. 8.28 left panel). *Right:* comparison of the excitation temperature measurements (Fig. 8.29 right panel minus Fig. 8.28 right panel). The black contours correspond to the IRAM 30m ^{12}CO J=2–1 peak map shown in Fig. 6.10 (contour levels: 0.25, 0.35, 0.45 and 0.75 times the maximum value across the map).

thin column density tracers (dust, molecular lines), *iii.) via* the diffuse γ-ray emission produced by the interaction of CRs with interstellar protons (Bolatto *et al.*, 2013). We adopted the following conversion factor, with a ±30% uncertainty:

$$X_{\rm CO} = 2 \times 10^{20}\ {\rm cm}^{-2}({\rm K\ km\ s}^{-1})^{-1} \tag{8.38}$$

Using this equation, the H_2 column density is directly determined by the product of $X_{\rm CO}$ with the velocity-integrated brightness temperature of the raw ^{12}CO J=1–0 line (without optical depth correction), and we infer the molecular mass from N_{H_2} *via* $M_{H_2} = (2m_{\rm H})\mathcal{A}N_{H_2}$ where $\mathcal{A}$ is the area of a pixel (as already described previously). We report the results of these measurements in the last column of Tab. 8.5, where they are referred to as $M_{X_{\rm CO}}^{J=1-0}$ ($M_\odot$). Within errorbars, our measurements are consistent with this rough estimate of the mass. However, with respect to the population diagram method, the '$X_{\rm CO}$ measurement method' tends to overestimate the molecular mass.

Discussion In Fig. 8.30, we compare the results obtained with the $\tau_{\rm ul} \ll 1$ population diagrams with the opacity-corrected measurements. Fig. 8.30 left panel shows that the column density is systematically increased by an non-negligible factor ($\times 2-30$). The areas of the extended G region that benefit the most from the optical depth correction are the quiescent cloudlet and ambient

region	$\overline{N_{\rm CO}}[10^{17}{\rm cm}^{-2}]$	Mass ($M_\odot$)	$\overline{T_{\rm ex}}$[K]	$\overline{\chi^2}$	$M_{X_{\rm CO}}^{J=1-0}$ ($M_\odot$)
cloudlet (A)	$2.6^{+1.2}_{-0.7}$	160^{+140}_{-60}	9^{+2}_{-3}	0.24	450±140
ring-like structure (B)	$3.8^{+2.0}_{-0.9}$	130^{+110}_{-40}	12^{+2}_{-4}	0.05	200±60
shocked clump (C)	$3.2^{+1.6}_{-0.8}$	90^{+80}_{-30}	19^{+4}_{-6}	0.04	190±60
shocked knot (D)	$2.5^{+1.3}_{-0.6}$	25^{+20}_{-10}	17^{+3}_{-10}	0.01	30±10
ambient cloud	$1.2^{+0.6}_{-0.3}$	470^{+400}_{-200}	9^{+2}_{-4}	2.04	1300±400
IC443G (extended)	$1.7^{+0.8}_{-0.4}$	850^{+700}_{-300}	10^{+2}_{-4}	2.38	2600±800

Notes. Average measurements corresponding to the spatial boxes defined in Fig. 8.23. The 'ambient cloud' corresponds to $\overline{\rm A} \cap \overline{\rm B} \cap \overline{\rm C} \cap \overline{\rm D}$, and the last row corresponds to the measurements performed on the entire PPV cubes. $\overline{N_{\rm CO}}$ is the average column density measurement. The mass is given by $M_{\rm H_2} = (2m_{\rm H})\mathcal{A}N_{^{12}{\rm CO}} \times 10^4$ where $\mathcal{A}$ is the area of a spatial bin (a pixel) and $m_{\rm H}$ the mass of one hydrogen atom. The mass uncertainties are determined by the uncertainties on the distance to IC443 ($d = 1.8 \pm 0.2$ kpc) and [^{12}CO/^{13}CO] isotopic ratio (60^{+30}_{-15}). The uncertainties on the average excitation temperature $\overline{T_{\rm ex}}$ take into account the linear fit errors and the temperature variations between Fig. 8.28 and Fig. 8.29. $\overline{\chi^2}$ is the average for all the opacity-corrected population diagrams in each boxe. For comparison, we indicate the estimate of the mass obtained by using the CO-to-H_2 conversion factor $X_{\rm CO} = 2 \times 10^{20}$ cm^{-2}(K km s^{-1})$^{-1}$ applied to the raw J=1–0 data (without optical depth correction). The values presented in this table cannot be directly compared to the values read in the maps (Fig. 8.29) because of the dilution caused by averaging the signal in the spatial boxes defined in Fig. 8.23.

Table 8.5 Quantitative summary of the opacity-corrected population diagrams analysis.

molecular cloud of Cornett *et al.* (1977). The column density variations are lower for the shocked clump because a significant fraction of the ^{12}CO emission is confined in the high-velocity wings of the lines, in which the optical depth is low (see Fig. 8.22). In contrast, the quiescent molecular lines are uniformly enhanced by the optical depth correction.

The excitation temperature variations are more puzzling. $T_{\rm ex}$ is systematically lowered across the field of observations, in particular within the periphery of the shocked clump. The interpretation of this significant excitation temperature decrease is given by the combination of Fig. 8.21 and Fig. 8.25. Since *i.)* the J=1–0 line opacity is greater than the J=2–1 and J=3–2 line opacities; then *ii.)* the upper level populations are displaced with respect to each other in the population diagram then *iii.)* it follows that the slope increases, hence the inferred excitation temperature decreases. This effect can explain the excitation temperature variations across the extended G region, but it is more acute towards the shocked clump where a NE-SW arm of quiescent gas is spatially confused with the shocked gas (see section 6.2.1). The spatial confusion between the ^{13}CO J=1–0 bright quiescent gas and the warm shocked clump causes a bias in the correction of the upper level populations: $\tau_{10} \gg \{\tau_{21},\ \tau_{32}\}$, hence $T_{\rm ex}$ is significantly lowered .

The excitation temperature measured in the ambient gas (down to $T_{\rm ex} \sim 5$ K) is far too low as well (with respect to the expected temperature of a cold dark molecular cloud). A critical limitation in our method is that we based our optical depth corrections on the comparison of ^{12}CO lines with ^{13}CO lines, which introduced a bias towards the $J = 1$ level population. In fact, we measured τ_{10} using IRAM 30m observations, and τ_{21}, τ_{32} using APEX observations. The combined effect of *i.)* the lower brightness temperature of the J=2–1 and J=3–2 ^{13}CO lines (with respect to the J=1–0 ^{13}CO line, see Fig. 6.21); *ii.)* the higher r.m.s of the APEX observations (see Tab. 6.1, Tab. 6.2: 25 mK *vs.* 80-84 mK) causes a detection bias when we apply a 3σ-clip to the spectra. Thus, in

low signal-to-noise data bins, sigma-clipping favors τ_{10} with respect to τ_{21} and τ_{32} (compare the left panel of Fig. 8.21 with the two other panels). It is likely that with a better signal-to-noise ratio in the J=2–1 and J=3–2 ^{13}CO data, the inferred excitation temperature would increase.

Certainly, it is also possible that the ^{12}CO lines are sub-thermal across the ambient cloud (see Fig. 8.27). Fig. 8.27 shows that there are significant deviations to LTE across the major part of the eastern and northeastern sections of the ambient cloud probed by our $10' \times 10'$ observations. If the local density of the cloud is low ($n \ll 10^4$ cm^{-3}) and the ^{12}CO lines are not fully thermalized, an excitation temperature of 5 K would be possible. In conclusion, the excitation temperatures found in this section should be interpreted very cautiously, because the correction of the optical depth introduces a significant bias.

8.2.5 non-LTE treatment of ^{12}CO and ^{13}CO lines (RADEX analysis)

In the previous section, we employed the 'population diagram method' presented in Chapter 4 to measure the column density of ^{12}CO. Our analysis relied on the assumption that *i.)* the lines are fully thermalized; *ii.)* the ^{12}CO and ^{13}CO lines share the same excitation conditions. The low excitation temperatures (down to 5 K) inferred in a fraction of the extended G field suggest that the LTE condition is not satisfied in all lines of sight.

In this section, we perform a least-square modelling of ^{12}CO and ^{13}CO lines with a radiative transfer code. `RADEX` is a one-dimensional non-LTE radiative transfer code that uses the escape probability formulation (or 'large velocity gradient') to solve statistical equilibrium equations in an isothermal, homogeneous medium (van der Tak *et al.*, 2007). In Chapter 4, we have described the characteristics of the program and its input parameters (see section 4.3.2). In section 8.2.5.1, we perform a least-square analysis of ^{12}CO and ^{13}CO lines on high signal-to-noise average spectra to infer average physical quantities from the main molecular features in the extended G region. In section 8.2.5.2, we present the preliminary results of pixel-per-pixel measurements of the column density and kinetic temperature in each line of sight of our PPV cubes.

8.2.5.1 Method 1: box-average least-square fitting

We aim to estimate the column density, kinetic temperature and density of the molecular gas in each spatial box defined in Fig. 8.23 (the shocked clump, quiescent cloudlet, *etc*). In order to fully exploit the potential of our observations, we simultaneously model the ^{12}CO and ^{13}CO lines, hence we have a total of six distinct data points to minimize *via* least-square fitting. Modeling both the ^{12}CO and ^{13}CO lines with `RADEX` should allow to lift the degeneracy induced by the saturation of ^{12}CO lines. In the `RADEX` settings `txt` file, we selected the expanding spherical shell geometry, for which the escape probability is related to the optical depth $\tau_{\rm ul}$ by the following formula (Mihalas, 1978):

$$\beta_{\rm ul} = \frac{1 - e^{-\tau_{\rm ul}}}{\tau_{\rm ul}}. \tag{8.39}$$

Description of our RADEX grid of models There are a total of 5 distinct physical input parameters to manage both for ^{12}CO and ^{13}CO: the total column density $N_{^{12}\rm CO}$ (respectively $N_{^{13}\rm CO}$), the full width at half-maximum of the lines Δv, the kinetic temperature $T_{\rm kin}$, the background brightness

temperature T_{bg} and the local density of the collisional partners (n_{H_2}). We assume that the background temperature is uniform across the extended G region and equal to the black body radiation of the CMB (T_{bg} = 2.7 K). The values of Δv are fixed for each average spectrum by measuring the line width with a gaussian line profile. Thus, only the parameters $N_{^{12}CO}$, T_{kin} and n_{H_2} are not fixed. We assume that ^{12}CO and ^{13}CO share the same kinetic temperature, and we assume that the ^{13}CO total column density is given by:

$$N_{^{13}CO} = \frac{N_{^{12}CO}}{[^{12}CO/^{13}CO]} \tag{8.40}$$

where $[^{12}CO/^{13}CO]$ is the adopted isotopic ratio. We fixed distinct values of the isotopic ratio for each molecular feature (indicated in Tab. 8.6), according to the best-fit parameters of the corresponding samples of data points in the histograms presented in Fig. 8.16 (right panel). ^{12}CO and ^{13}CO `RADEX` models are produced separately and stored in distinct `Python` arrays which are built such that a pixel (x, y) in the ^{12}CO and ^{13}CO arrays corresponds to the same `RADEX` input parameters ($N_{^{12}CO}$, T_{kin}, n_{H_2}).

We produced three-dimensional grids of `RADEX` models with logarithmically spaced densities ($N_{^{12}CO}$, n_{H_2}), linearly spaced temperatures (T_{kin}) and fixed parameters (T_{bg}, Δv). These input parameters are specified in Tab. 8.6 along with the results. During the preliminary 'exploration phase', we used broad ranges of column densities and kinetic temperatures in order to probe a large fraction of the parameter space. Once we identified the boundaries of the range of input parameters required to reproduce the observations in all spatial boxes, we produced model grids with narrow range of parameters in order to increase precision.

Least-square fitting Using a standard χ^2-minimization procedure, we compared `RADEX` outputs with our observations of ^{12}CO and ^{13}CO lines in order to constrain the physical conditions for each molecular feature indicated in Fig. 8.23. We compared the line velocity-integrated brightness temperature measurements of the first three pure rotational transitions of ^{12}CO and ^{13}CO with synthetic velocity-integrated brightness temperatures stored in our grids of `RADEX` models. In the same manner as in the population diagram approach, for consistency we convolved all maps to the same spatial resolution, using the nominal resolution of ^{13}CO J=2–1, such that we have a beam diameter of 30.1″. The spectral resolution was also set to 2 km s^{-1} for each transition in order to increase the signal-to-noise ratio. Using a `Python` algorithm, we applied the following steps:

1. We sigma-clipped the spectra of all transitions of ^{12}CO and ^{13}CO, using a threshold of 3σ in order to remove the low signal-to-noise data points.

2. We measured the velocity-integrated brightness temperature of the lines ($\int T_{mb} dv$). Then, in each element of the `RADEX` model grid we measured the following quantity, corresponding to a combined reduced-χ^2 statistical estimator:

$$\chi^2 = \frac{1}{N-p} \sum_{J_u=1}^{3} \left[\frac{(m_{12} - s_{12})^2}{\sigma_{12}^2} + \frac{(m_{13} - s_{13})^2}{\sigma_{13}^2} \right] \tag{8.41}$$

In this equation, J_u indicates the upper levels of each transition, m_{12} and m_{13} are respectively the synthetic velocity-integrated brightness temperatures of ^{12}CO and ^{13}CO lines produced

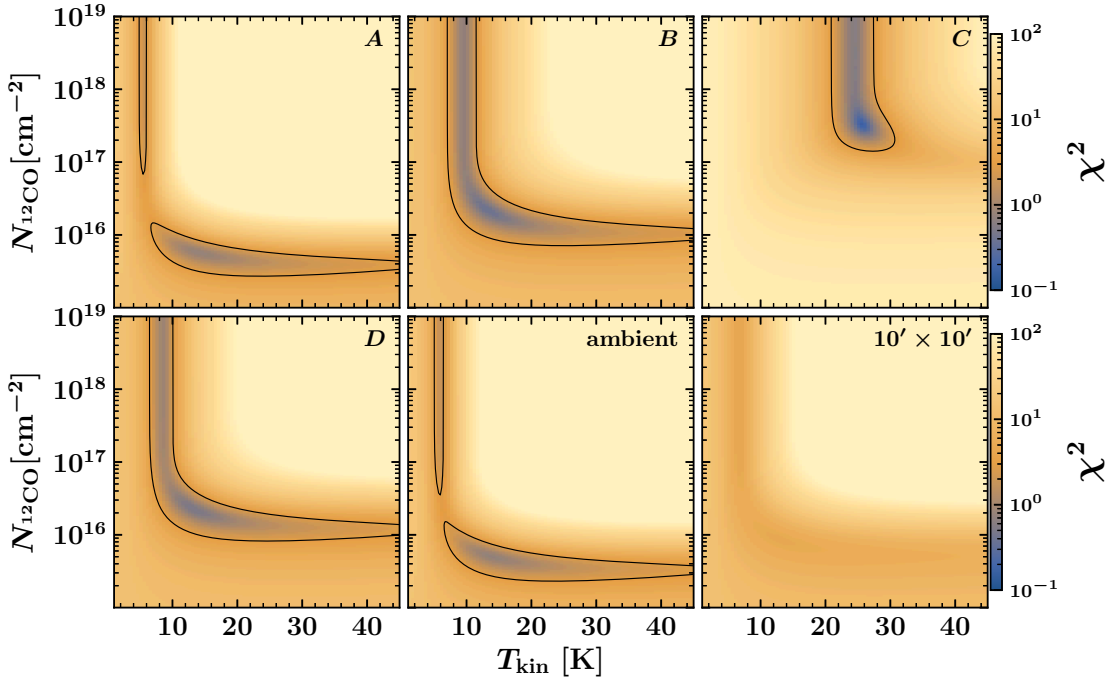

Figure 8.31 RADEX least-square diagrams of ^{12}CO lines in the extended G region (first term of Eq. 8.41). Each panel corresponds to a distinct average spectrum ('A', 'B', 'C', 'D' corresponding to the spatial boxes shown in Fig. 8.23 and 'ambient' corresponding to $\overline{\mathrm{A}} \cap \overline{\mathrm{B}} \cap \overline{\mathrm{C}} \cap \overline{\mathrm{D}}$). The black contours represent $\chi^2 = 3$. The adopted density is $n_{\mathrm{H_2}} = 10^5$ cm^{-3}.

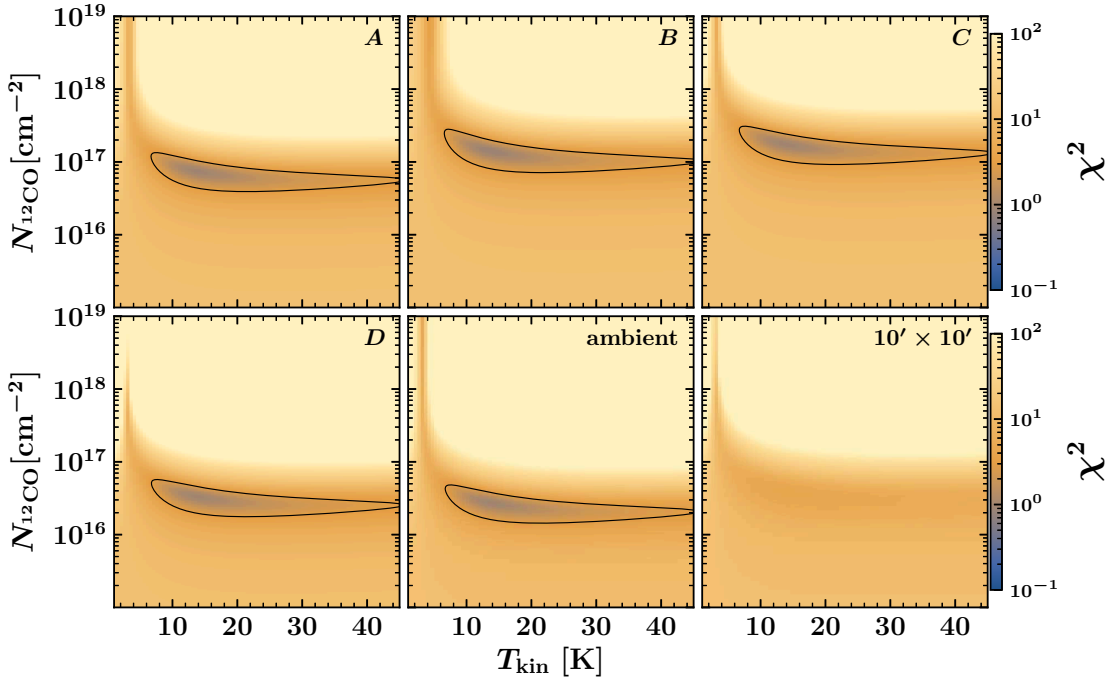

Figure 8.32 RADEX least-square diagrams of ^{13}CO lines in the extended G region (second term of Eq. 8.41). Each panel corresponds to a distinct average spectrum ('A', 'B', 'C', 'D' corresponding to the spatial boxes shown in Fig. 8.23 and 'ambient' corresponding to $\overline{\mathrm{A}} \cap \overline{\mathrm{B}} \cap \overline{\mathrm{C}} \cap \overline{\mathrm{D}}$). The black contours represent $\chi^2 = 3$. The adopted density is $n_{\mathrm{H_2}} = 10^5$ cm^{-3}.

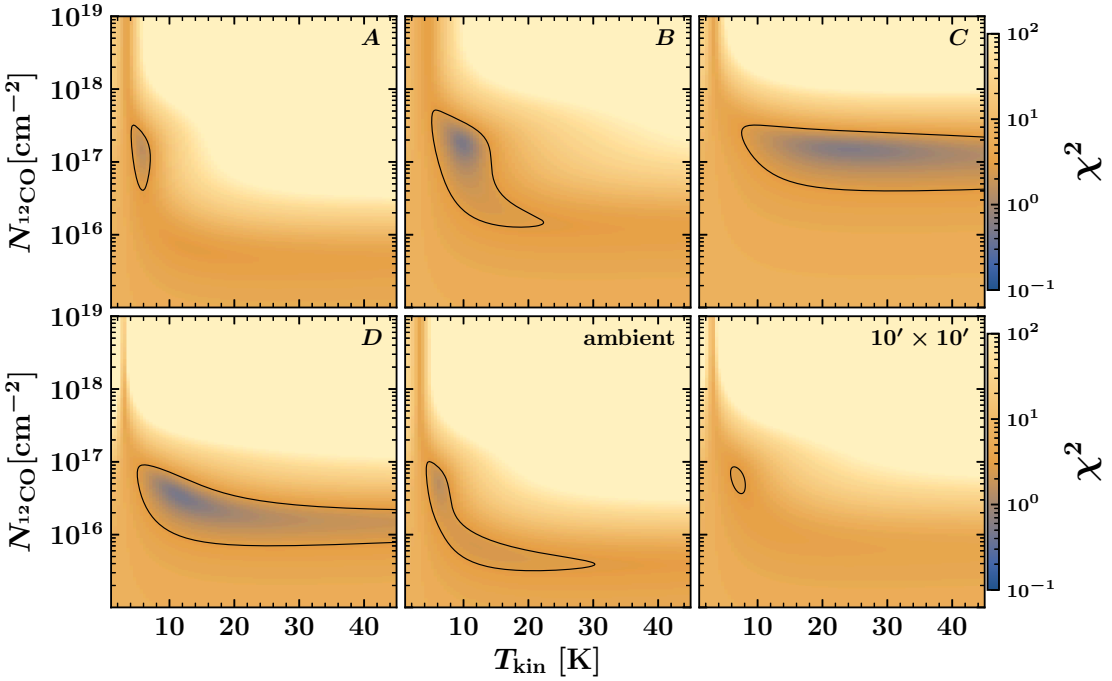

Figure 8.33 RADEX least-square diagrams of the combination of ^{12}CO and ^{13}CO lines in the extended G region (see Eq. 8.41). Each panel corresponds to a distinct average spectrum ('A', 'B', 'C', 'D' corresponding to the spatial boxes shown in Fig. 8.23 and 'ambient' corresponding to $\overline{\mathrm{A}} \cap \overline{\mathrm{B}} \cap \overline{\mathrm{C}} \cap \overline{\mathrm{D}}$). The black contours represent $\chi^2 = 3$. The adopted density is $n_{\mathrm{H_2}} = 10^5$ cm^{-3}.

by RADEX, s_{12}, s_{13} the velocity-integrated brightness temperature measurements and σ_{12}, σ_{13} the uncertainties associated with the measurements. $N = 6$ corresponds to the number of data points, and $p = 2$ is the number of free parameters (the kinetic temperature and total column density).

3. We inferred the physical conditions from the minimization of the quantity χ^2, *i.e.* we localized the minimum element of the resulting χ^2 grid and determined the quantities ($N_{^{12}CO}$, $n_{\mathrm{H_2}}$, T_{kin}) from the corresponding set of RADEX input parameters.

Uncertainties The errorbars on the total ^{12}CO column density, molecular mass and kinetic temperature are determined by: *(i.)* instrumental errors (systematic uncertainty on the brightness temperature (±12%, see section 8.2.1); *(ii.)* systematic errors on the adopted distance of IC443 (1.8±0.2 kpc); *(iii.)* systematic uncertainties on the adopted [^{12}CO/^{13}CO] isotopic ratio (±30%), *(iv.)* the uncertainty on the adopted H_2-to-^{12}CO abundance ratio (propagated into the uncertainty on the mass measurement).

Results The results of the RADEX least-square analysis of average spectra are shown in Fig. 8.31 (^{12}CO lines), Fig. 8.32 (^{13}CO lines) and Fig. 8.33 (combination of ^{12}CO and ^{13}CO lines) On these figures, we present the χ^2 grids corresponding to each spatial box defined in Fig. 8.23, and also the 'ambient molecular gas' measurement (corresponding to $\overline{\mathrm{A}} \cap \overline{\mathrm{B}} \cap \overline{\mathrm{C}} \cap \overline{\mathrm{D}}$) and the '10′ × 10′' measurement (corresponding to the entire PPV cubes).

Regions	cloudlet (A)	ring-like (B)	shocked clump (C)	shocked knot (D)	ambient
$N_{^{12}CO}$ [10^{17}cm^{-2}]	1.4-2.4	1.7-2.3	1.8-2.9	0.3-0.4	0.4-0.9
T_{kin} [K]	6±1	10±1	16±6	13±6	13±5
n_{H_2} [cm^{-3}]	$\sim 7\times10^5$	$> 10^4$	$> 10^4$	$> 10^4$	$\sim 3\times10^4$
$\log_{10}(\chi^2)$	0.37	0.25	0.55	0.53	0.88
M [$M_\odot$]	120-220	40-70	80-150	4-6	210-350
$N_{^{12}CO}$ [cm^{-2}]	[10^{15} – 10^{19}]	[10^{15} – 10^{19}]	[10^{15} – 10^{19}]	[10^{15} – 10^{19}]	[10^{15} – 10^{19}]
[^{12}CO/^{13}CO]	80	60	45	45	60
T_{grid} [K]	[1-100]	[1-100]	[1-100]	[1-100]	[1-100]
T_{bg} [K]	2.7	2.7	2.7	2.7	2.7
Δv [km s^{-1}]	4.0	3.5	25	35	3.0

Notes. Measurements performed on average spectra extracted within the spatial boxes defined in Fig. 8.23. The 'ambient cloud' corresponds to $\overline{A}\cap\overline{B}\cap\overline{C}\cap\overline{D}$. $N_{^{12}CO}$ is the total column density measurement. The mass is given by $M_{H_2} = (2m_H)\mathcal{A}N_{^{12}CO}\times10^4$ where $\mathcal{A}$ is the area of a spatial bin (a pixel) and m_H the mass of one hydrogen atom. We indicate lower boundaries on the local density n_{H_2} suggested by RADEX models. The mass uncertainties are determined by the uncertainties on the distance to IC443 ($d = 1.8\pm0.2$ kpc) and [^{12}CO/^{13}CO] isotopic ratio (±30%). The uncertainties on the kinetic temperature T_{kin} are determined by the $\pm1\sigma$ dispersion of χ^2 along the temperature axis. $\log_{10}(\chi^2)$ corresponds the minimum of χ^2 within the least-square grid. In the bottom part of the table (last 5 rows) we indicate the RADEX parameters used: total column density ($N_{^{12}CO}$) and kinetic temperature (T_{kin}) grids, [^{12}CO/^{13}CO] isotopic ratio (which determines the $N_{^{13}CO}$ grid), background temperature (T_{bg}) and line width (Δv). The line widths Δv were measured on the average spectra using gaussian models.

Table 8.6 Quantitative summary of the RADEX least-square analysis of ^{12}CO and ^{13}CO lines.

The 2D least-square grids shown in these figures correspond to the $n_{H_2} = 10^5$ cm^{-3} slice. We did not manage to consistently minimize our model grids along the local density axis, and in most cases the least-square analysis only provides a lower bound on the local density (χ^2 is minimal for $n_{H_2} \geq 10^4$ cm^{-3} and cannot be accurately constrained). The difficulty to constrain the local density and the minimal value found ($n_{H_2} \geq 10^4$ cm^{-3}) seem to confirm that the ^{12}CO J=1–0, J=2–1 and J=3–2 lines are indeed thermalized.

Except for the '$10'\times10'$' least-squares, all diagrams present low minimum chi-squares ($\chi^2 \ll 3$). The higher χ^2 in the '$10'\times10'$' least-square diagram is due to a mixture of different physical conditions (we adopted a single value of the isotopic ratio for this diagram: [^{12}CO/^{13}CO] = 60), hence it justifies the need to work with the sub-regions 'A', 'B', 'C', 'D'. Fig. 8.31 (^{12}CO least-squares) shows that the results of the RADEX analysis of ^{12}CO lines are partially degenerate in total column density, although the minimum χ^2 allows to converge to a solution for $N_{^{12}CO}$. In contrast, Fig. 8.32 (^{13}CO least-squares) shows that the column density inferred from ^{13}CO lines is constrained, but the temperature is partially degenerate.

The combined least-square analysis of ^{12}CO and ^{13}CO (see Fig. 8.33) allows to reduce the degeneracy of the physical parameters, except for the kinetic temperature in boxes 'C' and 'D' (shocked molecular structures) which remains weakly constrained for the lowest value of χ^2. We present the quantitative results of the combined analysis of ^{12}CO and ^{13}CO lines in Tab. 8.6.

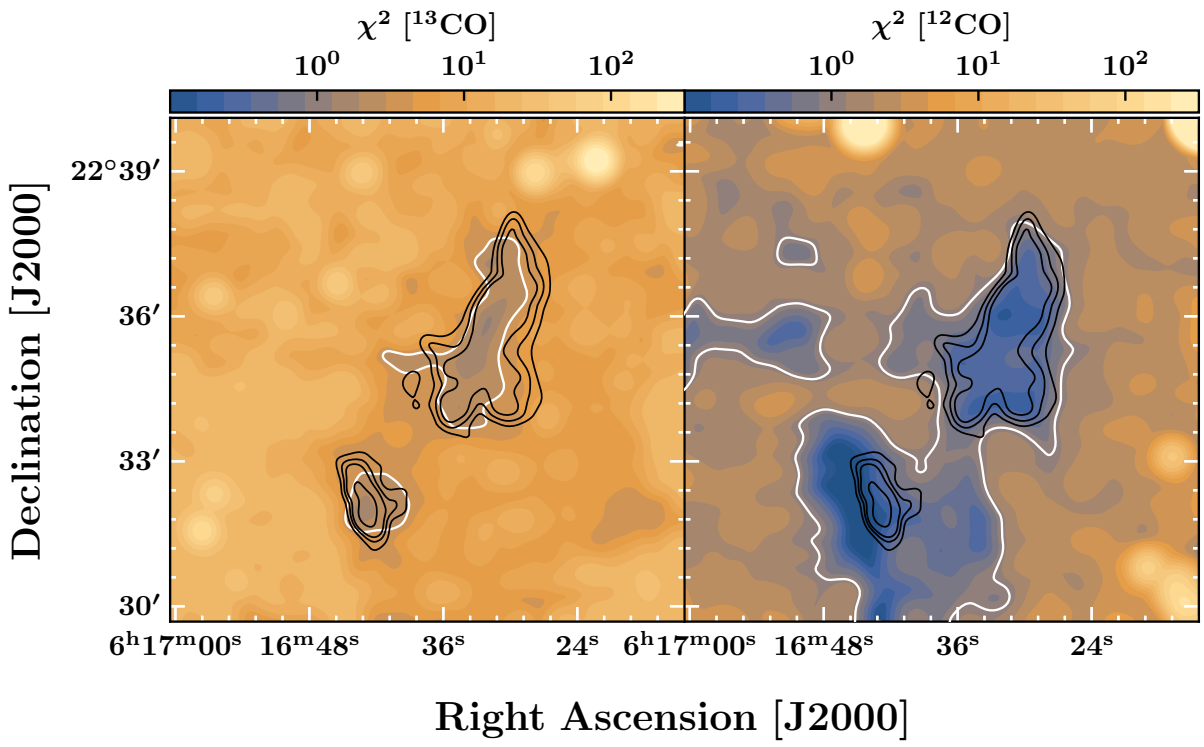

Figure 8.34 χ^2 maps (see Eq. 8.41). *Left:* χ^2 map associated with the ^{13}CO $J_u = 1, 2, 3$ RADEX least-square analysis (second term in Eq. 8.41). *Right:* χ^2 map associated with the ^{12}CO $J_u = 1, 2, 3$ RADEX least-square analysis (first term in Eq. 8.41). The white contour traces the area delimited by $\chi^2 = 3$ (in the left panel) and $\chi^2 = 1$ (in the right panel). The black contours correspond to the IRAM 30m ^{12}CO J=2–1 peak map shown in Fig. 6.10 (contour levels: 0.25, 0.35, 0.45 and 0.75 times the maximum value across the map).

8.2.5.2 Method 2: pixel-per-pixel least-square fitting (experimental)

We aim to apply the method described in the previous section in each pixel (*i.e.* in each line of sight) of our PPV cubes. The difficulty is that many pixels have low signal-to-noise ratios ($\ll 5$), and it can be a challenge to correctly interpret the results of the χ^2-minimization in noisy pixels. However, this method might be more accurate towards high signal-to-noise pixels because it reduces the confusion between distinct molecular features when working with average spectra. *Caution:* the results presented in the following paragraphs are preliminary.

Determination of the pixel-per-pixel input parameter Δv In the framework of the LVG assumption, the value of the optical depth τ_{ul} at line center determined by RADEX is proportional to $N_{^{12}CO}/\Delta v$ (see Eq. 4.39), where $N_{^{12}CO}$ is the column density and Δv the full width at half-maximum of the line. Thus, when using RADEX the choice of the parameter Δv is critical to correctly estimate the total column density.

In the previous section, we fixed Δv by measuring the line widths of average spectra of ^{12}CO and ^{13}CO extracted in manually defined spatial boxes (see Fig. 8.23). A limitation of this approach is that we adopted a single value of Δv to model the emission extracted over large areas of the extended G region, ignoring local variations.

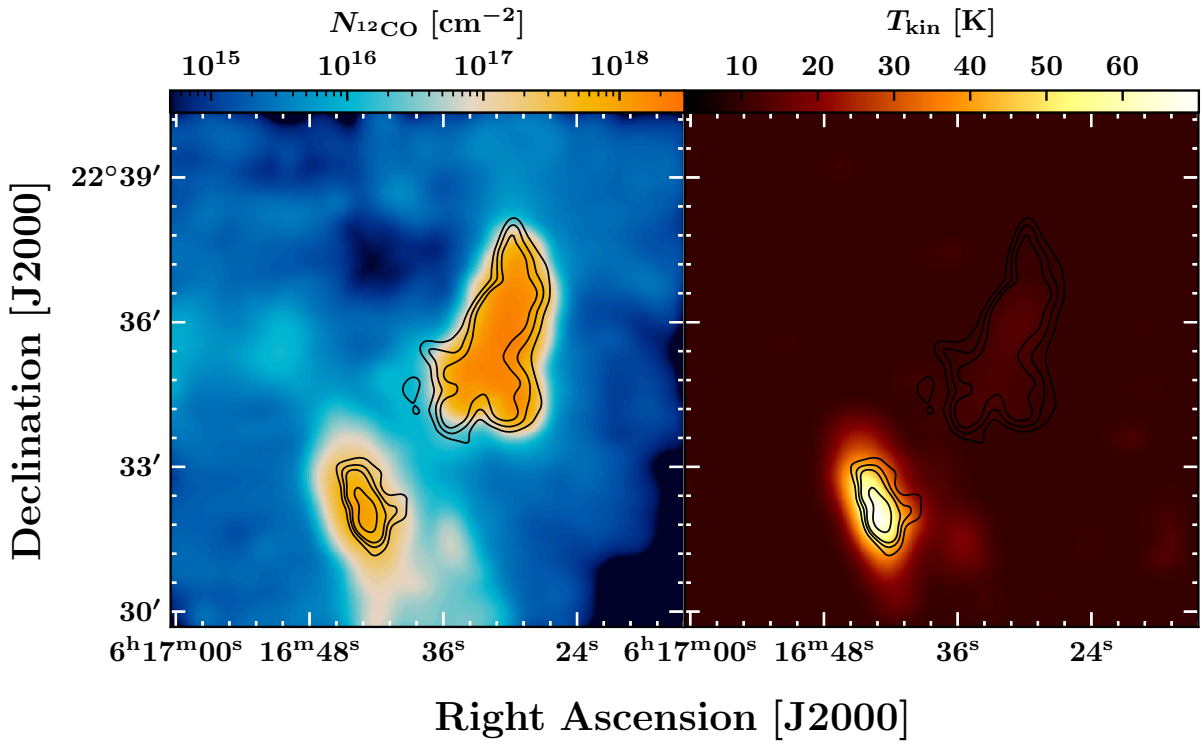

Figure 8.35 Results of the least-square RADEX analysis of ^{12}CO pure rotational lines only. *Left:* ^{12}CO column density map. The maximum value towards the quiescent cloudlet is $N_{^{12}CO} \sim 2\times10^{18}$ cm^{-2}. *Right:* excitation temperature map. The black contours correspond to the IRAM 30m ^{12}CO J=2–1 peak map shown in Fig. 6.10 (contour levels: 0.25, 0.35, 0.45 and 0.75 times the maximum value across the map).

The pixel-per-pixel method allows to be more accurate in the choice of the parameter Δv, which can be determined on a pixel-by-pixel basis. RADEX assumes that the line widths of all transitions are identical, hence we adopted the average value of the J=1–0, J=2–1 and J=3–2 line widths as a fixed value of the input parameter Δv in each line of sight. We obtained an estimate of the line widths in each pixel by producing the second moment map for each transition both for ^{12}CO and ^{13}CO (using the imperfect GILDAS procedure, in the same way as described in section 6.2.2, see Fig. 6.15, Fig. 6.17). For the rest of the parameters ($N_{^{12}CO}$, $N_{^{13}CO}$, T_{kin}, T_{bg}, n_{H_2}), we followed the same method as described in the previous section, using a uniform isotopic ratio [^{12}CO/^{13}CO] 60^{+30}_{-15} (see section 8.2.2).

8.2.5.3 Description of the pixel-per-pixel results

We have obtained a measurement of the column density and kinetic temperature in all lines of sight of our PPV cubes using RADEX. We did not manage to correctly constrain the local density. The minimization of n_{H_2} is difficult in low signal-to-noise pixels across the background, and there seems to be an anticorrelation between T_{kin} and n_{H_2} that perturbs the minimization of the kinetic temperature (a lower density n_{H_2} means a lower T_{ex}/T_{kin} ratio, and thus implies a higher T_{kin} to reproduce the same line intensity, for an optically thick line). The difficulty to constrain n_{H_2} may also indicate that ^{12}CO lines are thermalized.

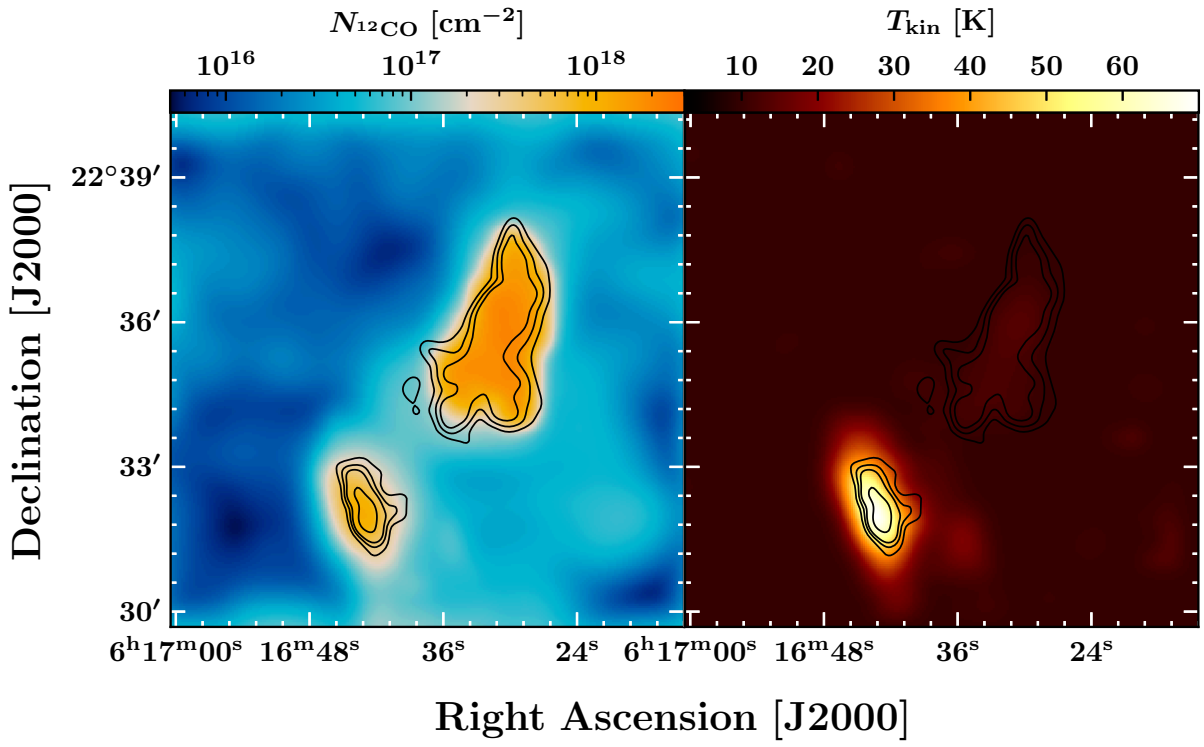

Figure 8.36 Results of the least-square RADEX analysis of ^{12}CO and ^{13}CO pure rotational lines. *Left:* ^{12}CO column density map. The maximum value towards the quiescent cloudlet is $N_{^{12}CO} \sim 2 \times 10^{18}$ cm^{-2}. *Right:* excitation temperature map. The black contours correspond to the IRAM 30m ^{12}CO J=2–1 peak map shown in Fig. 6.10 (contour levels: 0.25, 0.35, 0.45 and 0.75 times the maximum value across the map).

In order to accurately constrain $N_{^{12}CO}$ and T_{kin}, we fixed the local density in each pixel and found that the results converge for $n_{H_2} \geq 10^4$ cm^{-3} (as in the previous section). The results of the pixel-per-pixel χ^2-minimization are shown on Fig. 8.34 both for ^{12}CO and ^{13}CO lines. The resulting column density and kinetic temperature maps are shown on Fig. 8.35 and Fig. 8.36. The minimization of ^{12}CO data points is satisfying, with more than 90% of the pixels characterized by $\chi^2 \leq 3$. The minimization of ^{13}CO data points is more difficult due to lower signal-to-noise detections, but the minimized χ^2 is satisfying towards the shocked clump and quiescent cloudlet ($\chi^2 \leq 3$, see white contours on Fig. 8.34, left panel).

Results with ^{12}CO lines only To experiment with our method, we performed a run with ^{12}CO lines only (ignoring the second term in Eq. 8.41). The results are shown on Fig. 8.35. In comparison to the LTE analysis of ^{12}CO lines (corrected for optical depth, see Fig. 8.29), the inferred peak column densities are in agreement towards the shocked clump and quiescent cloudlet (respectively $\sim 10^{18}$ cm^{-2} and $\sim 2 \times 10^{18}$ cm^{-2}). Within errorbars, these values are in agreement with the results of the opacity-corrected population diagrams (see Fig. 8.29), hence RADEX seems to correctly treat the opacity of the lines. Both the kinetic and excitation temperatures found towards the shocked clump are higher than the LTE excitation temperature found in the previous section: at the core of the shocked clump, the excitation and kinetic temperatures determined with RADEX reach a maximum value of $\sim$ 80 K (in contrast to T_{ex} = 28 K). This discrepancy might be due to

region	$\overline{N_{\rm CO}}[10^{17}{\rm cm}^{-2}]$	Mass ($M_\odot$)	$\overline{T_{\rm kin}}$[K]	$\overline{\chi^2}$	$M_{X_{\rm CO}}^{J=1-0}$ ($M_\odot$)
cloudlet (A)	$3.1^{+1.6}_{-0.8}$	200^{+170}_{-80}	11±1	0.83	450±140
ring-like structure (B)	$5.7^{+2.9}_{-1.4}$	190^{+160}_{-80}	12±2	0.20	200±60
shocked clump (C)	$2.3^{+1.1}_{-0.5}$	70^{+50}_{-30}	29±8	0.14	190±60
shocked knot (D)	$0.7^{+0.3}_{-0.2}$	6^{+6}_{-2}	15±6	0.05	30±10
ambient cloud	$0.3^{+0.2}_{-0.1}$	120^{+100}_{-50}	9±2	5.9	1300±400
IC443G (extended)	$1.1^{+0.6}_{-0.3}$	570^{+500}_{-200}	11±1	7.1	2600±800

Notes. Average measurements corresponding to the spatial boxes defined in Fig. 8.23. The 'ambient cloud' corresponds to $\overline{\rm A} \cap \overline{\rm B} \cap \overline{\rm C} \cap \overline{\rm D}$, and the last row corresponds to the measurements performed on the entire PPV cubes. $\overline{N_{\rm CO}}$ is the average column density measurement. The mass is given by $M_{\rm H_2} = (2m_{\rm H})\mathcal{A}N_{^{12}{\rm CO}} \times 10^4$ where $\mathcal{A}$ is the area of a pixel and $m_{\rm H}$ the mass of one hydrogen atom. The mass uncertainties are determined by the uncertainties on the distance to IC443 ($d = 1.8 \pm 0.2$ kpc) and [^{12}CO/^{13}CO] isotopic ratio (60^{+30}_{-15}). The uncertainties on the average kinetic temperature $\overline{T_{\rm kin}}$ are determined by the $\pm1\sigma$ dispersion of χ^2 along the temperature axis. $\overline{\chi^2}$ is the average of $\chi^2(x, y)$ in each spatial box. For comparison, we indicate the estimate of the mass obtained by using the CO-to-H_2 conversion factor $X_{\rm CO} = 2 \times 10^{20}$ cm^{-2}(K km s^{-1})$^{-1}$ applied to the raw J=1–0 data (without optical depth correction).

Table 8.7 Summary of the pixel-per-pixel RADEX least-square analysis of ^{12}CO and ^{13}CO lines.

the single $T_{\rm ex}$ assumption in our LTE analysis, which causes confusion between warm and cold molecular gas along the line of sight.

Within the quiescent cloudlet, the kinetic temperature is $T_{\rm kin} \sim 15$ K. Additionally, the kinetic temperatures found in the 'background' ambient molecular gas are closer to physically plausible temperatures than the excitation temperatures inferred with the LTE analysis (with an average temperature $T_{\rm kin} \sim 10$ K, in contrast to $T_{\rm ex} = 5$ K[7]).

Results with the combined least-square fitting of ^{12}CO and ^{13}CO lines We applied the least-square analysis to the ^{12}CO and ^{13}CO lines simultaneously, as in Eq. 8.41. The results are shown in Fig. 8.36. The column density of the ambient molecular gas is increased with respect to the analysis of ^{12}CO lines only, but the column density towards the shocked clump and quiescent cloudlet remains approximately the same. The kinetic temperature map is almost unaffected by the addition of the ^{13}CO data points, but the excitation temperature returned by RADEX does change. The quantitative results of the combined RADEX least-square analysis of ^{12}CO and ^{13}CO lines are summarized in Tab. 8.7.

Within errorbars (and taking into account the modifications of the adopted isotopic ratios), the measurements are consistent with the results obtained with average spectra (Tab. 8.6) except for the ring-like structure for which we find an approximately three-fold higher mass (from $\sim$ 60 $M_\odot$ to $\sim$ 190 $M_\odot$). Notably, the inferred mass of the shocked clump is lowered by a factor $\sim$ 1.5, and the mass of the ambient molecular gas is also significantly lowered (from $\sim$ 280 $M_\odot$ to 120 $M_\odot$). These discrepancies are likely to be due to the more accurate treatment of the local variations of the parameter Δv. Naturally, the variation of the results between the average (section 8.2.5.1) and pixel-per-pixel approach (section 8.2.5.2) brings the RADEX measurements

[7]Assuming a local density $n = 5 \times 10^2$ cm^{-3}, a column density $N_{\rm CO} = 10^{16}$ cm^{-2} and a kinetic temperature $T_{\rm kin} = 10$ K, RADEX returns an excitation temperature $T_{\rm ex} = 5$ K for the ^{12}CO J=1–0 line.

closer to the results obtained with opacity-corrected population diagrams. This is in part due to the distinct assumptions made on the spatial variation of the isotopic ratio: we used a uniform ^{12}CO/^{13}CO isotopic ratio for both pixel-per-pixel methods (LTE and LVG), although we adopted distinct isotopic ratios in our first LVG analysis (see Tab. 8.6).

8.2.6 Discussion

Summary, limitations and future prospects We have inferred total ^{12}CO column density and excitation/kinetic temperature maps from the analysis of the first three pure rotational transitions of ^{12}CO and ^{13}CO using both LTE (section 8.2.4) and non-LTE (section 8.2.5) methods. A comparison and summary of the results obtained with these methods is shown in Tab. 8.8. We found that:

- Both approaches have their respective issues: on one hand, the LTE analysis relies on the assumption that all the lines are thermalized, and it requires to correct the optical depth assuming that ^{12}CO and ^{13}CO share the same excitation conditions and geometry. On the other hand, the `RADEX` analysis adopts a single line opacity for each line of sight (*i.e.* we cannot perform the calculation on a channel-per-channel basis), which is inaccurate towards areas where distinct molecular structures are spatially confused. Additionally, there are more parameters to manage with `RADEX`: the line width Δv and local density n_{H_2}, which requires additional assumptions and caution when interpreting the least-square results.

- The assumption on the [^{12}CO/^{13}CO] isotopic ratio is also an important source of uncertainties. By adopting [^{12}CO/^{13}CO]=60^{+30}_{-15}, we have propagated the isotopic uncertainty into our mass measurements (*via* the correction of the optical depth). The mass uncertainties shown in the third column of Tab. 8.8 are significant, but they would be reduced to a flat ±12% only (brightness temperature uncertainty) if both the [^{12}CO/^{13}CO] isotopic ratio and the distance to IC443 were accurately known.

- Additionally, the last column in Tab. 8.8 shows that both LTE and non-LTE mass measurements converge to the same values within ±30% for the quiescent cloudlet (box 'A'), ring-like structure (box 'B') and shocked clump (box 'C'), hence we consider that these measurements are robust. Only the shocked knot (box 'D', Fig. 8.23) and the ambient molecular gas are associated with significant discrepancies. For the ambient molecular gas, the discrepancy is caused by nonthermalization of the lines: the low excitation temperature inferred from opacity-corrected population diagrams (T_{ex} = 5 K) increases the inferred total column density with respect to `RADEX` measurements. For the shocked knot, the ^{12}CO line opacities are overestimated due to line of sight confusion with the ^{13}CO emission from the ambient molecular gas.

- In the future, observing more than the first three rotational transitions of ^{12}CO and ^{13}CO would allow to accurately disentangle the warm component from the cold, massive component of the molecular emission (using similar methods as in section 8.1). This would be particularly useful in the extended G region where there is spatial mixing between a cold foreground (the molecular cloud of Cornett *et al.* 1977) and shocked molecular structures along the line of sight, which causes confusion in the determination of T_{ex}. However, it

would not significantly modify our mass measurements since the mass of warm gas is negligible with respect to the mass of cold gas (see section 8.1, Fig. 8.12).

Comparisons with previous studies To our knowledge, there have been only two attempts to measure the molecular mass of 'clump G' that we can compare with our own estimate (that is, a mass 80^{+90}_{-40} $M_\odot$ if we take into account all measurements presented in this chapter):

– Dickman *et al.* (1992) measured a mass of 41.6 $M_\odot$ assuming that the ^{12}CO J=1–0 emission is optically thin.

– Using ^{12}CO J=3–2 observations, Xu *et al.* (2011) measured a mass of 2.06×10^3 $M_\odot$ for the so-called 'cloud G'. Their measurement included a larger field than the spatial box that we used (box 'C', see Fig. 8.23), and they lacked sufficient data to correctly estimate the optical depth.

The comparison with the measurement of Xu *et al.* (2011) is seemingly inadequate, because of a different spatial definition of 'clump G'. The measurement of Dickman *et al.* (1992) is consistent with our findings (within errorbars), although our mass value is higher because of optical depth correction.

Using a CO-to-H_2 conversion factor applied to their ^{12}CO J=1–0 observations, Lee *et al.* (2012) measured a mass of 57.7±0.9 $M_\odot$ for the small cloud 'SC03', which corresponds to the molecular structure that encompasses our boxes 'A' and 'B' (the quiescent cloudlet and ring-like structure). We found a total mass 340^{+380}_{-150} $M_\odot$ in these boxes. The discrepancy can be attributed to the correction of the optical depth (see Fig. 8.30, left panel).

region	$\overline{N_{CO}}[10^{17}cm^{-2}]$	Mass ($M_\odot$)	$\overline{T_{kin}}$[K]	n_{H_2} (cm^{-3})	$\overline{\chi^2}$(LTE/LVG)	M_{LTE}/M_{LVG}
cloudlet (A)	$2.9^{+1.8}_{-1}$	180^{+190}_{-80}	10^{+1}_{-4}	$1-5\times10^3$	0.72 / 0.83	0.8
ring-like structure (B)	$4.8^{+3.8}_{-1.9}$	160^{+190}_{-70}	12^{+2}_{-4}	$3-7\times10^3$	0.05 / 0.20	0.7
shocked clump (C)	2.8^{+2}_{-1}	80^{+90}_{-40}	24^{+13}_{-11}	$0.6-1.1\times10^4$	0.15 / 0.14	1.3
shocked knot (D)	$1.6^{+2.2}_{-1.1}$	15^{+30}_{-10}	16^{+7}_{-9}	$3-5\times10^3$	0.03 / 0.05	4.2
ambient cloud	$0.8^{+1}_{-0.6}$	300^{+600}_{-200}	9^{+2}_{-4}	$1-3\times10^2$	6.1 / 5.9	3.9
IC443G (extended)	$1.4^{+1.1}_{-0.6}$	700^{+900}_{-300}	10^{+2}_{-1}	-	7.1 / 7.1	1.5

Notes. This table presents a summary of the quantitative results of our LTE (corrected for line opacity, section 8.2.4) and non-LTE (section 8.2.5) analysis of ^{12}CO and ^{13}CO lines: each measurement is the average of the entries in Tab. 8.5 and Tab. 8.7, and the uncertainties represent the discrepancies between the two approaches. Refer to the notes below Tab. 8.5 and Tab. 8.7 for a detailed description of each column. In the last two rows, we compare the minimum χ^2 obtained for each method (LTE and non-LTE, *i.e.* 'LVG') and we indicate the ratio of the mass measurements (M_{LTE}/M_{LVG} = 1 if the measurements are identical). Additionally, the local density column (n_{H_2}) is inferred from the peak column density divided by the estimated length of the molecular structures (see text).

Table 8.8 Summary and comparison of the pixel-per-pixel opacity-corrected population diagram and `RADEX` least-square analysis of ^{12}CO and ^{13}CO lines.

Local density in the extended G region We aim to estimate the local density from the total ^{12}CO column density measurements. From our ^{12}CO J=2–1 observations (see chapter 6) we propose simple geometrical models for the main molecular features in the extended G region. We adopt a length l based on the mean diameter of each structure (manually measured from Fig. 6.10). For the ambient cloud, we use the ^{12}CO map of Lee *et al.* (2012) to obtain a rough estimate. We adopt a distance of 1.8 kpc (Ambrocio-Cruz *et al.* 2017, Yu *et al.* 2019) to convert the angular measurements into physical lengths. We adopt $\sim 0.5 - 1.5$ pc, $\sim 0.5 - 1$ pc, $\sim 0.3 - 0.6$ pc and $\sim 0.2 - 0.4$ pc respectively for the quiescent cloudlet, ring-like structure, shocked clump and shocked knot. We adopt a length of $\sim 3 - 10$ pc for the ambient cloud. Assuming that other sources of emission along the line of sight are negligible, the local density is given by the ratio of the measured column density and the length l, hence we have $n_{H_2} = N_{^{12}CO} \times 10^4 / l$, where 10^4 is the adopted H_2-to-^{12}CO abundance (Gordon and Burton 1976, Frerking *et al.* 1982). Results are shown in Tab. 8.8. These estimates should be interpreted cautiously, because *i.)* our measurements of the length of molecular structures are uncertain, *ii.)* if the molecular structures are clumpy then we are underestimating the local density, *iii.)* real density profiles are unlikely to be constant along the line of sight.

Assuming $T_{kin} = 10$ K, our estimates of the local density imply that the J=2–1 and J=3–2 lines might not be fully thermalized (see Tab. 4.4) for the most part of the extended G region. For the shocked clump only, the local density is consistent with the thermalization of the J=1–0 and J=2–1 lines. For the ambient molecular cloud, none of the lines are thermalized according to our estimates of the local density ($n_{H_2} \ll n_{crit}$ even for J=1–0). Nonthermalization of the lines emitted by the ambient molecular gas is consistent with the low excitation temperatures measured across the background (down to $T_{ex} = 5$ K, see section 8.2.4). Naturally, if the molecular gas has a clumpy distribution that is not sampled by the beam of the IRAM 30m and APEX telescopes, then the local density estimate would increase (assuming a filling factor $ff \simeq 0.2$, the ^{12}CO J=1–0 and J=2–1 lines would be fully thermalized).

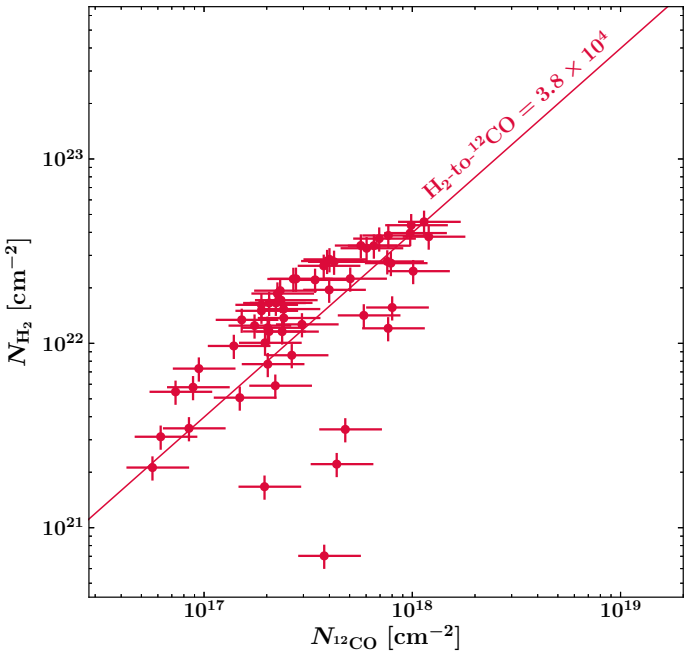

Figure 8.37 Direct pixel-per-pixel comparison of the ^{12}CO and H_2 total column density maps, restricted to the field of observations mapped both by *Spitzer*-IRS and the {IRAM 30m + APEX} telescopes. The ^{12}CO data points correspond to the measurements obtained with opacity-corrected population diagrams (Fig. 8.29). The H_2 data points correspond to the results obtained with the thermal admixture model (assuming $T_{min} = 25$ K and $T_{max} = 1500$ K, see section 8.1.3.2, Fig. 8.11). We show the linear fit associated with the sample of data points (determined with the `Python` package `curve_fit`) and the corresponding H_2-to-^{12}CO molecular abundance.

Comparison with H_2 measurements In section 8.1, we studied *Spitzer*-IRS spectral-line maps of H_2 in a subfield of the extended G region (see Fig. 8.1). With our thermal admixture model (in which we assume that the molecular hydrogen traced by pure rotational lines has a power-law kinetic temperature distribution between $T_{\rm min}$ = 25 K[8] and $T_{\rm max}$ = 1500 K, see section 8.1.3.2), we measured a peak H_2 column density $N_{\rm H_2} = 1.0 \pm 0.1 \times 10^{23}$ cm^{-2} towards the shocked clump. Our pixel-per-pixel opacity-corrected population diagrams yield a peak ^{12}CO column density $N_{^{12}\rm CO} = 1.2^{+0.4}_{-0.2} \times 10^{18}$ cm^{-2}, although we have to correct for beam dilution in order to allow direct comparison between the measurements.

We convolved our H_2 column density map with a gaussian kernel and resampled the data on the same spatial grid as in our ^{12}CO column density maps. A total of 54 pixels can be directly compared between the two column density maps, all characterized by high signal-to-noise ratios ($s/n \gg 6$). In Fig. 8.37, we show the pixel-per-pixel comparison between the H_2 and ^{12}CO column density maps (black data points). There is a quasi-linear relation between the column densities, and the H_2-to-^{12}CO abundance estimated from the linear fit is $\sim 3.8 \times 10^4$. The inferred abundance is high with respect to the standard abundance ($\sim 10^4$, Gordon and Burton 1976, Frerking *et al.* 1982). Towards the shocked clump, it is possible that ionization decreases the ^{12}CO abundance with respect to H_2 (*via* the depletion of ^{12}CO into C^+, see Fig. 10.7), or we could have overestimated the H_2 column density with our thermal admixture model.

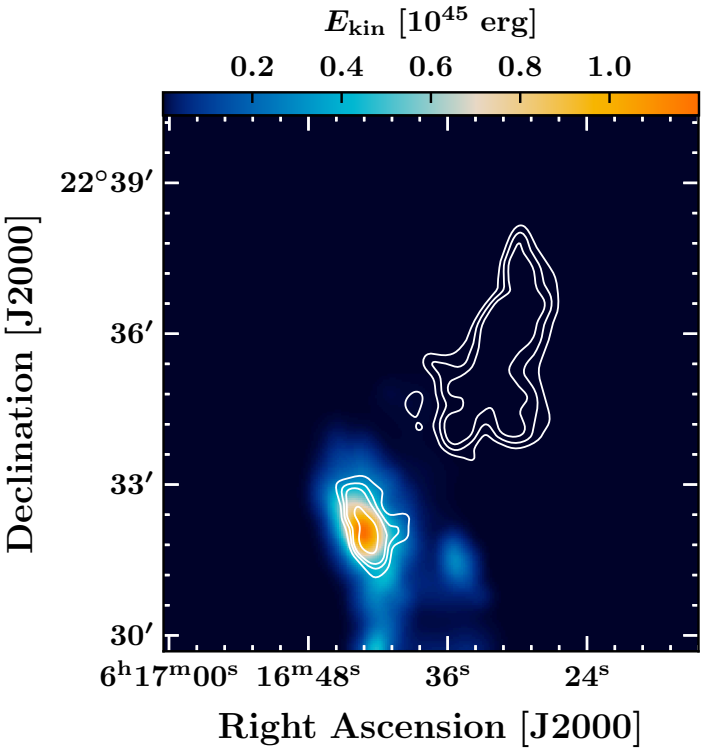

Figure 8.38 Turbulent kinetic energy measurements in the extended G region. $E_{\rm kin}$ (erg) is given by the quantity $m_{\rm H}\mathcal{A}N_{^{12}\rm CO}(\mathcal{M}_2)^2 \times 10^4$ where $N_{^{12}\rm CO}$ is the total ^{12}CO column density of the perturbed gas, $\mathcal{A}$ is the physical area of a pixel (assuming $d_{\rm IC443}$ = 1.8 kpc), $\mathcal{M}_2$ is the second moment of the ^{12}CO J=2–1 line and $m_{\rm H}$ the mass of one hydrogen atom (see text). $E_{\rm kin}$ is shown in units of 10^{45} erg (1 erg = 10^{-7} J). The maximum value towards the center of the shocked clump is 1.2×10^{45} erg. The sum over all pixels of the map is 3.4×10^{46} erg. The white contours correspond to the IRAM 30m ^{12}CO J=2–1 peak map shown in Fig. 6.10 (contour levels: 0.25, 0.35, 0.45 and 0.75 times the maximum value across the map).

Turbulent kinetic energy of the perturbed gas in the extended G region In section 8.2.3 we showed that the emission of the gas perturbed by the SNR can be separated from the emission of the quiescent molecular gas using the J=3–2/J=2–1 *vs.* J=2–1/J=1–0 ratio (see Fig. 8.19, right panel). We applied our 'opacity-corrected population diagram' method (described in section 8.2.4)

[8]Based on our estimate of the temperature of the molecular gas with ^{12}CO lines, see Fig. 8.29 and Fig. 8.36.

to the perturbed component only in order to obtain the total column density of shocked molecular gas. We then coupled the column density map with the second moment map $\mathcal{M}_2$ of the ^{12}CO J=2–1 line (Fig. 6.16) to obtain a rough estimate of the turbulent kinetic energy $E_{\rm kin}$:

$$E_{\rm kin}(x,y) = m_{\rm H}\mathcal{A}N_{^{12}{\rm CO}}(x,y)\mathcal{M}_2(x,y)^2 \times 10^4 \tag{8.42}$$

where $N_{^{12}{\rm CO}}$ is the total ^{12}CO column density of the perturbed gas, $\mathcal{A}$ is the physical area of a pixel (assuming $d_{\rm IC443} = 1.8$ kpc), $m_{\rm H}$ is the mass of one hydrogen atom and 10^4 is the adopted H_2-to^{12}CO abundance. The results are shown in Fig. 8.38 in units of 10^{45} erg. Both the main shocked clump and secondary shocked knot hold turbulent kinetic energy. The sum over the shocked knot is $2.4^{+2}_{-0.8} \times 10^{45}$ erg, and the sum over the shocked clump is $3.2^{+2.8}_{-1} \times 10^{46}$ erg, for a total of $3.4^{+3}_{-1} \times 10^{46}$ erg over the field of observations.

Adopting an initial kinetic energy $E_0 = 10^{51}$ erg for the explosion of the SN progenitor, our measurements suggest that in the extended G region, a kinetic energy $3.4^{+3}_{-1} \times 10^{-5} E_0$ is found in the form of turbulent motions at the time of the observations ($t_{\rm SNR} \sim 25 \pm 10$ kyr). This measurement is a lower boundary of the total turbulent kinetic energy injected by the SNR at the time of the observations, because the extended G region contains only a fraction of the molecular gas perturbed by the SNR blastwave (see Fig. 2.20).

- If we make the rough assumption that the molecular clumps 'B', 'C', 'D', 'E', 'F' and 'H' hold similar energies, then we find that the turbulent kinetic energy (injected by the SNR) in the fragmented molecular shell at the time of the observations is approximately $2 \times 10^{-4} E_0$.
- Alternatively, we can multiply our estimate by the ratio of the total area of the SNR divided by the area of our $10' \times 10'$ field of observation. The 2D surface of the SNR (projected on the sky) can be approximated by the sum of two hemispheres of respective diameters $\sim 30'$ and $\sim 50'$, thus our numerical factor is $[(\pi/2)(15^2 + 25^2)]/10^2 \simeq 13$. In that case, the turbulent kinetic energy in the SNR at the time of the observations is approximately $5 \times 10^{-4} E_0$.

Based on ^{12}CO J=2–1 and J=1–0 observations, Seta *et al.* (1998) estimated a total kinetic energy 6×10^{47} erg in the entire SNR, which is in agreement with our second estimate.

Comments on the interpretation of γ-ray emission in the extended G region Mass and density measurements are crucial for the interpretation of the interaction of CRs with the interstellar contents of SNRs (see Chapter 1). According to the TeV γ-ray significance map of Humensky and VERITAS Collaboration (2015), the extended G region is likely to be the primary target of interaction with high-energy CRs in the IC443 SNR. Our results put constraints on the amount of protons that are available to interact with CRs via bremsstrahlung and pion decay mechanisms. Torres *et al.* (2010) showed that the characteristics of the γ-ray spectra in IC443 suggest the interaction with two distinct molecular structures: *i.)* a lower mass cloud ($\sim$350 $M_\odot$) at distance of 4 pc from the SNR, and *ii.)* a higher mass cloud ($\sim$4000 $M_\odot$) at a distance of 10 pc. Their results were obtained from the analysis of the γ-ray spectra of the SNR over a larger field than the extended G region, yet they are consistent with out findings.

As it has been suggested by Lee *et al.* (2012), either the shocked clump or small cloud 'SC03' (or the combination of both) could correspond to the closer component, while the distant component would be the ambient cloud of Cornett *et al.* (1977). Within errorbars, the molecular masses

that we measured in the extended G region could fit with this scenario. According to our mass measurements, the small cloud 'SC03' is actually a greater reservoir of protons than the 'clump G', hence it should not be ruled out as a potential site of interactions with CRs. Fig. 8.13 shows that the errorbars on the location of the γ-ray peak are consistent with this target of interaction.

Conclusions of this section We have studied our IRAM 30m and APEX observations of ^{12}CO, ^{13}CO and C^{18}O pure rotational lines in the extended G region. Our main findings are the following:

(a) LTE radiative transfer models can reproduce the intensity ratios of the ^{12}CO, ^{13}CO and C^{18}O lines, and are consistent with a range of isotopic ratios [^{12}CO/^{13}CO]=60^{+30}_{-15}. The spread of the data points does not allow to detect nor constrain distinct excitation conditions for the different isotopologs.

(b) LTE radiative transfer models suggest an enhancement of the ^{13}CO/C^{18}O isotopic ratio, in particular towards the quiescent cloudlet. Such an enhancement might be the product of the fraction of carbon monoxide isotopologs caused by local protostars or radiative decay from X-ray irradiation in the SNR cavity.

(c) The ^{12}CO J=3–2/J=2–1 *vs.* J=2–1/J=1–0 allows to accurately separate the emission of the molecular gas perturbed by the SNR from the emission of the quiescent molecular gas.

(d) Using pixel-per-pixel LTE (opacity-corrected population diagrams) and non-LTE (`RADEX` models) methods, we measured the total ^{12}CO column density, the kinetic temperature of the gas phase and the molecular mass in the extended G region. The results are summarized in Tab. 8.8. Our mass measurements are systematically higher than in previous studies (Dickman *et al.* 1992, Lee *et al.* 2012) by virtue of our treatment of the optical depth.

(e) In the region of the IC443 SNR where the γ-ray peak has been detected (see Fig. 8.13), the total mass of shocked molecular gas is 100^{+120}_{-50} M$_\odot$ ('clump G' is identified to the combination of boxes 'C' and 'D' in Fig. 8.23). An additional 340^{+380}_{-150} M$_\odot$ of quiescent molecular gas is detected in the so-called quiescent 'cloudlet' and 'ring-like structure' (boxes 'A' and 'B'), corresponding to the small cloud 'SC03' of Lee *et al.* (2012). We also measured a total of 300^{+600}_{-200} M$_\odot$ across our $10' \times 10'$ map of the ambient cloud of Cornett *et al.* (1977).

(f) In the best scenario, a total of $\sim$ 1600 M$_\odot$ is available to interact with CRs *via* pion decay and bremsstrahlung in the extended G region. Our estimate is lowered to $\sim$ 700 M$_\odot$ if we exclude the contribution of the ambient molecular cloud of Cornett *et al.* (1977).

(g) Within the CR-ISM interaction scenario proposed by Torres *et al.* (2010), our mass measurements suggest that the small cloud 'SC03' is an adequate candidate for the interpretation of γ-ray observations in the IC443 SNR, and possibly a better candidate than the less massive shocked 'clump G'.

(h) Rough estimates of the local density (based on our total ^{12}CO column density measurements) suggest that the ^{12}CO lines are not thermalized across the ambient molecular cloud of Cornett *et al.* (1977), and only partially thermalized within the rest of the field of observations (boxes 'A', 'B', 'C', 'D').

(i) We compared our findings with the analysis of H_2 pure rotational lines towards the 'clump G' (section 8.1). Our measurements are consistent with a H_2-to-^{12}CO abundance ratio $3.8^{+1.2}_{-1.4}\times10^4$.

(j) Employing our pixel-per-pixel mass measurements of the perturbed gas component and our ^{12}CO J=2–1 second moment map of the extended G region, we estimate a turbulent kinetic energy $E_{\rm kin} = 3.4^{+3}_{-1} \times 10^{-5} E_0$ (where $E_0 = 10^{51}$ erg) in the form of turbulent motions within the fraction of the shocked molecular shell probed by our observations. We estimate a total kinetic energy $E_{\rm kin} \sim 5 \times 10^{-4} E_0$ in the entire SNR, in agreement (within $\sim$ 20%) with the results of Seta *et al.* (1998).

Chapter 9 | The dust contents of the IC443 supernova remnant

Contents

In this chapter, we aim to study the near-infrared to millimeter dust thermal emission in the IC443 SNR. Our goal is to cross-compare our results with the mass measurements obtained *via* the analysis of ^{12}CO, ^{13}CO and C^{18}O lines (described in Chapter 8), and to obtain as many additional constraints as possible to characterize the ISM in the region of the γ-ray peak (local interstellar radiation field, free-free and synchrotron relative contributions, *etc*).

Dust is a popular dark gas tracer (Grenier *et al.* 2005, Leroy *et al.* 2011) which offers the possibility to infer total column density measurements that are entirely independent of the assumptions and methods employed in Chapter 8, thus continuum observations of the IC443 SNR allow us to

address the shortcomings of our analysis of H_2 and ^{12}CO pure rotational lines (see the discussions in section 8.1.4 and section 8.2.6), although this method introduces new challenges.

In section 9.1, we present the available broadband observations in IC443 and provide a detailed description of the preliminary absolute flux calibration, background subtraction and characterization of line contamination. Section 9.2 comprises a Modified Black Body analysis of far-infrared to millimeter observations of the entire supernova remnant using the Bayesian algorithm `PPMAP` (see section 5.1.3 for a technical description), with a focus on the extended G region. In section 9.3, we perform a 'full dust model' analysis of near-infrared to millimeter observations of the extended G region, using the Hierarchical Bayesian algorithm `HerBIE` (see section 5.2 for a technical description) in combination with the THEMIS dust model. We discuss the results obtained with `PPMAP` and `HerBIE` in section 9.4.

Instrument	Central Wavelength	FWHM (″)	Spatial Coverage	peak s/n	Ref.	Continuum Contribution	Line Contribution
WISE	3.4 µm	2.1	full sky	210	*a*	VSGs, PAHs	-
WISE	4.6 µm	2.9	full sky	390	*a*	VSGs, PAHs	-
WISE	12 µm	7.6	full sky	340	*a*	VSGs, PAHs	H_2, Ne II
WISE	22 µm	13.8	full sky	320	*a*	VSGs	-
Spitzer/MIPS	24 µm	7.1	$\sim 1° \times 2°$	44	*b*	VSGs	H_2, Fe II, S I
Spitzer/MIPS	70 µm	20.7	$\sim 1° \times 2°$	25	*b*	VSGs, TEGs	O I
Spitzer/MIPS	160 µm	47.4	$\sim 1° \times 2°$	23	*b*	TEGs	C II, O I
AKARI/FIS	90 µm	78	full sky	6	*c*	TEGs	-
AKARI/FIS	140 µm	88	full sky	5	*c*	TEGs	O I
AKARI/FIS	160 µm	88	full sky	4	*c*	TEGs	C II, O I
LABOCA	870 µm	18.2	$\sim 40' \times 40'$	10	*d*	TEGs	^{12}CO J=3–2
NIKA2	1150 µm	9.7	$\sim 20' \times 20'$	28	*e*	TEGs	^{12}CO J=2–1
NIKA2	2000 µm	16.8	$\sim 20' \times 20'$	39	*e*	TEGs	^{12}CO J=1–0
VLA	330 MHz	17.3×15.8	$\sim 3° \times 3°$	12	*f*	free-free, sync.	-
VLA	74 MHz	36.5×31.8	$\sim 3° \times 3°$	6	*f*	free-free, sync.	-

Notes. 'VSGs', 'PAHs', 'TEGs', 'sync.' and 'peak s/n' respectively stand for 'very small grain', 'Polycyclic Aromatic Hydrocarbons', 'thermal equilibrium grains', 'synchrotron' and 'peak signal-to-noise ratio'. The spectral notation of the lines indicated in the last column are given in Tab 9.5.
a Wright *et al.* (2010).
b Pinheiro Gonçalves *et al.* (2011).
c Doi *et al.* (2015).
d A. Weiss, R. Güsten (MPIfR).
e Dell'Ova et al. 2020 (see Chapter 7).
f Castelletti *et al.* (2011).

Table 9.1 Summary of continuum observations towards the IC443 SNR.

9.1 | Pre-processing

9.1.1 Description of available data products

The continuum observations used throughout this chapter are listed in Tab. 9.1, in which we indicate the wavelength, angular resolution, spatial coverage, peak signal-to-noise ratio, and the

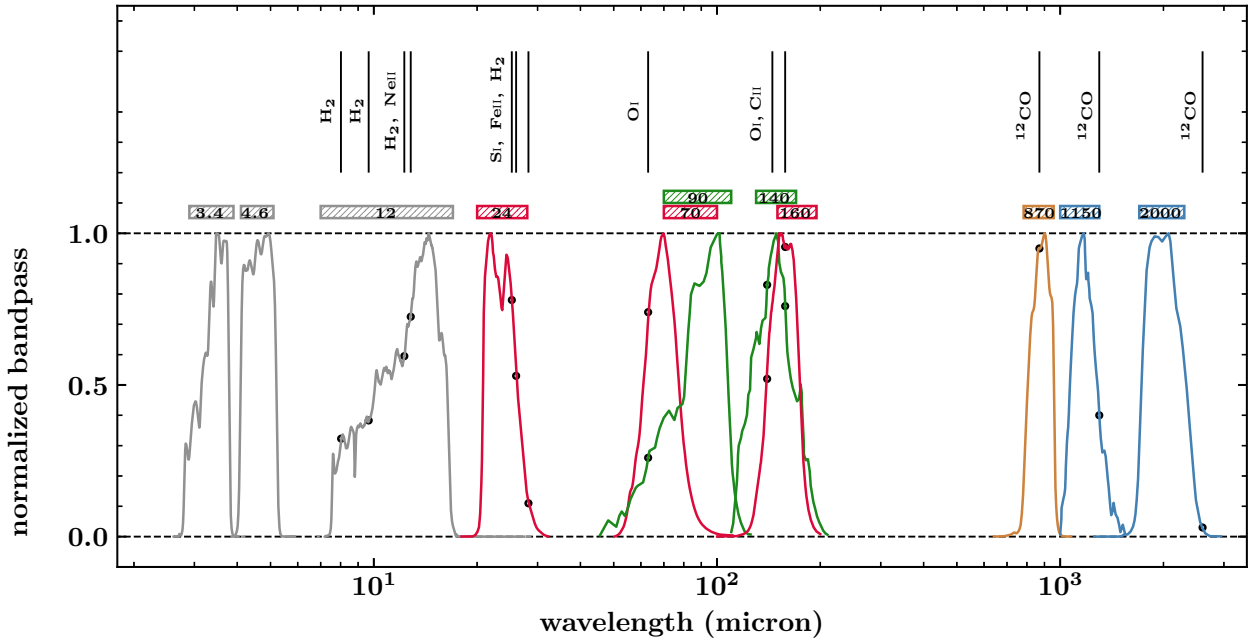

Figure 9.1 Instrumental bandpasses associated with the observations listed in Tab. 9.1: WISE photometric bands at 3.4 µm, 4.6 µm and 12 µm (in gray, Jarrett *et al.* 2011), *Spitzer*-MIPS bands at 24 µm, 70 µm and 160 µm (in red, Rieke *et al.* 2004), AKARI/FIS bands at 90 µm and 140 µm (in green, Kawada *et al.* 2007), LABOCA band at 870 µm (in yellow, Siringo *et al.* 2009) and NIKA2 bands at 1150 µm and 2000 µm (in blue, Adam *et al.* 2018). On the upper part of the figure, we indicate the main atomic, ionic and molecular lines which might contribute to the broadband flux measurements. For each line, the amplitude of the transmission is indicated by a black circle drawn on the bandpass curves.

corresponding continuum physical components that contribute to thermal emission (very small grains, thermal equilibrium grains, *etc*). Our set of observations is a mix of public archival data and new observations of the region (most notably NIKA2 observations at 1.15 mm and 2.0 mm, see Chapter 7).

In Fig. 9.1, we show the bandpasses of selected instruments between 3.4 µm and 2000 µm (the WISE 22 µm and AKARI/FIS 160 µm bands are not shown because they are redundant with the *Spitzer*/MIPS 24 µm and 160 µm bands, albeit with a worse angular resolution: *e.g.* from 47″ with *Spitzer*/MIPS to 88″ with AKARI/FIS at 160 µm). This figure also highlights the contamination of broadband measurements by ionic, atomic and molecular lines (H_2 and ^{12}CO pure rotational lines, O I, C II, *etc*, see also Fig. 5.1). We discuss and estimate the impact of line contamination in the subsection 9.1.4. In this section (9.1), we aim to fully prepare our set of continuum observations into a calibrated, scientific-ready product which can be used as an input for `PPMAP` and `HerBIE` models. We start with a description of each raw data product.

Near-infrared Observations with the wide infrared survey explorer (hereafter WISE, Wright *et al.* 2010) at 3.4 µm, 4.6 µm and 12µm offer coverage of the part of the continuum spectral energy distribution that is dominated by very small grains (VSGs) and polycyclic aromatic hydrocarbons (PAHs). We downloaded the 'WISE Atlas Image' public archival data products (both the intensity and uncertainty maps) directly from the Infrared Science Archive (IRSA). The maps are shown on the first row of Fig. 9.2. Towards near-infrared point sources, pixels are dominated by

stellar continuum emission (in particular at 3.4 μm and 4.6 μm, see Chapter 10).

Mid to far-infrared We cover the 22 μm to 160 μm wavelength range with three distinct instruments: WISE (22 μm), *Spitzer*-MIPS (Multiband Imaging Photometer for *Spitzer*: 24 μm, 70 μm, 160 μm, Pinheiro Gonçalves *et al.* 2011) and AKARI/FIS (Far Infrared Surveyor: 90 μm, 140 μm, 160 μm, Doi *et al.* 2015). These observations trace a mixture of VSGs and thermal equilibrium grains (TEGs). We downloaded these data products (both the intensity and uncertainty maps) from the Spitzer Heritage Archive (SHA, for *Spitzer*-MIPS data products) and Data ARchive and Transmission System (DARTS, for AKARI/FIS data products) public archives. The maps are shown on the second and third rows of Fig. 9.2.

Additional notes on the *Spitzer*-MIPS maps The raw *Spitzer*-MIPS 160 μm map downloaded from the SHA is characterized by strong stripe artifacts. Stripe patterns in the 160 μm are caused by sub-optimal sampling of the maps, due to a dead readout of 4 pixels in the non-contiguous MIPS array of photodetectors. A. Noriega Crespo (STScI) shared with us a 'destripped 160 μm map which looks cleaner. We checked that the destripped map can be used to perform photometric measurement *via* a pixel-per-pixel comparison of the flux. We found that the relative difference never exceeds $\sim 7\%$, which is reasonable in comparison to the rest of the systematic uncertainties associated with the absolute flux calibration of the *Spitzer*-MIPS 160 μm map (see section 9.1.2.1). Thus, we decided to use the destripped map over the raw map, because we do not want stripe patterns to propagate into our `PPMAP` and `HerBIE` final products.

(Sub)millimeter Sub-millimeter and millimeter data points are essential to trace the pure black body radiation emitted by large dust grains (*i.e.* TEGs). A. Weiss and R. Güsten (MPIfR) obtained a $40' \times 40'$ continuum map of the entire SNR molecular shell with APEX/LABOCA at 870 μm (345 GHz). We completed these sub-millimeter observations with two additional data points mapped in a $20' \times 20'$ field of view at 1.15 mm and 2.0 mm, *via* new observations of the region using the continuum camera NIKA2 installed on the IRAM 30m telescope (see Chapter 7). The maps are shown on the fourth row of Fig. 9.2.

Additional tracers In order to disentangle the contribution of thermal emission by dust grains from free-free and synchrotron continua at millimeter wavelengths, we contacted G. Castelletti who accepted to share her Very Large Array (VLA) observations of the IC443 SNR at 330 MHz and 74 MHz (Castelletti *et al.*, 2011).

9.1.2 Absolute flux calibrations

`PPMAP` and `HerBIE` require the input data products to be correctly calibrated and converted into the same unit (MJy/sr for `PPMAP`, and preferably W m^{-2} s^{-1} sr^{-1} for `HerBIE`). In the following subsections, we describe the transformations applied to our data in order to reach that goal, and the uncertainties associated with our absolute flux calibrations.

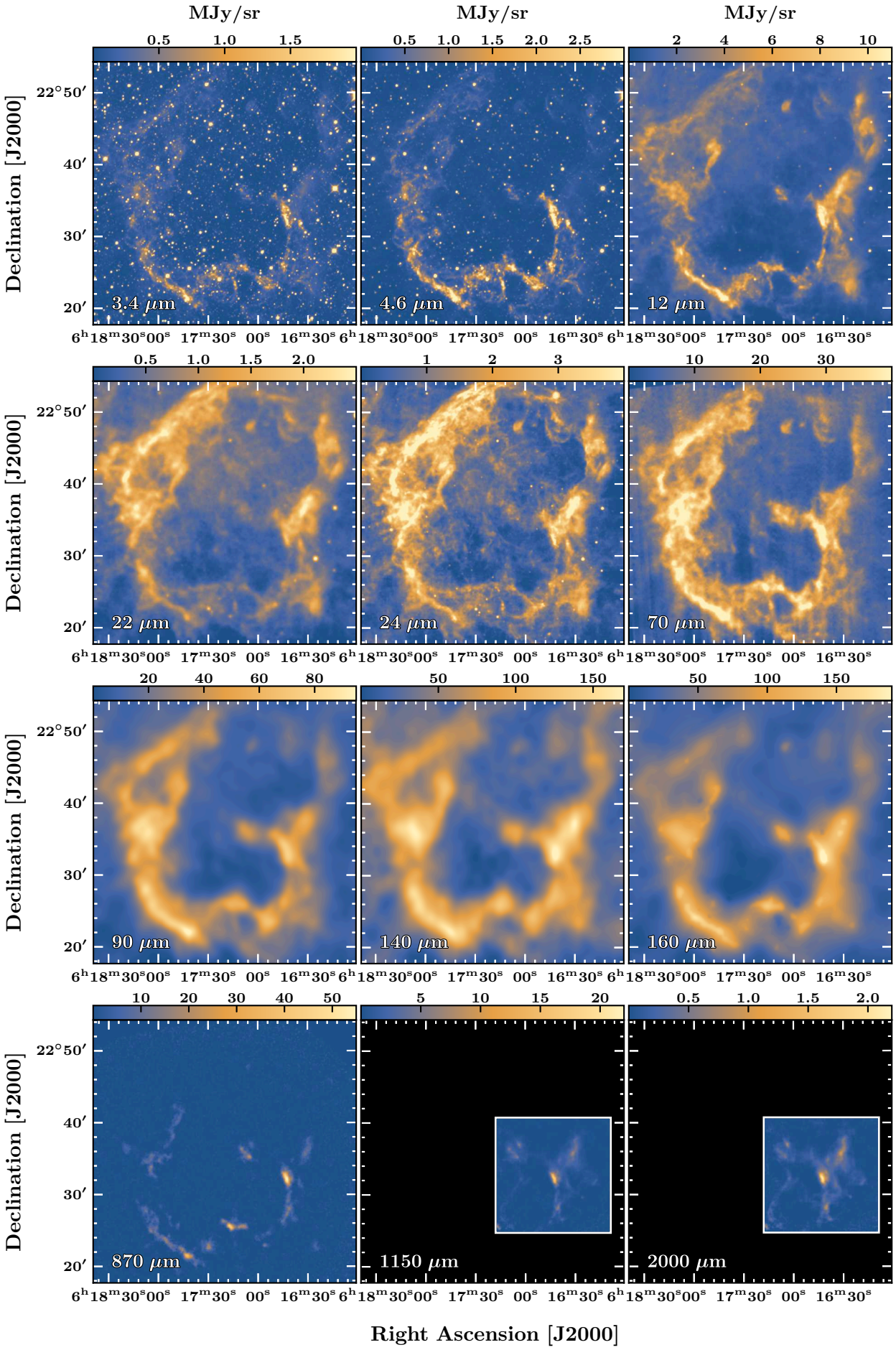

Figure 9.2 Continuum observations of the IC443 SNR. The wavelength is indicated in the bottom-left corner of each panel (the 160 μm map corresponds to *Spitzer*-MIPS data). See also Tab. 9.1.

9.1.2.1 Infrared data

***Spitzer*-MIPS and AKARI/FIS absolute flux calibrations** The *Spitzer*-MIPS and AKARI/FIS data products are shipped in the form of flux calibrated intensity maps (in units of MJy/sr). However, the Spitzer Telescope Handbook[1] warns the user that the 70 µm and 160 µm measurements are much more uncertain than the 24 µm measurement. The first *Spitzer*-MIPS receiver used Si:As photodetectors which were accurately calibrated (photometric uncertainty ∼1%, Rieke *et al.* 2004), whereas the Ge:Ga photodetectors installed on the second and third receivers had a poor photometric stability (photometric uncertainty ∼10%, Rieke *et al.* 2004). AKARI/FIS also used Ge:Ga photodetectors, and the photometric accuracy is estimated to 13% (90 µm), 10% (140 µm) and 50% (160 µm) by Shirahata *et al.* (2009) (see also Tab. 9.6).

Band	m_{ZP} [mag]	$m_{ZP,unc}$ [mag]	$f_0[F_\nu \sim \nu^0]$ [Jy]	$f_0[F_\nu \sim \nu^{-2}]$ [mag]	δm_{apc} [mag]	δm_{cal} [mag]	pixel size ($''$)
3.4 µm	20.5	0.0002	309.54	306.68	0.034	0	1.375
4.6 µm	19.5	0.0002	171.79	170.66	0.041	0	1.375
12 µm	17.5	0.0005	31.64	29.05	-0.030	0	1.375
22 µm	13.0	0.0013	8.63	8.28	0.029	0.92	1.375

Notes. m_{ZP} and $m_{ZP_{unc}}$ are respectively the zero-point magnitude and the associated uncertainty, $f_0[F_\nu \sim \nu^0]$ is the absolute flux for mag = 0 assuming a flat spectral energy distribution ($F_\nu \sim \nu^0$), and $f_0[F_\nu \sim \nu^{-2}]$ assumes that $F_\nu \sim \nu^{-2}$. The aperture correction factor and calibration correction factors are indicated by δm_{apc} and δm_{cal} (see text). These parameters are given in the section II.3 of the WISE Atlas Image user's guide and Jarrett *et al.* (2013).

Table 9.2 Calibration parameters for WISE Atlas Image photometry.

WISE absolute flux calibrations The WISE Atlas data products are delivered with fluxes expressed in 'Digital Number' (DN). WISE was designed primarily to build point source catalogs, and to our knowledge there are no official data releases for extended photometric measurements, although the user's guide[2] offers support to perform this task (see the calibration parameters in Tab. 9.2). In fact, the user's guide states that "even though the factors in Tab. 9.2 were mostly derived using point/compact-source photometry, they are also appropriate for calibrating extended/diffuse emission that can be measured in-excess of the local background level in an image". Using the parameters listed in Tab. 9.2, one can convert from DN/pixel to Jy/pixel by applying the following formulas:

$$m_{px} = m_{ZP} - 2.5\log_{10}(s_{px}) \tag{9.1}$$

where m_{px} is the magnitude measurement in a pixel, m_{ZP} the zero-point magnitude and s_{px} the background subtracted flux measured in a pixel (in units of DN/pixel). The magnitude measurement is then converted into a Jy/pixel flux f_{px} using the relation:

$$f_{px} = f_0 10^{-0.4 m_{px}} \tag{9.2}$$

[1] https://irsa.ipac.caltech.edu/data/SPITZER/docs/spitzermission/missionoverview/spitzertelescopehandbook/

[2] https://wise2.ipac.caltech.edu/docs/release

where f_0 is the absolute flux corresponding to mag = 0. The uncertainty in the zero-point flux-to-magnitude conversion is $\sim$ 1.5% for all bands (Jarrett *et al.*, 2013). We followed the method presented by Jarrett *et al.* (2011), Jarrett *et al.* (2013) and Ciesla *et al.* (2014) to produce absolute flux calibrations for each WISE Atlas data product. Jarrett *et al.* (2013) derived star formation rates of resolved galaxies using the four WISE photometric bands. They describe their absolute calibration method as follows:

1. Apply the guidelines of the WISE Preliminary Data Release Products user's guide (*i.e.* Eq. 9.1 and Eq. 9.2, using the calibration parameters listed in Tab. 9.2, and the background subtracted maps).

2. Apply an aperture correction factor $\delta m_{\rm apc}$ to correct the bias induced by PSF profile fitting calibrations (0.034, 0.041, -0.030 and 0.029 respectively at 3.4 µm, 4.6 µm, 12 µm and 22 µm, also listed in sixth column in Tab. 9.2).

3. Apply a color correction factor that accounts for the spectral signature of the source. In Tab. 9.2, we show the raw values of f_0 (assuming an isophotal spectral energy distribution, fourth column) and the values corrected for a dusty spectral energy distribution ($F_\nu \sim \nu^{-2}$, fifth column). In our absolute flux calibrations, we adopted the values corresponding to a dusty spectral energy distribution ($F_\nu \sim \nu^{-2}$).

4. Apply a magnitude correction factor to correct the calibration discrepancy between WISE photometric standard 'blue ' stars and 'red ' galaxies. This factor represents a 8% flux correction, and is only applied to the 22 µm band ($\delta m_{\rm cal}$ = 0.92, also listed in the seventh column of Tab. 9.2). *Remark:* in our study, we eventually decided not to include the WISE 22 µm map, since we put more trust in the absolute flux calibration of the *Spitzer*-MIPS 24 µm map.

Finally, Jy/pixel measurements can be converted into MJy/sr by dividing the fluxes by the area of a spatial bin (the pixel sizes are indicated in the last column of Tab. 9.2). Hence, following Eq. 9.1 and Eq. 9.2 we ultimately obtain a relation that can be used to convert from Jy/pixel to MJy/sr:

$$f_{\rm px} = 4.44 \times 10^{-17} \times f_0[F_\nu \sim \nu^{-2}] 10^{-0.4 m_{\rm px}},\ m_{\rm px} = m_{\rm ZP} - 2.5\log_{10}(s_{\rm px}) + \delta m_{\rm apc} + \delta_{\rm cal} \qquad (9.3)$$

where 4.44×10^{-17} is the area of a pixel (in radian) multiplied by 10^{-6} to convert from Jy/sr to MJy/sr, and the other parameters are given in Tab. 9.2. In this equation, $s_{\rm px}$ is the background subtracted flux (see section 9.1.3 and Tab. 9.3). Following Jarrett *et al.* (2011), we adopt a photometric uncertainty 2.4%, 2.7%, 4% and 6.2% respectively at 3.4 µm, 4.6 µm, 12 µm and 22 µm (see also Tab. 9.7).

Verifications We checked the validity of our absolute flux calibrations for WISE Atlas data products in three different ways:

1. We performed aperture photometry on 1819 points sources extracted in a 10′-diameter disk centered on the extended G region ($6^{\rm h}16^{\rm m}35^{\rm s}$, 22°35′). We then compared our magnitude measurements with WISE All-Sky catalogs of point sources (downloaded from the IRSA).

We found a satisfying agreement, in particular at 3.4 µm and 4.6 µm, although there are substantial discrepancies for a fraction of the point sources. We assume that these discrepancies are caused by the fact that the catalog measurements were performed with PSF profile-fitting photometry, which is more accurate for point sources embedded in extended emission.

2. We performed a pixel-per-pixel comparison between the *Spitzer*-MIPS map at 24 µm and the WISE Atlas map at 22 µm. We found discrepancies of the same magnitude as in '1'.

3. We performed a pixel-per-pixel comparison between the *Spitzer*-IRAC maps at 3.6 µm and 4.5 µm, and the WISE Atlas maps at 3.4 µm and 4.6 µm. We found discrepancies of the same magnitude as in '1'.

9.1.2.2 LABOCA, NIKA2 and VLA data

Our reduced LABOCA, NIKA2 and VLA data products are already calibrated in units of Jy/beam. We convert the fluxes from Jy/beam to W m^{-2} s^{-1} sr^{-1} *via* the following relation:

$$I_\nu[\mathrm{W\ m^{-2}s^{-1}sr^{-1}}] = I_\nu[\mathrm{Jy/beam}] \times 10^{-26} \times \frac{4\ln(2)}{\pi\theta_{\mathrm{min}}\theta_{\mathrm{maj}}} \tag{9.4}$$

where θ_{min} and θ_{maj} are the beam sizes along the minor and major axes (in radian), and 10^{-26} is the conversion factor from Jansky (Jy) to W m^{-2} s^{-1} sr^{-1}. The beam sizes are indicated in Tab. 9.1 for each instrument. The VLA data products are the only products with $\theta_{\mathrm{min}} \neq \theta_{\mathrm{maj}}$, because they were obtained *via* interferometric observations (Castelletti *et al.*, 2011).

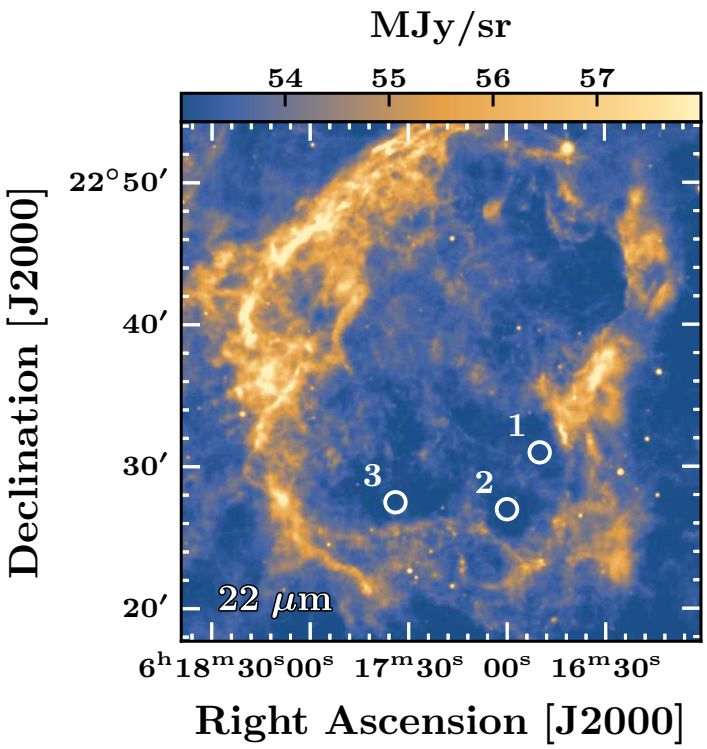

Figure 9.3 Raw (non background-subtracted) *Spitzer*-MIPS map of the IC443 SNR at 24 µm (Pinheiro Gonçalves *et al.*, 2011). White circles indicate the positions at which we measured the diffuse background emission in all infrared maps (*Spitzer-MIPS*, WISE Atlas and AKARI/FIS): (1) 6$^{\mathrm{h}}$16$^{\mathrm{m}}$50$^{\mathrm{s}}$, 22°31′; (2) 6$^{\mathrm{h}}$17$^{\mathrm{m}}$, 22°27′; (3) 6$^{\mathrm{h}}$17$^{\mathrm{m}}$34$^{\mathrm{s}}$, 22°27′30″ (J2000). Background emission measurements are shown in Tab. 9.3.

Instrument	Band	(1) $6^h16^m50^s$, 22°31′		(2) 6^h17^m, 22°27′		(3) $6^h17^m34^s$, 22°27′30″	
	(μm)	F_ν^{bg}	F_ν^{bg}/F_ν^{max}	F_ν^{bg}	F_ν^{bg}/F_ν^{max}	F_ν^{bg}	F_ν^{bg}/F_ν^{max}
WISE	3.4	8.868 DN	0.11	7.895 DN	0.10	17.25 DN	0.21
WISE	4.6	14.31 DN	0.10	13.96 DN	0.10	17.63 DN	0.12
WISE	12	780.5 DN	0.69	774.3 DN	0.68	774.0 DN	0.68
WISE	22	258.4 DN	0.99	258.2 DN	0.99	258.2 DN	0.99
Spitzer-MIPS	24	52.97 MJy/sr	0.88	52.87 MJy/sr	0.87	52.95 MJy/sr	0.88
Spitzer-MIPS	70	26.73 MJy/sr	0.19	27.74 MJy/sr	0.19	25.42 MJy/sr	0.18
Spitzer-MIPS	160	118.4 MJy/sr	0.38	103.3 MJy/sr	0.33	88.35 MJy/sr	0.29
AKARI/FIS	90	30.51 MJy/sr	0.28	30.62 MJy/sr	0.28	32.02 MJy/sr	0.30
AKARI/FIS	140	96.12 MJy/sr	0.37	93.33 MJy/sr	0.36	86.80 MJy/sr	0.33
AKARI/FIS	160	118.6 MJy/sr	0.34	106.3 MJy/sr	0.30	91.30 MJy/sr	0.26

Notes. Angular positions are in J2000 (shown on Fig. 9.3). F_ν^{bg} is the diffuse background emission measured in a 30″ disk, and F_ν^{max} is the maximum flux measured in the extended G region.

Table 9.3 Diffuse background flux measurements.

9.1.3 Background subtraction

Our raw WISE Atlas, *Spitzer*-MIPS and AKARI/FIS data products are characterized by nonzero background fluxes. Nonzero background emission can be caused either by physical processes (such as zodiacal light, see next paragraph) or introduced as an arbitrary digital number offset when a mosaic is generated from a combination of individual frames with distinct levels (in the case of WISE Atlas data products). Thus, background subtraction is required to perform a correct analysis of the spectral energy distribution of the thermal emission produced by dust associated with the IC443 SNR. We describe our method in the next paragraphs.

Zodiacal light Zodiacal diffuse emission produced by interplanetary dust particles is the dominant background radiation in the mid-infrared, and extends to the far-infrared range (Reach 1988, Reach *et al.* 1996). For *Spitzer*-MIPS data products, the estimated zodiacal fluxes are indicated in the headers of the `FITS` files (45.63 MJy/sr, 13.23 MJy/sr and 2.678 MJy/sr respectively at 24 μm, 70 μm and 160 μm). We experimented with these values and found that they do not entirely remove the background emission in the *Spitzer*-MIPS image. The residual flux might be related to foreground Galactic emission.

Systematic background subtraction The *Spitzer* `FITS` data products are the only ones that include an estimate of the zodiacal light written in the header[3]. The estimate is an average measurement over the entire field of observations, with no additional informations on time variability or gradient across the map.

Since *i.)* we do not have measurements of the zodiacal light for AKARI/FIS maps, *ii.)* the background emission in *Spitzer*-MIPS maps is greater than the zodiacal light estimates indicated in the `FITS` headers and *iii.)* the background emission is completely arbitrary in WISE Atlas maps, we decided to adopt a systematic background subtraction procedure that we applied to all

[3]The zodiacal light was measured by *Spitzer* during dedicated observations. See Tab. 4.1 in https://irsa.ipac.caltech.edu/data/SPITZER/docs/irs/irsinstrumenthandbook/IRS_Instrument_Handbook.pdf.

our infrared data products. We measured the background towards three distinct positions where we assume that the thermal contribution from dust that is physically associated with the SNR is zero. The positions are indicated in Fig. 9.3, in which we use the raw *Spitzer*-MIPS map at 24 μm as a reference. In Tab. 9.3, we indicate the results obtained in a disk of size 30″.

We checked that the variation of the measurements is negligible if we modify the size of the disk by ±10″. There are discrepancies (±10%) for the results at 3.4 μm and 4.6 μm because the WISE Atlas maps are crowded with bright, near-infrared point sources. There are also discrepancies (±10%) at 160 μm, because the diffuse background emission is not uniform across the frame (it is minimal towards the 3rd position both in *Spitzer*-MIPS and AKARI/FIS maps).

9.1.4 Broadband contamination

Instrument	Spectral Coverage	FWHM (″)	Spatial Coverage	Position (J2000)	Ref.	Line(s) of interest
IRS	5.2-37.0 μm	6	∼ 2′ × 2′	$6^h16^m42^s$, 22°31′45″	*a*	H_2, Ne II, S I, Fe II
PACS (B2A)	55-72 μm	9	∼ 1′ × 1′	$6^h16^m42^s$, 22°31′55″	*b*	O I
PACS (R1)	103-190 μm	11.5	47″ × 47″	$6^h16^m42^s$, 22°31′55″	*b*	O I, C II
EMIR (E090)	108-116 GHz	22.5	10′ × 10′	$6^h16^m35^s.5$, 22°35′	*c*	^{12}CO J=1–0
EMIR (E230)	228-236 GHz	11.2	10′ × 10′	$6^h16^m35^s.5$, 22°35′	*c*	^{12}CO J=2–1
FLASH345	342-348 GHz	19.2	10′ × 10′	$6^h16^m35^s.5$, 22°35′	*c*	^{12}CO J=3–2

Notes. The observations listed in this table were performed with *Spitzer*/IRS, *Herschel*/PACS, the IRAM 30m telescope EMIR receivers, and the APEX telescope FLASH345 receivers. The spectral notation of the lines indicated in the last column are given in Tab 9.5.
a Neufeld *et al.* (2007).
b Ossenkopf (2007).
c Dell'Ova *et al.* (2020). See also Chapter 6.

Table 9.4 Summary of spectral line observations towards the IC443 SNR.

9.1.4.1 Broadband contamination by ionic, atomic and molecular lines

An analysis of the near-IR to millimeter spectral energy distribution needs to account for non-broadband processes, which can be either subtracted and/or introduced as systematic uncertainties (Galliano *et al.*, 2018). Fig. 9.1 shows that several ionic, atomic and molecular lines are expected to contribute to the flux measured by broadband observations performed by WISE, *Spitzer*-MIPS, AKARI/FIS, LABOCA and NIKA2. Previous studies of the region have shown that the H_2 pure rotational lines are bright within the molecular shell of the SNR (∼ 10^{-3} erg cm^{-2} s^{-1} sr^{-1}, *e.g.* Cesarsky *et al.* 1999, Neufeld *et al.* 2007, Shinn *et al.* 2011, Reach *et al.* 2019, Kokusho *et al.* 2020), as well as [O I], [C II] and several other mid infrared lines (*e.g.* Burton *et al.* 1990, Oliva *et al.* 1999, Rho *et al.* 2001, Haas *et al.* 2003). In fact, Oliva *et al.* (1999) concluded that the observed IRAS flux in the 12 μm and 25 μm bands are saturated by strong [Ne II] and [Fe II] lines in the southern rim of the remnant. Therefore, it is clear that our infrared broadband measurements are sensitive to these spectral lines. We evaluate this issue in the following developments.

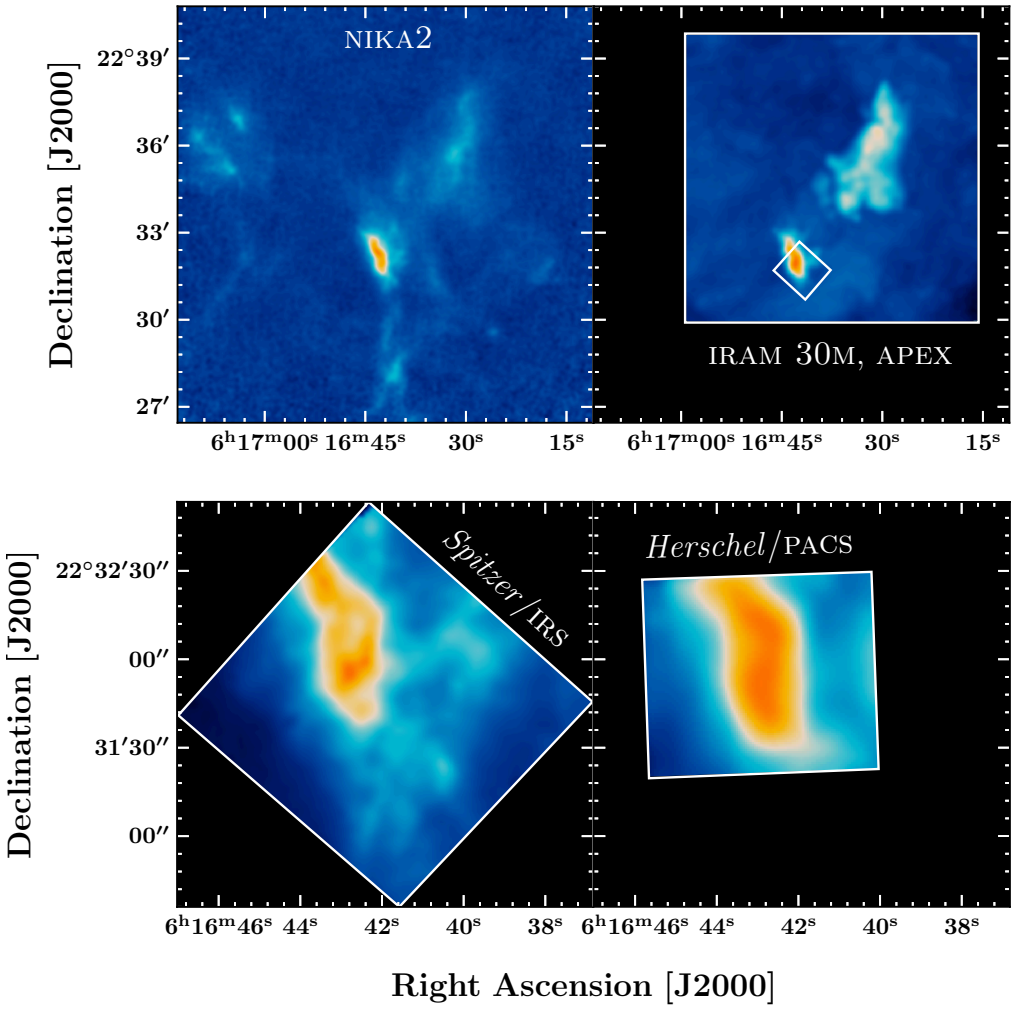

Figure 9.4 NIKA2 (top-left: 1.15 mm map), IRAM 30m (top-right: ^{12}CO J=2–1 map), *Spitzer*/IRS (bottom-left: H_2 S(1) map) and *Herschel*/PACS (bottom-right: [O I] 63 µm map) fields of observation. The smaller white box on the top-right panel represents the location of the *Spitzer*/IRS field of observations with respect to our IRAM 30m and APEX 10′ × 10′ maps.

Spectral-line observations To estimate the contribution of the lines, we can rely on several observations:

– Firstly, our $10' \times 10'$ IRAM 30m and APEX observations of the extended G region (see Chapter 6) can be used to determine the contribution of ^{12}CO lines to the LABOCA and NIKA2 continuum maps.

Additionally, both the *Spitzer* and *Herschel* space observatories mapped several near-IR and FIR lines towards the IC443G shocked clump (Pilbratt *et al.*, 2010):

– Neufeld *et al.* (2007) performed observations with *Spitzer*/IRS in a $\sim 2' \times 2'$ field of view between 5.2 µm and 37 µm.

– Ossenkopf (2007) performed observations in a $\sim 1' \times 1'$ field of view with the *Herschel* Photodetector Array Camera and Spectrometer (Poglitsch *et al.*, 2010).

We provide a summary of the observations in Tab. 9.4, and the respective fields of observations are shown in Fig. 9.4. This set of infrared spectral observations should allow us to determine the contribution of the H_2, Ne II, Fe II, S I, O I and C II lines to the broadband flux maps towards the shocked clump. These observations were performed in relatively small fields of view (with respect to our $10' \times 10'$ maps, see Fig. 9.4), but the shocked clump is likely to be the region in which the contamination of broadband measurements by infrared spectral lines is the most critical (due to the locally increased kinetic temperature and enhanced collisional excitation). Therefore, we aim to estimate the contribution of near-IR and FIR lines towards the shocked clump in order to use it as an upper limit on the contamination of the flux across our entire WISE, *Spitzer*-MIPS and AKARI/FIS maps.

Average estimate The width in frequency $\Delta\nu_{\rm line}$ of the spectral lines listed in Tab. 9.4 are negligible with respect to the spectral bandwidth of our broadband instruments ($\Delta\nu_{\rm line} \ll \Delta\nu_{\rm broadband}$). Under this assumption, for any broadband flux measurement the brightness F_ν (MJy/sr) contributed by a spectral line characterized by a velocity-integrated intensity W_ν (either in erg cm^{-2} s^{-1} sr^{-1} or K km s^{-1}) at a wavelength λ_{ij} is given by:

$$F_\nu = \frac{T(\lambda_{ij}) W_\nu}{\mathcal{B}} \tag{9.5}$$

where $T(\lambda_{ij})$ is the transmission of the bandpass at wavelength $\lambda = \lambda_{ij}$ (shown in the fourth column of Tab. 9.5) and $\mathcal{B}$ (Hz) is the bandwidth of the instruments (*e.g.* a few GHz for LABOCA). We measured $\mathcal{B}$ for each instrumental bandpass shown in Fig. 9.1 using Simpson's rule (*i.e.* we measured the areas below the curves with the `Python` module `scipy.integrate.simps`). We then started our evaluation of the broadband contamination by spectral lines with an average estimate over the extent of the *Spitzer*/IRS field of observations, except for the O I and C II spectral-line maps which are restricted to smaller fields (that is, smaller than our $10' \times 10'$ field of observations, see Fig. 9.4).

We estimate the *average* contribution C of spectral lines to broadband measurements *via* the following ratios, measured either in the *Spitzer*/IRS or *Herschel*/PACS fields of observations:

$$C = \overline{F_\nu^{\rm line}} / \overline{F_\nu^{\rm BB}}, \quad \sigma(C) = \sigma(F_\nu^{\rm line}) / \overline{F_\nu^{\rm BB}} \tag{9.6}$$

Line		Wavelength	Transmission	$\overline{F_\nu}$	$\sigma(F_\nu)$	Contribution		
		(μm)	$T(\lambda_{ij})$	(MJy/sr)	(MJy/sr)	(%)	band	(μm)
H_2 S(4)	J=6–4	8.0251	0.32	0.7	1.1	≤ 8	WISE	12
H_2 S(3)	J=5–3	9.6649	0.38	1.8	2.3	≤ 17	WISE	12
H_2 S(2)	J=4–2	12.2786	0.60	0.81	1.1	≤ 8	WISE	12
H_2 S(0)	J=2–0	28.2188	0.11	0.018	0.032	≤ 0.65	MIPS	24
Ne II	$^2P^0_{1/2}$ – $^2P^0_{3/2}$	12.8149	0.73	0.060	0.070	≤ 0.64	WISE	12
S I	$^3P_1$ – $^3P_2$	25.2490	0.79	0.15	0.38	≤ 6.8	MIPS	24
Fe II	$^6D_{7/2}$ – $^6D_{9/2}$	25.9882	0.52	0.12	0.13	≤ 3.2	MIPS	24
O I	$^3P_1$ – $^3P_2$	63.2274	0.74	58	32	50 ± 30	MIPS	70
O I	$^3P_0$ – $^3P_1$	145.6262	0.79	6.1	1.3	3 ± 1	MIPS	160
C II	$^2P_{3/2}$ – $^2P_{1/2}$	157.8501	0.96	15	6.2	7 ± 3	MIPS	160
^{12}CO	J=3–2	867.5636	0.95	5.4	4.1	20 ± 15	LABOCA	870
^{12}CO	J=2–1	1301.304	0.40	0.63	0.49	≤ 18	NIKA	1150
^{12}CO	J=1–0	2602.558	0.02	0.0030	0.0020	≤ 0.7	NIKA	2000
O I	$^3P_1$ – $^3P_2$	63.2274	0.25	18	9.9	20 ± 10	AKARI/FIS	90
O I	$^3P_0$ – $^3P_1$	145.6262	0.97	5.3	1.1	3 ± 1	AKARI/FIS	140
C II	$^2P_{3/2}$ – $^2P_{1/2}$	157.8501	0.71	7.9	3.3	5 ± 2	AKARI/FIS	140

Notes. See also Fig. 9.1 for a graphic representation of the spectral lines listed in this table (and the corresponding bandpasses). $\overline{F_\nu}$ and $\sigma(F_\nu)$ are respectively the mean and standard deviation of the flux produced by the lines and measured by broadband observations (see Eq. 9.5). These two statistical quantities are measured in the *Spitzer*/IRS field of observation (see Fig. 9.4, bottom-left panel), except for the O I and C II lines for which the measurements are performed on smaller fields of observation (see Fig. 9.4, bottom-right panel). The contribution in percent is calculated based on the ratio $F_\nu^{\rm line}/F_\nu^{\rm BB}$, where $F_\nu^{\rm line}$ is the quantity in the fifth column, and $F_\nu^{\rm BB}$ is the background subtracted broadband flux (see also Eq. 9.6). The errorbars correspond to $\pm 1\sigma(F_\nu)$.

Table 9.5 Spectral line average contribution measurements.

where $\overline{F_\nu^{\rm line}}$ and $\overline{F_\nu^{\rm BB}}$ are respectively the mean line and broadband fluxes (spatial averages over the field of observation), and $\sigma(F_\nu^{\rm line})$ is the standard deviation of the line flux. $F_\nu^{\rm BB}$ is directly measured on the background subtracted continuum maps (shown on Fig. 9.2), and $F_\nu^{\rm line}$ is measured *via* Eq. 9.5. The results of this analysis are shown in Tab. 9.5 for all lines, including the ^{12}CO J=1–0, J=2–1 and J=3–2 lines (also measured in the *Spitzer*/IRS field of observations to allow meaningful comparison with the rest of the lines). The estimated contribution of the lines is indicated in the seventh column. In cases where $\sigma(F_\nu^{\rm line})$ is approximately equal or greater than $\overline{F_\nu^{\rm line}}$, we indicate the upper limit of the contribution.

Comments on the results. We found that on the average, some of the spectral lines investigated in this section significantly contribute to our broadband continuum maps in IC443G:

– Most notably, the *Spitzer*-MIPS 70 μm and AKARI/FIS 90 μm maps are strongly affected by the [O I] 63 μm line (respectively $C_{\rm MIPS} = 50 \pm 30$ % and $C_{\rm FIS} = 20 \pm 10$ %). However, the strength of the [O I] line is non-uniform and is likely to decrease as the distance to the shocked molecular shell increases (in fact, the *Herschel*/PACS observations shown in the bottom-right panel in Fig. 9.4 confirm this trend).

– The *Spitzer*-MIPS 160 μm and AKARI/FIS 140 μm maps are (approximately) equally affected by the sum of the [O I] 145 μm and [C II] lines ($C \simeq 10 \pm 3$ %).

– The WISE 12 μm band is also significantly affected by H_2 S(2), S(3) and S(4) pure rotational lines (the sum of the lines yields $C \leq 35$ %). At $\lambda = 17.0348$ μm, the S(1) lines is not detected at all by the WISE bandpasses (the transmission is $\ll 1$).

– The ^{12}CO J=3–2 and J=2–1 lines contribute to the LABOCA 870 μm ($C = 20 \pm 15$ %) and NIKA2 1.15 mm measurements ($C \leq 18$ %). The NIKA2 2.0 mm band is virtually unaffected by the ^{12}CO J=1–0 band, because the transmission is negligible ($T(115\ \mathrm{GHz}) = 0.02$).

– The rest of the lines are characterized by relatively lower contributions ($C \ll 10$ %). However, the sum of the [S I] and [Fe II] represents $\sim$ 10 % of the *Spitzer*-MIPS 24 μm flux towards the inner region of the shocked clump.

A general conclusion of this analysis is that the contribution of spectral lines to the broadband continuum maps is (significantly) spatially variable. The line fluxes increase towards the shocked molecular shell, in particular the shocked clump G. Since the spatial coverage of the IC443 SNR is restricted to a $\sim 1' \times 1'$ field of observations for all the infrared lines, it is not possible to correctly account for spatial variations of the line intensities. As a consequence, we cannot accurately correct the contribution of all lines across the entire extent of our continuum maps. To take into account this issue, we will apply pixel-per-pixel corrections for ^{12}CO lines in the $10' \times 10'$ field of observations, and (spatially) *average* correction factors for the rest of the lines. The average correction factors are based on the mean of the line contribution across the smaller fields of observations. In addition, we will introduce systematic uncertainties associated with our correction of the broadband flux measurements to reflect the spatial variations of the line intensities.

^{12}CO lines: pixel-per-pixel estimate Using our $10' \times 10'$ ^{12}CO spectral line maps (see Chapter 6), we can perform a more accurate estimate of the broadband contamination of our LABOCA and NIKA2 maps in a significant fraction of the fields of observation (more than 50% of the area covered by NIKA2). Using the same assumptions as in the previous paragraph (see Eq. 9.5), we performed a pixel-per-pixel measurement of the contributions of ^{12}CO J=3–2 and J=2–1 lines. The intercalibration uncertainties associated with these pixel-per-pixel comparisons are minimal, since the observations were obtained with the same telescopes (the IRAM 30m for ^{12}CO J=2–1 and NIKA2 continuum observations, and the APEX telescope for ^{12}CO J=3–2 and LABOCA continuum observations). The results are shown in Fig. 9.5, we find that:

– The contamination of the (sub)millimeter continuum fluxes by ^{12}CO lines increases towards the shocked molecular shell. It is maximal in the shocked clump G.

– The ^{12}CO J=3–2 line contributes to the LABOCA 870 μm continuum map up to $C \sim 55$% towards the shocked molecular clump G, and $C \sim 30$% towards the 'quiescent cloudlet' (see sect. 6.2.1 for a description of the morphological structures).

– The ^{12}CO J=2–1 line contributes to the NIKA2 1.15 mm continuum map up to $C \sim 45$% towards the southern chunk of the shocked molecular shell ($C \sim 35$% within the clump G), and down to $C \sim 5 - 15$% towards the quiescent cloudlet.

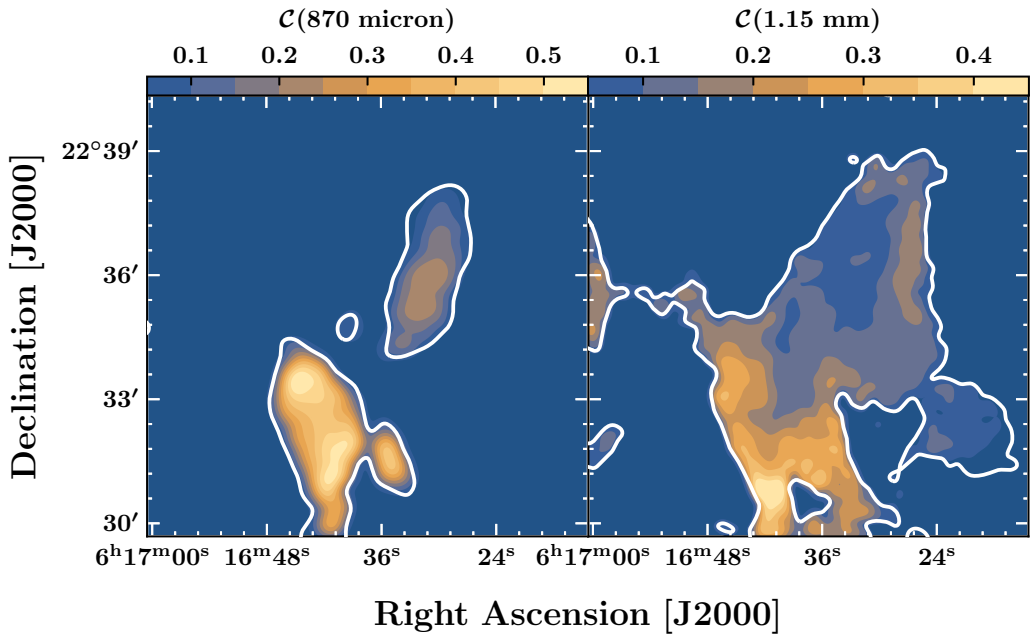

Figure 9.5 LABOCA (870 µm, left panel) and NIKA2 (1.15 mm, right panel) contamination maps. The quantity shown by filled contours is the pixel value of the proportion $F_\nu^{\rm line}/F_\nu^{\rm BB}$, where $F_\nu^{\rm line}$ is the ^{12}CO J=3–2 (for LABOCA) or J=2–1 (for NIKA2) line flux measured by the broadband instrument (see Eq. 9.5) and $F_\nu^{\rm BB}$ is the flux measured in the continuum map. White contours show the area where $F_\nu^{\rm BB} \geq 3\sigma$, where σ is the noise.

9.1.5 Convolution and spatial resampling

`HerBIE` requires the input maps to be convolved to the same angular resolution and spatially resampled on the same grid. For that reason, we decided not to include the AKARI/FIS maps (angular resolution $\sim$ 88″) and restricted our `HerBIE` input infrared data points to the WISE Atlas and *Spitzer*-MIPS data products. Therefore, we are limited by the angular resolution of the *Spitzer*-MIPS 160 µm (47.4″). We describe our method in the following subsection.

9.1.5.1 Method

The `Python` library offers two modules which can work on `FITS` files and fulfill our needs:

– The `astropy.convolution` functions `convolve` and `Gaussian2DKernel`. We generated gaussian kernels of suited size using the function `Gaussian2DKernel`, and then convolved all maps with the function `convolve` (Astropy Collaboration *et al.* 2013, Astropy Collaboration *et al.* 2018).

– We then reprojected all maps on the same spatial grids (pixel size 15.8″, *i.e.* one third of the angular resolution) using the function `reproject_exact` of the module `reproject`. The `reproject_exact` function uses the World Coordinate System informations stored in the headers of the `FITS` files and then uses a flux-conserving 'spherical polygon intersection algorithm' to re-grid the data on a reference frame (Robitaille, 2018).

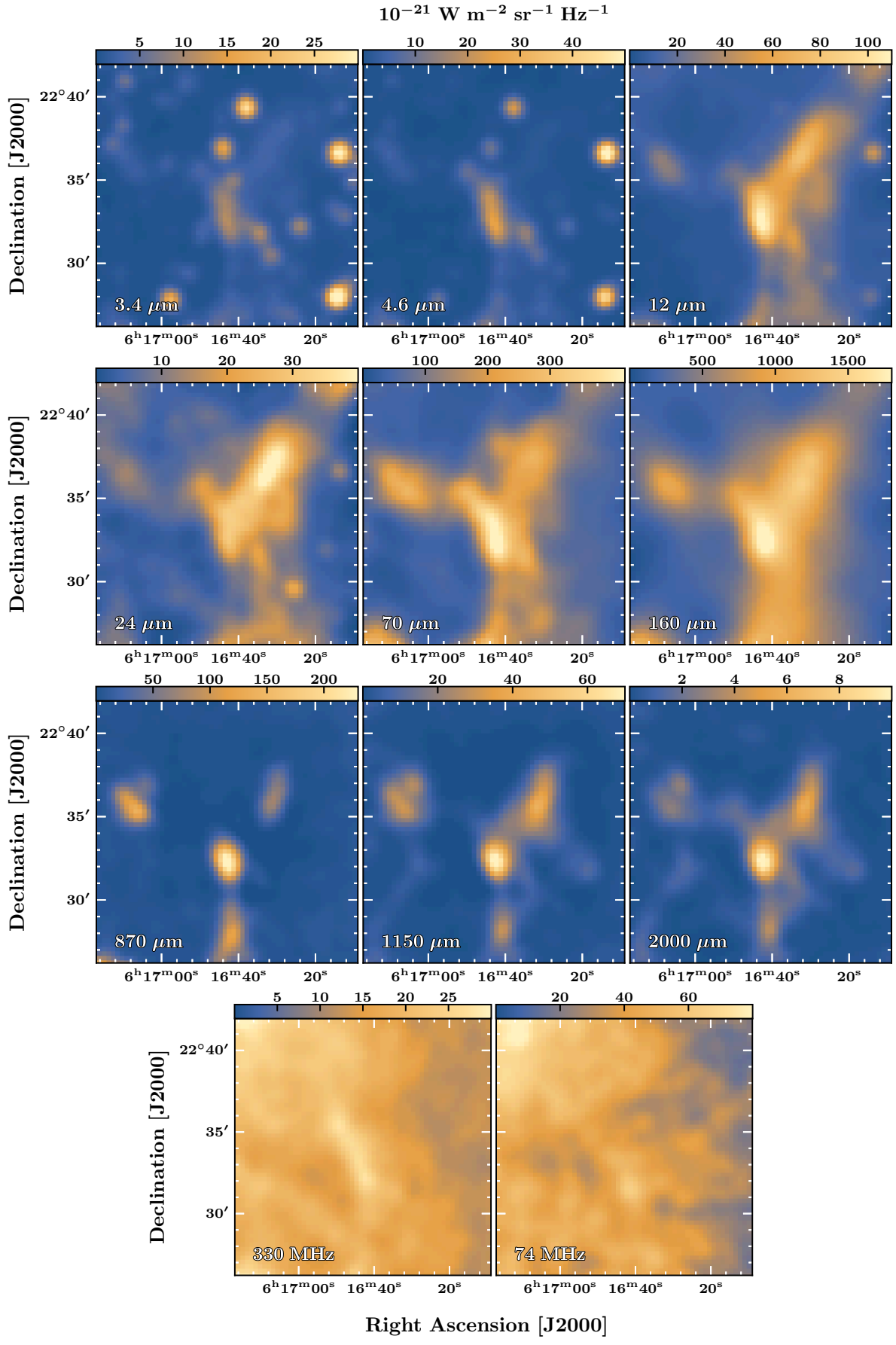

Figure 9.6 Background subtracted, decontaminated, convolved, spatially resampled continuum observations of the IC443 SNR (16′×16′ `HerBIE` input maps, see section 9.1.5.2). The wavelength is indicated in the bottom-left corner of each panel (the 160 μm map corresponds to *Spitzer*-MIPS data). See also Tab. 9.1 and Fig. 9.2 for comparison.

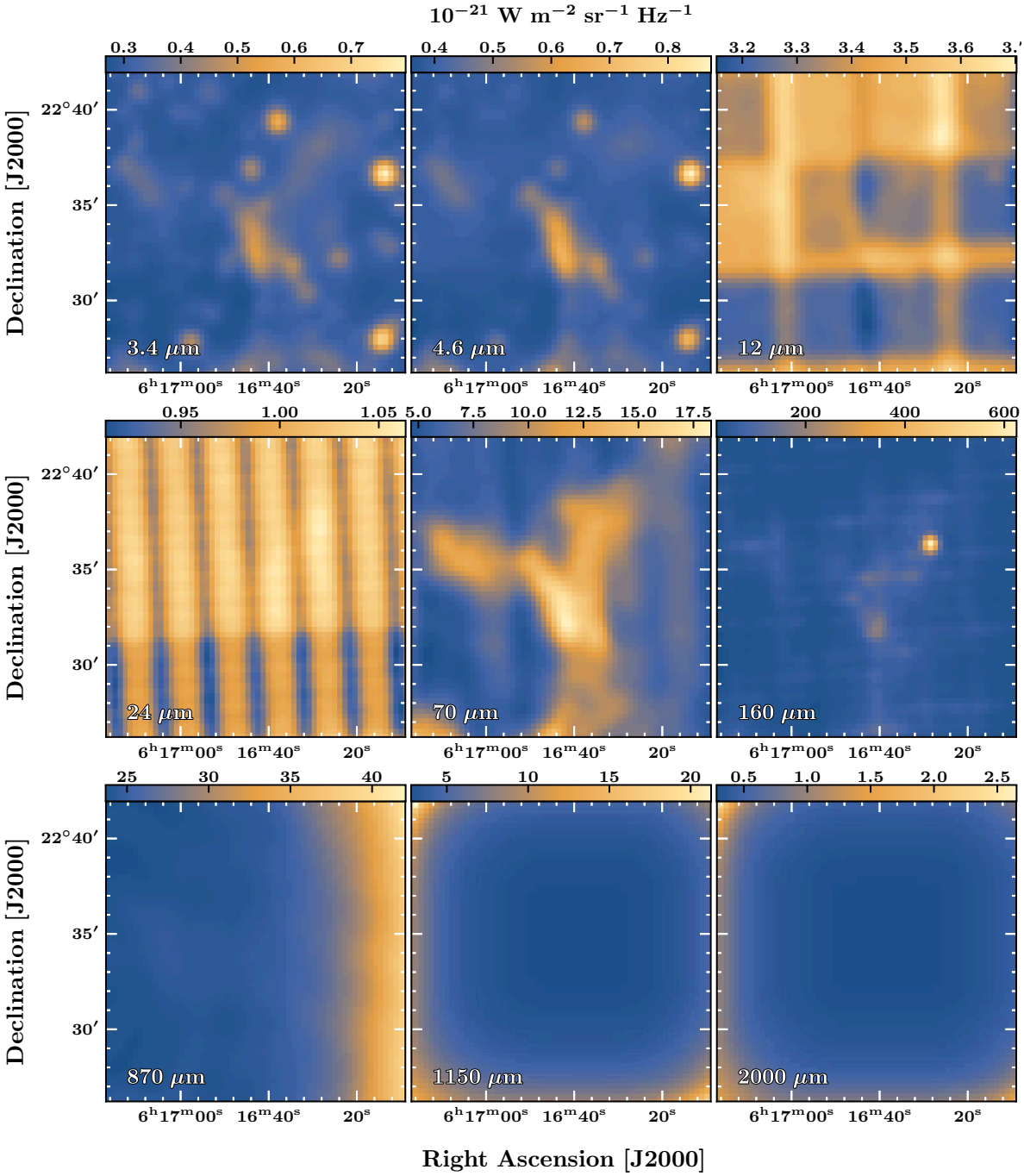

Figure 9.7 Convolved and spatially resampled noise maps of continuum observations of the IC443 SNR (16′ × 16′ `HerBIE` input noise maps, see section 9.1.5.2). The wavelength is indicated in the bottom-left corner of each panel (the 160 μm map corresponds to *Spitzer*-MIPS data). See also Tab. 9.1 and Fig. 9.6.

9.1.5.2 Summary, PPMAP and HERBIE datasets

Instrument	Central Wavelength	FWHM ($''$)	Spatial Coverage	C (%)	σ_{cal} (%)	σ_{bg} (%)	σ_{line} (%)	σ_{tot} (%)
Spitzer/MIPS	70 μm	20.7	$\sim 1^\circ \times 2^\circ$	50	10	1	30	32
AKARI/FIS	90 μm	78	full sky	20	13	2	10	17
AKARI/FIS	140 μm	88	full sky	8	10	4	3	11
Spitzer/MIPS	160 μm	47.4	$\sim 1^\circ \times 2^\circ$	10	10	9	4	14
LABOCA	870 μm	18.2	$\sim 40' \times 40'$	20†	15	0	15	21
NIKA2	1150 μm	9.7	$\sim 20' \times 20'$	10†	15	0	8	17
NIKA2	2000 μm	16.8	$\sim 20' \times 20'$	0	15	0	0	15

Notes. C corresponds to the average estimated contribution of the lines. The corrected flux is given by $(1 - C)F_\nu$, where F_ν is the raw flux. The quantities σ_{cal}, σ_{bg} and σ_{line} are the systematic uncertainties associated with the absolute flux calibration, background subtraction and line contribution, and σ_{tot} is the total systematic uncertainty, given by $(\sigma_{cal}^2 + \sigma_{bg}^2 + \sigma_{line}^2)^{1/2}$.

† The contribution of the lines to the LABOCA 870 μm and NIKA2 1150 μm maps is determined in each pixel across our $10' \times 10'$ observations of the region (see Fig. 9.5), and set either to zero or to the average value outside of the $10' \times 10'$ area (see text).

Table 9.6 PPMAP input dataset.

We have performed absolute flux calibrations (section 9.1.2) and background subtraction (section 9.1.3) of our continuum observations; we studied the broadband contamination by spectral lines (section 9.1.4) and adopted a method to convolve each map to the same angular resolution and intercalibrate the data products onto the same spatial grid (section 9.1.5.1). We can also estimate the total systematic uncertainty associated with each map, which is based on *i.)* the uncertainty on the absolute flux calibration (see section 9.1.2), *ii.)* the uncertainty on the background subtraction (inferred from discrepancies in Tab. 9.3) and *iii.)* the uncertainty on the measurement of the line contribution (inferred from the uncertainties in Tab. 9.5). We finally have all the required informations to produce input FITS files both for PPMAP and HerBIE. Based on the following remarks, we produced two distinct datasets:

– PPMAP can only model the thermal emission of TEGs and does not require to degrade the angular resolution of the maps. Therefore, we produced a first dataset that comprises the *Spitzer*-MIPS, AKARI/FIS, LABOCA and NIKA2 calibrated, background subtracted, decontaminated continuum maps at optimal resolution (see Tab. 9.6, Fig. 9.2). Tab. 9.6 contains the systematic uncertainties that we estimated for each map. This dataset covers the wavelength range 70-2000 μm with an angular resolution 9.7$''$-88$''$ (the average angular resolution is 39.8$''$). It is possible that the *Spitzer*/MIPS 70 μm maps also partially traces the non black body emission of VSGs, we will experiment with this issue in section 9.2. The dataset covers the entire SNR in 70-870 μm range, and only the extended G region in the 70-2000 μm range (limited by NIKA2 maps).

– HerBIE can model the thermal emission of VSGs, PAHs, TEGs and includes a model that accounts for free-free and synchrotron radio contina, but it requires to degrade the angular resolution of the maps to the coarsest common angular resolution (47.4$''$). Therefore,

Instrument	Central Wavelength	FWHM (″)	Spatial Coverage	C (%)	σ_{cal} (%)	σ_{bg} (%)	σ_{line} (%)	σ_{tot} (%)
WISE	3.4 µm	47.4	16′ × 16′	0	2.4	1	0[1]	3
WISE	4.6 µm	47.4	16′ × 16′	0	2.7	1	0[1]	3
WISE	12 µm	47.4	16′ × 16′	14	4	1	19	19
Spitzer/MIPS	24 µm	47.4	16′ × 16′	3	1	1	7	7
Spitzer/MIPS	70 µm	47.4	16′ × 16′	50	10	1	30	32
Spitzer/MIPS	160 µm	47.4	16′ × 16′	10	10	9	4	14
LABOCA	870 µm	47.4	16′ × 16′	20†	15	0	15	21
NIKA2	1150 µm	47.4	16′ × 16′	10†	15	0	8	17
NIKA2	2000 µm	47.4	16′ × 16′	0	15	0	0	15
VLA	91.4 cm	47.4	16′ × 16′	0	15	0	0	15
VLA	4.07 m	47.4	16′ × 16′	0	15	0	0	15

Notes. See notes below Tab. 9.6.
[1] Since we lack the required data to properly estimate the contribution of H_2 rovibrational lines and other potential sources of contamination in this wavelength range, we assume that $C = 0$.
The FWHM and spatial coverage indicated in the third and fourth columns correspond to the parameters of the convolved and regridded maps, based on the coarsest common angular resolution (*Spitzer*/MIPS 160 µm map) and shared field of view (limited by the NIKA2 observations).

Table 9.7 `HerBIE` input dataset.

we produced a second dataset that comprises the WISE Atlas, *Spitzer*-MIPS, AKARI/-FIS, LABOCA, NIKA2 and VLA convolved, calibrated, background subtracted, decontaminated, spatially resampled continuum maps (see Tab. 9.7, Fig. 9.6). We also show the noise maps in Fig. 9.7. Tab. 9.7 contains the systematic uncertainties that we estimated for each map. This dataset covers the wavelength range 3.4-2000 µm with an angular resolution 47.4″. The spatial extension of the dataset is limited by our NIKA2 continuum maps (*i.e.* a maximum size ∼ 20′ × 20′). We produced 16′ × 16′ maps in order to restrict the `HerBIE` analysis to the area mapped with a quasi-uniform signal-to-noise ratio.

9.2 | Modified Black Body approach (PPMAP analysis)

We start our analysis of the dust thermal emission between 70 µm and 2.0 mm with the Bayesian, modified black body model `PPMAP`. Firstly, we focus on the extended G region using our ∼ 20′×20′ NIKA2 continuum maps (section 9.2.2). We then extend the analysis to the entire SNR, using our wide field observations between 70 µm and 870 µm (section 9.2.3). Finally, we discuss the mass measurements in section 9.2.4.

9.2.1 Input files and parameters

Point Spread Functions `PPMAP` requires the point spread functions (hereafter PSFs) associated with the input observations, in order to correctly apply the point process algorithm (see section 5.1.3). `PPMAP` is shipped with six `FITS` files corresponding to the PSF of two *Herschel* instruments at 70 µm, 100 µm, 160 µm, 250 µm, 350 µm and 500 µm (respectively PACS Poglitsch *et al.* 2010, and SPIRE Griffin *et al.* 2010). Based on the format of these `FITS` files, we produced our own

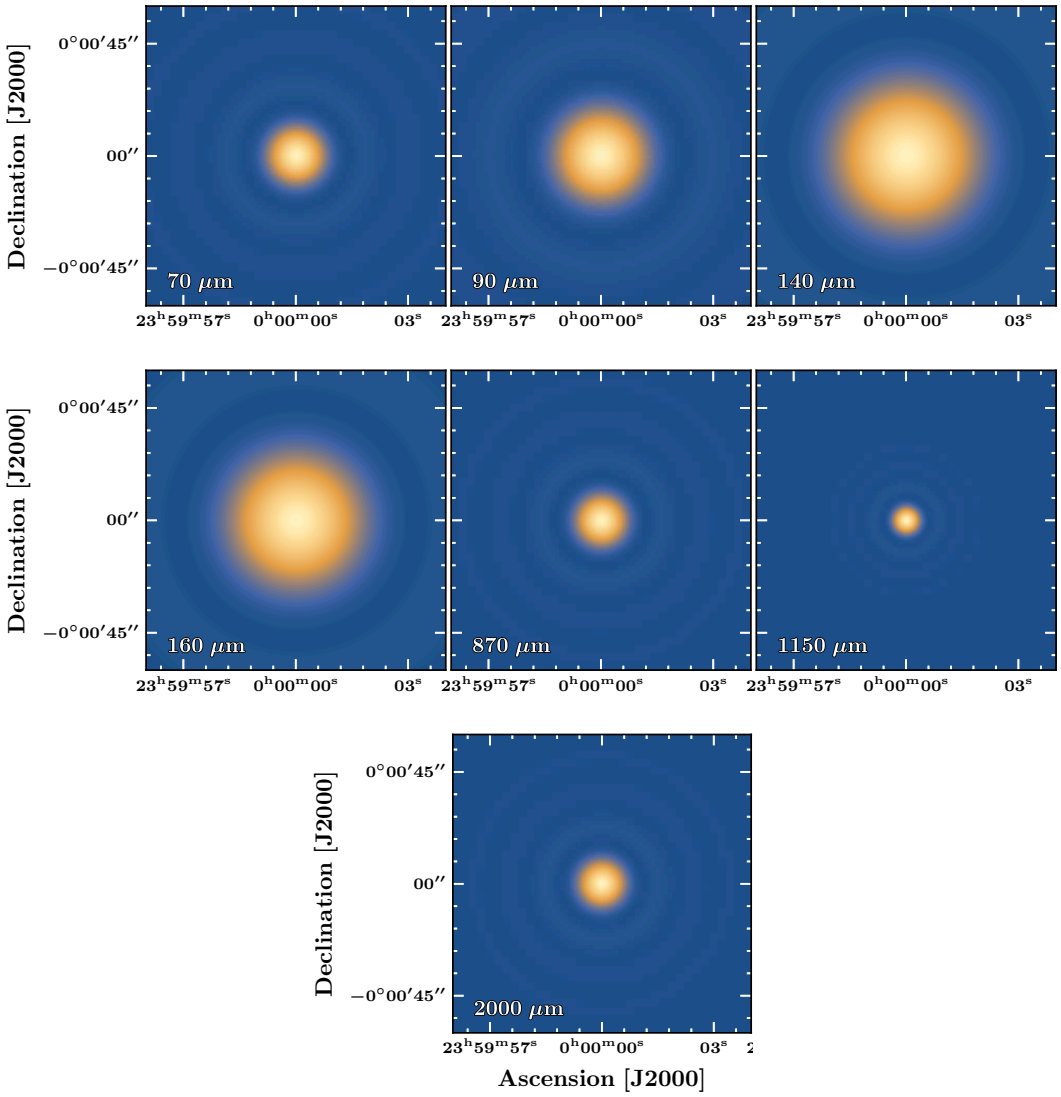

Figure 9.8 Synthetic point spread functions produced for PPMAP (represented with a linear color scale). The corresponding wavelengths are indicated in the bottom-left corner of each panel.

ideal PSFs associated with our continuum observations (listed in Tab. 9.6). We used the Python module `astropy.convolution.AiryDisk2DKernel` to produce synthetic PSFs of suited sizes sampled on 1024×1024 grids (see Fig. 9.8).

Fixed parameters In the algorithm 2, we have shown a typical PPMAP input file ('`premap.inp`'), in which all the input parameters are defined by the user (temperature grid, opacity, sampling, *etc*). Throughout this section, the only fixed parameters are the output sampling interval (`pixel`), distance of the source (`distance`, in parsec), reference opacity at 300 μm (`kappa`300, in cm^2 g^{-1}) and mosaic parameters (`ncells`, `noverlap`). The adopted values are indicated in Tab. 9.8. We set the parameters `ncells` and `noverlap` to their default, recommended values (respectively 40 and 20 pixels).

We experimented with different values for the size of a pixel in the output map (10″, 15″, 20″).

Table 9.8 Fixed PPMAP input parameters used in section 9.2. These are the parameters entered in the input file `premap.inp` (see also the algorithm 2). The reference opacity at 300 μm is defined with respect to the total mass (dust + gas, Marsh *et al.* 2015).

input parameter	description	adopted value
`pixel`	sampling (″)	15
`ncells`	cell size (px)	40
`noverlap`	cell overlap (px)	20
`distance`	distance (pc)	1800
`kappa300`	ref. opacity (cm^2 g^{-1})	0.1

We adopted a spatial sampling of 15″, which is a satisfying trade-off between computation time and angular resolution. We assume that the distance of the IC443 SNR is 1.8 kpc (Ambrocio-Cruz *et al.* 2017, Yu *et al.* 2019), and we adopt the default reference opacity $\kappa_{300} = 0.1$ cm^2 g^{-1}, defined with respect to the total mass and corresponding to a gas-to-dust ratio of 100 (Marsh *et al.* 2015, Hildebrand 1983).

Variable parameters: *i.)* temperature and opacity index grids The primary quantity that we aim to determine with PPMAP is the total column density of {dust + gas}. From a user-defined distribution of dust temperatures T_d (defined by the parameters `Nt`, `temprange`, see algorithm 2) and distribution of opacity law index values β (`nbeta`, `betagrid`, `betaprior`), PPMAP determines the best-fit parameters with respect to the response matrix (see Eq. 5.7). Since we have seven continuum data points (see Tab. 9.6), we should be allowed to optimize the fit for a maximum of six (T_d, β) pairs, *i.e.* a maximum of six distinct temperatures assuming a single value of β, or alternatively three values of T_d coupled with two values of β, *etc*. However, we noted that previous PPMAP studies did not satisfy this criterion:

- Marsh *et al.* (2017) adopted a single value of β and 12 values of T_d ($1\times12 = 12$ components) to model 5 Hi-GAL data points (*Herschel* observations at 70-500 μm).
- Howard *et al.* (2019) adopted 4 values of β and 12 values of T_d ($4 \times 12 = 48$ components) to model 5 *Herschel* data points (70-500 μm) and 1 SCUBA-2 data point (850 μm).
- Whitworth *et al.* (2019) adopted 4 values of β and 12 values of T_d ($4\times12 = 48$ components) to model 5 *Herschel* data points (70-500 μm).
- Chawner *et al.* (2020) adopted a single value of β and 12 values of T_d ($1 \times 12 = 12$ components) to model 5 *Herschel* data points (70-500 μm) and 1 *Spitzer*/MIPS data point (24 μm).
- Howard *et al.* (2021) adopted 3 values of β and 12 values of T_d ($3 \times 12 = 36$ components) to model 5 *Herschel* data points (70-500 μm) and 1 SCUBA-2 data point (850 μm).

Therefore, it seems to be approved by the developers of PPMAP (K. Marsh, A. Whitworth, A. Howard et al.) that one can model n continuum data points with a number $m \gg n$ of PPMAP (T_d, β) pairs of model components. In fact, if we adopt a very large number of state-variables (m) there will be a large uncertainty on their individual occupation numbers, and hence the uncertainty map will have larger values than the expectation-value map. From this point of view, the state of the system is identifiable by probabilistic calculations even if $m \gg n$, although the precision decreases. In order to study this issue, we experimented with PPMAP models that satisfy both $m \leq n-1$ (*i.e.* zero degrees of freedom) and $m \gg n$ (see the following developments, section 9.2.2, section 9.2.3).

Variable parameters: *ii.)* dilution The third variable parameter that we can experiment with is the '`dilution`' input parameter (hereafter denoted η). The default value in the `premap.inp` template file shipped with the program is `dilution` = 0.3, and Marsh *et al.* (2015) recommend a value in the range 0.1-0.01. The 'dilution' parameter represents the degree to which `PPMAP` is forced to minimize the number of (T_d, β) components used to reproduce the observations. Therefore, modifying the dilution η will change the differential column density distribution with respect to T_d and β. We experiment with the value of η in the following developments.

Run	Wavelength Range (μm)	Spatial Coverage	T_d (K) min.	T_d (K) max.	T_d (K) n	β (list)	η	`sigobs` (weighting)	χ^2
`A1` (Fig. B.1)	70-2000	$16' \times 16'$	10	30	12	{2.0}	0.3	$s/n = 100$	4.6
`A2` (Fig. B.2)	140-2000	$16' \times 16'$	10	30	12	{2.0}	0.3	$s/n = 100$	4.7
`B1` (Fig. B.3)	140-2000	$16' \times 16'$	10	30	12	{2.0}	0.3	$\overline{s/n}$	4.3
`B2` (Fig. B.4)	140-2000	$16' \times 16'$	10	30	8	{1.6, 1.7, 1.8, 1.9, 2.0}	0.3	$\overline{s/n}$	2.2
`C1` (Fig. B.5)	140-2000	$16' \times 16'$	10	30	8	{1.6, 1.7, 1.8, 1.9, 2.0}	0.03	$\overline{s/n}$	1.8
`C2` (Fig. B.6)	140-2000	$16' \times 16'$	10	30	8	{1.6, 1.7, 1.8, 1.9, 2.0}	3	$\overline{s/n}$	2.9
`D` (Fig. B.7)	140-2000	$16' \times 16'$	10	25	4	{1.8}	0.3	$\overline{s/n}$	1.6
`W1` (Fig. B.8)	140-870	$40' \times 40'$	10	30	8	{1.7, 1.8, 1.9}	0.3	$\overline{s/n}$	1.7
`W2` (Fig. B.9)	140-870	$40' \times 40'$	10	30	8	{1.7, 1.8, 1.9}	0.3	$\overline{s/n}^{\dagger}$	2.0

Notes. The first column indicates the name of the `PPMAP` run, and the corresponding figure. The wavelength range indicates the input `FITS` files (*e.g.* for a range 70-870 μm, the inputs are the 70 μm, 90 μm, 140 μm, 160 μm and 870 μm maps). Dust temperatures T_d are logarithmically spaced between the minimum and maximum boundaries, and the opacity index β is defined by a list of float numbers. η is the dilution parameter. The '`sigobs`' column indicates the method used to fill the `sigobs` input in `premap.inp`: '$s/n = 100$' signifies that we systematically used a signal-to-noise ratio equal to 100 (uniform weighting, see text) and '$\overline{s/n}$' signifies that we fixed the parameter `sigobs` based on the average value across the real noise maps (r.m.s weighting, see text). χ^2 is the statistical mean of the quantity defined in Eq. 9.9, over the pixels of the 1150 μm map where $F_\nu \geq 3\sigma$.

† the `sigobs` parameters of the '`PPMAP-W2`' run were tuned in order to increase the weight of the 870 μm data point (see second paragraph in section 9.2.3).

Table 9.9 `PPMAP` inputs for each run presented in sections 9.2.2 and 9.2.3.

Input parameters: *iii.)* summary We have performed several runs with `PPMAP` to determine the impact of the temperature distribution, opacity law index distribution and dilution, and other parameters (inclusion or not of the 70 μm map, data weighting, see sections 9.2.2 and 9.2.3). The fixed parameters are indicated in Tab. 9.8. For each run, we indicate the rest of the parameters in Tab. 9.9, as well as the input `FITS` files, weighting method and spatial coverage. The results obtained with each run are discussed in sections 9.2.2 and 9.2.3.

9.2.2 PPMAP analysis of the extended G region

Figure description Hereafter, we systematically present the results obtained with `PPMAP` in a multi-panel figure produced using the same template (Fig. B.1 to B.9). These figures are shown in the appendix, and Fig. B.4 is also reproduced in this section to provide an example (Fig. 9.9). The figure comprises three rows, each with three panels:

– On the top row, we show the total column density map ('`cdens.fits`', in cm^{-2}), mean dust temperature map ('`temp.fits`', in Kelvin) and mean opacity index map ('`beta.fits`')

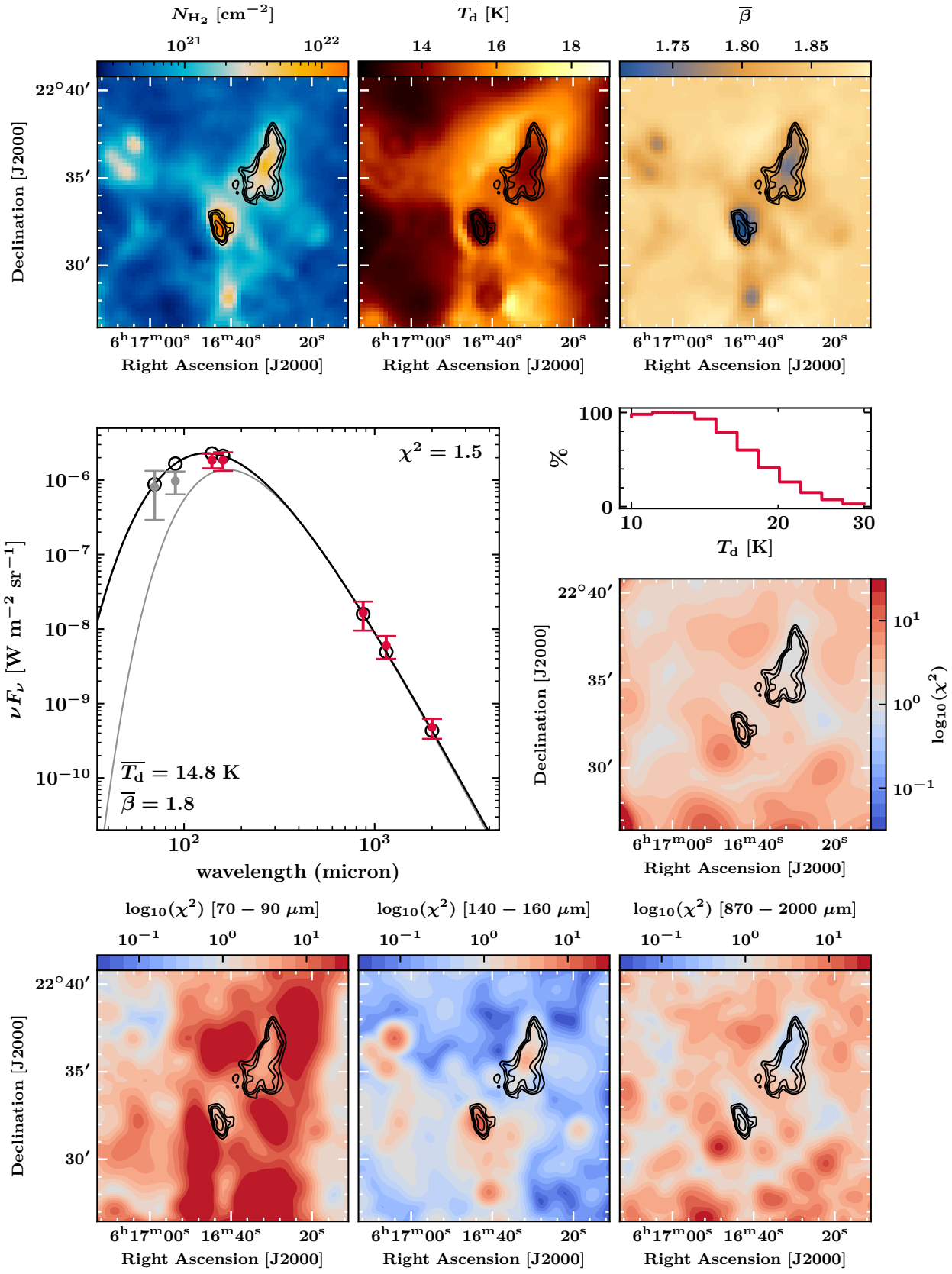

Figure 9.9 Results of the run '`PPMAP-B2`': analysis of the 140-2000 μm data points with eight dust temperatures in the range $T_d = 10 - 30$ K, $\beta = \{1.6, 1.7, 1.8, 1.9, 2.0\}$, $\eta = 0.3$ and r.m.s weighting (see Tab. 9.9). See the first paragraph in section 9.2.2 for a detailed description of the figure.

returned by the algorithm. The black contours correspond to the IRAM 30m ^{12}CO J=2–1 peak map shown in Fig. 6.10 (contour levels: 0.25, 0.35, 0.45 and 0.75 times the maximum value across the map).

– To the left-center of the figure, a panel shows the spectral energy distribution νF_ν (spatially averaged over the whole field of observations, in W m^{-2} sr^{-1}): *i.)* broadband observations are represented with $\pm 2\sigma$ errorbars in order to make them easier to read (in gray if the data point is excluded from the input, and in red if the data point is included), *ii.)* the black curve and circles correspond to the average synthetic fluxes computed from all SEDs in the field of observations (produced using Eq. 5.13 applied to '`tdenscube.fits`'), and *iii.)* the gray curve represent the single MBB model inferred from the statistical mean of '`cdens.fits`', '`temp.fits`' and '`beta.fits`'. The black data points and gray curve are not exactly identical, because the black curve takes into account the distribution $N(T_\mathrm{d}, \beta)$, whereas the gray curve is a single, average MBB model produced from $N(\overline{T_\mathrm{d}}, \overline{\beta})$. On the one hand, the equation of the black curve is:

$$\nu F_\nu = \sum_{k=1}^{N} \sum_{l=1}^{M} \left\{ \left(\frac{N(T_{\mathrm{d},k}, \beta_l)}{2.1 \times 10^{24}\ \mathrm{cm}^{-2}} \right) \left(\frac{\lambda}{300\ \mu\mathrm{m}} \right)^{-\beta_l} \nu B_\nu(T_{\mathrm{d},k}) \right\} \tag{9.7}$$

where $N(T_{\mathrm{d},k}, \beta_l)$ is extracted from `tdenscube.fits` (see also Eq. 5.13), and $T_{\mathrm{d},k}, \beta_l$ are the bins of the dust temperature and opacity index grids (listed in Tab. 9.9). On the other hand, the equation of the gray curve is:

$$\nu F_\nu = \left(\frac{N_\mathrm{tot}}{2.1 \times 10^{24}\ \mathrm{cm}^{-2}} \right) \left(\frac{\lambda}{300\ \mu\mathrm{m}} \right)^{-\overline{\beta}} \nu B_\nu(\overline{T_\mathrm{d}}) \tag{9.8}$$

where N_tot is extracted from `cdens.fits`, $\overline{\beta_l}$ from `beta.fits` and $\overline{T_\mathrm{d}}$ from `temp.fits`.

In addition, in order to show a significant spectral energy distribution in terms of signal-to-noise ratio (s/n), we extracted the spatially averaged observations and `PPMAP` models within the area of the 1.15 millimeter map where the measurements are at least 3σ detections (both for the 'gray' and 'red' curves; this region of higher s/n is represented by white contours in the right panel of Fig. 9.5). To the right-center, an upper-panel shows the distribution of the differential column density (in relative percents, normalized with respect to max$[N(T_\mathrm{d})]$ as a function of the dust temperature T_d, and a lower-panel represents the global reduced χ^2 map. The reduced χ^2 map is defined by:

$$\chi^2(x,y) = \frac{1}{n_\lambda - p} \sum_{i=1}^{n_\lambda} \left(\frac{\sum_{k=1}^{N} \sum_{l=1}^{M} \left\{ \left(\frac{N(T_{\mathrm{d},k},\ \beta_l,\ x,\ y)}{2.1 \times 10^{24}\ \mathrm{cm}^{-2}} \right) \left(\frac{\lambda_i}{300\ \mu\mathrm{m}} \right)^{-\beta_l} \nu_i B_\nu(T_{\mathrm{d},k}) \right\} - \nu_i F_\nu^\mathrm{obs}(\lambda_i, x, y)}{\nu_i \sigma_\mathrm{r.m.s}(\lambda_i, x, y) + [\sigma_\mathrm{cal}(\lambda_i) + \sigma_\mathrm{bg}(\lambda_i) + \sigma_\mathrm{line}(\lambda_i)] \nu_i F_\nu^\mathrm{obs}(\lambda_i, x, y)} \right)^2 \tag{9.9}$$

where $F_\nu^\mathrm{obs}(\lambda_i, x, y)$ corresponds to the flux measurements at wavelength λ_i in a pixel (x, y), n_λ is the number of measurements included in the `PPMAP` input, and $\sigma_\mathrm{r.m.s}$, σ_cal, σ_bg, σ_line are the uncertainties associated with the r.m.s, absolute flux calibration, background subtraction and line contributions (see Tab. 9.6). p is the number of free parameters.

– The bottom row represents the reduced χ^2 associated with distinct domains of the spectral energy distribution: 70-90 μm (left panel, corresponding to Eq. 9.9 for $\lambda_i = \{70,\ 90\}$ μm), 140-160 μm (center-panel, corresponding to Eq. 9.9 for $\lambda_i = \{140,\ 160\}$ μm) and 870-2000 μm (right panel, corresponding to Eq. 9.9 for $\lambda_i = \{870,\ 1150,\ 2000\}$ μm).

9.2.2.1 Weighting

Methods PPMAP requires to provide an estimate of the noise associated with each input continuum map (input parameter `sigobs`). The input file `premap.inp` does not allow to work with noise maps, since it only accepts a float number for each wavelength. We experimented with two distinct methods to determine the `sigobs` input:

– **'uniform weighting'**: in our first batch of PPMAP models, we arbitrarily set the value of `sigobs` such that the peak signal-to-noise s/n is uniform across the continuum measurements, *e.g.* $s/n(\lambda) = 100$ for any λ in $\{70,\ 90,\ 140,\ 160,\ 870,\ 1150,\ 2000\}$ (μm), assuming a constant flux uncertainty of 1%.

– **'r.m.s weighting'**: in our second batch of PPMAP models, we determined the value of `sigobs` based on the mean of the r.m.s across the noise maps.

On the one hand, the 'r.m.s weighting' method should be the most reliable and appropriate with respect to the quality of the observations, and it requires no assumptions at all. If we adopt this method, observations with lower signal-to-noise, such as the AKARI/FIS continuum maps (see Tab. 9.1), are associated with lower weights. On the other hand, the 'uniform weighting' allows to the same weight to each continuum map, so that the best-fit model is not dominated by the data points with greater signal-to-noise ratios.

PPMAP runs: experiments with the weighting method In this paragraph, we present the runs '`PPMAP-A1`' to '`PPMAP-B1`' and the corresponding results:

– We performed an initial PPMAP analysis of our 70-2000 μm maps with twelve dust temperatures and a single value of β, using the 'uniform weighting method' ('`PPMAP-A1`', see Tab. 9.9). Results are shown in Fig. B.1. The resulting spectral energy distribution shows that the best-fit models are dominated by the mid-IR data points, and as a consequence our 870 μm, 1150 μm and 2000 μm are not reproduced by the PPMAP models ($|F_\nu^{\rm mod} - F_\nu^{\rm obs}| \gg 3\sigma$: the distance between the observations and the model is greater than 3 σ). The global chi-square test yields $\chi^2 = 4.6$. It is likely that the 70 μm and 90 μm data points trace a mixture of VSGs and TEGs emission.

– Therefore, we performed a follow-up PPMAP analysis of our 140-2000 μm maps with the exact same input parameters ('`PPMAP-A2`', see Tab. 9.9). Results are shown in Fig. B.2. The spectral energy distribution shows that the quality of the best-fit model is enhanced for the millimeter data points, although the 870-2000 μm data points are still not correctly reproduced by PPMAP (global $\chi^2 = 4.7$).

– We then performed a PPMAP analysis of our 140-2000 μm maps with the same input parameters, only modifying the input parameter `sigobs` by shifting from the 'uniform weighting'

to the 'r.m.s weighting' method ('PPMAP-B1', see Tab. 9.9). Results are shown in Fig. B.3. The quality of the best-fit model for the 870-2000 µm data points is enhanced, such that the 870 µm is within 2σ and the 1150 µm, 2000 µm data points almost within 3σ of the PPMAP models (global $\chi^2 = 4.3$).

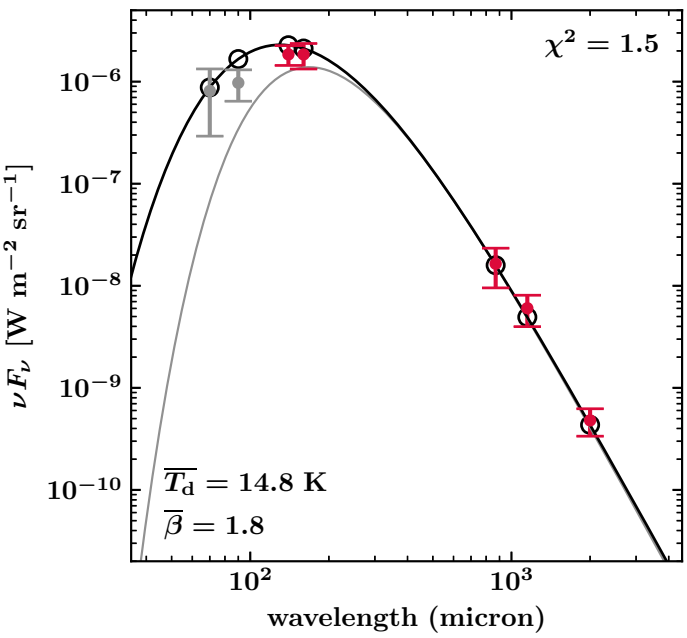

Figure 9.10 Average spectral energy distribution of dust thermal emission in statistically significant pixels of the extended G region. The black curve corresponds to the differential PPMAP model (Eq. 9.7), and the gray curve corresponds to the average PPMAP model with dust temperature $\overline{T_d}$ and opacity index $\overline{\beta}$ (Eq. 9.8). Red data points are included in the fit, and gray data points are excluded. The errorbars represent $\pm 2\sigma$, where σ is the r.m.s. The global χ^2 is indicated in the top-right corner of the figure.

Conclusions on the weighting method

1. The 70 µm and 90 µm data points might trace a mixture of VSGs and TEGs. We remove these data points from the PPMAP analysis.

2. The 'r.m.s weighting' method favors the longer wavelengths data points, since the NIKA2 maps are characterized by a greater signal-to-noise ratio than the mid-IR data points (*Spitzer*/MIPS and AKARI/FIS). Since the overall quality of the fit is superior when using the 'r.m.s weighting', we will adopt this method for the rest of the section.

9.2.2.2 Best-fit model ($m \gg n$)

Introduction of β as a variable parameter In order to improve our PPMAP modelling, instead of a single $\beta = 2$ input we adopted a grid of opacity indices $\beta = \{1.6, , 1.7, 1.8, 1.9, 2.0\}$ to account for local variations of β across the field of observation and along the line of sight. We also decreased the number of bins in the temperature grid from 12 to 8 to reduce the number of PPMAP components to $8 \times 5 = 40$ ('PPMAP-B2', see Tab. 9.9). The results of the analysis of the 140-2000 µm data points with this setup are shown in Fig. B.4, and we also reproduced the spectral energy distribution in Fig. 9.10. The global χ^2 is 2.3, and all the millimeter data points are within $\pm 2\sigma$ of the PPMAP model. We adopt this model as our preliminary PPMAP best-fit model, although it was obtained using a number of PPMAP components ($m = 40$) greater than the number of data points ($n = 5$).

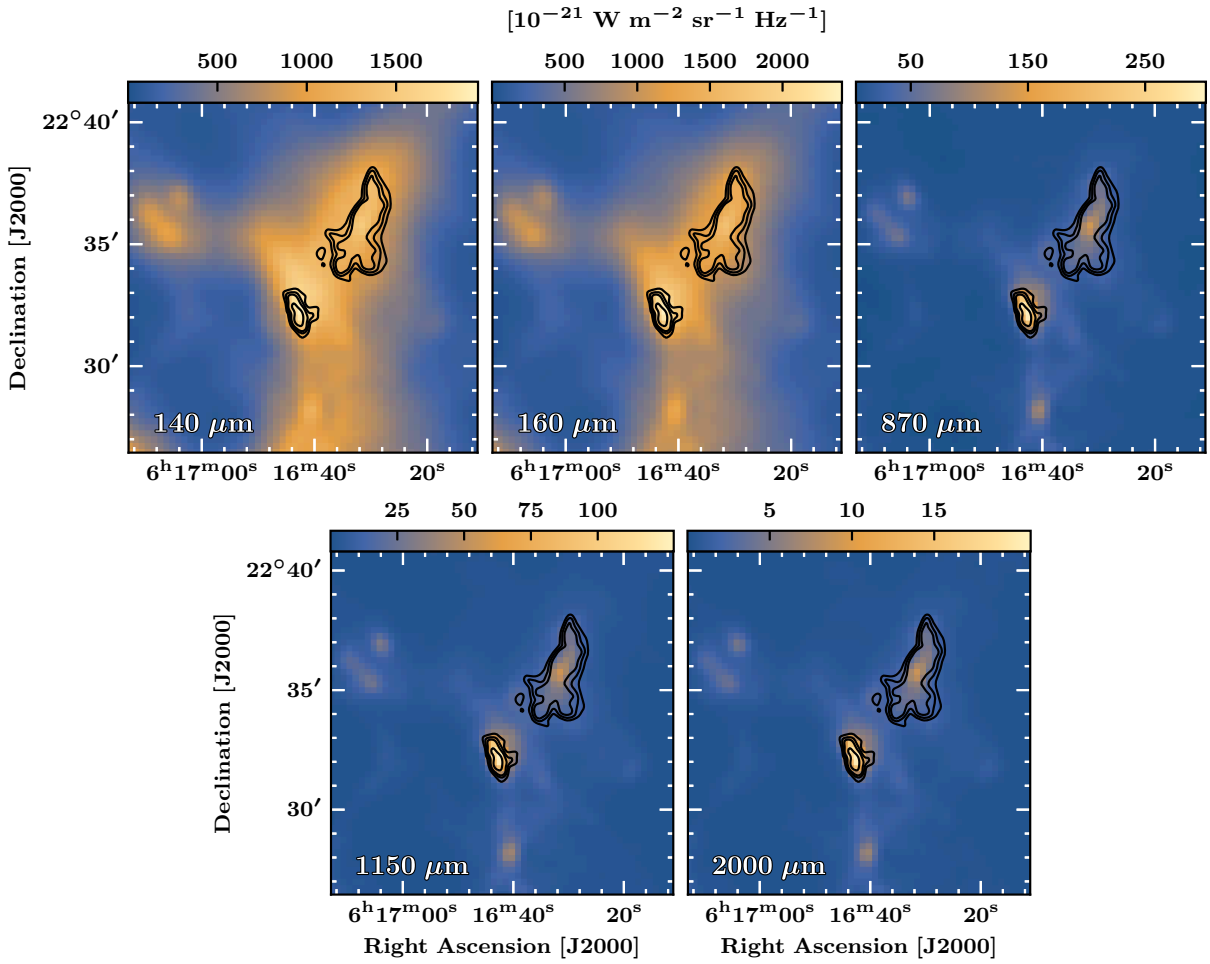

Figure 9.11 Synthetic PPMAP flux maps at 140 µm, 160 µm, 870 µm, 1150 µm and 2000 µm (produced *via* Eq. 9.7 applied to the results of the 'PPMAP-B2' model). The black contours correspond to the IRAM 30m ^{12}CO J=2–1 peak map shown in Fig. 6.10 (contour levels: 0.25, 0.35, 0.45 and 0.75 times the maximum value across the map)

Including the variations of β into the PPMAP models allows to attribute lower values of the opacity index towards the bright molecular structure (down to $\beta \simeq 1.75$) and higher values in the background (up to $\beta \simeq 1.85$). It is likely that the optical properties of dust grains vary between the diffuse cavity of the SNR, the ambient cloud of Cornett *et al.* (1977) and the dense molecular shell (due to grain coalescence and coagulation, Köhler *et al.* 2012), hence this variation of the PPMAP best-fit parameter β might trace physical variations of dust grain properties in the field of observations. Variations of β on a parsec-scale might trace local variations of $G_0/n_{\rm H}$. In fact, Köhler *et al.* (2012) found that the opacity index can vary between $\beta = 1.65$ ad $\beta = 1.8$ in a temperature range $T_{\rm d} = 14 - 17$ K (assuming an environment density $n_{\rm H} = 100$ cm^{-3} and up to $n_{\rm H} = 10^5$ cm^{-3} in dense molecular regions).

Synthetic flux maps Using Eq. 9.7, we produced the synthetic PPMAP flux maps at 140 µm, 160 µm, 870 µm, 1150 µm and 2000 µm. In addition to Eq. 9.7, we convolved the map with a gaussian kernel of suited size in order to produce synthetic maps with the same angular resolution as in the observations. The results are shown in Fig. 9.11. The 870-2000 µm synthetic maps seem to be dominated by the NIKA2 input maps.

Differential column density maps We produced differential column density maps by summing the '`tdenscube.fits`' cube over the opacity indices:

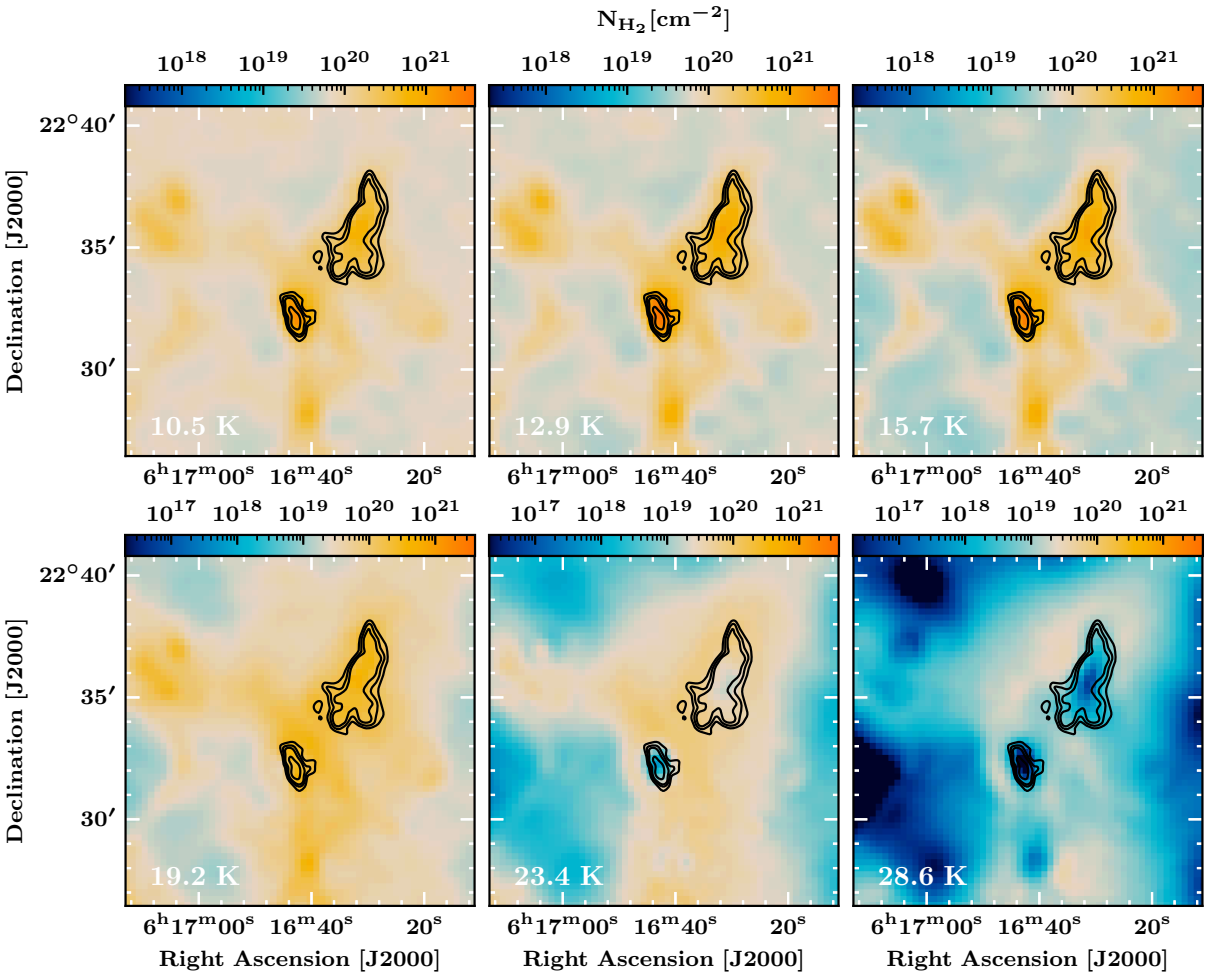

Figure 9.12 Differential column density maps obtained with the '`PPMAP-B2`' model. The temperature bins are indicated in the bottom-left corner of each panel. The colorbar is changed from $2 \times 10^{17} - 4 \times 10^{21}$ to $2 \times 10^{16} - 4 \times 10^{21}$ between the first and second rows. The black contours correspond to the IRAM 30m ^{12}CO J=2–1 peak map shown in Fig. 6.10 (contour levels: 0.25, 0.35, 0.45 and 0.75 times the maximum value across the map).

$$N_{\mathrm{T_d}}(x,y) = \sum_{l=1}^{M} N(T_{\mathrm{d},k}, \beta_l, x, y) \tag{9.10}$$

where $T_{\mathrm{d,k}}$ is a temperature bin in the `PPMAP` input T_{d} grid, β_l is an opacity index bin in the input β grid and $N(T_{\mathrm{d},k}, \beta_l, x, y)$ is an element of the '`tdenscube.fits`' cube. The results are shown in Fig. 9.12. The column density distribution is quasi-constant in the temperature range 10.5-15.7 K, in which the cold column density is concentrated in the dense molecular regions (clumps 'G' and 'D', quiescent cloudlet, molecular shell). The column density decreases in the higher temperature bins (19.2-28.6 K), and tends to be more extended. In the highest temperature bins ($T_{\mathrm{d}} = 23.4,\ 28.6$ K) the column density is anti-correlated with the bright molecular structures.

9.2.2.3 Experiments with the dilution parameter η

In this paragraph, we present the runs '`PPMAP-C1`' and '`PPMAP-C2`' and the corresponding results. We studied the impact of the dilution parameter η on our results. Using the best-fit model '`PPMAP-B2`' model as a baseline, we performed a batch of `PPMAP` models with a range of values $\eta = 0.01 - 10$. We show the results obtained with a dilution $10 \times \eta_{\rm default}$ and $0.1 \times \eta_{\rm default}$, where $\eta_{\rm default} = 0.3$ is the default, recommended value. The $\eta = 0.03$ model is shown in Fig. B.5 ('`PPMAP-C1`'), and the $\eta = 3$ model is shown in Fig. B.6 ('`PPMAP-C2`').

- With respect to the reference model ('`PPMAP-B2`', $\chi^2 = 2.2$) the increased dilution yields a higher global chi-square ($\chi^2 = 2.3$) whereas the lowered dilution yields a lower global chi-square ($\chi^2 = 1.8$).
- The column density, dust temperature and opacity index are significantly altered by the modification of the parameter η (compare the top row in Fig. B.5 with the top row in Fig. B.6).
- The lower panels in Fig. B.5 and Fig. B.6 show that the pixel-per-pixel `PPMAP` best-fit models converge in different ways with respect to the mid-IR and sub-mm/mm data points depending on the value of η. With $\eta = 3$, the best-fit models across the extended emission are dominated by the mid-IR data points and the emission of the bright molecular structures is dominated by the sub-mm/mm data points. In contrast, with $\eta = 0.03$ the mid-IR and sub-mm/mm data points seem to be equally reproduced by `PPMAP`.
- The total column density map obtained with $\eta = 0.03$ has a greater gradient than the $\eta = 3$ column density map, in which the transition between the bright structures and the background is smoother. Additionally, the inversion of temperature between the extended regions and the bright molecular structures is observed with $\eta = 0.03$, but not with $\eta = 3$.

9.2.2.4 Zero degrees of freedom best-fit model ($m \leq n$)

We performed an additional `PPMAP` analysis using a reduced number of physical components in order to satisfy the condition $m \leq n$, where m is the total number of bins in the temperature and opacity index grids, and n is the number of data points at distinct wavelengths. We adopted a single value of the opacity index ($\beta = 1.8$, based on the previous results) and a grid of four dust temperatures between 10 K and 25 K (see '`PPMAP-D`' in Tab. 9.9). We thus have $m = 4 \times 1$ components and $n = 5$ data points, and the best-fit model has zero degrees of freedom.

Results are shown in Fig. B.7. The global chi-square is $\chi^2 = 1.6$, and both the mid-IR and sub-mm/mm data points are correctly reproduced by `PPMAP`. The χ^2 of this model is lower than the χ^2 associated with the '`PPMAP-B2`' model because we shrinked the dust temperature grid from 10-30 K to 10-25 K. With the same temperature grid we obtained $\chi^2 = 2.1$. Since the opacity index is fixed, the total column density and dust temperature map are altered with respect to the '`PPMAP-B2`' model (compare the top panels in Fig. B.4 with the top panels in Fig. B.7).

In the following developments (comparisons with `HerBIE`, *etc*) we will keep the results of the run '`PPMAP-B2`' as the 'overall best-fit model', since it was obtained with the recommended value for the dilution parameter ($\eta = 0.3$) and it yields a satisfying chi-square ($\chi^2 = 2.2$) while allowing to measure variations of β.

9.2.3 PPMAP analysis of the entire SNR

Our NIKA2 maps at 1.15 mm and 2.0 mm maps are restricted to a $\sim 16' \times 16'$ field of observation, but the rest of our mid-IR and sub-millimeter observations cover the entire SNR. With only one data point in the sub-millimeter regime (LABOCA at 870 µm), the best-fit model might be uncertain, but we can obtain a rough estimate of the dust parameters over the full extent of the SNR cavity and molecular shell.

r.m.s weighting We used the most suited PPMAP input parameters that were previously determined in the extended G region to perform a preliminary PPMAP analysis of a $40' \times 40'$ field of observations in the wavelength range 140-870 µm ('PPMAP-W1, see Tab. 9.9). We adopted eight temperatures between 10 K and 30 K, and three values of the opacity index ($\beta = \{1.7,\ 1.8,\ 1.9\}$). The results are shown in Fig. B.8. The global chi-square is $\chi^2 = 1.7$, but the individual χ^2 values are not uniform between the mid-IR and sub-millimeter data points ($\chi^2 \gg 3\sigma$ at 870 µm).

The spectral energy distribution shows that the best-fit models are dominated by the mid-IR data points, and as a consequence the column density is decreased in the extended G region (from a peak column density $\sim 10^{22}$ cm^{-2} in the 'PPMAP-B2' output map to a peak column density $\sim 10^{21}$ cm^{-2}).

non-uniform r.m.s weighting In order to correctly reproduce the 870 µm data point, we tuned the sigobs input parameter. We define the weight w_λ of a data point at wavelength λ by:

$$w_\lambda = \frac{\sigma_{\text{r.m.s}}(\lambda)}{\sigma_{\texttt{sigobs}}(\lambda)} \tag{9.11}$$

where $\sigma_{\text{r.m.s}}$ is the true r.m.s uncertainty, and $\sigma_{\texttt{sigobs}}$ is the value used in the sigobs input parameter. By default, we use uniform weights equal to unity. We experimented with non-uniform weights in order to try to force PPMAP to reproduce the 870 µm data point. We used $w_{870} = 1 - 5$, and found that $w_{870} = 2.5$ is sufficient to obtain a fit that accounts both for the mid-IR data points and the 870 µm data points ('PPMAP-W2, see Fig. B.9). The global chi-square is slightly increased ($\chi^2 = 2.0$), and the resulting total column density is increased along the molecular shell, up to 10^{22} cm^{-2}. The spectral energy distribution in the extended G region (center-left panel in Fig. B.9) shows that the best-fit model is appropriate in the sub-mm/mm regime, in contrast to the results of the 'PPMAP-W1' model. Therefore, in our analysis of the entire SNR we keep the 'PPMAP-W2' run as the 'overall best-fit model'.

9.2.4 Mass measurements

The total mass estimated by PPMAP in a pixel is given by the following relation (Howard *et al.*, 2021):

$$\Delta M_{\text{px}} = [0.011\ \text{M}_\odot]\tau_0 \left(\frac{\Delta\Omega_{\text{px}}}{\text{arcsec}^2}\right)\left(\frac{D}{100\ \text{pc}}\right) \tag{9.12}$$

where τ_0 is the optical depth, given by $\tau_0 = N_{\text{H}_2}/2.1 \times 10^{24}$ cm^{-2}, where N_{H_2} is the quantity stored in the 'cdens.fits' PPMAP output file. $\Delta\Omega_{\text{px}}$ is the angular size of a pixel, and D is the

distance of the object. We adopted a distance $D = 1.8$ kpc for the IC443 SNR (Ambrocio-Cruz *et al.* 2017, Yu *et al.* 2019). We indicate the inferred masses for each PPMAP model in Tab. 9.10.

– *Total mass in the* $16' \times 16'$ *field of observations:* the best models (with respect to the value of χ^2) are the 'B2', 'C1' and 'C2' runs (respectively $\chi^2 = 2.2,\ 1.7,\ 2.0$). The inferred masses found with the 'B2' and 'C1' models are similar (around 700 $M_\odot$, with a relative difference $\sim 30\%$). However, the model with increased dilution ('C2', $\eta = 3$) yields a much greater mass $M \simeq 2 \times 10^3$ $M_\odot$.

– *Total mass in the entire SNR:* depending on the weight attributed to the 870 µm data point, the total mass varies between ~ 2500 $M_\odot$ ('W1') and ~ 5500 $M_\odot$ ('W2').

Conclusion: the total mass inferred with PPMAP is sensitive to the input parameters (dilution, weighting). PPMAP models with low global chi-square ($\chi^2 \sim 1$) can yield distinct total mass measurements. We will discuss these issues and compare the PPMAP results with HerBIE results, as well as ^{12}CO mass measurements in section 9.4.

Run	Wavelength Range (µm)	T_d (K) min.	T_d (K) max.	n	β (list)	η	sigobs (weighting)	χ^2	Mass ($M_\odot$)
A1 (Fig. B.1)	70-2000	10	30	12	{2.0}	0.3	$s/n = 100$	4.6	235
A2 (Fig. B.2)	140-2000	10	30	12	{2.0}	0.3	$s/n = 100$	4.7	318
B1 (Fig. B.3)	140-2000	10	30	12	{2.0}	0.3	$\overline{s/n}$	4.3	517
B2 (Fig. B.4)	140-2000	10	30	8	{1.6, 1.7, 1.8, 1.9, 2.0}	0.3	$\overline{s/n}$	2.2	844
C1 (Fig. B.5)	140-2000	10	30	8	{1.6, 1.7, 1.8, 1.9, 2.0}	0.03	$\overline{s/n}$	1.8	608
C2 (Fig. B.6)	140-2000	10	30	8	{1.6, 1.7, 1.8, 1.9, 2.0}	3	$\overline{s/n}$	2.9	2184
D (Fig. B.7)	140-2000	10	25	4	{1.8}	0.3	$\overline{s/n}$	1.6	703
W1 (Fig. B.8)	140-870	10	30	8	{1.7, 1.8, 1.9}	0.3	$\overline{s/n}$	1.7	2445
W2 (Fig. B.9)	140-870	10	30	8	{1.7, 1.8, 1.9}	0.3	$\overline{s/n}^{\dagger}$	2.0	5514

Notes. See the notes below Tab. 9.9. The mass is measured using Eq. 9.12, assuming a distance of 1.8 kpc (Ambrocio-Cruz *et al.* 2017, Yu *et al.* 2019). *Reminder:* the PPMAP models A1 to D are restricted to the $16' \times 16'$ field of observations, but the PPMAP models W1 and W2 are performed on a $40' \times 40'$ field of observations, hence they naturally encompass a greater total mass.

Table 9.10 PPMAP results for each run presented in sections 9.2.2 and 9.2.3.

9.3 | Full dust model approach (HERBIE analysis)

We continue our analysis of the dust thermal emission with the Hierarchical Bayesian model HerBIE. The HerBIE input dataset is shown in Tab. 9.7, it covers a $16' \times 16'$ field of observations with a total of 11 data points in the wavelength range 10^0 – 10^6 µm (3.4 µm, 4.6 µm, 12 µm, 24 µm, 70 µm, 160 µm, 870 µm, 1.55 mm, 2.0 mm, 91.4 cm, 4.07 m). In contrast to PPMAP, HerBIE allows to model the $\lambda \leq 100$ µm emission of VSGs, including near-IR PAH features. Therefore, our HerBIE analysis will provide a determination of the dust mass that relies on a larger number of data points, and additional constraints such as the spatial distribution and intensity of the radiation field and the fraction of PAHs (albeit with additional uncertainties related to the physical mechanisms introduced in the description of the dust emission by HerBIE).

9.3.1 Assumptions (adopted physical components)

Dust and stellar continua We used two `HerBIE` physical components: *i.)* the THEMIS grain mixture (Jones *et al.*, 2017) illuminated by a non-uniform interstellar radiation field (hereafter ISRF), using a power law of ISRF intensities and *ii.)* a near-IR stellar continuum. These `HerBIE` components are described in Chapter 5, specifically in Eq. 5.17 and Eq. 5.18. The 'illuminated dust mixture' (also referred to as '`deltaU`', Galliano 2018) monochromatic luminosity of a source s_i (*i.e.* a pixel) at frequency ν_j is given by:

$$\begin{aligned} L_\nu^{\rm mod}(\nu_j, M_i, U_i, q_i^{\rm PAH}, f_i^+) = M_i[&q_i^{\rm PAH} f_i^+ l_\nu^{\rm PAH^+}(U_i, \nu_j) \\ &+ q_i^{\rm PAH}(1 - f_i^+) l_\nu^{\rm PAH^0}(U_i, \nu_j) \\ &+ (1 - q_i^{\rm PAH}) l_\nu^{\rm non-PAH}(U_i, \nu_j)] \end{aligned} \tag{9.13}$$

where M_i is the dust mass, U_i is the intensity of the ISRF, $q_i^{\rm PAH}$ is the PAH mass fraction (which controls the strength of aromatic features) and f_i^+ is a control parameter that characterizes the ratio between C–C and C–H bands. The terms $l_\nu^{\rm PAH}$, $l_\nu^{\rm PAH^+}$ and $l_\nu^{\rm non-PAH}$ correspond to the monochromatic luminosities of neutral PAH, charged PAH and non-PAH dust grains, which are computed with a stochastic heating method applied to the adopted THEMIS distribution of grains (Guhathakurta and Draine, 1989).

The near-IR stellar continuum component (also referred to as '`starBB`', Galliano 2018) is modelled by assuming a black body emission corresponding to a temperature $T_\star = 50\,000$ K, and adjusting the stellar bolometric luminosity $L_i^\star$ to match the observations of a source s_i (*i.e.* a pixel) at frequency ν_j:

$$L_\nu^{\rm mod}(\nu_j, L_i^\star) = L_i^\star \frac{\pi}{\sigma T_\star^4} B_\nu(T_\star, \nu_j) \tag{9.14}$$

where σ is the Stefan-Boltzmann constant ($\sigma = 5.670 \times 10^{-8}$ W m^{-2} K^{-4}). This component is required to fit the observations at shorter wavelengths ($\lambda \leq 10^1$ µm) in pixels illuminated by stars.

Free-free and synchrotron radio continua Our VLA data points at 330 MHz and 74 MHz (respectively corresponding to 91.4 cm and 4.07 m wavelengths) allow to estimate the contribution of the radio continuum to our NIKA2 data points (Castelletti *et al.*, 2011). As we already presented in Chapter 5 (see Eq. 5.19), the millimeter continuum excess produced by free-free and synchrotron emission can be fitted by `HerBIE` based on a linear combination of two power laws:

$$L_\nu^{\rm mod}(\nu_j, L_{1,i}, f_{{\rm FF},i}, \alpha_{s,i}) = \frac{L_{1,i}}{\nu_1} \left(f_{{\rm FF},i} \left(\frac{\nu_j}{\nu_1} \right)^{-0.1} + (1 - f_{{\rm FF},i}) \left(\frac{\nu_j}{\nu_1} \right)^{-\alpha_{s,i}} \right) \tag{9.15}$$

where $L_{1,i}$ is the luminosity at $\lambda = 1$ cm (at $\nu = \nu_1$), $f_{{\rm FF},i}$ is the fraction of free-free emission at $\lambda = 1$ cm and $\alpha_{s,i}$ is the index of the synchrotron power law. As a matter of fact, we did not include this component into our `HerBIE` models, because the model grid maintained by F. Galliano is currently not designed to account for radio observations at $\lambda > 30$ cm. Therefore, to determine if it is required to update the `HerBIE` grid of models in order to include this additional component, we added an *a posteriori* radio continuum power-law model to our spectral energy distributions. We discuss this issue in the following developments (see Eq. 9.16).

9.3.2 Results: *i.*) Spectral energy distributions

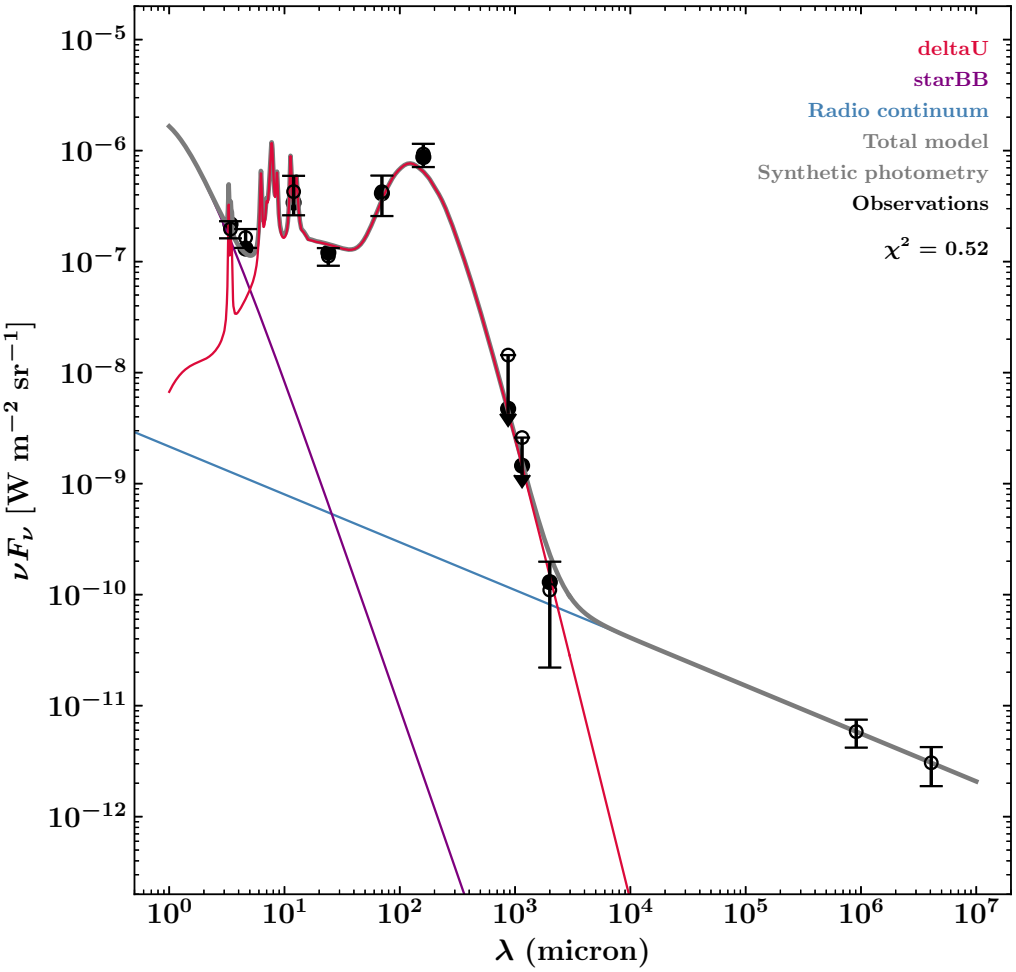

Figure 9.13 Average spectral energy distribution in the extended G region. Observations are shown in black, with $\pm 1\sigma$ errorbars. The `HerBIE` models of the illuminated dust mixture `deltaU`, stellar continuum `starBB` and the power-law model of the radio continuum are shown respectively by red, purple and blue curves. The total model and synthetic photometric data points are shown in gray.

Average spectral energy distribution of the extended G region In Fig. 9.13, we show the *average* spectral energy distribution (hereafter SED) obtained by measuring the mean SED in all pixels over the extent of our $16' \times 16'$ field of observations. The `HerBIE` analysis was performed on the 3.6-2000 µm data points only, since the grid of model cannot take into account the VLA observations. We added the VLA data points *a posteriori* to the SED, and we determined the best-fit power law that reproduces the 330 MHz and 74 MHz flux measurements based on the following relation:

$$\nu F_\nu = F_0 \nu^{-\alpha} \tag{9.16}$$

Using the `Python` module `curve_fit`, we optimized the parameters F_0 and α that correspond to best fit of the 330 MHz and 74 MHz data points in each pixel of our maps. This method is approximate, because self-absorption could disrupt the inferred index of the power law (Castelletti

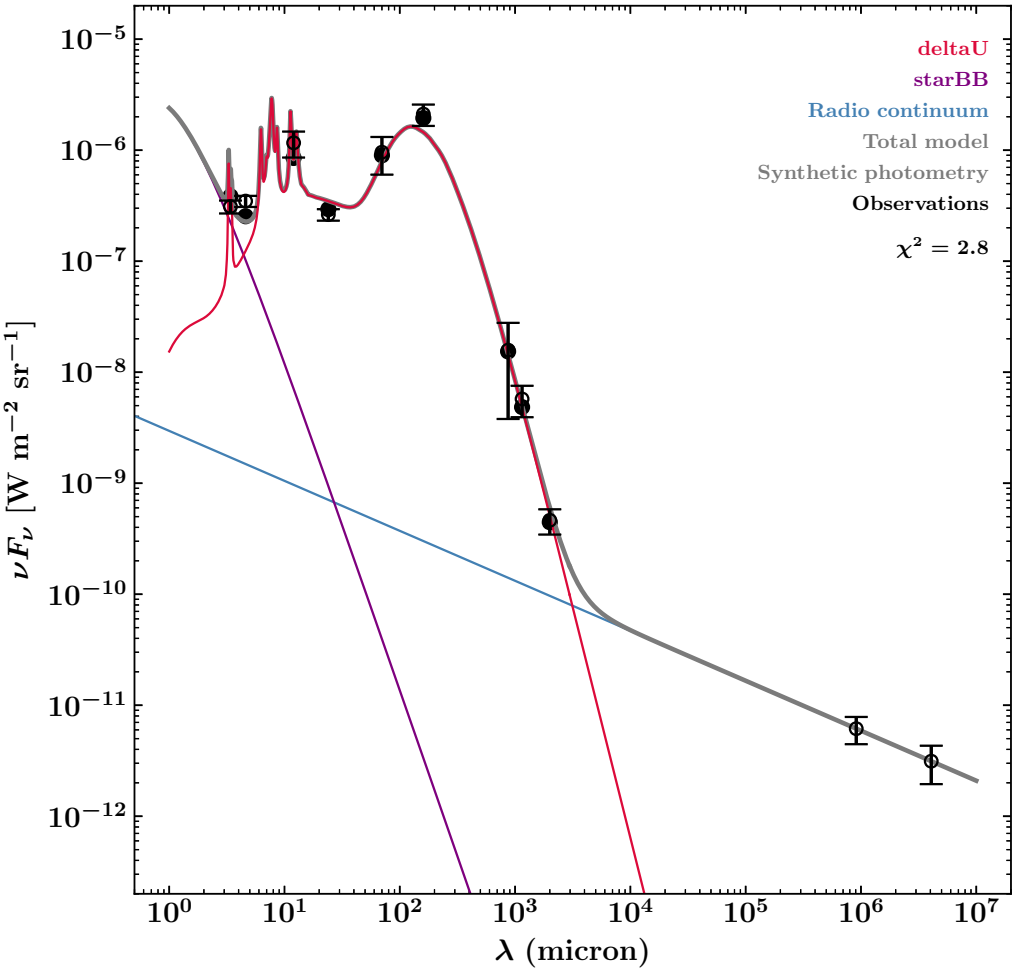

Figure 9.14 Average spectral energy distribution in the extended G region (restricted to statistically significant pixels: $F_\nu(\lambda) \geq 3\sigma$, where σ is the r.m.s). Observations are shown in black, with $\pm 1\sigma$ errorbars. The `HerBIE` models of the illuminated dust mixture `deltaU`, stellar continuum `starBB` and the power-law model of the radio continuum are shown respectively by red, purple and blue curves. The total model and synthetic photometric data points are shown in gray.

et al., 2007), although it provides a rough estimate of the contribution of the radio continuum to our 2.0 mm data point (we quantify and discuss the contribution of the radio continuum in the following developments). Therefore, the 'total model' represented by the gray curve in Fig. 9.13 is the sum of the illuminated dust mixture (`HerBIE` component `deltaU`), stellar continuum (`HerBIE` component `starBB`) and power-law model of the radio continuum (*a posteriori*, non-`HerBIE` component). In order to evaluate the quality of the best fit `HerBIE` model, we measure the following quantity:

$$\chi^2 = \frac{1}{n_\lambda - p} \sum_{i=1}^{n_\lambda} \left(\frac{\nu_i F_\nu^{\texttt{HerBIE}}(\lambda_i) - \nu_i F_\nu^{\text{obs}}(\lambda_i)}{\nu_i \sigma_{\text{r.m.s}}(\lambda_i) + [\sigma_{\text{cal}}(\lambda_i) + \sigma_{\text{bg}}(\lambda_i) + \sigma_{\text{line}}(\lambda_i)] \nu_i F_\nu^{\text{obs}}(\lambda_i)} \right)^2 \tag{9.17}$$

where $n_\lambda = 9$ is the number of data points given as input to `HerBIE`, $F_\nu^{\texttt{HerBIE}}$ and F_ν^{obs} are respectively the modelled and observed continuum fluxes, and $\sigma_{\text{r.m.s}}$, σ_{cal}, σ_{bg}, σ_{line} are respectively the uncertainties associated with the measurement r.m.s, absolute flux calibrations, background subtraction and line contamination. $p = 5$ is the number of free parameters (total dust mass, PAH

mass fraction, PAH charged fraction, ISRF intensity and ISRF power law index). The chi-square measured for the mean SED shown in Fig. 9.13 is $\chi^2 = 0.52$, hence the average quality of the fit is excellent. In fact, measuring a $\chi^2 \leq 1$ suggests that we might have overestimated the uncertainties associated with our measurements. The quality of the fit can be visualized in Fig. 9.13 by comparing the observations data points (in black) with the gray filled circles, which represent the synthetic photometric data points estimated by `HerBIE`. Synthetic photometric fluxes are distinct from the total model curve, because they take into account the instrument filters.

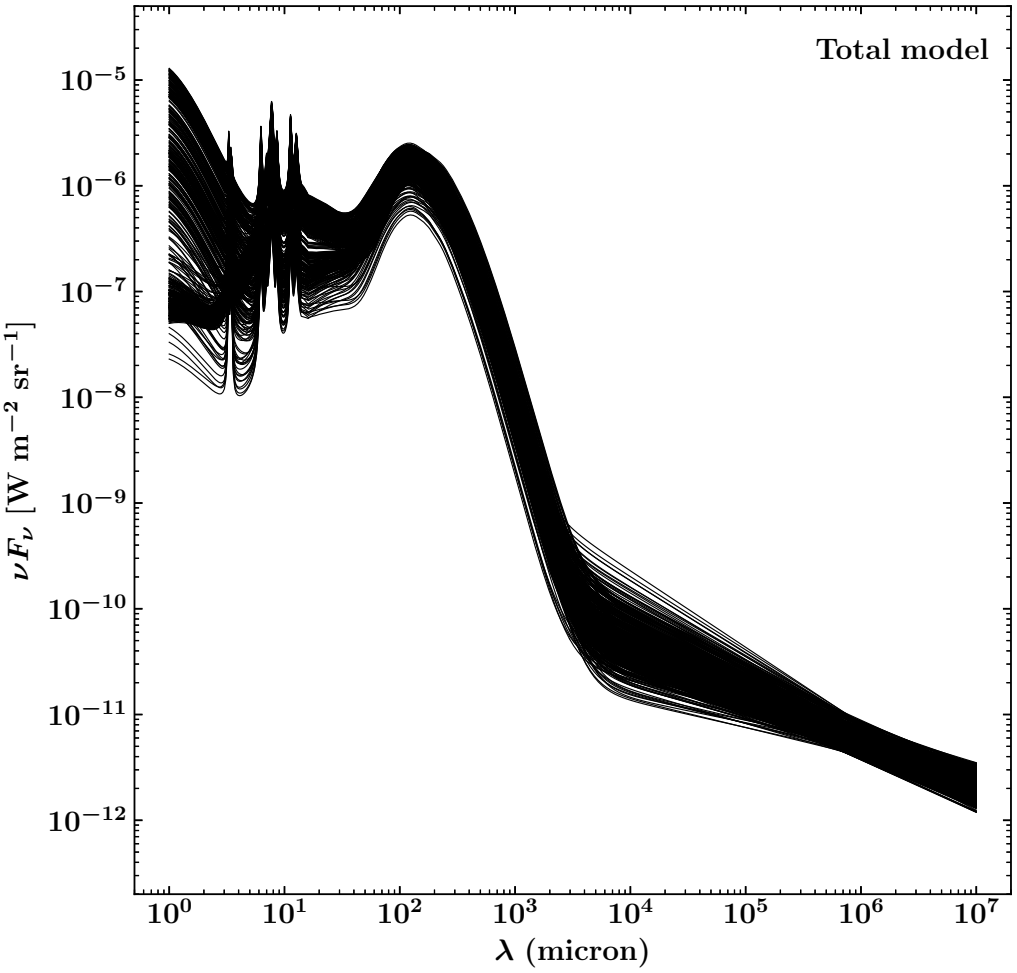

Figure 9.15 Individual spectral energy distributions in the extended G region (one curve corresponds to one pixel, restricted to statistically significant pixels: $F_\nu(\lambda) \geq 3\sigma$, where σ is the r.m.s). The 'total model' corresponds to the sum of the `HerBIE` models of the illuminated dust mixture `deltaU`, stellar continuum `starBB` and the power-law model of the radio continuum.

In order to evaluate the quality of the best fit in areas of the maps that are statistically significant, we produced an average SED restricted to the pixels of the map where the continuum flux is greater than 3σ (at any wavelength), where σ is the r.m.s measured in the noise map. The resulting average SED is shown in Fig. 9.14. The best fit is equally correct for the mid-IR to millimeter data points, although the global chi-square is $\chi^2 = 2.8$, because the near-IR data points are not reproduced as accurately as in Fig. 9.13, in particular at 4.6 μm. We discuss this near-IR discrepancy in the next paragraph. We also show the entire sample of individual best fits that are statistically significant ($F_\nu(\lambda) \geq 3\sigma$, where σ is the r.m.s) in Fig. 9.15. The figure suggests that a

few pixels might be characterized by a non-negligible contribution by the radio continuum in the millimeter wavelength range.

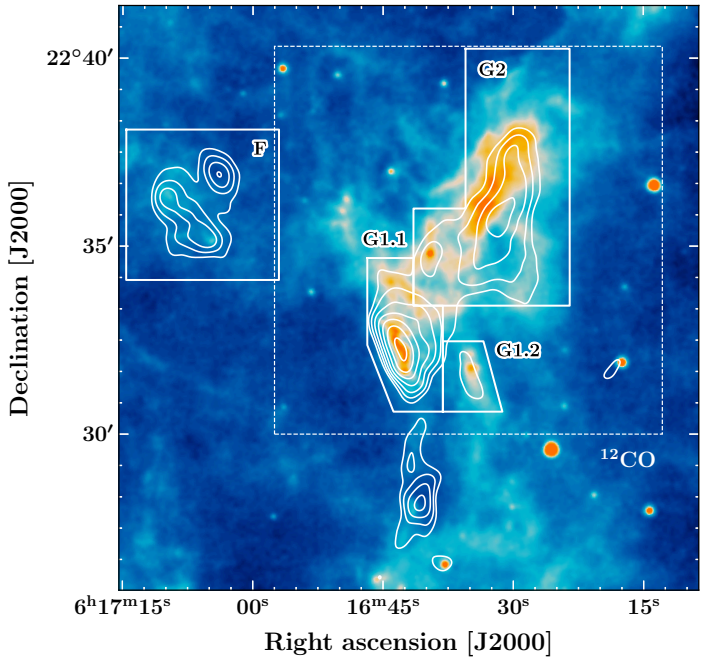

Figure 9.16 Definition of spatial boxes in the 16′ × 16′ field of observations. *Background: Spitzer*/MIPS map at 24 µm. White contours represent the emission at 1.15 mm (NIKA2 observations). The white boxes indicate the areas in which the signals corresponding to the 'G1.1', 'G1.2' and 'F' shocked clumps are extracted, as well as the box 'G2' that encompasses the ring-like structure and quiescent cloudlet (see also Fig. 6.19). These boxes are used to produce the average SEDs shown in Fig. 9.17. The white dashed box represents our 10′×10′ ^{12}CO field of observations.

Characteristic spectral energy distributions In order to study local variations of the SEDs (illustrated by Fig. 9.15), we produced average SEDs corresponding to distinct areas of the field of observations. We defined arbitrary boxes to enclose the brightest features in the 16′ × 16′ field of observations. The boxes are shown in Fig. 9.16. To study the features in the extended G region, we used the same boxes as in Chapter 6 (see Fig. 6.19), and we added a square box to include the shocked clump 'F'. We measured the (spatially) average fluxes and extracted the (spatially) average `HerBIE` SED models in each box to plot the results in Fig. 9.17.

– **IC443G1.1** (main shocked clump 'G'). With χ^2 = 17.3, the global chi-square is increased with respect to the previous SEDs (Fig. 9.13, 9.14), although the FIR, sub-millimeter and millimeter data points are correctly reproduced. The discrepancies between the modelled and observed near-IR data points suggest that we might have missed the correction of additional H_2 rovibrational lines towards the shocked clump, or that we have calibration issues. The contribution of the radio continuum is negligible. A small excess at 870 µm ($< 1\sigma$) indicates that the correction of the ^{12}CO J=3–2 line contribution could be inaccurate.

– **IC443G1.2** (secondary shocked clump 'G'). χ^2 = 7.12. The SED is similar to the IC443G1.1 SED. The global chi-square is reduced with respect to the IC443G1.1 SED, mostly as a result of the decrease of the signal-to-noise ratio. The radio continuum contribution to the 2.0 mm data point might be non-negligible ($\sim 1\sigma$), hence it could be required to perform a new `HerBIE` analysis including the 'free-free and synchrotron radio continua' component (see Eq. 9.15).

– **IC443G2** (quiescent small cloud). With χ^2 = 0.47, the quality of the fit is greater than for the shocked clump 'G': near-IR data points are accurately reproduced (within 1σ).

– **IC443F** (shocked clump 'F'). The global chi-square for the shocked clump 'F' is satisfying ($\chi^2 = 0.68$), although the 870 µm and 1150 µm data points are systematically in excess with respect to the best fit. This is expected, since we could not correct the contribution of the ^{12}CO J=3–2 and J=2–1 lines towards this area, for which we lack observations (our ^{12}CO observations are restricted to a $10' \times 10'$ field of observations that covers only a fraction of the $16' \times 16'$ `HerBIE` input, see the white dashed box in Fig. 9.16). Additionally, the radio continuum contribution to the 2.0 mm data point seems to be non-negligible ($\sim 1\sigma$) in this region as well.

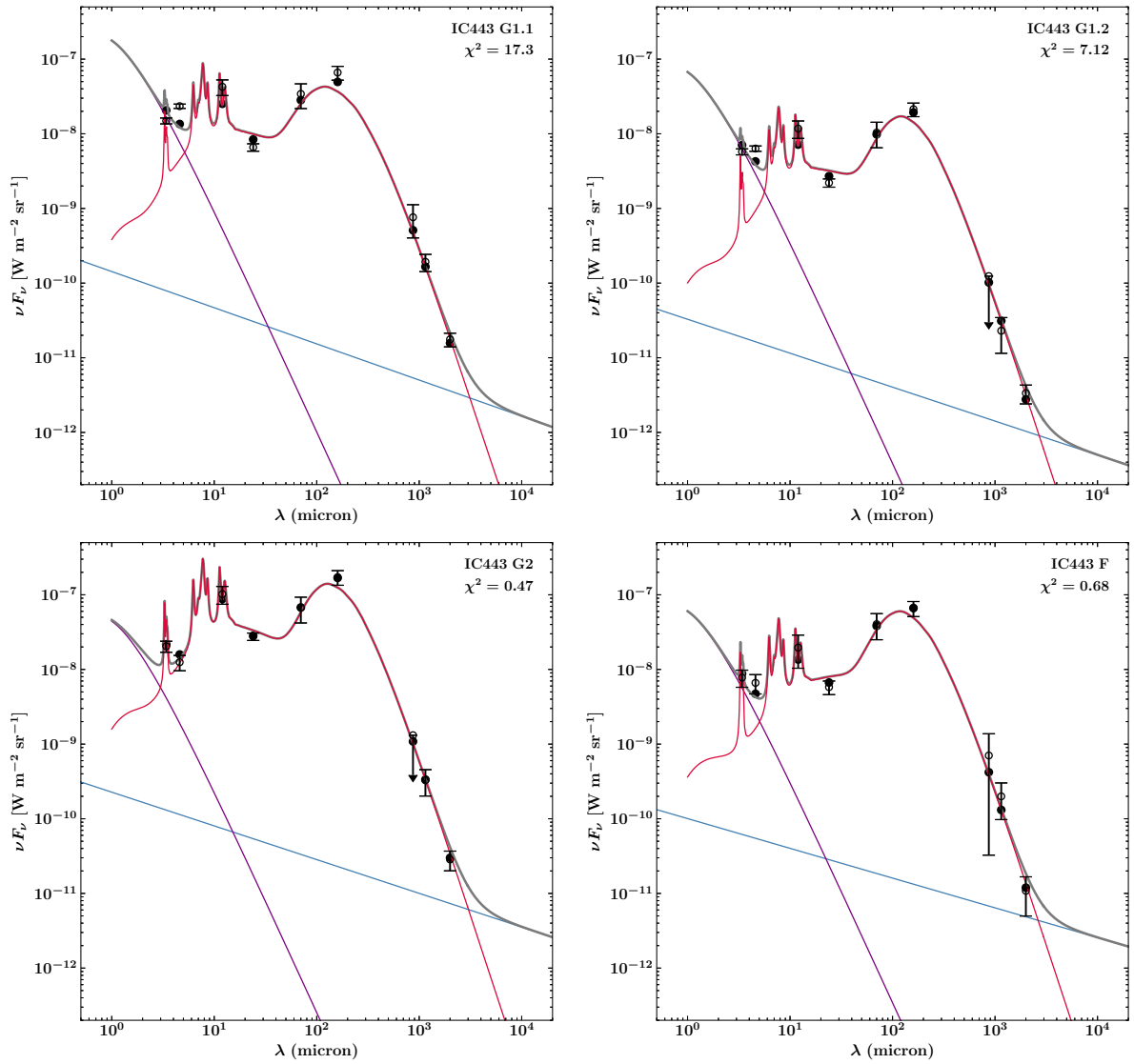

Figure 9.17 Average spectral energy distribution for the shocked clumps (IC443G1.1, G1.2 in the top row, IC443F in the bottom-left panel) and quiescent molecular structure (IC443G2, bottom-right panel). The average SEDs are measured in the boxes defined in Fig. 9.16. Observations are shown in black, with $\pm 1\sigma$ errorbars. The `HerBIE` models of the illuminated dust mixture `deltaU`, stellar continuum `starBB` and the power-law model of the radio continuum are shown respectively by red, purple and blue curves. The total model and synthetic photometric data points are shown in gray. The value of χ^2 is indicated in the top-right corner of the panels.

9.3.3 Results: *ii.*) Maps

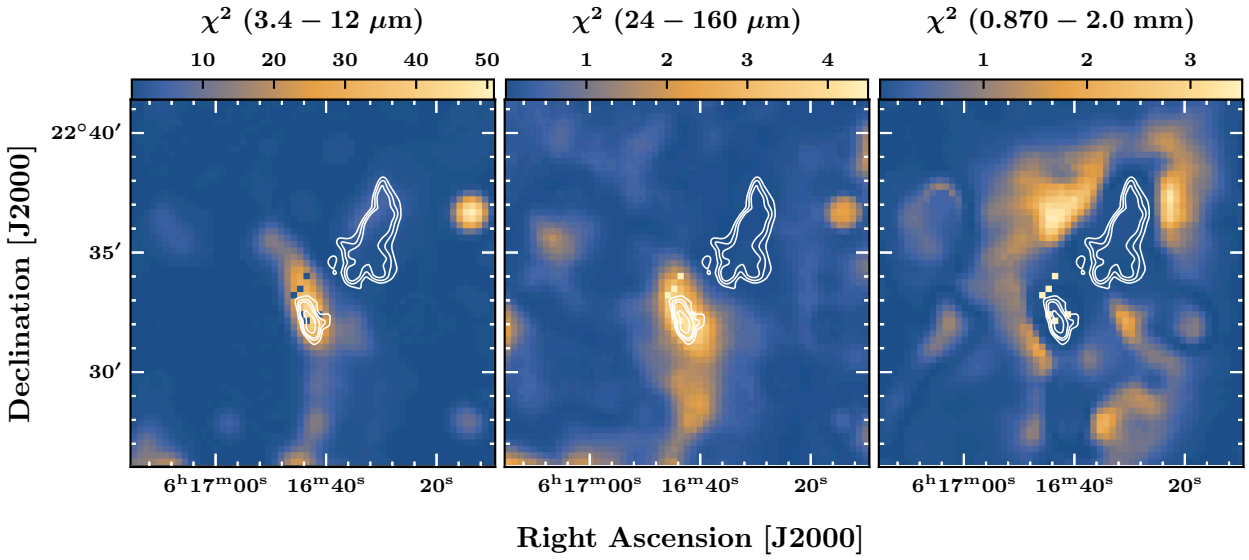

Figure 9.18 `HerBIE` reduced χ^2 maps in the wavelength ranges 3.4 – 12 μm (left panel), 24 – 160 μm (center-panel) and 0.870 – 2.0 mm (right panel). See Eq. 9.17.

9.3.3.1 Chi-square map

We produced *a posteriori* χ^2 maps by applying Eq. 9.17 in each pixel of the maps. We measured the χ^2 for specific wavelength ranges and produced the corresponding χ^2 maps:

- 'near-IR χ^2' (3.4 μm, 4.6 μm, 12 μm data points).
- 'mid-IR χ^2' (24 μm, 70 μm, 160 μm data points).
- 'millimeter χ^2' (870 μm, 1.15 mm, 20 mm data points).

The χ^2 maps are shown in Fig. 9.18. The maps show that the quality of the fit is correct between 24 μm and 2.0 mm ($0 \leq \chi^2 \leq 3$ for the most part of the field of observation). However, the 'near-IR χ^2' increases significantly towards the SNR molecular shell ($\chi^2 \sim 10^1$). In fact, both the 'near-IR χ^2' and 'mid-IR χ^2' trace the molecular shell, suggesting that we failed to remove entirely the contribution of spectral lines in these data points (that is, H_2 rovibrational lines at shorter wavelengths, and atomic and ionized lines such as O I and C II at intermediate wavelengths).

"Bad pixels" Our `HerBIE` output maps contain 6 "bad pixels" in which the best fit models did not converge correctly (see right panel in Fig. 9.18, towards the shocked clump). These errors might be caused by significant flux gradients coupled with PSF uncertainties. In all `HerBIE` output maps, we masked the bad pixels and replaced their values using a simple nearest interpolation algorithm.

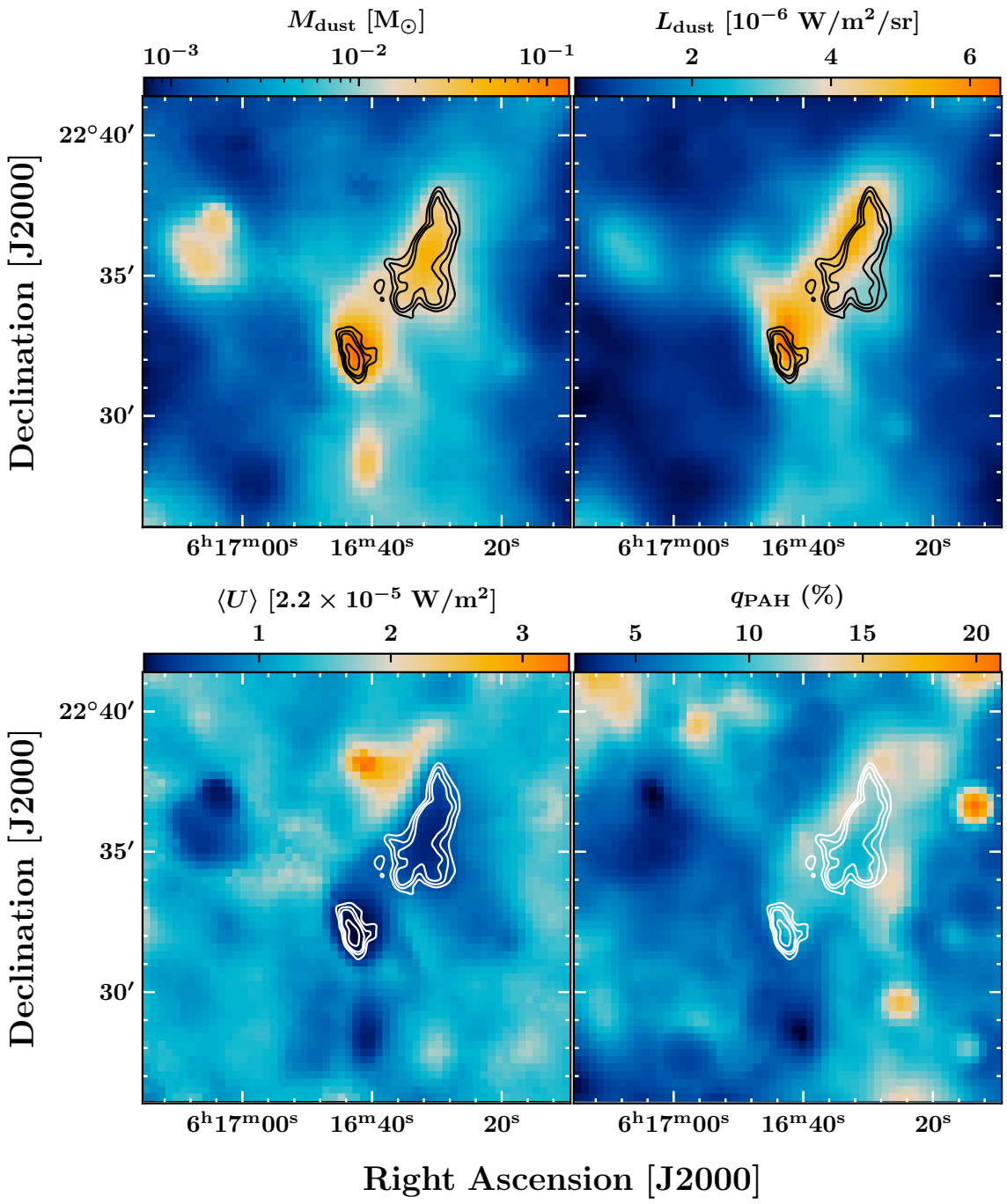

Figure 9.19 `HerBIE` output maps (1/2). *Top row:* total dust mass (left panel) and total dust luminosity (right panel). *Bottom row:* average starlight intensity heating the dust, $U = 1$ for the diffuse Galactic ISRF, corresponding to $4\pi \int J_\lambda d\lambda = 2.2 \times 10^{-5}$ W/m^2 between 0.0912 μm and 8 μm (shown on the left panel) and PAH mass fraction (right panel). The contours represent the IRAM 30m ^{12}CO J=2–1 peak map shown in Fig. 6.10 (contour levels: 0.25, 0.35, 0.45 and 0.75 times the maximum value across the map).

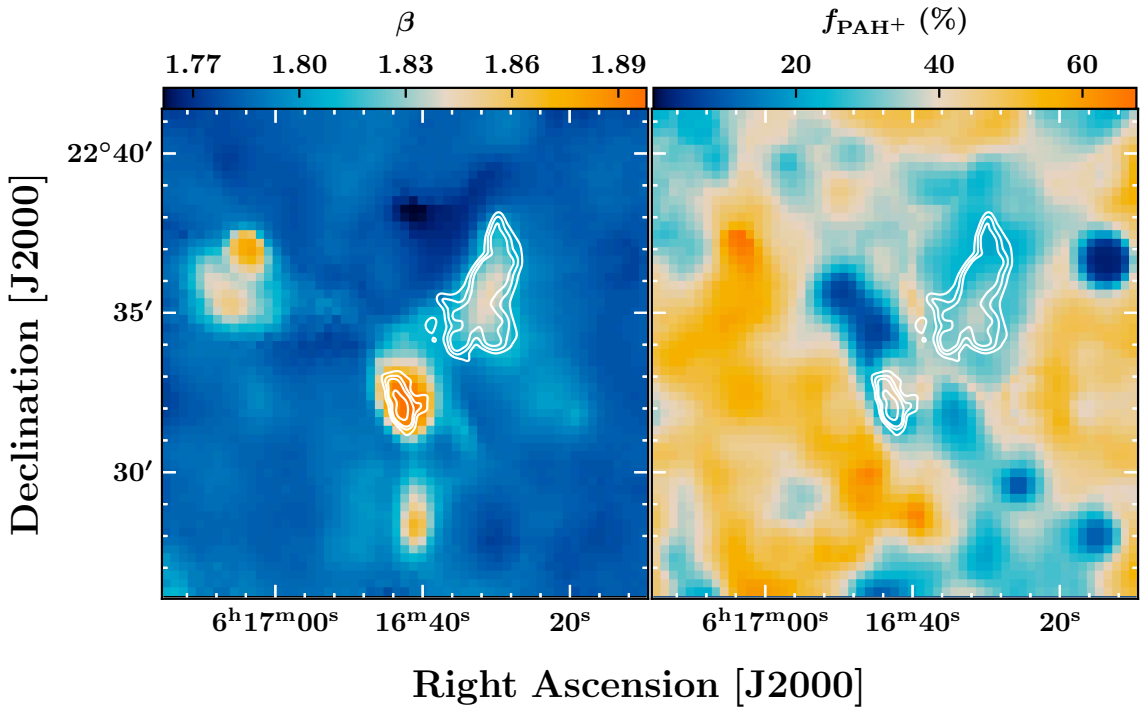

Figure 9.20 HerBIE output maps (2/2). *Left:* dust opacity index β. *Right*: charged PAH fraction. The white contours represent the IRAM 30m ^{12}CO J=2–1 peak map shown in Fig. 6.10 (contour levels: 0.25, 0.35, 0.45 and 0.75 times the maximum value across the map).

9.3.3.2 Physical parameters maps

In addition to the spectral energy distribution, the HerBIE output contains several maps tracing the spatial distribution of the physical components used by the model. In Fig. 9.19 and Fig. 9.20, we present the maps of the total dust mass, total dust luminosity, average ISRF intensity between 0.0912 µm and 8 µm, PAH mass fraction, dust opacity index and charged PAH fraction. The six bad pixels in these maps were replaced using nearest interpolation (see previous section).

Total dust mass In contrast to PPMAP, HerBIE does not directly output the total (dust + gas) mass, but only the total dust mass. The distribution of the total dust mass is shown in the top-left panel in Fig. 9.19. We produced the map from the '`im_M_powerU_mean.fits`' HerBIE output, in which the masses are given in kg m^{-2} sr^{-1}. We converted the mass measurements ΔM_{px} into solar mass units *via* the following equation:

$$\Delta M_{\mathrm{px}}\ [\mathrm{M}_\odot] = \Delta M_{\mathrm{px}}\ [\mathrm{kg\ m^{-2}\ sr^{-1}}] \left(\frac{4\pi D^2}{2 \times 10^{30}\ \mathrm{kg}} \right) \Delta\Omega_{\mathrm{px}}^2 \tag{9.18}$$

where $\Delta\Omega_{\mathrm{px}}$ is the angular size of a pixel (in radian), and D is the distance of the object. We adopted a distance $D = 1.8$ kpc (Ambrocio-Cruz *et al.* 2017, Yu *et al.* 2019). Fig. 9.19 shows that the bulk of the mass is held by the brightest structures (the shocked clumps 'G' and 'F', and the quiescent cloudlet), although there is also diffuse mass along the axis of the ambient cloud of Cornett *et al.* (1977). The total dust mass (summed over the $16' \times 16'$ field of observation) is $M_{\mathrm{dust}} = 18.6\ \mathrm{M}_\odot$.

Total dust luminosity The total luminosity emitted by thermal dust is shown in the top-right panel in Fig. 9.19 (corresponding to the `HerBIE` output '`im_Ldust_powerU_mean.fits`'). The total luminosity is dominated by the mid-IR data points (70 µm and 160 µm observations, see Fig. 9.6), and it is not completely correlated to the spatial distribution of the dust mass.

ISRF intensity The average ISRF intensity is shown in the bottom-left panel in Fig. 9.19 (corresponding to the `HerBIE` output '`im_Uav_powerU_mean.fits`'). The quantity shown in each pixel of the map is the average of the power-law distribution of U (denoted by $\langle U \rangle$). U is defined such that $U = 1$ for the diffuse Galactic ISRF, which is defined by:

$$4\pi \int_{0.0912\ \mu\mathrm{m}}^{8\ \mu\mathrm{m}} J_\lambda \mathrm{d}\lambda = 2.2 \times 10^{-5}\ \mathrm{W\ m^{-2}} \tag{9.19}$$

where J_λ is the local radiation field. In our $16' \times 16'$ field of observations, we observe roughly three regimes:

- In the interclump background, the intensity of the ISRF is mostly in the range $\langle U \rangle \simeq 1.1 - 1.4$, hence slightly higher than the diffuse Galactic ISRF.
- Within the dense molecular clumps where the dust grains are shielded from heating radiation, the intensity of the ISRF decreases down to $\langle U \rangle \simeq 0.1 - 0.3$.
- On the northeastern border of the quiescent cloudlet, a region of relatively intense ISRF extends from a point-like source, with $\langle U \rangle \simeq 2 - 3.4$. In addition, several sites of local enhancement of $\langle U \rangle$ are found across the map.

PAH mass fraction and charged fraction The PAH mass fraction ('q_{PAH}', introduced by Draine and Li 2007) is shown in the bottom-right panel in Fig. 9.19 (corresponding to the `HerBIE` output '`im_q_PAH_powerU_mean.fits`'), and the charged PAH fraction is shown in the right panel in Fig. 9.20 (corresponding to the `HerBIE` output '`im_fionPAH_powerU_mean.fits`'). Across the shocked SNR molecular shell, the PAH mass fraction is lower ($q_{\mathrm{PAH}} \simeq 0 - 5\%$.) than in the rest of the field of observation (the average fraction across the map is $\overline{q_{\mathrm{PAH}}} = 8\%$). In addition, there are several point-like sources associated with higher PAH mass fraction. The edges of the quiescent cloudlet are also correlated with a PAH enhancement $q_{\mathrm{PAH}} \simeq 10 - 15\%$.

In comparison with our results, the Galactic diffuse neutral medium q_{PAH} lies around 4.6% (Li and Draine 2001, Weingartner and Draine 2001), and the PAH mass fraction is known to be larger in molecular regions than in the diffuse ISM (*e.g.* from $\sim 0.6\%$ to $\sim 1\% - 2\%$ in the low-metallicity Small Magellanic Cloud (SMC), Sandstrom *et al.* 2010). There are several parameters to take into account to interpret our relatively high measurement of q_{PAH} in IC443:

- Coagulation and growth of PAHs and dust grains in dense molecular regions (Sandstrom *et al.* 2010, Köhler *et al.* 2012). Assuming that q_{PAH} increases by $\times 2 - 3$ from the diffuse ISM to molecular regions (as in the SMC) then our measurement would be consistent with the Galactic diffuse neutral medium PAH mass fraction ($q_{\mathrm{PAH}} = 4.6$, Li and Draine 2001).
- Dust synthesis and processing by interstellar shocks in the SNR (Jones *et al.* 1994, Micelotta *et al.* 2010, Biscaro and Cherchneff 2014, Bocchio *et al.* 2014, Bocchio *et al.* 2016, Micelotta

et al. 2018b, Sarangi *et al.* 2018). If the survival rate of PAHs is greater than the survival rate of non-PAH dust grains, then $q_{\rm PAH}$ might increase locally.

The charged PAH fraction varies between $\sim$ 1% and $\sim$ 60%. Lower PAH^+ fractions are correlated with the SNR shell, whereas the SNR cavity is characterized by a higher PAH^+ fraction.

Dust opacity index The dust opacity index map (β) is not directly produced by `HerBIE`. We measured the opacity index in each pixel of the map *a posteriori*, using the `Python` module `curve_fit` to find the best linear fit of the SED between 500 µm and 2.0 mm. The results are shown in Fig. 9.20 (left panel). The results are consistent with `PPMAP`, with an average $\beta \simeq 1.8$ across the map. However, there is an inversion of the variation between the background and the dense regions with respect to `PPMAP` (see *e.g.* Fig. B.4).

9.3.3.3 Estimate of the electron density from the PAH ionization fraction

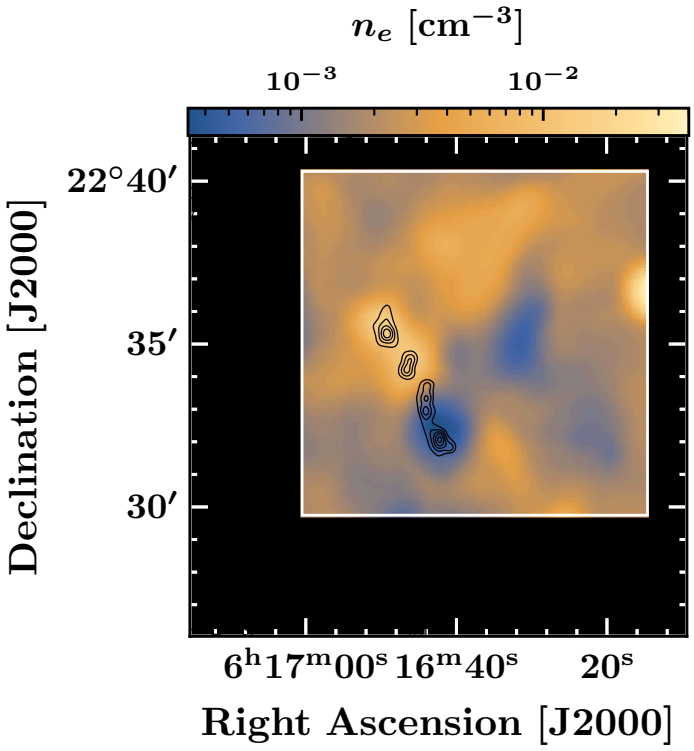

Figure 9.21 10′×10′ electron density map shown with respect to the 16′ × 16′ frame corresponding to `HerBIE` outputs (see also Fig. 9.19, Fig. 9.20). The quantity n_e is measured in each pixel based on Eq. 9.20 (Galliano *et al.* 2008, Boersma *et al.* 2015), using the rescaled $\langle U \rangle$ map as the G_0 parameter, in addition to the PAH charged fraction and gas temperature maps (respectively from Fig. 9.20 and Fig. 8.36). Black contours represent the radio continuum at 330 MHz (five contour levels between 20 mJy/beam and 30 mJy/beam).

The ionization state of the PAH population is directly related to the local radiation field and physical conditions of the gas (ionization and temperature, Tielens 2005). Following Boersma *et al.* (2015), the ionized/neutral PAH density ratio is tied to the strength of the radiation field G_0, gas temperature $T_{\rm gas}$ and electron density n_e:

$$n_{\rm PAH^+}/n_{\rm PAH} = 3.76 \times 10^{-5} G_0 T_{\rm gas}^{1/2}/n_e \tag{9.20}$$

where G_0 is the 'Habing field', *i.e.* the ISRF integrated between 0.09 µm and 0.24 µm (UV/optical radiation field, Habing 1968). This empirical relation was calibrated *via* ISO and *Spitzer*

observations of Galactic regions, Magellanic H II regions and galaxies of various types (Galliano *et al.*, 2008). The quantity $n_{\mathrm{PAH^+}}/n_{\mathrm{PAH}}$ corresponds to our $f_{\mathrm{PAH^+}}$ map (Fig. 9.20, right panel), and we have measured T_{gas} in Chapter 8 (see Fig. 8.36). In addition, G_0 is directly proportional to our measurement of the ISRF obtained with `HerBIE` ($\langle U \rangle$, Fig. 9.19, bottom-left panel). Using the knowledge of the ISRF SED, we can rescale $\langle U \rangle$ into G_0 (*e.g.* Le Petit *et al.* 2006). Therefore, we can use Eq. 9.20 to determine the electron density n_e.

We present the results in Fig. 9.21. Our map size is restricted by the field of view of our ^{12}CO observations ($10' \times 10'$). We find that the electron density is $n_e \sim 5 \times 10^{-4} - 10^{-3}$ cm^{-3} towards the molecular features, and up to $n_e \sim 10^{-2}$ cm^{-3} in the rest of the field of observations. Based on our estimate of the local density (see section 8.2.6, Tab. 8.8), the ionization fraction is $\sim 10^{-7}$ towards the shocked clump and quiescent small cloud, and up to $\sim 10^{-4}$ in the more diffuse background.

Our estimates are consistent with studies of the ionization fraction in dense molecular gas ($10^{-7.5} - 10^{-6.5}$, Williams *et al.* 1998) and in the cold neutral medium ($\sim 10^{-3}$, McKee and Ostriker 1977). We compared our electron density map with the continuum emission at 330 MHz (black contours in Fig. 9.21, Castelletti *et al.* 2011). We find that the bright 330 MHz knots are correlated with the increased electron density patch to the northeast of the shocked clump, which provides an interpretation for free-free/synchrotron enhancement in this region.

9.4 | Discussion

9.4.1 HERBIE/PPMAP results comparison

Spectral energy distribution In Fig. 9.22, we compare the average spectral energy distribution obtained with `HerBIE` and `PPMAP` in the $16' \times 16'$ field of observations. The `PPMAP` model used in the comparison is our 'overall best fit' model, *i.e.* the '`PPMAP-B2`' run (obtained with eight temperatures between 10 K and 30 K, and $\beta = \{1.6, \ , 1.7, \ 1.8, \ 1.9, \ 2.0\}$, see Tab. 9.9).

We produced the average SED corresponding to statistically significant pixels only (*i.e.* pixels that satisfy the condition $F_\nu(\lambda) \geq 3\sigma$ for any observed λ, where σ is the r.m.s). In Fig. 9.22, we also show the decomposition in individual `PPMAP` components corresponding to distinct dust temperatures T_{d} and opacity indices β (represented by thin, semi-transparent blue curves). The total `PPMAP` model is the sum of all components (solid blue curve). Between 70 µm and 160 µm (TEGs emission), the total `PPMAP` model is in close agreement with the total `HerBIE` model (average relative difference $\sim 1\%$).

Mass measurements We compare the total mass maps inferred with `HerBIE` and `PPMAP` in Fig. 9.23 (using the '`PPMAP-B2`' model, see Tab. 9.9). We used Eq. 9.12 to produce the `PPMAP` total mass map (dust + gas) from the '`cdens.fits` output file. We also convolved the `PPMAP` mass map with a gaussian kernel for consistency with the `HerBIE` map. `HerBIE` returns the total dust mass only (see Eq. 9.18). Therefore, we converted the dust mass measurement into a total mass estimate using the gas-to-dust ratio $GDR = 100$, for consistency with `PPMAP` assumptions (Marsh *et al.* 2015, Hildebrand 1983). Fig. 9.23 shows that `HerBIE` recovers more mass than `PPMAP`, both towards the bright molecular structures and in the extended region that corresponds to the molecular cloud of Cornett *et al.* (1977).

Using the `Python` module `reproject`, we spatially regridded the `PPMAP` outputs onto the

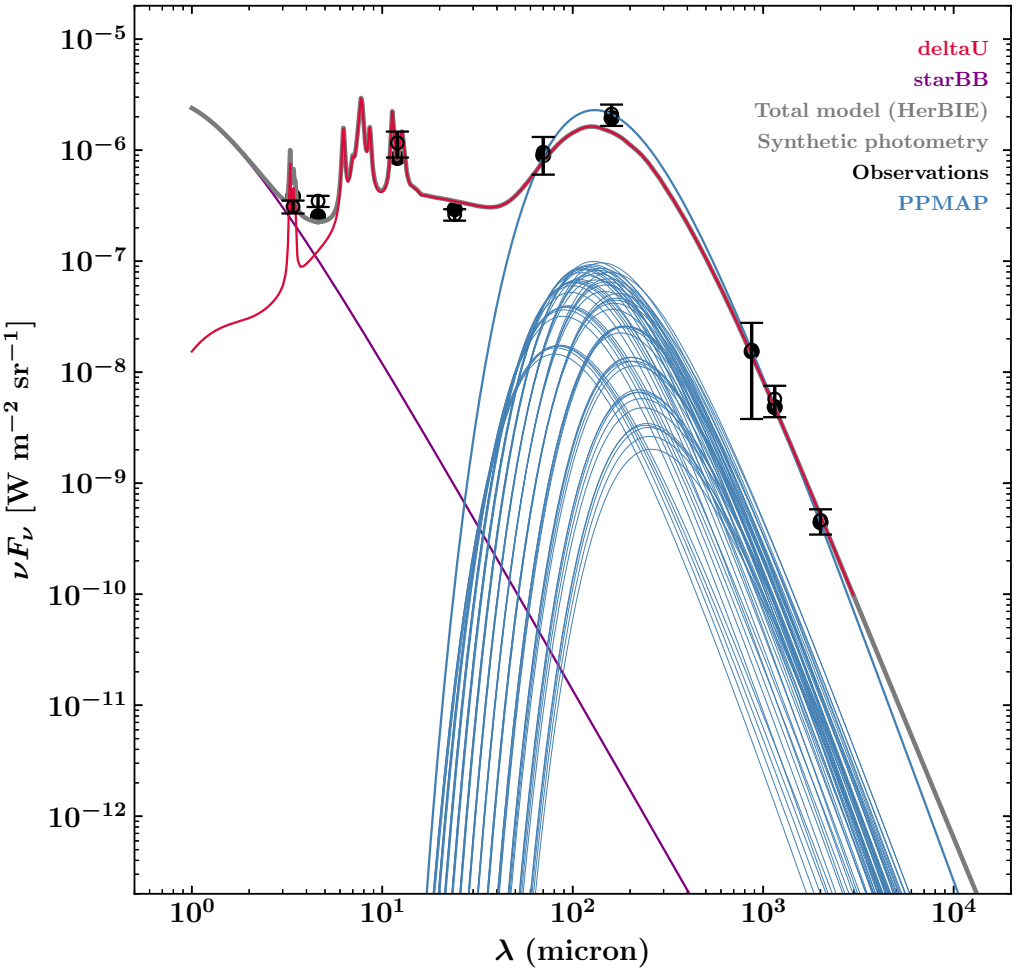

Figure 9.22 Comparison between the `HerBIE` and '`PPMAP-B2`' average spectral energy distribution in the $16' \times 16'$ field of observations (restricted to statistically significant pixels: $F_\nu(\lambda) \geq 3\sigma$, where σ is the r.m.s). Observations are shown in black, with $\pm 1\sigma$ errorbars. The `HerBIE` models of the illuminated dust mixture `deltaU` and stellar continuum `starBB` are shown respectively by the red and purple curves. The `HerBIE` total model and synthetic photometric data points are shown in gray. The `PPMAP` total model and individual $N(T_{\rm dust}, \beta)$ components are shown in blue.

`HerBIE` products and performed a pixel-per-pixel comparison between the `PPMAP` and `HerBIE` mass maps (see Fig. 9.24). The maps are well correlated, but the relation between the `PPMAP` and `HerBIE` masses is not linear. More than 95% of the pixels satisfy the condition $M_{\rm PPMAP} \leq M_{\rm HERBIE} \leq 6M_{\rm PPMAP}$, where $M_{\rm PPMAP}$ and $M_{\rm HERBIE}$ are respectively the total (dust + gas) mass inferred by `PPMAP` and `HerBIE`. The pixels in which the discrepancy is the most important are the pixels that hold the greater masses, whereas the pixels with the lowest masses tend to a 1:1 ratio between the `PPMAP` and `HerBIE` mass measurements.

The combination of Fig. 9.22 and Fig. 9.24 shows that `HerBIE` and `PPMAP` can both reproduce the observations in the FIR-millimeter range with quasi-identical best fit SEDs (relative difference $\sim$ 1%) and yet provide distinct mass measurements (in some pixels, up to a six-fold mass enhancement from `PPMAP` to `HerBIE` results).

This discrepancy in the measurement of the total mass might be caused by the choice of the PPMAP normalization constant (2.1×10^{24} cm^{-2} in Eq. 9.7, related to $\kappa_{300} = 10$ cm^2 g^{-1}). In

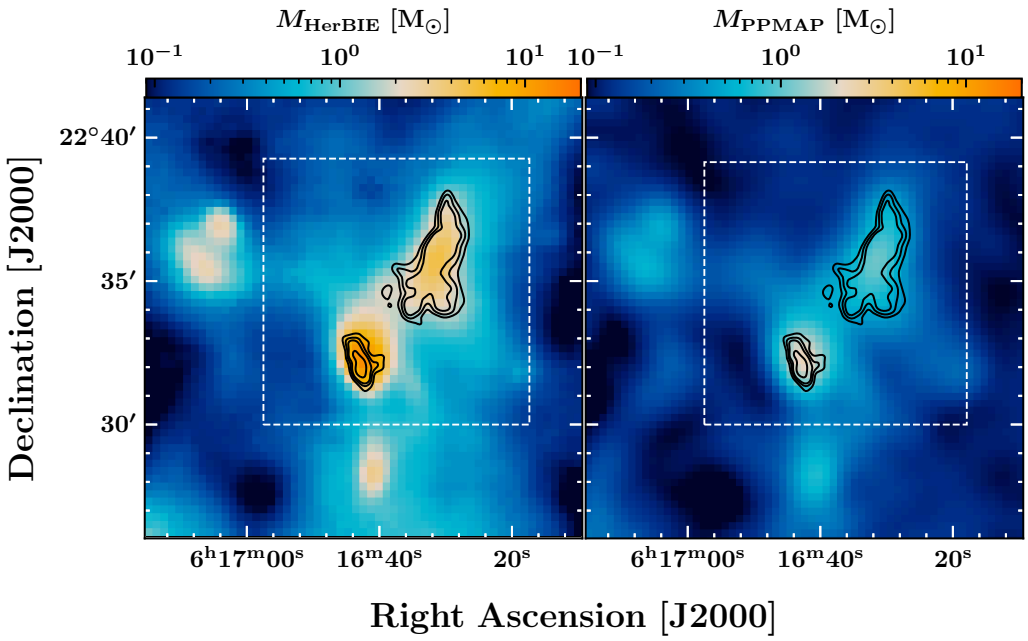

Figure 9.23 Comparison between the `HerBIE` and '`PPMAP-B2`' total mass maps (assuming a gas-to-dust ratio GDR = 100). The white dashed box represents the 10′ × 10′ IRAM 30m / APEX field of observation. Black contours represent the IRAM 30m ^{12}CO J=2–1 peak map shown in Fig. 6.10 (contour levels: 0.25, 0.35, 0.45 and 0.75 times the maximum value across the map).

addition, `PPMAP` and `HerBIE` are based on distinct assumptions. `PPMAP` is based on a simple sum of MBB models in which all the dust grain optical properties are modelled by a power-law opacity (see Eq. 5.13), whereas `HerBIE` uses a THEMIS grain mixture stochastically heated by a non-uniform ISRF (see Eq. 5.17). The description of dust emission by `HerBIE` is more accurate, although more physical parameters also means more uncertainty on the determination of these parameters.

9.4.2 Comparison with ^{12}CO mass measurements

Comparison of the dust and molecular gas mass spatial distributions In Chapter 8, we obtained several maps of the total molecular mass in a 10′ × 10′ field of observations (the 'extended G region'). Our estimate of the total molecular mass relied on an analysis of the emission of ^{12}CO lines (see section 8.2.6 for a summary). We convolved our ^{12}CO-inferred molecular mass map with a gaussian kernel for consistency, and then spatially regridded the map onto the `HerBIE` outputs. In Fig. 9.25, we compare the dust mass map obtained with `HerBIE` with our LTE ^{12}CO-inferred molecular mass map:

– The respective spatial distributions of the total dust mass and molecular gas mass are partially correlated. There is a higher correlation towards the main molecular features than in the background. The ^{12}CO-inferred molecular mass map is more correlated to the molecular cloud of Cornett *et al.* (1977) than the `HerBIE` map.

– Assuming a gas-to-dust ratio GDR = 100 (Hildebrand, 1983), the total mass found towards the main molecular features with `HerBIE` is larger than the mass found with ^{12}CO lines (in

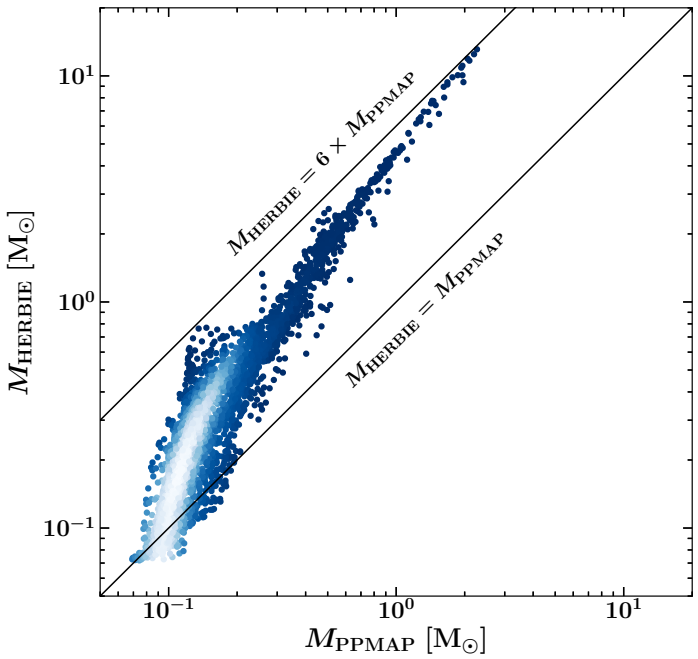

Figure 9.24 Direct, pixel-per-pixel comparison between the `HerBIE` and `PPMAP` total mass maps (dust + gas mass, respectively denoted $M_{\rm HERBIE}$ and $M_{\rm PPMAP}$). Each point in the diagram represents a measurement corresponding to a pixel (in solar mass units). The color of the points represents the kernel density estimate of the sample (*i.e.* the local density of the data points, produced using the `Python` module `scipy.stats.gaussian_kde`). In addition, two black straight lines indicate the boundaries of the domain in which $M_{\rm PPMAP} \leq M_{\rm HERBIE} \leq 6M_{\rm PPMAP}$.

particular for the shocked clump 'G'), although it is lower across the south-western area that corresponds to the ambient cloud of Cornett *et al.* (1977).

– The local molecular gas depletion on the north-eastern edge of the quiescent cloudlet is spatially correlated with the area characterized by an enhanced ISRF intensity $\langle U \rangle = 3$ (see bottom-left panel in Fig. 9.19). The dust mass map does not display the same depletion, hence this region seems to be associated to a higher dust-to-gas ratio that is characteristic of the diffuse ISM.

pixel-per-pixel comparison In Fig. 9.26, we compare the dust mass found with `HerBIE` ($M_{\rm dust}$) to the molecular gas mass inferred with the analysis of ^{12}CO lines in each pixel of the maps. In addition, we drew straight lines that represent constant gas-to-dust mass ratios (GDR = 12.5, 100, 400). More than 99% of the pixels satisfy the condition $12.5 \leq GDR \leq 400$. The distribution is scattered, but the mean and median of the gas-to-dust ratio are respectively $\overline{GDR} = 99.3$ and median(GDR) = 89.7, which is close to the expected ratio ($GDR = 100$, Hildebrand 1983). Hence, although there are significant local variations, on average the gas-to-dust ratio inferred from the comparison of our `HerBIE` dust masses with the molecular mass found in Chapter 8 is consistent with the expected gas-to-dust ratio ($GDR = 100$).

Mass measurements: quantitative summary We measured the total masses obtained with the `PPMAP` and `HerBIE` results in distinct areas of the maps (assuming a standard gas-to-dust ratio $GDR = 100$, Hildebrand 1983). For consistency with the result presentation in Chapter 8, we used the boxes defined in Fig. 8.23 (including the double-peaked shocked clump 'G' and the quiescent cloudlet) and Fig. 9.16 (including the IC443 'F' clump). The measurements are summarized in Tab. 9.11, which allows to directly compare the continuum-based mass measurements (`HerBIE` and `PPMAP`) with the ^{12}CO-based mass measurements.

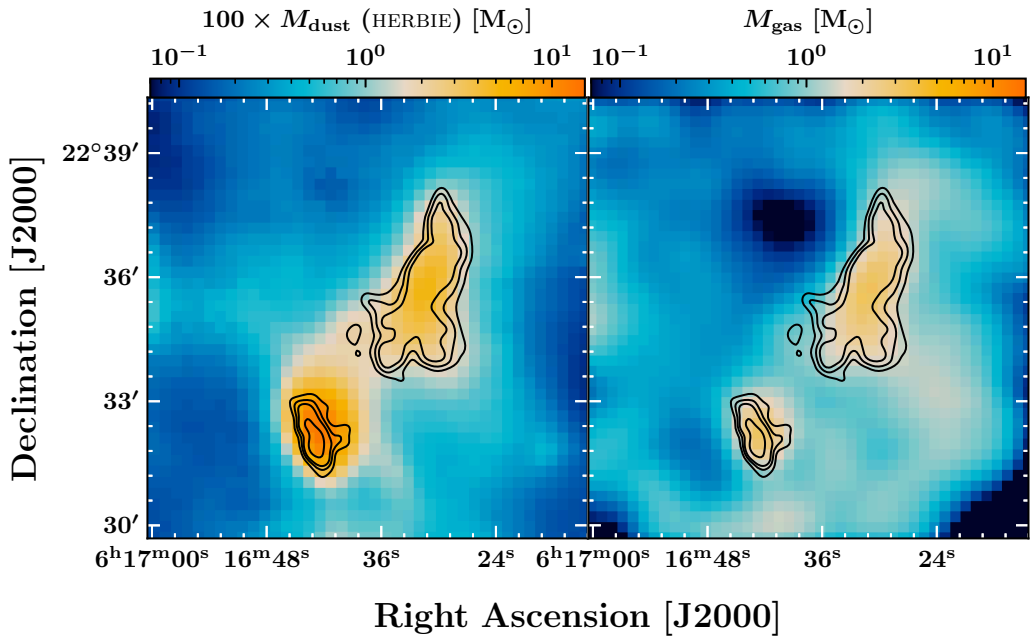

Figure 9.25 Comparison between the `HerBIE` dust mass (multiplied by the gas-to-dust ratio $GDR = 100$, Hildebrand 1983) and ^{12}CO-inferred molecular gas mass maps in the $10' \times 10'$ shared field of observations (see Chapter 8). Black contours represent the IRAM 30m ^{12}CO J=2–1 peak map shown in Fig. 6.10 (contour levels: 0.25, 0.35, 0.45 and 0.75 times the maximum value across the map).

9.4.3 Summary

Conclusions of this section Using new continuum observations with NIKA2 at 1.15 mm and 2.0 mm and archival data at shorter wavelengths, we have studied the thermal emission of dust grains (between 3.4 µm and 2.0 mm) in the IC443 SNR. We have obtained results with the Bayesian MBB-approximation algorithm `PPMAP`, and with the Hierarchical Bayesian stochastic-heating algorithm `HerBIE` coupled with the THEMIS dust model. Our main findings are the following:

(a) From an analysis of spectral-line observations (*Spitzer*/IRS, *Herschel*/PACS, IRAM 30m, APEX) we found that several ionic, atomic and molecular lines contribute significantly to the flux of our near-IR to millimeter broadband observations (see the measurements in Tab. 9.5). Most importantly, H_2 lines contribute to our near-IR and mid-IR data points (WISE, *Spitzer*/MIPS), [O I] and [C II] lines to our FIR data points (*Spitzer*/MIPS, AKARI/FIS) and ^{12}CO lines contribute in the millimeter range (LABOCA, NIKA2).

(b) Since our spectral-line observations do not entirely cover the extent of our $16' \times 16'$ NIKA2 field of observations, the correction of line contribution is associated with significant uncertainties (see Tab. 9.6 and Tab. 9.7). The correction of the contribution by ^{12}CO J=2–1 and J=3–2 lines is performed pixel-per-pixel in a restricted $10' \times 10'$ area, and the correction of the rest of the lines is based on average measurements in smaller fields towards the shocked clump (typical size $\sim 1' \times 1'$, see Tab. 9.4 and Tab. 9.5). In the future, the correction of the contribution by spectral lines could be improved by including additional observations in the analysis and/or producing pixel-per-pixel templates extrapolated from a reference map.

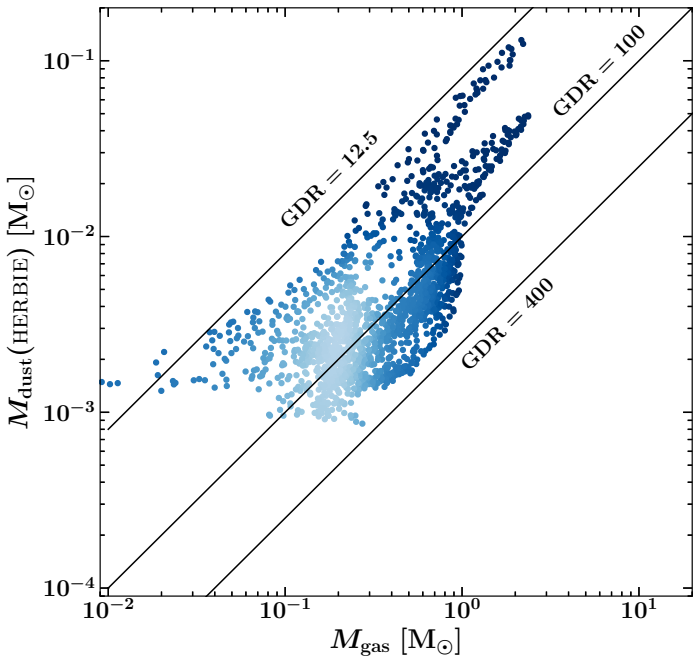

Figure 9.26 Direct, pixel-per-pixel comparison between the `HerBIE` dust mass and ^{12}CO-inferred molecular gas mass maps (respectively denoted $M_{\rm dust}$ and $M_{\rm gas}$). Each point in the diagram represents a measurement corresponding to a pixel (in solar mass units). The color of the points represents the kernel density estimate of the sample (*i.e.* the local density of the data points, produced using the `Python` module `scipy.stats.gaussian_kde`). In addition, black straight lines indicate the corresponding values of the gas-to-dust ratio $GDR = M_{\rm gas}/M_{\rm dust}$.

(c) In addition to spectral lines, our continuum observations trace a mixture of zodiacal light, line-of-sight emission and intrinsic emission from the supernova remnant itself. The background removal in the *Spitzer*/MIPS 160 µm map represents an additional significant uncertainty ($\sim$ 10%).

(d) Our preliminary `PPMAP` results suggested that our 70 µm and 90 µm maps trace a mixture of thermal emission from equilibrium grains (TEGs) and stochastically heated smaller grains (VSGs). We removed these observations from our `PPMAP` analysis.

(e) We successfully reproduced the continuum observations with `PPMAP` modelled SEDs (average global $\chi^2 = 2.2$ in statistically significant pixels with the '`PPMAP-B2`' best fit model). The best fit obtained with `PPMAP` favors an opacity power-law index $\beta = 1.8 \pm 0.1$ (see Tab. 9.9), which is $\sim$ 10% higher than the average Milky Way opacity index ($\beta = 1.62$, Planck Collaboration *et al.* 2014a).

(f) We experimented with different `PPMAP` weighting approaches. Based on the quality of the best fit with respect to the millimeter data points, we found that the 'r.m.s weighting' method (based on noise measurements) yields more accurate results (in terms of eventual chi-square values) than the 'uniform weighting' method (see section 9.2.2).

(g) The results obtained with `PPMAP` are sensitive to the dilution parameter η. The total (dust + gas) mass is characterized by a near four-fold enhancement if the dilution is modified from $\eta = 0.03$ to $\eta = 3$ (see Tab. 9.10), and the differential column density distribution in temperature is altered (see Fig. B.5, Fig. B.6).

(h) Using a restricted sample of continuum observations (three data points in the wavelength range $\lambda = 140 - 870$ µm) we performed a `PPMAP` analysis of the entire IC443 SNR (results are

region (name)	Mass ($M_\odot$) (^{12}CO analysis)	Mass ($M_\odot$) (HerBIE)	Mass ($M_\odot$) (PPMAP)	$\overline{GDR}$ (gas-to-dust mass ratio)
cloudlet	180^{+190}_{-80}	220 ± 50	80^{+70}_{-20}	80^{+50}_{-40}
ring-like structure	160^{+190}_{-70}	240 ± 60	70^{+30}_{-15}	70^{+50}_{-20}
shocked clump 'G'	80^{+90}_{-40}	400 ± 100	100 ± 20	20^{+20}_{-10}
shocked knot 'G'	15^{+30}_{-10}	40 ± 10	15^{+15}_{-5}	40^{+50}_{-20}
ambient cloud	300^{+600}_{-200}	350 ± 100	200^{+300}_{-50}	85^{+115}_{-45}
shocked clump 'F'	-	170 ± 40	70^{+70}_{-15}	-
IC443G ($10' \times 10'$)	700^{+900}_{-300}	1200 ± 300	500^{+500}_{-200}	60^{+50}_{-20}
IC443 ($16' \times 16'$)	-	1900 ± 400	800^{+1400}_{-200}	-
IC443 ($40' \times 40'$)	-	-	5500 ± 1500	-

Notes. The masses are measured in the boxes defined in Fig. 8.23 and Fig. 9.16. The masses from the ^{12}CO analysis correspond to the masses in the third column of Tab. 8.8. The second column is produced by multiplying the HerBIE dust masses by the standard gas-to-dust ratio $GDR = 100$ (Hildebrand, 1983). The PPMAP masses correspond to the 'PPMAP-B2' model, and the errorbars are based on the 'PPMAP-C1' and 'PPMAP-C2' models (variation of the dilution parameter η). In the last column, we indicate the average gas-to-dust ratio $\overline{GDR}$ inferred from our measurements, defined by the ratio of the '^{12}CO-inferred' (second column) molecular mass and HerBIE dust mass.

Table 9.11 Summary and comparison of the mass measurements based on the analysis of ^{12}CO lines and continuum observations with PPMAP and HerBIE.

shown in Fig. B.8 and B.9). We found a total (dust + gas) mass $M = 2500 - 5500\ M_\odot$.

(i) We successfully reproduced the continuum observations with HerBIE modelled SEDs (average global $\chi^2 = 2.8$ in statistically significant pixels). Along the molecular shell, we observe an increased χ^2 (up to $\sim 10^1$ in some pixels) for the near-IR data points. It is likely that we missed the correction of additional spectral lines contributing to our near-IR broadband flux measurements (such as H_2 $v = 1,\ 2,\ 3,\ ...$ rovibrational lines, Kokusho *et al.* 2020).

(j) We included VLA observations at 330 MHz and 74 MHz in our analysis of the HerBIE best fit spectral energy distribution. Using an *a posteriori* power-law model to study the contribution of the free-free and synchrotron continua to our millimeter data points, we found that the contribution is mostly negligible (with the exception of the IC443 'G1.2' and IC443 'F' average SEDs in which the contribution at 2.0 mm is of order 1σ, see Fig. 9.17).

(k) With the HerBIE pixel-per-pixel best fit models, we obtained maps of the total dust mass, total dust luminosity, ISRF intensity, dust opacity index, PAH mass fraction and charged PAH fraction (see Fig. 9.19, Fig. 9.20).

– The ISRF intensity map shows a local enhancement of the radiation field ($\langle U \rangle = 2 - 3.4$) towards the north-eastern edge of the quiescent cloudlet, which is correlated with an area where the molecular gas is depleted (see Fig. 9.25, right panel). The average ISRF in the rest of the field varies between $\langle U \rangle = 1.1 - 1.4$ (in the diffuse background) and $\langle U \rangle = 0.1 - 0.3$ (in the shielded, dense molecular shell).

– The average PAH mass fraction in our $16' \times 16'$ field of observations is $\overline{q_{\rm PAH}} = 17\%$. The PAH mass fraction increases on the edge of the quiescent cloudlet ($q_{\rm PAH} = 25 - 30\%$) and decreases within the dense molecular shell of the SNR ($q_{\rm PAH} = 0 - 10\%$). Our results suggest either the destruction of PAHs in the shocked molecular shell, or coagulation and coalescence into non-PAH dust grains.

(l) We compared our `HerBIE` and `PPMAP` total (dust + gas) mass measurements. We found that `PPMAP` is associated with a reduced total mass ($\sim 50\%$ of the mass found with `HerBIE`). In some pixels of the `HerBIE` mass map, the discrepancy corresponds to a six-fold enhancement with respect to the `PPMAP` mass map (see Fig. 9.24). Interestingly, there is an inversion of the variation of the opacity index β from the background to denser regions (between `PPMAP` and `HerBIE`: compare Fig. 9.20 with Fig. 9.9).

(m) We compared our `HerBIE` dust mass map with the molecular gas mass map obtained from the analysis of ^{12}CO lines in Chapter 8. Assuming a gas-to-dust ratio $GDR = 100$ (Hildebrand, 1983), we compare the total (dust + gas) mass maps in Tab. 9.11. We find that within errorbars, the `HerBIE` and '^{12}CO-based' measurements are in agreement (although the `HerBIE` mass measurements are systematically higher). The only exception is the shocked clump, for which the `HerBIE` mass is approximately $\times 5$ higher.

(n) From our pixel-per-pixel measurements of the charged PAH fraction and ISRF intensity, we estimated the electron density in a $10' \times 10'$ field of observations (see Fig. 9.21). We found that the electron density varies between $\sim 5 \times 10^{-4}$ cm^{-3} and $\sim 10^{-2}$ cm^{-3}. The enhancement of the electron density is correlated with the emission at 330 MHz, and the ionization fraction varies between $\sim 10^{-7}$ and $\sim 10^{-4}$.

We will discuss these conclusions with respect to our initial scientific goals in section 10.5 (general conclusion).

Chapter 10 | The stellar contents of the IC443 supernova remnant

Contents

Introduction In chapters 8 and 9, we studied the interstellar contents of the IC443 SNR. Firstly, we studied the cold molecular phase traced by ^{12}CO rotational lines in the $10' \times 10'$ 'extended G region' mapped with the IRAM 30m and APEX telescopes. In addition, we studied the warm molecular phase in a $2' \times 2'$ area mapped with *Spitzer*/IRS observations of H_2 pure rotational lines. Secondly, we studied the interstellar dust phase traced by 3.4 μm to 2.0 mm broadband flux measurements in a $16' \times 16'$ region mapped with new NIKA2 observations (the IRAM 30m continuum camera performing at 1.15 mm and 2.0 mm).

Ultimately, we have obtained maps of the molecular and dust masses and column densities, molecular gas temperature (both for the cold and warm phases towards the shocked clump 'G'), dust temperature, interstellar radiation field intensity (ISRF), molecular gas turbulent kinetic energy and PAH mass fraction. In this chapter, we aim to characterize the local star formation in the IC443 SNR, and to discuss our findings in relation to the interstellar measurements obtained in the previous chapters, and also in relation to several tracers (synchrotron features traced by radio continuum emission, ionized gas tracers, interferometric high-resolution observations, *etc*).

In the following sections, we study the distribution of optical, infrared and near-infrared point sources in the $16' \times 16'$ field of observations. We aim to check if these infrared point sources can be identified as young stellar objects (YSO) and if so, to constrain their evolutionary stage based on their infrared fluxes. Finally, we aimed to study their spatial distribution and their association with the molecular phase, dust phase and ISRF features found in our interstellar analysis. A question

that we aim to answer is whether or not YSOs could contribute to inject fresh CRs in the extended G region, which would contribute to the γ-ray spectrum.

Table 10.1 Photometric parameters summary for each band of the telescopes WISE (W_1, W_2, W_3, W_4, Wright *et al.* 2010), 2MASS (J, H, K, Skrutskie *et al.* 2006) and Gaia (Gaia Collaboration *et al.* 2016, Gaia Collaboration *et al.* 2018) used in this chapter. λ is the central wavelength of the band, $\Delta\lambda$ the band width and 'FWHM' is the full width at half maximum of the point spread function (corresponding to a 2.5″ seeing for the 2MASS ground-based observations, and to the diffraction limit for the WISE and Gaia space observatories).

band	λ (µm)	$\Delta\lambda$ (µm)	FWHM (″)
WISE W_1	3.35	0.66	6.1
WISE W_2	4.60	1.04	6.4
WISE W_3	11.56	5.51	6.5
WISE W_4	22.09	4.10	12.0
2MASS J	1.235	0.162	2.5
2MASS H	1.662	0.251	2.5
2MASS K	2.159	0.262	2.5
band	λ (nm)	$\Delta\lambda$ (nm)	FWHM (″)
Gaia G	673	440	0.4
Gaia G_{BP}	532	253	0.4
Gaia G_{RP}	797	296	0.4
Gaia G_{RVS}	860	28	0.4

10.1 | near-IR/mid-IR point source census

Available data The IC443 SNR was fully mapped both by the 2MASS and WISE all-sky surveys. 2MASS operates between 1.235 μm and 2.159 μm, and WISE between 3.4 μm and 22 μm. The exact photometric parameters for each band of 2MASS and WISE are given in Tab. 10.1 (see also Chapter 3).

Data acquisition In order to obtain point source catalogs in the extended G region from the WISE and 2MASS all-sky surveys, we used the NASA/IPAC infrared science archive. We set up a query to obtain all entries in a 16 arcmin sized square box around the field center $\alpha_{[J2000]}$=6^{h}16^{m}43.5^s, $\delta_{[J2000]}$=+22°34′00″, corresponding to the field mapped with NIKA2 continuum camera.

A total of 1244 point sources in the 2MASS All-Sky Point Source Catalog (PSC) and 1304 point sources in the AllWISE Source Catalog were found using this query. At this stage, we did not perform a study of simultaneous detections by both WISE and 2MASS (see next section). Both catalogs provide position coordinates, photometric measurements for each band and their uncertainties, signal-to-noise ratio, as well as several flags specifying contamination by extended emission, quality of the PSF-profile fit and other possible sources of bias.

10.1.1 WISE and 2MASS census

Preliminary filtering In order to reject false positives, we applied several selection criteria to our primary catalogs of point sources detected by 2MASS and WISE:

1. We required a complete detection in the WISE bands W_1, W_2 and 2MASS bands J, H and K (*i.e.* the measurement is not an upper limit).

2. We selected only the sources characterized by a signal-to-noise ratio greater than 2 for the photometric bands W_1, W_2, W_3, J, H and K.

3. We rejected the WISE point sources that were flagged for confusion and/or contamination of the photometric bands by image artifacts.

4. We rejected the 2MASS point sources that were flagged for low quality photometric measurements.

Double detections After this preliminary selection, 494 out of 1304 point sources remain for the AllWISE Source Catalog and 915 out of 1244 for the 2MASS PSC. We checked the catalogs to determine if some point sources are detected by both surveys. We parsed the catalogs and measured the distances between each source, assuming that a 2MASS and WISE source are matched if the angular distance that separates the two sources is below 10″. With this distance criterion, we found that a total of 263 point sources are detected both by 2MASS and WISE.

Extended sources AllWISE point sources marked with a value of *ext_flg* flag different from zero are indicated as extended sources. Either their morphology is not consistent with the point spread function of any band or they are spatially associated with a known extended source of the 2MASS Extended Source Catalog (XSC). 2MASS point sources with *gal_contam* = 0 are also sources that overlap with the elliptical profile of a known extended source. A search in the 2MASS XSC catalog shows that 28 extended sources are found in our 16′ × 16′ field. The shocked clump is particularly crowded, suggesting that the extended emission of bright knot of shocked material are detected by the survey in this area.

This was our biggest issue when looking for possible YSOs: their signature can often not be differentiated from local knots of shocked material traced in *e.g.* H_2 lines that are contained in the 2MASS and WISE bands. The photometric measurements are likely to be contaminated by this extended emission, hence the identification of these sources as YSO candidates is uncertain. Nonetheless we do not completely rule out these entries in the catalog since this extended emission might be produced by outflows, and not only by the SNR shock structure at the location where it interacts with the local molecular cloud(s).

10.1.2 Color-color filtering

2MASS color-color filtering We applied color-color criteria to our near-infrared point source catalogs to select point sources that could possibly be YSOs. To identify the nature of a YSO candidate detected by 2MASS, we compared the relative flux in the J, H and K photometric bands. We used the following empirical color criteria (Xu *et al.* 2011), based on the idea that YSOs have an infrared excess in the 1.235-2.159 µm range that determines their position in the JHK color-color space and that is directly related to their evolutionary stage (Lada and Adams 1992):

$$\begin{aligned} (J-H) - 1.7 \cdot (H-K) + 0.450 &= 0 \\ (J-H) - 0.493 \cdot (H-K) - 0.439 &= 0 \\ (J-H) - 1.7 \cdot (H-K) + 1.400 &= 0 \\ (J-H) &= 0.2 \end{aligned} \tag{10.1}$$

Within the color-color diagram, this system of equations defines the color-color domains which mark out the different types of sources (see Fig. 10.1, right panel). This method allows to filter

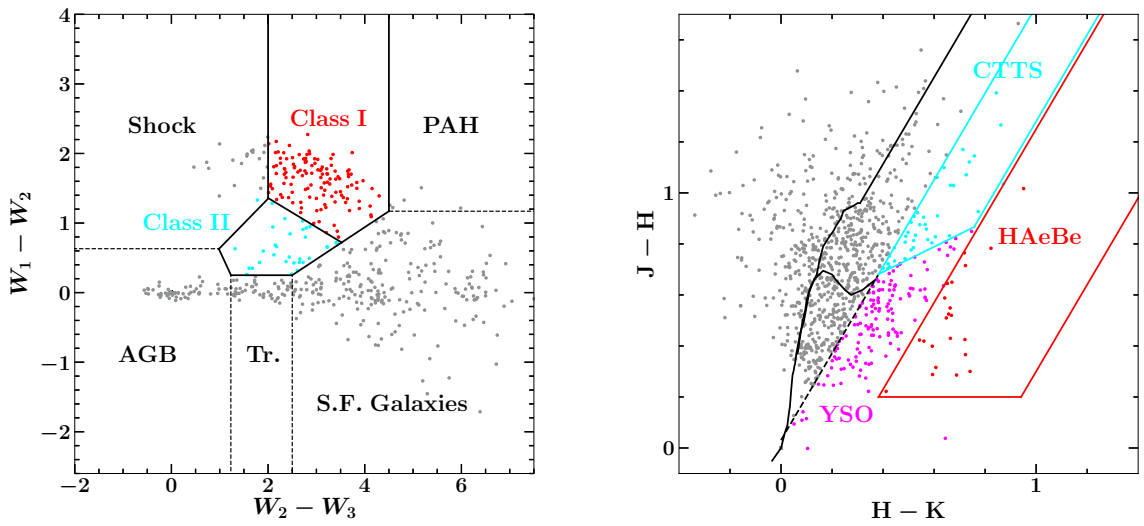

Figure 10.1 *Left*: WISE census of YSO candidates in our 16′ × 16′ field of observations in the IC443 SNR. Cyan dots are Class II candidates, red dots are Class I candidates and gray dots are point sources detected by WISE and rejected by our color-color filtering based on photometric bands W_1, W_2 and W_3. *Right*: 2MASS census of YSO candidates in the same region. Cyan dots are CTTS candidates, red dots are HAeBe candidates, magenta dots are YSO candidates and gray dots are point sources detected by 2MASS and rejected by our JHK color-color filtering.

the sample of point sources and to produce a subset of different types of candidate YSOs:

– Classical T Tauri stars (CTTS)[1].

– Herbig Ae/Be stars (HAeBe)[2].

– YSOs that do not fall into the above groups.

WISE color-color filtering Similarly, we used the color-color criteria introduced by Koenig and Leisawitz (2014) to characterize the point sources from the relative flux measurements of the three first AllWISE bands (W_1, W_2 and W_3). Fischer *et al.* (2016) proposed a slightly modified version of these filtering criteria that excludes an area of the color-color diagram that would be considered as Class II in the original diagram. This area of the diagram is instead interpreted as characteristic of shock emission (traced by a W_3/W_2 excess), thus all point sources that are beyond the left branches of the Class II and Class I areas are identified as unresolved shocked structures. Interestingly, this shock category doesn't systematically correlate with the places where we know for sure that shocks are propagating based on *e.g.* H_2 emission seen by *Spitzer* or the wide spectral lines we observed in CO. In this version of the diagram, there are two well-defined domains of color-color space:

1. A first region is defined by the following system of 4 equations that constrain the infrared

[1]Classical T Tauri stars are Class II pre-main sequence YSOs.
[2]Herbig Ae/Be stars are higher-mass analogs of CTTS, *i.e.* Class II pre-main sequence YSOs.

excess observed in Class I YSOs:

$$\begin{aligned} W_2 - W_3 &> 2.0 \\ W_1 - W_2 &> -0.42 \cdot (W_2 - W_3) + 2.2 \\ W_1 - W_2 &> 0.46 \cdot (W_2 - W_3) - 0.9 \\ W_2 - W_3 &< 4.5 \end{aligned} \tag{10.2}$$

2. A second, adjacent region is defined by the following system of 5 equations that constrain the infrared excess observed in Class II YSOs:

$$\begin{aligned} W_1 - W_2 &> 0.25 \\ W_1 - W_2 &< 0.71 \cdot (W_2 - W_3) - 0.07 \\ W_1 - W_2 &> -1.5 \cdot (W_2 - W_3) + 2.1 \\ W_1 - W_2 &> 0.46 \cdot (W_2 - W_3) - 0.9 \\ W_2 - W_3 &< 4.5 \end{aligned} \tag{10.3}$$

In the color-color diagram represented in Fig. 10.1 (left panel), this system of 9 equations allows to distinguish two samples from the rest of the catalog and enables to sort the YSO candidates into two distinct expected evolutionary stage based on their infrared excess:

– Class I YSOs.

– Class II YSOs.

In addition to the shocked emission area of the color-color diagram, Fischer *et al.* (2016) added the labels 'Polycyclic Aromatic Hydrocarbon (PAH) emission', 'AGB stars', 'Tr. (Transition) disks' and 'Star-forming galaxies' to differents parts of the diagram based on the expected emission of these objects in the WISE photometric bands. We defined arbitrary branches to separate the areas corresponding to each label and identified point sources falling into one of these areas.

Results After the color-color filtering of the catalogs, the total amount of remaining point sources is 201 out of 915 for 2MASS and 155 out of 494 for WISE. In total, 17 YSO candidates are detected both by 2MASS and WISE (using a maximum separation of 10″).

The spatial distribution of 2MASS and WISE YSO candidates is shown in Fig. 10.2. The correlation between the SNR molecular shell and WISE YSOs is striking, and 2MASS YSOs seem to be correlated with the southern shocked H_2 ridge (see Fig. 2.10), in particular towards IC443G. This figure either suggests enhanced star formation in the molecular shell, or it suggests that both WISE and 2MASS are sensitive to contamination by infrared spectral lines (or a combination of both). We further discuss the interpretation of these findings in section 10.4.1. In fact, we know that our results are uncertain due to extended emission:

– *2MASS*. 5.5% of the YSO candidates found in the 2MASS PSC are contaminated by extended emission.

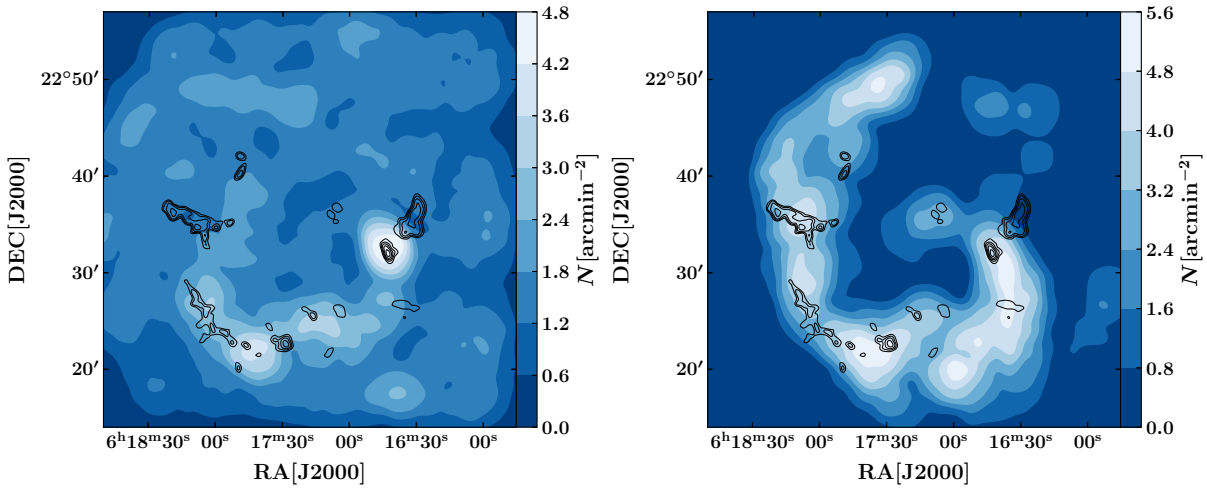

Figure 10.2 Density map of the YSO candidates detected by 2MASS (left panel) and WISE (right panel) in the IC443 SNR: the quantity shown is the density of point sources measured in $1' \times 1'$ boxes. Black contours represent the emission of ^{12}CO J=2–1 lines (see also Fig. 2.20).

– *WISE*. 69.7% of the YSO candidates found in the AllWISE catalog are contaminated by extended emission towards the crowded shocked clump.

Using color-color diagrams, we identified the following YSO candidates:

– *2MASS*. In total, 40 CTTS candidates, 22 HAeBe candidates and 139 additional YSO candidates are identified based on their J, H, K photometric measurements.

– *WISE*. In total, 122 class I protostar candidates and 33 class II YSO candidates are identified in our field based on their W_1, W_2, W_3 photometric measurements.

10.2 | Gaia point source census

We used the second release of the Gaia all-sky optical survey (see Tab. 10.1 for exact photometric parameters) to complete our point source census with optical sources and search for multiple detection by Gaia, WISE and 2MASS. We queried the ESA Gaia science archive to obtain all entries in a 16 arcmin sized square box around the same field center. A total of 1427 point sources were found within our $16' \times 16'$ field of observations. In order to estimate the amount of optical point sources that might be evolved stars physically associated with the SNR, we also used a distance criterion to filter the result.

Assuming that the distance of IC443 is ~1.8 kpc (Ambrocio-Cruz *et al.* 2017, Yu *et al.* 2019), we rejected the point sources with distance greater than 2200 pc or lower than 1400 pc (*i.e.* the point sources that are not within ±400 pc of IC443), using the lower and upper bounds of the confidence interval on the estimated distance determined by parallax measurements[3] (Bailer-Jones *et al.*, 2018).

There are 57 point sources in the interval 1400-2200 pc. We repeated the same process with a different distance criterion in order to assess the variability of the result with respect to the

[3] http://vizier.u-strasbg.fr/viz-bin/VizieR?-source=I/347

amplitude of distance interval applied as a filter. We found a total of 113 optical point sources which relative distance is greater than 1200 pc and lower than 2400 pc. We checked if our samples of optical point sources is correlated with candidate YSOs found in our WISE and 2MASS census (using a maximum angular separation of 10″):

1. Among the 57 Gaia point sources found with the first distance check ($1400 \leq d$ (pc) ≤ 2200), 8 point sources are also detected by 2MASS, and 5 are spatially correlated with a WISE point source.

2. For the 113 Gaia point sources detected with the second distance check ($1200 \leq d$ (pc) ≤ 2400), 18 point sources are also detected by 2MASS, and 10 with a WISE point source.

Hence, a fraction of the YSO detections by WISE and 2MASS are confirmed by the Gaia all-sky survey (Gaia is sensitive to Class II-III pre-main sequence stars, see Fig. 1.23, *e.g.* Kounkel *et al.* 2018). The distance estimates allow to strengthen the assumption that these sources are physically associated with the SNR.

10.3 | Spectral index α of YSO candidates in the 3.4-12 micron range

Method We measured the spectral index $\alpha = \mathrm{d}\ln(\lambda F_\lambda)/\mathrm{d}\ln\lambda$ of our YSO candidates detected by 2MASS and WISE to derive an identification based on their infrared spectral energy distribution (SED) (Adams *et al.*, 1987). We used the classification system of Greene *et al.* (1994) to attribute an evolutionary stage to each point source and rule out the sources characterized by a flat SED. With this classification scheme, near-IR point sources fall into four distinct categories based on the slope of their SED in the 3.4-12 μm range:

– Class I: $\alpha \geq 0.3$

– Flat-SED: $-0.3 \leq \alpha \leq 0.3$

– Class II: $-1.6 \leq \alpha \leq -0.3$

– Class III: $\alpha < -1.6$

Results We used the photometric fluxes of bands W_1, W_2 and W_3 to compute the slope of the SED in the range 3.4-12 μm for each YSO candidate found in the extended G region. Results are given in Tab. C.1, in which we compare the identification based on the $W_1/W_2/W_3$ color-color diagram with the results obtained with the measurement of the slope α. In addition, we present the SEDs of the 17 YSO candidates that are detected both by 2MASS and WISE in Fig. 10.3 (including the W_4 data point at 22 μm). In regard to the comparison between the classification based on the value of the infrared spectral index α and the classification based on color-color criteria, our results are the following:

– 33 Flat-SED point sources are found within our sample of 65 AllWISE YSO candidates (ID 9-15 and ID 40-65).

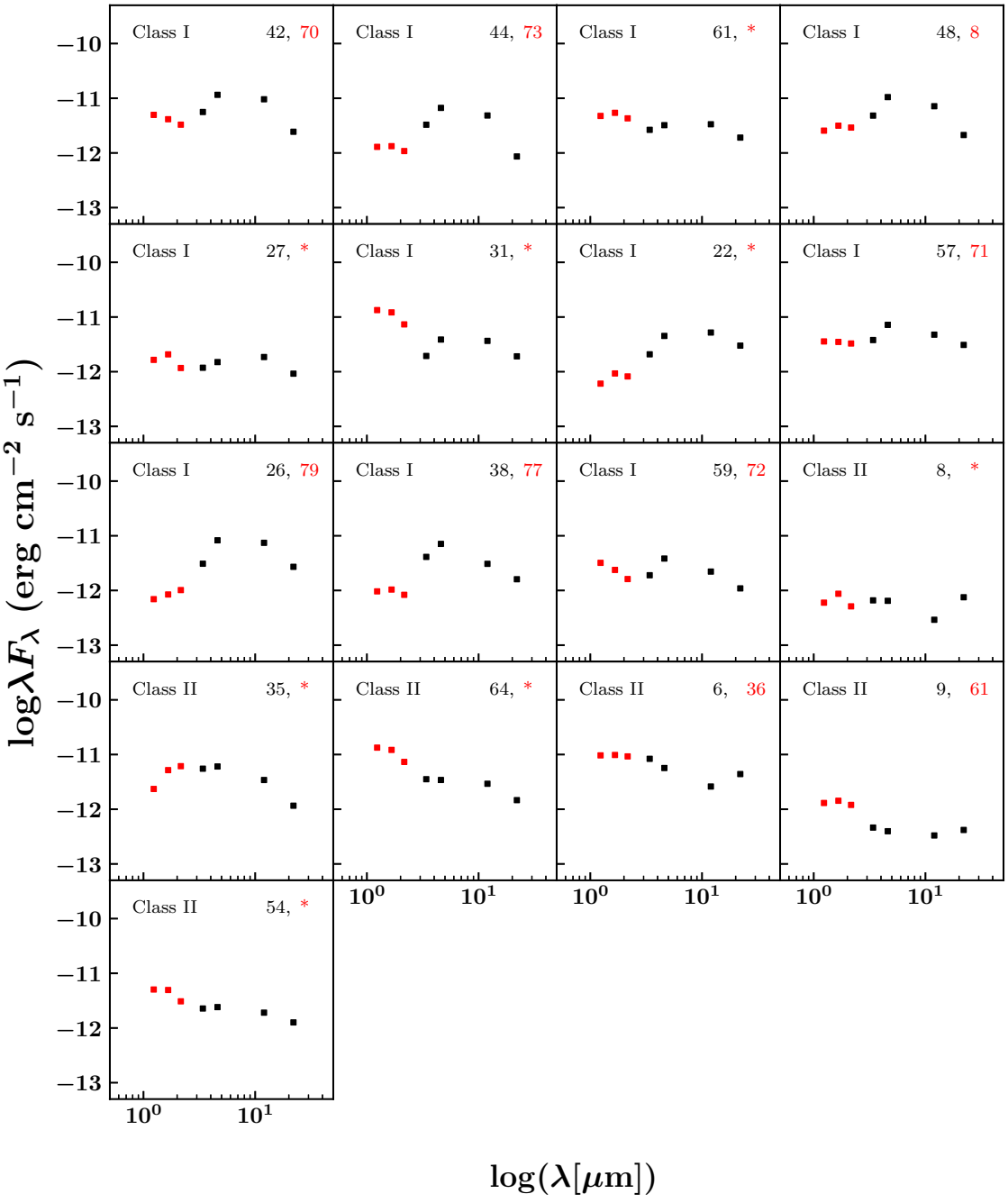

Figure 10.3 Spectral energy distributions of the 17 YSO candidates that are detected both by 2MASS and WISE. Their corresponding ID in Tab. C.1-C.2 and Tab. C.3-C.4 are indicated in the upper-left corner of each box when available (marked with a '*' if not corresponding to any point source identified by a label). Red markers correspond to 2MASS photometric measurements and black markers correspond to WISE measurements.

– Every single point source classified as Class I by our measurement of α was also identified as Class I using the color-color diagram (ID 1-4 and ID 16-34).

– In contrast, there is only partial agreement between the two methods for the identification of Class II YSO candidates: excluding Flat-SED sources, 75% of the identifications were confirmed by both approaches (ID 5-8 and ID 35-39).

– No Class III were identified in our sample.

10.4 | Multiwavelength comparisons

10.4.1 Spatial distribution of YSO candidates

Results We represent the spatial distributions of all the sub-populations of YSO candidates in Fig. 10.4, Fig. 10.8 and Fig. 10.9. We used the `Python` package `mistree` to produce the minimal spanning trees corresponding to our samples of point sources (Naidoo, 2019). The minimal spanning tree is defined as the network of lines, or branches, that connect a set of points together such that the total length of the branches is minimized and there are no closed loops (Cartwright and Whitworth 2004, Gutermuth *et al.* 2009). We discuss our findings in the next paragraphs.

Minimal spanning trees In Fig. 10.8 and Fig. 10.9, each panel represents the minimal spanning tree (hereafter MST) corresponding to a type of point source (identified *via* color-color criteria). Originally, the MST is a concept from graph theory, which represents the unique connection of all points of a data set, so that there are no closed loops (a 'tree'), and so that the total length of all edges between the points is minimal (Kruijssen *et al.*, 2012). In our case, the MST allows to locate clusters of YSOs that are likely to be physically associated:

– We find signs of clustering of Class I protostar candidates along the molecular shell (see Fig. 10.8, bottom-left panel), although we have to take into account contamination by H_2 lines to interpret this result (see following developments).

– We also find a clustering of 'Galaxies/PAH emission' sources that is partly correlated to the *Spitzer*/MIPS observations at 24 μm (see Fig. 10.9, second row, left panel; we discuss the interpretation of these sources in the following developments).

– Finally, the distribution of 'shock emission' point sources (see Fig. 10.9, second row, right panel) is clustered towards the north-east of the shocked clump.

The rest of the MSTs do not show obvious clustering.

Discussion: *i.)* contamination by H_2 lines in the shocked molecular shell As said above, we find a higher concentration of YSO candidates detected by WISE within the shocked clump and along the molecular shell (see also Fig. 10.2), suggesting that this might be a star-forming region. However, the third photometric band of WISE W_3 (central wavelength λ=11.56 μm, bandwidth $\Delta\lambda$=5.51 μm) is partially sensitive to three pure rotational transitions of H_2, namely the transitions S(2) (λ=12.28 μm), S(3) (λ=9.665 μm) and S(4) (λ=8.026 μm). Moreover, several H_2 rovibrational transitions are detected by WISE bands (see also Fig. 9.1). Hence, our detections might be

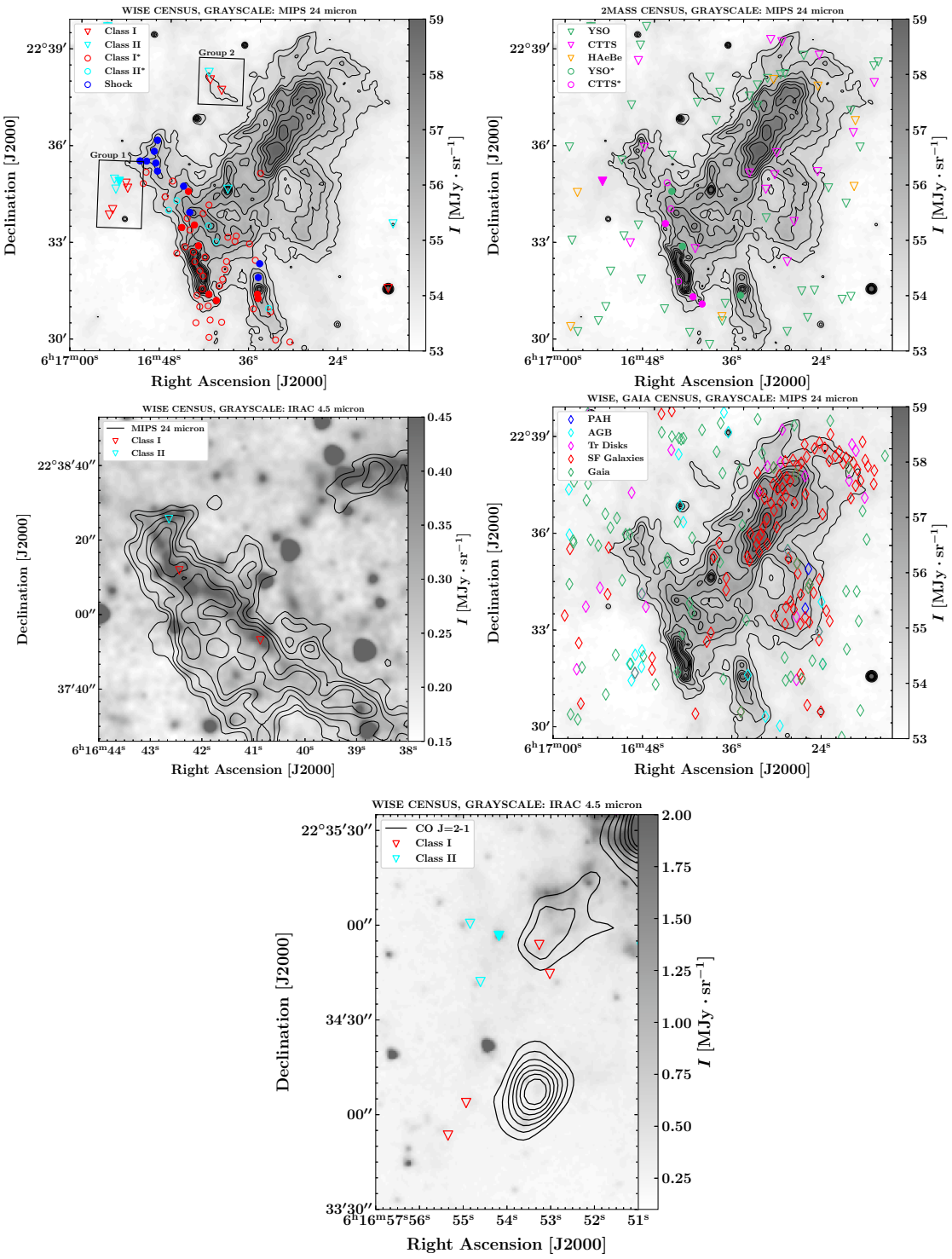

Figure 10.4 *Upper-left panel:* WISE census of Class I and Class II YSO candidates, with shock emission indicated. Based on the selection criteria by Fischer *et al.* (2016). *Upper-right panel:* 2MASS census of YSO, CTTS and HAeBe candidates. Based on the selection criteria by Xu *et al.* (2011). *Center-left panel:* Close-up on the box corresponding to the 'cluster 1' (see text). *Center-right panel:* Transition disks, AGB star, star-forming galaxies emission and PAH emission candidates, based on the selection criteria by Fischer *et al.* (2016); and Gaia point sources. *Lower panel:* Close-up on the box corresponding to the 'cluster 2' (see text). On all panels, triangle-shaped markers correspond to well-detected point sources, and circle-shaped markers (labels marked with a '*') correspond to point sources that were flagged for contamination by extended emission. Filled markers represent point sources that were detected both by 2MASS and WISE. Figure reproduced from Dell'Ova *et al.* (2020).

contaminated by the emission of warm H_2 clumps that are excited by the propagation of the SNR shock (or *via* radiative pumping).

Gutermuth *et al.* (2009) reported that when trying to build YSO samples, unresolved knots of shock emission are regularly detected in all IRAC bands (3.6 - 8 μm). As a consequence, warm and shocked condensations of H_2 with sizes smaller than the spatial resolution might be detected as infrared point sources by the survey. Fischer *et al.* (2016) provides a quantitative distinction between shock emission and the signature of YSO candidates in the WISE color-color diagram, yet almost none of the point sources located along the bright shocked clump are identified as shock emission, casting doubts about the reliability of this criterion to adequately detect shock emission (see Fig. 10.9).

A few point sources associated with faint, extended *Spitzer*-MIPS 24 μm emission are identified as shock emission to the north-east of the main shocked clump (see Fig. 10.9, second row, right panel). The clumpy and filamentary morphology of the structure in which these point sources are embedded, seen in *Spitzer*-IRAC 4.5 μm, is similar to that of the shocked clump. The spatial trend in the identification of 'shock emission' point sources might indicate that this region is dominated by non-stellar emission, whereas the point sources detected in the shocked clump are dominated by YSO emission despite the contamination by extended shock structures.

The 2MASS census might also be biased by the emission of warm H_2, since band K (central wavelength λ=2.159 μm, bandwidth $\Delta\lambda$=0.262 μm) is sensitive to the H_2 rovibrational line $v = 1 - 0$ S(1) at 2.12 μm (Kokusho *et al.*, 2020). The clumpy and bright extended emission displayed in the band K map of the southern ridge makes it clear that the flux of point sources might be contaminated by extended emission, in particular along the bright shocked clump. Rho *et al.* (2001) confirmed that the band K extended emission from this region of the remnant is dominated by H_2 emission, and to a lesser extent bands J and H.

On the one hand, if the flux of band K is overestimated due to H_2 emission, then the correction would lead to a positive displacement along the H-K axis, which means that more YSO candidates would be detected towards the shocked clump where the emission of warm H_2 is significant. This might explain why the higher density of YSO candidates found in the WISE census is not reproduced by our 2MASS census. On the other hand, it would be possible that a number of point sources detected by 2MASS are unresolved knots of shocked H_2, in a similar fashion as what is expected for WISE. In fact, the high correlation between WISE point sources and the SNR shell is not reproduced by 2MASS, hence it is likely that 2MASS is less sensitive to H_2 lines (2MASS bandpasses are more narrow, see Fig. 3.4 and Fig. 3.5).

Discussion: *ii.)* quiescent molecular cloudlet and ring-like structure A greater amount of point sources is found on the edges of the 24 μm bright knot that is spatially associated with the eastern edge of the quiescent molecular cloudlet. Excluding the shocked clump, there is an anti-correlation between both 2MASS and WISE YSO candidates and the MIPS-24μm flux map, in particular in the vicinity of the quiescent cloudlet seen in ^{12}CO (see Fig. 10.4). We suppose that the absence of optical (Gaia) point sources within this region is due to the extinction caused by this massive, dark small cloud. No IR point sources are found at the center of the gap within the ring-like molecular structure seen in ^{12}CO (neither on its surface).

Discussion: *iii.)* higher-certainty YSO candidates Interestingly, the few point sources that were not flagged for contamination by extended sources are primarily organized in clusters (identified based on the combination of the Class I and Class II MSTs) in the eastern and north-eastern part of the $10' \times 10'$ field, and beyond the molecular shell (see the magenta circles in Fig. 10.5, left panel; see also Fig. 10.4):

- The cluster '1' is located on the north-eastern edge of the quiescent cloudlet seen in ^{12}CO. It overlaps with the region of enhanced ISRF (see Fig. 10.5, left panel).
- The cluster '2' is located to the north-east of the shocked clump and is also associated with an enhancement of the ISRF (see Fig. 10.5, left panel).
- Clusters '3' and '4' are close to each other and might be physically associated. They are located beyond the molecular shell of the SNR, to the south-west corner of the field of observations (see Fig. 10.5, left panel).

All these candidates were positively identified by both methods as Class I and Class II YSOs. The Class I protostar candidates on the north-eastern edge of the quiescent molecular cloudlet (cluster '1' in Fig. 10.5, left panel, see also Fig. 10.4) are associated with *Spitzer*-IRAC filamentary structures at 4.5 μm, at the edge of a faint structure detected by *Spitzer*-MIPS at 24 μm. This bright filament has no counterpart in ^{12}CO, hence it is likely to correspond to the cooling of dust grains heated by stellar UV photons (see Fig. 9.19). We discuss the spatial distribution of these higher-certainty YSO candidates in relation to the interstellar radiation field map in section 10.4.2.

Discussion: *iv.)* SNR-induced star formation? Most IR sources with YSO signatures are spatially correlated with the molecular shell in the extended G region (see Fig. 10.8, bottom-left panel), suggesting enhanced star formation along the rims of the SNR. Given the protostellar collapse phase timescale of $\sim 10^5$ yr (Lefloch and Lazareff, 1994) we dot not establish any causal relation between the SNR shocks and the formation of Class I and Class II YSOs.

Based on our color-color census for the 155 YSO candidates detected by WISE, the Class II / Class I ratio is equal to 0.27. Following Dunham *et al.* (2015), we assumed a Class II duration of 2 Myr and used the standard method to infer the age of a stellar population from this ratio (Wilking *et al.* 1989, Evans *et al.* 2009). We obtain an age of ∼500 kyr for the YSO population found in the $16' \times 16'$ field of observations, which is not consistent with the scenario in which the formation of these YSOs was triggered by interaction of the SNR with its environment.

In fact, it is likely that the collapse of molecular clouds in the vicinity of the high-mass progenitor was triggered by the compression driven by stellar winds (Xu *et al.*, 2011). To find evidence of enhanced star formation by the SNR itself would require to detect deeply embedded prestellar cores (age $<$ 100 kyr), which is not attainable with the data at our disposal since these have signatures at longer wavelengths (although we present preliminary NOEMA observations in the appendix D).

In the future, sensitive, high-resolution (∼1″) sub-millimeter and millimeter observations will be required to disentangle the kinematics of large-scale shock structure and outflows, and to eventually uncover prestellar cores in the molecular shell (*e.g.* as Louvet *et al.* 2016 and Motte *et al.* 2018 did for the W43-MM1 star forming region). Nonetheless, our catalog of YSO candidates

provides a useful baseline to study star formation in an environment that is subject to intense γ-ray flux and shock dynamical feedback, and to put constraints on the amount of YSOs that might inject fresh CRs in the environment.

Comparison with previous studies We compared our results with respect to previous studies on the star formation in the IC443 SNR:

- Based on 2MASS point source catalogs, Xu *et al.* (2011) found a total of 1666 YSO candidates, 154 CTTS and 419 HAeBe stars in a search circle around IC443 within a 25′ radius. Their YSO candidates were mostly concentrated around the ^{12}CO molecular shell, in particular towards *i.* the clump C; *ii.* the extended G region where their YSO candidates are spatially correlated with the shocked clump. They proposed that the formation of these YSOs have been triggered by the stellar wind of the IC443 progenitor.
- Based on 2MASS and WISE point source catalogs, Su *et al.* (2014) found a total of 98 YSO candidates in the entire SNR. They proposed a sample of 62 YSO candidates concentrated along the boundary of the radio shell. They also proposed that the formation of these YSOs is likely to have been triggered by the stellar winds of the SNR progenitor. In contrast with our results and the findings of Xu *et al.* (2011), their distribution does not show a strong correlation with the molecular structures in the extended G region.

10.4.2 Comparison with molecular and dust phase measurements

Local ISRF enhancement In Fig. 10.5 (left panel), we compare our Class I/II candidates found in the AllWISE catalog with our ISRF map obtained with `HerBIE` in section 9.3.3 (see Fig. 9.19). We find that all clusters of higher-certainty YSO candidates are correlated with local enhancement of the ISRF ($\langle U \rangle \geq 1.5$). At the peak of the higher ISRF intensity area on the north-eastern edge of the quiescent molecular cloudlet, according to our census a single Class II and two Class I YSOs might be the main sources of radiation. The identification of these YSOs is robust, since they were not flagged for contamination by extended emission. However, we cannot confirm their association with IC443 since they were not detected by Gaia (hence, there are no constraints on their distance).

PAH emission The spatial distribution of point sources identified as star-forming galaxies from their location in the color-color diagram is structured. These sources are correlated with the bright ridge located on the north-eastern rim of the quiescent cloudlet and the spiral-shaped, bright and extended infrared features mapped by *Spitzer*-MIPS at 24 µm. Most of these sources might as well be identified as PAH emission, since our arbitrary criterion of selection puts a significant uncertainty on the cut between the two categories of sources, in particular along the W_1 - W_2 axis (Koenig *et al.*, 2012).

In fact, there is no reason to believe that there would be any correlation between the quiescent cloudlet and background galaxies, hence it is more likely that these point sources are associated with PAH emission driven by the PDR to the northeast of the cloudlet (see Fig. 10.5, left panel). With our current criterion, only a few sources identified as PAH emission are found and located

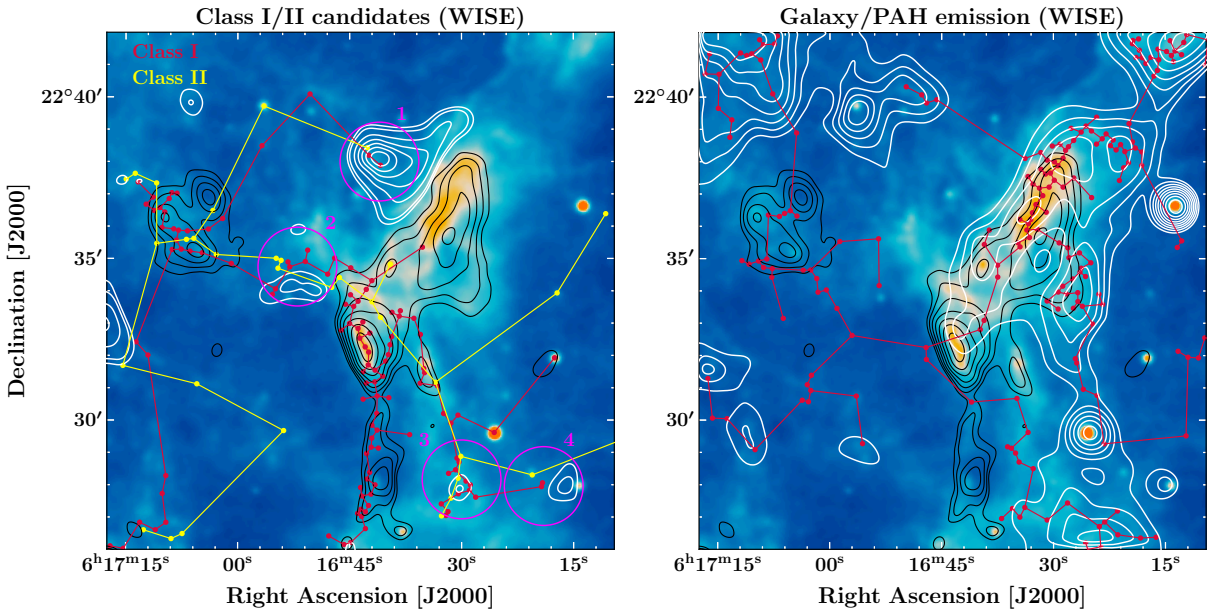

Figure 10.5 *Left:* minimal spanning tree of Class I/II YSO candidates detected by AllWISE in the IC443 SNR 16′ × 16′ field of observations. The background map is the *Spitzer*/MIPS map at 24 µm. Black contours represent the continuum emission at 1.15 mm (NIKA2). White contours represent the ISRF intensity ($\langle U \rangle \geq 1.5$ contour levels, see also Fig. 9.19). Magenta circles indicate the location of clusters of higher-certainty YSO candidates. *Right:* minimal spanning tree of galaxy/PAH emission detected by AllWISE. The background map is the *Spitzer*/MIPS map at 24 µm. Black contours represent the continuum emission at 1.15 mm (NIKA2). White contours represent the PAH mass fraction ($q_{\rm PAH} \geq 20\%$ contour levels, see also Fig. 9.19).

in the same area as point sources that were labeled 'star-forming galaxies'. If most of these detections are actually arising from PAH emission, this result would support the assumption that the bright infrared extended emission arise from a dark dust lane that is spatially associated with the molecular cloudlet detected by our CO observations.

In Fig. 10.5 (right panel), we compare our 'Galaxy/PAH' emission point sources found in the AllWISE catalog with our PAH mass fraction map obtained with `HerBIE` in section 9.3.3 (see Fig. 9.19). We find that the point sources identified either as 'PAH' or 'star-forming galaxy' are well correlated to the PAH mass fraction map, in particular towards the 24 µm features associated with the quiescent molecular cloudlet.

Radio continuum In Fig. 10.6, we study the correlation between the distribution of Class I/II YSO candidates, the total dust mass and the radio continuum emission at 330 MHz (Castelletti *et al.*, 2011). The emission at 330 MHz is driven either by synchrotron radiation (free electrons gyrating around the locally increased magnetic field), free-free radiation (which is also expected in ionized regions), or a combination of both.

This figure shows that the shocked clump 'G' is a region that combines *i.)* a high density of YSO candidates, *ii.)* a large reservoir of mass and *iii.)* several peaks of emission at 330 MHz (which are likely to be driven by the locally enhanced magnetic field and ionization fraction). The emission at 330 MHz is resolved into several 'bullets' located along the molecular shell and partially correlated with the shocked clump. The 'bullets' which are spatially coincident with the shocked clump are privileged candidates for the production of leptonic cosmic rays in ionized bub-

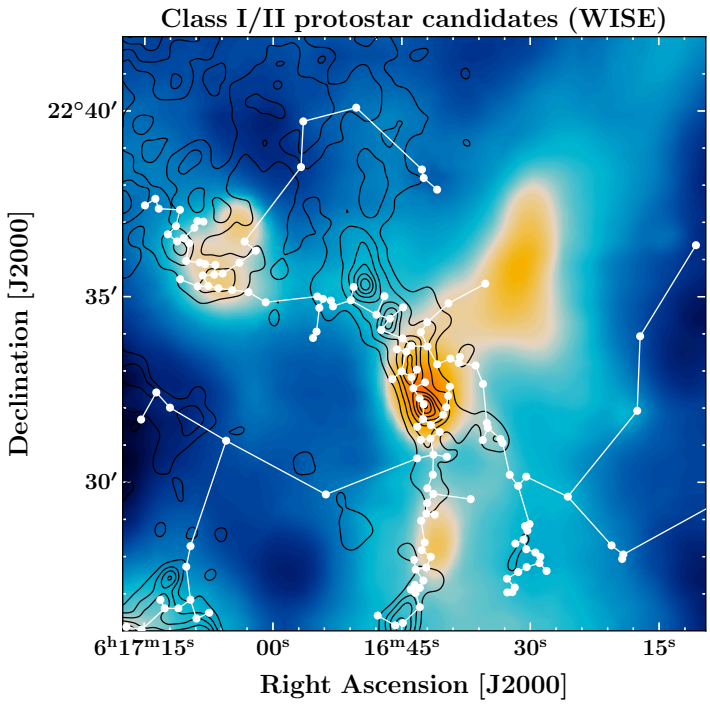

Figure 10.6 Spatial distribution and minimal spanning tree of all Class I/II YSO candidates detected by AllWISE in the IC443 SNR 16′ × 16′ field of observations (point sources are represented by white circles). The background map is the `HerBIE` total dust mass map obtained in section 9.3.3 (see also Fig. 9.19). Black contours represent the continuum emission at 330 MHz (Very Large Array observations, Castelletti *et al.* 2011, 8 linearly spaced contour levels between 15 mJy/beam and 30 mJy/beam).

bles (although we do not find any evidence of increased ionization fraction towards the bubbles, see following developments). These high-energy electrons would in turn produce synchrotron radiation *via* the interaction with the magnetic field.

In addition, the protons accelerated by YSOs might provide a source of fresh mid-energy CRs (up to 10-13 GeV and 26-37 GeV respectively for jet acceleration and protostellar surface shock acceleration in lower-mass stars, Padovani *et al.* 2016). With jet velocities up to 1000 km s^{-1}, high-mass protostellar shocks could contribute to the TeV γ-ray peak in the extended G region.

Warm molecular phase with H_2 pure rotational lines In Chapter 8, from the analysis of H_2 lines we obtained $\sim 2' \times 2'$ maps of the warm molecular gas mass and temperature towards the 'G' clump (at an angular resolution $\sim 8''$). In Fig. 10.7, we compare the spatial distribution of 2MASS and WISE YSO candidates with the 330 MHz map, in addition to our H_2 mass and temperature maps (top row), and with other tracers mapped with *Spitzer*/IRS (second and third rows: Ne II, Fe II, Si II and S I).

All YSO candidates shown in this figure are flagged for contamination by extended emission (see also Fig. 10.4). We find that a few H_2 temperature peaks ($\sim 10^2$ K) are correlated with YSO candidates. These YSOs might contribute to the local heating of molecular gas. The 330 MHz map is well correlated with the H_2 column density map, but there are no significant correlations between the 330 MHz bullets and the local H_2 temperature enhancements.

Synchrotron radiation *vs.* [Ne II] and [Si II] emission In Fig. 10.7, the synchrotron radiation (white contours) is compared with several ions:

– The emission at 330 MHz is partly correlated with the emission of Si II and Fe II, although there are no strong correlations between the 330 MHz 'bubbles' and the emission of these two ions.

– The emission of the Ne II line is not correlated to the emission at 330 MHz. In fact, it is shifted towards the eastern edge of the shocked clump (in the cavity of the SNR).

Therefore, *Spitzer*/IRS tracers of ionization seem to suggest that the 330 MHz bubbles are primarily tracing local enhancements of the magnetic field (*via* compression by the shocks) rather than enhancements of the ionization fraction.

10.5 | Summary

Conclusions of this section Using the AllWISE, 2MASS and Gaia point source catalogs, we have studied the local star formation in the IC443 SNR. *Via* color-color filtering, we identified a population of YSOs candidates in the extended G region. We compared the distribution of YSO candidates with respect to several tracers (molecular mass, temperature, continuum emission, atomic and ionic lines, *etc*). Our main findings are the following:

(a) Color-color filtering of the AllWISE and 2MASS point source catalogs allows to identify 122 Class I, 33 Class II, 40 'classical T Tauri stars', 22 'Herbig Ae/Be stars' and 139 additional YSOs in our $16' \times 16'$ field of observation (Xu *et al.* 2011, Fischer *et al.* 2016).

(b) We measured the spectral index of our point sources to confirm their identification as YSO candidates (Adams *et al.* 1987, Lada 1987). We found that Class I and Class II candidates are respectively recovered at 100% and 75% by spectral index measurements.

(c) Our identification of YSO candidates is uncertain due to two factors:

– Contamination by extended emission (69.7% of AllWISE YSO candidates and 5.5% of 2MASS YSO candidates are flagged for contamination by extended emission).

– Contamination by H_2 rovibrational lines (in particular along the shocked molecular shell). WISE seems to be more sensitive to H_2 lines than 2MASS.

(d) Using the second release of the Gaia all-sky optical survey, we found that a total of 13 YSO candidates have distances $1400 \leq d\ (\mathrm{pc}) \leq 2200$ (consistent with the adopted distance of IC443: $d = 1.8 \pm 0.2$ kpc, Ambrocio-Cruz *et al.* 2017, Yu *et al.* 2019).

(e) We found several clusters of YSO candidates that are associated with local enhancement of the interstellar radiation field (measured with `HerBIE`, section 9.3.3, Fig. 9.19). Two Class I and a single Class II candidates might be at the origin of the photodissociation region (hereafter PDR) to the northeast of the quiescent small cloud (see Fig. 10.5, left panel: cluster '1').

(f) We did not find evidence of SNR-induced star formation in IC443. The formation timescale for Class I and Class II YSOs is not consistent with a SNR-induced scenario. It is likely that the formation of these YSOs was triggered by the SN progenitor (Xu *et al.*, 2011).

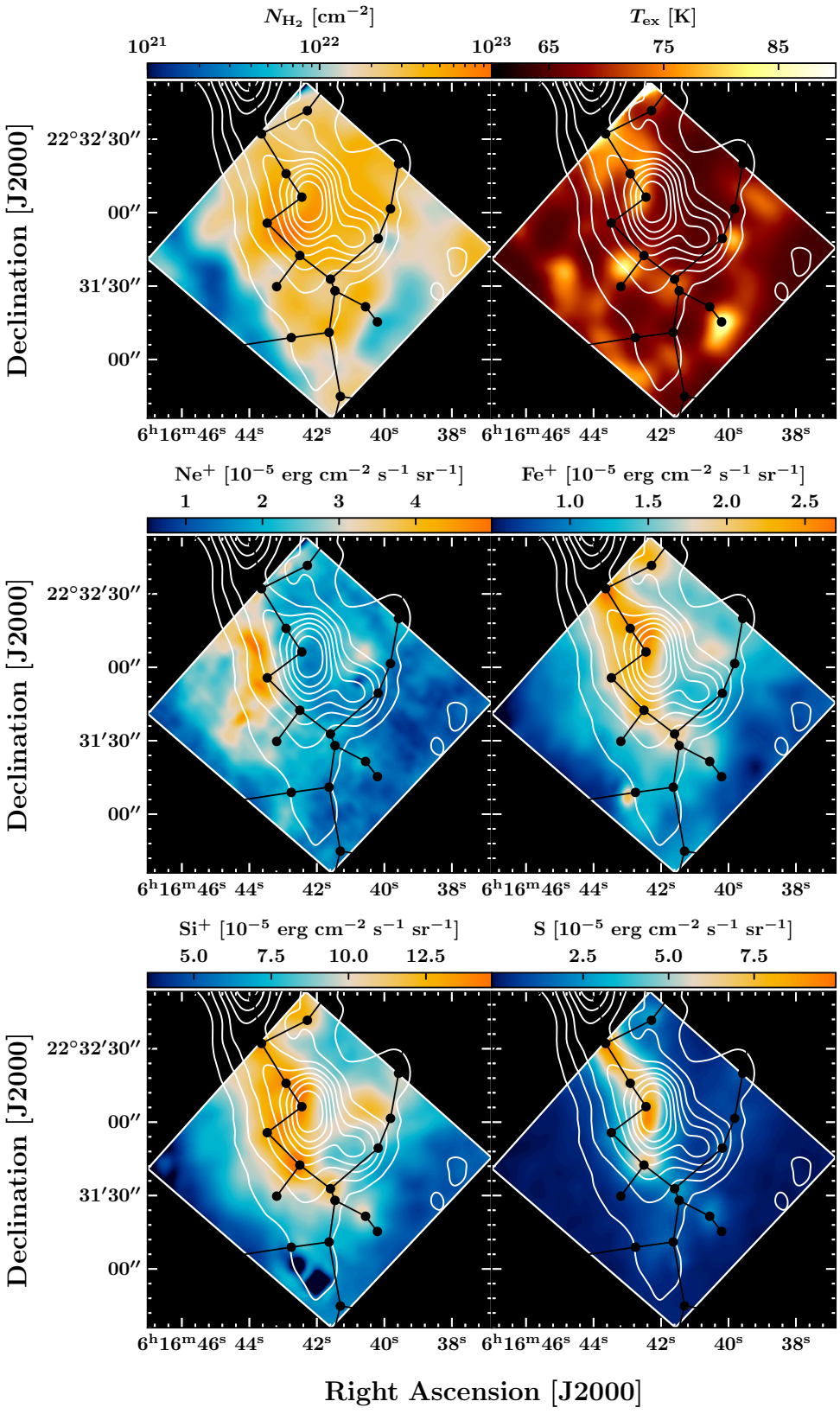

Figure 10.7 Minimal spanning tree of 2MASS and WISE YSO candidates towards the $\sim 2' \times 2'$ *Spitzer*/IRS field of observation (shocked clump 'G'). White contours represent the continuum emission at 330 MHz. In the top row, the background images represent the total column density and average excitation temperature inferred from the analysis of H_2 pure rotational lines (section 8.1.3.2, Fig. 8.11). In the second and third rows, additional *Spitzer*/MIPS observations are shown.

(g) The interstellar and stellar contents (total mass, 330 MHz emission, YSOs) of the shocked clump 'G' makes it a privileged target for the injection of fresh CRs by YSOs (10-37 GeV, Padovani *et al.* 2016) and their interaction with a significant mass reservoir. We discuss the implications of these findings in section 10.5.

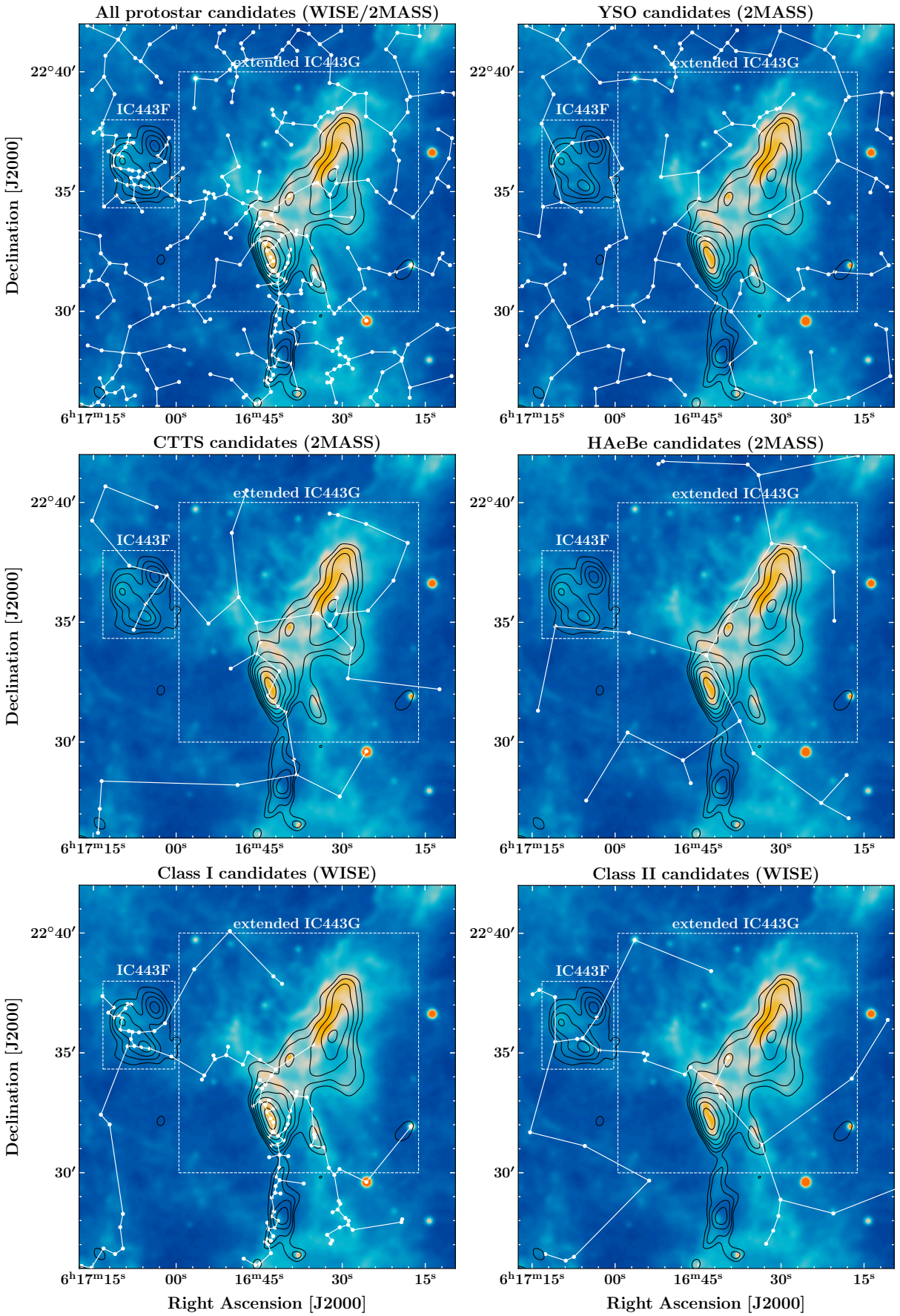

Figure 10.8 Minimal spanning tree of YSO candidates in the IC443 SNR 16′ × 16′ field of observations (see text). The background map is the *Spitzer*/MIPS map at 24 µm. Black contours represent the continuum emission at 1.15 mm (NIKA2).

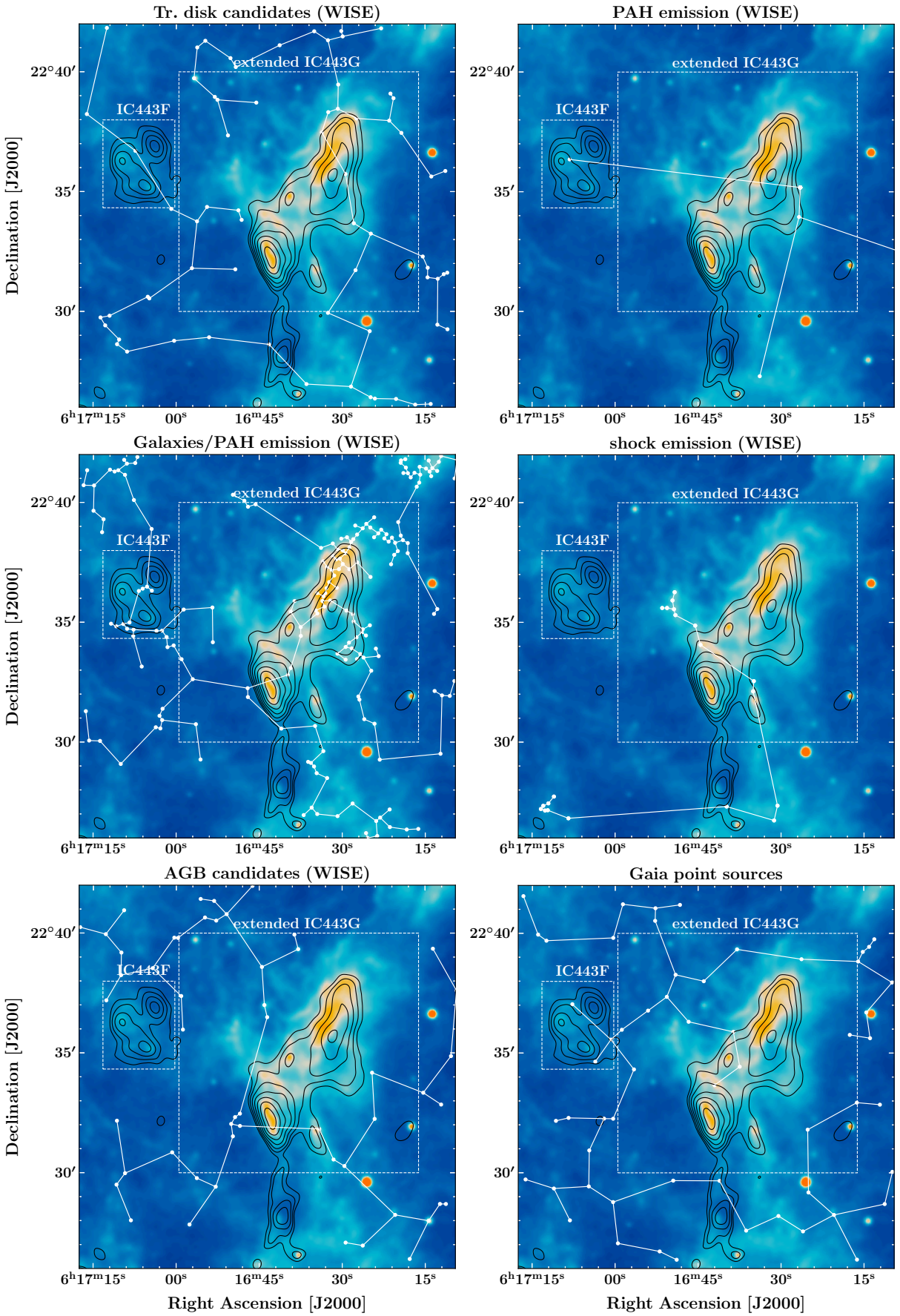

Figure 10.9 Minimal spanning tree of YSO candidates and non-YSO detections in the IC443 SNR $16' \times 16'$ field of observations (see text). The background map is the *Spitzer*/MIPS map at 24 µm. Black contours represent the continuum emission at 1.15 mm (NIKA2).

Conclusion

Interstellar measurements for the interpretation of γ-ray spectra in the IC443 SNR

In Chapter 8 and Chapter 9, we have produced maps of several interstellar parameters that are essential to tackle the interpretation of γ-ray spectra, in addition to the energetic, chemical impacts and star-forming conditions in the IC443 SNR. In Fig. 10.10, we present a summary of all the interstellar measurements obtained in this work:

- PAH mass fraction $q_{\rm PAH}(\%)$ (`HerBIE` output).
- Total dust mass $M_{\rm dust}$ (`HerBIE` output).
- Interstellar radiation field intensity $\langle U \rangle$ (`HerBIE` output. $U = 1$ corresponds to the diffuse Galactic interstellar radiation field: $\int_{0.0912\ \mu\rm m}^{8\ \mu\rm m} J_\lambda {\rm d}\lambda = 2.2 \times 10^{-5}$ W m^{-2}).
- Charged PAH fraction $f^+(\%)$ (`HerBIE` output).
- Total dust luminosity $L_{\rm dust}$ (`HerBIE` output).
- Average dust opacity index β (in the sub-millimeter/millimeter range, measured *a posteriori* from the `HerBIE` SEDs).
- Average dust temperature $T_{\rm dust}$ (`PPMAP` output).
- Systemic velocity $v_{\rm LSR}$ (inferred from ^{13}CO J=1–0 observations).
- Systemic velocity $v_{\rm LSR}$ (inferred from ^{12}CO J=2–1 observations).
- Molecular gas total mass $M_{\rm gas}$ (inferred from ^{12}CO and ^{13}CO lines, using population diagrams and `RADEX`).
- Molecular gas temperature $T_{\rm gas}$ (inferred from ^{12}CO and ^{13}CO lines, using population diagrams and `RADEX`).
- Velocity dispersion σ_v (inferred from the second moment map of our ^{12}CO J=2–1 hyperspectral map).
- Spatial distribution of the quiescent molecular gas, traced by the ^{12}CO J=2–1 spectral line intensity map ($\int T dv$) of the velocity channels with low ^{12}CO [J=2–1]/[J=1–0] line ratios (see Eq. 8.29).

– Spatial distribution of the molecular gas perturbed by the SNR, traced by the ^{12}CO J=2–1 spectral line intensity map ($\int T dv$) of the velocity channels with high ^{12}CO [J=2–1]/[J=1–0] line ratios (see Eq. 8.29).

– Electron density n_e inferred from the charged PAH fraction, ISRF strength (`HerBIE` outputs) and gas temperature (see Eq. 9.20).

These measurements were obtained either in $10' \times 10'$ or $16' \times 16'$ field of observations located within the peak of γ-ray emission determined by Humensky and VERITAS Collaboration 2015, at an angular resolution that varies between $\sim 11.2''$ and $\sim 47.4''$. Therefore, they constitute a high-resolution description of the interstellar contents of the region with respect to the forthcoming next-generation γ-ray observations. The Cherenkov Telescope Array will map the IC443 SNR between 20 GeV and 300 TeV, up to an angular resolution $\sim 1.5'$.

In addition to our $\sim$ $10''$ – $20''$ kinematic and morphologic description of the molecular phase (see Chapter 6), our interstellar measurements allow to accurately constrain the total mass of protons available to interact with cosmic rays in this area of the SNR (*via* pion decay and Bremsstrahlung). Furthermore, our estimates of the interstellar radiation field ($\langle U \rangle$) and total dust luminosity ($L_{\rm dust}$) constitute additional constraints to determine the contribution of inverse Compton scattering to the γ-ray spectra.

Summary and future prospects

Summary We have thoroughly studied the molecular and dust phases in the GeV/TeV bright shell of an evolved SNR interacting with a molecular cloud. Firstly, in order to estimate the total molecular mass, we have studied the emission of molecular tracers (H_2, ^{12}CO) in IC443.

We performed new IRAM 30m and APEX observations of ^{12}CO, ^{13}CO and C^{18}O rotational lines in a $10' \times 10'$ field of observations (the 'extended G region'). Using LTE (opacity-corrected population diagrams) and non-LTE methods (`RADEX`), we measured the total mass and temperature of the molecular gas. Our measurements rely on several critical assumptions: *i.)* we assumed that ^{12}CO and ^{13}CO share the same geometry and that the isotopic ratio is uniform across the field of observations; *ii.)* we adopted a standard ^{12}CO/^{13}CO isotopic ratio in order to measure the optical depth of the lines; *iii.)* we assumed that ^{12}CO and ^{13}CO share the same excitation temperatures. Therefore, the uncertainty on the isotopic ratio results in large uncertainties on our mass measurements. The results obtained with CO lines are consistent with our separate LTE analysis of H_2 pure rotational lines towards the shocked clump 'G' (assuming a H_2-to-^{12}CO abundance $\sim 4 \times 10^4$).

We then studied the thermal emission of dust grains in the same region, based on continuum observations. In a $\sim 16' \times 16'$ field of observations, we performed new observations with NIKA2, the continuum camera at the IRAM 30m telescope. Using two distinct Bayesian models (`PPMAP` and `HerBIE`) and the dust model THEMIS, we analyzed the pixel-per-pixel spectral energy distributions between 3.4 µm and 2.0 mm, in addition to radio continuum measurements at 74 MHz and 330 MHz.

The two models used in our analysis of dust emission have synergies: on one hand, `PPMAP` can work with observations characterized by distinct angular resolution without requiring to smooth the data to the coarsest resolution, however it is limited to $\lambda > 100$ µm observations since it is

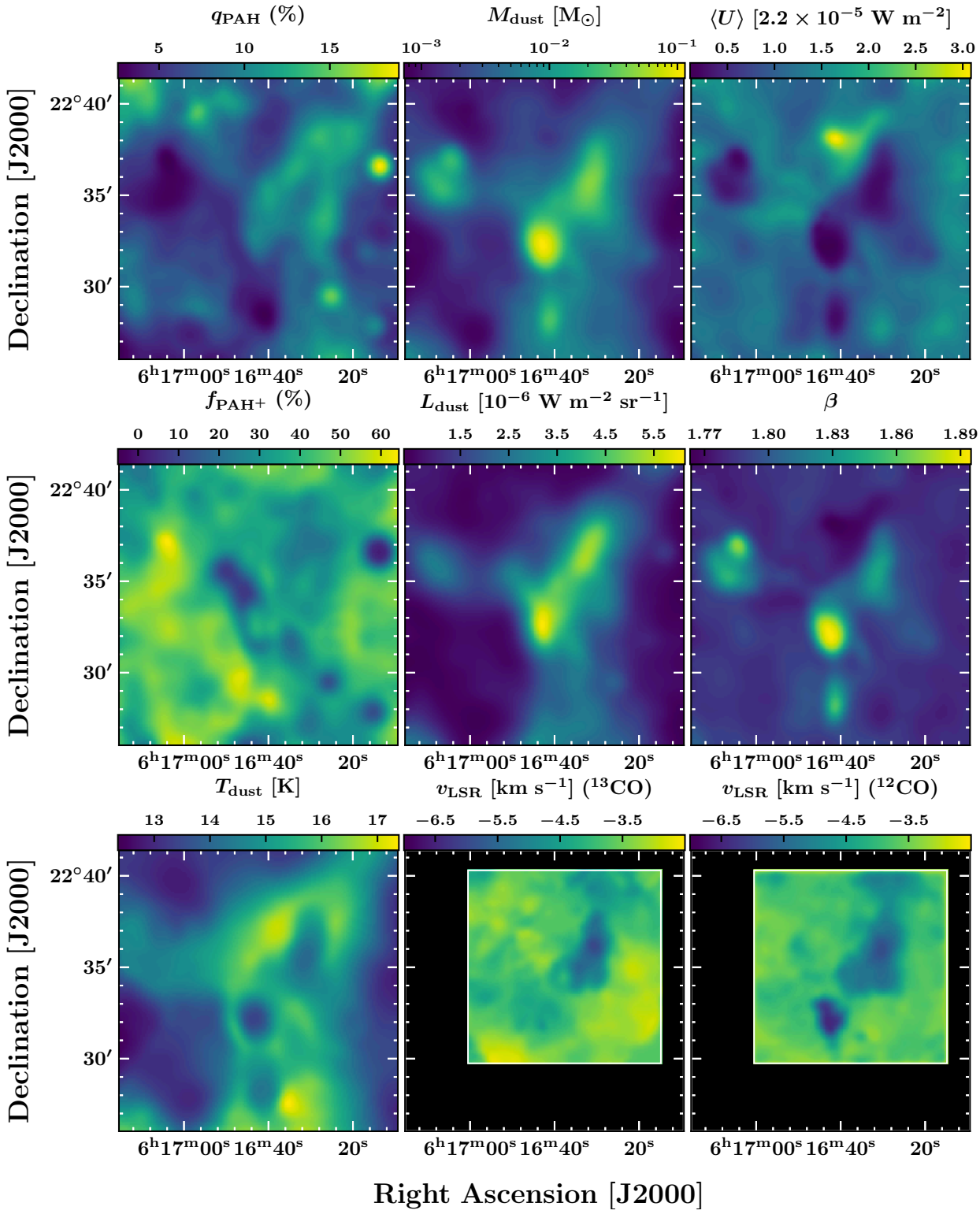

Figure 10.10 Interstellar measurements in the IC443 SNR (1/2): PAH mass fraction q_{PAH}, total dust mass M_{dust}, ISRF intensity $\langle U \rangle$, charged PAH fraction f_{PAH}, total dust luminosity L_{dust}, dust opacity index β, dust temperature T_{dust} and systemic velocity v_{LSR} (see text, see also Fig. 9.19, Fig. 9.12, Fig. 6.16, Fig. 6.17, Fig. 8.29).

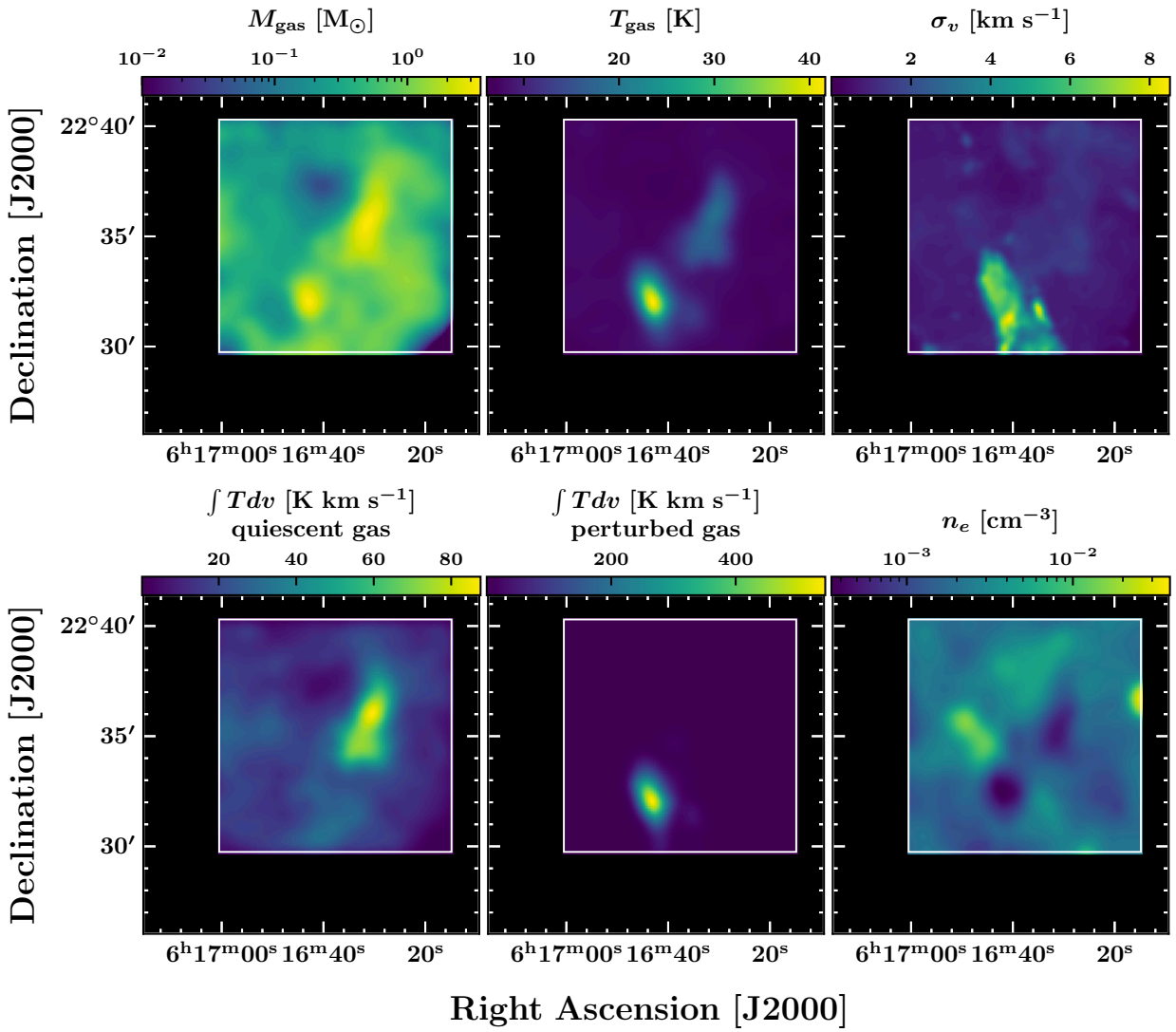

Figure 10.11 Interstellar measurements in the IC443 SNR (2/2): total molecular gas mass $M_{\rm gas}$, molecular gas temperature $T_{\rm gas}$, molecular gas velocity dispersion σ_v, ^{12}CO J=2–1 spectral-line intensity $\int Tdv$ of the quiescent and perturbed molecular gas, and electron density n_e (see text, see also Fig. 9.19, Fig. 9.12, Fig. 6.16, Fig. 6.17, Fig. 8.29, Fig. 9.21).

based on a modified blackbody model. On the other hand, `HerBIE` does require to convolve the maps to the same resolution, but provides an accurate description of dust thermal emission, based on the THEMIS dust model and stochastic heating by a non-uniform radiation field. However, our mass measurements derived from the analysis of dust SEDs are uncertain due to the difficulty to correctly subtract the contribution of atomic, ionic and molecular lines from broadband measurements, in addition to the uncertainty related to the assumption on the dust-to-gas mass ratio. Moreover, we found discrepancies between the results obtained with `PPMAP` and `HerBIE` (the mass found with `PPMAP` is approximately 50% lower than the mass found with `HerBIE`).

Following our analysis of the molecular and dust phases of the SNR, we found that there are two conspicuous interstellar features that constitute likely candidates for the interaction with cosmic rays in IC443. The shocked clump 'G' (mass $\sim$ 250 $M_\odot$) and its neighboring quiescent small cloud (mass $\sim$ 400 $M_\odot$) both represent privileged targets for the production of γ-rays *via* pion decay. The mass of the small cloud is accurately constrained, with a $\sim$ 25% relative difference

between our measurements based on molecular lines and dust SEDs (which are entirely independent). The mass of the shocked clump is less certain (100 – 400 $M_\odot$). In total, we find that around $\sim$ 1100 $M_\odot$ is available to interact with CRs in the extended G region (including the mass of the ambient cloud of Cornett *et al.* 1977).

Finally, we probed the star-forming conditions in the extended G region based on 2MASS, WISE and Gaia point source catalogs. Using basic procedures (color-color filtering, spectral index measurements) we isolated a sample of protostar candidates from the catalogs and we estimated their current evolutionary stage. The identification of protostars with these methods is challenged by the contamination by extended emission and bright H_2 rovibrational lines. However, we found several clusters of young stellar object candidates associated with localized enhancement of the interstellar radiation field (estimated by `HerBIE`), thus increasing the certainty on their identification. Due to the formation timescale constraints for Class I/II protostars, we do not find evidence of SNR-induced star formation. Nonetheless, these protostars could inject fresh mid-energy cosmic rays in the environment (with energies up to 10-37 GeV, Padovani *et al.* 2016) and thus contribute to drive the γ-ray emission.

This work brings together the first steps towards a detailed description of the interstellar and stellar contents of a galactic TeVatron, with the purpose of collecting the essential parameters to interpret the γ-ray spectra based on accurate constraints on the total mass, radiation field ($\langle U \rangle$ and $L_{\rm dust}$), electron density, and local CR injection. These new measurements will allow to lift the current degeneracy between hadronic and leptonic scenarios for the interpretation of the γ-ray emission in IC443 (pion decay *vs.* Bremsstrahlung models *vs.* inverse Compton scattering, see Fig. 2.14). We have also obtained constraints on the energetic and chemical impact of the SNR on its environment, with measurements of the turbulent kinetic energy injected in the SNR molecular shell and the physical conditions of the molecular gas, dust grains and PAHs (temperature, abundances, charged fraction, dust opacity index).

Future prospects There are many aspects of this study that can be further refined and expanded upon. Performing new observations of IC443 in order to entirely map the SNR both with spectral-line measurements (^{12}CO, ^{13}CO, C^{18}O) and continuum measurements (NIKA2) will allow to extend the analysis to the rest of the molecular shell. In addition, gathering more observational data might allow to use statistical methods in order to perform structure identification, such as meanshift clustering (Bron *et al.*, 2018), Regularized Optimization for HyperSpectral Analysis (Marchal *et al.*, 2019) or General Morphological Component Analysis (Picquenot *et al.*, 2019). We could also improve our analysis of the lines using a more advanced LTE excitation/radiative transfer approach based on the Cramer Rao Bound (Roueff *et al.*, 2021), and Paris-Durham shock models for the analysis of H_2 lines.

One of the most important tasks that remains is to accurately determine the magnetic field in IC443. In the near future, we aim to constrain the orientation and strength of the magnetic field based on the anisotropic resonant scattering technique developed by Houde *et al.* 2013. In addition to polarization mode observations, the parameters required for this analysis are the excitation temperature, the line profiles and the continuum flux at the radiation frequency, which we all have already determined with our ^{12}CO observations.

In the near future, we aim to re-invest our knowledge of the total mass, radiation field, electron density (and forthcoming measurement of the magnetic field) to start modelling the γ-ray spectra

with accurate input parameters. We plan to work in collaboration with S. Gabici, P. Cristofari, M. Padovani and A. Marcowith to characterize the interaction of CRs with the molecular shell and ambient cloud of Cornett *et al.* 1977, in order to reproduce the γ-ray observations with dedicated models (*e.g.* Gabici *et al.* 2009b). We will also evaluate the contribution of our protostars candidate to the local injection of CRs, based on the model of Padovani *et al.* 2015, Padovani *et al.* 2016. Ultimately, we aim to constrain the electron/nuclei proportion, particle escape rate and re-acceleration scenarios from very high-energy γ-ray observations in IC443.

Finally, expanding upon our preliminary census of the star formation in the extended G region will require to perform sensitive interferometric observations, in order to disentangle the emission of molecular shock structures from the contribution of potential protostellar outflows. High-resolution observations will allow to identify protostars and evaluate their evolutionary stage with certainty. On the long term, we aim to build the CMF in the extended G region and determine the star-forming conditions to study the impact of shock and CR feedback.

Bibliography

B. P. Abbott *et al.*, Living Reviews in Relativity **21**, 3 (2018).
A. A. Abdo *et al.*, ApJ **706**, L1 (2009).
A. A. Abdo *et al.*, ApJ **712**, 459 (2010).
V. A. Acciari *et al.*, ApJ **698**, L133 (2009).
A. Achterberg, R. D. Blandford, and S. P. Reynolds, A&A **281**, 220 (1994).
M. Ackermann *et al.*, Science **334**, 1103 (2011).
M. Ackermann *et al.*, Science **339**, 807 (2013).
R. Adam *et al.*, A&A **609**, A115 (2018).
F. C. Adams, C. J. Lada, and F. H. Shu, ApJ **312**, 788 (1987).
F. A. Aharonian *et al.*, Nature **432**, 75 (2004).
F. Aharonian *et al.*, A&A **460**, 365 (2006).
F. A. Aharonian, Astroparticle Physics **43**, 71 (2013).
F. Aharonian, R. Yang, and E. de Oña Wilhelmi, Nature Astronomy **3**, 561 (2019).
M. Ahlers and F. Halzen, Progress in Particle and Nuclear Physics **102**, 73 (2018).
K. Akabane, PASJ **18**, 96 (1966).
A. Alarie and L. Drissen, MNRAS **489**, 3042 (2019).
J. Albert *et al.*, ApJ **664**, L87 (2007).
M. G. Allen *et al.*, ApJS **178**, 20 (2008).
J. Alves, M. Lombardi, and C. J. Lada, A&A **462**, L17 (2007).
P. Ambrocio-Cruz *et al.*, MNRAS **472**, 51 (2017).
S. Anderl, A. Gusdorf, and R. Güsten, A&A **569**, A81 (2014).
M. Andersen *et al.*, ApJ **742**, 7 (2011).
P. Andre and T. Montmerle, ApJ **420**, 837 (1994).
P. Andre, D. Ward-Thompson, and M. Barsony, ApJ **406**, 122 (1993).
P. André, in *The Cold Universe*, edited by T. Montmerle, C. J. Lada, I. F. Mirabel, and J. Tran Thanh Van (1994) p. 179.
P. Andre, D. Ward-Thompson, and M. Barsony, in *Protostars and Planets IV*, edited by V. Mannings, A. P. Boss, and S. S. Russell (2000) p. 59.
P. André *et al.*, A&A **518**, L102 (2010).
P. André *et al.*, in *Protostars and Planets VI*, edited by H. Beuther, R. S. Klessen, C. P. Dullemond, and T. Henning (2014) p. 27.
B. Armstrong, J. Quant. Spec. Radiat. Transf. **7**, 61 (1967).
J. W. Armstrong, B. J. Rickett, and S. R. Spangler, ApJ **443**, 209 (1995).
I. Asaoka and B. Aschenbach, A&A **284**, 573 (1994).
Astropy Collaboration *et al.*, A&A **558**, A33 (2013).
Astropy Collaboration *et al.*, AJ **156**, 123 (2018).
W. I. Axford, E. Leer, and G. Skadron, in *International Cosmic Ray Conference*, International Cosmic Ray Conference, Vol. 11 (1977) p. 132.
W. Baade and R. Minkowski, ApJ **119**, 215 (1954).
W. Baade and F. Zwicky, Proceedings of the National Academy of Science **20**, 254 (1934).
W. Baade, ApJ **97**, 119 (1943).
W. Baade, ApJ **102**, 309 (1945).
J. W. M. Baars *et al.*, A&A **175**, 319 (1987).
R. Bachiller, ARA&A **34**, 111 (1996).
R. Bachiller *et al.*, A&A **372**, 899 (2001).
B. T. Chiad, L. T. Ali, and A. S. Hassani, International Journal of Astronomy and Astrophysics **5**, 125 (2015).
C. A. L. Bailer-Jones *et al.*, The Astronomical Journal **156**, 58 (2018).
J. Bally and C. J. Lada, ApJ **265**, 824 (1983).
J. Bally, Annual Review of Astronomy and Astrophysics **54**, 491 (2016), https://doi.org/10.1146/annurev-astro-081915-023341 .
A. Bamba *et al.*, ApJ **589**, 827 (2003).

M. J. Barlow, MNRAS **183**, 367 (1978).
E. E. Barnard, Astronomy and Astro-Physics (formerly The Sidereal Messenger) **13**, 177 (1894).
J. Baselmans, Journal of Low Temperature Physics **167**, 292 (2012).
N. Bastian, K. R. Covey, and M. R. Meyer, ARA&A **48**, 339 (2010).
M. R. Bate, I. A. Bonnell, and V. Bromm, MNRAS **339**, 577 (2003).
G. Bazin *et al.*, A&A **499**, 653 (2009).
S. V. W. Beckwith *et al.*, AJ **99**, 924 (1990).
M. Beech and R. Mitalas, ApJS **95**, 517 (1994).
A. R. Bell, MNRAS **182**, 147 (1978).
A. R. Bell *et al.*, MNRAS **431**, 415 (2013).
M. Benedettini *et al.*, A&A **598**, A14 (2017).
E. A. Bergin and M. Tafalla, ARA&A **45**, 339 (2007).
J. P. Bernard *et al.*, A&A **518**, L88 (2010).
H. A. Bethe, Reviews of Modern Physics **62**, 801 (1990).
S. Bianchi and R. Schneider, MNRAS **378**, 973 (2007).
M. E. Biot, *Connaissance des temps, Additions*, , 60 (1864).
C. Biscaro and I. Cherchneff, A&A **564**, A25 (2014).
G. A. Blake *et al.*, ApJ **315**, 621 (1987).
R. Blandford and D. Eichler, Phys. Rep. **154**, 1 (1987).
R. D. Blandford and J. P. Ostriker, ApJ **221**, L29 (1978).
P. Blasi, A&A Rev. **21**, 70 (2013).
L. Blitz, in *Protostars and Planets III*, edited by E. H. Levy and J. I. Lunine (1993) p. 125.
H. Bloemen, The High-Energy Component of the ISM-Cosmic-Ray Phenomena, in *Interstellar Processes*, Vol. 134, edited by D. J. Hollenbach and J. Thronson, Harley A. (1987) p. 143.
J. M. Blondin *et al.*, ApJ **500**, 342 (1998).
J. M. Blondin, R. A. Chevalier, and D. M. Frierson, ApJ **563**, 806 (2001).
R. Blundell and C.-Y. E. Tong, IEEE Proceedings **80**, 1702 (1992).
F. Bocchino and A. M. Bykov, A&A **376**, 248 (2001a).
F. Bocchino and A. M. Bykov, A&A **400**, 203 (2003).
F. Bocchino and A. M. Bykov, A&A **362**, L29 (2000).
F. Bocchino and A. M. Bykov, A&A **376**, 248 (2001b).
M. Bocchio, A. P. Jones, and J. D. Slavin, A&A **570**, A32 (2014).
M. Bocchio *et al.*, A&A **587**, A157 (2016).
C. Boersma, J. Bregman, and L. J. Allamandola, ApJ **806**, 121 (2015).
B. J. Bok and E. F. Reilly, ApJ **105**, 255 (1947).
A. D. Bolatto, M. Wolfire, and A. K. Leroy, ARA&A **51**, 207 (2013).
H. E. Bond *et al.*, ApJ **765**, L12 (2013).
I. A. Bonnell *et al.*, MNRAS **323**, 785 (2001).
I. A. Bonnell, S. G. Vine, and M. R. Bate, MNRAS **349**, 735 (2004).
I. A. Bonnell, R. B. Larson, and H. Zinnecker, in *Protostars and Planets V*, edited by B. Reipurth, D. Jewitt, and K. Keil (2007) p. 149.
S. Bontemps *et al.*, A&A **311**, 858 (1996).
S. Bontemps *et al.*, A&A **524**, A18 (2010).
C. M. Booth *et al.*, ApJ **777**, L16 (2013).
A. P. Boss, ApJ **439**, 224 (1995).
M. T. Botticella *et al.*, A&A **479**, 49 (2008).
D. Branch and G. A. Tammann, ARA&A **30**, 359 (1992).
B. H. Bransden and C. J. Joachain, *Physics of Atoms and Molecules; 2nd ed.* (Prentice-Hall, Harlow, 2003).
R. Braun and R. G. Strom, A&A **164**, 193 (1986).
E. Bron *et al.*, A&A **610**, A12 (2018).
R. Hanbury Brown and C. Hazard, Nature **170**, 364 (1952).
A. Burrows and D. Vartanyan, Nature **589**, 29 (2021).
M. G. Burton *et al.*, MNRAS **231**, 617 (1988).
M. G. Burton *et al.*, ApJ **355**, 197 (1990).
A. M. Bykov and I. N. Toptygin, Ap&SS **138**, 341 (1987).
A. M. Bykov, F. Bocchino, and G. G. Pavlov, ApJ **624**, L41 (2005).
Bykov *et al.*, ApJ **538**, 203 (2000).
A. M. Bykov *et al.*, Space Sci. Rev. **214**, 41 (2018).
A. M. Bykov *et al.*, Space Sci. Rev. **216**, 42 (2020).
S. Cabrit and C. Bertout, ApJ **307**, 313 (1986).

S. Cabrit, in *Star-Disk Interaction in Young Stars*, Vol. 243, edited by J. Bouvier and I. Appenzeller (2007) pp. 203–214.
M. Calvo *et al.*, Journal of Low Temperature Physics **184**, 816 (2016).
A. G. W. Cameron and J. W. Truran, Icarus **30**, 447 (1977).
M. Cardillo, E. Amato, and P. Blasi, A&A **595**, A58 (2016).
M. Carter *et al.*, A&A **538**, A89 (2012).
A. Cartwright and A. P. Whitworth, MNRAS **348**, 589 (2004).
G. Castelletti, G. Dubner, C. Brogan, and N. E. Kassim, A&A **471**, 537 (2007).
G. Castelletti *et al.*, A&A **534**, A21 (2011).
J. Castor, R. McCray, and R. Weaver, ApJ **200**, L107 (1975).
G. Cazzoli, C. Puzzarini, and A. V. Lapinov, ApJ **611**, 615 (2004).
C. Ceccarelli *et al.*, ApJ **740**, L4 (2011).
S. Celli *et al.*, MNRAS **487**, 3199 (2019).
D. Cesarsky *et al.*, A&A **348**, 945 (1999).
G. Chabrier, PASP **115**, 763 (2003).
G. Chabrier, The Initial Mass Function: From Salpeter 1955 to 2005, in *The Initial Mass Function 50 Years Later*, Vol. 327, edited by E. Corbelli, F. Palla, and H. Zinnecker (2005) p. 41.
S. Chandrasekhar, ApJ **74**, 81 (1931).
H. Chawner *et al.*, MNRAS **499**, 5665 (2020).
C. H. R. Chen *et al.*, ApJ **695**, 511 (2009).
I. Cherchneff and S. Lilly, ApJ **683**, L123 (2008).
I. Cherchneff, arXiv e-prints , arXiv:1405.1216 (2014).
I. Cherchneff and E. Dwek, ApJ **713**, 1 (2010).
I. Cherchneff and A. Sarangi, in *The Molecular Universe*, Vol. 280, edited by J. Cernicharo and R. Bachiller (2011) pp. 228–236.
Cherenkov Telescope Array Consortium *et al.*, *Science with the Cherenkov Telescope Array* (2019).
D. F. Chernoff, ApJ **312**, 143 (1987).
R. A. Chevalier and E. P. Liang, ApJ **344**, 332 (1989).
R. A. Chevalier, ApJ **188**, 501 (1974).
R. A. Chevalier, ARA&A **15**, 175 (1977).
R. A. Chevalier, R. P. Kirshner, and J. C. Raymond, ApJ **235**, 186 (1980).
R. A. Chevalier, ApJ **258**, 790 (1982a).
R. A. Chevalier, ApJ **259**, 302 (1982b).
R. A. Chevalier, ApJ **511**, 798 (1999).
J. P. Chieze, G. Pineau des Forets, and D. R. Flower, MNRAS **295**, 672 (1998).
L. Ciesla *et al.*, A&A **565**, A128 (2014).
D. F. Cioffi, C. F. McKee, and E. Bertschinger, ApJ **334**, 252 (1988).
D. H. Clark and F. R. Stephenson, in *Supernovae: A Survey of Current Research*, NATO Advanced Study Institute (ASI) Series C, Vol. 90, edited by M. J. Rees and R. J. Stoneham (1982) pp. 355–370.
G. W. Clark, G. P. Garmire, and W. L. Kraushaar, ApJ **153**, L203 (1968).
B. G. Clark, A&A **89**, 377 (1980).
P. C. Clark, R. S. Klessen, and I. A. Bonnell, MNRAS **379**, 57 (2007).
M. J. Claussen *et al.*, ApJ **489**, 143 (1997a).
M. J. Claussen *et al.*, ApJ **489**, 143 (1997b).
M. J. Claussen *et al.*, AJ **117**, 1387 (1999).
L. I. Cleeves *et al.*, ApJ **799**, 204 (2015).
S. A. Colgate, ApJ **187**, 333 (1974).
M. Compiègne *et al.*, A&A **525**, A103 (2011).
R. H. Cornett, G. Chin, and G. R. Knapp, A&A **54**, 889 (1977).
L. L. Cowie, ApJ **225**, 887 (1978).
D. P. Cox, ApJ **178**, 159 (1972a).
D. P. Cox, ApJ **178**, 143 (1972b).
D. P. Cox and B. W. Smith, ApJ **189**, L105 (1974).
R. M. Crutcher, ApJ **520**, 706 (1999).
R. M. Crutcher, ARA&A **50**, 29 (2012).
A. C. Cummings *et al.*, ApJ **831**, 18 (2016).
C. J. Cyganowski *et al.*, ApJ **796**, L2 (2014).
T. Dahlen *et al.*, ApJ **757**, 70 (2012).
J. E. Dale, T. J. Haworth, and E. Bressert, MNRAS **450**, 1199 (2015).
T. M. Dame, D. Hartmann, and P. Thaddeus, ApJ **547**, 792 (2001).
I. J. Danziger *et al.*, IAU Circ. **4746**, 1 (1989).
E. Dartois *et al.*, A&A **557**, A97 (2013).
E. Dartois *et al.*, Nuclear Instruments and Methods in Physics Research B **365**, 472 (2015a).
E. Dartois *et al.*, A&A **576**, A125 (2015b).
E. Dartois *et al.*, A&A **618**, A173 (2018).
R. Davé, MNRAS **385**, 147 (2008).

J. G. Davies, A. G. Lyne, and J. H. Seiradakis, Nature **240**, 229 (1972).
T. de Jong, S. Chu, and A. Dalgarno, ApJ **199**, 69 (1975).
I. De Looze *et al.*, MNRAS **465**, 3309 (2017).
P. Dell'Ova *et al.*, A&A **644**, A64 (2020).
L. K. Denoyer, ApJ **212**, 416 (1977).
L. K. Denoyer and M. A. Frerking, ApJ **246**, L37 (1981).
L. K. Denoyer, MNRAS **183**, 187 (1978).
L. K. Denoyer, ApJ **228**, L41 (1979a).
L. K. Denoyer, ApJ **232**, L165 (1979b).
K. P. Dere *et al.*, A&A **498**, 915 (2009).
K. M. Desai *et al.*, AJ **140**, 584 (2010).
S. Dib, E. Bell, and A. Burkert, ApJ **638**, 797 (2006).
J. R. Dickel and D. K. Milne, Australian Journal of Physics **29**, 435 (1976).
J. R. Dickel *et al.*, AJ **98**, 1363 (1989).
J. R. Dickel, Astrophys. Lett. **15**, 61 (1973).
J. M. Dickey, M. M. Hanson, and G. Helou, ApJ **352**, 522 (1990).
R. L. Dickman *et al.*, ApJ **400**, 203 (1992).
B. Dincel *et al.*, in *Supernova Remnants: An Odyssey in Space after Stellar Death* (2016) p. 37.
B. Dincel, *Massive runaway stars inside supernova remnants*, Ph.D. thesis, Astrophysikalisches Institut Und Universitäts-sternwarte (2017).
Y. Doi *et al.*, PASJ **67**, 50 (2015).
A. Z. Dolginov and T. F. Stepinski, ApJ **427**, 377 (1994).
M. A. Dopita and R. S. Sutherland, ApJS **102**, 161 (1996).
M. A. Dopita, D. S. Mathewson, and V. L. Ford, ApJ **214**, 179 (1977).
D. Downes, Radio Astronomy Techniques, in *Evolution of Galaxies: Astronomical Observations*, Vol. 333, edited by I. Appenzeller, H. J. Habing, and P. Lena (1989) p. 351.
B. T. Draine and N. Anderson, ApJ **292**, 494 (1985).
B. T. Draine and A. Li, ApJ **657**, 810 (2007).
B. T. Draine and C. F. McKee, ARA&A **31**, 373 (1993).
B. T. Draine and E. E. Salpeter, J. Chem. Phys. **67**, 2230 (1977).
B. T. Draine, *Physics of the Interstellar and Intergalactic Medium* (2011).
B. T. Draine, ApJ **241**, 1021 (1980).
B. T. Draine, W. G. Roberge, and A. Dalgarno, ApJ **264**, 485 (1983).
B. T. Draine and B. Sutin, ApJ **320**, 803 (1987).
B. T. Draine, ARA&A **41**, 241 (2003).
B. T. Draine *et al.*, ApJ **663**, 866 (2007).
L. O. Drury and T. P. Downes, MNRAS **427**, 2308 (2012).
L. O. Drury, F. A. Aharonian, and H. J. Voelk, A&A **287**, 959 (1994).
L. O. Drury, MNRAS **415**, 1807 (2011).
G. Dubner and E. Giacani, A&A Rev. **23**, 3 (2015).
G. M. Dubner *et al.*, AJ **120**, 1933 (2000).
R. M. Duin and H. van der Laan, A&A **40**, 111 (1975).
W. W. Duley and D. A. Williams, MNRAS **196**, 269 (1981).
C. Dullemond, in *Radiative Transfer in Astrophysics. Theory, Numerical Methods and Applications.* (2013).
M. M. Dunham *et al.*, ApJS **220**, 11 (2015).
L. Dunne *et al.*, Nature **424**, 285 (2003).
E. Dwek and R. G. Arendt, ARA&A **30**, 11 (1992).
Y. N. Efremov and B. G. Elmegreen, MNRAS **299**, 643 (1998).
E. Egron *et al.*, MNRAS **470**, 1329 (2017).
J. H. Elias *et al.*, ApJ **296**, 379 (1985).
M. Elitzur, ApJ **203**, 124 (1976).
B. G. Elmegreen and D. M. Elmegreen, ApJ **220**, 1051 (1978).
B. G. Elmegreen and C. J. Lada, ApJ **214**, 725 (1977).
B. G. Elmegreen, in *Origins*, Astronomical Society of the Pacific Conference Series, Vol. 148, edited by C. E. Woodward, J. M. Shull, and J. Thronson, Harley A. (1998) p. 150.
C. P. Endres *et al.*, Journal of Molecular Spectroscopy **327**, 95 (2016).
M. L. Enoch *et al.*, ApJ **638**, 293 (2006).
J. A. Esposito *et al.*, ApJ **461**, 820 (1996).
I. Evans, Neal J. *et al.*, ApJS **181**, 321 (2009).
C. Evoli, The cosmic-ray energy spectrum (2018).
E. Falgarone *et al.*, A&A **331**, 669 (1998).

M. Fardin, On the rheology of cats (2014).
G. Fazio and J. Hora, Studying Stellar Ejecta on the Large Scale using SIRTF-IRAC, Spitzer Proposal (2004).
C. Federrath and R. S. Klessen, ApJ **761**, 156 (2012).
E. Fermi, Physical Review **75**, 1169 (1949).
K. Ferrière, ApJ **503**, 700 (1998).
K. M. Ferrière, Reviews of Modern Physics **73**, 1031 (2001).
R. A. Fesen, W. P. Blair, and R. P. Kirshner, ApJ **292**, 29 (1985).
R. A. Fesen and R. P. Kirshner, ApJ **242**, 1023 (1980).
R. A. Fesen, ApJ **281**, 658 (1984).
G. B. Field, ApJ **142**, 531 (1965).
G. B. Field, W. B. Somerville, and K. Dressler, ARA&A **4**, 207 (1966).
D. Field *et al.*, MNRAS **285**, 839 (1997).
W. J. Fischer *et al.*, The Astrophysical Journal **827**, 96 (2016).
V. L. Fish, L. O. Sjouwerman, and Y. M. Pihlström, ApJ **670**, L117 (2007).
D. J. Fixsen and J. C. Mather, ApJ **581**, 817 (2002).
N. Flagey *et al.*, ApJ **701**, 1450 (2009).
D. R. Flower and G. Pineau des Forets, MNRAS **275**, 1049 (1995).
D. R. Flower and G. Pineau des Forêts, A&A **578**, A63 (2015).
D. R. Flower and G. Pineau des Forêts, MNRAS **343**, 390 (2003).
D. R. Flower and E. Roueff, Journal of Physics B Atomic Molecular Physics **31**, 2935 (1998a).
D. R. Flower and E. Roueff, Journal of Physics B Atomic Molecular Physics **31**, L955 (1998b).
D. R. Flower, G. Pineau des Forets, and T. W. Hartquist, MNRAS **216**, 775 (1985).
D. R. Flower *et al.*, MNRAS **280**, 447 (1996).
D. R. Flower, MNRAS **288**, 627 (1997).
D. R. Flower, E. Roueff, and C. J. Zeippen, Journal of Physics B Atomic Molecular Physics **31**, 1105 (1998).
D. R. Flower, MNRAS **297**, 334 (1998).
D. R. Flower and G. Pineau des Forêts, MNRAS **308**, 271 (1999).
D. R. Flower *et al.*, MNRAS **341**, 70 (2003).
D. Flower, Flows in Molecular Media, in *Lecture Notes in Physics, Berlin Springer Verlag*, Vol. 793, edited by P. J. V. Garcia and J. M. Ferreira (2010) p. 161.
D. A. Frail and S. R. Kulkarni, Nature **352**, 785 (1991).
D. A. Frail and G. F. Mitchell, ApJ **508**, 690 (1998).
D. A. Frail *et al.*, AJ **111**, 1651 (1996).
P. François *et al.*, A&A **421**, 613 (2004).
C. Fransson *et al.*, The Messenger **127**, 44 (2007).
M. A. Frerking, W. D. Langer, and R. W. Wilson, ApJ **262**, 590 (1982).
S. Gabici, F. A. Aharonian, and S. Casanova, MNRAS **396**, 1629 (2009a).
S. Gabici *et al.*, arXiv e-prints , arXiv:1903.11584 (2019).
S. Gabici and F. A. Aharonian, ApJ **665**, L131 (2007).
S. Gabici, F. A. Aharonian, and S. Casanova, MNRAS **396**, 1629 (2009b).
B. M. Gaensler and P. O. Slane, ARA&A **44**, 17 (2006).
B. M. Gaensler *et al.*, ApJ **648**, 1037 (2006).
B. M. Gaensler and S. Johnston, MNRAS **277**, 1243 (1995).
B. M. Gaensler, ApJ **493**, 781 (1998).
D. Gaggero *et al.*, Phys. Rev. Lett. **119**, 031101 (2017).
Gaia Collaboration *et al.*, A&A **595**, A2 (2016).
Gaia Collaboration *et al.*, A&A **616**, A1 (2018).
T. K. Gaisser, R. J. Protheroe, and T. Stanev, ApJ **492**, 219 (1998).
F. Galliano *et al.*, ApJ **679**, 310 (2008).
F. Galliano *et al.*, A&A **536**, A88 (2011).
F. Galliano, M. Galametz, and A. P. Jones, ARA&A **56**, 673 (2018).
F. Galliano, MNRAS **476**, 1445 (2018), arXiv:1801.06660 [astro-ph.GA] .
J. Gao, *The Physics of Superconducting Microwave Resonators*, Ph.D. thesis, California Institute of Technology (2008).
R. P. Garden *et al.*, ApJ **374**, 540 (1991).
P. M. Garnavich *et al.*, ApJ **493**, L53 (1998).
A. Gatto *et al.*, MNRAS **449**, 1057 (2015).
T. R. Geballe and T. Oka, Nature **384**, 334 (1996).

S. Geen *et al.*, MNRAS **463**, 3129 (2016).
R. D. Gehrz *et al.*, Review of Scientific Instruments **78**, 011302 (2007).
F. A. Gent *et al.*, MNRAS **432**, 1396 (2013).
Y. M. Georgelin, Ph.D. thesis, - (1975).
C. L. Gerardy *et al.*, AJ **119**, 2968 (2000).
R. Giacconi *et al.*, ApJ **165**, L27 (1971).
R. Giacconi *et al.*, ApJS **27**, 37 (1974).
A. Ginsburg *et al.*, ApJ **842**, 92 (2017).
R. Giovanelli and M. P. Haynes, ApJ **230**, 404 (1979).
P. Girichidis *et al.*, ApJ **816**, L19 (2016).
A. E. Glassgold, P. J. Huggins, and W. D. Langer, ApJ **290**, 615 (1985).
B. Godard and J. Cernicharo, A&A **550**, A8 (2013).
B. Godard *et al.*, A&A **622**, A100 (2019).
P. F. Goldsmith, E. A. Bergin, and D. C. Lis, ApJ **491**, 615 (1997).
P. F. Goldsmith and W. D. Langer, ApJ **517**, 209 (1999).
H. L. Gomez *et al.*, ApJ **760**, 96 (2012).
M. A. Gordon and W. B. Burton, ApJ **208**, 346 (1976).
K. D. Gordon *et al.*, ApJ **797**, 85 (2014).
W. M. Goss, ApJS **15**, 131 (1968).
R. J. Gould and E. E. Salpeter, ApJ **138**, 393 (1963).
D. A. Gouliermis *et al.*, ApJ **688**, 1050 (2008).
J. R. Graham, G. S. Wright, and A. J. Longmore, ApJ **313**, 847 (1987).
D. Graham and G. C. Hunt, Nature Physical Science **242**, 86 (1973).
E. Greco *et al.*, A&A **615**, A157 (2018).
D. A. Green and F. R. Stephenson, Historical Supernovae, in *Supernovae and Gamma-Ray Bursters*, Vol. 598, edited by K. Weiler (2003) pp. 7–19.
D. A. Green, MNRAS **221**, 473 (1986).
D. A. Green, Bulletin of the Astronomical Society of India **42**, 47 (2014).
D. A. Green, Journal of Astrophysics and Astronomy **40**, 36 (2019).
D. A. Green, MNRAS **238**, 737 (1989).
T. P. Greene *et al.*, ApJ **434**, 614 (1994).
I. A. Grenier, J. H. Black, and A. W. Strong, ARA&A **53**, 199 (2015a).
I. A. Grenier, J.-M. Casandjian, and R. Terrier, Science **307**, 1292 (2005).
I. A. Grenier, J. H. Black, and A. W. Strong, ARA&A **53**, 199 (2015b).
A. Greve, C. Kramer, and W. Wild, A&AS **133**, 271 (1998).
M. J. Griffin *et al.*, A&A **518**, L3 (2010).
F. Gueth *et al.*, A&A **323**, 943 (1997).
P. Guhathakurta and B. T. Draine, ApJ **345**, 230 (1989).
V. Guillet, G. Pineau Des Forêts, and A. P. Jones, A&A **476**, 263 (2007).
V. Guillet, A. P. Jones, and G. Pineau Des Forêts, A&A **497**, 145 (2009).
V. Guillet, G. Pineau Des Forêts, and A. P. Jones, A&A **527**, A123 (2011).
S. Guilloteau and R. Lucas, in *Imaging at Radio through Submillimeter Wavelengths*, Astronomical Society of the Pacific Conference Series, Vol. 217, edited by J. G. Mangum and S. J. E. Radford (2000) p. 299.
P. Gulliford, Ap&SS **31**, 241 (1974).
A. Gusdorf *et al.*, A&A **482**, 809 (2008a).
A. Gusdorf *et al.*, A&A **490**, 695 (2008b).
A. Gusdorf, R. Gusten, Y. Yuan, D. Neufeld, and Herschel Wadi Team, in *The Molecular Universe*, Vol. 280, edited by J. Cernicharo and R. Bachiller (2011) p. 185.
A. Gusdorf *et al.*, A&A **542**, L19 (2012).
A. Gusdorf *et al.*, A&A **575**, A98 (2015).
M. Gustafsson *et al.*, A&A **513**, A5 (2010).
R. Güsten *et al.*, A&A **454**, L13 (2006).
R. A. Gutermuth *et al.*, ApJS **184**, 18 (2009).
HESS Collaboration *et al.*, Nature **531**, 476 (2016).
M. R. Haas *et al.*, in *American Astronomical Society Meeting Abstracts #202*, American Astronomical Society Meeting Abstracts, Vol. 202 (2003) p. 30.08.
E. Habart *et al.*, Space Sci. Rev. **119**, 71 (2005).
H. J. Habing, Bull. Astron. Inst. Netherlands **19**, 421 (1968).
E. E. Haller *et al.*, NTD germanium: A novel material for low-temperature bolometers, NASA STI/Recon Technical Report N (1982).
Y. Hanabata *et al.*, ApJ **786**, 145 (2014).
D. E. Harris, ApJ **135**, 661 (1962).
T. Hartwig *et al.*, ApJ **799**, 114 (2015).

A. Heger *et al.*, ApJ **591**, 288 (2003).
C. Heiles and R. Crutcher, Magnetic Fields in Diffuse HI and Molecular Clouds, in *Cosmic Magnetic Fields*, Vol. 664, edited by R. Wielebinski and R. Beck (2005) p. 137.
C. Heiles *et al.*, in *Protostars and Planets III*, edited by E. H. Levy and J. I. Lunine (1993) p. 279.
D. J. Helfand, E. V. Gotthelf, and J. P. Halpern, ApJ **556**, 380 (2001).
D. J. Helfand, B. F. Collins, and E. V. Gotthelf, ApJ **582**, 783 (2003).
F. P. Helmich *et al.*, A&A **283**, 626 (1994).
P. Hennebelle and G. Chabrier, ApJ **684**, 395 (2008).
P. Hennebelle and O. Iffrig, A&A **570**, A81 (2014).
P. Hennebelle and R. Teyssier, A&A **477**, 25 (2008).
P. Hennebelle *et al.*, A&A **486**, L43 (2008).
W. Herbst and G. E. Assousa, ApJ **217**, 473 (1977).
J. J. Hester, ApJ **314**, 187 (1987).
J. J. Hester, ARA&A **46**, 127 (2008).
J. W. Hewitt *et al.*, ApJ **652**, 1288 (2006).
J. W. Hewitt, F. Yusef-Zadeh, and M. Wardle, ApJ **683**, 189 (2008).
J. W. Hewitt, F. Yusef-Zadeh, and M. Wardle, ApJ **706**, L270 (2009a).
J. W. Hewitt *et al.*, ApJ **694**, 1266 (2009b).
S. Heyminck *et al.*, A&A **454**, L21 (2006).
T. Hezareh *et al.*, A&A **558**, A45 (2013).
R. H. Hildebrand, QJRAS **24**, 267 (1983).
L. E. Hill, MNRAS **157**, 419 (1972).
A. C. Hindmarsh, Scientific Computing (1983).
A. Hirschauer *et al.*, ApJ **696**, 1533 (2009).
B. Hnatyk and O. Petruk, Condensed Matter Physics **1**, 655 (1998).
P. Y. Ho, Vistas in Astronomy **5**, 127 (1962).
I. T. Ho *et al.*, MNRAS **444**, 3894 (2014).
I. M. Hoffman *et al.*, ApJ **583**, 272 (2003).
J. A. Högbom, A&AS **15**, 417 (1974).
D. E. Hogg, ApJ **140**, 992 (1964).
J. Holder, in *6th International Symposium on High Energy Gamma-Ray Astronomy*, American Institute of Physics Conference Series, Vol. 1792 (2017) p. 020013.
J. Holdship *et al.*, arXiv e-prints (2021).
D. Hollenbach and C. F. McKee, ApJS **41**, 555 (1979).
D. Hollenbach and C. F. McKee, ApJ **342**, 306 (1989).
D. J. Hollenbach and A. G. G. M. Tielens, Reviews of Modern Physics **71**, 173 (1999).
P. F. Hopkins, MNRAS **430**, 1653 (2013).
J. R. Houck *et al.*, ApJS **154**, 18 (2004).
M. Houde *et al.*, ApJ **764**, 24 (2013).
A. D. P. Howard *et al.*, MNRAS **489**, 962 (2019).
A. D. P. Howard *et al.*, MNRAS **504**, 6157 (2021).
I. Howard, William E. and H. R. Dickel, PASP **75**, 149 (1963).
F. Hoyle and J. G. Ireland, MNRAS **120**, 173 (1960).
Y. L. Huang, R. L. Dickman, and R. L. Snell, ApJ **302**, L63 (1986).
B. Humensky and VERITAS Collaboration, in *34th International Cosmic Ray Conference (ICRC2015)*, International Cosmic Ray Conference, Vol. 34 (2015) p. 875.
R. M. Humphreys, ApJS **38**, 309 (1978).
L. K. Hunt *et al.*, A&A **576**, A33 (2015).
J. D. Hunter, Computing In Science & Engineering **9**, 90 (2007).
O. Iffrig and P. Hennebelle, A&A **576**, A95 (2015).
E. Iglesias, ApJ **218**, 697 (1977).
S. Ikeuchi and J. Spitzer, L., ApJ **283**, 825 (1984).
S. A. Ilovaisky and J. Lequeux, A&A **18**, 169 (1972).
R. Indebetouw *et al.*, ApJ **782**, L2 (2014).
N. Indriolo and B. J. McCall, Chemical Society Reviews **42**, 7763 (2013).
N. Indriolo *et al.*, ApJ **724**, 1357 (2010).
J. G. Ingalls *et al.*, ApJ **743**, 174 (2011).
T. Inoue *et al.*, ApJ **744**, 71 (2012).
K. Isensee *et al.*, ApJ **725**, 2059 (2010).
A. V. Ivlev *et al.*, ApJ **812**, 135 (2015).
K. G. Jansky, Nature **132**, 66 (1933).
T. H. Jarrett *et al.*, ApJ **735**, 112 (2011).
T. H. Jarrett *et al.*, AJ **145**, 6 (2013).
E. B. Jenkins and D. A. Meloy, ApJ **193**, L121 (1974).

H. L. Johnson, R. I. Mitchell, and B. Iriarte, ApJ **136**, 75 (1962).
D. Johnstone *et al.*, ApJ **545**, 327 (2000).
A. P. Jones and N. Ysard, A&A **627**, A38 (2019).
E. Jones *et al.*, SciPy: Open source scientific tools for Python (2001).
A. P. Jones, W. W. Duley, and D. A. Williams, QJRAS **31**, 567 (1990).
F. C. Jones and D. C. Ellison, Space Sci. Rev. **58**, 259 (1991).
A. P. Jones *et al.*, ApJ **433**, 797 (1994).
A. P. Jones *et al.*, A&A **558**, A62 (2013).
A. P. Jones *et al.*, Faraday Discussions **168**, 313 (2014).
A. P. Jones, M. Köhler, N. Ysard, M. Bocchio, and L. Verstraete, A&A **602**, A46 (2017).
J. K. Jørgensen *et al.*, ApJ **659**, 479 (2007).
M. K. R. Joung and M.-M. Mac Low, ApJ **653**, 1266 (2006).
M. Jubelgas *et al.*, A&A **481**, 33 (2008).
B.-I. Jun and M. L. Norman, ApJ **465**, 800 (1996).
M. Juvela *et al.*, A&A **556**, A63 (2013).
O. Kargaltsev *et al.*, Journal of Plasma Physics **83**, 635830501 (2017).
V. M. Kaspi *et al.*, ApJ **503**, L161 (1998).
M. Kawada *et al.*, PASJ **59**, S389 (2007).
M. T. Kawasaki *et al.*, ApJ **572**, 897 (2002).
B. C. Kelly *et al.*, ApJ **752**, 55 (2012).
J. W. Keohane *et al.*, ApJ **484**, 350 (1997).
I.-J. Kim *et al.*, ApJ **784**, 12 (2014).
C.-G. Kim and E. C. Ostriker, ApJ **802**, 99 (2015).
G. Klapper *et al.*, Journal of Molecular Spectroscopy **201**, 124 (2000a).
G. Klapper *et al.*, Zeitschrift Naturforschung Teil A **55**, 441 (2000b).
G. Klapper *et al.*, ApJ **582**, 262 (2003).
B. Klein *et al.*, A&A , this volume (2012a).
B. Klein *et al.*, A&A **454**, L29 (2006).
B. Klein *et al.*, A&A **542**, L3 (2012b).
T. Klein *et al.*, IEEE Transactions on Terahertz Science and Technology **4**, 588 (2014).
R. S. Klessen, ApJ **556**, 837 (2001).
M. Köhler *et al.*, A&A **548**, A61 (2012).
M. Köhler, A. Jones, and N. Ysard, A&A **565**, L9 (2014).
M. Köhler, N. Ysard, and A. P. Jones, A&A **579**, A15 (2015).
X. P. Koenig and D. T. Leisawitz, ApJ **791**, 131 (2014).
X. P. Koenig *et al.*, ApJ **744**, 130 (2012).
T. Kokusho *et al.*, ApJ **899**, 49 (2020).
A. Konigl and R. E. Pudritz, in *Protostars and Planets IV*, edited by V. Mannings, A. P. Boss, and S. S. Russell (2000) p. 759.
V. Könyves *et al.*, A&A **463**, 1227 (2007).
V. Könyves *et al.*, A&A **518**, L106 (2010).
B.-C. Koo and D.-S. Moon, ApJ **475**, 194 (1997a).
B.-C. Koo and D.-S. Moon, ApJ **485**, 263 (1997b).
B.-C. Koo *et al.*, ApJ **673**, L147 (2008a).
B.-C. Koo *et al.*, AJ **140**, 262 (2010).
B.-C. Koo *et al.*, ApJ **673**, L147 (2008b).
B. Koralesky *et al.*, AJ **116**, 1323 (1998).
M. J. Korpi *et al.*, A&A **350**, 230 (1999).
R. Kotak *et al.*, ApJ **704**, 306 (2009).
M. Kounkel *et al.*, AJ **156**, 84 (2018).
K. Koyama, R. Petre, E. V. Gotthelf, U. Hwang, M. Matsuura, M. Ozaki, and S. S. Holt, Nature **378**, 255 (1995).
T. Kozasa *et al.*, in *Cosmic Dust - Near and Far*, Astronomical Society of the Pacific Conference Series, Vol. 414, edited by T. Henning, E. Grün, and J. Steinacker (2009) p. 43.
C. Kramer, J. Stutzki, R. Rohrig, and U. Corneliussen, A&A **329**, 249 (1998).
L. M. Krauss and B. Chaboyer, Science **299**, 65 (2003).
L. E. Kristensen *et al.*, A&A **477**, 203 (2008).
P. Kroupa, MNRAS **322**, 231 (2001).
P. Kroupa *et al.*, The Stellar and Sub-Stellar Initial Mass Function of Simple and Composite Populations, in *Planets, Stars and Stellar Systems. Volume 5: Galactic Structure and Stellar Populations*, Vol. 5, edited by T. D. Oswalt and G. Gilmore (2013) p. 115.
J. M. D. Kruijssen *et al.*, MNRAS **419**, 841 (2012).
M. R. Krumholz, Phys. Rep. **539**, 49 (2014).
M. R. Kundu and T. Velusamy, A&A **20**, 237 (1972).
M. L. Kutner and B. L. Ulich, ApJ **250**, 341 (1981).

J. Kwan and N. Scoville, ApJ **210**, L39 (1976).
J. H. Kwan *et al.*, ApJ **216**, 713 (1977).
C. J. Lada and F. C. Adams, ApJ **393**, 278 (1992).
C. J. Lada and B. A. Wilking, ApJ **287**, 610 (1984).
C. J. Lada, ARA&A **23**, 267 (1985).
C. J. Lada, in *Star Forming Regions*, Vol. 115, edited by M. Peimbert and J. Jugaku (1987) p. 1.
I. Lamperti *et al.*, MNRAS **489**, 4389 (2019).
L. D. Landau and E. M. Lifshitz, *Fluid mechanics* (1959).
W. D. Langer *et al.*, ApJ **277**, 581 (1984).
W. D. Langer, R. W. Wilson, and C. H. Anderson, ApJ **408**, L45 (1993).
W. D. Langer and A. A. Penzias, ApJ **408**, 539 (1993).
M. F. Larsen and S. Schick, in *Cryogenic Optical Systems and Instruments XI*, Society of Photo-Optical Instrumentation Engineers (SPIE) Conference Series, Vol. 5904, edited by J. B. Heaney and L. G. Burriesci (2005) pp. 166–177.
R. B. Larson, MNRAS **145**, 271 (1969).
R. B. Larson, MNRAS **194**, 809 (1981).
J. Le Bourlot *et al.*, MNRAS **332**, 985 (2002).
F. Le Petit *et al.*, ApJS **164**, 506 (2006).
D. A. Leahy and J. E. Williams, AJ **153**, 239 (2017).
D. A. Leahy, AJ **127**, 2277 (2004).
D. A. Leahy, ApJ **837**, 36 (2017).
J. Le Bourlot, G. Pineau des Forêts, and D. R. Flower, MNRAS **305**, 802 (1999).
J.-J. Lee *et al.*, AJ **135**, 796 (2008).
J.-J. Lee *et al.*, ApJ **749**, 34 (2012).
Y.-N. Lee *et al.*, Space Sci. Rev. **216**, 70 (2020).
B. Lefloch and B. Lazareff, A&A **289**, 559 (1994).
A. Leger and J. L. Puget, A&A **500**, 279 (1984).
A. Lehmann *et al.*, A&A **643**, A101 (2020).
S. Lepp, A. Dalgarno, and R. McCray, ApJ **358**, 262 (1990).
J. Lequeux, E. Falgarone, and C. Ryter, *Le milieu interstellaire*, EDP sciences, CNRS éditions. (2002).
A. K. Leroy *et al.*, ApJ **737**, 12 (2011).
P. Lesaffre *et al.*, A&A **427**, 147 (2004a).
P. Lesaffre *et al.*, A&A **427**, 157 (2004b).
P. Lesaffre *et al.*, A&A **550**, A106 (2013).
S. Leurini *et al.*, A&A **422**, 573 (2004).
N. A. Levenson *et al.*, ApJS **118**, 541 (1998).
A. Levine *et al.*, ApJ **228**, L99 (1979).
A. Li and B. T. Draine, ApJ **554**, 778 (2001).
Z.-Y. Li and F. Nakamura, ApJ **640**, L187 (2006).
W. Li *et al.*, MNRAS **412**, 1473 (2011).
A. Li, Nature Astronomy **4**, 339 (2020).
I. D. Litovchenko *et al.*, Astronomy Reports **55**, 978 (2011).
S. Lizano and F. H. Shu, ApJ **342**, 834 (1989).
J. L. Locke, J. A. Galt, and C. H. Costain, ApJ **139**, 1071 (1964).
P. Lockett, E. Gauthier, and M. Elitzur, ApJ **511**, 235 (1999).
M. Lombardi, J. Alves, and C. J. Lada, A&A **454**, 781 (2006).
R. London, R. McCray, and S. I. Chu, ApJ **217**, 442 (1977).
S. N. Longmore *et al.*, in *Protostars and Planets VI*, edited by H. Beuther, R. S. Klessen, C. P. Dullemond, and T. Henning (2014) p. 291.
L. W. Looney, J. J. Tobin, and W. Kwon, ApJ **670**, L131 (2007).
S. Loru *et al.*, MNRAS **482**, 3857 (2019).
F. Louvet *et al.*, A&A **595**, A122 (2016).
F. Louvet *et al.*, A&A **653**, A157 (2021).
A. W. Love, Radio Science **11**, 671 (1976).
F. J. Low, Journal of the Optical Society of America (1917-1983) **51**, 1300 (1961).
T. A. Lozinskaya, Soviet Astronomy Letters **7**, 17 (1981).
T. A. Lozinskaya, Soviet Ast. **13**, 192 (1969).
T. A. Lozinskaia, Soviet Astronomy Letters **1**, 35 (1975).
L. B. Lucy *et al.*, Dust Condensation in the Ejecta of SN 1987 A, in *IAU Colloq. 120: Structure and Dynamics of the Interstellar Medium*, Vol. 350, edited by G. Tenorio-Tagle, M. Moles, and J. Melnick (1989) p. 164.
M. Luisi *et al.*, Science Advances **7**, eabe9511 (2021).
K. Lundmark, Publ. Astron. Soc. Pacific **33**, 225 (1921).
D. Ma, *Wen-Xian-Tang-Kao (Historical Investigation of Public Affairs), Vol. 294*, (1254).

M.-M. Mac Low and R. McCray, ApJ **324**, 776 (1988).
P. Madau and M. Dickinson, ARA&A **52**, 415 (2014).
P. Madau, M. della Valle, and N. Panagia, MNRAS **297**, L17 (1998).
R. Malina, M. Lampton, and S. Bowyer, ApJ **207**, 894 (1976).
J. Malinen *et al.*, A&A **530**, A101 (2011).
M. A. Malkov and L. O. Drury, Reports on Progress in Physics **64**, 429 (2001).
J. G. Mangum, D. T. Emerson, and E. W. Greisen, A&A **474**, 679 (2007).
J. G. Mangum and Y. L. Shirley, PASP **127**, 266 (2015).
V. N. Mansfield and E. E. Salpeter, ApJ **190**, 305 (1974).
A. Marchal *et al.*, A&A **626**, A101 (2019).
K. A. Marsh, A. P. Whitworth, and O. Lomax, MNRAS **454**, 4282 (2015).
K. A. Marsh *et al.*, MNRAS **471**, 2730 (2017).
D. Martizzi, C.-A. Faucher-Giguère, and E. Quataert, MNRAS **450**, 504 (2015).
J. W. Mast and J. Goldstein, S. J., ApJ **159**, 319 (1970).
A. Mastichiadis, A&A **305**, L53 (1996).
J. C. Mather, Appl. Opt. **23**, 584 (1984).
J. S. Mathis, P. G. Mezger, and N. Panagia, A&A **500**, 259 (1983).
T. Matsumura *et al.*, Journal of Low Temperature Physics **176**, 733 (2014).
M. Matsuura *et al.*, Science **333**, 1258 (2011).
M. Matsuura *et al.*, ApJ **800**, 50 (2015).
F. Matteucci, *Chemical Evolution of Galaxies* (2012).
S. Mattila *et al.*, ApJ **756**, 111 (2012).
A. J. Maury *et al.*, A&A **621**, A76 (2019).
P. W. May *et al.*, MNRAS **318**, 809 (2000).
C. F. McKee and L. L. Cowie, ApJ **195**, 715 (1975).
C. F. McKee and D. J. Hollenbach, ARA&A **18**, 219 (1980).
C. F. McKee and J. P. Ostriker, ApJ **218**, 148 (1977).
C. F. McKee and J. C. Tan, Nature **416**, 59 (2002).
C. F. McKee, ApJ **188**, 335 (1974).
C. F. McKee, ApJ **345**, 782 (1989).
C. F. McKee, in *The Evolution of the Interstellar Medium*, Astronomical Society of the Pacific Conference Series, Vol. 12, edited by L. Blitz (1990) pp. 3–29.
C. F. McKee, in *The Origin of Stars and Planetary Systems*, NATO Advanced Study Institute (ASI) Series C, Vol. 540, edited by C. J. Lada and N. D. Kylafis (1999) p. 29.
M.-M. Mac Low and R. S. Klessen, Reviews of Modern Physics **76**, 125 (2004).
M.-M. Mac Low, ApJ **524**, 169 (1999).
R. McCray and M. Kafatos, ApJ **317**, 190 (1987).
R. McCray and J. Snow, T. P., ARA&A **17**, 213 (1979).
K. E. McDonnell, M. Wardle, and A. E. Vaughan, MNRAS **390**, 49 (2008).
J. Meaburn *et al.*, A&A **227**, 191 (1990).
M. Meneguzzi, J. Audouze, and H. Reeves, A&A **15**, 337 (1971).
E. R. Micelotta, M. Matsuura, and A. Sarangi, Space Sci. Rev. **214**, 53 (2018a).
E. R. Micelotta, A. P. Jones, and A. G. G. M. Tielens, A&A **510**, A36 (2010).
E. R. Micelotta, M. Matsuura, and A. Sarangi, Space Sci. Rev. **214**, 53 (2018b).
D. Mihalas, *Stellar atmospheres* (1978).
G. E. Miller and J. M. Scalo, ApJS **41**, 513 (1979).
J. S. Miller, ApJ **189**, 239 (1974).
R. A. Millikan and G. H. Cameron, Physical Review **32**, 533 (1928).
D. K. Milne, Australian Journal of Physics **23**, 425 (1970).
D. K. Milne, Australian Journal of Physics **24**, 429 (1971).
D. K. Milne, Australian Journal of Physics **32**, 83 (1979).
M. Min *et al.*, A&A **462**, 667 (2007).
R. Minkowski, PASP **53**, 224 (1941).
R. Minkowski, ApJ **96**, 199 (1942).
R. Minkowski, PASP **58**, 305 (1946).
R. Minkowski, in *URSI Symp. 1: Paris Symposium on Radio Astronomy*, IAU Symposium, Vol. 9, edited by R. N. Bracewell (1959) p. 315.
M. R. Mokiem *et al.*, A&A **465**, 1003 (2007).
J. Molet *et al.*, A&A **626**, A132 (2019).
A. Monfardini *et al.*, ApJS **194**, 24 (2011).

T. Montmerle, ApJ **231**, 95 (1979a).
T. Montmerle, ApJ **231**, 95 (1979b).
A. Moorhouse *et al.*, MNRAS **253**, 662 (1991).
F. Motte, P. Andre, and R. Neri, A&A **336**, 150 (1998).
F. Motte, P. Schilke, and D. C. Lis, ApJ **582**, 277 (2003).
F. Motte *et al.*, A&A **476**, 1243 (2007).
F. Motte *et al.*, Nature Astronomy **2**, 478 (2018).
D. Muders *et al.*, A&A **454**, L25 (2006).
M. W. Mueller and W. D. Arnett, ApJ **210**, 670 (1976).
S. L. Mufson *et al.*, AJ **92**, 1349 (1986).
D. J. Mullan, MNRAS **153**, 145 (1971).
H. S. P. Müller *et al.*, A&A **370**, L49 (2001).
H. S. P. Müller *et al.*, Journal of Molecular Structure **742**, 215 (2005).
R. Mundt and J. W. Fried, ApJ **274**, L83 (1983).
P. C. Myers *et al.*, ApJ **442**, 177 (1995).
P. C. Myers *et al.*, ApJ **319**, 340 (1987).
T. Naab and J. P. Ostriker, ARA&A **55**, 59 (2017).
K. Naidoo, The Journal of Open Source Software **4**, 1721 (2019).
T. Nakamura *et al.*, Science **333**, 1113 (2011).
T. Nakano, ApJ **494**, 587 (1998).
A. V. Nesterenok *et al.*, MNRAS **489**, 4520 (2019).
D. A. Neufeld and M. J. Kaufman, ApJ **418**, 263 (1993).
D. A. Neufeld and Y. Yuan, ApJ **678**, 974 (2008).
D. Neufeld *et al.*, IRS Spectroscopy of Shocked Molecular Gas in Supernova Remnants: Probing the Interaction of a Supernova with a Molecular Cloud, Spitzer Proposal (2004).
D. A. Neufeld *et al.*, ApJ **664**, 890 (2007).
D. A. Neufeld *et al.*, ApJ **706**, 170 (2009).
D. A. Neufeld *et al.*, ApJ **781**, 102 (2014).
D. A. Neufeld and M. G. Wolfire, ApJ **845**, 163 (2017).
G. Neugebauer *et al.*, ApJ **278**, L1 (1984).
M. Nicholl *et al.*, Nature Astronomy **4**, 893 (2020).
T. Nony *et al.*, A&A **618**, L5 (2018).
A. Noriega-Crespo *et al.*, in *The Evolving ISM in the Milky Way and Nearby Galaxies* (2009) p. 46.
C. Norman and J. Silk, ApJ **238**, 158 (1980).
C. A. Norman and A. Ferrara, ApJ **467**, 280 (1996).
T. Nozawa *et al.*, ApJ **598**, 785 (2003).
T. Nozawa *et al.*, ApJ **666**, 955 (2007).
T. Nozawa *et al.*, ApJ **736**, 45 (2011).
S. F. Odenwald and K. Shivanandan, ApJ **292**, 460 (1985).
M. S. Oey, ApJ **467**, 666 (1996).
S. S. R. Offner *et al.*, in *Protostars and Planets VI*, edited by H. Beuther, R. S. Klessen, C. P. Dullemond, and T. Henning (2014) p. 53.
Y. Ohira, K. Murase, and R. Yamazaki, A&A **513**, A17 (2010).
C. M. Olbert *et al.*, ApJ **554**, L205 (2001a).
C. M. Olbert *et al.*, in *Young Supernova Remnants*, American Institute of Physics Conference Series, Vol. 565, edited by S. S. Holt and U. Hwang (2001) pp. 341–344.
E. Oliva, A. F. M. Moorwood, and I. J. Danziger, A&A **214**, 307 (1989).
E. Oliva *et al.*, A&A **341**, L75 (1999).
J. H. Oort, in *Problems of Cosmical Aerodynamics* (1951) p. 118.
E. J. Opik, Irish Astronomical Journal **2**, 219 (1953).
V. Ossenkopf, KPGT_vossenko_1: The warm and dense ISM, Herschel Space Observatory Proposal (2007).
D. E. Osterbrock, in *American Astronomical Society Meeting Abstracts*, American Astronomical Society Meeting Abstracts, Vol. 199 (2001) p. 15.01.
X. Ouyang and Q. Song, *Xin-Tang-Shu (New History of Tang Dynasty), Astronomy 2*, **32**, 839 (1061).
P. Padoan and Å. Nordlund, ApJ **576**, 870 (2002).
P. Padoan *et al.*, ApJ **661**, 972 (2007).
P. Padoan and Å. Nordlund, ApJ **730**, 40 (2011).
P. Padoan *et al.*, ApJ **840**, 48 (2017).
M. Padovani *et al.*, A&A **582**, L13 (2015).
M. Padovani *et al.*, A&A **590**, A8 (2016).
M. Padovani, D. Galli, and A. E. Glassgold, A&A **501**, 619 (2009).
M. Padovani, P. Hennebelle, and D. Galli, A&A **560**, A114 (2013).
M. Padovani *et al.*, A&A **614**, A111 (2018).

M. Padovani *et al.*, A&A **630**, A72 (2019).
M. Padovani *et al.*, Space Sci. Rev. **216**, 29 (2020).
P. Palmeirim *et al.*, A&A **550**, A38 (2013).
M. E. Palumbo *et al.*, in *Journal of Physics Conference Series*, Journal of Physics Conference Series, Vol. 101 (2008) p. 012002.
D. Paradis *et al.*, A&A **520**, L8 (2010).
D. Paradis *et al.*, A&A **537**, A113 (2012).
J. Pardo, J. Cernicharo, and E. Serabyn, in *Astronomical Site Evaluation in the Visible and Radio Range*, Astronomical Society of the Pacific Conference Series, Vol. 266, edited by J. Vernin, Z. Benkhaldoun, and C. Muñoz-Tuñón (2002) p. 188.
R. A. R. Parker, ApJ **149**, 363 (1967).
R. A. R. Parker, *The physical conditions pertaining to some possible supernova remnants*, Ph.D. thesis, California Institute of Technology (1963).
R. A. R. Parker, ApJ **139**, 493 (1964).
G. E. Parkes *et al.*, MNRAS **179**, 55 (1977).
N. Peretto *et al.*, A&A **518**, L98 (2010).
S. Perlmutter *et al.*, Nature **391**, 51 (1998).
R. Petre *et al.*, ApJ **335**, 215 (1988).
S. J. Petuchowski *et al.*, ApJ **342**, 406 (1989).
J. Pety, in *SF2A-2005: Semaine de l'Astrophysique Francaise*, edited by F. Casoli, T. Contini, J. M. Hameury, and L. Pagani (2005) p. 721.
H. M. Pickett *et al.*, J. Quant. Spec. Radiat. Transf. **60**, 883 (1998).
A. Picquenot *et al.*, A&A **627**, A139 (2019).
Y. M. Pihlström *et al.*, ApJ **676**, 371 (2008).
Y. M. Pihlström *et al.*, AJ **147**, 73 (2014).
G. L. Pilbratt *et al.*, A&A **518**, L1 (2010).
D. Pinheiro Gonçalves *et al.*, AJ **142**, 47 (2011).
Planck Collaboration *et al.*, A&A **564**, A45 (2014a).
Planck Collaboration *et al.*, A&A **571**, A11 (2014b).
E. K. Plyler, L. R. Blaine, and W. S. Connor, Journal of the Optical Society of America (1917-1983) **45**, 102 (1955).
A. Poglitsch *et al.*, A&A **518**, L2 (2010).
A. Poveda, in *Novae, Novoides et Supernovae* (1965) p. 221.
S. S. Prasad and S. P. Tarafdar, ApJ **267**, 603 (1983).
M. Punturo *et al.*, Classical and Quantum Gravity **27**, 194002 (2010).
V. Radhakrishnan, PASP **72**, 296 (1960).
J. C. Raymond, ApJS **39**, 1 (1979).
J. C. Raymond *et al.*, ApJ **246**, 100 (1981).
W. T. Reach, ApJ **335**, 468 (1988).
W. T. Reach *et al.*, A&A **315**, L381 (1996).
W. T. Reach, J. Rho, and T. H. Jarrett, ApJ **618**, 297 (2005).
W. T. Reach *et al.*, AJ **131**, 1479 (2006).
W. T. Reach *et al.*, ApJ **884**, 81 (2019).
J. E. Reed *et al.*, ApJ **440**, 706 (1995).
S. P. Reynolds, ApJ **493**, 375 (1998).
J. Rho and R. Petre, ApJ **503**, L167 (1998).
J. Rho *et al.*, ApJ **547**, 885 (2001).
J. Rho *et al.*, ApJ **693**, L39 (2009).
J. Rho *et al.*, in *EAS Publications Series*, EAS Publications Series, Vol. 46, edited by C. Joblin and A. G. G. M. Tielens (2011) pp. 169–175.
J. A. Rich *et al.*, ApJ **721**, 505 (2010).
J. M. Richardson and K. A. Marsh, Acoustical Imaging **615** (1987).
J. M. Richardson and K. A. Marsh, Maximum Entropy and Bayesian Methods **213** (1992).
J. S. Richer *et al.*, in *Protostars and Planets IV*, edited by V. Mannings, A. P. Boss, and S. S. Russell (2000) p. 867.
M. J. Richter, J. R. Graham, and G. S. Wright, ApJ **454**, 277 (1995a).
M. J. Richter *et al.*, Ap&SS **233**, 67 (1995b).
M. J. Richter *et al.*, ApJ **449**, L83 (1995c).
G. H. Rieke *et al.*, ApJS **154**, 25 (2004).
A. G. Riess *et al.*, AJ **116**, 1009 (1998).
A. G. Riess *et al.*, ApJ **659**, 98 (2007).
A. M. Ritchey *et al.*, ApJ **897**, 83 (2020).
H.-W. Rix and J. Bovy, A&A Rev. **21**, 61 (2013).
W. G. Roberge and B. T. Draine, ApJ **350**, 700 (1990).
W. W. Roberts, ApJ **158**, 123 (1969).
T. Robitaille, Reproject: Astronomical Image Reprojection In Python (2018).
M. Rosado, E. Le Coarer, and Y. P. Georgelin, A&A **286**, 231 (1994).
A. Rosen and J. N. Bregman, ApJ **440**, 634 (1995).

G. Van Rossum and F. L. Drake, *Python 3 Reference Manual* (CreateSpace, Scotts Valley, CA, 2009).
A. Roueff *et al.*, A&A **645**, A26 (2021).
H. Roussel *et al.*, ApJ **669**, 959 (2007).
G. B. Rybicki and A. P. Lightman, *Radiative processes in astrophysics* (1979).
M. Salem and G. L. Bryan, MNRAS **437**, 3312 (2014).
E. E. Salpeter, ApJ **121**, 161 (1955).
K. M. Sandstrom *et al.*, ApJ **715**, 701 (2010).
K. M. Sandstrom *et al.*, ApJ **777**, 5 (2013).
H. Sano *et al.*, ApJ **724**, 59 (2010).
H. Sano *et al.*, ApJ **799**, 175 (2015).
A. Sarangi, M. Matsuura, and E. R. Micelotta, Space Sci. Rev. **214**, 63 (2018).
B. D. Savage and J. S. Mathis, ARA&A **17**, 73 (1979).
J. M. Scalo, Fund. Cosmic Phys. **11**, 1 (1986).
J. M. Scalo, Theoretical Approaches to Interstellar Turbulence, in *Interstellar Processes*, Vol. 134, edited by D. J. Hollenbach and J. Thronson, Harley A. (1987) p. 349.
P. Schilke *et al.*, A&A **321**, 293 (1997).
W. Schmidt *et al.*, A&A **516**, A25 (2010).
N. Schneider *et al.*, A&A **520**, A49 (2010).
N. Schneider *et al.*, A&A **540**, L11 (2012).
N. Schneider *et al.*, PASP **132**, 104301 (2020).
K. M. Schure *et al.*, Space Sci. Rev. **173**, 491 (2012).
K.-F. Schuster *et al.*, in *Radio Telescopes*, Society of Photo-Optical Instrumentation Engineers (SPIE) Conference Series, Vol. 4015, edited by H. R. Butcher (2000) pp. 260–267.
J. S. Scott and R. A. Chevalier, ApJ **197**, L5 (1975).
N. Z. Scoville *et al.*, ApJ **216**, 320 (1977).
L. I. Sedov, *Similarity and Dimensional Methods in Mechanics* (1959).
L. Sedov, *Similitude et dimensions EN mecanique* (1977).
M. Seta *et al.*, ApJ **505**, 286 (1998).
G. A. Shajn and V. F. Gaze, Dokl. Akad. Nauk SSSR **96**, 713 (1954).
P. R. Shapiro and G. B. Field, ApJ **205**, 762 (1976).
S. Sharpless, Distribution of Associations, Emission Regions, Galactic Clusters and Supergiants, in *Galactic structure. Edited by Adriaan Blaauw and Maarten Schmidt. Published by the University of Chicago Press, Chicago, ILL USA, 1965., p.131* (1965) p. 131.
R. L. Shelton, ApJ **521**, 217 (1999).
R. Shetty *et al.*, ApJ **696**, 2234 (2009).
C. N. Shingledecker *et al.*, ApJ **830**, 151 (2016).
C. N. Shingledecker, J. Tennis, R. Le Gal, and E. Herbst, ApJ **861**, 20 (2018).
J.-H. Shinn *et al.*, ApJ **732**, 124 (2011).
M. Shirahata *et al.*, PASJ **61**, 737 (2009).
I. S. Shklovsky, Dokl. Akad. Nauk SSSR **97**, 53 (1954).
F. H. Shu, F. C. Adams, and S. Lizano, ARA&A **25**, 23 (1987).
F. Shu *et al.*, ApJ **429**, 781 (1994).
J. M. Shull and C. F. McKee, ApJ **227**, 131 (1979).
J. M. Shull, D. G. York, and L. M. Hobbs, ApJ **211**, L139 (1977).
J. M. Shull, R. A. Fesen, and J. M. Saken, ApJ **346**, 860 (1989).
G. Siringo *et al.*, A&A **497**, 945 (2009).
M. F. Skrutskie *et al.*, AJ **131**, 1163 (2006).
P. Slane *et al.*, ApJ **616**, 403 (2004).
M. D. Smith and P. W. J. L. Brand, MNRAS **245**, 108 (1990).
J. D. T. Smith *et al.*, PASP **119**, 1133 (2007).
R. L. Snell, R. B. Loren, and R. L. Plambeck, ApJ **239**, L17 (1980).
R. L. Snell *et al.*, ApJ **325**, 853 (1988).
R. L. Snell *et al.*, ApJ **620**, 758 (2005).
V. V. Sobolev, *Cambridge: Harvard University Press, 1960* (1960).
P. M. Solomon, D. B. Sanders, and N. Z. Scoville, in *The Large-Scale Characteristics of the Galaxy*, Vol. 84, edited by W. B. Burton (1979) p. 35.
L. Spitzer, *Physical processes in the interstellar medium* (1978).
J. Spitzer, L., ApJ **262**, 315 (1982).
J. Spitzer, Lyman, ARA&A **28**, 71 (1990).
J. Spyromilio and B. Leibundgut, MNRAS **283**, L89 (1996).
A. Sternberg *et al.*, ApJ **790**, 10 (2014).

J. M. Stone, E. C. Ostriker, and C. F. Gammie, ApJ **508**, L99 (1998).
S. M. Straal and J. van Leeuwen, A&A **623**, A90 (2019).
S. J. Sturner and C. D. Dermer, A&A **293**, L17 (1995).
Y. Su *et al.*, ApJ **694**, 376 (2009).
Y. Su *et al.*, ApJ **788**, 122 (2014).
J. Surdej, A&A **62**, 135 (1978).
J. Surdej, A&A **60**, 303 (1977).
R. S. Sutherland, G. V. Bicknell, and M. A. Dopita, ApJ **414**, 510 (1993).
D. A. Swartz *et al.*, ApJ **808**, 84 (2015).
S. Tachibana *et al.*, ApJ **639**, L87 (2006).
M. Tafalla *et al.*, A&A **573**, L2 (2015).
G. A. Tammann, W. Loeffler, and A. Schroeder, ApJS **92**, 487 (1994).
X. Tang, MNRAS **482**, 3843 (2019).
A. Tappe, J. Rho, and W. T. Reach, ApJ **653**, 267 (2006).
V. Tatischeff and S. Gabici, Annual Review of Nuclear and Particle Science **68**, 377 (2018).
J. A. Tauber *et al.*, ApJ **421**, 570 (1994).
M. Tavani *et al.*, ApJ **710**, L151 (2010).
G. Taylor, Proceedings of the Royal Society of London Series A **201**, 192 (1950).
C. J. Taylor *et al.*, ApJ **750**, L15 (2012).
J. Tennyson, in *Astronomical Spectroscopy: An Introduction to the Atomic and Molecular Physics of Astronomical Spectroscopy.* (2019).
G. Tenorio-Tagle and P. Bodenheimer, ARA&A **26**, 145 (1988).
L. Testi and A. I. Sargent, ApJ **508**, L91 (1998).
F.-K. Thielemann, K. Nomoto, and M.-A. Hashimoto, ApJ **460**, 408 (1996).
M. A. Thompson *et al.*, MNRAS **421**, 408 (2012).
A. G. G. M. Tielens *et al.*, ApJ **431**, 321 (1994).
A. G. G. M. Tielens, *The Physics and Chemistry of the Interstellar Medium* (2005).
J. Tigé *et al.*, A&A **602**, A77 (2017).
M. Tiwari *et al.*, ApJ **914**, 117 (2021).
P. Todini and A. Ferrara, MNRAS **325**, 726 (2001).
K. Tomisaka, A. Habe, and S. Ikeuchi, Ap&SS **78**, 273 (1981).
D. F. Torres *et al.*, Phys. Rep. **382**, 303 (2003).
D. F. Torres, A. Y. Rodriguez Marrero, and E. de Cea Del Pozo, MNRAS **387**, L59 (2008).
D. F. Torres, A. Y. R. Marrero, and E. de Cea Del Pozo, MNRAS **408**, 1257 (2010).
L. N. Tram *et al.*, MNRAS **473**, 1472 (2018).
R. R. Treffers, ApJ **233**, L17 (1979).
V. Trimble, A&A Rev. **3**, 1 (1991).
E. Troja, F. Bocchino, and F. Reale, ApJ **649**, 258 (2006).
E. Troja *et al.*, A&A **485**, 777 (2008).
J. K. Truelove and C. F. McKee, ApJS **120**, 299 (1999).
W. H. Tucker, Science **172**, 372 (1971).
M. Turatto, Classification of Supernovae, in *Supernovae and Gamma-Ray Bursters*, Vol. 598, edited by K. Weiler (2003) pp. 21–36.
B. E. Turner *et al.*, ApJ **399**, 114 (1992).
B. E. Turner, VLA observations of OH masers and associated ultracompact continuum sources, in *In: Regions of recent star formation; Proceedings of the Symposium on Neutral Clouds near HII Regions - Dynamics and Photochemistry, Penticton, British Columbia, Canada, June 24-26, 1981. (A82-47601 24-90) Dordrecht, D. Reidel Publishing Co., 1982, p. 425-431; Discussion, p. 432.*, Astrophysics and Space Science Library, Vol. 93, edited by R. S. Roger and P. E. Dewdney (1982) pp. 425–431.
Y. Uchiyama *et al.*, Nature **449**, 576 (2007).
Y. Uchiyama and F. A. Aharonian, ApJ **677**, L105 (2008).
Y. Uchiyama *et al.*, ApJ **723**, L122 (2010).
M. Uhlig *et al.*, MNRAS **423**, 2374 (2012).
H. Ungerechts *et al.*, in *Imaging at Radio through Submillimeter Wavelengths*, Astronomical Society of the Pacific Conference Series, Vol. 217, edited by J. G. Mangum and S. J. E. Radford (2000) p. 190.
S. Ustamujic *et al.*, A&A **649**, A14 (2021).
B. van Veelen *et al.*, A&A **503**, 495 (2009).
S. van den Bergh and K. W. Kamper, ApJ **218**, 617 (1977).
S. van den Bergh, ApJ **327**, 156 (1988).
H. van der Laan, MNRAS **124**, 125 (1962a).
H. van der Laan, MNRAS **124**, 179 (1962b).
E. van der Swaluw *et al.*, A&A **397**, 913 (2003).
F. F. S. van der Tak *et al.*, A&A **468**, 627 (2007).

S. van der Walt, S. C. Colbert, and G. Varoquaux, Computing in Science and Engineering **13**, 22 (2011).
E. F. van Dishoeck, D. J. Jansen, and T. G. Phillips, A&A **279**, 541 (1993).
H. A. T. Vanhala and A. P. Boss, ApJ **575**, 1144 (2002).
H. A. T. Vanhala and A. G. W. Cameron, ApJ **508**, 291 (1998).
S. Vaupré *et al.*, A&A **568**, A50 (2014).
E. Vázquez-Semadeni, A. Palau, J. Ballesteros-Paredes, G. C. Gómez, and M. Zamora-Avilés, MNRAS **490**, 3061 (2019).
M. Veneziani *et al.*, ApJ **772**, 56 (2013).
J. Vink and J. M. Laming, ApJ **584**, 758 (2003).
J. Vink, J. S. Kaastra, and J. A. M. Bleeker, A&A **328**, 628 (1997).
J. Vink, A&A Rev. **20**, 49 (2012).
J. Vink, Supernova remnant evolution, in *Physics and Evolution of Supernova Remnants* (Springer International Publishing, Cham, 2020) pp. 87–116.
H. J. Voelk, L. O. Drury, and J. F. McKenzie, A&A **130**, 19 (1984).
H. J. Völk, E. G. Berezhko, and L. T. Ksenofontov, A&A **433**, 229 (2005).
R. V. Wagoner, W. A. Fowler, and F. Hoyle, ApJ **148**, 3 (1967).
V. Wakelam *et al.*, Molecular Astrophysics **9**, 1 (2017).
S. K. Walch *et al.*, MNRAS **427**, 625 (2012).
Z. Wang and N. Z. Scoville, ApJ **386**, 158 (1992).
Z. R. Wang *et al.*, PASJ **44**, 303 (1992).
K. Wang *et al.*, MNRAS **439**, 3275 (2014).
M. Wardle and F. Yusef-Zadeh, Science **296**, 2350 (2002).
M. Wardle, ApJ **525**, L101 (1999).
R. Weaver *et al.*, ApJ **218**, 377 (1977).
K. W. Weiler and N. Panagia, A&A **70**, 419 (1978).
J. C. Weingartner and B. T. Draine, ApJ **548**, 296 (2001).
S. Weinreb *et al.*, Nature **200**, 829 (1963).
B. Y. Welsh and S. Sallmen, A&A **408**, 545 (2003).
T. V. Wenger *et al.*, ApJ **856**, 52 (2018).
M. W. Werner *et al.*, ApJS **154**, 1 (2004).
B. E. Westerlund, AJ **74**, 879 (1969a).
B. E. Westerlund, AJ **74**, 882 (1969b).
J. Whelan and J. Iben, Icko, ApJ **186**, 1007 (1973).
G. J. White *et al.*, A&A **173**, 337 (1987).
P. A. Whitelock *et al.*, MNRAS **240**, 7P (1989).
A. P. Whitworth *et al.*, MNRAS **489**, 5436 (2019).
D. Wilgenbus *et al.*, A&A **356**, 1010 (2000).
B. A. Wilking, C. J. Lada, and E. T. Young, ApJ **340**, 823 (1989).
J. P. Williams and P. C. Myers, ApJ **537**, 891 (2000).
J. Williams, *Chinese Observations of Comets, London*, (1871).
J. P. Williams, E. J. de Geus, and L. Blitz, ApJ **428**, 693 (1994).
J. P. Williams, L. Blitz, and A. A. Stark, ApJ **451**, 252 (1995).
J. P. Williams *et al.*, ApJ **503**, 689 (1998).
J. P. Williams, L. Blitz, and C. F. McKee, in *Protostars and Planets IV*, edited by V. Mannings, A. P. Boss, and S. S. Russell (2000) p. 97.
B. J. Williams *et al.*, ApJ **741**, 96 (2011).
F. O. Williamson *et al.*, ApJ **193**, L133 (1974).
T. L. Wilson and R. Rood, ARA&A **32**, 191 (1994).
G. P. Wilson, *Candidates for historical supernovae and their comparison against known Chinese records*, Ph.D. thesis, Durham University (2003).
T. L. Wilson, K. Rohlfs, and S. Hüttemeister, *Tools of Radio Astronomy* (2009).
T. L. Wilson and F. Matteucci, A&A Rev. **4**, 1 (1992).
J. Winkler, P. Frank and G. W. Clark, ApJ **191**, L67 (1974).
L. Woltjer, ARA&A **10**, 129 (1972).
C. A. Wood, S. L. Mufson, and J. R. Dickel, AJ **102**, 224 (1991).
J. M. Woodall and M. D. Gray, MNRAS **378**, L20 (2007).
D. H. Wooden *et al.*, ApJS **88**, 477 (1993).
S. E. Woosley and T. A. Weaver, ApJS **101**, 181 (1995).
S. E. Woosley, W. D. Arnett, and D. D. Clayton, ApJS **26**, 231 (1973).

S. E. Woosley, A. Heger, and T. A. Weaver, Reviews of Modern Physics **74**, 1015 (2002).
A. Wootten, ApJ **245**, 105 (1981).
A. Wootten and A. R. Thompson, IEEE Proceedings **97**, 1463 (2009).
S. A. Wrathmall, A. Gusdorf, and D. R. Flower, MNRAS **382**, 133 (2007).
E. L. Wright *et al.*, AJ **140**, 1868 (2010).
Z. Xi and S. Bo, Acta Astron. Sinica **13**, 1 (1965).
Z. Xi, Acta Astron. Sinica **8**, 183 (1955).
S. Xu and A. Lazarian, ApJ **833**, 215 (2016).
S. Xu and A. Lazarian, ApJ **850**, 126 (2017).
J.-L. Xu, J.-J. Wang, and M. Miller, ApJ **727**, 81 (2011).
R. Yamaguchi *et al.*, PASJ **53**, 959 (2001).
H. Yamaguchi *et al.*, ApJ **705**, L6 (2009).
I. Yamamura *et al.*, (2010).
B. Yang *et al.*, ApJ **718**, 1062 (2010).
D. G. York and SDSS Collaboration, AJ **120**, 1579 (2000).
N. Ysard *et al.*, A&A **577**, A110 (2015).
B. Yu *et al.*, MNRAS **488**, 3129 (2019).
Y. Yuan and D. A. Neufeld, ApJ **726**, 76 (2011).
F. Yusef-Zadeh *et al.*, ApJ **585**, 319 (2003).
A. Zavagno *et al.*, A&A **472**, 835 (2007).
Y. B. Zeldovich and Y. P. Raizer, *Elements of gas dynamics and the classical theory of shock waves* (1966).
Z. Zhang, Y. Gao, and J. Wang, Science China Physics, Mechanics, and Astronomy **53**, 1357 (2010).
S. Zhang *et al.*, ApJ **859**, 141 (2018).
H. Zinnecker and H. W. Yorke, ARA&A **45**, 481 (2007).
L. M. Ziurys, R. L. Snell, and R. L. Dickman, ApJ **341**, 857 (1989).
V. Zubko, E. Dwek, and R. G. Arendt, ApJS **152**, 211 (2004).
B. Zuckerman and I. Evans, N. J., ApJ **192**, L149 (1974).
P. Zyla *et al.*, Progress of Theoretical and Experimental Physics (2020).
R. Zylka, MOPSIC: Extended Version of MOPSI (2013), ascl:1303.011 .

Appendices

Appendix **A** | **Additional figures**

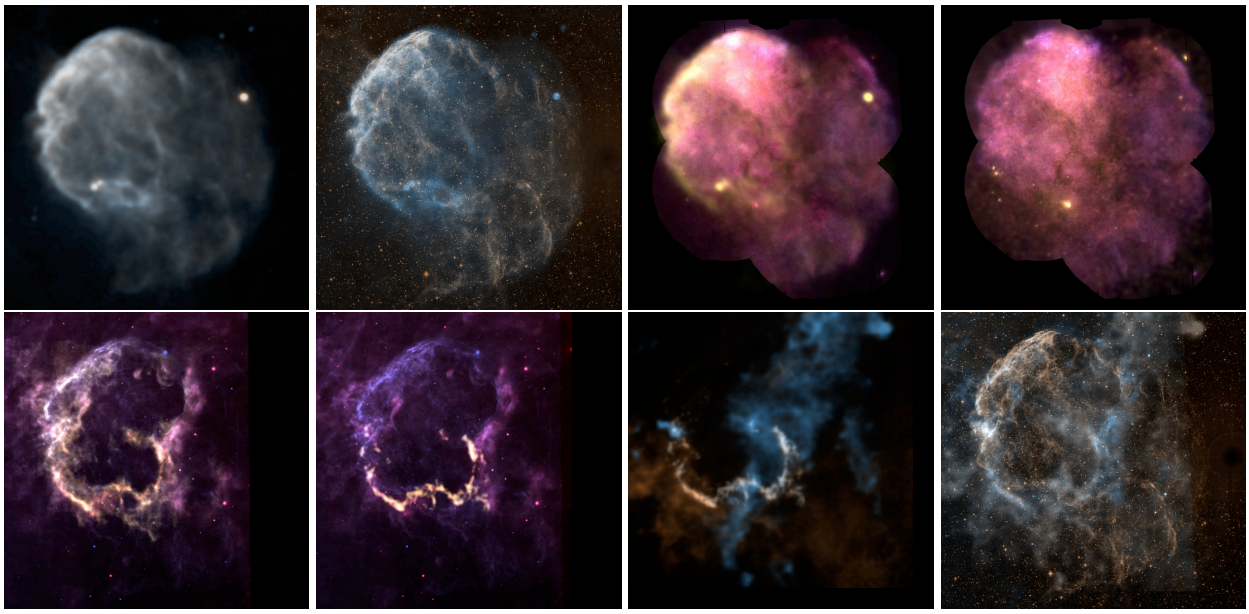

Figure A.1 Mosaic of composite images reproduced from the figures 2.16, 2.17, 2.18 and 2.19. See captions therein.

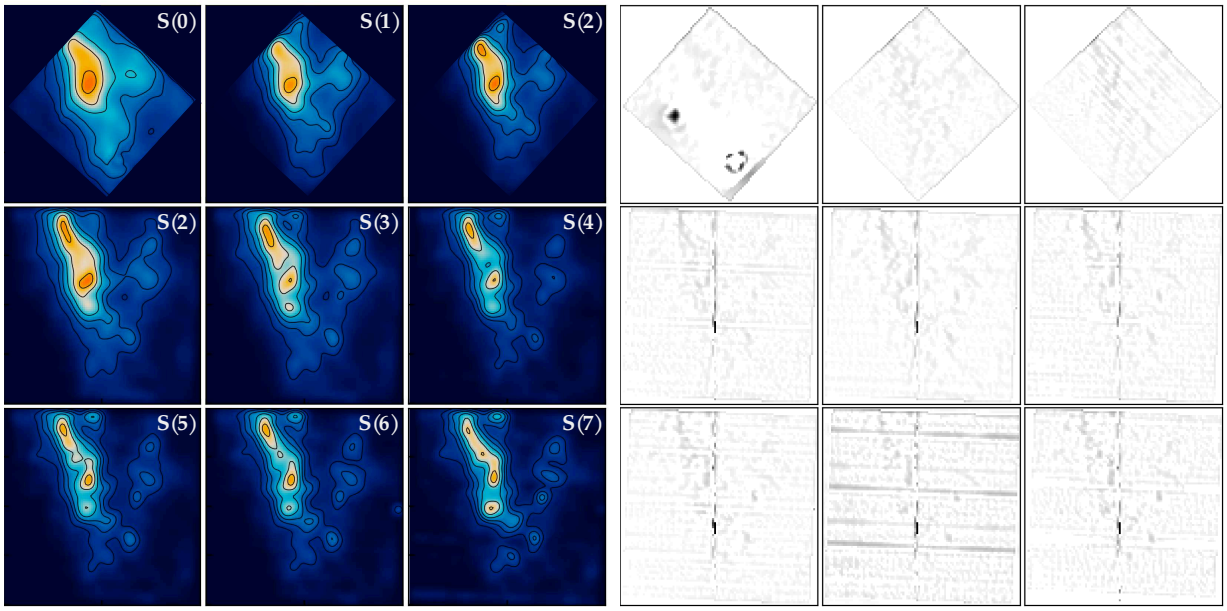

Figure A.2 H_2 $v = 0-0$ S(0) to S(7) maps obtained with *Spitzer*-IRS towards the region IC443G. *Left:* pre-processed maps (see text). *Right:* residuals between the raw and pre-processed maps. The S(2) line was mapped both by the SH (top-row) and SL (second-row) modules. See also Fig. 8.3 for the numerical values.

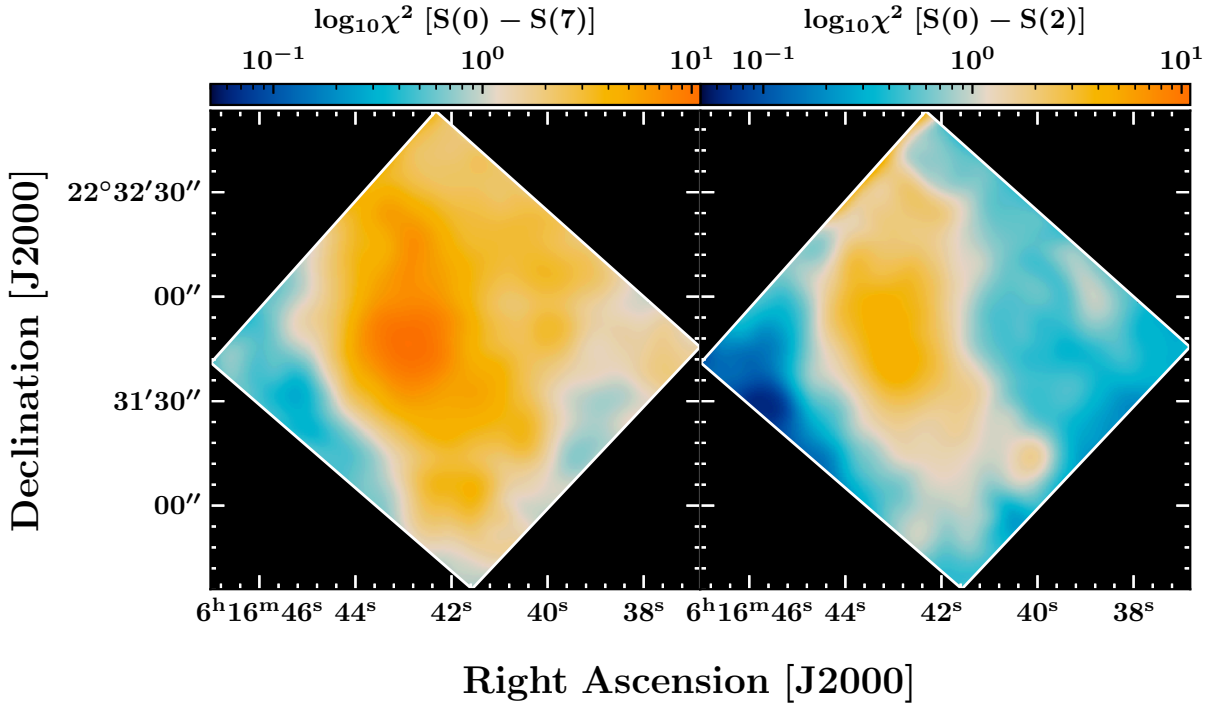

Figure A.3 χ^2 map corresponding to the pixel-per-pixel population diagram analysis of H_2 spectral-line maps S(0) to S(7) (see section 8.1.2). Left panel: χ^2 corresponding to the transitions S(0) to S(7). Right panel: χ^2 corresponding to the 'cold' component (S(0) to S(2) lines).

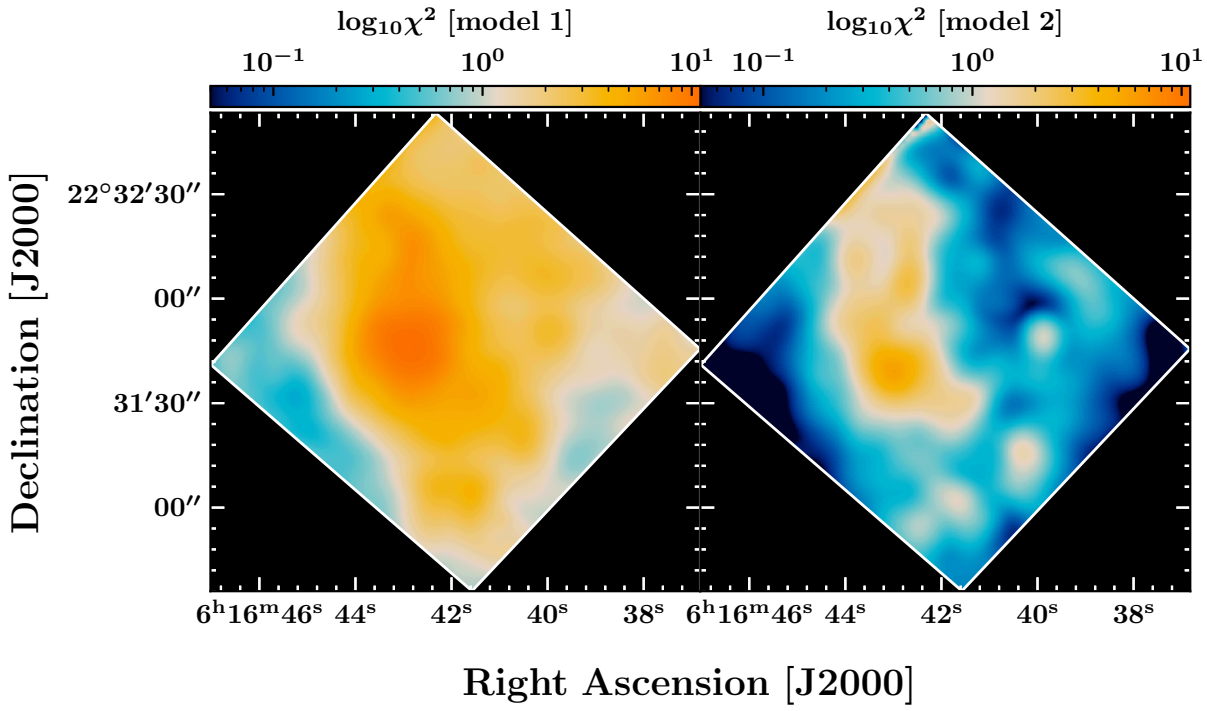

Figure A.4 χ^2 map corresponding to the pixel-per-pixel population diagram analysis of H_2 spectral-line maps S(0) to S(7) (see section 8.1.2). Left panel: χ^2 corresponding to the first model (standard population diagram). Right panel: χ^2 corresponding to the second model (H_2 thermal admixture).

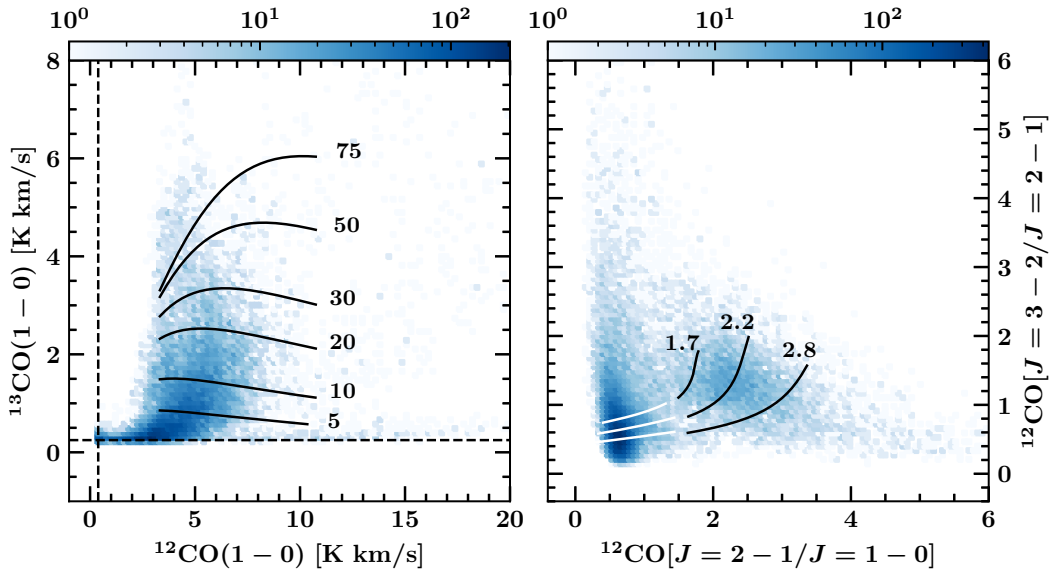

Figure A.5 *Left:* ^{13}CO *v.s.* ^{12}CO J=1–0 histogram. Black curves represent the radiative transfer models obtained for different opacities (indicated by numeric values on the right end of the curves). *Right:* ^{12}CO [J=3–2]/[J=2–1] *v.s.* [J=2–1]/[J=1–0] histogram. Black curves (τ = 40) and white curves (τ = 5) represent the radiative transfer models obtained for different T_{2-1}/T_{1-0} ratios (indicated by numeric values on the top end of the curves). See also Fig. 8.15.

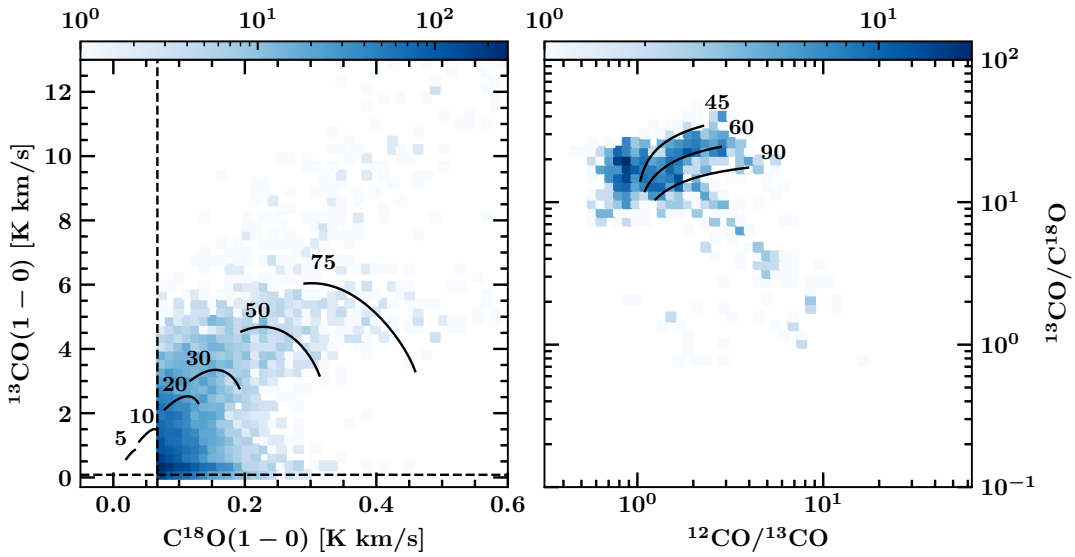

Figure A.6 *Left:* kernel density estimate of the ^{13}CO *v.s.* C^{18}O J=1–0 histogram. Black curves represent the radiative transfer models obtained for different opacities (indicated by numeric values on top of the curves). *Right:* kernel density estimate of the [^{13}CO/C^{18}O] *v.s.* [^{12}CO/^{13}CO] (J=1–0) histogram. Black curves represent the radiative transfer models obtained for different ^{12}CO/^{13}CO isotopic ratios (indicated by numeric values on the right end of the curves). See also Fig. 8.16.

Appendix B | PPMAP results

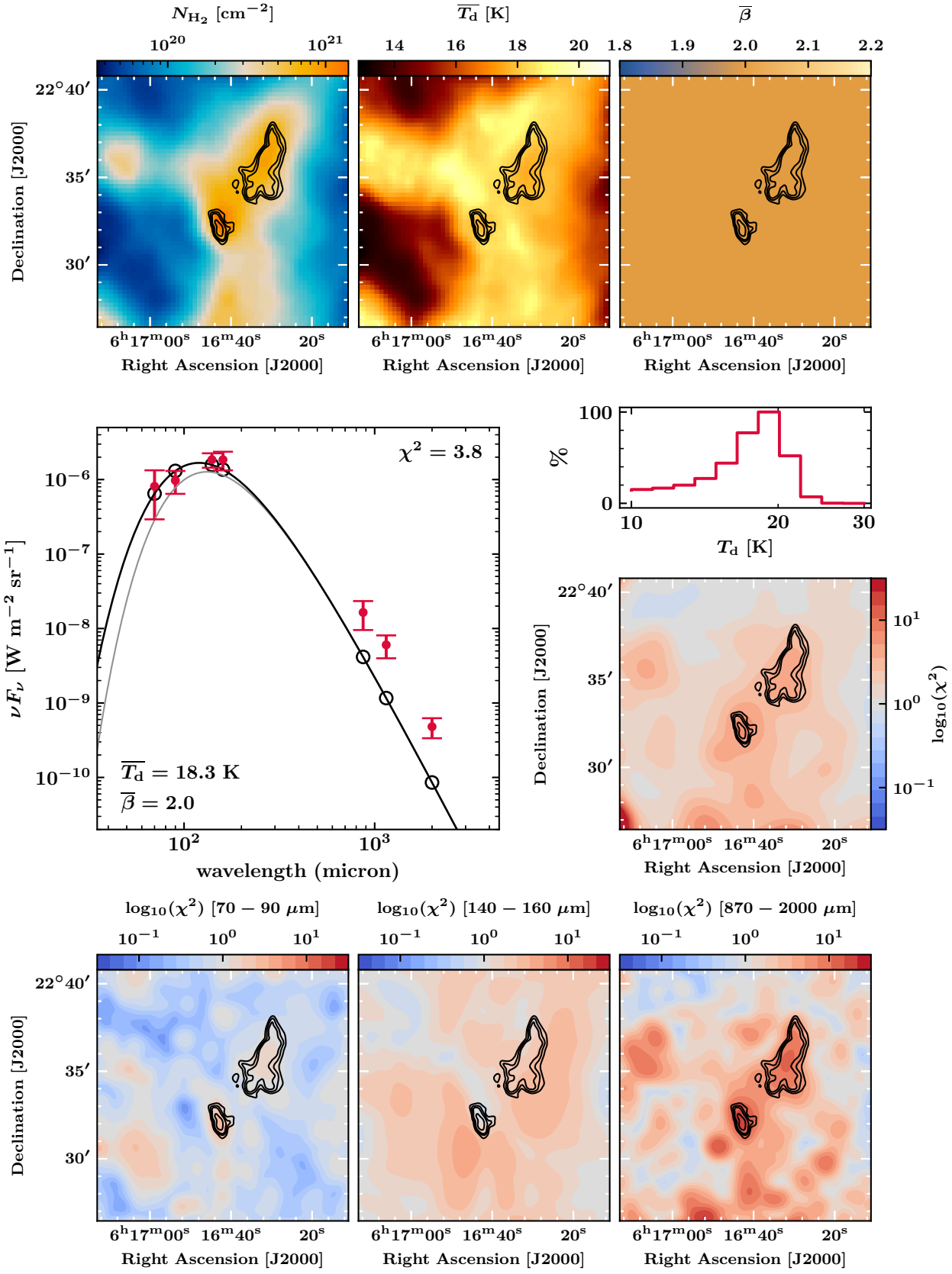

Figure B.1 Results of the run '`PPMAP-A1`': analysis of the 70-2000 µm data points with twelve dust temperatures in the range $T_d = 10 - 30$ K, $\beta = 2$, $\eta = 0.3$ and uniform weighting (see Tab. 9.9). See the first paragraph in section 9.2.2 for a detailed description of the figure.

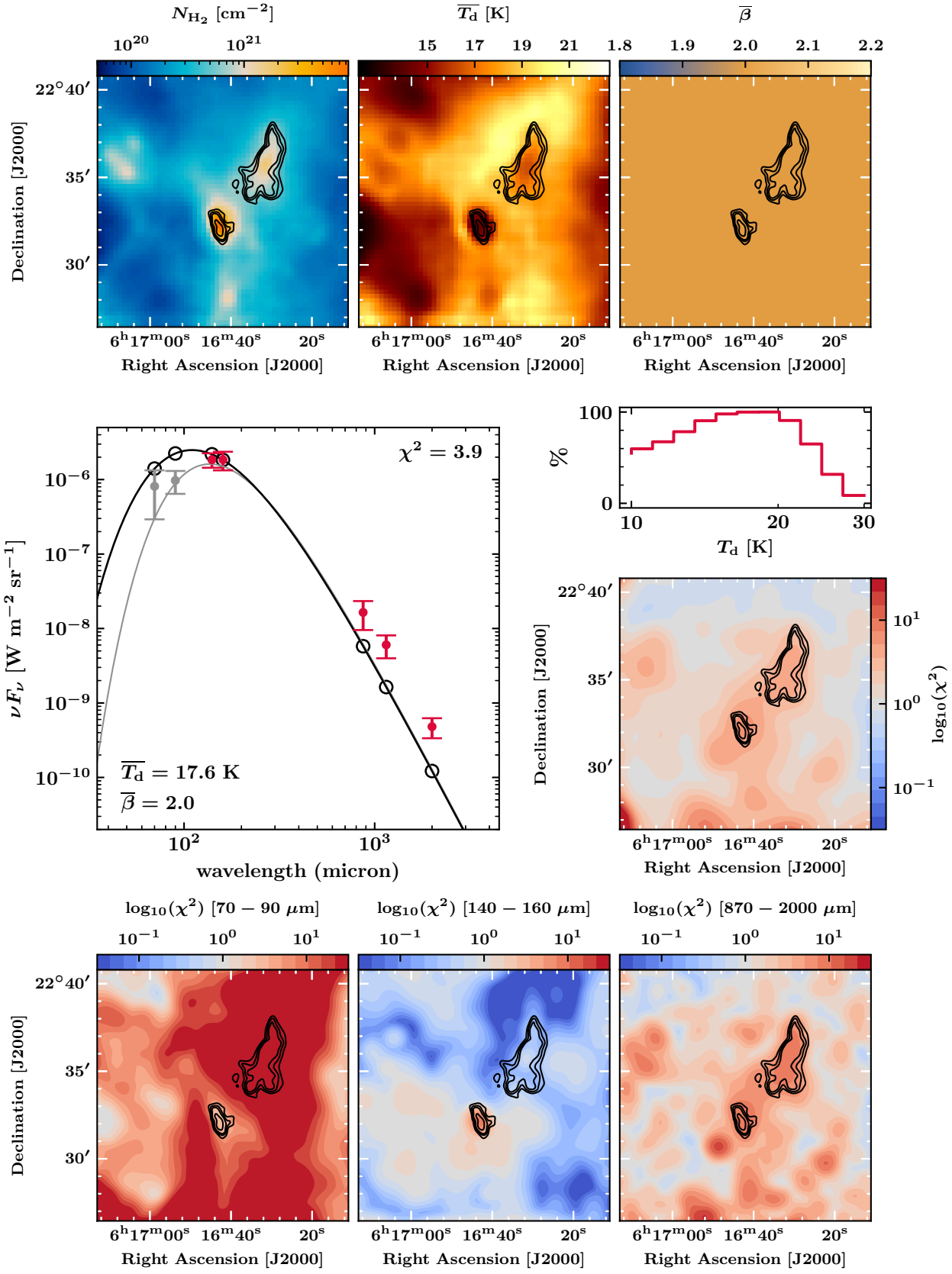

Figure B.2 Results of the run '`PPMAP-A2`': analysis of the 140-2000 µm data points with twelve dust temperatures in the range $T_d = 10 - 30$ K, $\beta = 2$, $\eta = 0.3$ and uniform weighting (see Tab. 9.9). See the first paragraph in section 9.2.2 for a detailed description of the figure.

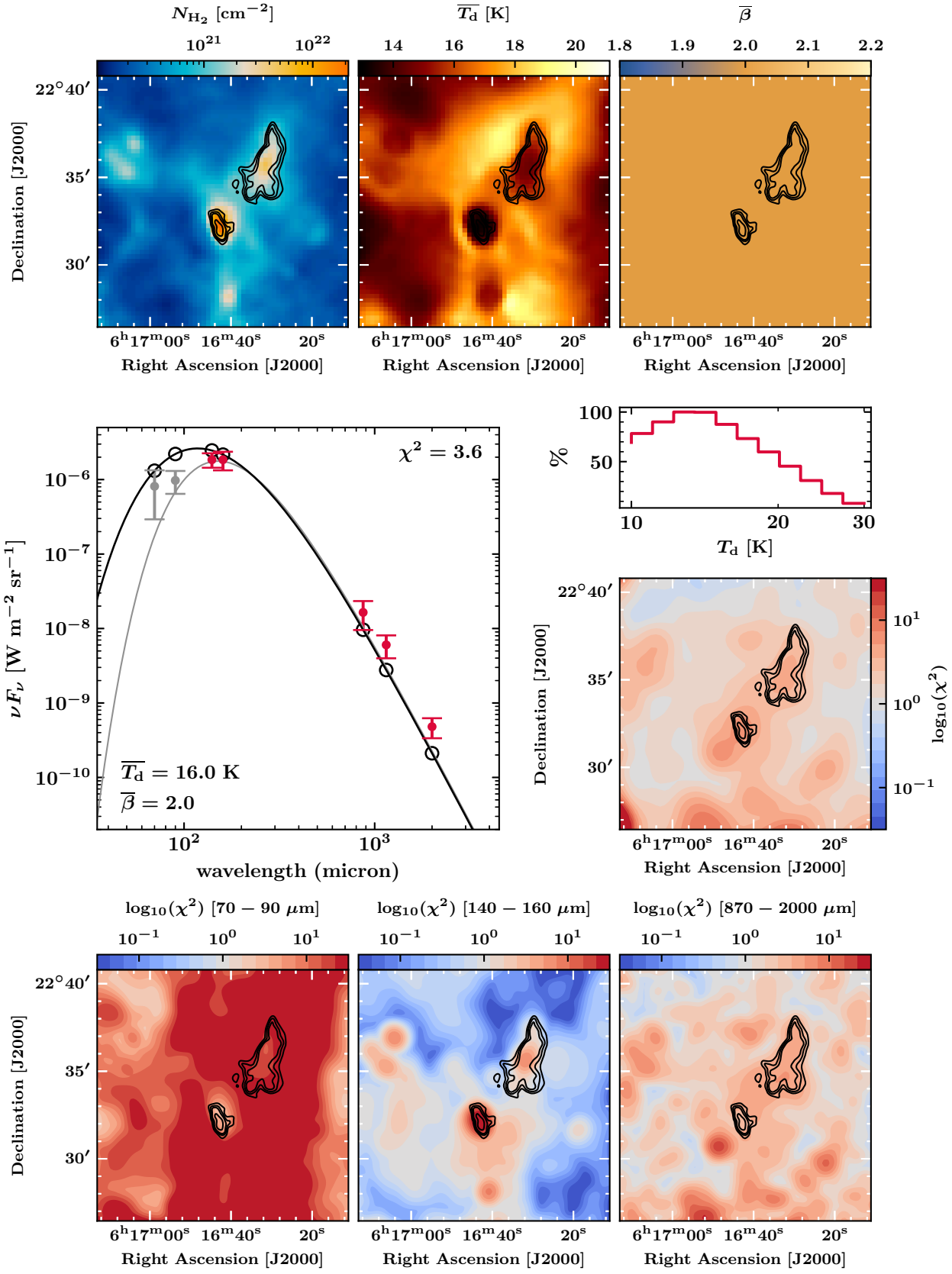

Figure B.3 Results of the run 'PPMAP-B1': analysis of the 140-2000 µm data points with twelve dust temperatures in the range $T_d = 10 - 30$ K, $\beta = 2$, $\eta = 0.3$ and r.m.s weighting (see Tab. 9.9). See the first paragraph in section 9.2.2 for a detailed description of the figure.

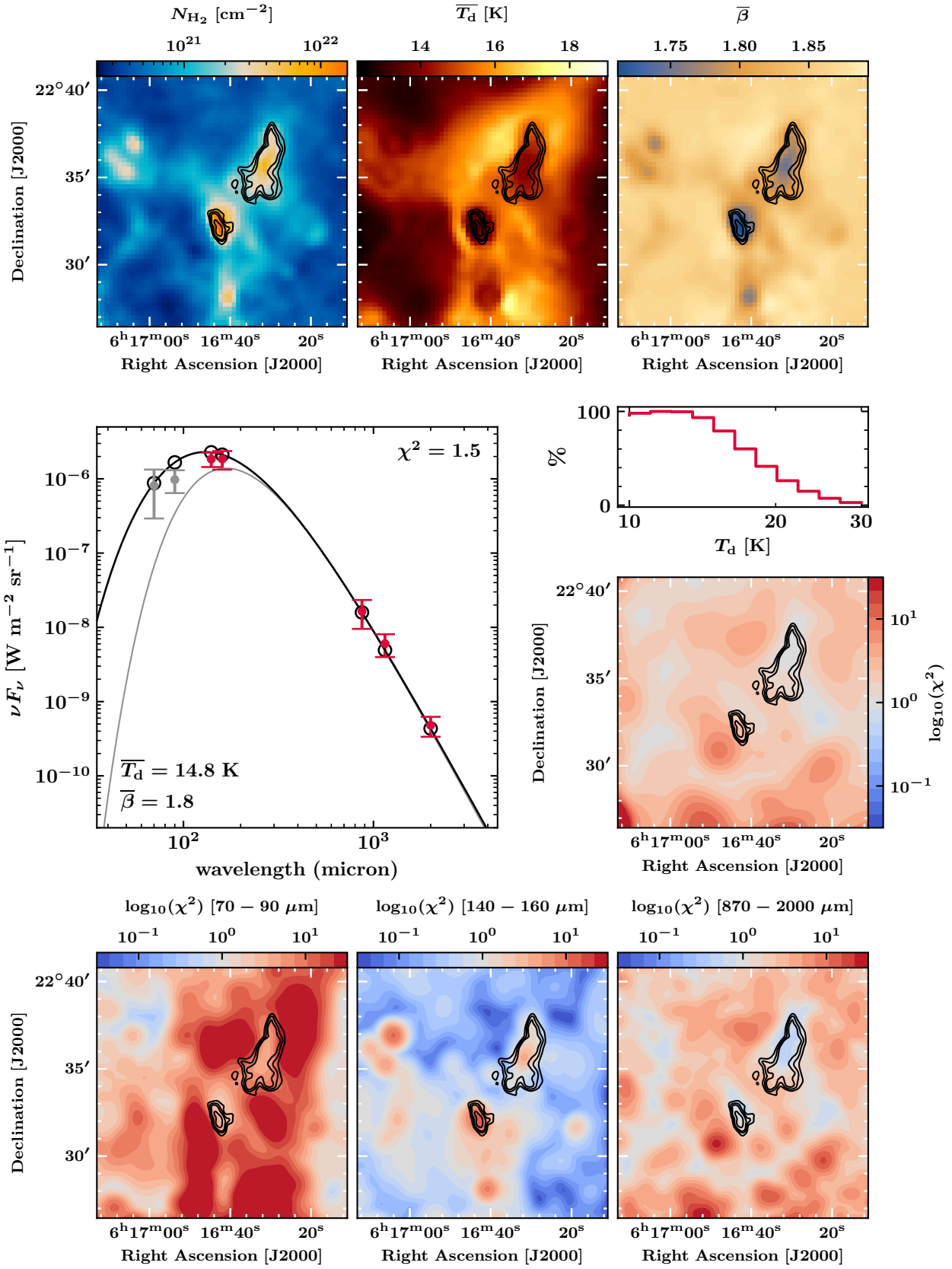

Figure B.4 Results of the run '`PPMAP-B2`': analysis of the 140-2000 µm data points with eight dust temperatures in the range $T_d = 10 - 30$ K, $\beta = \{1.6, 1.7, 1.8, 1.9, 2.0\}$, $\eta = 0.3$ and r.m.s weighting (see Tab. 9.9). See the first paragraph in section 9.2.2 for a detailed description of the figure.

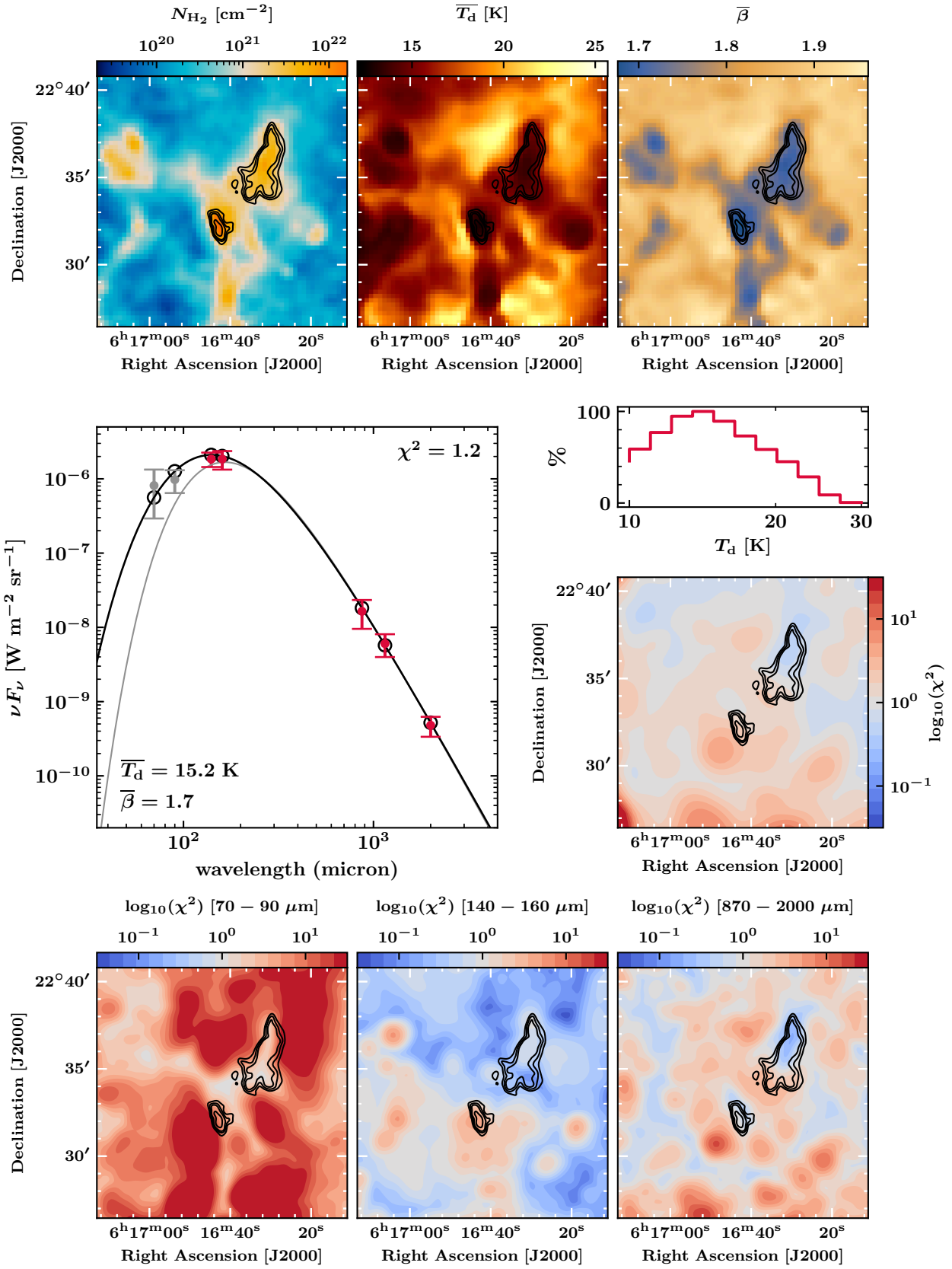

Figure B.5 Results of the run '`PPMAP-C1`': analysis of the 140-2000 µm data points with eight dust temperatures in the range $T_d = 10 - 30$ K, $\beta = \{1.6,\ 1.7,\ 1.8,\ 1.9,\ 2.0\}$, $\eta = 0.03$ and r.m.s weighting (see Tab. 9.9). See the first paragraph in section 9.2.2 for a detailed description of the figure.

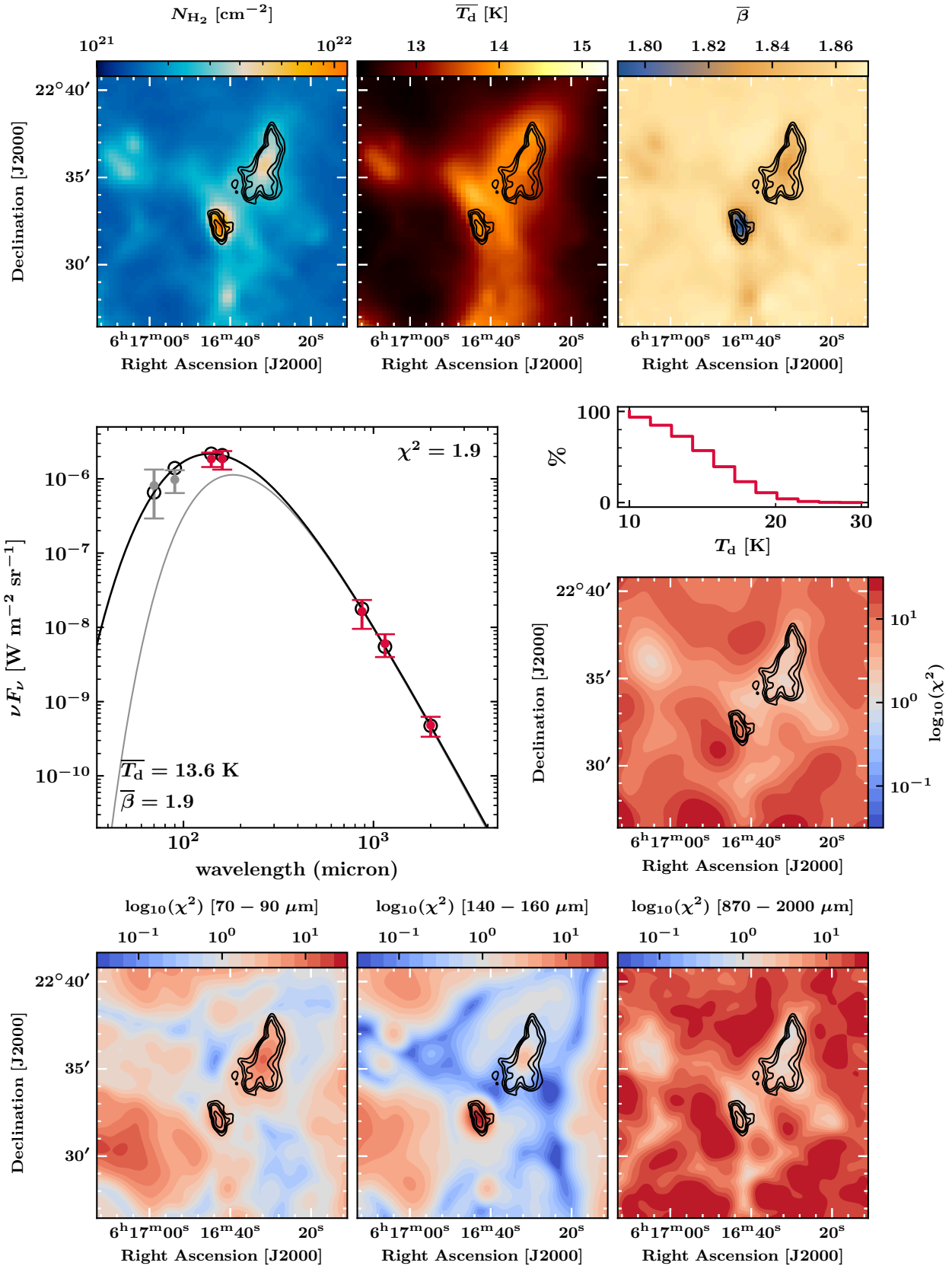

Figure B.6 Results of the run '`PPMAP-C2`': analysis of the 140-2000 µm data points with eight dust temperatures in the range $T_d = 10 - 30$ K, $\beta = \{1.6, 1.7, 1.8, 1.9, 2.0\}$, $\eta = 3$ and r.m.s weighting (see Tab. 9.9). See the first paragraph in section 9.2.2 for a detailed description of the figure.

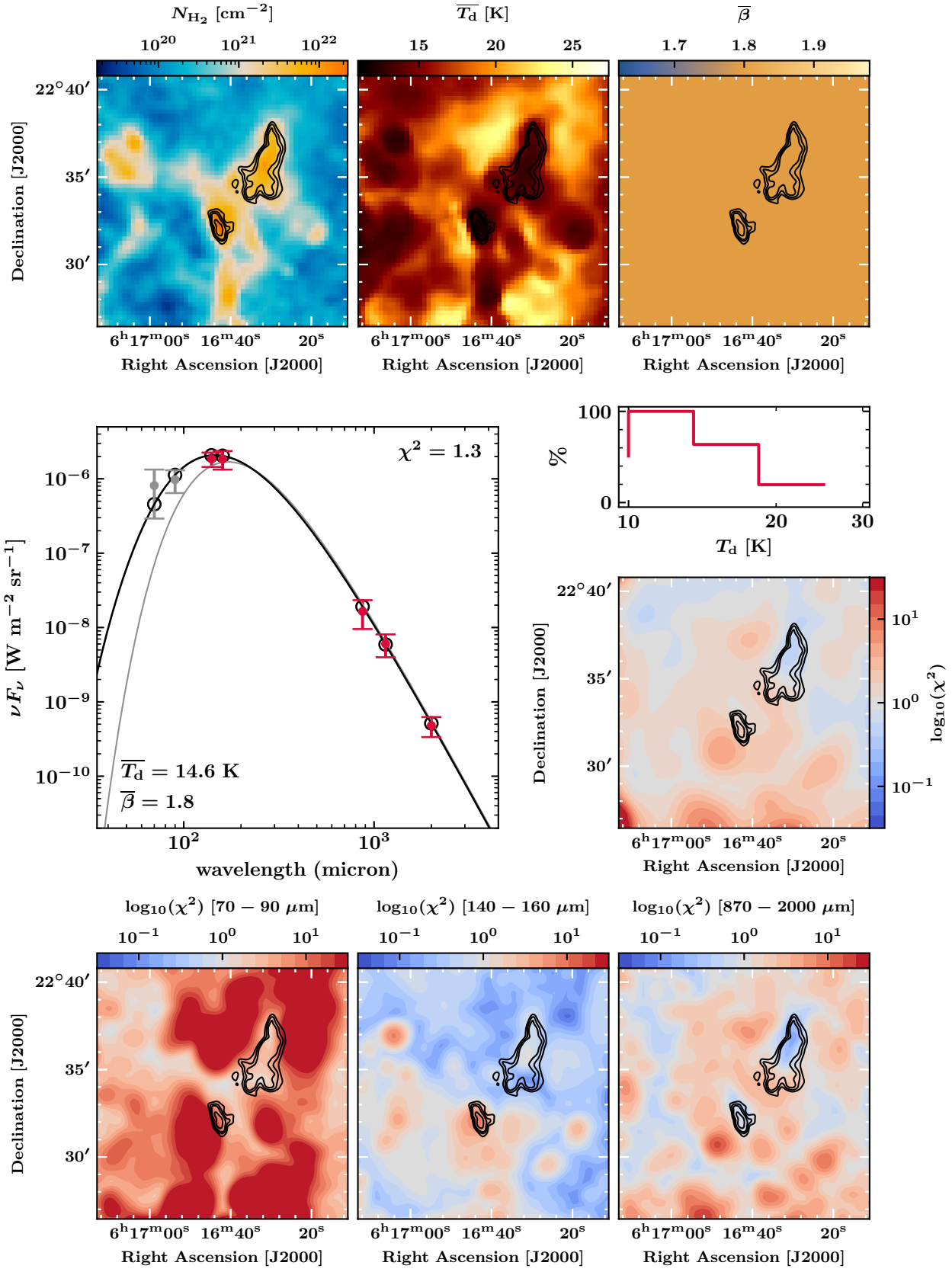

Figure B.7 Results of the run '`PPMAP-D`': analysis of the 140-2000 µm data points with four dust temperatures in the range $T_d = 10 - 25$ K, $\beta = 1.8$, $\eta = 0.3$ and r.m.s weighting (see Tab. 9.9). See the first paragraph in section 9.2.2 for a detailed description of the figure.

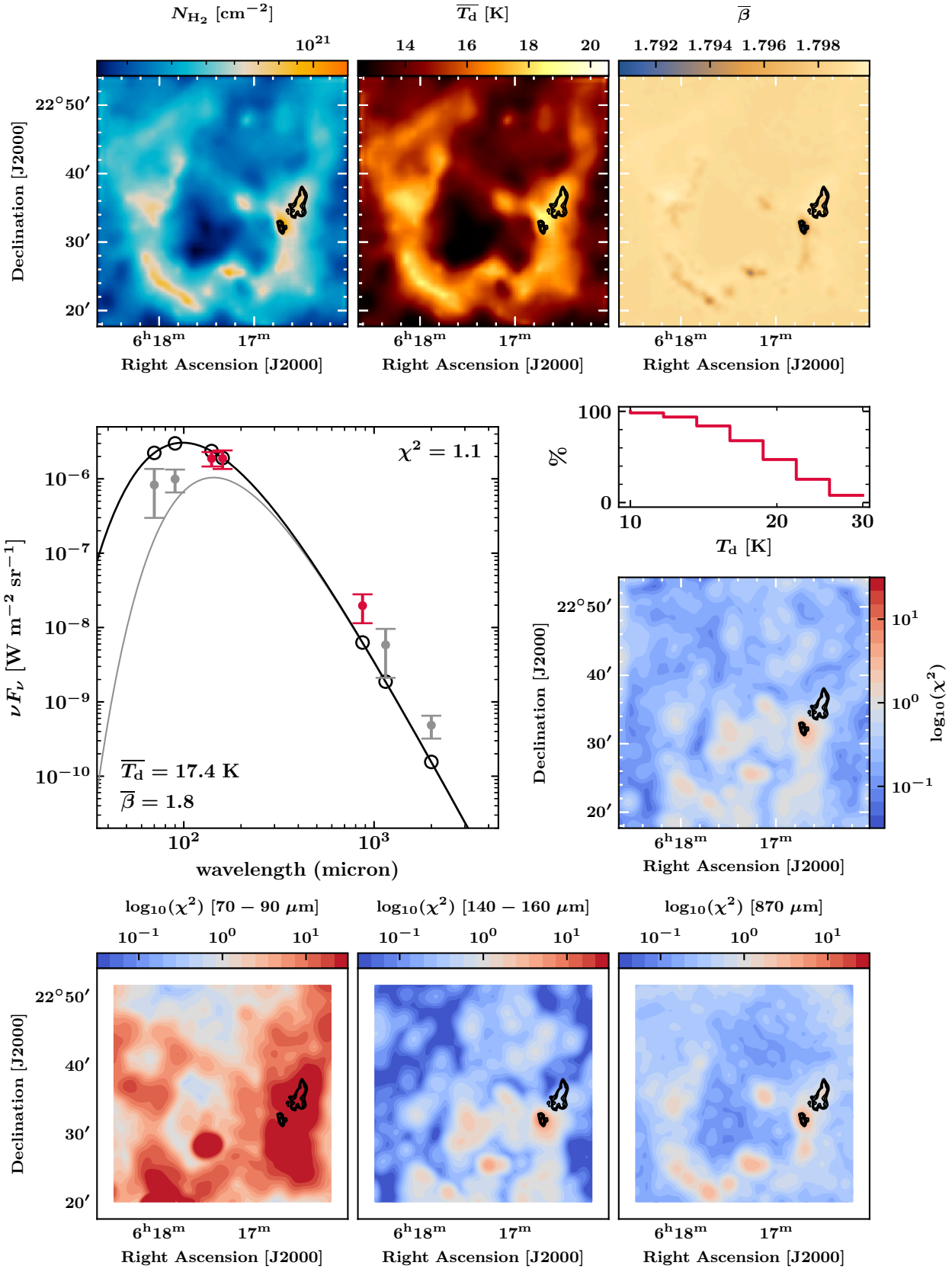

Figure B.8 Results of the run 'PPMAP-W1': analysis of the 140-870 µm data points with eight dust temperatures in the range $T_d = 10 - 30$ K, $\beta = \{1.7,\ 1.8,\ 1.9\}$, $\eta = 0.3$ and r.m.s weighting (see Tab. 9.9). See the first paragraph in section 9.2.2 for a detailed description of the figure.

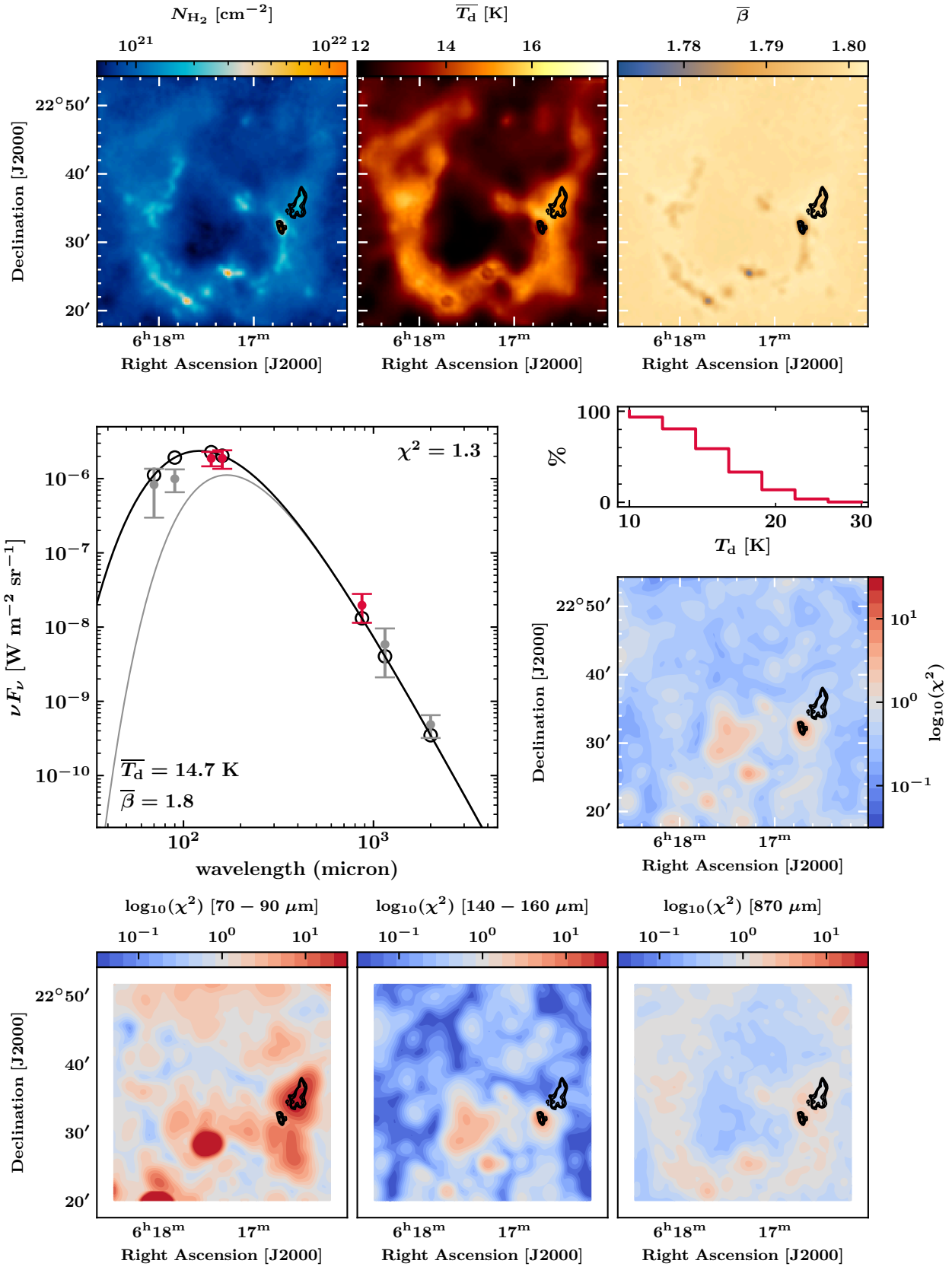

Figure B.9 Results of the run 'PPMAP-W2': analysis of the 140-870 µm data points with eight dust temperatures in the range $T_d = 10 - 30$ K, $\beta = \{1.7,\ 1.8,\ 1.9\}$, $\eta = 0.3$ and modified r.m.s weighting (see Tab. 9.9). See the first paragraph in section 9.2.2 for a detailed description of the figure.

Appendix C | Tables: YSO candidates

Table C.1 Infrared photometric magnitudes and spectral index of YSO candidates detected by WISE in the extended IC443G region.

ID	Catalog name	W1(3.4 μm) (mag)	W2(4.6 μm) (mag)	W3(12 μm) (mag)	W4(22 μm) (mag)	Fig. 10.1 (label)	α	FLAG
1	J061654.93+223403.6	17.132 ± 0.205	16.04 ± 0.25	11.906 ± 0.458	8.09	Class I	0.99	0
2	J061655.34+223353.3	16.925 ± 0.206	15.716 ± 0.225	11.828 ± 0.52	8.654 ± 0.508	Class I	0.86	0
3	J061653.26+223453.7	15.348 ± 0.053	13.717 ± 0.042	10.316 ± 0.085	8.234	Class I	0.71	0
4	J061656.75+223829.3	15.752 ± 0.068	14.049 ± 0.05	10.926 ± 0.142	8.257	Class I	0.53	0
5	J061617.53+223155.6	12.36 ± 0.025	11.021 ± 0.021	8.844 ± 0.03	5.952 ± 0.049	Class I	-0.41	0
6	J061656.48+223943.2	11.276 ± 0.029	10.733 ± 0.027	8.612 ± 0.036	6.027 ± 0.090	Class II	-0.9	0
7	J061642.63+223825.6	15.152 ± 0.048	14.492 ± 0.066	12.316 ± 0.489	8.392 ± 0.431	Class II	-0.79	0
8	J061617.19+223356.0	14.033 ± 0.031	13.089 ± 0.032	10.99 ± 0.197	7.944 ± 0.219	Class II	-0.69	0
9	J061654.18+223456.6	14.42 ± 0.034	13.622 ± 0.038	10.85 ± 0.132	8.582 ± 0.398	Class II	-0.24	0
10	J061653.02+223444.5	15.494 ± 0.056	14.695 ± 0.077	11.238 ± 0.244	8.687	Class I	0.29	0
11	J061639.55+223449.3	13.393 ± 0.042	12.444 ± 0.029	9.577 ± 0.371	6.398 ± 0.141	Class II	-0.09	0
12	J061642.43+223811.8	15.687 ± 0.077	14.321 ± 0.062	11.897 ± 0.407	8.415 ± 0.377	Class I	-0.2	0
13	J061654.60+223442.0	15.628 ± 0.056	14.91 ± 0.094	11.505 ± 0.258	8.369 ± 0.310	Class II	0.21	0
14	J061654.84+223500.4	15.476 ± 0.054	14.818 ± 0.08	11.6 ± 0.299	8.268	Class II	0.03	0
15	J061640.86+223753.0	15.845 ± 0.069	14.826 ± 0.082	11.77 ± 0.382	8.51 ± 0.493	Class I	0.1	0
16	J061638.20+223322.9	14.555 ± 0.049	12.846 ± 0.035	9.626 ± 0.113	7.84 ± 0.366	Class I	0.61	1
17	J061638.34+223313.0	14.453 ± 0.059	13.053 ± 0.035	9.533 ± 0.249	7.877 ± 0.323	Class I	0.68	1
18	J061643.64+223232.1	11.158 ± 0.028	9.394 ± 0.021	6.363 ± 0.015	6.11 ± 0.145	Class I	0.49	3
19	J061646.10+223246.9	13.34 ± 0.028	11.706 ± 0.023	8.424 ± 0.029	8.667	Class I	0.62	3
20	J061641.30+223044.8	15.073 ± 0.053	13.683 ± 0.044	9.385 ± 0.087	8.617	Class I	1.28	3
21	J061642.50+223142.4	11.168 ± 0.025	9.246 ± 0.021	6.51 ± 0.015	6.217 ± 0.090	Class I	0.35	3
22	J061634.95+223128.1	12.786 ± 0.036	10.981 ± 0.024	7.86 ± 0.027	6.443 ± 0.071	Class I	0.59	3
23	J061639.57+223219.9	13.203 ± 0.045	11.801 ± 0.037	8.653 ± 0.13	8.272	Class I	0.39	5
24	J061632.40+223012.2	14.098 ± 0.036	12.352 ± 0.028	8.965 ± 0.037	7.88 ± 0.305	Class I	0.76	1
25	J061642.44+223206.3	11.228 ± 0.028	9.299 ± 0.023	6.521 ± 0.018	6.171 ± 0.103	Class I	0.39	5
26	J061643.86+223340.7	12.358 ± 0.048	10.323 ± 0.027	7.473 ± 0.053	6.553	Class I	0.5	3
27	J061642.75+223108.9	13.4 ± 0.026	12.176 ± 0.026	8.98 ± 0.035	7.724 ± 0.211	Class I	0.32	3
28	J061641.63+223111.0	12.829 ± 0.027	11.003 ± 0.023	8.096 ± 0.029	7.607 ± 0.289	Class I	0.43	5
29	J061635.24+223521.1	14.723 ± 0.057	13.606 ± 0.042	9.478 ± 0.202	7.199 ± 0.156	Class I	1.0	1
30	J061639.81+223201.5	12.88 ± 0.031	10.896 ± 0.023	8.251 ± 0.083	8.371	Class I	0.31	3
31	J061633.23+223103.7	12.862 ± 0.027	11.146 ± 0.023	8.242 ± 0.043	6.932 ± 0.098	Class I	0.37	3

Table C.2 Infrared photometric magnitudes and spectral index of YSO candidates detected by WISE in the extended IC443G region (continued).

ID	Catalog name	W1(3.4 μm) (mag)	W2(4.6 μm) (mag)	W3(12 μm) (mag)	W4(22 μm) (mag)	Fig. 10.1 (label)	α	FLAG
32	J061635.54+223108.5	13.757 ± 0.03	12.12 ± 0.026	8.638 ± 0.039	7.456 ± 0.162	Class I	0.78	3
33	J061642.91+223215.9	11.159 ± 0.024	9.3 ± 0.02	6.33 ± 0.014	5.976 ± 0.084	Class I	0.5	3
34	J061639.38+223234.8	14.358 ± 0.046	13.055 ± 0.038	9.669 ± 0.23	7.606	Class I	0.52	3
35	J061640.86+223310.8	11.727 ± 0.023	10.662 ± 0.02	8.315 ± 0.036	7.473 ± 0.244	Class II	-0.43	5
36	J061647.39+223406.4	13.909 ± 0.03	13.397 ± 0.033	10.958 ± 0.212	7.292	Class II	-0.66	3
37	J061642.00+223339.7	10.74 ± 0.024	10.143 ± 0.02	8.244 ± 0.085	6.939 ± 0.193	Class II	-1.04	3
38	J061645.55+223335.1	12.046 ± 0.025	10.487 ± 0.021	8.433 ± 0.032	7.121	Class I	-0.39	5
39	J061635.51+223239.1	14.932 ± 0.044	13.438 ± 0.035	11.349 ± 0.366	8.485	Class I	-0.4	3
40	J061644.88+223352.6	12.305 ± 0.039	10.132 ± 0.02	7.963 ± 0.031	7.454 ± 0.442	Class I	0.04	3
41	J061642.28+223241.6	11.956 ± 0.034	10.024 ± 0.023	7.769 ± 0.105	6.777 ± 0.128	Class I	-0.02	3
42	J061643.22+223302.2	11.709 ± 0.027	9.96 ± 0.021	7.198 ± 0.018	6.666 ± 0.254	Class I	0.27	3
43	J061647.94+223431.0	13.987 ± 0.032	12.795 ± 0.028	9.7 ± 0.078	7.89	Class I	0.23	3
44	J061640.55+223121.5	12.291 ± 0.025	10.557 ± 0.023	7.939 ± 0.026	7.795 ± 0.259	Class I	0.15	5
45	J061630.48+223009.3	14.817 ± 0.041	13.375 ± 0.042	10.875 ± 0.17	8.639	Class I	-0.1	1
46	J061643.19+223038.8	15.019 ± 0.043	13.721 ± 0.04	11.043 ± 0.184	8.752	Class I	-0.04	1
47	J061650.62+223515.5	13.783 ± 0.032	11.77 ± 0.024	9.615 ± 0.062	8.559 ± 0.490	Class I	-0.06	1
48	J061641.59+223132.8	11.874 ± 0.029	10.064 ± 0.023	7.515 ± 0.022	6.815 ± 0.146	Class I	0.14	3
49	J061640.18+223149.4	12.626 ± 0.031	10.845 ± 0.029	8.508 ± 0.088	7.898	Class I	-0.04	5
50	J061639.32+223320.1	14.693 ± 0.061	12.991 ± 0.035	10.655 ± 0.284	7.322 ± 0.192	Class I	-0.09	1
51	J061636.38+223308.9	13.925 ± 0.038	12.355 ± 0.027	10.027 ± 0.396	7.67	Class I	-0.17	1
52	J061642.01+223418.9	14.356 ± 0.057	12.241 ± 0.026	9.799 ± 0.462	7.823 ± 0.482	Class I	0.23	3
53	J061639.74+223041.6	14.382 ± 0.036	12.701 ± 0.034	9.991 ± 0.347	8.641	Class I	0.2	1
54	J061646.36+223424.7	12.69 ± 0.027	11.661 ± 0.024	8.949 ± 0.045	7.379 ± 0.251	Class II	-0.16	3
55	J061645.01+223259.5	11.93 ± 0.024	10.383 ± 0.02	7.495 ± 0.019	7.311 ± 0.138	Class I	0.26	3
56	J061643.87+223250.1	11.07 ± 0.024	9.276 ± 0.02	6.732 ± 0.016	6.358 ± 0.194	Class I	0.13	5
57	J061635.06+223135.9	12.134 ± 0.026	10.475 ± 0.023	7.958 ± 0.025	6.41 ± 0.073	Class I	0.03	3
58	J061647.01+223500.8	14.047 ± 0.035	11.907 ± 0.024	9.892 ± 0.103	7.989	Class I	-0.1	3
59	J061644.84+223442.6	12.885 ± 0.029	11.157 ± 0.026	8.788 ± 0.035	7.539 ± 0.240	Class I	-0.05	3
60	J061641.36+223012.4	13.6 ± 0.037	11.791 ± 0.027	9.673 ± 0.122	7.951	Class I	-0.2	3
61	J061643.18+223129.7	12.525 ± 0.022	11.347 ± 0.023	8.34 ± 0.024	6.933 ± 0.111	Class I	0.15	3
62	J061650.94+223454.3	14.969 ± 0.049	12.959 ± 0.032	10.635 ± 0.144	8.476	Class I	0.07	1
63	J061644.45+223331.1	12.396 ± 0.035	10.456 ± 0.022	7.952 ± 0.027	7.341	Class I	0.18	3
64	J061633.49+223110.4	12.208 ± 0.024	11.279 ± 0.027	8.486 ± 0.039	7.219 ± 0.144	Class II	-0.16	3
65	J061642.76+223402.6	12.266 ± 0.028	10.421 ± 0.021	7.897 ± 0.071	7.022 ± 0.162	Class I	0.14	3

Table C.3 Infrared photometric magnitudes of YSO candidates detected by 2MASS in the extended IC443G region.

ID	r.a. (J2000)	dec. (J2000)	J(1.25 μm) (mag)	H(1.65 μm) (mag)	K(2.17 μm) (mag)	Fig. 10.1 (label)	FLAG
1	$6^h16^m21.16^s$	$22^d37^m25.37^s$	16.073 ± 0.078	15.449 ± 0.108	14.932 ± 0.093	YSO	0
2	$6^h16^m21.35^s$	$22^d34^m32.27^s$	15.3 ± 0.048	14.92 ± 0.087	14.708 ± 0.075	YSO	0
3	$6^h16^m32.01^s$	$22^d33^m59.85^s$	16.83 ± 0.140	15.981 ± 0.182	15.234 ± 0.120	YSO	0
4	$6^h16^m23.77^s$	$22^d34^m59.89^s$	15.138 ± 0.055	14.519 ± 0.064	14.094 ± 0.046	YSO	0
5	$6^h16^m19.73^s$	$22^d36^m17.92^s$	15.439 ± 0.074	14.997 ± 0.094	14.576 ± 0.070	YSO	0
6	$6^h16^m21.42^s$	$22^d31^m33.23^s$	15.4 ± 0.052	14.815 ± 0.069	14.347 ± 0.067	YSO	0
7	$6^h16^m20.25^s$	$22^d31^m39.30^s$	16.75 ± 0.150	16.051 ± 0.192	15.478 ± 0.136	YSO	0
8	$6^h16^m54.05^s$	$22^d30^m37.07^s$	16.742 ± 0.165	16.013 ± 0.188	15.451 ± 0.145	YSO	0
9	$6^h16^m39.00^s$	$22^d30^m00.26^s$	16.22 ± 0.109	15.587 ± 0.144	15.226 ± 0.123	YSO	0
10	$6^h16^m41.73^s$	$22^d30^m21.36^s$	15.163 ± 0.049	14.663 ± 0.067	14.226 ± 0.054	YSO	0
11	$6^h16^m45.23^s$	$22^d31^m03.71^s$	16.753 ± 0.170	16.174 ± 0.222	15.604 ± 0.168	YSO	0
12	$6^h16^m37.41^s$	$22^d30^m45.04^s$	16.45 ± 0.120	16.011 ± 0.188	15.756 ± 0.189	YSO	0
13	$6^h16^m28.65^s$	$22^d30^m29.60^s$	15.273 ± 0.061	14.65 ± 0.090	14.086 ± 0.059	YSO	0
14	$6^h16^m25.18^s$	$22^d31^m48.32^s$	13.487 ± 0.027	13.011 ± 0.038	12.658 ± 0.025	YSO	0
15	$6^h16^m25.96^s$	$22^d30^m57.38^s$	15.913 ± 0.072	15.315 ± 0.105	14.878 ± 0.107	YSO	0
16	$6^h16^m26.89^s$	$22^d31^m46.11^s$	15.278 ± 0.044	14.761 ± 0.075	14.47 ± 0.068	YSO	0
17	$6^h16^m37.10^s$	$22^d31^m17.74^s$	16.608 ± 0.148	15.972 ± 0.194	15.335 ± 0.134	YSO	0
18	$6^h16^m18.27^s$	$22^d38^m49.88^s$	14.252 ± 0.034	13.7 ± 0.034	13.392 ± 0.030	YSO	0
19	$6^h16^m17.72^s$	$22^d38^m57.65^s$	16.62 ± 0.132	16.029 ± 0.190	15.464 ± 0.145	YSO	0
20	$6^h16^m27.76^s$	$22^d39^m04.81^s$	16.348 ± 0.106	15.627 ± 0.162	15.161 ± 0.121	YSO	0
21	$6^h16^m39.20^s$	$22^d36^m57.77^s$	17.06 ± 0.183	16.282 ± 0.235	15.662 ± 0.170	YSO	0
22	$6^h16^m38.84^s$	$22^d37^m50.51^s$	13.85 ± 0.027	13.508 ± 0.039	13.307 ± 0.031	YSO	0
23	$6^h16^m34.85^s$	$22^d37^m45.31^s$	13.714 ± 0.031	13.268 ± 0.038	12.954 ± 0.027	YSO	0
24	$6^h16^m32.52^s$	$22^d38^m19.35^s$	14.745 ± 0.036	14.165 ± 0.055	13.813 ± 0.039	YSO	0
25	$6^h16^m30.79^s$	$22^d38^m27.47^s$	14.896 ± 0.036	14.202 ± 0.034	13.762 ± 0.039	YSO	0
26	$6^h16^m30.19^s$	$22^d38^m29.64^s$	15.996 ± 0.079	15.408 ± 0.114	14.843 ± 0.087	YSO	0
27	$6^h16^m33.70^s$	$22^d37^m27.99^s$	14.368 ± 0.032	13.821 ± 0.047	13.487 ± 0.031	YSO	0
28	$6^h16^m33.83^s$	$22^d38^m06.52^s$	15.865 ± 0.072	15.212 ± 0.087	14.83 ± 0.078	YSO	0
29	$6^h16^m56.77^s$	$22^d30^m15.22^s$	15.112 ± 0.042	14.755 ± 0.070	14.461 ± 0.060	YSO	0
30	$6^h16^m53.13^s$	$22^d31^m03.76^s$	15.879 ± 0.082	15.605 ± 0.149	15.273 ± 0.131	YSO	0
31	$6^h16^m57.99^s$	$22^d33^m04.98^s$	14.739 ± 0.037	14.366 ± 0.057	14.057 ± 0.048	YSO	0
32	$6^h16^m48.47^s$	$22^d31^m57.35^s$	11.835 ± 0.023	11.741 ± 0.030	11.69 ± 0.023	YSO	0
33	$6^h16^m49.15^s$	$22^d33^m37.91^s$	16.26 ± 0.100	15.794 ± 0.152	15.355 ± 0.129	YSO	0
34	$6^h16^m51.04^s$	$22^d33^m16.69^s$	16.806 ± 0.178	16.093 ± 0.223	15.637 ± 0.169	YSO	0
35	$6^h16^m52.65^s$	$22^d32^m10.02^s$	15.536 ± 0.056	14.916 ± 0.077	14.473 ± 0.063	YSO	0
36	$6^h16^m56.50^s$	$22^d39^m43.29^s$	14.008 ± 0.038	13.187 ± 0.041	12.502 ± 0.028	YSO	0
37	$6^h16^m49.04^s$	$22^d39^m47.80^s$	14.418 ± 0.033	14.196 ± 0.048	13.853 ± 0.044	YSO	0
38	$6^h16^m49.76^s$	$22^d39^m12.79^s$	15.869 ± 0.078	15.481 ± 0.123	15.182 ± 0.117	YSO	0
39	$6^h16^m58.80^s$	$22^d35^m58.44^s$	11.262 ± 0.022	10.979 ± 0.030	10.796 ± 0.021	YSO	0
40	$6^h16^m52.79^s$	$22^d39^m39.43^s$	16.178 ± 0.103	16.14 ± 0.228	15.496 ± 0.164	YSO	0
41	$6^h16^m51.69^s$	$22^d35^m37.42^s$	15.277 ± 0.052	14.827 ± 0.074	14.372 ± 0.081	YSO	0
42	$6^h16^m40.28^s$	$22^d38^m17.54^s$	15.355 ± 0.056	14.797 ± 0.082	14.487 ± 0.068	YSO	0

Table C.4 Infrared photometric magnitudes of YSO candidates detected by 2MASS in the extended IC443G region (continued).

ID	r.a. (J2000)	dec. (J2000)	J(1.25 μm) (mag)	H(1.65 μm) (mag)	K(2.17 μm) (mag)	Fig. 10.1 (label)	FLAG
43	$6^h16^m41.82^s$	$22^d37^m30.09^s$	16.673 ± 0.158	16.052 ± 0.215	15.654 ± 0.167	YSO	0
44	$6^h16^m44.95^s$	$22^d35^m49.96^s$	15.919 ± 0.081	15.28 ± 0.100	14.832 ± 0.086	YSO	0
45	$6^h16^m50.66^s$	$22^d37^m20.93^s$	14.637 ± 0.040	14.328 ± 0.057	14.092 ± 0.055	YSO	0
46	$6^h16^m18.14^s$	$22^d38^m18.74^s$	16.236 ± 0.102	15.326 ± 0.118	14.713 ± 0.069	CTTS	0
47	$6^h16^m20.71^s$	$22^d36^m44.49^s$	16.83 ± 0.163	16.054 ± 0.190	15.544 ± 0.151	CTTS	0
48	$6^h16^m31.07^s$	$22^d35^m20.79^s$	17.069 ± 0.203	15.948 ± 0.175	15.21 ± 0.128	CTTS	0
49	$6^h16^m28.25^s$	$22^d33^m54.94^s$	15.992 ± 0.094	15.117 ± 0.090	14.573 ± 0.072	CTTS	0
50	$6^h16^m32.20^s$	$22^d34^m52.98^s$	17.311 ± 0.228	15.919 ± 0.169	15.075 ± 0.112	CTTS	0
51	$6^h16^m25.32^s$	$22^d35^m29.40^s$	16.402 ± 0.098	15.57 ± 0.136	14.91 ± 0.093	CTTS	0
52	$6^h16^m41.39^s$	$22^d32^m57.89^s$	16.827 ± 0.180	15.657 ± 0.153	14.944 ± 0.111	CTTS	0
53	$6^h16^m28.97^s$	$22^d32^m39.40^s$	15.688 ± 0.056	14.903 ± 0.064	14.459 ± 0.064	CTTS	0
54	$6^h16^m25.67^s$	$22^d39^m06.09^s$	17.201 ± 0.219	16.343 ± 0.262	15.773 ± 0.198	CTTS	0
55	$6^h16^m34.49^s$	$22^d35^m22.21^s$	16.21 ± 0.084	15.149 ± 0.084	14.537 ± 0.063	CTTS	0
56	$6^h16^m30.92^s$	$22^d36^m01.72^s$	16.564 ± 0.128	15.298 ± 0.110	14.436 ± 0.062	CTTS	0
57	$6^h16^m30.75^s$	$22^d39^m28.69^s$	16.132 ± 0.079	15.328 ± 0.099	14.737 ± 0.077	CTTS	0
58	$6^h16^m32.27^s$	$22^d39^m32.10^s$	16.987 ± 0.166	15.842 ± 0.152	15.084 ± 0.107	CTTS	0
59	$6^h16^m50.15^s$	$22^d33^m04.16^s$	16.416 ± 0.122	15.609 ± 0.138	15.122 ± 0.105	CTTS	0
60	$6^h16^m49.96^s$	$22^d38^m43.88^s$	16.521 ± 0.136	15.645 ± 0.143	15.08 ± 0.113	CTTS	0
61	$6^h16^m54.18^s$	$22^d34^m56.75^s$	16.184 ± 0.098	15.279 ± 0.107	14.72 ± 0.076	CTTS	0
62	$6^h16^m48.71^s$	$22^d36^m02.72^s$	16.682 ± 0.152	15.854 ± 0.171	15.249 ± 0.126	CTTS	0
63	$6^h16^m20.50^s$	$22^d37^m06.78^s$	15.847 ± 0.074	15.298 ± 0.102	14.635 ± 0.083	HAeBe	0
64	$6^h16^m20.35^s$	$22^d35^m04.23^s$	15.896 ± 0.073	15.477 ± 0.110	14.917 ± 0.100	HAeBe	0
65	$6^h16^m37.47^s$	$22^d30^m53.17^s$	16.922 ± 0.187	16.207 ± 0.243	15.484 ± 0.150	HAeBe	0
66	$6^h16^m25.69^s$	$22^d38^m08.44^s$	16.448 ± 0.140	15.86 ± 0.161	15.218 ± 0.132	HAeBe	0
67	$6^h16^m31.69^s$	$22^d38^m17.72^s$	16.433 ± 0.108	16.133 ± 0.215	15.392 ± 0.138	HAeBe	0
68	$6^h16^m57.74^s$	$22^d30^m24.12^s$	16.068 ± 0.092	15.669 ± 0.144	15.076 ± 0.101	HAeBe	0
69	$6^h16^m57.50^s$	$22^d34^m34.24^s$	16.757 ± 0.159	16.112 ± 0.217	15.46 ± 0.157	HAeBe	0
70	$6^h16^m43.12^s$	$22^d33^m01.40^s$	14.73 ± 0.042	14.126 ± 0.053	13.625 ± 0.086	YSO	2
71	$6^h16^m35.10^s$	$22^d31^m33.98^s$	15.086 ± 0.048	14.306 ± 0.051	13.628 ± 0.056	YSO	2
72	$6^h16^m44.82^s$	$22^d34^m42.82^s$	15.207 ± 0.049	14.728 ± 0.067	14.395 ± 0.061	YSO	2
73	$6^h16^m40.21^s$	$22^d31^m15.34^s$	16.192 ± 0.104	15.358 ± 0.119	14.831 ± 0.119	CTTS	2
74	$6^h16^m41.46^s$	$22^d31^m28.03^s$	15.451 ± 0.061	14.421 ± 0.058	13.757 ± 0.061	CTTS	2
75	$6^h16^m43.47^s$	$22^d31^m55.73^s$	16.435 ± 0.121	15.65 ± 0.139	15.131 ± 0.135	CTTS	2
76	$6^h16^m44.87^s$	$22^d34^m10.32^s$	14.743 ± 0.046	14.039 ± 0.057	13.62 ± 0.072	CTTS	1
77	$6^h16^m45.52^s$	$22^d33^m42.53^s$	16.511 ± 0.132	15.626 ± 0.144	15.116 ± 0.162	CTTS	2
78	$6^h16^m45.50^s$	$22^d34^m58.63^s$	16.432 ± 0.130	15.51 ± 0.140	14.975 ± 0.135	CTTS	1
79	$6^h16^m43.49^s$	$22^d33^m37.44^s$	16.867 ± 0.189	15.85 ± 0.178	14.899 ± 0.148	HAeBe	2

Appendix D | Northern Extended Millimeter Array observations of the IC443 'G' clump

In Chapter 10, we used the 2MASS and WISE all-sky surveys to identify a sample of YSO candidates in the IC443 SNR, based on their SED and infrared excess in the near/mid-infrared range. The certainty of our results is limited by several issues: *i.)* contamination by bright H_2 rovibrational lines from molecular shocks, *ii.)* contamination by extended emission. In addition, we cannot detect Class 0 protostars with IR observations, since they are only detectable in the submillimeter/millimeter range (see Fig. 1.23). In order to tackle these issues, we performed millimeter interferometric observations. These new observations are paramount to study the star-forming conditions in the extended G region:

- High-resolution observations ($\sim$ 1″) would allow to disentangle the contribution of the large-scale shock structures from individual outflows.
- Millimeter observations of the region could allow to eventually confirm our identifications of YSO candidates, to detect Class 0 protostars, prestellar cores and to evaluate their evolutionary stage. If we map a large enough field of observations with sufficient sensitivity, we could also build a statistically significant CMF.

Proposed observations We submitted several ALMA and NOEMA proposals since 2018 (ALMA Cycle 7, IRAM S18, S19, S20). We proposed to perform continuum and spectral-line mapping of the 'ring-like structure' (see Fig. 6.13, section 6.2.1) with ALMA at 1.3 mm and 3 mm, at an angular resolution $\sim$ 0.2″. We also proposed to perform continuum and spectral-line mapping of the ring-like structure and shocked clump 'G' (see Fig. 6.13, section 6.2.1) with NOEMA at 1.3 mm and 3 mm, with a requested angular resolution $\sim$ 1″ (1000-1500 AU at 2 kpc). *Results of the proposal committee:* our ALMA proposal was declined, and our NOEMA proposal was ranked 'B' multiple times. The NOEMA observations that we requested were partially performed between 2019 and 2020:

1. The ring-like structure was mapped at 3 mm only, in February-march 2019.
2. The shocked clump 'G' was also mapped at 3 mm only, in March-April 2020.

D.1 | Observations

D.1.1 Interferometric observations

Mapping strategy We requested the spectral-line and continuum mapping of $2' \times 2'$ fields of observation towards the shocked clump 'G' and ring-like structure. This represents two mosaics of 46 individual fields.

Spectral setup We optimized our spectral windows to include SiO, DCO^+, $C^{18}O$, ^{13}CO, ^{12}CO, CS at 1.3 mm, and CH_3OH, ^{13}CS, SiO, SO_2, HNC, HCO^+, SO at 3 mm. *Reminder:* only our 3 mm setup was observed at the moment.

Data reduction with CLIC and MAPPING We used the IRAM data reduction modules `CLIC` and `MAPPING` offered by the `GILDAS` package (Guilloteau and Lucas, 2000). The reduction included the following steps:

1. Run the pipeline on `.IPB` files (*e.g.* `clic -nw @pipeline w18af002 19-feb-2019`). The pipeline produces `.hpb` files (which contains the list of visibilities and calibrations), in addition to meteo and calibration reports. We found that there are amplitude calibration drops due to atmospheric effects in the observations done on February the 28th, 2019. We manually flagged the drops to ignore these calibrations in the rest of the reduction.

2. Produce UV tables with `CLIC` (in mosaic mode). This step is repeated for each `.hpb` file, and for each line of interest.

3. Open UV tables with `MAPPING` to build the hyperspectral cubes. We produced a cube for each line of interest, and the continuum maps. To produce the continuum map, we removed all strong lines from the data.

4. Clean the hyperspectral cubes. We used the hogbom algorithm to clean the maps (Högbom 1974, Clark 1980). We optimized the number of iteration `niter` based on the accumulated flux of the final cleaned maps.

D.1.2 Short-spacings

We requested short-spacing with the IRAM 30m telescope. We performed spectral-line maps of HCO^+, HCN, HNC, HCS^+, SiO, $H^{13}CO^+$, C_2H and C_3H_2O. We did not include short-spacing observations into our reduction of NOEMA data yet, since we were primarily interested in the detection of the smallest possible structures both in the continuum (possible protostars) and line (possible protostellar jets/outflows *vs.* SNR shock) observations.

D.2 | Preliminary results

Since our NOEMA proposals were ranked 'B', we have obtained preliminary observations with reduced observing time ($\sim$ 7.1 hours). Therefore, we have unfinished mosaics with low signal-to-noise ratios. In the following paragraphs, we present some preliminary results towards the shocked clump.

PPV cubes We obtained hyperspectral (PPV) cubes of several spectral lines (most importantly: HCO^+, SiO, N_2H^+). In Fig. D.1, we show the velocity-integrated intensity maps of the lines detected with the highest signal-to-noise ratios. The maps shown in Fig. D.1 show that there is absorption (negative flux values) in the `MAPPING` outputs. We also show a comparison between HCO^+ and near-IR continuum emission (*Spitzer*/IRAC at 8 μm) in Fig. D.4. We might need to improve the cleaning step with more iterations or a different algorithm.

Continuum maps We manually removed the velocity channels characterized by line emission and produced maps based on the lower and upper sidebands (respectively LSB, USB). We show the results in Fig. D.5. There are no 3σ detections. A few point sources can be distinguished from the background on the left-panel (LSB), although they are not reproduced in the USB. Hence, they could correspond to faint spectral lines that were not manually removed from the LSB. These "point sources" can also be produced by noise (see Fig. D.6). We might require additional observing time to confirm these detections.

Possible outflows? We produced maps of the high-velocity signal to try to identify outflows in the field of observations (see Fig. D.3). We represent the 'blue-shifted' and 'red-shifted' signal with respect to the systemic velocity of the shocked clump, $v_{\rm LSR} = -4.5$ km s^{-1}. There are no obvious signatures of bipolar outflows, although it is difficult to disentangle the emission of the large-scale shocked gas from possible outflows.

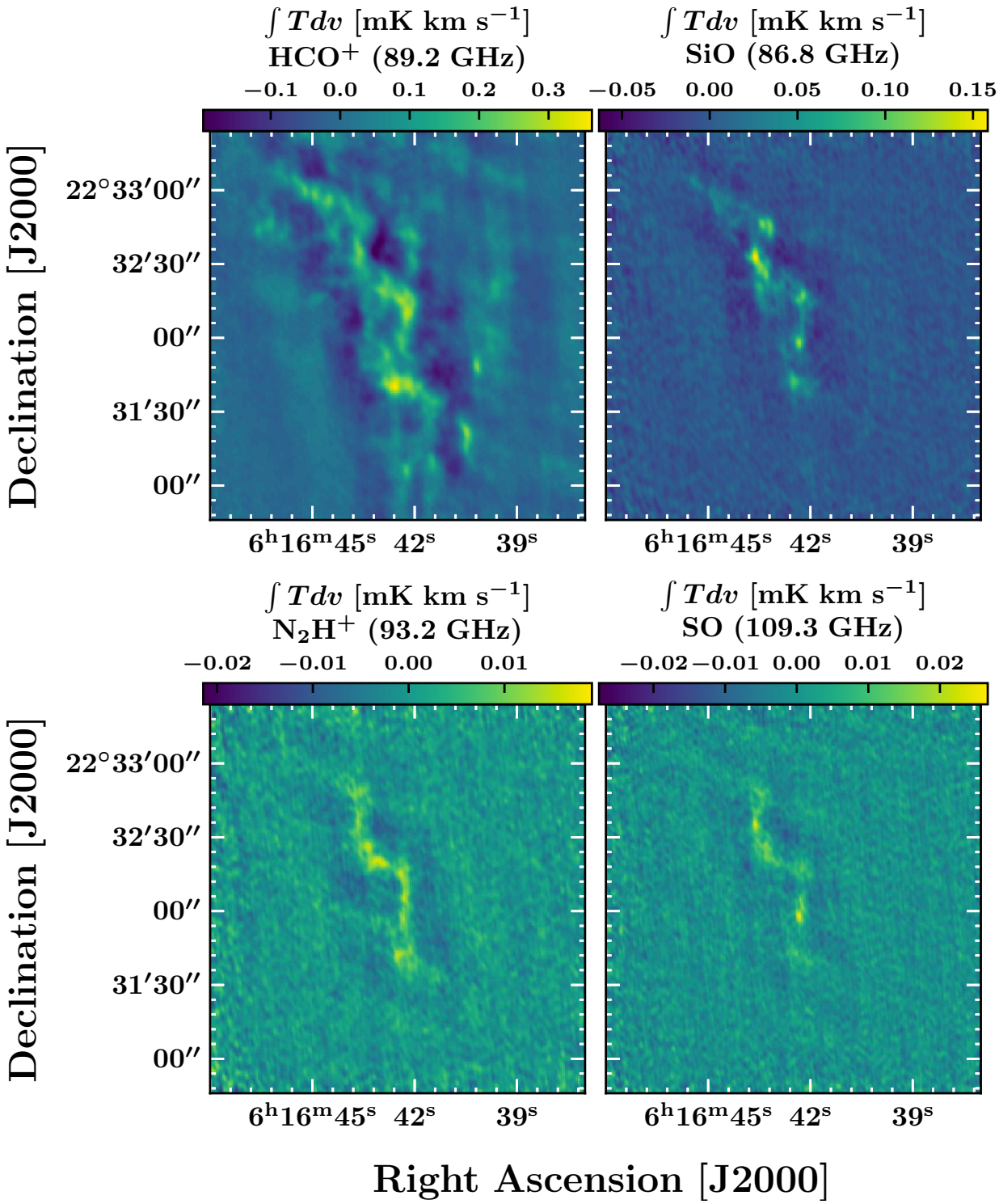

Figure D.1 NOEMA HCO$^+$, SiO, N_2H^+ and SO spectral-line maps (velocity-integrated temperature brightness $\int Tdv$, between -40 km s^{-1} and +30 km s^{-1}).

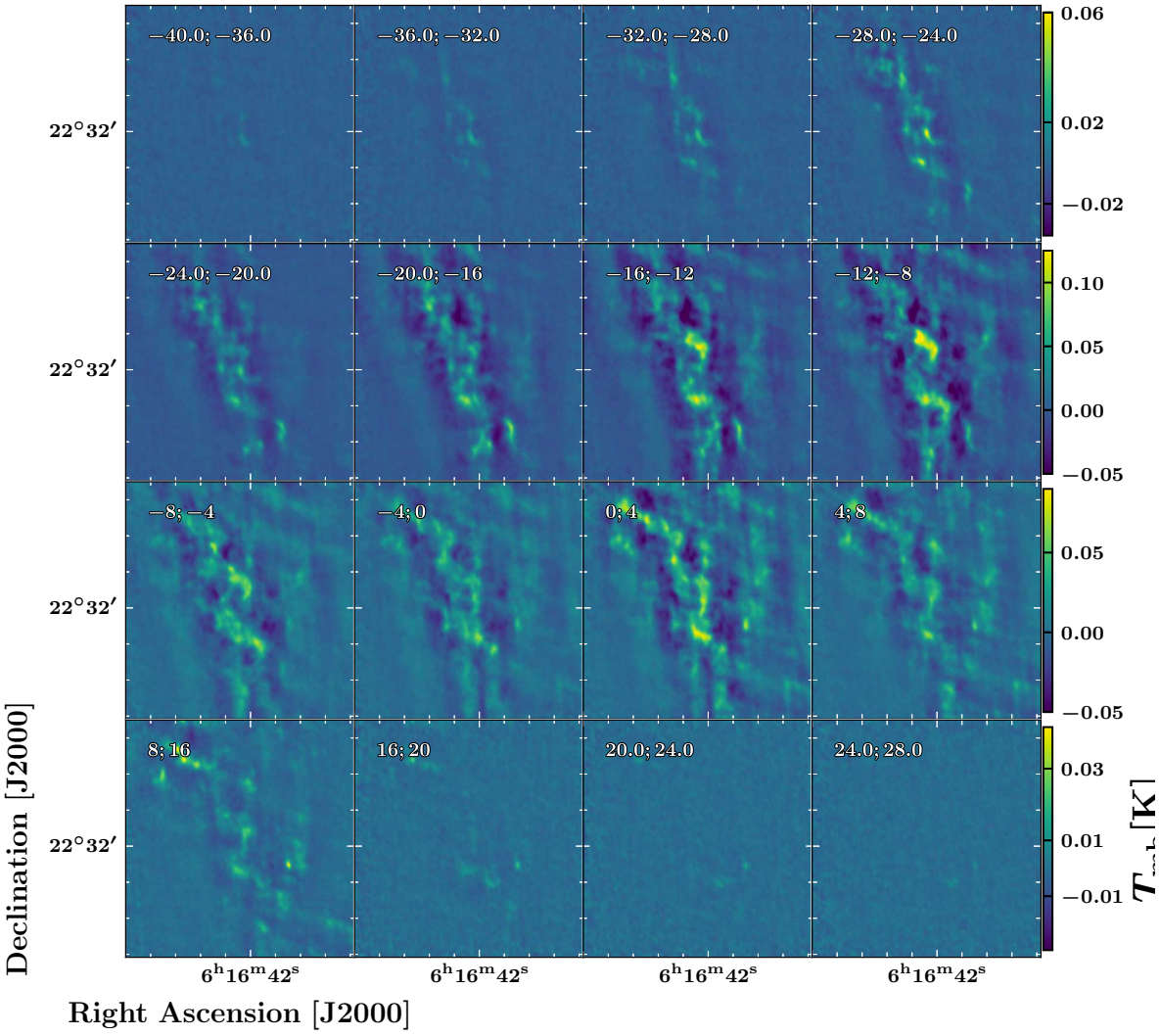

Figure D.2 Channel map of our HCO^+ PPV cube obtained with NOEMA observations. Each panel represents the velocity-integrated emission in the same area, between −40 km s^{-1} and 28 km s^{-1}. The boundaries of the velocity intervals (in km s^{-1}) are indicated on the top left corner of each panel.

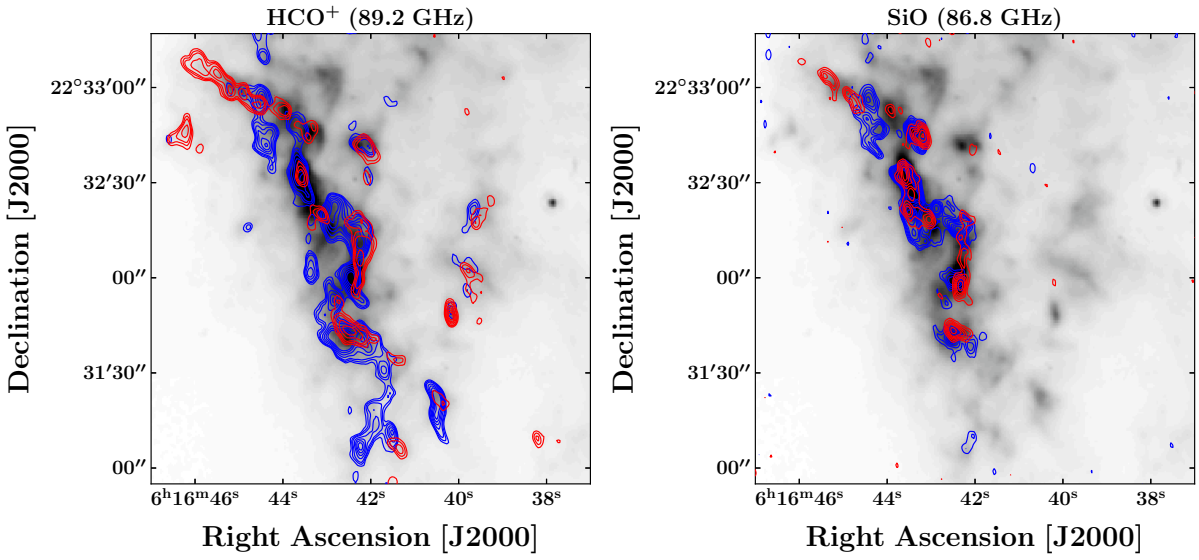

Figure D.3 NOEMA HCO^+ (left) and SiO (right) emission maps. *Blue contours*: $\int T dv$ between -40 km s^{-1} and -9.5 km s^{-1}). *Red contours*: $\int T dv$ between 0.5 km s^{-1} and +30 km s^{-1}). *Background: Spitzer*/IRAC 8 μm map.

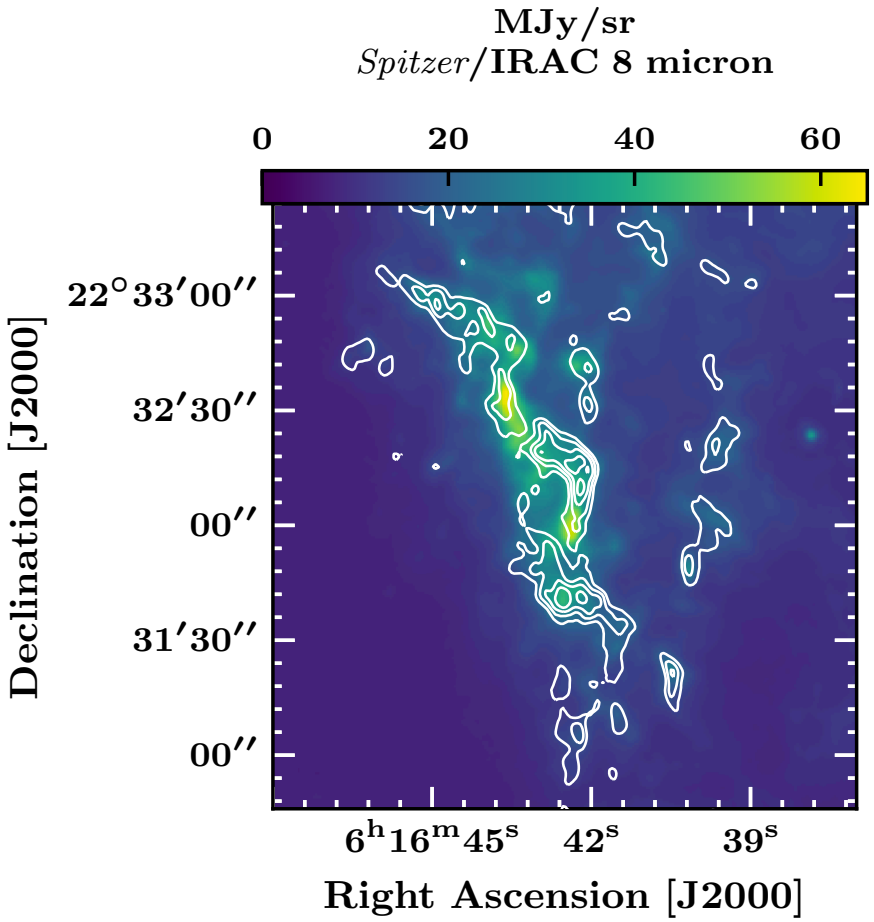

Figure D.4 *Background*: *Spitzer*/IRAC map at 8 µm. *White contours:* NOEMA HCO^+ spectral-line map (velocity-integrated temperature brightness $\int T dv$, between -40 km s^{-1} and +30 km s^{-1}).

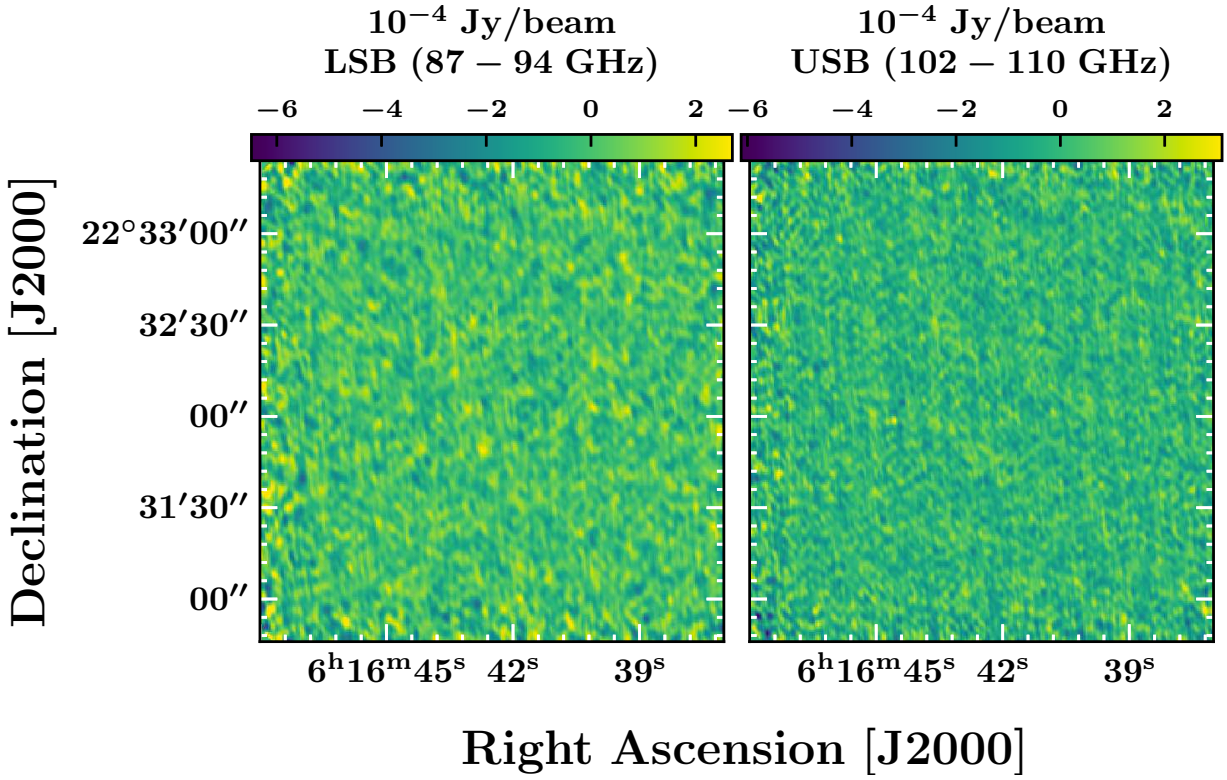

Figure D.5 NOEMA continuum maps extracted from the LSB (left-panel) and USB (right-panel) bands after spectral-line removal.

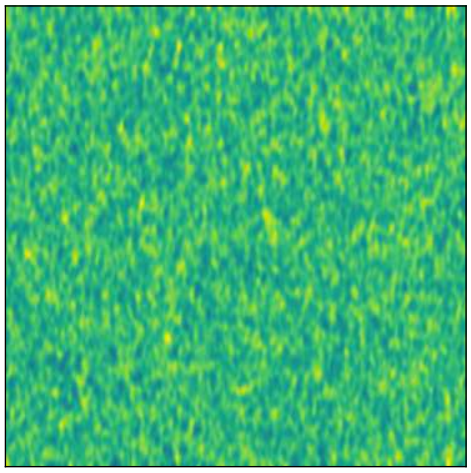

Figure D.6 Synthetic gaussian 2D noise produced with `Python`. We convolved the noise map with an asymetric $1'' \times 2''$ gaussian kernel to mimic the NOEMA beam.

RÉSUMÉ

Les supernovae ont un impact majeur sur l'évolution du milieu interstellaire des galaxies. Ces explosions stellaires injectent 10^{51} erg dans leur voisinage direct, soit l'équivalent de l'énergie émise par le Soleil durant toute son existence. Ces événements réguliers à l'échelle d'une galaxie (environ deux par siècles dans la Voie Lactée) produisent une onde de choc rapide (jusqu'à 10^4 km s^{-1}) qui interagit avec le milieu ambiant durant plusieurs centaines de millier d'années. En plus d'être temporairement le siège de l'accélération de rayons cosmiques de haute énergie (TeV−PeV), les restes de supernovae déposent de l'énergie cinétique sur plusieurs dizaines de parsecs avant de se dissiper entièrement sous forme de rayonnement et de turbulence. Cette injection d'énergie et de rayons cosmiques participe à la régulation de la turbulence, à l'enrichissement chimique et à la structuration des multiples phases du milieu interstellaire. De plus, après refroidissement des régions denses comprimées par les chocs plus lents (10^1 km s^{-1}) qui se propagent tardivement, la formation de nouvelles étoiles peut être déclenchée. Situé à 1.8 kpc et âgé d'environ 25,000 ans, le reste de supernova IC443 offre la possibilité d'étudier ces mécanismes de rétro-action avec précision. L'étude des rayons cosmiques est poursuivie à travers le produit de leur interaction avec le milieu interstellaire, source de photons de haute énergie (rayons X/γ) émis *via* quatre mécanismes : décomposition de pions neutres, Bremsstrahlung, effet Compton inverse et rayonnement synchrotron. L'interprétation des observations de rayons γ requiert une connaissance fine des caractéristiques physiques et chimiques de l'environnement, tel que la masse totale du gaz, l'intensité et la distribution en énergie du champ de rayonnement, et la présence de sources d'injection de nouveaux rayons cosmiques. En direction du pic d'intensité des rayons γ, nous avons réalisé de nouvelles observations du reste de supernova IC443 avec le télescope de 30m de l'IRAM ainsi que le télescope APEX. Dans un champ $10' \times 10'$, nos observations spectrales de ^{12}CO, ^{13}CO, C^{18}O et nos observations continuum avec la caméra NIKA2 révèlent le contenu interstellaire de la région avec une résolution angulaire de $10'' - 20''$. À l'aide de modèles de transfert de rayonnement, nous avons d'abord produit des cartes de la masse totale de gaz dans la région à partir de l'émission de ^{12}CO et ^{13}CO. Nous avons ensuite utilisé des modèles d'émission de poussière pour étudier le continuum entre 3.4 μm et 2.0 mm (WISE, Spitzer, LABOCA, NIKA2). L'utilisation des algorithmes Bayésiens PPMAP et HerBIE permet de déterminer la densité de colonne et la température des poussières, ainsi que plusieurs paramètres supplémentaires avec HerBIE. Nos mesures de masses *via* l'émission des poussières et *via* la molécule ^{12}CO sont indépendantes et en accord. Ces mesures indiquent l'existence de deux candidats pour l'interaction du milieu dense avec les rayons cosmiques à l'origine de la production de rayons γ: un amas de gaz choqué de masse ~ 250 M$_\odot$, et un amas de gaz froid et non perturbé de masse ~ 400 M$_\odot$. D'une part, ces cartes de masse posent des contraintes précises sur l'émission de rayons γ *via* la décomposition de pions neutres et le Bremsstrahlung dans la région étudiée. D'autre part, notre carte du champ de rayonnement déterminée *via* HerBIE nous permet aussi de poser une contrainte sur l'effet Compton inverse. Enfin, à l'aide de catalogues de sources ponctuelles nous avons déterminé l'existence de potentielles protoétoiles dans la région. Ces dernières peuvent également participer à l'injection de rayons cosmiques de moyennes énergies (MeV−GeV). Ces résultats pourront être ré-investis en tant que paramètres d'entrée dans un modèle d'émission de rayons γ afin de déterminer la composition (hadronique ou leptonique) et les mécanismes principaux d'interaction des rayons cosmiques avec le milieu interstellaire dans IC443.

MOTS CLÉS

Milieu interstellaire, *Restes de supernova*, *Cinématique et dynamique*, *Chocs*, *Formation des étoiles*, *Rayons cosmiques*

ABSTRACT

Supernovae have a major impact on the evolution of the interstellar medium of galaxies. These stellar explosions inject 10^{51} erg into their neighborhood, which is equivalent to the energy emitted by the Sun during its entire existence. These regular events at the scale of a galaxy (about two per century in the Milky Way) produce a fast shock wave (up to 10^4 km s^{-1}) that interacts with the surrounding medium for several hundred thousand years. In addition to being temporary sites of acceleration of high-energy cosmic rays (TeV−PeV), supernova remnants deposit kinetic energy over several tens of parsecs before they entirely decay into radiation and turbulence. This injection of energy and cosmic rays participates in the regulation of the turbulence, the chemical enrichment and the structuring of the multiple phases of the interstellar medium. Moreover, when dense regions are compressed by the slower shocks (10^1 km s^{-1}) that propagate lately, the cold and dense medium that is left after a characteristic cooling time constitutes a potential site for the formation of new stars. Located at 1.8 kpc and about 25,000 years old, the supernova remnant IC443 offers the possibility to study these feedback mechanisms with accuracy. In this kind of objects, the study of cosmic rays is pursued through the product of their interaction with the interstellar medium, which is a source of high energy photons (X-ray/γ-ray) emitted *via* four mechanisms: decay of neutral pions, Bremsstrahlung, inverse Compton scattering and synchrotron radiation. The interpretation of γ-ray observations requires a detailed knowledge of the physical and chemical characteristics of the environment, such as the total mass of the gas, the intensity and energy distribution of the radiation field, and the existence of new cosmic-ray injection sources. In the direction of the γ-ray intensity peak, we have made new observations of the supernova remnant IC443 with the IRAM 30m telescope and the APEX telescope. In a $10' \times 10'$ field of observations, our spectral observations of ^{12}CO, ^{13}CO, C^{18}O pure rotational lines and our continuum observations with the NIKA2 camera reveal the interstellar content of the region with an angular resolution of $10'' - 20''$. Using radiative transfer models, we first produced maps of the total molecular gas mass in the region from the emission of ^{12}CO and ^{13}CO lines. We then used dust emission models to study the continuum between 3.4 μm and 2.0 mm (WISE, Spitzer, LABOCA, NIKA2). The use of the Bayesian algorithms PPMAP and HerBIE allows us to determine the column density and temperature of the dust, as well as several additional parameters with HerBIE. Our mass measurements *via* dust emission and *via* the ^{12}CO molecule are independent and in agreement. These measurements indicate the existence of two candidates for the interaction of the dense medium with cosmic rays at the origin of the γ-ray production: a shocked molecular clump of ~ 250 M$_\odot$, and a cold, quiescent molecular cloudlet of ~ 400 M$_\odot$. On the one hand, these mass maps put precise constraints on the γ-ray emission *via* neutral pion decay and Bremsstrahlung in the studied region. On the other hand, our radiation field map determined *via* HerBIE also allows us to constrain the inverse Compton scattering. Finally, with the help of point-source catalogs we have determined the existence of potential protostars in the region. These protostars can also participate in the injection of medium energy cosmic rays (MeV−GeV). These results can be re-invested as input parameters in a γ-ray emission model in order to determine the composition (hadronic or leptonic) and the main mechanisms of interaction of cosmic rays with the interstellar medium in IC443.

KEYWORDS

Interstellar medium, *Supernova remnants*, *Kinematics and Dynamics*, *Shocks*, *Star formation*, *Cosmic rays*